CHARACTERIZING SINGLE VENTRICLE HEMODYNAMICS USING PHASE CONTRAST MAGNETIC RESONANCE IMAGING

A Dissertation
Presented to
The Academic Faculty

by

KARTIK SIVARAM SUNDARESWARAN

In Partial Fulfillment
of the Requirements for the Degree
Doctor of Philosophy in the
School of Biomedical Engineering

Georgia Institute of Technology
December 2008

CHARACTERIZING SINGLE VENTRICLE HEMODYNAMICS USING PHASE CONTRAST MAGNETIC RESONANCE IMAGING

Approved by:

Dr. Ajit P. Yoganathan, Advisor
School of Biomedical Engineering
Georgia Institute of Technology

Dr. John N. Oshinski
School of Biomedical Engineering
Georgia Institute of Technology

Dr. Mark A. Fogel, MD
Division of Cardiology
Children's Hospital of Philadelphia

Dr. Oskar Skrinjar
School of Biomedical Engineering
Georgia Institute of Technology

Dr. Kirk R. Kanter, MD
Cardiothoracic Surgery
Children's Healthcare of Atlanta

Date Approved: November 13, 2008

To Amma and Appa…for all their hard work and sacrifices…

ACKNOWLEDGEMENTS

The last 5 years or so have been the most challenging and intellectually satisfying years of my life. There are so many people to thank for this work, that a few pages maybe insufficient. I still remember the fateful day in fall 2002, when I was trying to decide between pursuing a career as a software engineer in Dell Inc, and a Masters degree in electrical and computer engineering. On that day, Dr. Mark Smith (my professor for digital image processing) made an announcement about an opening for an undergraduate research assistantship position in the Biomedical Engineering department. I decided to apply for that position, and the rest is history.

A PhD was never on my radar screen as to something I would do after I got my undergraduate degree. The one person who convinced me, and deserves as much accolades for this thesis as I do is Dr. David H. Frakes. He was the person who recruited me to the cardiovascular fluid mechanics laboratory (CFML) as an undergraduate, and convinced me that I had the potential to complete a PhD. Back then, he believed more in me than I believed in myself. If it wasn't for him, I would be somewhere else, doing mundane computer programming. I would like to sincerely thank him for being an excellent mentor and a great friend. I wish him the best of luck for a career as a professor at Arizona State University.

I would like to thank Dr. Ajit Yoganathan, my advisor, for giving an undergraduate with hardly any research experience, the opportunity to work in his lab. He has constantly been an inspiration, leading by example on several occasions when it came to doing research the right way. His rigorous work ethic and devotion to excellence has helped bring out the best in me. I thank him for all the guidance and direction he has

provided, and for allowing me to work on such a fascinating problem. There are many lessons I have learnt from him, and I hope I can apply them in real life. I wish him the best of health, and success in the future.

I would also like to thank my committee members Dr. John Oshinski, Dr. Oskar Skrinjar, Dr. Mark Fogel, and Dr. Kirk Kanter, for making this thesis a reality. Dr. Oshinski provided all the guidance that I needed from an MRI perspective, and helped me analyze the PC MRI data the right way. If it wasn't for Dr. Skrinjar's guidance on divergence free interpolation, specific aim 3 of my thesis would not have been possible. Thanks to Dr. Fogel for providing all the data that I ever requested, as well as for all the clinical guidance he gave over the course of my PhD. It has been a lot of fun working with Dr. Fogel. Thanks to Dr. Kanter for all the surgical input, that helped me shape the clinical aspects of my thesis. I have been very lucky to have worked with such an esteemed committee.

Thanks to my colleagues in the CFML, for making the entire CFML experience fun. I would like to specifically single out Diane de Zelicourt and Hiroumi Kitajima for sharing all the leadership responsibilities in the Fontan group. If it wasn't for them, my productivity in the lab would not have been as profound. Diane receives special credit, for having read the entire 400 + pages of my thesis, and for patiently providing the critical feedback that has no doubt significantly improved the quality of this work. Her productivity and energy continues to amaze me every day. On the same note, Chris Haggerty deserves a lot of credit as well, for not only reading my thesis, but also for taking over my work without many complaints. Thanks to Dennis D. Soerensen for teaching me how to run PC MRI experiments and the corresponding post processing

methods involved. I thank him for helping me with the development of Flow Finder and the development of the velocity database. Thanks to Helene for help with all the presentations, Jorge for all his “wise” advice, and Prasad for almost being my second advisor. Thanks to Dr. Kerem Pekkan for all the help with the lumped parameter model, and of course for being a great mentor when he was at Georgia Tech. I wish him the best of luck as a professor at Carnegie Mellon University. Thanks to all the newcomers: Erin, David Icenogle, and Yap for all the fun discussions on topics ranging from politics to football. I will truly cherish their friendship for a lifetime. I would like to also acknowledge all my undergraduates: Jin Sol Oh, Gopinath Jayaprakash, Colleen Sherwin, Jessica Kanter, and Sunny Lee who have worked with me in the last 5 years. Special credit goes to Jin Sol Oh, who helped me streamline and optimize several components of the segmentation process. I wish him the best of luck in his future endeavors in medical school.

I would also like to thank everyone in the BME department, for helping with all the administrative tasks associated with my PhD. Special thanks to Sally Gerrish for providing me with so many opportunities to participate in departmental activities that have been so much fun, Colly Mitchell for being a great friend and a shock absorber in times of great strife, and Lakeisha Wheaton for making all the group administrative tasks smooth and efficient. Thanks to Dr. Wendy Newstetter and Dr. Paul Benkeser, who have gave me the wonderful opportunity to be a teaching assistant from them. The problem based learning class, was a phenomenal learning experience for me. I would also like to thank all the administrative personnel: Tracie Dinkins, Sandra Wilson, Shuana Durham, Penelope Pollard, Rachel Arnold, Shannon Sullivan, Beth Bullock, Michelle Mayberry,

Chris Ruffin, Steven Marzec, and everyone in the department who has helped me out on several occasions.

If it wasn't for my friends in the last 5 years, it would be very difficult to survive the rigor of graduate school. Two people Kartik Balachandran (KB) and Murali Padala deserve special mention. These two have been my colleagues as well as my closest friends over the last 5 years. I would never forget the coffee breaks, the deep discussions, the arguments about nothing, football analysis, and the hours of hanging out. KB's cooking from first principles, and Murali's experiments with food and drinks will forever be etched in my memory. Thanks to KB's wife Smitha for being a great support, all the wonderful food, great coffee, discussions on politics, and of course for being a close friend as well. Thanks to her for being a great sport when KB, Murali, and I kept rambling about research.

How can I forget Yash and Ayona for being the greatest event organizers I have known, the soccer, the food, and all the wonderful parties? Yash is perhaps one of the most thorough people I have met, who pays attention to every little detail. It is this very attention to detail, why he was the captain of our soccer team and has successfully led our team to playoffs the last couple of years. Thanks to Yash's wife Ayona, for being a great friend and a great cook for making some of the most innovative dishes that I have had. I love the peanut salad AY! I have had a lot of fun with you guys, and I am looking forward to your visit to San Francisco in the Spring of 2009! I would also like to give a shout out to my buddy from the west coast: Rahul Sathe; for all the fun we have had at Monroe Place, playing soccer, making pizzas, and of course our dedication to Seinfeld. I wish all of you the best of luck for the future.

When I started graduate school in Fall 2003, there were 4 people whom I got really close to (and still am), and I would like to thank each one of them. First of all I would like to thank Udita Adurkar Goyal, who has perhaps been my closest friend over the last 5 years. I have learnt a lot from her, on how to be thoughtful, humble, and a good hearted person. I have really cherished her friendship, and I wish her the best of luck in her new role as a wife and daughter in law. Thanks to Mamta Patel, for being a great friend and an inspiration in many forms. I have always admired her determination and will power in getting things done, and hopefully some of that has rubbed off in me as well. I have been lucky to have her as my friend and neighbor, and I wish her all the best in her future endeavors. Another person I would like to thank is my namesake Kartik Sundar. Our lives have always been intertwined right from the time I received his acceptance letter from the department. We have been close friends since then. I have tremendously enjoyed relaxing in his humongous mansion of an apartment. I can never forget his attention to detail to everything non-academic, his smooth demeanor with women, the great parties he has thrown at his place, and his obsession with Toronto Raptors. Don't worry Kartik; I am sure they will win the NBA world championship at some-point in your lifetime. Thanks to Abhiruchi Agarwal for all the great potluck dinners and lunches, and the great times we have shared over the course of the last 5 years. I would also like to give a shout out to all my friends in the BME: Mike Heffernan, Stephen Yang, David Dumbauld, Sean Coyer, Andrea Para, David Bark, Tony Dickherber, Brandon Fornwalt, Srinidhi Nagaraja, Swathi Ravi, Priya Santhanam, Rekha Nair, Laveeta Joseph, Ryan Maladen, Nick Willett, Jana Delfino, Abbey Wojtowicz, Daniel Conway, and Christian Gumera who have made this entire experience a

memorable one.

Finally, the two people who deserve this thesis more than I do are my parents (Mr. T.S. Sundareswaran and Seethalakshmy Sundareswaran). This thesis is entirely dedicated to them. I can never forget the amount of hard work it took them, and the sacrifices they made in order to send me and my sister to a great institution such as Georgia Tech for higher education. If it wasn't for their endless love, blessings, and support over the entire course of my PhD, it would not have been possible for me to take up and complete such a daunting task. They will always be my role models on how to lead a life the right way, and I hope I can be as good a son to them, as the parents they have been to me. I would also like to thank my sister Sowmya, for being of such great support in the last few years. She had to put up with all my moodiness and crankiness during days when things didn't go well, and she has always been a good sport in dealing with it. Of course, if it wasn't for her cooking, I would have gone hungry on many evenings. Thanks to her for being a wonderful sister. I would also like to thank my uncle and aunt in Dallas, for providing a "home away from home", and for being there at all times. I could always count on escaping to Dallas and relaxing there, whenever things got too hot. Without the love and support of all my family, I would never have come so far.

TABLE OF CONTENTS

LIST OF TABLES

LIST OF FIGURES

NOMENCLATURE

Proximal: Near to the center or point of attachment to the body

Distal: Far away from the center or point of attachment to the body

Anterior: Front side of the body

Posterior: Backside of the body

Superior: Upper side of the body

Medial: Towards the middle

Lateral: Towards the outer

LIST OF ABBREVIATIONS

ACGI: Adaptive Control Grid Interpolation

AP: Atriopulmonary

AP: Anterior-Posterior

Ao: Aortic Valve

ASO: Arterial Switch Operation

AV: Atrioventricular

BDG: Bidirectional Glenn

CHB: Children's Hospital of Boston

CHD: Congenital Heart Disease

CHOA: Children's Healthcare of Atlanta

CHOP: Children's Hospital of Philadelphia

CVP: Central Venous Pressure

DC: Dextrocardia

DFI: Divergence Free Interpolation

DILV: Double Inlet Left Ventricle

DORV: Double Outlet Right ventricle

D-TGA: D Transposition of the Great Arteries

DVM: Distance from the Vector Median

Ea: Arterial elastance (Afterload)

EDV: End Diastolic Volume

Ees: End Systolic Elastance (Preload)

EF: Ejection Fraction

ESP: End Systolic Pressure

ESV: End Systolic Volume

FAVMF: Fuzzy Adaptive Vector Median Filters

FIESTA: Fast Imaging Employing Steady State Acquisition

HF: Hemi-Fontan

HLHS: Hypoplastic Left Heart Syndrome

HRHS: Hypoplastic Right Heart Syndrome

IRB: Institutional Review Board

IVC: Inferior Vena Cava

IV: Innominate Vein

LA: Left Atrium

LE: Entrance Length

LPF: Low Pass Filter

LPM: Liters per Minute

LSVC: Left Superior Vena Cava

LV: Left Ventricle

Mi: Mitral Valve

MRI: Magnetic Resonance Imaging

MSE: Mean Squared Error

NMSE: Normalized Root Mean Squared Error

PA-IVS: Pulmonary Atresia – Intact Ventricular Septum

PAVM: Pulmonary Arteriovenous Malformations

PC MRI: Phase Contrast Magnetic Resonance Imaging

PLE: Protein Losing Enteropathy

Pu: Pulmonary Valve

RA: Right Atrium

RL: Right-Left

RMS: Root Mean Square

RPA: Right Pulmonary Artery

RSVC: Right Superior Vena Cava

RV: Right Ventricle

SD: Standard Deviation

SE: Standard Error

SI: Superior-Inferior

SV: Stroke Volume / Single Ventricle

SVC: Superior Vena Cava

TA: Tricuspid Atresia

TGA: Transposition of the Great Arteries

TPS: Thin Plate Splines

Tr: Tricuspid Valve

TR: Repetition Time

TE: Echo Time

True-FISP: true Fast Imaging with Steady State Precession

VMF: Vector Median Filters

WU: Woods Units

LIST OF SYMBOLS

A: Area (cm^2)

C: Compliance (L/mmHg)

C: Active contour

C(s): Parametric active contour

$\boldsymbol{C_0}$: Initial contour

$\boldsymbol{C_p}$: Active contour with parameter invariance

CVD: Compliance at end diastole (L/mmHg)

CVS: Compliance at end systole (L/mmHg)

d: Distance function (cm)

E: Energy (joules)

E: Elastance (Chapter 7 and 11) (mmHg/L)

$\dot{E}_{Loss}$: Power loss (W)

$\boldsymbol{E_{ext}}$: External energy function

$\boldsymbol{E_{int}}$: Internal energy function

$\vec{f}$: Body force vector (cm/s^2)

F: Contour propagating force

I: Image (pixels)

i, j, k: Directional index

$\vec{k}$: Image position vector

M: Number of rows in an image

M: Median filter

MI: Magnitude image intensity

N: Number of points

N: Number of columns in an image

N: Normal vector

P: Pressure (mmHg)

p_v: Noise probability

Q: Flow rate (Liter/Minute)

Qs: Systemic flow rate (Liter/Minute)

Qp: Pulmonary flow rate (Liter/Minute)

r: Radius (cm)

R: Resistance (mmHg-Minute-m^2/Liter)

Re: Reynold's number

s: Parameterization vector

T_C: Contraction time for the myocardial muscle (s)

T_R: Relaxation time for the myocardial muscle (s)

TS: Length of systole (s)

T: Duration of cardiac cycle (s)

u: x component of velocity (cm/s)

U: Distance from the vector median

v: y component of the velocity (cm/s)

V: Velocity vector

w: z component of the velocity (cm/s)

W: Window size

$\vec{x}$: Position vector

x: Position component (cm)

y: Position component (cm)

z: Position component (cm)

α: Contour's tension control (Chapter 5)

α: Fuzzy membership function (Chapter 5)

α: Radial basis function support (Chapter 6)

β: Active contour's rigidity

ε: Energy functional

ϕ: Dissipation function (s^{-2})

Φ(x, t): Level set function (Chapter 5)

Φ(x, t): Divergence free radial basis function (Chapter 6)

κ: Curvature

μ: Term governing the trade-off between smoothness and accuracy

μ: Arithmetic mean

μ: Dynamic viscosity (centipoise)

γ: Kinematic viscosity (centistokes)

γ: Number of components of velocity (Chapter 5)

Ω_0 : Region defined by the level set contour (Chapter 5)

Ω : Image domain

ρ: Density (Kg/m^3)

σ: Standard deviation

τ: Shear stress ($g/cm/s^2$)

ω: Frequency related to heart rate (1/s)

ψ (x,t): Scalar valued infinitely supported radial basis function

SUMMARY

Single ventricle congenital heart defects afflict 2 per every 1000 births. They are characterized by cyanotic mixing between the de-oxygenated blood coming back from the systemic circulation and the oxygenated blood from the pulmonary circulation. Prior to introduction of the Fontan procedure in 1971, surgical options for single ventricle patients were limited. The Fontan operation involves a series of three palliative procedures aimed at the separation of systemic and pulmonary circulations and reducing the long term effects of chronic hypoxia and ventricular volume overload. The total cavopulmonary connection (TCPC) is completed in the final stage of the surgery with the anastomosis of the inferior vena cava (IVC) and superior vena cava to the pulmonary arteries.

Improved quantification and visualization of flow structures within the TCPC has the potential to aid in the planning and design of the Fontan operation. Despite significant development of phase contrast magnetic resonance imaging (PC MRI) for *in vivo* flow measurements, it is not routinely applied in children with single ventricle congenital heart disease. Limited technologies available for post-processing of PC MRI data has prevented clinicians and scientists from conducting the detailed hemodynamic analyses necessary to better understand the physiology of the single ventricle circulation. This thesis attempts to bridge the gap between PC MRI and fluid dynamics, by developing the necessary post-processing technologies for PC MRI, and then applying these techniques for characterizing single ventricle hemodynamics.

.

CHAPTER 1

INTRODUCTION

Two out of every one thousand live births are born with single ventricle congenital heart defects that are characterized by cyanotic mixing between the systemic and pulmonary circulation. Prior to the introduction of the Fontan procedure in 1971[1], surgical options for single ventricle patients were limited. The Fontan operation involves a series of three palliative procedures aimed at the separation of systemic and pulmonary circulations and reducing the long term effects of chronic hypoxia and ventricular volume overload. The first stage comprises of a systemic to pulmonary shunt to increase pulmonary circulation along with an aortic reconstruction when needed. In the second stage the superior vena cava is anastomosed to the pulmonary arteries in a configuration known as the bidirectional cavopulmonary connection. The total cavopulmonary connection (TCPC) is completed in the final stage of the surgery with an anastomosis of the inferior vena cava to the pulmonary arteries.

The introduction of the TCPC significantly improved the outcomes of children born with single ventricle congenital heart disease. However, the marked improvement in surgical outcome is balanced by the numerous and serious long term consequences experienced by Fontan patients. Some of these complications include: congestive heart failure, systemic venous hypertension, hepatic and pulmonary congestion, valvular and myocardial dysfunction, thromboembolism, arrhythmias, protein losing enteropathy, poor exercise capacity and a decreased quality of life[2]. Although the exact mechanism for these complications is unknown, there is evidence that hemodynamics of the unusual Fontan circulation is directly responsible in some manner.

An increase in impedance as a result of the pulmonary vascular bed and the TCPC in series, results in a contractility-afterload mismatch in Fontan patients. Such a mismatch significantly reduces the cardiac reserve available to these patients, as well as accelerates the onset of heart failure. Therefore, the efficiency of the TCPC could govern to a large degree, the functional capacity of the single ventricle in a Fontan circulation.

This has been shown in clinical studies evaluating atriopulmonary connections where the kinetic energy loss in the atrial chamber rose nearly exponentially with increased cardiac output. These findings lead to a paradigm shift in surgical procedures from thinking of the right atrium as a potential pumping chamber to be incorporated into the Fontan circuit, to a more streamlined connection where the right atrium is excluded or only minimally incorporated into the systemic venous pathway. While these advances have had significant impact clinically, the design of the TCPC to date has focused on geometric considerations with little attention being paid to flow dynamics or interaction between the flow dynamics and geometry. This is, in great part, due to the limitations associated with the *in vivo* measurement and quantification of hemodynamics in Fontan patients. With improvements in magnetic resonance imaging and the development of phase velocity encoding, a new era of evaluating cavopulmonary connections has begun, incorporating flow dynamics into our measures of circulation efficiency, and further refining the Fontan operation as it is performed today.

One such modality is phase contrast magnetic resonance imaging (PC MRI), which has emerged in recent times as an imaging modality to non invasively probe the fluid dynamics of the cardiovascular system and has shown promise in its application to congenital heart disease. Unlike other imaging modalities such as ultrasound and

computed tomography, PC MRI can be used for quantifying the velocity fields in all three directions. This powerful capability of PC MRI can be used for characterizing the hemodynamics of Fontan patients in great detail.

This thesis explores the applicability of PC MRI for probing the hemodynamics of Fontan patients from both the systemic venous and systemic arterial side. A two pronged approach is undertaken comprising of a methodology development arm and a clinical application arm. Novel approaches for segmentation, filtering, and interpolation of PC MRI data are developed and validated in the methodology development arm. Using these methodologies, global and regional hemodynamics are quantified in a large cohort of Fontan patients. At the conclusion of this thesis, a much better understanding of the Fontan circulation is expected to be achieved.

CHAPTER 2

HYPOTHESIS AND SPECIFIC AIMS

Improved quantification and visualization of flow structures within the total cavopulmonary connection (TCPC) has the potential to aid in the planning and design of the Fontan operation. Numerous attempts in this direction have used *in vitro* experiments, animal models, and numerical simulations to model the hemodynamics of the TCPC. Few studies have done so *in vivo*, and those that do exist have been cursory. Despite significant development of phase contrast magnetic resonance imaging (PC MRI) for *in vivo* flow measurements, it is not routinely applied in children with single ventricle congenital heart disease. Limited technologies available for post-processing of PC MRI data has prevented clinicians and scientists from conducting the detailed hemodynamic analyses necessary to better understand the physiology of the single ventricle circulation. This thesis attempts to bridge the gap between PC MRI and fluid dynamics, by developing the necessary post-processing technologies for PC MRI, and then using these techniques for characterizing single ventricle hemodynamics. Hence, the driving hypothesis of this thesis is that: **PC MRI combined with the application of advanced image processing techniques can be used to characterize the hemodynamics of patients with a single ventricle physiology.** This hypothesis will be investigated using four specific aims:

Specific Aim 1: Assess the feasibility of high resolution PC MRI towards characterizing TCPC hemodynamics. *Sub-Hypothesis: 3D PC MRI can be used to reconstruct velocity fields within the TCPC.* Previous *in vitro* PC MRI studies in our lab

have primarily focused on idealized TCPC models, and no studies until now have evaluated the applicability of high resolution PC MRI to quantify the detailed 3D hemodynamics in anatomically realistic TCPC models. To accomplish this aim, *in vitro* PC MRI experiments will be conducted on anatomically realistic TCPC phantom models created using *in vivo* MRI. A dense stack of PC MRI through the TCPC with velocity encoding in all three directions will be acquired. Three-dimensional velocity vectors reconstructed from PC MRI will then be qualitatively and quantitatively compared to those numerically evaluated using computational fluid dynamics.

Specific Aim 2: Quantify the *in vivo* flow characteristics of different Fontan configurations in a large group of single ventricle patients using PC MRI. *Sub-Hypothesis: A large velocity and flow database can be used to characterize the flow features within the TCPC.* In order to quantify the global hemodynamics of different Fontan types, a large velocity and flow database is required. No large series currently exists that has systematically characterized the hemodynamics in Fontan patients. Towards achieving this objective, a novel two-step segmentation and filtering algorithm will be first developed and validated. This approach will then be applied to the TCPC and the ascending aorta of a large cohort (> n=100) of single ventricle patients to establish a Fontan flow and velocity database. Differences in flow rates, flow velocities, flow splits, pulsatility, and vessel area will be evaluated and analyzed for different types of TCPCs and single ventricle pathologies.

Specific Aim 3: Compare the *in vivo* time-periodic hemodynamics of three-dimensional velocity field reconstructions for intraatrial and extracardiac TCPCs. *Sub-Hypothesis: There are significant differences in hemodynamics between extracardiac*

and intraatrial TCPCs, and these differences can be quantified using 3D PC MRI. Two variations of the TCPC commonly performed by the surgical community are the intraatrial and extracardiac connections. There is no consensus currently in the surgical community as to which one of the two methods is superior. Previous studies were conducted using *in vitro* and computational fluid dynamics and the 3D hemodynamics have never been investigated *in vivo*. To accomplish this objective, a new method for reconstructing the 4D (space + time) hemodynamics from a stack of sparsely sampled 3D *in vivo* PC MRI slices will be developed and validated. The approach will utilize the fundamental principle of incompressible fluid flows for interpolating the velocity fields in locations where PC MRI data is unavailable. The technique will be first validated using synthetic and *in vitro* Phantom models, and then applied to a stack of *in vivo* 3D PC MRI obtained from intraatrial and extracardiac Fontan patients. Quantitative hemodynamic parameters extracted from the 3D velocity fields will then be used to elucidate the differences between the two types of TCPCs.

Specific Aim 4: Investigate the differences in output power between single left and single right ventricles using PC MRI of the ascending aorta. *Sub-Hypothesis: Significant differences in aortic flow dynamics exist between patients with morphological right ventricles and morphological left ventricles*. Morphological right ventricles in a systemic configuration have a higher risk for heart failure compared to morphological left ventricles. To investigate the underlying mechanics associated with this phenomenon, PC MRI of the ascending aorta will be used for evaluating the power output, and then correlated with ventricular function assessed using short axis cine MRI.

To further evaluate the possible impact of TCPC hemodynamics on the single

ventricle circulation a lumped parameter mathematical model of the single ventricle circulation will be developed and used to relate the TCPC hemodynamics to cardiac function at rest and exercise. This study does not specifically fall under any of the 4 specific aims. Figure 2.1 shows the overall interaction between the specific aims.

This thesis is arranged as follows:

- The Background and Significance for the entire thesis is provided as part of Chapter 3.
- Materials and Methods for specific aim 1 are described in Chapter 4, and the results are presented as part of Chapter 8.
- Materials and Methods for the implementation of specific aims 2 and 4 are the same, and are described as part of Chapter 5. The results are presented in Chapter 9.
- Materials and Methods for the implementation of specific aim 3 are described in Chapter 6, and the results are presented as part of Chapter 10.
- Materials and Methods for the lumped parameter mathematical model relating the TCPC hemodynamics to the entire single ventricle circulation, is described in Chapter 7, and the results are presented as part of Chapter 11.
- Conclusions of this thesis are described in Chapter 12.

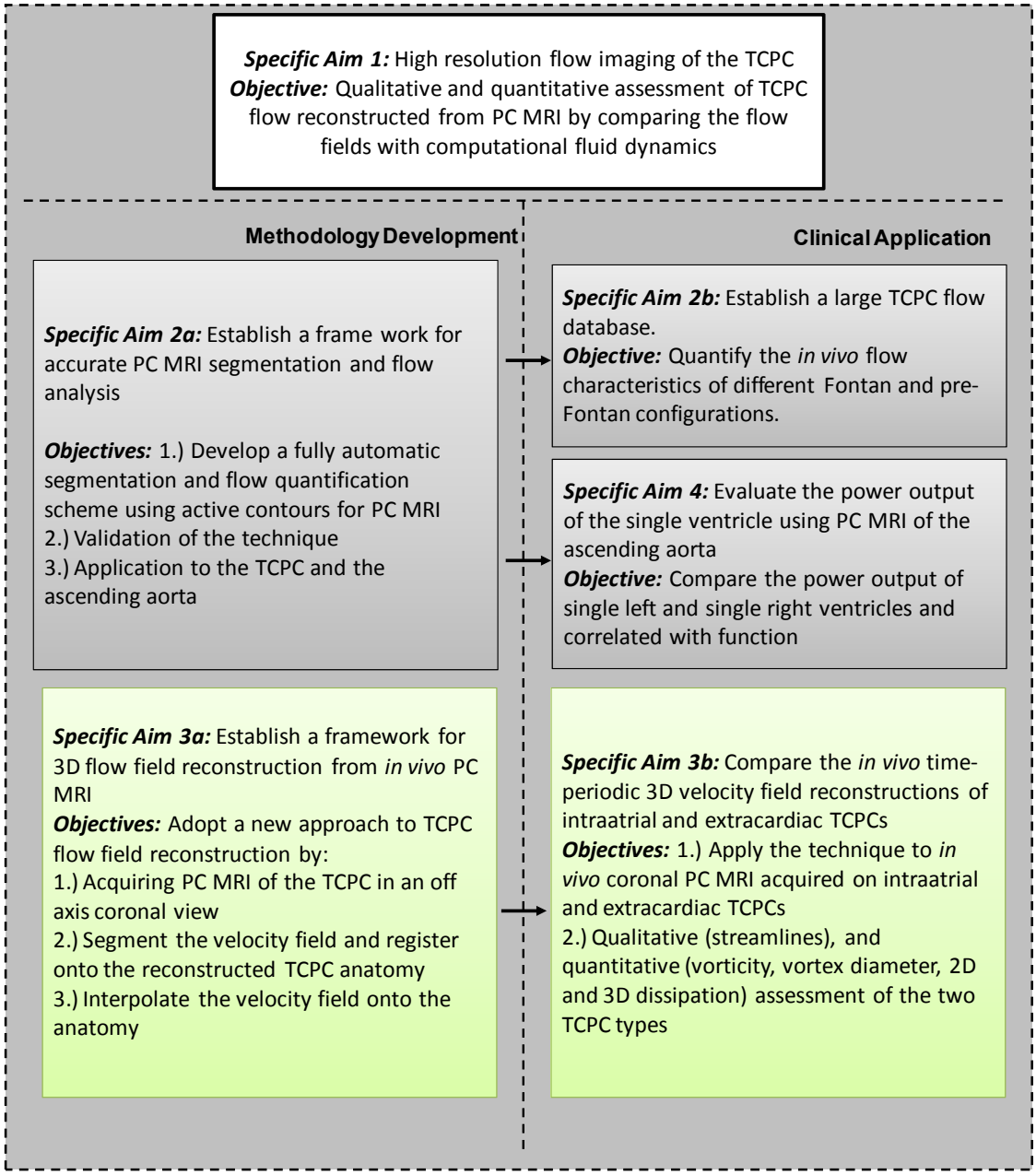

Figure 2.1: Overall research design of the thesis

CHAPTER 3

BACKGROUND AND SIGNIFICANCE

3.1 Normal Biventricular Circulation

The need for efficient transfer of oxygen and nutrients in multi-cellular organisms necessitated the evolutionary development of a circulatory system to move fluid between the body surface and its deepest parts. In simpler animals, peripheral muscular activity was sufficient for generating the necessary pressure to drive fluid flow. As more complex animals evolved, a dedicated muscle for circulating internal fluid was necessary for the transport of nutrients. Depending upon the particular species of animals' different type of hearts evolved to control the circulatory system.

The human heart is a complex muscular organ that is responsible for the transport of oxygen and other nutrients required to sustain life. Each day the average heart beats about 100,000 times and pumps about 2000 gallons of blood (American Heart Association). It is an integral component of the human circulatory system which is a network of elastic tubes that carries blood to the different parts of the body. The system includes the heart, lungs, arteries, arterioles, capillaries, venules, and veins. Arteries, arterioles, and capillaries carry blood away from the heart and allow the exchange of nutrients from the thin walls of the capillaries to different organs and tissues. The venous system then carries the nutrient and oxygen depleted blood from the rest of the body back to the heart. Figure 3.1 shows a schematic highlighting the main components of the entire circulatory system.

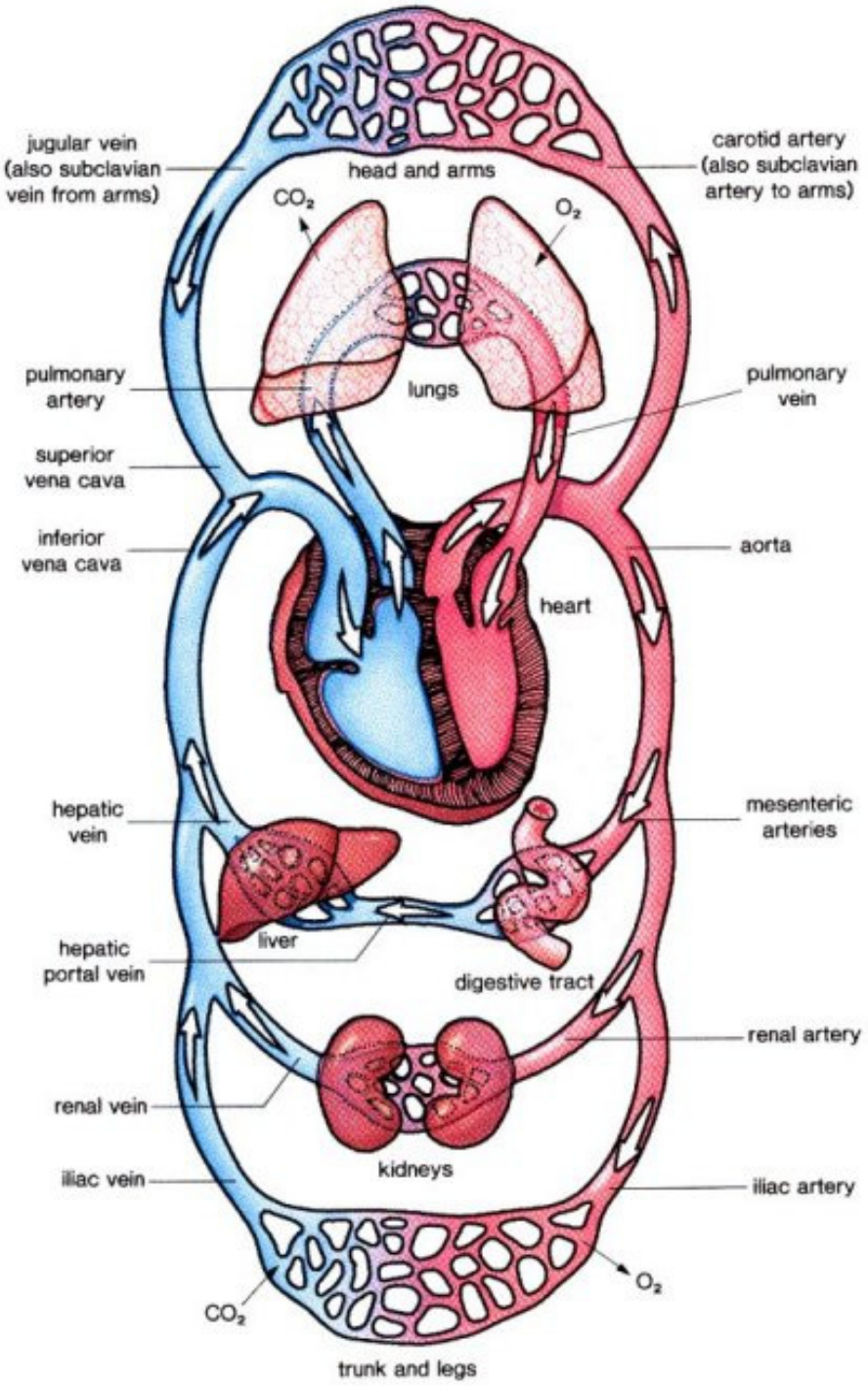

Figure 3.1: Schematic of the entire cardiovascular system

The heart lies in the thoracic cavity, held in place by ligaments connected to the spine. The pointed apex of the heart angles down to the left side of the body, while the broader base lies behind the breastbone. It is encased in a tough membraneous sac, the pericardium. A thin layer of clear pericardial fluid inside the pericardium lubricates the motion of the heart as it moves around. The heart itself is composed mostly of cardiac muscle or myocardium covered by a thin outer and inner layers of epithelium and connective tissue.

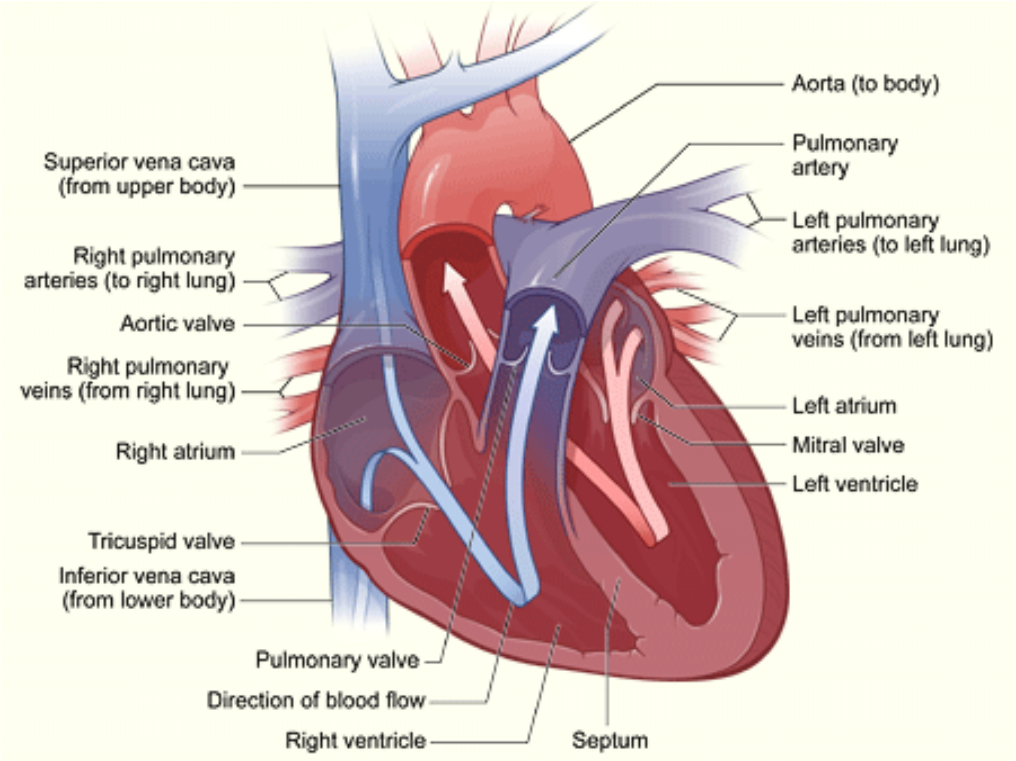

Figure 3.2: Schematic of the Heart

There are four chambers within the heart (Figure 3.2). The upper chambers are called the right and left atria, while the lower chambers are called the right and left ventricles respectively. A muscular wall separates the right and left side of the heart

known as the septum. As depicted in figure, oxygen deficient blood from the superior (SVC) and inferior vena cava (IVC) drain into the right atrium. The right atrium pumps blood into the right ventricle when the tricuspid valve is open. The deoxygenated blood is then pumped to the lungs for oxygenation by the right ventricle through the pulmonary valve and the pulmonary arteries. The oxygenated blood from the lung first enters the left atrium during systole and then to the left ventricle during diastole. Overall, the systemic and pulmonary circulations are in parallel with two pumps driving flow through each of the two circuits.

3.2 Congenital Heart Defects

The incidence of children born in the USA with congenital heart defects (CHD) is about 8 out of every 1000 live births, which translates to about 35,000 births every year. According to the March of Dimes, CHDs are the number 1 form of birth defect in the world. These defects are problems with the heart's structure that can involve the interior walls of the heart, valves, and the orientation of the arteries / veins that are the medium of blood flow transportation. CHDs happen because of incomplete or abnormal development of the fetus heart during the very early weeks of pregnancy. Some of these are associated with genetic disorders such as Down syndrome, although the causes of most CHDs are vastly unknown.

Common types of CHDs that can affect the heart or any of the surrounding structures include: Aortic Stenosis, Atrial Septal Defect, Atrioventricular Canal Defect, Coarctation of the Aorta, Hypoplastic Left Heart Syndrome, Patent Ductus Arteriosus, Pulmonary Atresia, Pulmonary Stenosis, Tetralogy of Fallot, Total Pulmonary Venous

Connection, Transposition of the Great Arteries, Tricuspid Atresia, Truncus Arteriosus, and Ventricular Septal Defects. Most of these defects are cyanotic in nature, i.e., the heart's ability to pump blood and deliver oxygen to the different tissues in the body is compromised. Signs and symptoms include a bluish tinge or color to the skin around the mouth or on the lips and tongue, increased rate of breathing, difficulty feeding, abnormal heart murmur, sweating, and diminished pulse strength. Most of CHDs, if detected early, can be treated surgically and the prognosis is generally excellent. However, a quarter of these patients are born with complex defects that result in a functional single ventricle, where there is a significant amount of mixing between the oxygenated and deoxygenated blood in the heart. These defects constitute the most complex forms of heart defects, where mortality rates are quite high despite significant progress in the treatment and management of these patients.

3.3 Single Ventricle Congenital Heart Defects

Many complex cardiac malformations are characterized by the existence of only one functional ventricle. The incidence of children born with a single congenital heart defect, in which there is one effective pumping chamber, is about 2 per 1000 births (about 25% of all CHDs). The most common forms of single ventricle heart defects are tricuspid atresia, hypoplastic left heart syndrome, hypoplastic right heart syndrome (pulmonary atresia with intact ventricular septum), mitral valve atresia, double outlet left ventricle, heterotaxy syndrome, and double outlet right ventricle. The ventricular structure may resemble the normal left ventricle or the normal right ventricle, or neither. Single ventricle defects tend to be the most complex forms of congenital heart defects

known. Some of the commonly occurring single ventricle CHDs are described below.

3.3.1.1 Hypoplastic Left Heart Syndrome

Hypoplastic Left Heart Syndrome (HLHS) is the most common form of cyanotic congenital heart defect, occurring in roughly 1/3rd of all patients born with single ventricle disease. In this defect, the left side of the heart including the aorta, aortic valve, left ventricle, and the mitral valve is under-developed. Blood returning from the lungs must flow through the opening between the left and right atrium (Atrial septal defect) or the left and right ventricle (ventricular septal defect). The right ventricle pumps the blood into the pulmonary artery and blood reaches the aorta through the patent ductus arteriosus (Figure 3.3). The most critical aspect of HLHS is the small and underdeveloped left

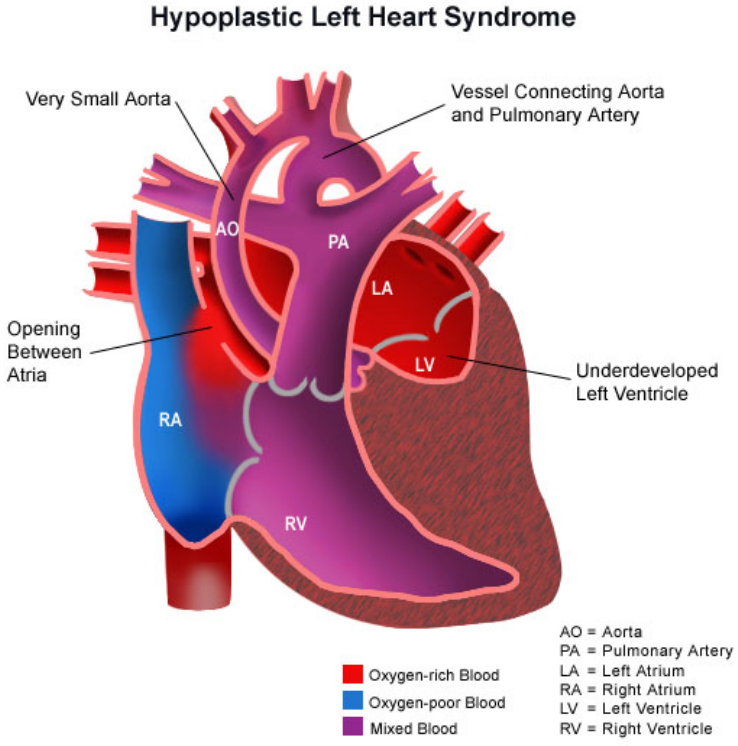

Figure 3.3: Hypoplastic Left Heart Syndrome

ventricle. In a normal heart, this chamber is very strong and muscular so it can pump blood to the high resistance systemic circuit. This makes HLHS the most complex and debilitating form of cyanotic single ventricle heart defect, with a 100% mortality rate within the first year of birth, if left untreated.

3.3.1.2 Tricuspid Atresia

In tricuspid atresia, the valve between the right atrium and the right ventricle fails to develop (Figure 3.4). The absence of a tricuspid valve is usually associated with an under developed right ventricle. As a consequence, deoxygenated blood that returns from the body to the right atrium cannot enter the right ventricle. The child's survival depends

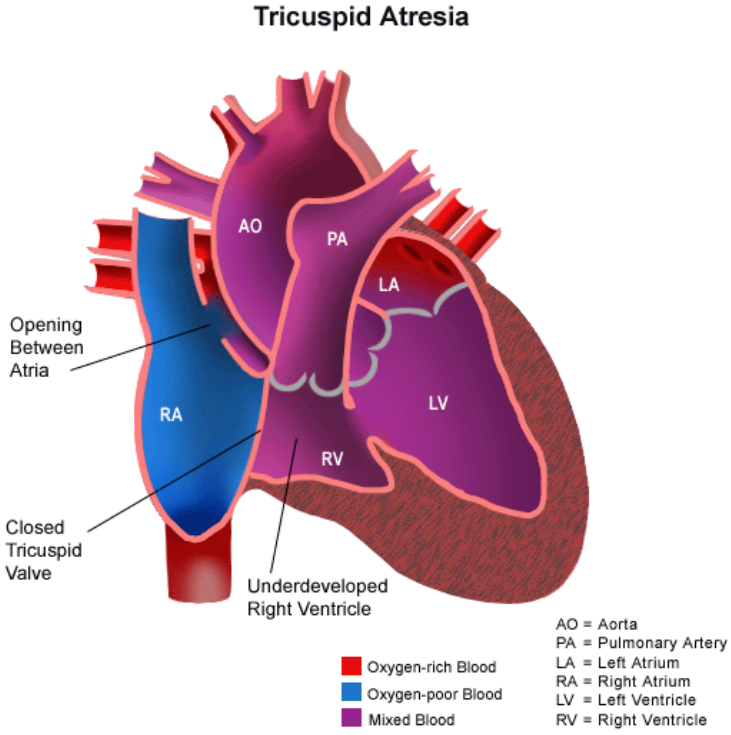

Figure 3.4: Tricuspid Atresia

upon the presence and size of an atrial septal defect allowing blood to travel from the right to the left atrium. This results in the mixing of systemic and pulmonary circulations in the left ventricle. Most of the poorly oxygenated mixture goes from the left ventricle through the aorta to the rest of the body.

3.3.1.3 Other Single Ventricle Heart Defects

Besides Tricuspid Atresia and HLHS, the other common forms of single ventricle congenital heart disease include double inlet left ventricle (DILV), some forms of double outlet right ventricle (DORV), hypoplastic right heart syndrome (HRHS) and heterotaxy syndromes. In DILV, both the atria are connected to the left ventricle. Usually there is a small right ventricle, and the arteries are switched (i.e. the pulmonary arteries rise from the left ventricle while the aorta rises from the right ventricle). There is significant mixing in the left ventricle resulting in a high degree of cyanosis. In DORV, both the aorta and pulmonary arteries rise from the right ventricle. The blood from the left ventricle mixes with the blood in the right ventricle via a ventricular septal defect. Most DORVs are corrected via the arterial switch operation (ASO) when there is an adequately shaped left ventricle. In situations where the left ventricle is underdeveloped or if a biventricular repair is not possible, these patients are eligible for single ventricle repair.

Heterotaxy syndromes are rare CHDs, where the configuration of the thoracic and abdominal organs is indeterminate. In these patients, there is a presence of multiple small spleens that are accompanied by thoracic isomerism. Thoracic isomerism implies that the heart and the blood vessels do not have the correct “sidedness”. For example, in bilateral “right-sidedness” both sides of the heart look like the right side, while in bilateral “left-

sidedness", both sides of the heart look like the left side. A characteristic anomaly is infrahepatic interruption of the inferior vena cava with the azygous vein draining into the superior vena cava. There is mixing of the oxygenated and de-oxygenated blood within the single ventricle resulting in a significant reduction in oxygen saturation. Heterotaxy syndromes are considered to be the rarest forms of single ventricle CHDs, and the most challenging to manage. Figure 3.5 shows a schematic of heterotaxy syndrome with left isomerism.

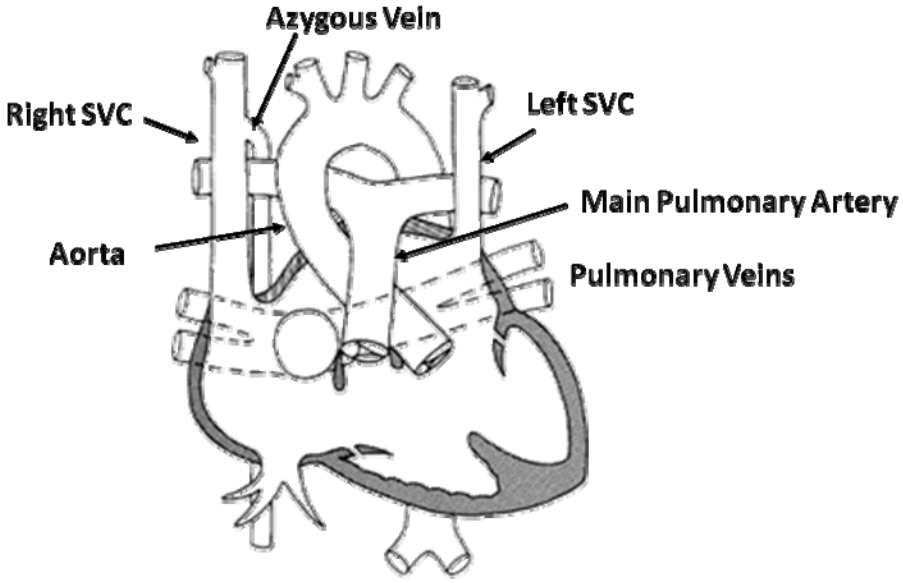

Figure 3.5: Heterotaxy syndrome with bilateral left sidedness

3.4 Surgical Palliation of Single Ventricle Physiology: Multi-Stage Fontan Repair

The single ventricle has to maintain both systemic and pulmonary circulations which are not connected in series but in parallel. Such a circuit has a few disadvantages: a) significant arterial oxygen de-saturation due to mixing; b) chronic volume overload on the single ventricle. Chronic volume overload over time will impair ventricular function,

and will eventually lead to congestive heart failure. Without surgical intervention this set of lesions is generally lethal, resulting, if untreated, in 95% mortality within the first month of life. The concept of a total right ventricular bypass, first introduced by Fontan and Baudet in 1971[1], is a palliative surgical procedure aimed at separating the systemic and pulmonary circulations thereby eliminating venous blood mixing. The parallel circuit of the single ventricle circulation is now converted to a series circuit of the Fontan circulation (Figure 3.6). In a "Fontan Circulation", the systemic venous return is connected to the pulmonary arteries without the interposition of an adequate ventricle. In such a circuit, the post capillary energy is no longer wasted, but is collected and used to drive the flow through the pulmonary circulation.

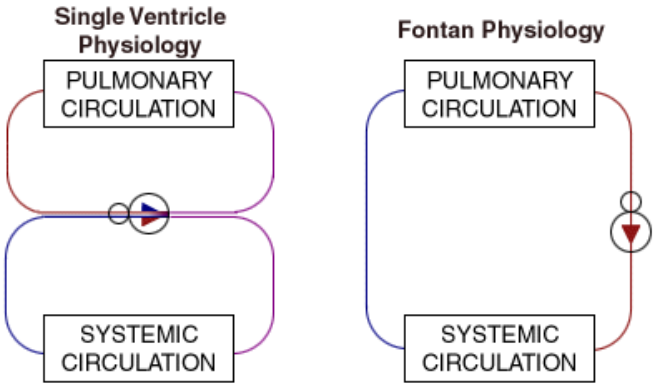

Figure 3.6: Schematic describing the pre-Fontan single ventricle physiology and the Fontan physiology. The systemic and pulmonary circulations are successfully separated after the Fontan operation.

3.4.1 Evolution of the Fontan operation

The Fontan operation was first introduced in 1971[1], when Fontan and Baudet successfully implemented an atriopulmonary (AP) connection in a patient with tricuspid

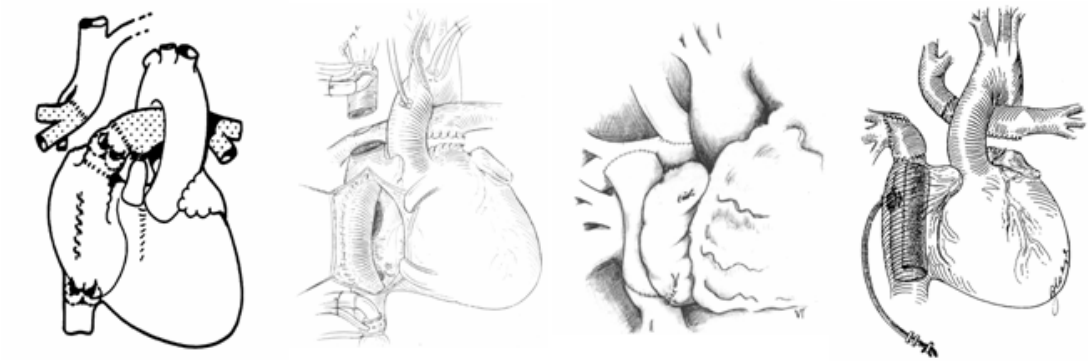

a. b. c. d.

Figure 3.7: Schematics showing the a) original Fontan repair for Tricuspid Atresia; b) lateral tunnel Fontan; c) completed extracardiac Fontan; d) Fontan unidirectional cavopulmonary connection with adjustable atrial septal defect

atresia, and this operation became the repair option of choice for patients who qualified i.e., those who had reasonable anatomy and normal pulmonary vascular resistance (Figure 3.7a). The classic Fontan procedure had 5 main steps: (1) end-to-side anastomosis of the distal end of the right pulmonary artery (RPA) to the SVC; (2) end-to-end anastomosis of the right atrial (RA) appendage to the proximal end of the RPA by means of an aortic homograft; (3) closure of the atrial septal defect; (4) insertion of a pulmonary valve homograft into the IVC; and (5) ligation of the main pulmonary artery (MPA). In 1971, Kreutzer and colleagues independently reported success with a similar type of anastomosis, a single valveless AP connection that diverted the entire venous return to the pulmonary circulation[3].

In 1988, de Leval presented both *in vitro* and *in vivo* evidence for use of a total cavopulmonary connection (TCPC) as a logical alternative to the traditional AP connections described above[4]. The TCPC was characterized as an anastomosis of the

SVC directly (end-to-side) to the superior wall of the RPA, followed by creation of an intraatrial caval channel through the RA connecting the IVC to the inferior wall of the RPA (Figure 3.7b). de Leval hypothesized that the lateral tunnel-type (intraatrial) Fontan demonstrated more streamlined flow patterns with less turbulence and fluid energy losses, savings that would more than compensate for benefits that may have been derived from the RA pumping capabilities.

In 1990, Marcelletti and colleagues modified the TCPC by replacing the intraatrial channel with an extracardiac conduit between the IVC and the RPA (Figure 3.7c)[5]. In 1993, Laschinger and colleagues modified the extracardiac approach by constructing an external tunnel between the IVC and RPA using the external atrial wall and a synthetic material or pericardium, hypothesizing that the tunnel would prove superior due to growth of the atrial wall[6]. In 1995, Laks and colleagues further modified the TCPC approach with a procedure that independently connected the SVC to the LPA and the IVC to the RPA using an intraatrial connection (Figure 3.7d)[7]. Though this approach had many advantages from a hemodynamic standpoint, the exclusion of hepatic venous flow from the left lung appeared detrimental to left lung development and led to unilateral pulmonary arteriovenous malformations on the left side. After twenty years of evolution, the Fontan operation is now performed in multiple stages, where the complete separation of systemic and pulmonary circulations takes place in 3 stages.

3.4.2 Current approaches to single ventricle palliation

The Fontan circulation is almost impossible to complete at birth. The pulmonary vascular resistance is high, and the vessel sizes are too small for a successful

cavopulmonary connection. The staged approach allows the body to gradually get adapted to substantially different hemodynamic conditions. The aims of the different stages are as follows:

Stage1: Achieve unrestricted flow from the heart to the aorta and limited flow to the lungs

Stage 2: Increase the amount of lung perfusion

Stage 3: Complete separation of systemic and pulmonary circulations

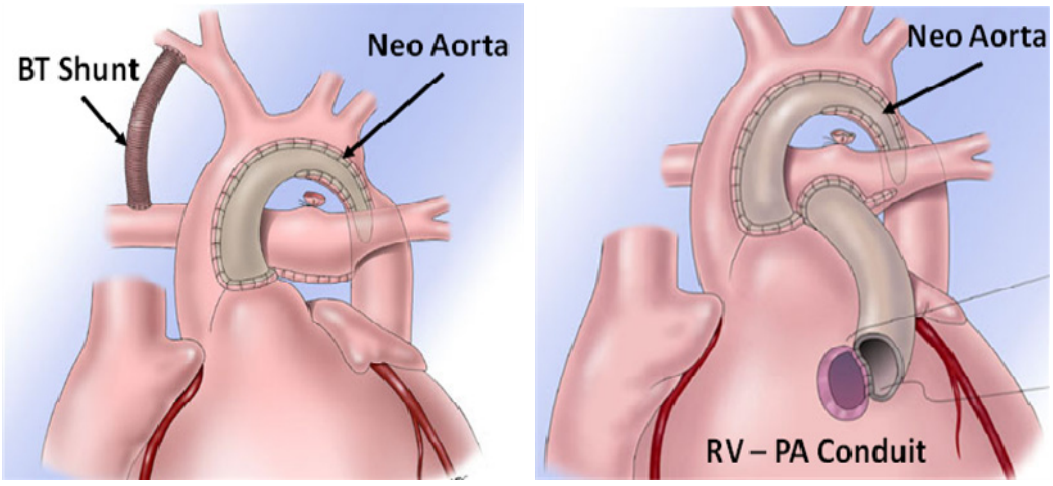

a. b.

Figure 3.8: The Norwood procedure done today using a) Classic BT Shunt;
b) Right ventricle to pulmonary artery shunt (Sano)
(Images Courtesy: Children's Hospital of Boston, Boston, MA)

The first stage is completed using the Norwood procedure introduced by Norwood[8] and associates in 1980. There are two primary steps involved: a) achieve unrestricted flow from the ventricle; b) increase pulmonary circulation. In children with HLHS, the first step is done by a patch augmentation of the hypoplastic aortic arch. Alternatively, a Damus-Kaye-Stansel procedure can be performed by anastomosing the

main pulmonary artery to the aorta[9]. The second step is usually performed using a modified Blalock-Taussig shunt (MBTS) (Figure 3.8a). The shunt consists of a 3-4 mm non-valved polytetrafluoroethylene (PTFE) conduit (Goretex, Gore, Flagstaff, Arizona) with the proximal end connected to the subclavian artery and the distal end to the right pulmonary artery[8]. MBTS physiology is characterized by flow through the shunt to the right pulmonary artery during diastole. The diastolic runoff results in decreased flow to the coronary arteries, which is a risk factor for post-operative mortality and morbidity[10].

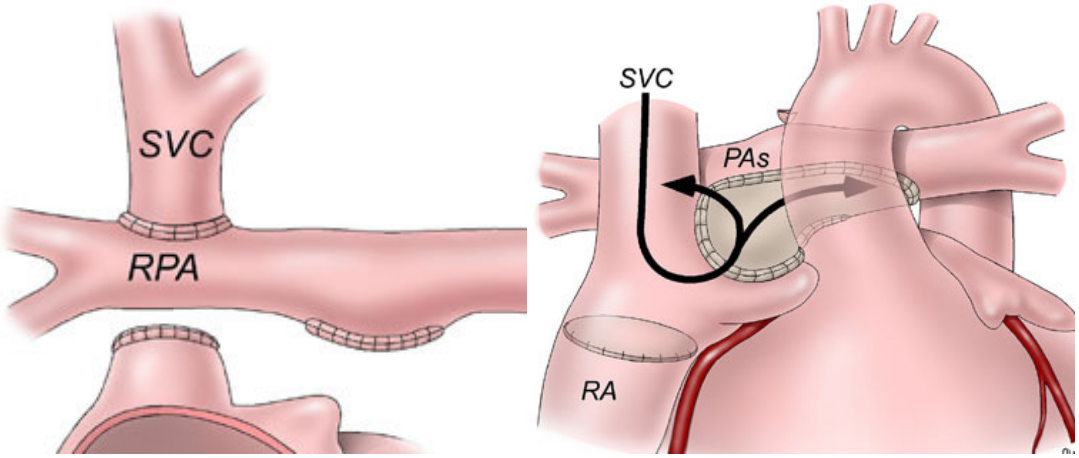

a. b.

Figure 3.9: Stage two bidirectional cavopulmonary anastomosis performed using the: a) bidirectional Glenn approach; b) Hemi-Fontan approach
(Images Courtesy: Children's Hospital of Boston, Boston, MA)

The hemodynamic instability associated with MBTS procedure prompted the introduction of an alternative approach using a Right Ventricle to Pulmonary Artery Conduit, also known as the "Sano Procedure" (Figure 3.8b)[11]. The Sano modification consists of a 4-6 mm non-valved PTFE conduit anastomosed in the proximal end to the infundibulum of the right ventricle, and the distal end to the confluence of the pulmonary arteries. The physiology of the Sano modification is characterized by pulsatile antegrade

flow to the pulmonary arteries. In addition, there is diastolic backflow that results in volume overload and decreased growth of the pulmonary arteries. Although some studies have reported improved early hospital survival and mortality after the Sano procedure[12, 13], other studies have shown little or no difference between the procedures[14, 15]. However, none of these studies were prospective or randomized which is critical when the benefit of one surgical procedure over the other has to be demonstrated. A prospective randomized trial comparing the MBTS and Sano is currently going on which should demonstrate the benefit of using either the MBTS or the Sano.

At 4-12 months of age, most surgical centers introduce either a bidirectional Glenn (BDG) shunt or a Hemi-Fontan (HF) connection with the superior vena cava (SVC) being anastomosed to the pulmonary artery[16](Figure 3.9). A BDG is an end to side anastomosis of the SVC with the right pulmonary artery. In a HF connection, the right atrium is connected to the pulmonary artery, and a patch within the right atrium redirects the SVC flow to the pulmonary artery. Although no clear clinical benefit exists of choosing one procedure over the other, hemodynamics induced by a HF and BDG are clearly different. Furthermore, the choice of stage two procedures determines to a large extent the type of third stage TCPC procedure that can be performed. It should be noted that the HF significantly simplifies the stage-three Fontan procedure. At 1-5 years of age the TCPC surgery is performed and the Fontan circulation is completed by connecting the IVC to the BCPA. In such a configuration, the right side of the heart is bypassed that places an extensive volume load upon the single ventricle. The ventricle must morphologically and anatomically adapt itself to the increased burden.

3.4.3 Types of Fontan

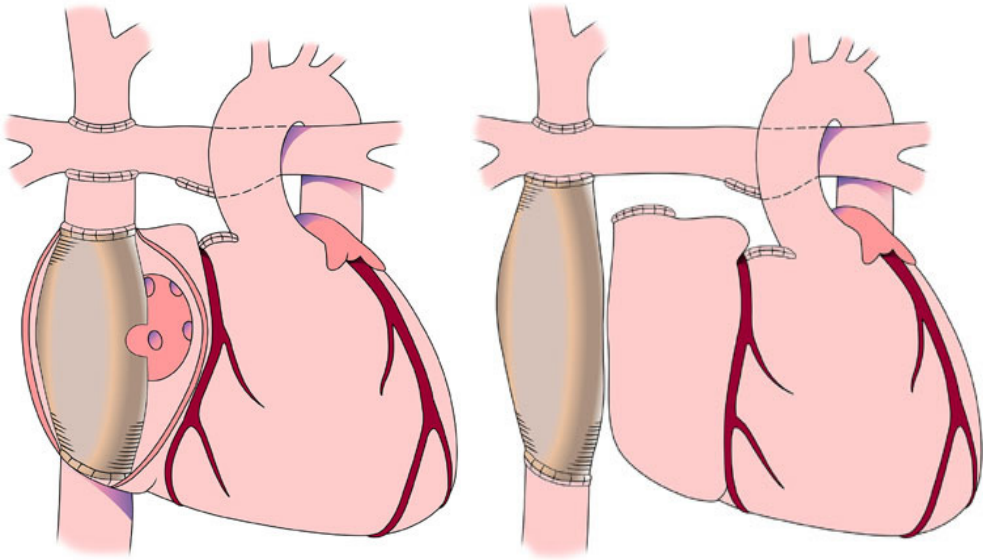

a. b.

Figure 3.10: Stage three Fontan procedure using the: a) Lateral tunnel (intraatrial) approach; b) extra cardiac approach.
(Images Courtesy: Children's Hospital of Boston, Boston, MA)

The two most commonly performed TCPCs are the intraatrial and the extracardiac connections (Figure 3.10). The original AP connection is no longer performed due to significant late complications. While the intraatrial connection is the most common Fontan procedure, there are trends in the current clinical practice to deviate from this procedure due to the presence of extensive secondary swirls created in the intraatrial pouch[17-19]. As it requires creating an incision in the right atrium, there is potential to disrupt the cardiac electrophysiology as well, leading to possible arrhythmias. The extracardiac conduit on the other hand involves using a smooth conduit that results in a comparatively smoother flow profile and consequently an unharmed right atrium[20]. However, the extracardiac conduit does not allow for growth which is viewed as a

shortcoming of this procedure. Significant debate continues to exist in the clinical community about the benefits of using either of these options, as clinically there is very little evidence demonstrating the benefit of using one procedure over the other.

3.4.4 Eligibility of Fontan Operation

Not all single ventricle patients are candidates for a Fontan repair. In 1978, Choussat and Fontan described their recommendations for a successful Fontan operation[21]. The primary criteria is that after repair, left atrial pressure and the transpulmonary gradient must be low. The list provided by Choussat and Fontan are as follows:

1.) Age at the operation between 4 and 15 years.

2.) Presence of sinus rhythm

3.) Normal systemic venous return

4.) Normal right ventricle volume

5.) Mean pulmonary artery pressure <16 mmHg

6.) Pulmonary arteriole resistance < 4 WU/m^2

7.) Ratio of pulmonary artery diameter to Aorta diameter > 0.75

8.) Left Ventricular ejection fraction > 60%

9.) Competent Aortic valve

10.) No adverse affect from prior pulmonary artery operation

Cardiac requirements nowadays are: unobstructed ventricular inflow (no atrioventricular valve stenosis and no regurgitation), reasonable ventricular function, unobstructed outflow (no subaortic stenosis, no arterial hypertension, no coarctation),

good size pulmonary artery, a well developed distal vascular bed, and a normal pulmonary vascular resistance.

Since its inception, modifications of the Fontan procedure have steadily improved surgical outcomes, reducing the post-operative mortality to the level of simpler congenital heart disease repairs. However, the marked improvement in surgical outcome is balanced by the numerous and serious long-term complications encountered by the Fontan patients. In fact, even though the incidence of these defects is only 0.2%, clinicians report that a disproportionate 50% of their time is spent in the care and management of single ventricle defects. Possible complications include: aging in pulmonary vascularity, congestive heart failure, systemic venous hypertension, hepatic and pulmonary congestion, valvular and myocardial dysfunction, thromboembolism, arrhythmias and protein loss, poor exercise performance and quality of life [2]. The current Fontan procedure is the total cavopulmonary connection (TCPC) that is performed in three stages, ultimately resulting in the anastomosis of the inferior (IVC) and superior (SVC) vena cavae directly onto the pulmonary arteries (PAs) bypassing the right side of the heart. The single ventricle thus drives the blood flow through the systemic and pulmonary circulation.

3.4.5 Perioperative Outcome

Initial operative survival after the Fontan procedure has been reported to be as high as 95% in some centers[22], with some reporting a post-operative mortality rate as low 2%[23]. Ten year survival rate ranges from 50-80%, while the 15 year survival is about 50-80%. Risk factors for mortality are determined to be the timing of surgery (early vs. late),

ventricular morphology (single right vs. single left), elevated pulmonary vascular resistance and presence of liver disorders prior to surgery. In a study published by Gaynor and colleagues, the presence of a common atrioventricular valve, and an increased preoperative pulmonary artery pressure were associated with an increased risk of early death[24]. The presence of a single punch fenestration in both the intraatrial and extracardiac Fontans as well as the use of modified ultrafiltration decreased the chances of early death. The risk of prolonged pleural effusions lasting more than 14 days was lesser in patients with extra-cardiac conduit with a side-by-side fenestration and in patients who underwent lateral tunnel Fontan with a single punch fenestration compared to those with AP connections.

Lemler et al. specifically investigated the impact of a fenestration on perioperative performance[25]. They observed that patients with a fenestrated Fontan had total chest tube drainage that was 55% less, a length of stay that was 41% shorter, and 67% fewer additional procedures in the postoperative period than those without a fenestration. The conclusion of this study was that fenestration at the time of the Fontan surgery improves short term outcome in standard-risk patients by decreasing pleural drainage, hospital length of stay, and the need for additional postoperative procedures. These findings have provided compelling evidence that has encouraged cardiac surgeons to incorporate a fenestration into the Fontan procedure.

3.4.6 Long Term Complications in Patients with a Fontan Circulation

Despite marked improvements in early survival rates and midterm outcomes after the Fontan operation, the single ventricle physiology tends towards several

complications[2]. These include, but are not limited to, systemic arterial and venous hemodynamic abnormalities, decreased exercise capacity, protein losing enteropathy, neo-aortic valve root dilation and insufficiency, diminished cognitive development, and thromboembolic complications[2]. Even after Fontan completion, studies have found ventricular hypertrophy, increased muscle mass and poor myocardial function to be a significant risk factor for death[8, 26]. The presence or absence of a systemic left ventricle also seems to affect the clinical outcome. For example, the absence of a systemic left ventricle (e.g. HLHS) results in RV volume overload and eventual dysfunction and failure as the morphologic design is poorly suited for such loads[27, 28]. Joshi et al., examined differences in exercise tolerance between patients with HLHS and other Fontan (single ventricle) patients and reported no significant differences, although the study was limited by a very small sample size (n=7)[29]. Fogel et al have demonstrated significant differences in flow patterns in the aorta of patients with a single ventricular physiology when compared to normal children [27, 28, 30-34]. As these patients grow older, questions continue to be posed about their long term clinical outcome, cognitive abilities, socio-economic status, and quality of life.

3.4.7 Fontan Failure

Fontan patients are at high risk for both acute and late stage Fontan failure. Early failure is typically associated with the drastic change in hemodynamics that results from the Fontan procedure. The sudden increase in central venous pressure may lead to ascites, pleural effusions, decreased pulmonary compliance and increased pulmonary vascular resistance. If no remedial action can be taken, then the only real option is to take down

the Fontan and leave the circulation with a bidirectional cavopulmonary anastomosis (BCPA)[35].

Late failure is typically associated with some of the chronic problems that are a consequence of the Fontan circulation. Obstruction of the systemic and pulmonary venous returns, atrioventricular valve regurgitation, persistant cyanosis, poor ventricular function, atrial arrhythmias, and protein losing enteropathy are some of the causes of late Fontan failure. Some of these can be directly attributed to the surgically created Fontan connection. For example, the original AP connection introduced by Fontan and Baudet was susceptible to systemic venous pathway blockage due to thrombus formation in the atrial pouch. Platelet adhesion as a result of slow, re-circulating flow gradually led to the accumulation of emboli in the atrial pouch eventually leading to complete IVC blockage. In addition, the enlarged right atrium also had a tendency to pinch on the pulmonary veins resulting in the obstruction of flow to the left atrium. Such obstruction resulted in the accumulation of fluid in the lungs eventually causing pulmonary edema and cardiac failure. Lastly, the AP connections were also susceptible to atrial arrhythmias as a result of the suture lines in the right atrium. The isthmus of tissue created by the suture lines, allowed the reentry of action potentials into the atrial wall. These action potentials interfered with signals originating from the sinus node, leading to atrial flutter and rhythm disturbance. Right atrial distension and hypertension, as well as areas of slow conduction and sinus dysfunction that occur after the Fontan procedure further aggravated the problem. Revision of the Fontan circuit to the cavopulmonary connection turned out to be the primary approach for dealing with failures associated with the AP connection[35].

The introduction of the TCPC alleviated many of the problems associated with the AP connections. However, as these patients started to get older, newer modes of Fontan failure started to emerge with the most common being: a) Ventricular dysfunction; b) Protein Losing Enteropathy (PLE); c) Pulmonary Arteriovenous Malformations (PAVMs). The chronic pressure overloaded condition of the single ventricle in a Fontan circulation makes it susceptible for ventricular dysfunction and heart failure. For example, Fogel et al. demonstrated that the presence of the lateral tunnel baffle restricted the motion of the atrioventricular valve plane consequently resulting in increased afterload and decreased cardiac function[36]. Senzaki and colleagues argued that increased afterload, decreased preload (ventricular filling), and abnormal ventricular-vascular coupling are contributing factors for the decreased cardiac reserve and function in patients with a Fontan circulation[37]. Similar increased afterload and decreased preload were reported by Szabo et al. as well using pressure-volume analysis conducted on measurements made in a canine single ventricle model[38]. Besides experimental studies, theoretical models have also predicted similar changes in afterload, preload, and cardiac reserve in a Fontan circulation[39, 40].

Although these studies have demonstrated a strong link between cardiac function and functional outcome, the role of TCPC still remains unclear. As the TCPC resistance is in series to the lungs, it has an effect similar to increasing the pulmonary vascular resistance (PVR) as pictured by Guyton's isolated venous theory[41, 42]. According to Guyton, single ventricle cardiac output is highly sensitive to the PVR which is located downstream of the venous compliance. Recent experimental and computational studies have repeatedly demonstrated the elevated energy losses due to the highly complex

nature of flow structures in the TCPC, which have a compounding effect on the overall resistance experienced by the venous system[43, 44]. This hints that the TCPC resistance could play a major role in regulating cardiac function in Fontan patients.

In order to cope up with the increased resistance and maintain the desired cardiac output in the absence of a pulmonary ventricle, there is a significant drop in venous compliance of the Fontan physiology (-400%)[45]. Consequently, there is a ten-fold increase in central venous pressures (CVP). Such elevated CVP causes problems in the hepatic system that could potentially lead to the development of PLEs. Kiesewetter and colleagues provided histological evidence elevated CVP correlated with changes in hepatic physiology[46]. The liver is lodged between the hepatic portal veins coming out of the digestive tract and the central venous system (Figure 3.1). Elevated pressures in the central and the portal venous system, along with depressed cardiac output provide the ideal substrate for hepatocyte hypoxia, congestion, and stimulation of the fibrotic response. Although the exact mechanism is unknown, increased CVP seem to cause an increase in collagen deposition, and changes in hepatic arterial and venous perfusion. These events lead to liver fibrosis and eventually liver damage. Therefore, elevated CVP as a consequence of the Fontan circulation could indirectly impact the development of PLEs.

Another major complication that results in Fontan failure is progressive cyanosis due to the development of unilateral PAVMS [47-51]. PAVMs are intrapulmonary arterial to venous shunts where the systemic venous blood reaches the pulmonary venous system through abnormal vascular connections proximal to the gas exchange units. The primary consequence of PAVMS is increasing cyanosis and decreased oxygen saturation. Studies

have shown that liver derived factors present in the hepatic venous blood prevent the formation of PAVMs[48, 50-52]. Therefore, any abnormalities in the distribution of hepatic flow in a TCPC configuration could potentially lead to PAVMs. In addition, the intrapulmonary shunts lead to a drop in pulmonary vascular resistance which tends to direct more flow to the diseased lung creating a positive feedback loop of increasing cyanosis. Once the oxygen saturation drops to a certain level, the only palliative option is to re-operate and re-orient the TCPC such that a better hepato-pulmonary flow distribution is achieved[52-56].

One single-ventricle subgroup that is especially at risk for PAVMs is children having an interrupted IVC with an azygous vein continuation (Kawashima Procedure)[57]. In such cases, the azygous vein tends to carry a majority of the IVC flow, while the hepatic flow is directed to the pulmonary system via an extracardiac or intraatrial shunt. This results in a configuration that is much more complex than a typical TCPC geometry. Although several palliative options have been discussed in the literature such as the use of a bifurcated extracardiac conduit, or drainage of the hepatic vein to the persistent azygous vein through an extracardiac conduit[54], there is no "exact" geometric solution to achieving the adequate hepato-pulmonary flow split. The inherent challenges associated with visualizing hepatic flow splits pre-operatively based on geometry alone make it difficult to identify the surgical option that will distribute the hepatic flow "equally" to both the lungs. The development of significant PAVMs constitutes Fontan failure, and requires a Fontan revision with the conduit being placed in a configuration where the hepatic flow can be distributed equally to both the lungs.

3.5 Characterization of Fontan Hemodynamics

A bulk of the literature has focused on evaluating the TCPC hemodynamics using computational fluid dynamics (CFD) and *in vitro* experimental fluid dynamics[18, 19, 43, 58-72]. Most of these studies have attempted to quantify energy losses as a parameter for evaluating single ventricle performance. These studies have significantly improved the understanding of Fontan flow physiology, and have optimized the design of the TCPC. Some of the major contributions have come from the collaborations between de Leval's group in London, England and Migliavacca's group in Milan, Italy. For example, Dubini et al studied the fluid dynamics of the TCPC using CFD, lumped parameter modeling, and fluid-structure interactions[59]. As a consequence, de Leval et al. suggested (using CFD) that forming the systemic venous pathway as a cylindrical tube (such as an extracardiac connection) minimizes energy losses and creates a uniform flow pattern[4, 17]. Further studies by Migliavacca illustrated that the extracardiac connection tends to divert more flow towards the right lung, and induce more power losses compared to the intraatrial connection[73-77]. More recently, Pekkan and Yoganathan have refuted this claim by demonstrating that flows in an anatomically realistic intraatrial connection are quite complex, and have the potential for higher energy losses under increased cardiovascular demand [43, 69].

CFD studies have been adequately supplemented with adequate *in vitro* experiments as well, that have corroborated and confirmed some of the findings from CFD. Early *in vitro* experiments consisted of idealized blown glass models and involved parametric studies to investigate the effect of offsets, angle of connections and presence of pouches on hemodynamics[18, 19, 61, 62, 70, 72, 78, 79]. Amodeo et al. demonstrated the

benefits of a vortex created in an extracardiac model in reducing power losses[58]. Kim et al. compared the fluid dynamics of AP connections and TCPCs using blown glass models[80]. Sharma et al. showed that the incorporation of an offset between the SVC and the IVC was the most efficient configuration from an energy loss perspective[72]. de Zelicourt studied the effects of pouches formed in intraatrial connections using idealized parametric models, and demonstrated its effect on energy losses[19]. Recent trends in experimental research has indicated a shift from idealized models to more anatomically accurate TCPC models built from *in vivo* magnetic resonance imaging[18, 19, 43, 68, 73, 74, 78, 81]. In most of these studies, *in vitro* experiments were used as a validation for computational simulations.

These computational and experimental studies have improved our understanding of the Fontan hemodynamics, and have helped in the optimization of the TCPC geometry. Despite their capabilities of providing hemodynamic data in significant detail, both CFD and *in vitro* experiments suffer from the same limitation: they are not *in vivo* methods. As a result, they can only provide a cursory approximation of *in vivo* physiology. In order to truly understand the *in vivo* flow dynamics, a clinical diagnostic imaging modality such as magnetic resonance imaging has to be utilized. The progress in phase contrast magnetic resonance imaging (PC MRI) in the last couple of decades has allowed for the precise measurements of *in vivo* blood flow velocity fields, and has shown considerable promise in their application to congenital heart disease. In the forthcoming sections, the potential role of PC MRI in single ventricle hemodynamics is disussed.

3.6 Phase Contrast Magnetic Resonance Imaging[82]

Phase contrast magnetic resonance imaging (PC MRI) is a flow imaging technique that measures velocities of water molecules based on phase shifts of moving protons. Magnetic spins of intravascular protons that flow within the magnetic field acquire a phase shift that is proportional to their velocity. By applying a bipolar gradient pulse pair, a velocity dependent phase can be introduced into the signal. This bipolar gradient pulse pair can be applied in all 3 orthogonal directions, to obtain a velocity vector for each pixel in the image. For a bipolar gradient G and –G, the corresponding phase shift is:

$$\phi = \int_{t=0}^{\tau/2} \gamma\, G\, x(t)\, dt + \int_{t=\tau/2}^{\tau} \gamma\, (-G)\, x(t)\, dt$$

In this equation, γ is the gyromagnetic ratio of protons, φ is the phase shift, τ is the length of the gradient signal, and x(t) is the location where the phase shifts are being measured. If the protons in the region of interest are not moving, then the phase shift is 0. However, for protons in blood flowing with velocity v_x, v_y, v_z, the value of φ in each given direction is given by:

$$\phi_x = \gamma\, v_x \tau^2 G_x$$
$$\phi_y = \gamma\, v_y \tau^2 G_y$$
$$\phi_z = \gamma\, v_z \tau^2 G_z$$

Gx, Gy, and Gz are the bipolar gradients that are applied in the three orthogonal directions for inducing phase shifts in each direction. To measure the velocities, a bipolar gradient pulse with reversed polarity is first applied having a negative waveform which is immediately followed by a positive waveform. The phase of the precessing protons

remains the same in static tissue compared to the phase of protons in blood flowing at a constant velocity. Subtraction of the phase images therefore gives a net phase shift of:

$$\Delta\varphi = 2\gamma v_x \tau^2 G$$

The image created as a result of these phase shifts constitute a PC MRI acquisition. When applied in all three directions, a phase image for each component of the velocity vector is obtained. Figure 3.11 shows an example of a PC MRI acquisition in a coronal orientation with phase images corresponding to three spatial dimensions of

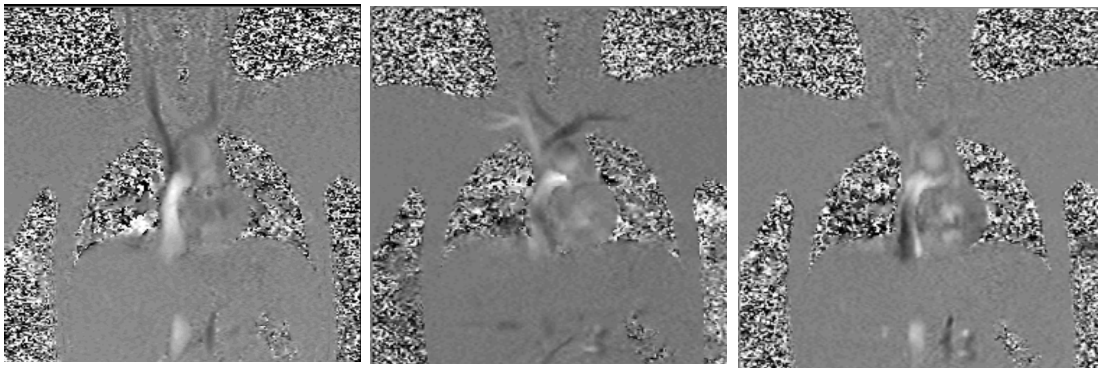

a. b. c.

Figure 3.11: PC MRI acquired in a coronal orientation with velocity encoding in the a) Foot-Head Direction; b) Left-Right Direction; c) Anterior Posterior Direction

Foot-Head, Right-Left, and Anterior-Posterior respectively. In a typical phase image, the pixel intensity is linearly proportional to the velocity component, and by applying a linear transformation, a velocity field within a region of interest can be quantified. At the time of acquisition, a velocity encoding value (venc) is specified and the intensities of phase image lie within this value. For instance, if the intensities of the image range from 0 (black) to 255 (white), 0 corresponds to the lowest velocity (-venc), 128 corresponds to 0 velocity, and 255 corresponds to the highest velocity (venc). By applying this

transformation, a vector field can be generated for the entire phase image. Several post-processing steps are involved in this process for extracting the vector field and clinically relevant parameters from the PC MRI acquisition. Development and validation of these processes is critical if the clinical potential of PC MRI has to be fully harnessed.

3.7 PC MRI Post Processing Methods

PC MRI is the only imaging modality available that can be used for visualizing and quantifying blood flow velocity fields *in vivo*. Besides the measurement of flow rates, it has been used to quantify wall shear stress (WSS)[83-87], pressure drops[84], and flow related phenomena like coherent structures and viscous dissipation energy losses[88]. In addition, PC MRI has also been used to identify regions prone to atherosclerosis[89, 90], aneurysms[91], and the patency of heart valves[92, 93]. In order to meaningfully extract these parameters, an accurate post-processing methodology is crucial.

One of the key post-processing steps is the segmentation of the velocity field within the blood vessel of interest. Typically, the segmentation process consists of detecting the vessel boundary, and the velocity field inside this boundary is then used for quantifying the clinical parameters of interest. Most users employ manual outlining techniques for the purposes of segmentation, although they can be quite time consuming and tedious, especially in situations where large sets of data have to be processed. Automatic segmentation techniques that can significantly speed up the time taken to process and analyze these datasets are highly desirable. The most popular method in the literature for automatic PC MRI segmentation is active contours[94, 95]. Active contours, or snakes, are curves defined within an image domain that move under the influence of both

external forces (based on image data) and internal forces (based on the contour itself). These forces are defined such that the snake will be attracted towards specific features within the image, and in most cases towards the edge of a vessel. Different formulations of the external force can be chosen. Options include gradient magnitude of phase images[96], velocity vector based forces[97, 98], and statistical models[99], that are selected based on the desired segmentation application.

Active contours work well for detecting the morphology of the vessels. However, in situations when the vessel boundary is blurred there are no suitable edges for a contour to converge upon and hence only an approximation of the vessel boundary can be obtained. In such a scenario, vectors that are not part of the desired velocity field get incorporated into the segmentation (Figure 3.12). This effect is pronounced when the vessel is in close proximity to the lungs where the signal to noise ratio is significantly lower. Consequently, the presence of noise along the wall distorts the computation of quantities like wall shear stress, viscous dissipation, etc., that depend upon the spatial derivatives of the velocity field. Therefore filtering this noise is critical especially if PC MRI is to be used as a reliable technique for computing these parameters.

The most frequently cited technique for noise removal in PC MRI is the one proposed by Walker et al., which uses a standard deviation-based measure[100]. This technique classifies regions of high standard deviation as noise, and regions of low standard deviations as flow. The technique is widely used because of its ease of implementation and effectiveness in removing noise. However, the primary drawback of this filter is that it is a scalar technique, and 3D PC MRI produces a vector field. When the Walker filter is applied to a vector field, there is a tendency of the filter to remove

vectors that are actually part of the flow field. This is because the technique treats each component of the vector as an independent quantity, and does not factor in the local characteristics of the velocity field in the filtering process.

Once the vector field is segmented, the next step is to reconstruct a 3D velocity field that can be used for conducting higher order flow field analysis. Performing a 3D *in vivo* flow analysis in patients with a Fontan circulation has always been challenging due to: a) extended acquisition time to obtain a volumetric PC MRI dataset; b) lack of accurate interpolation strategies for reconstructing these flow fields. Normally, the ideal sequence for performing a detailed quantitative flow analysis would be a stack of thinly spaced PC MRI slices in the axial direction with all 3 components of velocity encoded. However, due to limited time available for pediatric scans, this approach is really not feasible.

By adopting a suitable interpolation strategy, the velocity field within the entire TCPC domain can be reconstructed with only a sparse number of acquisitions. Since PC MRI is a relatively new imaging modality, not many approaches are available for interpolating PC MRI datasets. Frakes et al introduced an adaptive control grid interpolation (ACGI) technique for interpolating the velocity field between two successive slices using motion models[81]. One drawback of this approach is that it is a scalar technique where each component of the velocity vector is interpolated separately. Although significantly better than existing methods, this approach did not take the properties of fluid mechanics into account when performing the interpolation. Fatouree et al, used a calculus of variations based approach to reconstruct a 3D velocity field using divergence as a parameter of optimization[101]. Although this approach was very

promising, the technique was idealized for vessels with a purely cylindrical morphology. Besides, the technique was quite complex and challenging to implement, making it a difficult approach for applying it routinely for clinical applications. Therefore, new, simpler approaches for post-processing of PC MRI data have to be developed and validated so that more clinically relevant information can be extracted and utilized.

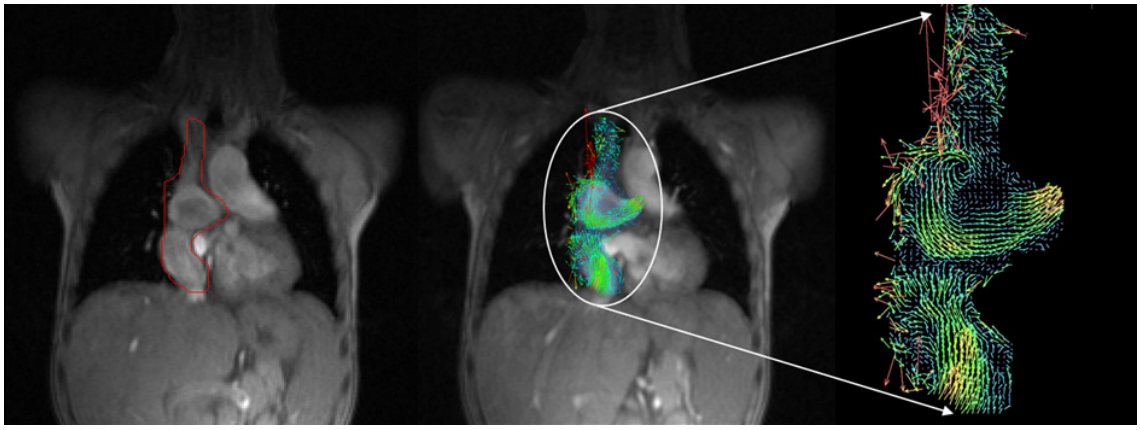

Figure 3.12: Noise vectors being included into the segmentation process

3.8 Clinical Applications of Three Component PC MRI

3 Component PC MRI (also called MRI Phase Velocity Mapping (MR PVM)) has been around for over 20 years, although only recently have clinicians routinely started using some of this information for clinical decision making. Some of the limitations of 3D PC MRI for applicability in a clinical setting include: a) extended acquisition time; b) poor signal to noise ratio for measuring low velocities; c) presence of background phase errors; d) inability to measure turbulent flow structures. Since the vessels in the human circulation have complex shape and structure, there is a need for validating 3D PC MRI for each targeted application. Most validation studies that have been performed have

primarily focused on using idealized phantom models for each designed application[102-110]. In these studies, a physical replica of the anatomic domain of interest is constructed and an *in vitro* experiment is conducted by simulating *in vivo* conditions. The measured velocities using PC MRI are then compared to theoretically expected values. The results have demonstrated errors ranging from 10-20% for the measurement of flow rates and velocities.

In more complex situations, where the velocities within the flow domain need to be quantitatively compared, a second modality such as Doppler ultrasound, particle image velocimetry, or computational fluid dynamics is typically used as a control. The comparisons range from poor to excellent depending upon the chosen application. For example Delfino et al., reported excellent comparisons between PC MRI and Tissue Doppler Imaging for measuring myocardial velocities in normal subjects and patients with dyssynchrony[111]. For the efficacy of PC MRI to measure velocities in all three directions, Canstein and colleagues compared PC MRI with computational fluid dynamics on realistic phantoms of the aorta, and observed a good correlation between the two modalities[112]. Several investigators have attempted to compare the flow velocities and wall shear stresses acquired from 3D PC MRI to those obtained from CFD on the carotid bifurcation phantom[113-116]. These studies showed that PC MRI and CFD correlate very well in regions where the flow is laminar and well behaved, but tend to disagree significantly when vortices and swirls are present in the flow field. Therefore, care must be taken before using PC MRI directly for evaluating 3D hemodynamics in complex vascular structures.

In the cardiovascular realm, a majority of investigators have primarily been using

3D PC MRI for establishing a better understanding of cardiac physiology. As early as 1993, Kilner and colleagues used PC MRI to investigate the jet patterns in mitral and aortic valve stenosis[117]. This study attempted to validate PC MRI for measuring high jet velocities against a more established modality in echocardiography. The same group reported helical and retrograde secondary flow patterns in the ascending aortic arch using 3D PC MRI[118]. In another elegant study that was published in Nature, the group showed the complex structure of flow fields in the heart[119]. For the first time, the morphometry of flow structures were visualized which demonstrated the underlying fluid dynamic benefits of heart's anatomic structure. When the flow goes from SVC and the IVC to the right atrium, the orientation of the atrium redirects the flow towards the tricuspid valve. At late diastole, a vortex ring is formed under the leaflets that helps valve close at end diastole. During systole, when the tricuspid valve is closed, a large vortex is formed within the atrium that reduces the dissipative effects of flow collision. Similar phenomenon was reported on the left side as well. This landmark study brought to fore the strength of PC MRI for understanding the physiology of the human circulation. More recently, Delfino et al. have gone one step further in attempting to quantify the mechanics of the ventricular wall using 3D PC MRI[111, 120, 121]. They reported that PC MRI can be used to accurately quantify the low magnitude velocity fields of the myocardial wall, which can then be used for quantifying metrics of biomechanical relevance such as myocardial strain and strain rates. Such parameters have immense clinical significance as they can be used for identifying patients having ventricular dyssynchrony with high a degree of sensitivity and specificity.

Besides the heart itself, hemodynamics in other major vessels have been

investigated in significant detail as well. One of the key areas of research is the estimation of wall shear stresses from PC MRI[85, 122, 123]. Wall shear stress has been to shown to have implications for progression of atherosclerosis by several investigators, and the ability to make these measurements has the potential to screen patients at risk of developing this disease. Chatzimavroudis and colleagues optimized and validated PC MRI imaging sequences for accurately measuring mitral and aortic regurgitation[105, 124-127]. Frydrychowicz et al. extensively used a newly developed volumetric 3D PC MRI sequence for quantifying the hemodynamics in a variety of cardiovascular structures[128-137]. For example, in one of the studies, they showed significant recirculation patterns taking place inside cerebral aneurisms[129]. They demonstrated the potential benefit of using 3D PC MRI for following up patients with aneurisms to determine when surgical intervention is necessary. In another study, they looked at the swirling patterns in the ascending aorta and identified critical structures during normal and pathological conditions. They showed significant changes in local flow patterns even during the presence of small vascular pathologies.

It should be noted that a majority of the studies thus far have focused on using 3D PC MRI in adult cardiovascular applications. Applications to pediatrics, especially in those having congenital heart disease have been very few.

3.9 TCPC Flow Characterization using PC MRI

TCPC flow characterization using PC MRI has been limited to few *in vitro* experiments and *in vivo* applications. Imaging time constraints as well as lack of PC MRI analysis methods optimized for pediatric applications. Although *in vitro* PC MRI

experiments using flow phantoms is an attractive option option, few people have taken this approach due to the challenges involved in setting up an *in vitro* flow loop in the MRI scanner. Ensley et al. used *in vitro* PC MRI for reconstructing three dimensional (3D) flow fields and compared the resulting flow structures with particle image velocimetry (PIV) on an idealized model with a one-diameter offset[62]. In this study, a good overall match in the large scale flow structures were observed between PC MRI and PIV. However, there were significant discrepancies in small scale features which indicated some of the key limitations of PC MRI.

Most of the *in vivo* MRI studies for evaluating TCPC hemodynamics, have involved using MRI as boundary conditions for computational and experimental studies[43, 67-69, 74-77, 138-140]. Few studies have directly used MRI to study Fontan hemodynamics. Fogel et al., used bolus tagging to study the flow structure in the systemic venous pathway[141]. They showed that flow was essentially laminar throughout its course, and was found to be phasic to both cardiac and respiratory cycles. In another study by the same group, PC MRI was used to show that the SVC blood flow was directed more towards the RPA, while the IVC blood tended to flow toward into the LPA[142]. The study also showed that even though the right lung is larger compared to the left lung, the LPA/RPA flow split was 50/50.

Be'eri et al. studied the hemodynamic efficiency of the AP connection and compared it to the TCPC using *in vivo* multi-dimensional PC MRI[143]. Areas of flow reversal, flow stagnation, and circular flow were observed within the AP connections but not in the TCPC. Analysis of quantitative flow indices showed that compared to the AP group, flow velocities in the TCPC patients were significantly higher, less variable, and

more unidirectional. In a comparison with normal patients, Morgan et al. demonstrated that velocities in the pulmonary arteries were not significantly different in patients after the Fontan operation[144]. However, they did observe that flows and cross-sectional areas were higher in the normal group than in the Fontan operations indicating higher flow rates in normal volunteers. Pedersen et al. evaluated the flow during exercise in Fontan patients using PC MRI[145]. They showed that supine leg exercise resulted in a more than two fold increase in IVC flow. Hjortdal et al studied the effect of exercise and respiration on blood flow in the TCPC using real time PC MRI[146]. They demonstrated that Fontan children have significantly lower cardiac output, and $VO_{2,\ max}$ consumption compared to normal children. More recently, they compared the exercise performance of children with intraatrial and extracardial TCPCs and found no significant difference[147]. Their results also showed that the IVC flow increased during exercise, and that inspiration augments the IVC flow at rest. In a study by Sharma et al, *in vivo* PC MRI was utilized for studying the TCPC hemodynamics and concluded that the flow in the IVC was disturbed irrespective of the Fontan type[71].

Despite all these studies, our understanding of the *in vivo* Fontan hemodynamics is quite limited. A detailed characterization of the global and regional 3D hemodynamics of *in vivo* Fontan flow phenomena is necessary to take the next step in improving the overall performance of patients with single ventricle congenital heart diseases. This thesis makes an attempt to address some of the limitations of PC MRI, so that it can be used to fill in some of the gaps in knowledge associated with single ventricle congenital heart defects.

3.10 Significance

A better understanding of the flow dynamics in the TCPC as well as the energetics of the single ventricle may lead to improved surgical planning and further refinement of the Fontan procedure as it is done today. Numerous attempts in this direction have been conducted using *in vitro* experiments, animal models, and numerical simulations. However, for a convenient clinical use there is a strong need for equivalent *in vivo* evaluation methods. In this thesis, new methods for image processing are developed that will be used for quantifying the hemodynamics and energetics of the Fontan circulation directly from *in vivo* data. Quantitative comparisons are made between different types of Fontan connections as well as different single ventricle morphologies. Particularly, the differences in hemodynamics between intraatrial and extracardiac Fontan types, single left and single right ventricle morphologies are investigated in detail.

CHAPTER 4

IN VITRO PHASE CONTRAST MRI EXPERIMENTS

4.1 Overview

The prohibitively long scanning times associated with high resolution PC MRI, makes *in vivo* volumetric acquisition impractical. This problem can be circumvented using anatomically accurate TCPC phantom models within an experimental flow loop in the MRI scanner. Previous *in vitro* PC MRI studies in our lab have only focused on idealized TCPC models and no study to date exist that has used 3D PC MRI for 3D flow quantification in the TCPC. Hence, the primary objective of this study is to conduct high resolution PC MRI experiments on anatomically accurate TCPC models and compare the resulting hemodynamics to computational fluid dynamics (CFD). The overall approach is depicted in Figure 4.1.

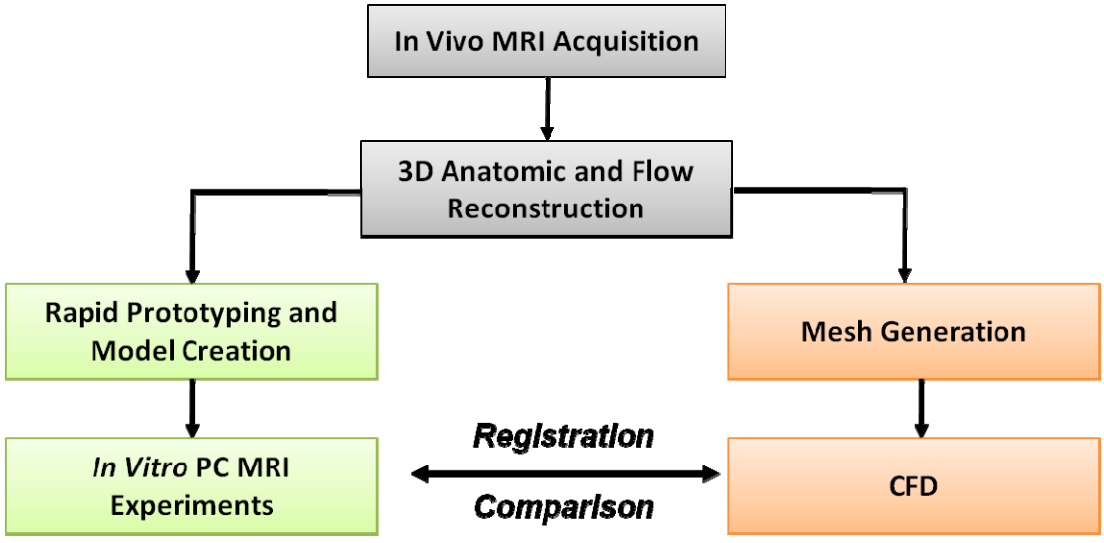

Figure 4.1: Overall approach for *in vitro* PC MRI studies

4.2 TCPC Model Creation

The first step prior to performing the experiments is to succeed in manufacturing anatomically accurate transparent experimental models. Traditionally this was achieved by reverse engineering the morphology of interest, through tedious casting/curing operations, ultimately producing a transparent Slygard enclosure for the TCPC lumen. For the small, complex, and variable nature of pediatric anatomies, this process was found to be expensive and difficult to apply. To circumvent these issues, another path is adopted here, where the design is inverted using computer aided design (CAD) and the physical model is built directly using transparent stereolithographic resins[78]. This approach presents the following advantages: a) It is very accurate and allows for identical experimental and CFD models which is critical for quantitative comparison between the two modalities; b) It is cheaper than the earlier methods; c) It is time effective with the entire design and manufacturing process taking about 1-2 days.

In order to manufacture anatomically realistic TCPC phantom models, a 3D reconstruction of the anatomy is necessary. MRI provides an attractive avenue for this purpose, as it is non invasive, has minimum radiation, and can provide flow information for boundary conditions. Patients are recruited at the Children's Hospital of Philadelphia (CHOP), Children's Healthcare of Atlanta (CHOA), and the University of North Carolina at Chapel Hill (UNC). Informed consent is obtained from all patients, and all protocols are approved by the institutional review boards (IRB) of each institution. This approach has been applied to over 250 patients with a single ventricle anatomy, and a large Fontan MRI database has been established.

4.2.1 MRI Scanning Protocol

Anatomy: A GE 1.5T Signa (General Electric Healthcare, Chalfont St. Giles, United Kingdom) is used for patients from CHOA (sequence name: fast imaging employing steady state acquisition (FIESTA)) with an average repetition time (TR) of 6s and echo time (TE) of 1.5-3 ms. A Siemens 1.5T Sonata or Avanto scanner (Siemens Medical Solutions, Erlangen, Germany) is used for patients from CHOP (sequence name: true fast imaging with steady state precession (trueFISP)) having a TR of 150-250 ms and a TE of 1.1-1.5ms. Axial slices of 3-5 mm thickness with approximately 1 mm^2 in plane resolution are obtained spanning the entire thorax region (Figure 4.2). Angiographic methods are not used because younger patients are not systematically administered the gadolinium contrast agent.

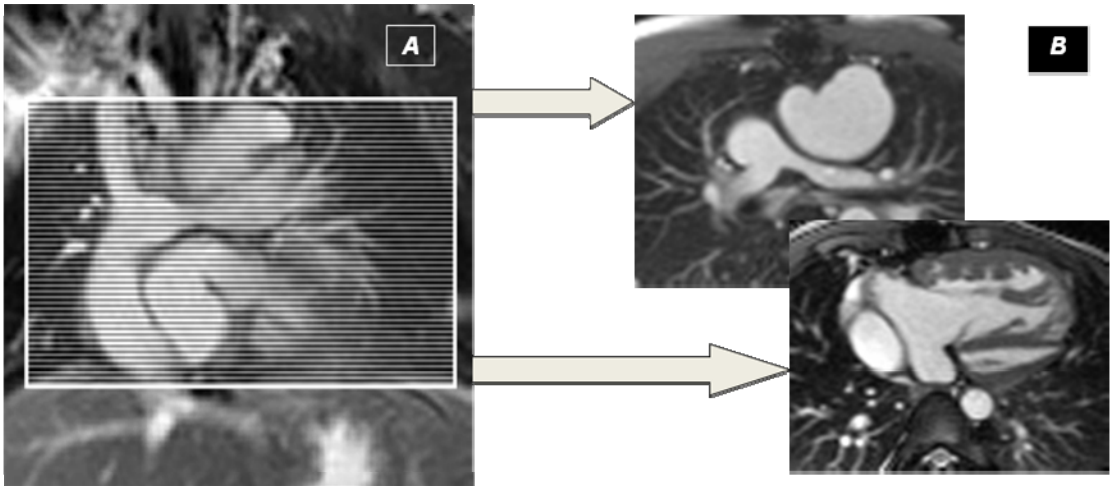

Figure 4.2: Example of obtaining axial images throughout the thorax region using steady state free precession. A) Axial stack acquisition; B) Axial slice at the location of the pulmonary arteries (upper panel B) and the ventricle (lower panel B) are shown.

Velocity: In addition to the anatomic acquisition, a PC MRI acquisition is performed at the inlets (SVC and IVC), the outlets (LPA and the RPA) and the ascending aorta to serve as boundary conditions. The transverse slices acquired for the anatomy are imported in a software program for multi-planar reconstruction. Using this software program, the exact locations for the imaging planes are identified. A segmented k-space fast field echo (FFE) sequence with 3 segments per acquisition is used to obtain phase encoded velocity maps in the 5 vessels. Care is taken to make sure that the slices are perpendicular to the flow of blood to ensure maximum signal to noise ratio. All acquisitions are retrospectively gated, with a typical R-R time interval of 750 ms resulting in about 20 cardiac phases for each vessel. The TR and TE are set to be 50 and 3.8 ms respectively. The slice thickness is 6 mm with an average in-plane resolution of 1x1 mm^2. Figure 4.3 shows the acquisition protocol used. The acquired datasets are processed using the methodology outlined in Chapter 5.

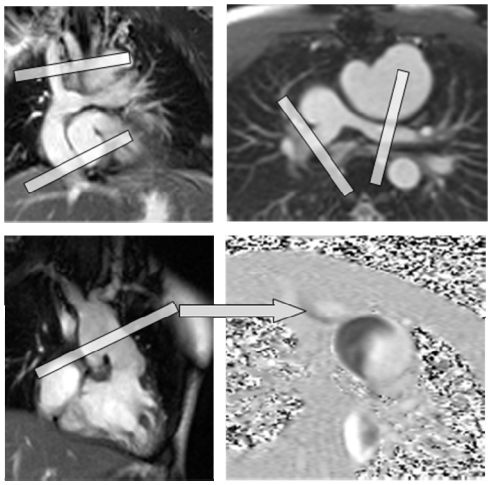

Figure 4.3: Example of a PC MRI acquisition. Upper row describes the vessel locations for the TCPC, while the bottom rows shows the locations for the aorta

4.2.2 Interpolation

In order to extract a smooth TCPC geometry from a stack of axial anatomic images, isotropic voxels are required. Since the data acquired from the institutions have anisotropic voxel sizes (1x1x5 mm^3), there is a need for image interpolation. Although several techniques are available in the literature for this purpose, the adaptive control grid interpolation (ACGI) technique developed by Frakes et al, is used in the current application[148]. This technique combines optical flow with block matching approaches to evaluate a continuous interpolating function for the entire MRI stack. The number of slices required for achieving isotropic voxel size is estimated based on the pixel size and slice thickness. ACGI is then used for interpolating the missing slices. Figure 4.4 shows the original MRI and the interpolated stack from a coronal perspective.

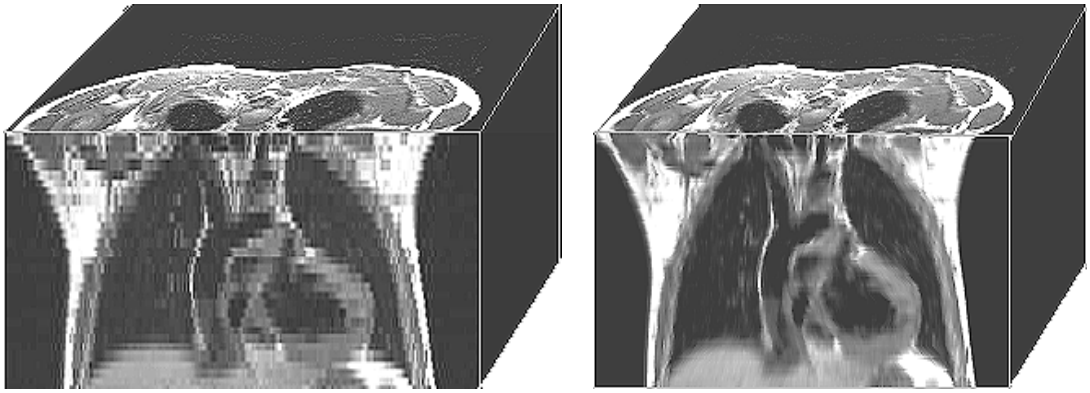

a. b.

Figure 4.4: The benefits of using ACGI for interpolation of the MRI dataset. a) Original acquisition. Notice the step-like pattern due to anisotropic voxel sizes; b) Enhanced dataset using ACGI. Notice how smooth the structures look, which is more representative of the human anatomy.

4.2.3 Segmentation

An integral component for a 3D geometric reconstruction is the segmentation process where the morphology of the vessel is extracted from a stack of images. Traditional approaches such as thresholding, edge detection, and region growing popular in most software packages, are ineffective since the vessel boundaries are poorly defined. A new approach developed by Frakes et al. addresses this problem by using a shape element segmentation approach[149]. The incomplete borders are used as scaffolds, within which the areas of interest are reconstructed. By determining the maximum size of edge gaps *a priori*, a shape element of predetermined size is initialized inside this scaffold. The shape element then bounces within this structure until the entire TCPC is segmented (Figure 4.5). This shape element segmentation approach has been shown to perform superiorly to other techniques available for geometric reconstruction.

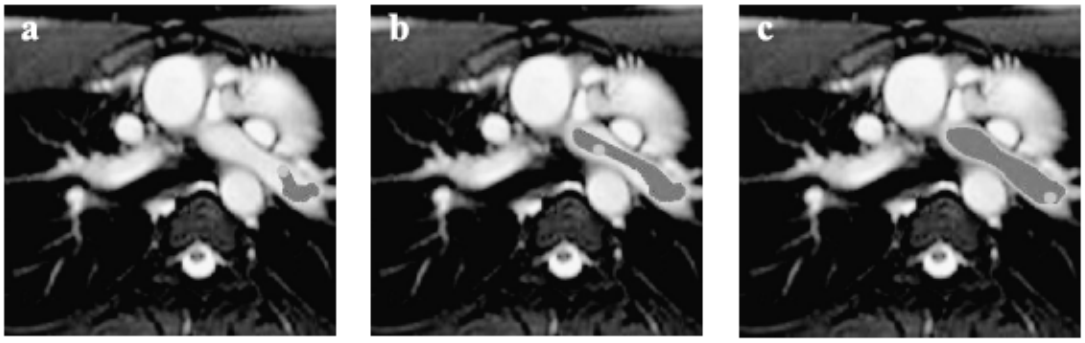

Figure 4.5: Frames associated with the segmentation process. a) The shape element is first initialized within the vessel of interest; b) The state of segmentation after 15 iterations; c) The final segmented product after the algorithm converges.

4.2.4 3D Reconstruction

The output of the shape element segmentation approach is a stack of binary segmented slices. In order to obtain a 3D morphology from these slices, a surface connectivity needs to be established between the vessel borders. Doing so is computationally intensive, and hence a commercial software package is used. The segmented binary slices from the shape element segmentation are then imported into Mimics software (Materialize, Ann Arbor, MI). The pixel sizes and the interpolated slice thickness are specified during the process of importing. A smooth triangulated surface is then fit to the segmented slices to get a 3D representation of the vessel anatomy. Any unwanted structures included as part of the segmentation are cleaned out in this phase. Figure 4.6 shows the transformation of going from a 2D segmented dataset to a 3D reconstruction in a stereolithographic (STL) format.

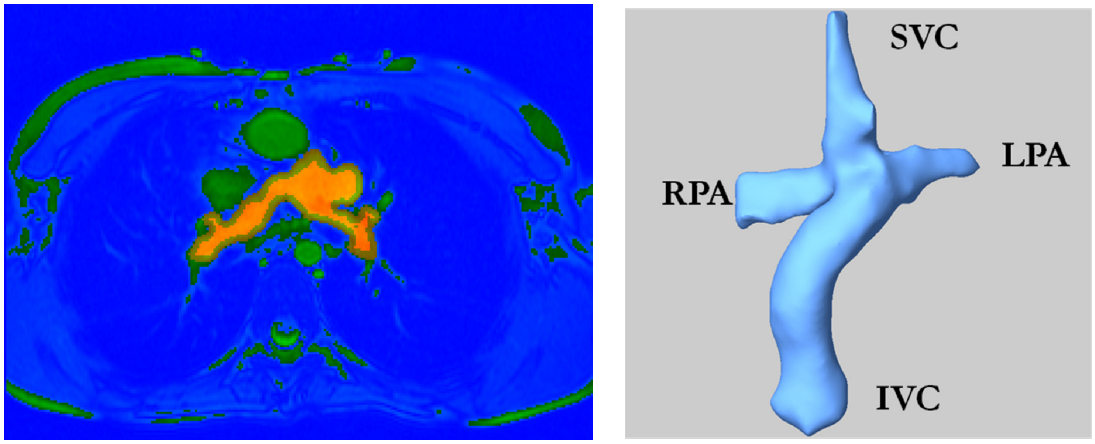

Figure 4.6: a) The segmented slice after the shape element segmentation. Only the region colored in orange is retained; b) 3D reconstruction of an extracardiac TCPC anatomy with the different vessels labeled.

4.2.5 Rapid Prototyping and Physical Model Creation

De Zelicourt et al have previously described a method for designing and manufacturing physical replicas from 3D anatomic reconstructions[78]. In this approach, the STL files are first converted to international graphics exchange format (IGES) in Geomagics Studio (Raindrop Geomagic, Research Triangle Park, NC) to aid in the computer aided design (CAD) manipulation and mesh generation. At this point the vessels are sectioned at locations where the velocity images are acquired (Figure 4.3). The sectioned geometry is then imported into Pro/ENGINEER (Parametric Technology Corporation, Needham, MA), where a rapid prototyping replica is designed around the vessel volume defined by the volumetric anatomic reconstruction. Vessel extensions with circular outer cross-sections are included in the design to facilitate the connection of tubes. All walls of the rapid-prototype replica are at least 4 mm in thickness to avoid the construction of an excessively fragile model. The model is then exported into a rapid prototyping system (SLA 3500, 3D systems, Valencia, CA) for 3D printing. The physical models are polished to prevent any power losses due to friction with the vessel walls. Figure 4.7 shows a schematic of the process.

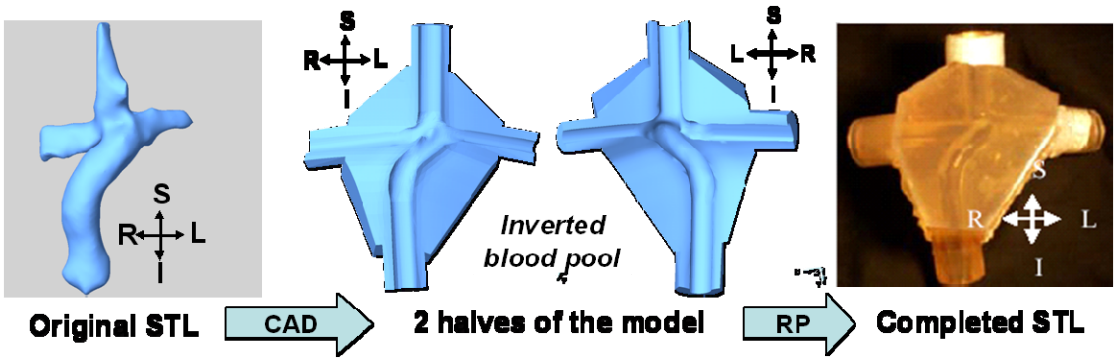

Figure 4.7: Process associated with the phantom model creation

4.2.6 Selected Models

Given the diversity of the Fontan population, it is important to select TCPC geometries that are representative of the overall patient population. Towards this end, 3 models are selected: a) CHOA006 (IVC-MPA Extracardiac TCPC); CHOA007 (Extracardiac TCPC); b) CHOA011 (Intraatrial TCPC). Table 4.1 shows the details of the patients selected for this study. The above described process was followed for each patient, and 3 TCPC phantom models were manufactured (Figure 4.8).

Table 4.1: Demographics of the patients used in this study

Patient	Template Type	Diagnosis	Gender	Age	Race	BSA (m^2)
CHOA006	IVC-MPA	AVCD	Male	7	White	1.03
CHOA007	Extracardiac	HLHS	Male	6	White	0.79
CHOA011	Intraatrial	HLHS	Female	11	White	1.19

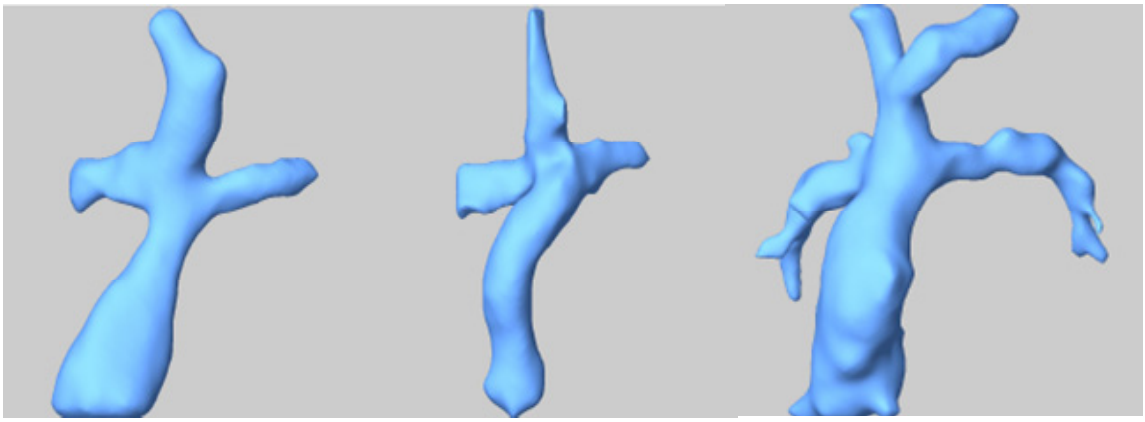

a. b. c

Figure 4.8: TCPC models used in this study: a) CHOA006 (IVC MPA Connection); b) CHOA007 (Extracardiac Connection); c) Intraatrial Connection

4.3 Experimental Protocol

4.3.1 Flow Loop Setup

An MRI compatible experimental flow loop is setup inside the Philips Intera 1.5T and the Philips Intera 3.0T scanners located at the Emory University Hospital. The stereolithographic replica of the TCPC is connected to this flow loop, consisting of a steady pump (Model 4E-34N, Little Giant Pump Company, Oklahoma City, OK), a pump regulator (Type 3PN1010, Staco Energy Products Company, Dayton, OH) to adjust the flow rates, rotameters (Model 75302317C02, King Instrument Company, Inc., Garden Grove, CA) with turn knobs to accurately control the caval and pulmonary flow splits, long vinyl tubing, plastic clamps, and a reservoir for the water/glycerin mixture.

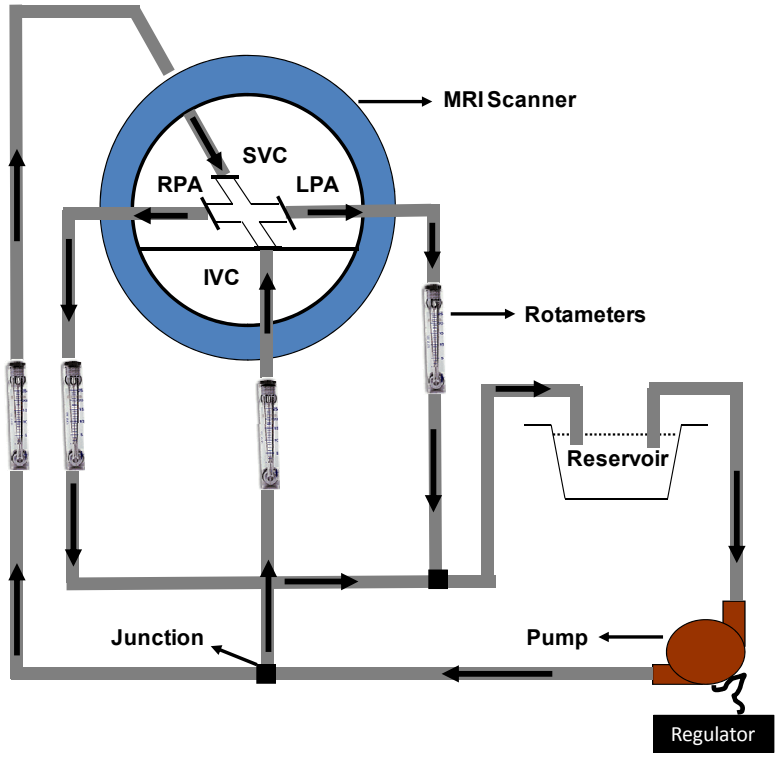

Figure 4.9: Schematic showing the MRI flow loop. The arrows indicate the direction of flow,

To ensure that no air bubbles get mixed into the solution and into the flow loop, the tubes are submerged under the water/glycerin solution in the reservoir. Teflon tape is wound around the inlets and outlets at all tube connection sites before the tubes are fitted to the pump and the model. Plastic clamps are used instead of metal clamps, to ensure MRI compatibility. Since is experimentally not possible to make the flow loop completely air tight, the loop is flushed after every experimental condition to make sure that all air-bubbles are removed before the start of each experiment. This is done by opening up the rotameters completely, and running the pump at its maximum capacity. In models with a pouch in the IVC baffle (such as the intraatrial TCPC CHOA011), the pouch is placed facing downwards instead of the usual physiological upward configuration to prevent the accumulation of air bubbles in the region. Figure 4.9 shows a schematic of the flow loop setup and Figure 4.10 shows an actual picture of the MRI flow loop.

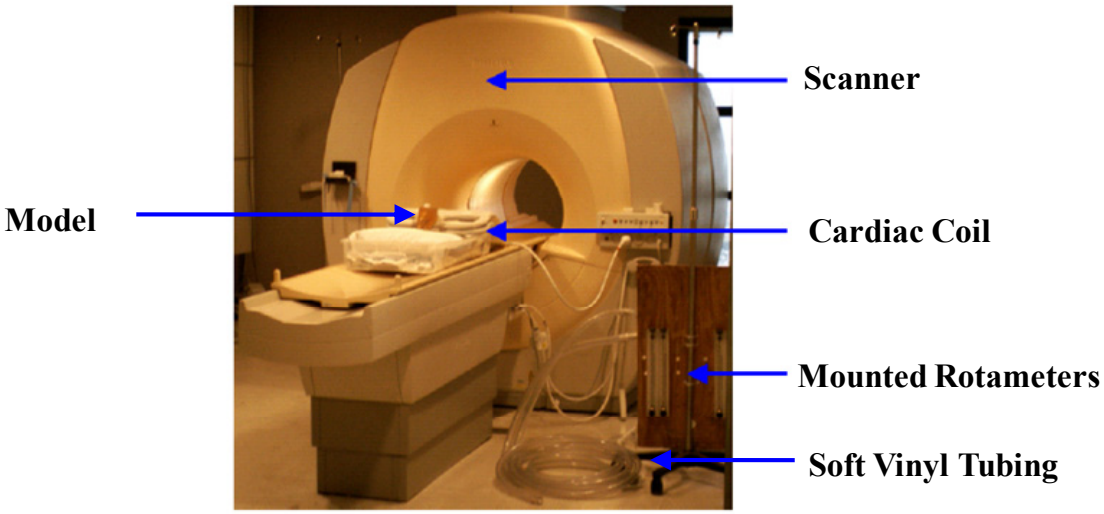

Figure 4.10: A snapshot of the flow loop setup inside the MRI scanner

The soft vinyl tubing used in the experimental loop, has a tendency to expand and contract during the experiment which slowly and steadily changes the flow rates. This makes it necessary to constantly monitor the flow rates during the course of the experiment to ensure that the desired flow rates are maintained. Using stiff tubing may fix this problem, but it is not possible to do so due to the significant space constraints associated with setting up the flow loop inside the MRI scanner.

The tubes feeding the SVC and the IVC have at least 2 meters of straight tube to ensure fully developed flow into the two inlets. In a typical configuration, the SVC goes into the scanner first, and hence is farthest away from the pump. This required much longer tubes (> 6 meters) for the SVC compared to the other vessels. To minimize the number of kinks, tubing of larger diameter is used for the SVC (1 inch vs. ¾ inch for the rest).

The entrance length requirement for fully developed laminar flow is determined based on the following equation:

$$LE = \frac{0.06 * 4 * Q}{\pi \gamma} \qquad \text{Equation 4-1}$$

In this equation, LE is the entrance length, Q is the desired flow rate, and γ is the kinematic viscosity of the water/glycerin mixture. The lowest flow rate used is 0.8 Liters per minute (LPM) that translates to an entrance length of .29 m, and the highest flow rate through an inlet is 4.8 LPM that translates to an entrance length of 1.74 m, which is well within the 2 m tube length used in conducting the experiments.

The pump (Model 4E-34N, Little Giant Pump Company, Oklahoma city, OK) is a metal pump and cannot be placed close to the loop. The magnetic field near the scanner is

so strong, that keeping the pump close to the scanner can be disastrous as it can cause significant equipment damage. For this reason, the pump is kept far away in the corner of the room, away from the magnetic field. The pump also generates a lot of heat, and if run for an extended period of time, it will tend to burn out. To keep the pump cool, it is immersed in a bucket of ice for experiments conducted over an extended period of time. The ice inside the bucket is replenished every 2 hours to maintain the temperature of pump operation.

The rotameters serve as flow meters for controlling the inlet and outlet boundary conditions and are stable and easy to use with turn knob adjustable valves for accurate flow adjustment. Rotameters consist of two basic elements: a tapered tube and a float. When fluid flows through the rotameter, fluid enters the tapered tube and the float is lifted to height that balances the gravitational force and the fluid force experienced by the float. Therefore, the readings depend upon the specific gravity, fluid viscosity, the operating temperature and the specific gravity of the float. This requires the rotameters to be calibrated for the solution before they can be used in the experiment. The readout scale of the rotameters is in gallons per minute (GPM), and is normally calibrated to distilled water.

The specific model 75302317C02 (King Instrument Company, Garden Grove, CA) is chosen since it is made of acrylic which is MRI compatible, has a sensitive readout scale ranging from 0.2 to 2 GPM with an accuracy of ± 2% of full scale flow, a repeatability of 1%, and is a stable and easy to use system. Four rotameters are used to control the flows going into the SVC, IVC, LPA, and RPA respectively. They have to be maintained in a vertical position for accurate flow reading and operation. This is achieved

by attaching them to a wooden board and mounting the wooden board on a stand so that the position is maintained over entire course of the experiment.

To mimic *in vivo* conditions, a blood analog solution of water and glycerin is used as the working fluid. A 60/40 ratio of water/glycerin mixture has a kinematic viscosity of 3.5 centristokes (cSt) which is similar to flowing blood. In addition, 20 mL of Magnevist Gadopentate dimeglumine also known as Gadolinium (Berlex, Montville, NJ) is added to every 20L of solution to boost the MRI signal. Gadolinium decreases the T1 relaxation time, thereby increasing the contrast and the signal to noise ratio of the flowing solution. The total volume of fluid used in the experiments is about 30 L, and hence about 30 mL of contrast agent is used. To calibrate the rotameters, a correction factor is applied to account for the water/glycerin mixture. The manufacture supplied correction factor is 1.047 for the working fluid.

Once the flow loop is setup, it is first tested for leaks using just plain water as the working fluid. The mixture of water and glycerin is quite slimy and slippery, and if there is a leak, then it makes a mess in the MRI scanner. This is unacceptable as the same scanner is also used for clinical purposes and the area needs to be devoid of any harmful chemicals that maybe around. After ensuring that the flow loop is leak-free, water is replaced with the water/glycerin mixture and the flow loop is now setup for the *in vitro* PC MRI experiments. The pump is set to drive at a power necessary for maintaining the desired flow rates and rotameters are adjusted to achieve the desired flow split.

4.3.2 Experimental Conditions

For each model selected in the study, *in vivo* flow conditions are acquired from

PC MRI data. Specifically, flow rates through the SVC/IVC are obtained to get an estimate of the total flow rate through the TCPC, and the LPA/RPA to estimate the pulmonary artery flow split. SVC/IVC flow splits are always kept at 40/60 and the flow rates are rounded off to the nearest whole number for experimental simplicity. All experiments are conducted under steady flow conditions. Although there is some pulsatility in the IVC of the TCPC, the variation is quite low and is not expected to have a significant impact on the flow fields. Furthermore, conducting a pulsatile experiment *in vitro* is very challenging for a TCPC since it requires the synchronization of two independent piston pumps. In an MRI scanner the space constraints prevent the use of two piston pumps. Keeping these caveats in mind, the cost/benefit ratio of conducting pulsatile *in vitro* experiments is much higher for the presented application and hence steady flow experimental conditions are chosen.

Table 4.2: Experimental conditions for the 3 TCPC Models

Model	Total Flow Rate (LPM)	LPA/RPA (LPM)	Exp. Flow Conditions	Exp. Flow Splits (%RPA)
CHOA006	2.8	1.5/1.3	3, 5	30, 50, 70
CHOA007	2	0.93/1.07	2, 4	50, 60, 70
CHOA011	4	2.4/1.6	4, 6	30, 50, 70

Experiments are conducted at resting and exercise flow conditions which is a 2 LPM increase over the resting flow rate. For each flow condition, 3 different flow splits are used to account for different lung resistances. Table 4.2 shows the *in vivo* measurements, and the experimental conditions for each model used in the study. For CHOA007, the LPA is much smaller in diameter than the RPA, and hence no more than

50% of the total flow could be forced through the LPA. For the other two models (CHOA006, and CHOA011), the flow splits are varied from 30-70% going to the RPA in 20% increments.

4.3.3 MRI Data Acquisition

All experiments, but one, are conducted on a Philips 1.5T Intera MRI scanner (Philips, Vantaa, Finland), and one is conducted on a Philips 3.0T Intera MRI scanner. Both are located at the Emory University Hospital. CHOA007 (extracardiac) and CHOA011 (intraatrial) are the models selected for imaging in the 1.5T scanner, while CHOA006 is the model scanned in the 3.0T scanner. The purpose of conducting experiments in a 3.0T scanner is to investigate the potential benefit of increased SNR at higher field strengths on the accuracy of the TCPC flow reconstruction. As MRI evolves towards higher field strengths, there are unanswered questions about its benefits in the quantification of flow structures in complex vascular anatomies. Recent studies indicating the benefit of 3.0T are only based on simple flow geometries using theoretical flow regimes and few studies have been conducted on anatomically realistic geometries[150]. The experiment conducted at 3.0T is meant to be a preliminary study to investigate the feasibility of 3.0T for quantifying flow structures in the TCPC. For both the scanners, significant attempt is made to make sure that the exact same protocol is used for data acquisition.

4.3.3.1 Scanner Protocol

An MRI protocol is developed to acquire dense PC MRI slices through the entire domain of the TCPC. For each experimental condition, a stack of contiguous T1

weighted, fast-field echo (FFE) slices with a thickness of 2 mm are obtained. The field of view used is 102 mm x 51 mm with a matrix size of 256 pixels x 128 pixels to obtain an in-plane resolution of 0.4 mm. A TR of 30 ms, a TE of 13 ms, a flip angle of 30°, and a signal average of 2 is used to optimize the signal to noise ratio. Three sets of data are acquired corresponding to the three components of velocity. These are the Anterior-Posterior (AP), Right-Left (RL), and Superior-Inferior (SI) directions respectively. Care is taken to place the model at the isocenter of the magnet to minimize any interference from the eddy currents induced in the coil due to magnetic field inhomogeneities.

Prior to conducting the experiments, a velocity encoding (venc) value is determined based on the vessel diameter and expected velocities within the TCPC model. To get full use of the dynamic range in this gray scale, venc values are selected close to the maximum expected velocities inside the MRI scanner. However, care is taken not to make the velocity encoding values too small either, as that can lead velocity aliasing. The maximum expected velocities are evaluated prior to the experiment using the following simplified formula:

$$V_{Max} = 2 * \frac{Q}{A} = \frac{2 * Q}{\pi * r^2} \qquad \text{Equation 4-2}$$

Q is the flow rate through the vessel, A is the cross-sectional area and r is the radius of the vessel. The formula holds when the cylinder is straight and the flow is steady, and fully developed (laminar), in which case the maximum velocity is twice the mean velocity. To investigate whether the flow is laminar or turbulent under the experimental conditions, the Reynold's number, Re is evaluated for flow through each vessel as follows:

$$Re = \frac{Q}{\pi * r * v}$$ Equation 4-3

The Reynold's number is evaluated for each experimental condition to check for turbulence. Table 4.3 shows the radii of the different vessels used in the study. Tables A1, A2, and A3 (Appendix) show the expected mean, maximum velocities, and the Reynold's numbers within the different vessels for different experimental conditions. The maximum velocities and the Reynold's numbers are observed in the LPA and the RPA, which is expected due to their relatively smaller diameters compared to the IVC and the SVC. Based on these data, the velocity encoding values are determined for each experimental condition (Table 4.4). The velocity encoding value is kept higher than the maximum observed velocities to ensure that wrap around is kept to a minimum.

Table 4.3: Radii of the different models used in the study

Model	IVC (cm)	SVC (cm)	LPA (cm)	RPA (cm)
CHOA006	1.0	0.72	0.82	0.72
CHOA007	1.04	0.83	0.61	0.60
CHOA011	1.21	0.84	0.55	0.77

Table 4.4: Maximum theoretical velocities, and the chosen velocity encoding (venc) for the models used in the study

Model	Flow Rate (LPM)	Theoretical V_{Max} (cm/s)	AP Venc (cm/s)	RL Venc (cm/s)	FH Venc (cm/s)
CHOA006	3	33.14	120	150	150
CHOA006	5	71.57	200	250	250
CHOA007	2	41.27	60	90	90
CHOA007	4	82.54	100	180	180
CHOA011	4	98.23	75	100	100
CHOA011	6	147.35	120	150	150

A summary of the protocol is shown in Table 4.5:

Table 4.5: Summary of the MRI acquisition protocol

Parameter	Value
Sequence Name	Balanced Fast Field Echo
Coil Type	SENSE – BODY
Acquisition Direction	Axial
FOV	10.2 – 15.4 cm
Phase FOV	25% (2.6-3 cm) or 50% (5.1-6 cm)
Acquisition Matrix	256x256 – 384x384 Pixels
Pixel Size	0.4 mm
Slice Thickness	4 mm
Reconstructed Slice Thickness	2 mm
Number of Slices	50
Flip Angle	30°
TR	30 ms
TE	13 ms

This protocol is applied to all the models except CHOA011 which required a larger FOV due to its larger size. Figure 4.11 shows the magnitude and phase images associated with CHOA007. The acquisition orientation of this dataset is similar to the *in vivo* orientation with the SVC going first into the MRI scanner (head first configuration), and the chest of the patient facing the ceiling. In such an orientation the direction of acquisition is from the IVC going towards the SVC for an axial acquisition. The MRI orientation axis is then Left-Posterior-Superior, implying that X corresponds to the Right -> Left direction, Y corresponds to the Anterior -> Posterior direction, and Z corresponds to the Inferior -> Superior direction. This approach is followed for CHOA006 and CHOA007. For CHOA011, the Right-Anterior-Superior orientation is chosen to

minimize the accumulation of air bubbles in the intraatrial pouch which is anterior to the pulmonary arteries.

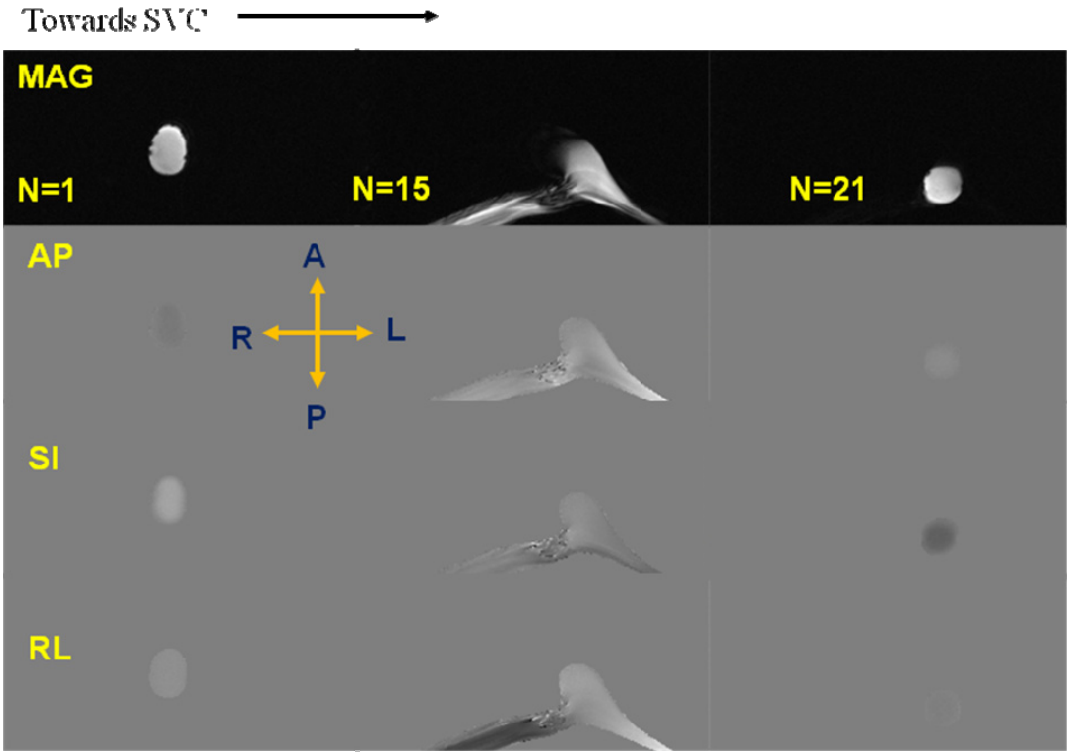

Figure 4.11: A sample of PC MRI acquired in CHOA007 at 3 different locations: at the IVC (N=1), the connection region (N=15), and the SVC (N=21). The first row shows the magnitude or speed images, the second row are the images with encoding in the Anterior-Posterior (AP) direction, Superior-Inferior (SI) direction, and the Right-Left Direction (RL). Notice that the intensities closer to white in the AP, SI, and RL encoding directions, correspond to increasing velocities in the posterior, superior, and left directions respectively, while the intensities closer to black correspond to increasing velocities in the opposite direction

Each acquisition lasts for about 12 minutes, which corresponds to a total acquisition time of approximately 36 minutes for each experimental condition. The images are inspected to check for any wrap around or aliasing that may have occurred. If any wrap around is observed, then the scan is redone with new velocity encoding values.

4.4 PC MRI Post Processing

Once the images are acquired, a set of post processing steps are followed for converting the images to a format conducive for fluid dynamic analysis. Figure 4.12 shows the overall process associated with PC MRI post processing. The images are first imported into a dicom viewer (Dicomworks, Freeware) which allows for the inspection

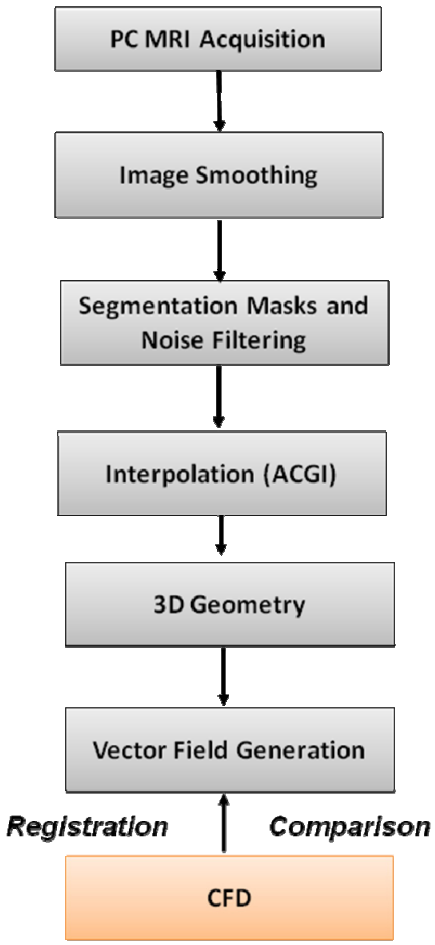

Figure 4.12: The process associated with the post processing of PC MRI data

of the data. The relevant images associated with the experiments are then exported in dicom format for further analysis.

4.4.1 Image Smoothing and Segmentation

Due to complexities in the velocity field inside the TCPC, the intensity of images within the TCPC is not uniform. Therefore, the magnitude images have to smoothened in order to homogenize the pixel intensities within the TCPC so that a suitable segmentation mask can be created. Traditional smoothing approaches such as Gaussian smoothing have the effect of blurring out edges as well which is not desirable if the borders of the vessel have to be accurately identified. To get around this issue, Perona and Malik first proposed the idea of edge preserving filters[151]. The idea is to use the principle of diffusion to smoothen only regions within objects in the image, and not across the boundaries. This is accomplished by smoothing perpendicular to the primary gradient direction. Mathematically this translates to:

$$It = |\nabla I| \cdot div\left(\frac{\nabla I}{|\nabla I|}\right) \qquad \text{Equation 4-4}$$

Here, I is the image to be smoothened. This equation simplifies to:

$$It = \Delta I - \frac{I_x^2 \cdot I_{xx} + I_y^2 \cdot I_{yy} - 2 \cdot I_x \cdot I_y \cdot I_{xy}}{|\nabla I|^2} \qquad \text{Equation 4-5}$$

I_t is the time derivative governing the evolution of the image and is applied iteratively until the desired smoothing effect is reached. A segmentation mask is then created by applying a suitable threshold to the image. The results of this approach are demonstrated on a magnitude PC MRI image in Figure 4.13. Figure 4.14 shows the components of the velocity images with and without the segmentation masks. Prior to the application of the segmentation masks, the presence of noise pixels within the image is evident.

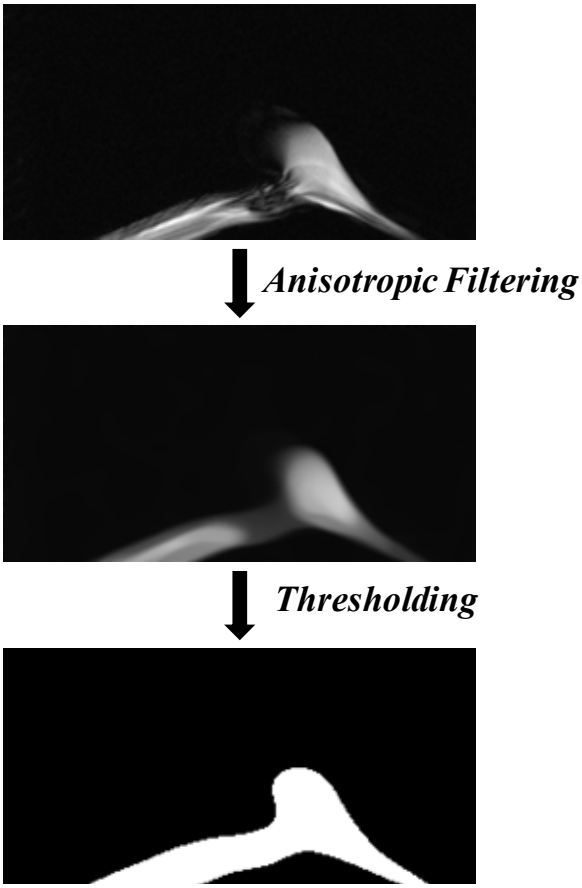

Figure 4.13: Anisotropic diffusion filtering and the generation of segmentation masks

After the segmentation process, it can be seen that the images are clean, and only the velocities within the TCPC flow domain are retained. This process also facilitates an accurate comparison of flow fields between the PC MRI data and the CFD simulations. Once the images are smoothened, segmented, and masked, they are used as inputs to the interpolation algorithm for conversion to a denser volumetric stack with isotropic voxel sizes. The goal of this step is to generate a smooth geometry of the TCPC as well as to reconstruct a dense representation of the flow field.

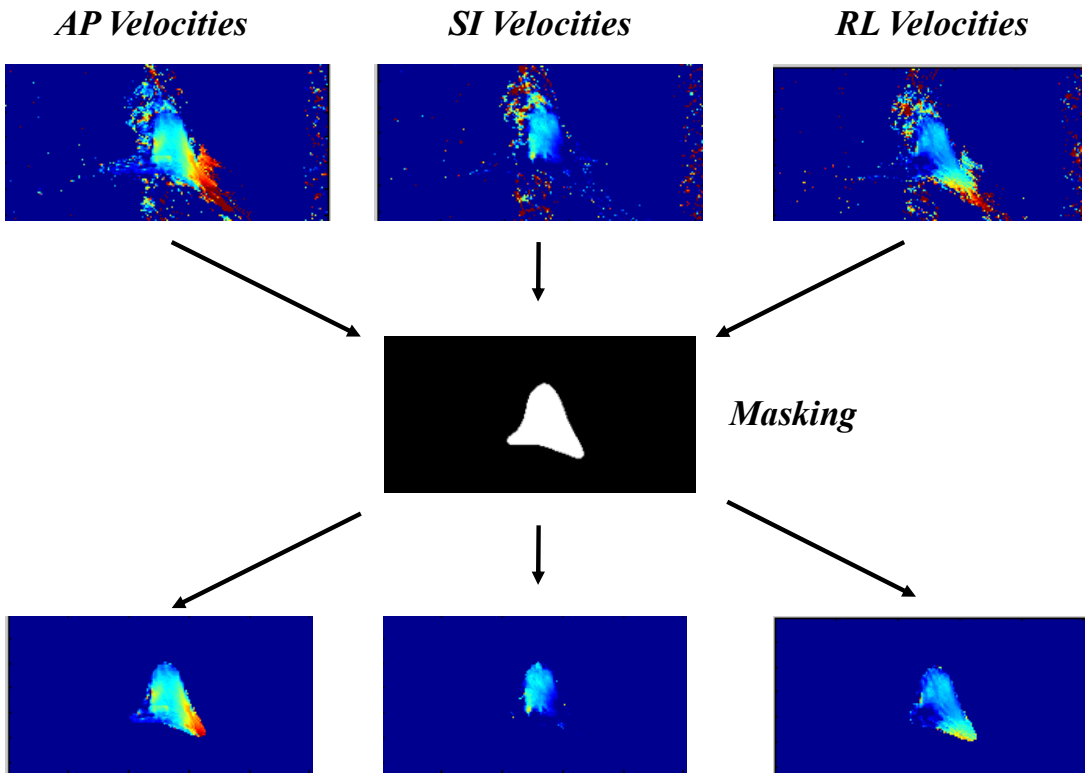

Figure 4.14: The benefit of using segmentation masks on the PC MRI velocity images. As can be observed, only the velocities within the TCPC flow domain are retained, and the noise vectors in the rest of the image are discarded.

4.4.2 Interpolation

As discussed previously in Section 4.2.2, isotropic voxel sizes are needed for reconstructing smooth geometries from serial axial MRI datasets. In addition, a denser volumetric stack is also needed for accurate flow analysis. Hence, the interpolation process in this section consists of two parts: a) Interpolation of the magnitude images of *in vitro* PC MRI acquisition for 3D mesh generation; b) Interpolation of the velocity field for volumetric flow analysis. For a) the process detailed out in section 4.2.2 is directly

applied. Since the TCPC flow domain is already segmented there is no need for running the shape element segmentation algorithm (section 4.2.3). The marching cubes algorithm is applied to establish the connectivity between the different nodes and generating the mesh from the segmented interpolated slices. This Cartesian mesh (Mi) serves two purposes: a) facilitate velocity field analysis; b) enable registration with the CFD mesh.

The interpolation approach proposed by Frakes et al, can also be applied for reconstructing velocity images and has been shown to be more accurate than linear and cubic interpolation methods[81]. However, one of the drawbacks of this approach is that it is a scalar interpolation technique, i.e., each velocity component is interpolated independently and as a consequence the fundamental properties of fluid mechanics, such as incompressibility, are not preserved. This necessitated the development of a newer interpolation approach that combines ACGI with a divergence free interpolation algorithm that preserves the incompressibility property of the velocity field. Details of this approach can be found in Chapter 6 of this thesis. A set of equally distributed control points are initialized within this 3D Cartesian mesh (Mi) generated from the magnitude images. Using the PC MRI velocity measurements, a divergence free interpolating function is determined and is used to interpolate the velocity values at all the mesh points (Mi). This 3D velocity field is used for comparing the overall 3D flow structures between CFD and PC MRI.

4.5 Computational Fluid Dynamic Simulations

CFD simulations are conducted on identical TCPC geometries for comparing the flow fields obtained from PC MRI. The motivation behind doing this is to evaluate the

effectiveness of PC MRI for quantifying, visualizing and reconstructing the complex 3D hemodynamics within the TCPC. In this case, CFD is used as a control for the PC MRI acquisition. CFD simulations are carried using an in-house unstructured, sharp interface immersed boundary method, based upon the structured formulation of Gilmanov and Sotiropoulos[152, 153]. The efficacy, validity, and the accuracy of this methodology is demonstrated in simplified and patient-specific TCPC geometries, confronting the numerical results to controlled *in vitro* experiments. The surface of the original TCPC anatomic geometries (from section 4.2.4) is first discretized using an unstructured triangular mesh and immersed in a uniform, isotropic cartesian grid of resolution h=0.028 D_{IVC} where D_{IVC} is the equivalent hydraulic diameter of the IVC. Inflow and outflow boundary conditions are prescribed identical to those imposed on the *in vitro* PC MRI experiments. Fully-developed velocity profiles are prescribed at all inlet planes. Time accurate simulations are carried out until the running average of the velocity components converged. All subsequent CFD results and discussions are based on the velocity fields obtained from converged CFD running averages.

4.6 PC MRI – CFD Registration

In vitro PC MRI experiments are conducted on a different MRI scanner compared to the original *in vivo* MRI acquisition. Since CFD simulations are based on the *in vivo* geometry, the two sets of data have to be registered so that a point-by-point comparison can be made. This is accomplished in a fully automatic fashion using the "Best Fit Alignment" feature of Geomagic Studio. The 3D geometry reconstructed from *in vitro* PC MRI experiments and the original *in vivo* TCPC geometry are both imported into

Geomagic Studio. The co-ordinate system associated with the *in vitro* PC MRI acquisition is kept as the reference co-ordinate system (alternatively the *in vivo* geometry can be used as the reference frame as well). The "Best Fit Alignment" feature then automatically determines the optimum coordinate transformation matrix for registering the *in vivo* geometry with the *in vitro* geometry. To register the two velocity fields, the

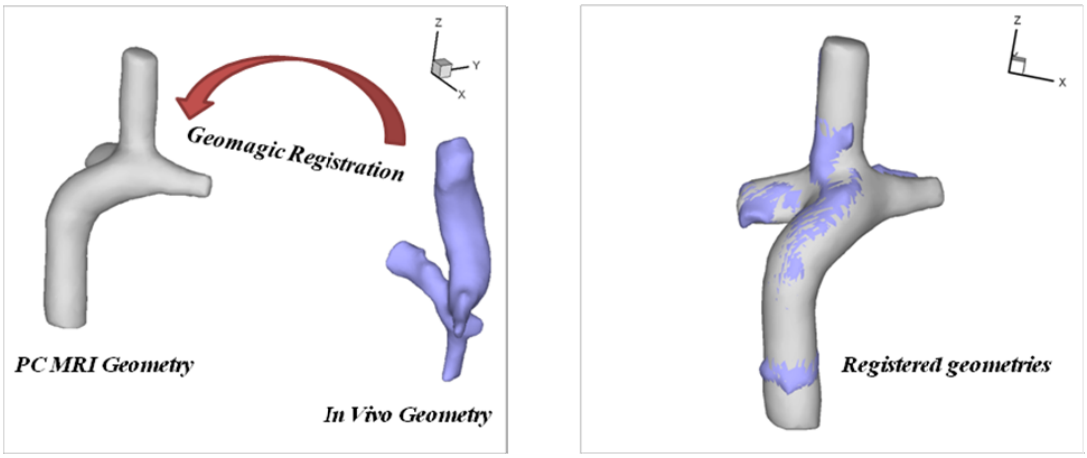

Figure 4.15: The two geometries before and after the automatic registration. As can be observed, a perfect overlap is achieved.

PC MRI velocity fields and the CFD solution are imported into Tecplot 360 (Tecplot, Bellevue, WA) and the transformation matrix is applied to the CFD solution. Once registered, the CFD velocity fields are interpolated onto the PC MRI mesh for a point-wise comparison between PC MRI and CFD velocities. Figure 4.15 shows the two geometries before and after the registration process.

4.7 PC MRI-CFD Comparison

The velocity fields from PC MRI measurements and CFD simulations are imported into Tecplot 360 (Tecplot, Bellevue, WA) for analysis. The transformation

matrix obtained from Geomagic Studio is then applied to register the velocity fields from both the modalities. In order to conduct a quantitative comparison between the two modalities, both CFD and PC MRI velocities have to be available at each node. This is accomplished by interpolating the CFD velocities onto the PC MRI mesh. If the interpolation is performed the other way around, then there will be additional interpolation errors that will be added as the CFD simulation is performed at a much finer resolution compared to the PC MRI acquisition.

Quantitative comparisons between CFD and PC MRI measurements are made by evaluating error metrics. First the error in velocity measurements are evaluated as follows:

Equation 4-6

$$RMS_{Error}(cm/s) = \sqrt{\sum_{FlowDomain}(u_{CFD}-u_{MRI})^2 + (v_{CFD}-v_{MRI})^2 + (w_{CFD}-w_{MRI})^2}$$

$$Normalized\ RMS_{Error}(\%) = \frac{100 * \sqrt{\sum_{FlowDomain}(u_{CFD}-u_{MRI})^2 + (v_{CFD}-v_{MRI})^2 + (w_{CFD}-w_{MRI})^2}}{\sqrt{\sum_{FlowDomain}u_{CFD}^2 + v_{CFD}^2 + w_{CFD}^2}}$$

$$Average\ Error(u)(cm/s) = \frac{\sqrt{\sum_{FlowDomain}(u_{CFD}-u_{MRI})^2}}{N}$$

$$Percentage\ Error\ (\%) = \frac{100 \cdot \sqrt{(\bar{u}_{CFD}-\bar{u}_{MRI})^2}}{\bar{u}_{CFD}}$$

Here, u, v, and w are the RL, AP, and SI components of the velocity fields respectively. These metrics are evaluated in 180 different locations of the registered PC MRI- CFD volumetric vector fields. Characteristics of the error fields are determined using correlation and Bland-Altman analysis for each TCPC model and experimental

condition. In addition to quantitative measures, a thorough qualitative comparison is conducted as well. This includes a comparison of flow profiles at different planes along the TCPC model, flow structures in the form of 3D vector fields. It should be noted that only the PC MRI measurements are used for performing the quantitative assessment.

CHAPTER 5

PC MRI SEGMENTATION METHODS

5.1 Overview

One of the key steps in the post processing of PC MRI data is the segmentation of the vessel of interest. There are several approaches outlined in the literature on automatic segmentation for anatomic applications, but few have been optimized for PC MRI data. There are two important issues that have to be tackled for PC MRI segmentation: a) how to use both magnitude and phase information in the segmentation; b) how to filter out noise from the segmented velocity field in order to accurately analyze the velocity fields. To tackle these issues two new approaches are presented: a) a hybrid magnitude-velocity active contour model, and b) a multidimensional Fuzzy noise filter. The overall approach of this two-step process is described in the Figure 5.1.

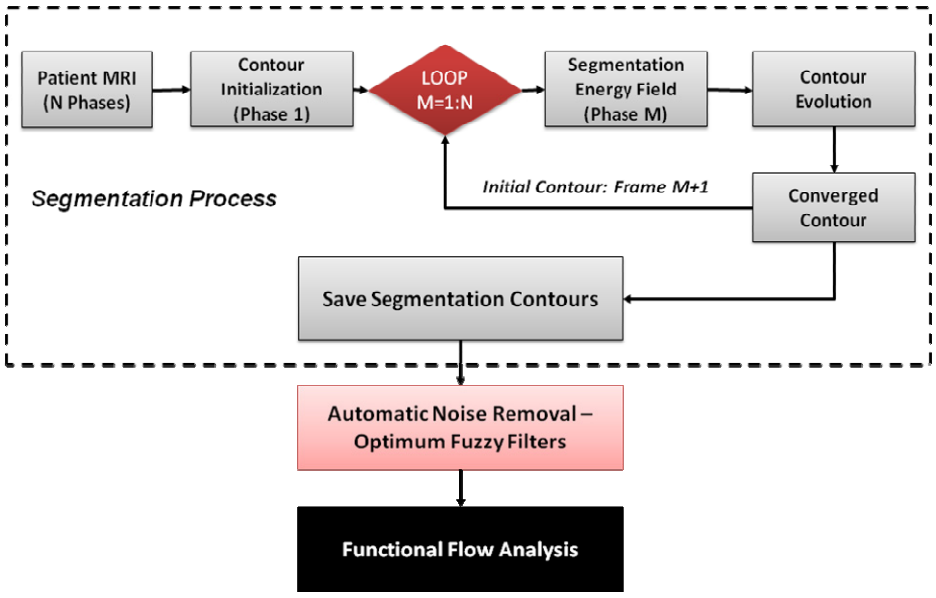

Figure 5.1: Overall segmentation approach

5.2 Active Contour Models (Snakes)

Active contours, or snakes, are curves defined within an image-domain that can move under the influence of external image-based forces as well as internal elastic forces of the contour itself[154]. The classical approach is based on deforming an initial contour $\boldsymbol{C_0}$ towards the boundary of the vessel to be detected. The deformation is obtained via minimization of an energy function designed such that the local minima is on the edge of the vessel. The energy functional is composed of two components: one controls the smoothness of the curve and the other attracts the curve towards the object boundary. Since its first introduction by Kass et al[154], extensive work has been done in using active contours for boundary detection. Applications of active contours range from segmentation to object tracking and shape modeling.

There are two different formulations of active contours: a) Parametric or explicit active contours, which use Lagrangian approaches for contour evolution; b) Level-set or implicit active contours, which use Eulerian approaches for contour evolution. Each has its own benefits, although level-set based methods are more robust and can handle topological changes in the image easily. Since the presented application is primarily 2D (single plane PC MRI), both approaches work equally well. However, if the segmentation has to be performed in 3D, then implicit active contour models are preferred as no explicit parameterization is necessary. Both the formulations will be discussed in the following sections.

5.2.1 Parametric Active Contours

A parametric active contour is defined as a curve $\boldsymbol{C}(s) = \{x(s), y(s)\}$ where $s \in (0,$

S) and **S** is the length of the curve that evolves in the image domain so as to minimize the energy functional given by:

$$E = \int_0^S \frac{1}{2}[\alpha |C'(s)|^2 + \beta |C''(s)|]^2 + E_{ext}(C(s))ds \qquad \text{Equation 5-1}$$

Here α and β are weights that control the contour's tension and rigidity respectively, while ***C'(s)*** and ***C''(s)*** are the first and second derivatives of the curve with respect to the parameter 's'. The parameter '**s'** is used to define the contour in any arbitrary dimension. The most common choice for '**s'** is the arc length or the distance between two contour mesh points. The external energy $\boldsymbol{E_{ext}}$ (**s**) is derived from the image and is a discrete energy field that guides the contour in the image domain. Various external energy functions can be generated in order to guide the contour to the desired structures of interest. In segmentation applications, where the objective is to detect an object boundary, the most commonly used energy functional is the gradient magnitude of the image $-|\nabla I\ (x, y)|^2$ or other variants of the image gradient. The Euler-Lagrange equation minimizing Equation 5-1 is as follows:

$$\alpha C''(s) - \beta C''''(s) - \nabla E_{ext} = 0 \qquad \text{Equation 5-2}$$

This equation can be viewed as an energy balance equation $\boldsymbol{E_{int}} + \boldsymbol{E_{ext}}=0$, where $\boldsymbol{E_{int}}= \alpha\mathbf{C}''(s) - \beta\mathbf{C}''''(s)$, and $\boldsymbol{E_{ext}}= -\nabla \boldsymbol{I}$, where I is the image. $\boldsymbol{E_{int}}$ is the internal energy function controlling the rigidity and elasticity of the contour, and $\boldsymbol{E_{ext}}$ is the external energy function guiding the contour to the desired features of interest. Given an initial curve $\boldsymbol{C_0(s)}$, a time dependent evolution criteria can be established based on the Euler

equation:

$$C_t(s,t) = \alpha C''(s,t) - \beta C''''(s,t) - \nabla E_{ext} \qquad \text{Equation 5-3}$$

When the contour stabilizes, the left side of the equation vanishes and the desired vessel is segmented. The above equation is discretized and solved iteratively until a convergent solution is obtained.

5.2.1.1 Gradient Vector Flow

Parametric active contours are drawn towards the edge of the vessel by potential energy functions which are typically the negative gradient of some underlying potential function ($\boldsymbol{E_{Ext}}$). Any desired forces can be included into the model via this external energy term. Along these lines, there are two primary deficiencies associated with the implementation of the active contour algorithm in the traditional sense using just the image gradient as the energy function: 1.) limited capture range, i.e., the initialized contour must be close to the object to be segmented or it will converge to the wrong result; 2.) inability of the snake to identify and pass through boundary concavities. These weaknesses prevent the application of the active contour approach for a wider variety of segmentation problems. To address this issue and increase the robustness of parametric active contours, Xu and Prince first introduced the gradient vector flow (GVF) approach[155]. These energy fields are dense vector fields, derived from images by minimizing an energy functional in a variational framework. The minimization is accomplished by solving a pair of decoupled partial differential equations that diffuse the gradient vector fields of a gray level edge map derived from the image. Such an implementation is also known as a GVF snake, and is different from other active contour

formulations as it is directly specified from the energy balance equation. Particular advantages of the GVF approach are: a) insensitivity to contour initialization, and b) ability to move into boundary concavities.

The GVF field is a vector field $\boldsymbol{E}(x, y)=\{u(x, y), v(x,y)\}$ that minimizes the following energy functional:

$$\varepsilon = \iint \mu(u_x^2 + u_y^2 + v_x^2 + v_y^2) + |\nabla f|^2 |E - \nabla f|^2 \, dxdy \qquad \text{Equation 5-4}$$

Here u_x, u_y, v_x, v_y are spatial derivatives of the components of the GVF energy field, and $f(x,y) = -\boldsymbol{E}_{Ext}(x, y)$ is a static energy field computed directly from the image. This variational formulation allows for the vector field E(x, y) to be smooth in regions where there is no useful image data especially, where $|\nabla \mathbf{f}|$ is small. When $|\nabla \mathbf{f}|$ is small, the second term vanishes, and the first term dominates resulting in a smoothly varying energy field. In regions close to the edges, the second term dominates since $|\nabla \mathbf{f}|$ is large, and the resulting energy field $\boldsymbol{\varepsilon}(x, y)$ becomes $|\nabla \mathbf{f}|$ in those regions. Consequently, the final energy field is equal to the gradient of the static energy field near the structures of interest, but is non-zero in homogenous regions far away from the object. Hence the energy field is extended to regions far away from the object itself. The parameter $\boldsymbol{\mu}$ takes a value in the range of (0, 1) and governs the tradeoff between the first and second terms of the equation. If the original image is noisy, then a higher value of $\boldsymbol{\mu}$ is used for a smoother flow field, while a smaller value is used if more emphasis is to be laid out on $|\nabla \mathbf{f}|$. Using calculus of variations, the above equation can be analytically solved to yield the following set of partial differential equations:

$$\mu\nabla^2 u-(u-f_x)(f_x^{\,2}+f_y^{\,2})=0$$
$$\mu\nabla^2 v-(v-f_y)(f_x^{\,2}+f_y^{\,2})=0$$

Equation 5-5

These equations are decoupled and can be solved iteratively by artificially imposing time dependence into the equations, yielding the following set of evolution schemes:

$$u_t(x,y,t)=\mu\nabla^2 u-(u-f_x)(f_x^{\,2}+f_y^{\,2})$$
$$v_t(x,y,t)=\mu\nabla^2 v-(v-f_y)(f_x^{\,2}+f_y^{\,2})$$

Equation 5-6

When u(x, y) and v(x, y) stabilize, the left side of the equation disappears (or becomes very small) resulting in the desired GVF field. The equations are discretized as:

$$u_{i,j}^{n+1}=(1-b_{i,j}\Delta t)u_{i,j}^{n}+r(u_{i+1,j}^{n}+u_{i,j+1}^{n}+u_{i-1,j}^{n}+u_{i,j-1}^{n}-4u_{i,j}^{n})+c_{i,j}^{1}\Delta tv$$
$$v_{i,j}^{n+1}=(1-b_{i,j}\Delta t)v_{i,j}^{n}+r(v_{i+1,j}^{n}+v_{i,j+1}^{n}+v_{i-1,j}^{n}+v_{i,j-1}^{n}-4v_{i,j}^{n})+c_{i,j}^{2}\Delta t$$
$$r=\frac{\mu\,\Delta t}{\Delta x\Delta y}$$
$$b(x,y)=f_x(x,y)^2+f_y(x,y)^2$$
$$c^1(x,y)=b(x,y)\,f_x(x,y)$$
$$c^2(x,y)=b(x,y)\,f_y(x,y)$$

Equation 5-7

Here i, j, and n are the indices that correspond to x, y, and t respectively, Δx and Δy are the pixel spacings in the x and y directions, and Δt is the time-step for each iteration. The benefit of gradient vector flow is evident in Figure 5.2 and Figure 5.3 for synthetic images generated in Matlab (Mathworks, Natick, MA). If just the gradient magnitude is used, the resulting energy field is localized very close to the image edges. This limits the capture range of the active contour in situations where the object has boundary concavities. On the other hand if the GVF algorithm is applied, the capture

range is automatically increased to regions far away from the object itself.

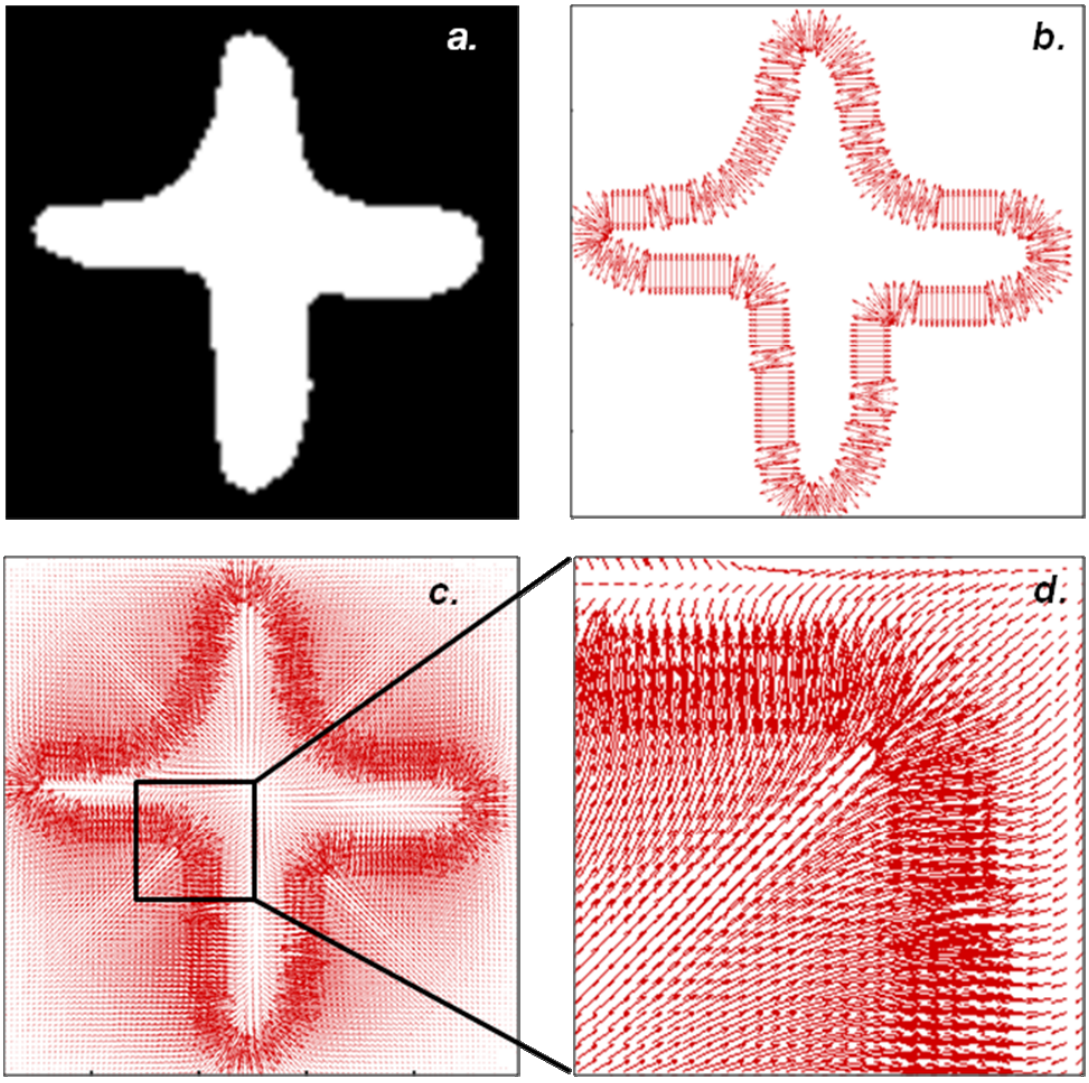

Figure 5.2: The benefit of using the gradient vector flow algorithm: a) Synthetic binary image; b) Gradient magnitude energy field; c) Gradient vector flow energy field; d) Close up view of the GVF energy field

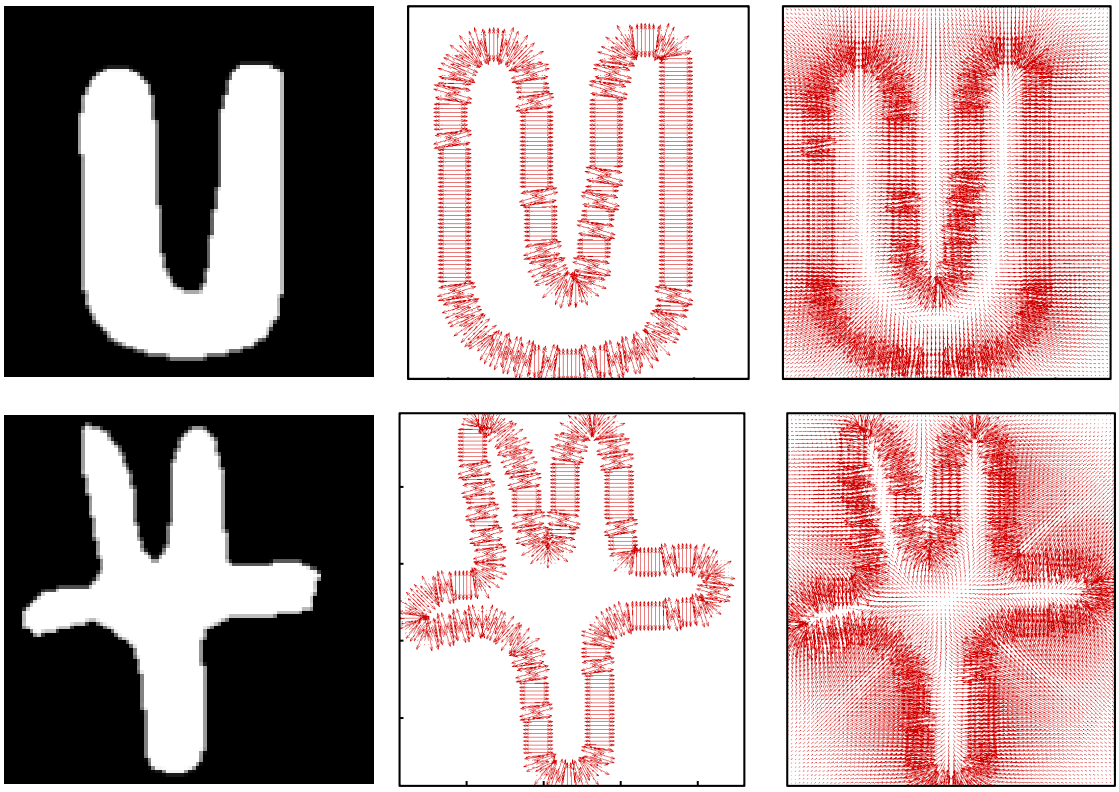

a. b. c.

Figure 5.3: Some more examples of Gradient Vector Flow Images: a) Synthetically generated shape; b) Gradient magnitude flow; c) Gradient Vector Flow. As can be observed the energy field is diffused to regions far away from the object itself.

5.2.1.2 Implementation of Parametric Active Contours

The implementation of parametric active contours consists of the following steps: a) Initialization; b) Evolution; c) Resampling; d) Convergence. In the first step, the user first initializes a contour by drawing around the object or structure of interest. If the algorithm needs to be fully automated, then an arbitrary contour can be initialized within the image. This contour is sampled at equal intervals to maintain the discrete spacing between the points at less than 1 pixel. The locations of these points are saved in a

periodic data structure, with the first and last point being the same. It should be noted that as the contour ***C(s)*** evolves, additional parameterization issues are introduced because the contour length (ds) changes as Equation 5-3 is solved. The first step in solving this problem is to change the formulation from an implicit parameterization by the arc length parameter s Є (0, **S**), to an explicit version where the parameterization is not time-dependent. A new parameterization in the form of p Є (0, 1) is introduced. To make this change correctly, recall the definition of arc length:

$$S = \oint_{C(p)} \|Cp\| dp = \oint_{C(s)} ds \quad \Rightarrow \quad \|Cp\| dp = ds \qquad \text{Equation 5-8}$$

Having made this change, the contour is re-parameterized as ***C(p)***={x(p), y(p)} and Equation 5-3 is re-written as:

$$\begin{aligned} C_t &= \alpha\kappa \mathrm{N} + E_{ext} \\ \kappa &= \frac{x_p\, y_{pp} - y_p\, x_{pp}}{\left(x_p^2 + y_p^2\right)^{3/2}} \\ \mathrm{N} &= (-y_p, x_p) \end{aligned} \qquad \text{Equation 5-9}$$

Here, x_p and y_p are first derivatives; x_{pp} and y_{pp} are the second derivatives of the contour with respect to the parameter ‘p’. The central differencing approach is used to evaluate these derivatives as follows:

$$x_p = \frac{x(p+1) - x(p-1)}{2\Delta p}$$
$$y_p = \frac{y(p+1) - y(p-1)}{2\Delta p}$$
$$x_{pp} = \frac{x(p+1) - 2x(p) + x(p-1)}{\Delta p^2}$$
$$y_{pp} = \frac{y(p+1) - 2y(p) + y(p-1)}{\Delta p^2}$$

Equation 5-10

The discretized evolution equation now becomes:

$$C(t+1) = C(t) + \Delta t(\alpha\kappa \cdot \mathrm{N} + E_{Ext}(x(p), y(p)))$$
$$\Delta t = \Delta p / 25$$

Equation 5-11

After five iterations, the contour is resampled, interpolated, and reparameterized using the Spline function. This is necessary to maintain the contour's integrity and stability and the accuracy of the derivatives over the entire evolution process. Equation 5-11 is iteratively solved until ||C(t+1)-C(t)|| is less than some predetermined error value. Figure 5.4 shows the segmentation results of the active contour model applied on the binary shape shown in Figure 5.2. The classic active contour implementation fails in this case as the initialized contour is far away from the object, and there are no forces pulling the object towards the object. The GVF algorithm is beneficial in this regard, where the contour passes through boundary concavities and successfully extracts the shape of the object. An alternative implementation is to apply a constant force which uniformly shrinks the contour, and the external energy is used to stop the contour itself. This is the general idea behind the implicit active contour implementation, which is discussed in the following sections.

a. b. c.

Figure 5.4: Parametric Implementation of the active contour algorithm a) initial contour (b) Converged solution without GVF (c) Converged solution with GVF

5.2.2 Implicit Active Contour Models

The parametric active contour approach suffers from the following drawbacks:

a.) The time-step required to achieve a stable convergence of the contour evolution is impractically small.

b.) As the contour evolves, the discrete marker points tend to clump around regions of high curvature that may cause numerical instability. This requires regular re-gridding, re-parameterization, and interpolation of the curve to maintain stability.

c.) As the parametric approach is primarily Lagrangian, there is inherent difficulty in the handling of topological changes associated when the object or vessel of interest changes morphology. As the contour splits or merges, ad hoc techniques are required to make the parametric approach work.

d.) A 3D implementation of the algorithm is quite complicated and requires

significant amount of computation for representing the different 3D shapes and objects.

For 2D segmentation of imagery with a single object of interest, Lagrangian approaches are sufficient. For this reason, a 2D version of the parametric active contour implementation works fine for single slice MRI applications. However, if the segmentation has to be performed in 3D (as needed and explained in Chapter 6), then a more robust approach is preferred that can handle topological changes with ease. Osher and Sethian proposed the level-set approach for describing contour motion set in an Eulerian framework (written in a fixed coordinate system)[156]. Advantages of such an approach are as follows:

- The underlying mesh points are fixed, and do not move, which circumvents the stability problems associated with Lagrangian approximates.
- Topological changes are handled naturally and automatically
- The moving front is captured regardless of whether it contains cusps or sharp corners
- There is no need for interpolation as the underlying implicit level-set function is continuous and can be used to evaluate the level-set function at any grid resolution.

The central idea of the level-set formulation is to implicitly represent the contour as the zero level-set of an underlying function $\boldsymbol{\varphi}$. The motion of this evolving function $\boldsymbol{\varphi}$ is determined from a partial differential equation in a higher dimension that permits cusps, sharp corners, and changes in topology in the zero level-set describing the interface. Since its introduction, the level-set approach has been used to compute and analyze a broad spectrum of physical and mathematical phenomena in image analysis

applications, combustion, shape recognition, and fluid mechanics. The generality of this approach makes it very attractive, especially for problems in 3 dimensions, and problems with complex changes in topology.

5.2.2.1 Level Set Theory

Let the curve to be tracked, ***C_0 (C(t=0))***, be a closed nonintersecting curve, moving in a direction normal to itself with speed ***F***. Shown in Figure 5.5 is the evolution of an active contour with a constant force ***F***. Assume $\varphi(\mathbf{x}, t)$, $\mathbf{x} \in R^N$ is a scalar function such that at time *t*, the zero level-set of the function is the curve ***C(t)***. This scalar function $\varphi(\mathbf{x}, t)$, is typically defined as a distance function such that:

$$\phi(\mathbf{x}, t = 0) = \pm d \qquad \text{Equation 5-12}$$

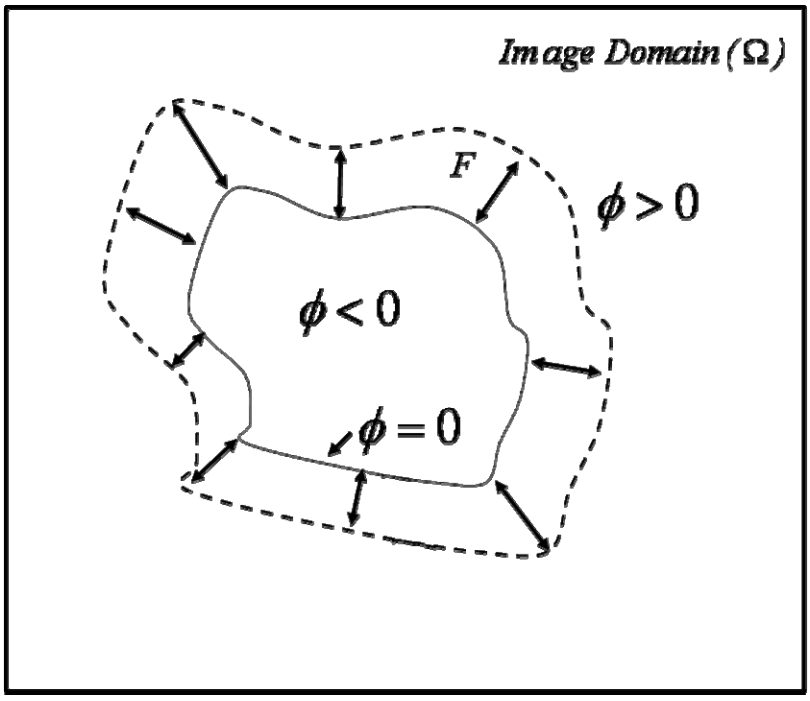

Figure 5.5: Shown is the evolution of the zero level-set with a constant speed function **'F'**

Here *d* is the distance of any point **x** from the initial contour $\boldsymbol{C_0}$, and the +(-) choice is chosen for any point outside (inside) the contour. Thus the initial level-set function φ(**x**, t=0), $R^N \rightarrow R$, has the property:

$$C_0 = (\mathbf{x} \mid \phi(\mathbf{x}, t = 0) = 0) \qquad \text{Equation 5-13}$$

The goal is to formulate an equation for the evolution of this propagating interface φ(**x**, t), which contains the embedded motion of ***C(t)*** as the zero level-set { **x**(t) | φ(**x**, t) = 0}. Let $\mathbf{x}_t$, t Є [0, ∞) be the path of a point on the propagating front. That is, **x** (t=0) is a point on the initial front $\boldsymbol{C_0}$, and $\mathbf{x_t}=\boldsymbol{F}(\mathbf{x},t)$ with the vector $\mathbf{x_t}$ is the particle trajectory normal to the front at **x(t)**. Since the evolving surface φ(**x (t)**, t) is always zero on the propagating surface, then according to Mulder and Sethian[157]:

$$\phi(\mathbf{x}(t), t) = 0 \qquad \text{Equation 5-14}$$

Differentiating this function with respect to time and applying the chain rule, we get:

$$\phi_t + \sum_{i=1}^{N} \phi_{x_i} x_{i_t} = 0 \qquad \text{Equation 5-15}$$

Here N is the dimension of **x**, and x_i is the i^{th} component of **x**. If x_{it} is to be considered the speed at which each component of the contour moves, then $(x_{1t}, x_{2t}, .., x_{Nt})=(f_1, f_2, .., f_N) = \boldsymbol{F}(\mathbf{x}, t)$. The equation simplifies to:

$$\phi_t + F \mid \nabla\phi \mid = 0 \qquad \text{Equation 5-16}$$

Such a formulation is also known as the Hamilton-Jacobi "type" equation because for certain forms of the speed function ***F***, the Hamilton-Jacobi equation is obtained.

5.2.2.2 Level Set Approach to Image Segmentation

In order to adapt the level-set framework to image segmentation, image information needs to be introduced into the level-set equation. This is accomplished via the speed term $\boldsymbol{F}$. Since the goal is to extract the object's shape, the force should vanish in the vicinity of the object. To accomplish this, a force field is generated such that it comprises two terms: a) An image derived force $\boldsymbol{F_I}$ identical to the external energy function $\boldsymbol{E_{Ext}}$ in the explicit parametric active contour equation; b) An internal force term $\boldsymbol{F_G}$ based on the geometry of the propagating surface. If **I(x, y)** is the image of interest, one external force function that can be constructed is as follows:

$$F_I(x,y) = \frac{1}{1+\left|\nabla I(x,y)\right|^2} \qquad \text{Equation 5-17}$$

In such a force field, the magnitude is small closer to the vessel boundaries and large away from the object edges. In order to remove the effect of noise from this system, the image can be smoothened prior to the gradient operation. Thus, the new level-set evolution function can be written as:

$$\phi_t + F_I(x,y)\,|\nabla\phi|\,(F_G + \alpha) = 0 \qquad \text{Equation 5-18}$$

Here, the force term consists of a geometric term $\boldsymbol{F_G}$ that controls the morphology of the contour that helps to maintain the desired smoothness, and α is a constant speed term similar to the balloon force term in explicit parametric active contour models (Equation 5-3). The entire force equation is weighted by the image-based term that ensures that the force field has a small value close to the object edge. The value of α can be chosen according to the necessary speed associated with the curve evolution. $\boldsymbol{F_G}$ is the

internal force of the level-set function and is usually set to be the curvature of the propagating front.

$$F_G = \kappa = div\left(\frac{\nabla\phi}{|\nabla\phi|}\right) = \frac{\phi_{xx}\phi_y^2 - 2\phi_x\phi_y\phi_{xy} + \phi_{yy}\phi_x^2}{\left(\phi_x^2 + \phi_y^2\right)^{\frac{3}{2}}} \qquad \text{Equation 5-19}$$

Such a formulation is similar to the implicit geodesic active contour model proposed by Casseles and Sapiro[158], where the contour ***C(t)*** is embedded into an energy functional inspired by the explicit active contour model, and takes the form:

$$\phi_t + |\nabla\phi|(div\left(F_I(x,y)\frac{\nabla\phi}{|\nabla\phi|}\right) + \alpha F_I(x,y)) = 0 \qquad \text{Equation 5-20}$$

It should be noted that the image-based speed terms ($\boldsymbol{F_I}$) only have meaning on the zero level-set, and do not hold true for the entire level-set function. Since all the level-sets have to be evolved simultaneously while still maintaining the form of the signed distance function, a force field has to be designed for each level-set in the domain. Therefore, the image based function $\boldsymbol{F_I}$ has to be *extended* to all possible level-sets. There are several methods discussed in the literature for constructing the extensions of velocities on the level-set domains[156, 158-161]. One of the most common approaches is the one proposed by Malladi et al[161]:

1. For each level-set function on a specific grid point in the image P (φ=C), the closest point Q on the zero level-set function (φ=0) is determined.
2. The image based external velocity for the point P is set to be the same as the value on point Q.

Such an approach is effective, but results in prohibitively large computation times. Another problem is that discontinuous velocity extensions are formed in regions far away from the zero level-set. One alternative is to re-initialize the level-set function after every fixed set of iterations by re-computing the distance function at every grid point. This adds further computational complexity of $O(N^3)$ assuming there are N points in each co-ordinate direction plus N points on the zero level-set. Several approaches have been proposed such as the Narrowband extension which significantly reduces the computation time[159, 160]. However for a robust implementation and to ensure stable convergence of the active contour, a curve evolution technique without this re-initialization step is preferred. Towards this extent, a new approach is proposed by Li and Fox where the signed distance function is maintained over the entire course of contour evolution and does not require the re-initialization step during the contour evolution[162].

5.2.2.3 Adopted Approach: Level Set Implementation Without Re-Initialization[162]

The re-initialization step associated with the level-set evolution can be avoided, if the level-set function resembles the signed distance function at every step of the evolution. In Euclidian space, the signed distance function is differentiable everywhere and satisfies the eikonal equation:

$$\left|\nabla \phi\right| = 1 \qquad \text{Equation 5-21}$$

Naturally, any function φ that satisfies this equation is the distance function plus a constant and hence the following integral is defined for characterizing how close the function φ is to a signed distance function:

$$P(\phi) = \int_{\Omega} \frac{1}{2}(|\nabla\phi| - 1)^2 \, dxdy \qquad \text{Equation 5-22}$$

In order to govern the tradeoff between the external velocities obtained from the image and the above described penalizing equation, the following variational formulation is proposed:

$$\varepsilon(\phi) = \mu P(\phi) + \varepsilon_M(\phi) \qquad \text{Equation 5-23}$$

where μ is the parameter governing the effect of penalizing the deviation of φ from a signed distance function, and $\varepsilon_M(\varphi)$ is the external force function ($\boldsymbol{F_I}$) governing the motion of the zero level-set function. Accordingly, P(φ) can be thought of as the internal energy and $\varepsilon_M(\varphi)$ as the external energy, respectively. Taking the first variation of the functional ε results in the following gradient flow equation:

$$\phi_t = -\frac{\partial\varepsilon}{\partial\phi} \qquad \text{Equation 5-24}$$

In order to incorporate the image-based force function $\boldsymbol{F_I}$ into such a level-set formulation, a new external energy function is defined for the above evolution equation:

$$\varepsilon_{F_I,\alpha,\nu} = \alpha L_{F_I}(\phi) + \nu A_{F_I}(\phi) \qquad \text{Equation 5-25}$$

Here α >0 and ν are constants and the terms L(φ) and A(φ) are defined as follows:

$$L_{F_I}(\phi) = \int_{\Omega} F_I \delta(\phi)|\nabla\phi| \, dx \, dy$$

and $\qquad \text{Equation 5-26}$

$$A_{F_I}(\phi) = \int_{\Omega} F_I H(-\phi) \, dx \, dy$$

Geometrically, the term L(φ) corresponds to the external energy function integrated over

the length of the zero level-set curve, and A(φ) corresponds the external energy function integrated over the inner region of the zero level-set contour (or over the area of the region associated with the negative level-set function). The parameter α has the same meaning as in Equation 5-20, while ν controls the speed with which the contour evolves. If the initial contour is outside the object of interest, then the value of ν is set to be a positive value. On the opposite, if the initial contour is set inside the object of interest then ν is set to a negative value. H (φ) is the Heaviside or the step function, and δ (φ) is the Dirac delta function. Therefore, the new total energy functional can be defined as:

$$\varepsilon(\phi) = \mu P(\phi) + \varepsilon_{F_I,\alpha,\nu}(\phi) \qquad \text{Equation 5-27}$$

Using calculus of variations, the steepest descent of the minimization of this functional is determined to be:

$$\phi_t = \mu\left(\Delta\phi - div\left(\frac{\nabla\phi}{|\nabla\phi|}\right)\right) + \alpha\delta(\phi)div\left(F_I\frac{\nabla\phi}{|\nabla\phi|}\right) + \nu F_I\delta(\phi) \qquad \text{Equation 5-28}$$

This is the level-set formulation without re-initialization as proposed by Li et al., and is the primary approach adopted in this thesis for the level-set implementation of active contours.

5.2.2.4 Numerical Implementation of the Level Set Active Contour Method

Step 1: A contour is first initialized and the corresponding level-set function is generated as follows:

$$\phi_0(x,y) = \begin{cases} -\eta & (x,y) \in \Omega_0 - \partial\Omega_0 \\ 0 & (x,y) \in \partial\Omega_0 \\ \eta & (x,y) \in \Omega - \Omega_0 \end{cases}$$ Equation 5-29

Step 2: The constants (μ, α, and ν) are initialized to be 0.04, 5, and 3.0 respectively. These values can be changed depending upon the application.

Step 3: The external energy function is evaluated from the given image using Equation 5-17.

Step 4: The Dirac delta function with support ε is defined as follows:

$$\delta(x) = \begin{cases} 0 & |x| > \varepsilon \\ \frac{1}{2\varepsilon}\left[1 + cos\left(\frac{\pi x}{\varepsilon}\right)\right] & |x| < \varepsilon \end{cases}$$ Equation 5-30

Step 5: Equation 5-28 is solved using standard central differencing schemes, and the level-set is evolved according to the following equation:

$$\phi_{i,j}^{k+1} = \phi_{i,j}^{k} + \tau\, L(\phi_{i,j}^{k})$$ Equation 5-31

Here $L(\phi_{i,j}^{k})$ is the right side of Equation 5-28, and τ is the selected time-step. The typical time-step requirement is similar to the one from the GVF algorithm and the constraint is that $\mu\tau < 0.25$. There is clearly a tradeoff between the size of the time-step used and the accuracy with which the boundary is detected, and for this reason a small time-step value is preferred. Figure 5.7 shows the evolution of the contour on a synthetic image with two objects in the image. Figure 5.6 shows the difference between the parametric active contour implementation and the level-set implementation. Notice that the change of topology is handled easily by the level-set approach, while that is not the

case for parametric approach, where the splitting is not handled naturally by the active contour algorithm. Figure 5.6 shows a comparison of the level-set with the parametric implementation.

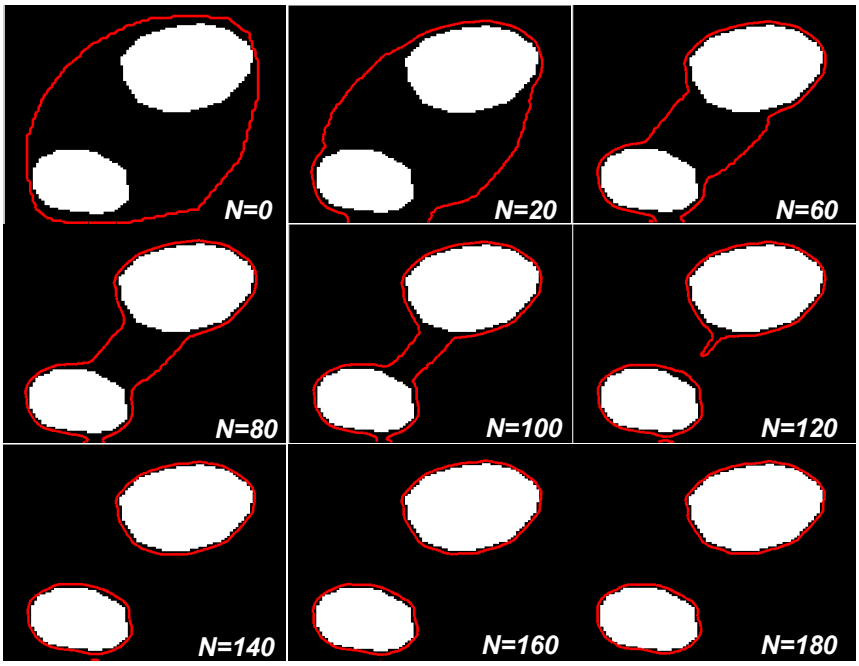

Figure 5.7: The evolution of the active contour over different iterations.

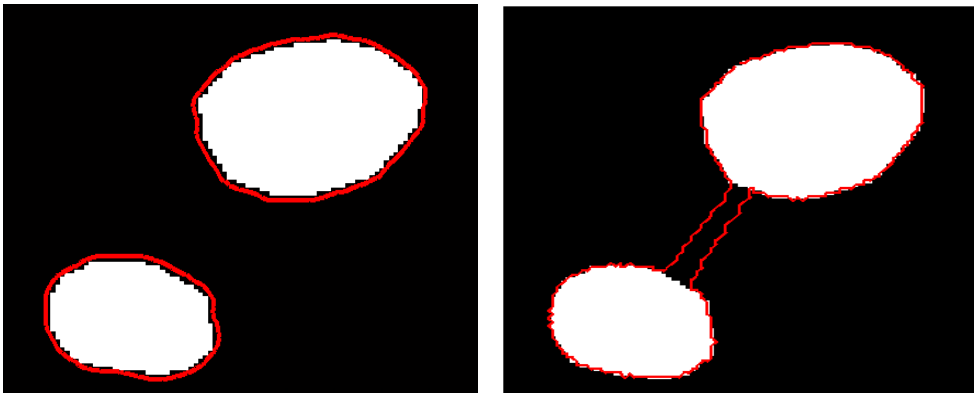

Figure 5.6: Comparison of the parametric active contour approach (right) and the level-set algorithm (left)

5.2.3 Summary of the Active Contour Approach

In section 5.2, two image segmentation approaches using the active contour model are presented namely a) the explicit active contour formulation (parametric); b) the implicit active contour formulation (level-sets). Although, the objective of both the approaches is the same, i.e. to propagate a contour in a desired direction, the underlying physics is significantly different. In the parametric approach, the contour is explicitly defined and evolved according to the active contour equation of motion. The benefits of this approach are: a) Computational efficiency; b) Image based information can be easily incorporated into the model. In the implicit approach, the contour is represented as the zero level-set of an underlying distance function. The active contour model of motion is then applied to all the level-sets in the specified model. Implicit active contours present several advantages over the explicit approach, some of which are:

1) The formulation is set in an Eulerian framework, and hence the stability issues associated with Lagrangian implementations are avoided
2) There is no need for re-parameterization as the underlying level-set function is continuous and can be evaluated at each discrete grid location
3) Changes in contour topology are handled naturally without the need for explicit splitting and merging strategies
4) The moving front is captured regardless of the presence of cusps and corners
5) A multidimensional implementation is straightforward and does not require complex parameterization for the multidimensional surface.

Given these benefits, the level-set approach is chosen as the favorable implementation for segmentation of PC MRI data.

5.3 Active Contours for PC MRI Segmentation

The segmentation tools developed in the previous section can be applied for object detection in any imaging modality. Since a PC MRI acquisition comprises of magnitude and phase images, a modified approach is needed in order to fully utilize all available information in the segmentation process. The overall approach is shown in Figure 5.8.

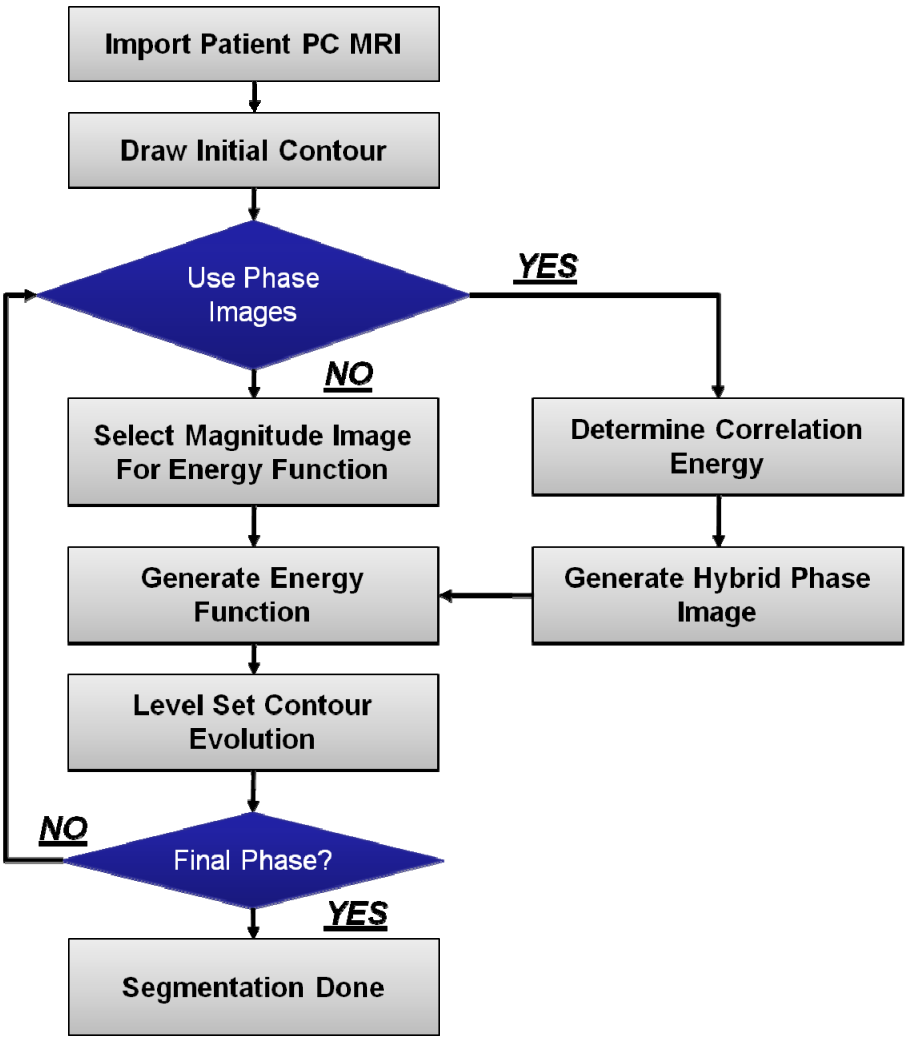

Figure 5.8: Flow chart demonstrating the automatic segmentation of PC MRI data

5.3.1 Incorporation of Phase Velocity Images in the Active Contour Model

Active contour models using just magnitude images have previously been shown to underestimate the vessel sizes in PC MRI applications[96], and hence the phase images have to be incorporated into the segmentation process. Compared to anatomic imaging data, such as MRI and computed tomography (CT), very little work has been done on the segmentation of phase velocity data. Previous researchers have approached this problem in the following ways: a) Generate external energy functions directly from phase images and use them in the active contour algorithm[96, 98]; b) Use pulsatility of the velocity field to determine the pixels that are part of the same blood vessel[163]; c) Incorporate the phase images in a Markov random field framework as *a priori* information for vascular segmentation of PC MRI[94, 95]. These techniques have their own strengths and weaknesses. For example, if only phase images are used in the active contour model, then problems are experienced when there is little or no flow going through the vessel. The pulsatility based approach alleviates this problem to a certain degree, although it fails to capture the changes in vessel morphology over the cardiac cycle as a single segmentation mask is generated for an entire cardiac cycle. Statistical approaches such as those proposed by Chung et al[94, 95], are powerful for reconstructing 3D geometries but do not necessarily capture the entire velocity field.

To alleviate some of these issues, and fully exploit the robustness and effectiveness of implicit active contour models, a novel approach is presented here that utilizes both magnitude and phase images for PC MRI segmentation. The algorithm is based on the assumption that the velocity-time profiles of pixels within the blood vessel of interest are highly correlated. Recall that the cross correlation between two signals

X(n) and Y(n) of length 'N' is defined as:

$$P(X(n),Y(n)) = \frac{\sum_{n=1:N}(X(n)-\overline{X})(Y(n)-\overline{Y})}{\sum_{n=1:N}(X(n)-\overline{X})^2 \sum_{n=1:N}(Y(n)-\overline{Y})^2} \qquad \text{Equation 5-32}$$

If each pixel in the PC MRI image is thought of as a time periodic signal, then:

- It should be possible to cross-correlate the velocity signals of each pixel with every other pixel in the image
- The correlation value should be high between pixels of the same vessel and low in situations when the two pixels are from different structures

This idea can be used to generate a cross correlation energy field for the entire phase velocity image. To implement this idea, a reference waveform within the blood vessel of interest is required. Recall that the first step in the segmentation process (Figure 5.8), the user first draws a contour to select the vessel of interest. Since this is a rough initial approximation of the vessel, all pixels within this region can be considered as reference waveforms. Let the number of pixels within this manually selected region be **M**, and the reference waveforms be denoted as **R**. A cross correlation energy map between the reference waveform and any velocity pixel **V**(n) can then be created as follows:

$$P(\mathbf{R}(m,n),\mathbf{V}(n)) = \sum_{m=1:M} \frac{\sum_{n=1:N}(R(m,n)-\overline{R(m)})(V(n)-\overline{V})}{\sum_{n=1:N}(R(m,n)-\overline{R(m)})^2 \sum_{n=1:N}(V(n)-\overline{V})^2} \qquad \text{Equation 5-33}$$

The desired feature of the cross correlation energy matrix is that it should be high inside the blood vessel to be segmented and low elsewhere.

Although the cross correlation map is powerful in isolating the vessel of interest, it cannot be used by itself as a segmentation mask especially since it is static image. Since blood vessels move and change in size during the cardiac cycle, a dynamic energy function is preferred. For this purpose, a hybrid velocity magnitude image is created by multiplying the normalized cross correlation map with the magnitude image as follows:

$$H(x,y) = \frac{P(x,y)}{P_{max}(x,y)} I_{Mag}(x,y) \qquad \text{Equation 5-34}$$

Figure 5.9 shows the original magnitude image, the cross correlation energy matrix, and the hybrid image used for segmenting the SVC and IVC from PC MRI respectively.

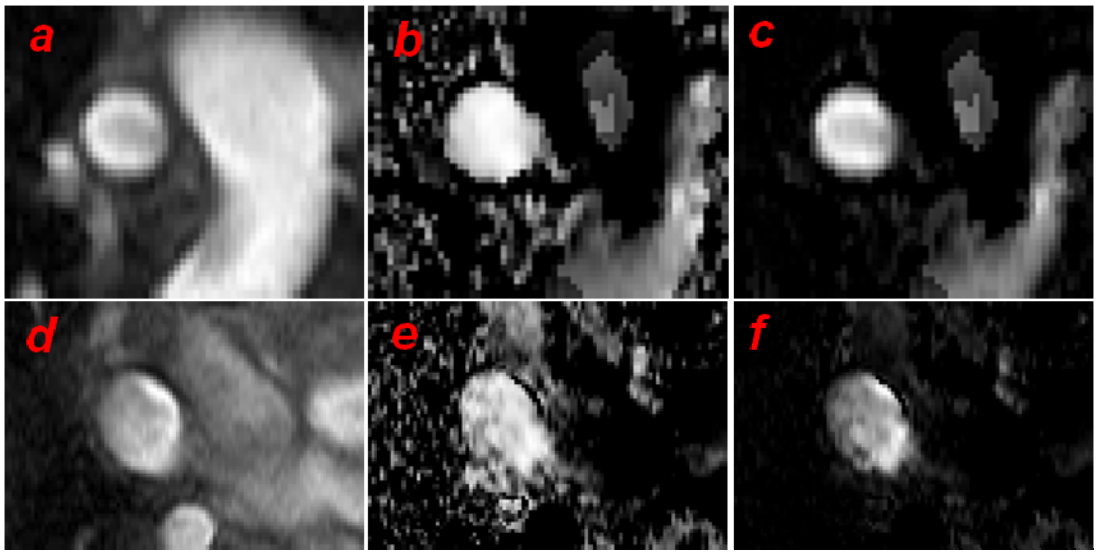

Figure 5.9: a) Original magnitude image of the SVC; b) Cross correlation energy matrix of the SVC; c) Hybrid magnitude velocity image of the SVC; d) Original magnitude image of the IVC; e) Cross correlation energy matrix of the IVC; f) Hybrid magnitude velocity image of the IVC. Notice how the signal from the surrounding structures are suppressed

5.3.2 Implementation of the Hybrid Active Contour Algorithm

The entire implementation of the level-set active contour algorithm is done in Matlab (Mathworks, Natick, MA). A custom in-house program called ***Flow Finder*** is developed to facilitate the segmentation and analysis of the PC MRI datasets. Figure 5.10 shows the Graphical User Interface (GUI) of this program.

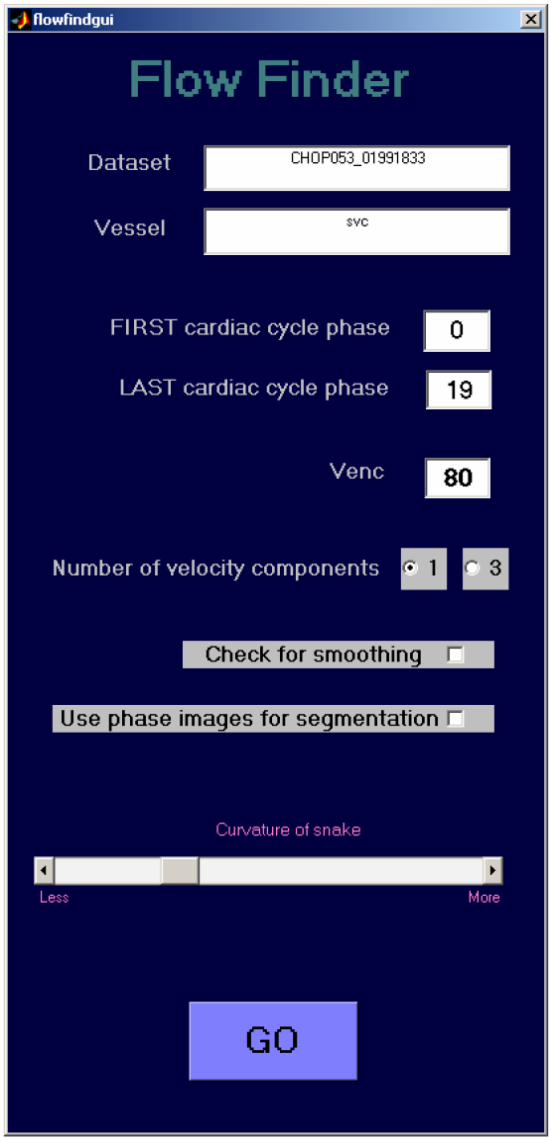

Figure 5.10: Graphical user interface used for PC MRI Segmentation

At this stage, the user is given an option to use the phase velocity images in addition to the magnitude images for generating the external energy field for the active contour model. If this option is selected, then the hybrid magnitude-velocity energy field is used in the level-set active contour model; otherwise only the magnitude image is used. The curvature parameter controls the tradeoff between the internal and external energy in the active contour model (parameter α in Equation 5-28). A value close to 0 implies that the contour purely evolves based on the external energy derived from the image. Conversely, if the value is closer to 1, the contour evolution is governed purely by the curvature of the front (internal energy).

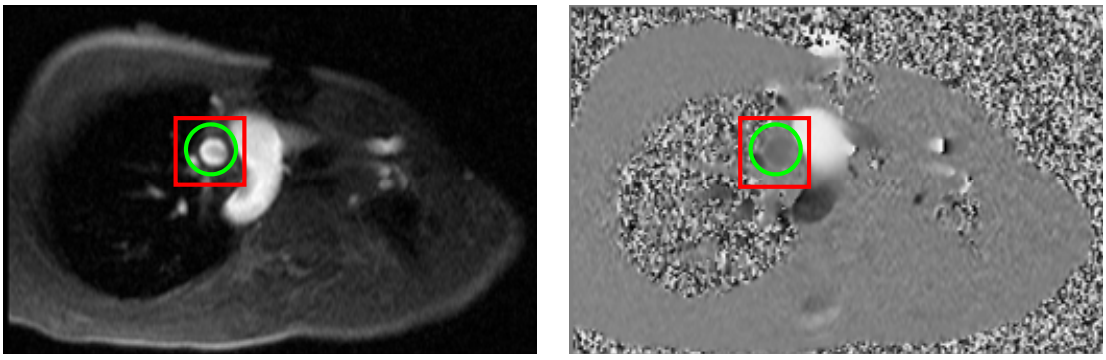

Figure 5.11: The contour selection process. The user crops a certain region around the vessel and selects the vessel of interest by drawing a contour. On the left side is the magnitude image and on the right side is the phase image.

Once the user hits the "GO" button, the cine PC MRI is assembled as a 4D dataset (x, y, u, t) for a single velocity component, or a 6D dataset (x, y, u, v, w, t) for 3 velocity components. Since the vessel of interest normally comprises only a small portion of the image, the region of interest is first reduced in size by cropping a smaller region within the image that contains this vessel (red square, Figure 5.11). This significantly reduces

the computation time as the level-set algorithm now has to be applied to a much smaller image. A contour is then initialized within this structure, which serves as the zero level-set for the signed distance function (C_{t0}). The level-set solver developed in the previous section is then used iteratively to minimize Equation 5-28 until the contour converges on the vessel of interest. The segmented contour in the current phase is then used as the initial contour in the subsequent cardiac phase, and the process is iteratively repeated until the vessel is segmented in all cardiac phases. At the end of the automatic segmentation process, the user is given the option to accept the resulting contours, or manually correct the ones where the active contour algorithm failed.

5.3.3 Calculation of Parameters

When the segmentation of the vessel is complete, the resulting binary mask is applied to the velocity images, and several parameters are consequently evaluated. Since the PC MRI slices are acquired perpendicular to the vessel, these include mean flow over the cardiac cycle, area of the vessel, mean flow rate per heart beat, quadrant flow, mean velocities, maximum velocities, velocity derived pulsatility and resistance indices. For each vessel segmented, this information is stored in a Matlab data file as well as in Microsoft Excel compatible text files for future analysis.

5.3.3.1 Vessel Cross Sectional Area

To calculate the vessel area, the pixel spacing value is first determined from the dicom header files. The name of the parameter in the dicom header file is “Pixel Spacing” and is usually in mm. The area of each pixel is calculated by multiplying the pixel spacing in both the directions, and the total area of the vessel is evaluated by multiplying

the total number of pixels in the segmented image by the pixel area.

5.3.3.2 Flow and Velocity over the Cardiac Cycle

The pixel intensities in the phase images represent the velocity of the flow going through the image slice for the given velocity encoding direction. The flow rate calculation is performed using the through-plane velocity component. For decoding the velocity images from different scanners, the reader is directed to Section 7.2.7 of Dennis' D. Soerensen's Master's thesis, where the issues associated with images of different MRI scanners are elegantly discussed[164]. Using the velocity encoding value (Venc) extracted from the dicom images, the velocity in cm/s for each pixel is evaluated as follows:

$$Velocity = \frac{venc}{2^{bitdepth-1}} \cdot (pixel\,intensity - 2^{bitdepth-1} + 1) \qquad \text{Equation 5-35}$$

The flow rate for each cardiac phase is then calculated to yield a time-varying flow curve given by:

$$Flow\,Rate(t) = \sum_{i=1}^{M}\sum_{j=1}^{N} Velocity(i,j,t) \cdot Pixel\,Area \qquad \text{Equation 5-36}$$

The mean value of this time varying flow rate curve is the average flow through the vessel in one cardiac cycle. In addition to the flow rate, the mean, minimum, and maximum velocity curves over the cardiac cycle are also evaluated.

5.3.3.3 Quadrant Flow

In order to quantitatively analyze the flow profiles obtained from the PC MRI scans, Fogel et al. first introduced the method of quadrant flow analysis[33]. This feature is implemented in the current version of ***Flow Finder*** as follows:

- Step 1: The centroid of vessel is computed in each cardiac phase using the binary segmentation masks
- Step 2: Based on the centroid, the vessel is divided into four quadrants, with the two splitting directions being parallel to the XY axes, and the net flow through each quadrant is then calculated.
- Step 3: Check to make sure that the sum of flow through each quadrant adds up to the total flow through the vessel.

Figure 5.12 shows the schematic associated with the calculation of quadrant flow.

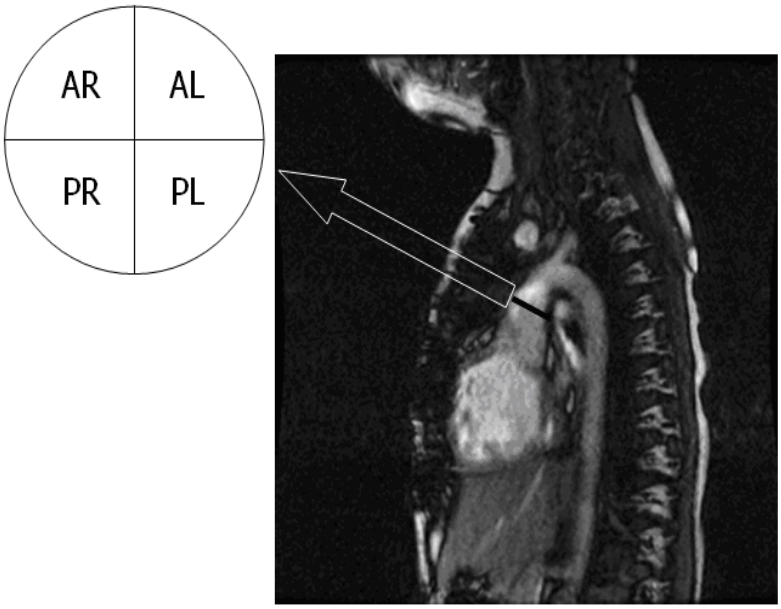

Figure 5.12: The methodology associated with the calculation quadrant flow for an axially acquired PC MRI dataset on an ascending aorta. In this case, the vessel is divided into four quadrants: AR = Anterior Right; AL = Anterior Left; PR= Posterior Right; PL = Posterior Left. This is the general configuration adopted for the SVC and the IVC as well, while for the LPA and the RPA the quadrants are divided into: Superior-Posterior, Superior-Anterior, Inferior Anterior, and Inferior-Posterior respectively.

5.3.3.4 Pulsatility and Resistance Index

Pulsatility index (PI) is a parameter that indicates how much the flow changes over the cardiac cycle. It is defined as:

$$Pulsatility\ Index = \frac{Maximum\ Flow - Minimum\ Flow}{Mean\ Flow} \qquad \text{Equation 5-37}$$

Similarly, the Resistance Index (RI) is evaluated as:

$$Resistance\ Index = \frac{Maximum\ Flow - Minimum\ Flow}{Max\ Flow} \qquad \text{Equation 5-38}$$

RI is a normalized parameter and has a value between 0 and 1. If the pulsatility is high, the value of RI is closer to 1; otherwise it is closer to 0. RI is greater than 1 only when the minimum flow is less than zero. This typically happens when there is significant backflow in one of the cardiac phases. If this happens, then the maximum value of 1 is assigned. Both PI and RI are quantitative metrics that can be used for characterizing the flow within then TCPC.

5.3.4 Comparison of Traditional and Hybrid Active Contour Models

Consider the segmentation of the SVC shown in Figure 5.11, which is in proximity to the ascending aorta where the signal intensity of the magnitude images is much higher than the SVC. If only the magnitude images are used, there is a tendency for the contour to be attracted towards the aorta especially in systole when the flow velocities are much higher within the aorta (Figure 5.13). Figure 5.14 shows the corresponding flow, area, and velocity curves extracted from the segmented vessel over the cardiac cycle. Notice how the maximum velocity profile does not follow the mean velocity

profile, and that there is an un-physiological spike in the computed area of the vessel. Figure 5.14 shows the color contour maps associated with this segmentation, that demonstrates why that is the case.

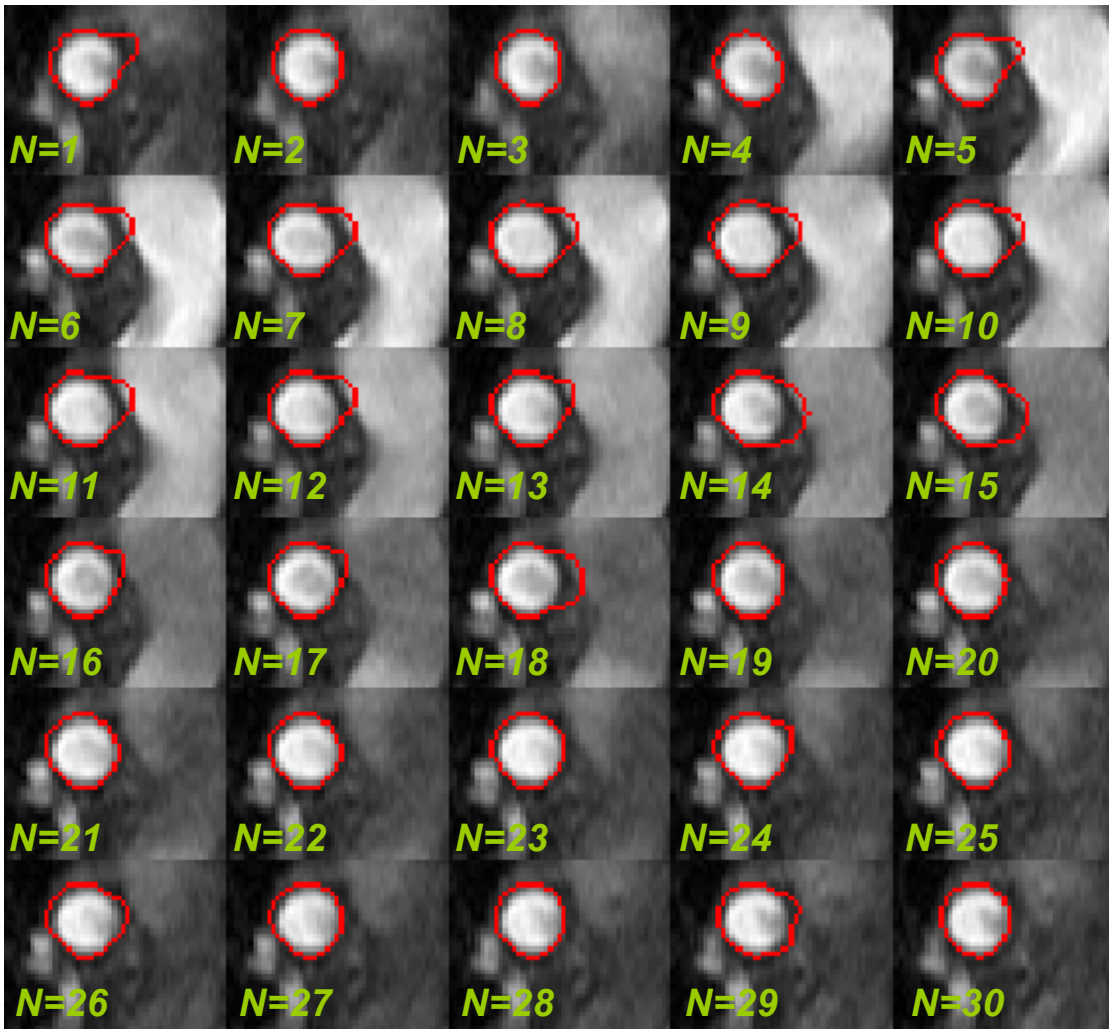

Figure 5.13: Segmentation results of the traditional active contour model.

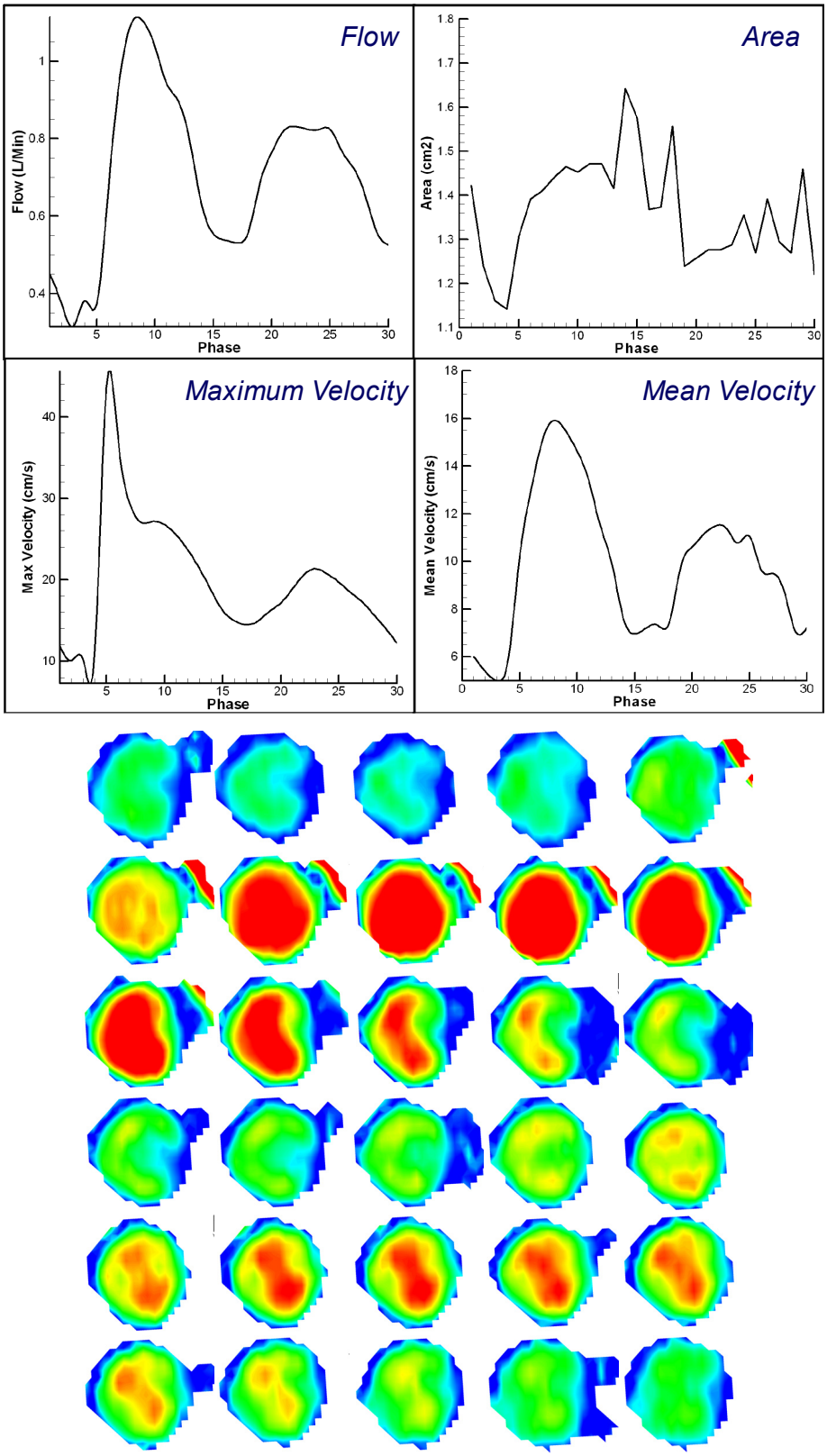

Figure 5.14: The flow, area, velocity curves (top) and the associated contour maps associated with the segmented SVC.

Now, if the hybrid velocity image from Figure 5.9 is used in the segmentation process, then this problem is avoided and only the SVC is segmented. Figure 5.15 shows the contour outlines, and Figure 5.16 shows the calculated flow, area, and velocity curves as well as the velocity color contour maps associated with this segmentation. Compared to the earlier segmentation, the area curve is more physiologic, and the pulsatile characteristics of the maximum velocity curve match the mean velocity curve.

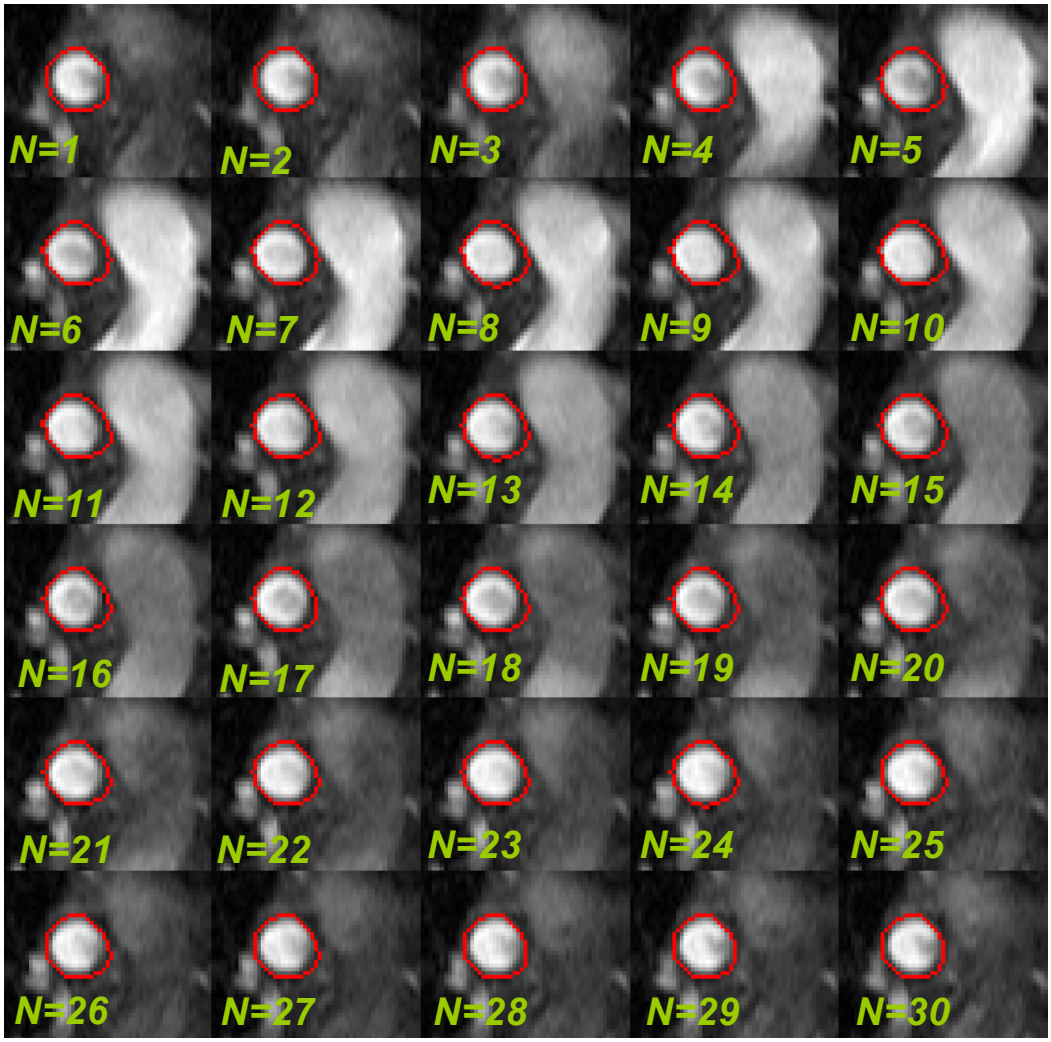

Figure 5.15: Segmentation contours using the hybrid magnitude velocity energy map

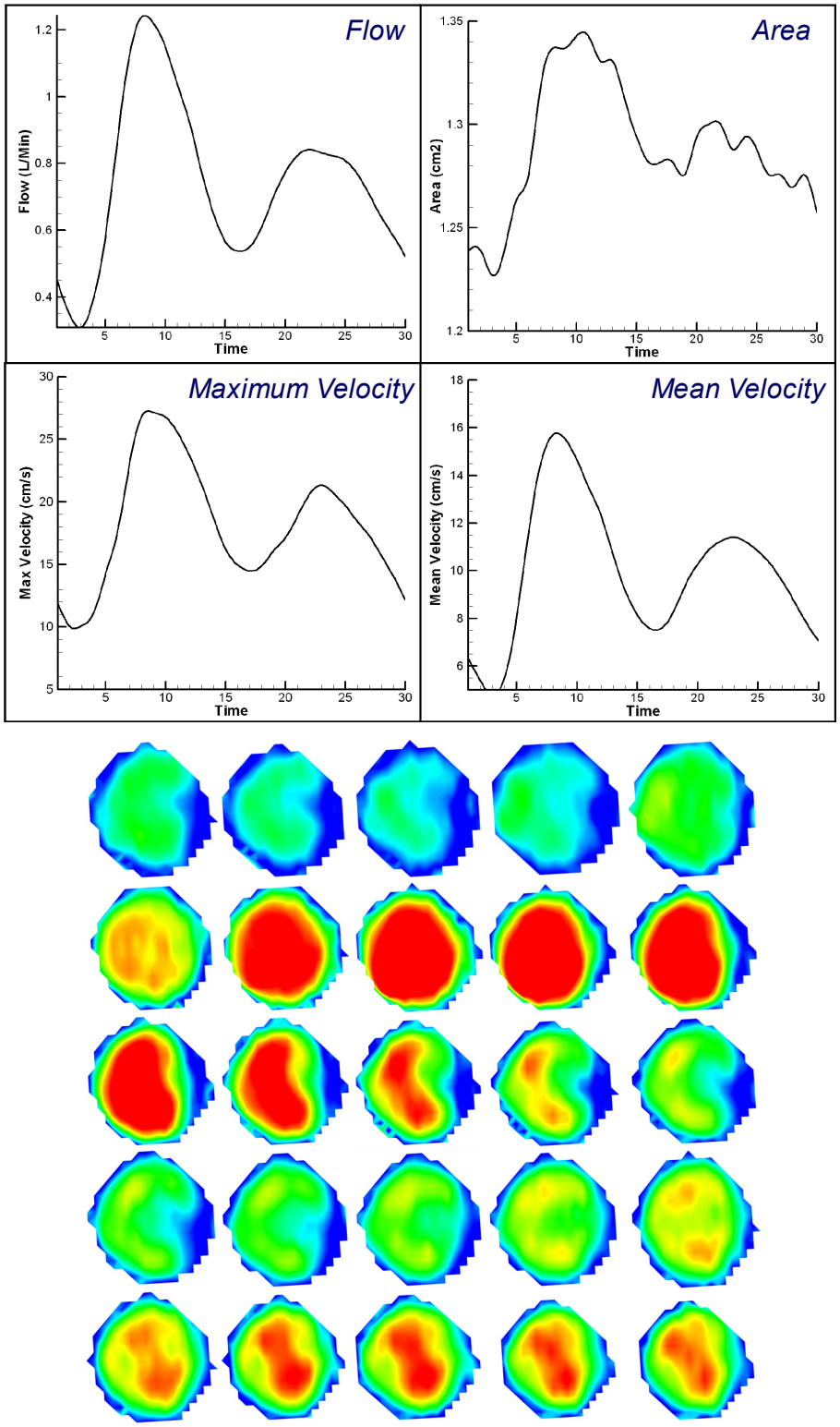

Figure 5.16: The flow, area, velocity curves and the associated velocity contour maps with the hybrid magnitude velocity segmentation

5.4 Summary of the Segmentation Process

Thus far, the first step in the post processing of PC MRI data has been presented. The active contour model is chosen as the primary segmentation tool, as it offered the following benefits: a) Significant control can be exercised over the segmentation process by choosing appropriate energy functions; b) *A priori* information about the vessel to be segmented can easily be incorporated into model via internal energy functions. The Eulerian level-set implementation of the active contour model is ultimately selected over its Lagrangian parametric counterpart as it offered significant advantages in the handling of complex vessel shapes and topologies. This model is adapted for the segmentation of PC MRI data using a novel external energy map generated using both magnitude and phase velocity information from the PC MRI datasets. This concludes step 1 of the two step segmentation process. The following sections discuss the filtering component, which is a critical component for performing quantitative vector field analysis accurately from PC MRI.

5.5 Optimum Fuzzy Filters

Active contours work well for detecting the morphology of the vessels. However, in situations when the vessel boundary is blurred there are no suitable edges for a contour to converge upon and hence only an approximation of the vessel boundary can be obtained. This happens quite often in the TCPC, as the flow fields are typically quite disturbed and complex, which results in edge blurring and low signal to noise ratio (SNR) near vessel borders. This effect is further pronounced when the vessel is in close proximity to the lungs where the SNR is significantly lower for pixels near the vessel

walls. In such a scenario, vectors that are not part of the desired velocity field get incorporated into the segmentation. Figure 5.17 shows an example of such a phenomenon, where spurious noise vectors become part of the segmentation. Consequently, the computation of quantities such as wall shear stress, viscous dissipation, etc., that depend upon the spatial derivatives of the 3D velocity field are distorted. Therefore filtering this noise is critical especially if PC MRI is to be used as a reliable technique for computing such quantitative parameters. In the following section, a novel multi-dimensional Fuzzy filter is proposed that selectively filters out noise vectors from the velocity field, while preserving the true velocity field.

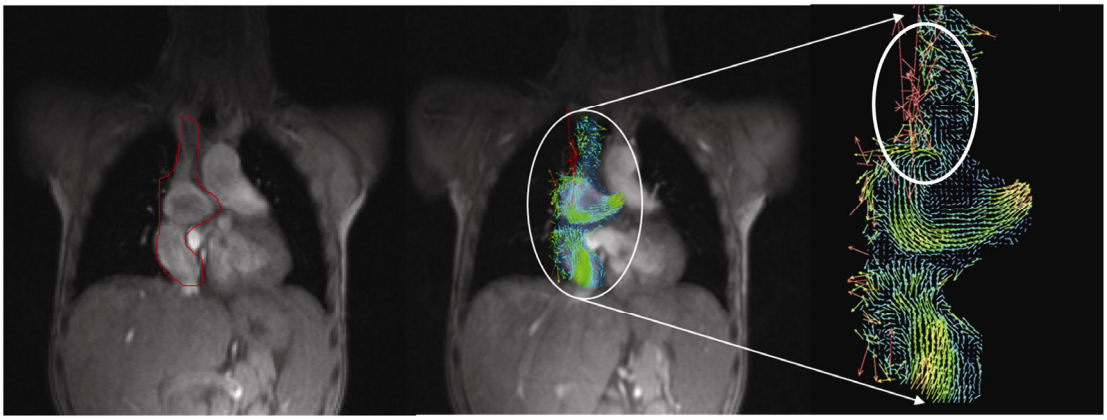

Figure 5.17: Example of noise being incorporated into the segmentation process

5.5.1 Filter Model

Two critical aspects to consider in the filtering of PC MRI velocity fields are: a) The detection of a noise pixel within the segmented vector field (if any), and b) The determination of an appropriate value to replace this noise pixel. A new filter is proposed to tackle both (a) and (b) that is based on a hybrid multi-channel framework (Figure

5.18):

$$y(\vec{k}) = \alpha(\vec{k})I(\vec{k}) + \left(1 - \alpha(\vec{k})\right)M(\vec{k}) \qquad \text{Equation 5-39}$$

Here, $\vec{k} = (k1, k2)$ is the pixel co-ordinate vector, I($\vec{k}$) is the input vector, α($\vec{k}$) is a continuous fuzzy membership function that takes a value between 0 and 1 (this determines to what extent I($\vec{k}$) is a flow pixel), and M($\vec{k}$) is the chosen filter value for replacing the noisy component of the vector. If α($\vec{k}$) equals, or is close to, one then I($\vec{k}$) is classified as part of the flow field and is retained. If it is close to zero then I($\vec{k}$) is considered random noise and is replaced by M($\vec{k}$). Several choices for M($\vec{k}$) are investigated including both scalar and vector based techniques. Since a segmented PC MRI dataset is a vector field with each data point having three components, a filter that is optimized for vector quantities is desirable. One such filtering technique is vector median filtering, which is the choice for M($\vec{k}$) in current filtering framework. The benefit of

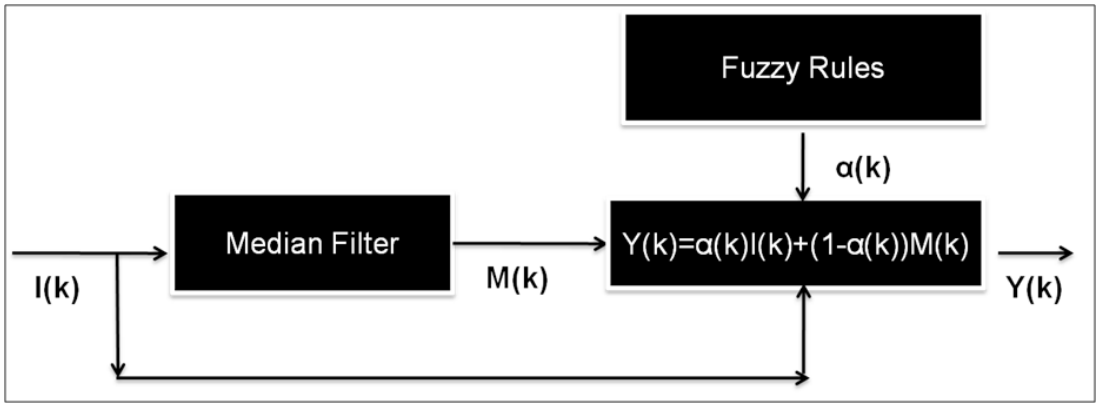

Figure 5.18: The Hybrid multi-channel filtering framework. A set of Fuzzy rules are used to determine a Fuzzy membership function associated with each pixel, and accordingly the pixel in question is either filtered or allowed to pass through unfiltered.

using vector median filtering will be demonstrated in the following sections.

5.5.2 Vector Median Filters

A 3D PC MRI dataset can be thought of as a multi-channel image, where each component of the velocity field is a single channel of the image. To determine the filter output for the vector quantity I($\vec{k}$), an interrogation window is selected around I($\vec{k}$). Let this window be W={I_i: i = 1,2,…, w}, where w is the size of the window (w=9 for a 3x3 window, 25 for 5x5 window, and so on) and I_1, I_2,...I_w is a set of vectors inside this window. Each component of the velocity vector is expressed as I_{i1}, I_{i2}, and I_{i3}. For each multi-channel image, I_i is associated with a distance measure:

$$D_i = \sum_{j=1}^{w} || I_i - I_j ||_\gamma$$

$$where,$$

$$|| I_i - I_j ||_\gamma = (\sum_{k=1}^{3} | I_{ik} - I_{jk} |^\gamma)^{1/\gamma}$$

Equation 5-40

and γ is the chosen distance norm with a value greater than 1. This distance is computed for each vector in the window, and the values are ordered according to the criteria $D_1<D_2..<D_w$ with D_1 being the smallest. If the same ordering is applied to the input set, then the ordered input sequence becomes $I_1<I_2…<I_w$. The sample I_1 associated with distance D_1 becomes the output of the vector median filter[165, 166]. Simply put, the output is the vector that has the smallest sum of vector distances to all of the other vectors in the interrogation window, or equivalently:

$$\sum_{i=1}^{w} || I_{VMF} - Ii ||_\gamma \leq \sum_{i=1}^{w} || I_j - Ii ||_\gamma$$

Equation 5-41

5.5.3 Determination of Fuzzy Rules

The second component of the noise filtering algorithm is to determine a fuzzy membership function ($\alpha(\vec{k})$) for use in the hybrid multi-channel framework shown in Figure 5.18. A set of rules are employed for this purpose, which are established by studying the physical characteristics of flow and noise. The parameters used for establishing these rules as well as a description of how they are evaluated are discussed below.

5.5.3.1 Distance from the Vector Median (DVM, U(k))

Let $I(\vec{k})$ be the vector at the current location and $M(\vec{k})$ be the output of the median filter defined above for the interrogation window. The DVM is calculated as

$$U(\vec{k}) = || I(\vec{k}) - M(\vec{k}) ||_{\gamma} \qquad \text{Equation 5-42}$$

where γ is the chosen distance norm for the VMF implementation. The larger the distance of the given pixel from the vector median within the interrogation window, the higher is the probability for the pixel to be a noise vector. The distances are normalized to be between 0 and 1.

5.5.3.2 Vector Direction Homogeneity (VDH, L(k))

Since random noise has random direction, this property can be used to differentiate between noise and flow. Let u_i be the vector at location i, $d_i(\vec{k})$ the difference in orientation between u_k and u_i, where u_k is the vector that is in question, and $L(\vec{k})$ be the VDH metric for the interrogation window centered on k. Then the VDH

metric can be evaluated as

$$L(\vec{k}) = \sum_{j=1}^{w} d_i(j) \qquad \text{Equation 5-43}$$

Where:

$$d_i(\vec{k}) = \frac{\vec{u}(i) \cdot \vec{u}(\vec{k})}{||\vec{u}(i)|| \cdot ||\vec{u}(\vec{k})||} \qquad \text{Equation 5-44}$$

If the orientation of the directions within the interrogation window is random, then L($\vec{k}$) tends to be 0, otherwise it has a high value. The histogram distribution for both random noise and flow regions within a 3 component PC MR image are shown as part of Figure 5.19. Notice the differences in VDH distribution for noise and flow.

5.5.3.3 *Vector Field Standard Deviation (SD, S (k))*

Another property that can be used to aid in noise detection is the standard deviation of the velocity field within the interrogation window. In this work, a standard deviation map S($\vec{k}$) is evaluated for each component. This is accomplished as follows:

$$S(\vec{k}) = \sqrt{\frac{\sum_{j=1}^{3} (I(\vec{k}, j) - \mu(j))^2}{3}} \qquad \text{Equation 5-45}$$

Here, μ (j) is the mean of the velocity component of each of the 3 vector components within the interrogation window W, and I ($\vec{k}$) is the vector that has to be filtered. The histogram distribution of the standard deviation map for both noise and flow pixels are shown in Figure 5.19. As can be observed, the distributions are markedly

different, with noise having a higher standard deviation compared to flow.

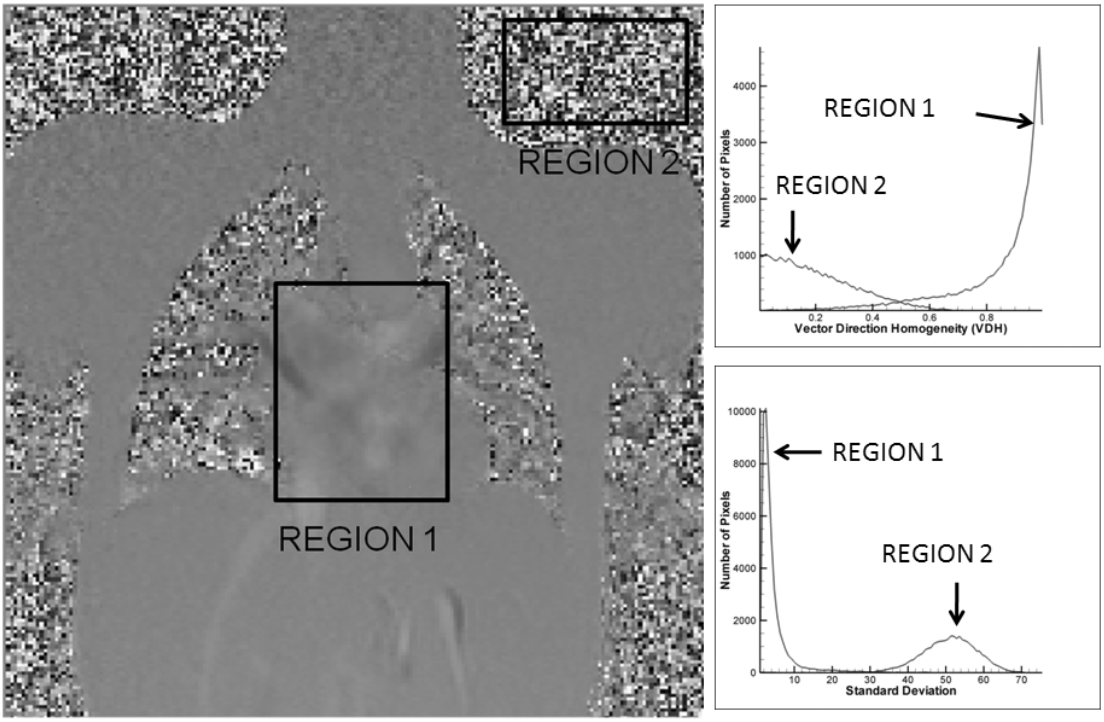

Figure 5.19: The properties of noise and flow in different regions of the PC MR image. The top right graph shows the histogram distribution of the vector direction homogeneity and the bottom right graph shows the histogram distribution of the standard deviation of the velocity field. Region 1 is Flow and Region 2 is Noise

5.5.3.4 Magnitude Image Intensity (MI, MI(k))

Another aspect that can be used towards the filtering process is the intensity of the magnitude images. In the magnitude images, the regions of flow are white (having a value of 1), while the noise regions are typically black (0). Therefore, if a pixel has a magnitude image intensity closer to 1 it has a higher probability of being a flow pixel, while if it is closer to 0 then it is a noise pixel.

5.5.3.5 *Fuzzy Rules*

Based on the analysis and behavior of these four metrics in a PC MR Image, a set of general rules can be defined that can now characterize flow and noise. These are:

Rule #1: DVM is high for noise and low for flow

Rule #2: VDH is low for noise and high for flow

Rule #3: SD is high for noise and low for flow

Rule #4: MI is low for noise and high for flow.

Once these rules are established, the next step in the filtering technique is to determine the Fuzzy membership function α ($\vec{k}$). This is accomplished using the Fuzzy C-Means Clustering technique[167].

5.5.4 Adaptive Fuzzy C-Means Clustering

The four parameters evaluated above can be stacked such that every pixel is characterized by a four-dimensional vector:

$$\vec{F}(\vec{k}) = \left\{U(\vec{k}), L(\vec{k}), S(\vec{k}), MI(\vec{k})\right\} \qquad \text{Equation 5-46}$$

Let C be the number of clusters of interest. In our case the two clusters are C1=flow and C2=noise. Therefore two membership functions that will be simultaneously estimated: one for the degree of membership of a pixel $\vec{k}$ to noise ($\alpha_{c1}(\vec{k})$), and a second for the degree of membership of a pixel $\vec{k}$ to flow (($\alpha_{c2}(\vec{k})$). According to fuzzy set theory:

$$\sum_{j=1}^{C} \alpha_j\left(\vec{k}\right) = \alpha_{c1}(\vec{k}) + \alpha_{c2}(\vec{k}) = 1 \qquad \text{Equation 5-47}$$

This effectively simplifies this process to estimating just a single function. For every cluster $j \in \{1, \mathrm{C}\}$, we define $\vec{C}_F(j)$ as the centroid of the 4-parameter vectors weighted by their membership to cluster j:

$$\vec{C}_F(j) = \frac{\sum_{i=1}^{MxN} \alpha_j(i)\vec{F}(i)}{\sum_{i=1}^{MxN} \alpha_j(i)} \qquad \text{Equation 5-48}$$

where MxN is the size of the image and $i \in \{1, \mathrm{MxN}\}$ spans all pixels in the image. Using the above Equation 5-48, can simultaneously estimate the membership function $\alpha_j : \{1, \mathrm{MxN}\} \to [0,1]$ and the centroid vector $\vec{C}_F(j)$ by minimizing the following expression with respect to alpha, gives:

$$J = \sum_{i=1}^{MxN} \sum_{j=1}^{C} \alpha_j(i)^2 \, \| \vec{F}(i) - \vec{C}_F(j) \|^2 \qquad \text{Equation 5-49}$$

where MxN is the size of the image, and C is the number of clusters and $\vec{F}(i)$ is the four-parameters vector associated with each pixel $i \in \{1, \mathrm{MxN}\}$. If the steepest descent algorithm is used, the corresponding update equations become:

$$\alpha_j(i) = \frac{1}{\sum_{l=1}^{C} \left\{ \frac{\| \vec{F}(i) - \vec{C}_F(j) \|}{\| \vec{F}(i) - \vec{C}_F(l) \|} \right\}^2} \qquad \text{Equation 5-50}$$

Equations 5-50 and 5-48 are used to concurrently update α_j and $\vec{C}_F(j)$ at every iterations. Iterations are continued until the value of α converges. Once the value of

α is determined, it is used in the hybrid multi-channel filtering framework and is applied to every pixel in the segmented vessel until all noise is filtered.

5.6 Algorithm Validation

Each step of the PC MRI post processing algorithm (Figure 5.1) is quantitatively validated using *in vivo* PC MRI and synthetic PC MRI generated from computational fluid dynamic (CFD) simulations. The active contour segmentation methodology (step 1) is validated on *in vivo* datasets using a manually defined contour as the reference standard. The filtering algorithm (step 2) is validated using synthetic datasets generated from CFD simulations as well as *in vivo* datasets. The reference standard for the CFD simulations are the original velocity field themselves, while for the *in vivo* case, a manual filtering strategy is designed and implemented that serves as the reference standard. The benefit of using the proposed fuzzy adaptive vector median filtering (FAVMF) is demonstrated by comparing the velocity error/pixel, maximum wall velocities, maximum wall velocities/core velocities ratio, and wall shear rates with and without the filter.

5.6.1 Generation of Synthetic Datasets

To generate the synthetic datasets, a CFD simulation is conducted on a 3D patient specific TCPC model reconstructed from *in vivo* MRI[43, 149]. The TCPC model is first meshed using Gambit (FLUENT Inc.,) having 400,000 tetrahedral elements. The meshed geometry is imported into a commercial CFD solver FLUENT, and the governing Navier-Stokes equations are solved to obtain a 3D vector field within the entire geometry of the TCPC. The CFD simulation is then sampled at 111 equally spaced planes (Figure 5.20a) to obtain 3 sets of phase images with velocity encoding in the anterior-posterior

(AP), right-left (RL), and superior-inferior (SI) directions respectively (Figure 5.20b). The pixel size is kept at 1 mm^2, the slice thickness 1.2 mm, and the velocity encoding is 100 cm/s to obtain images having intensities ranging from $0\text{-}2^{16}$, which is the standard clinical dicom range. These images are noise free and serve as the reference standard for comparing the performance of different noise filters.

In order to test the robustness of the filtering algorithm, artificial noise is embedded into the images (Figure 5.20c). An image (n ($\vec{k}$)) having random noise with values ranging between 0-216 is generated for each image slice in the dataset. This image is added to the original phase images according to the formula:

$$x(\vec{k}) = (1 - p_v) * o(\vec{k}) + p_v * n(\vec{k}) \qquad \text{Equation 5-51}$$

where n($\vec{k}$) is the noise pixel, p_v is the noise level, and o($\vec{k}$)is the original value of the vector field. The value of p_v is uniformly varied from 0 to 0.5 at intervals of 0.1 and various filters are quantitatively compared using the normalized mean squared error (NMSE) metric:

$$NMSE = \frac{\sqrt{\sum_{i=1}^{M}\sum_{j=1}^{N}(o_{ap}(i,j) - \hat{o}_{ap}(i,j))^2 + (o_{fh}(i,j) - \hat{o}_{fh}(i,j))^2 + (o_{rl}(i,j) - \hat{o}_{rl}(i,j))^2}}{\sqrt{\sum_{i=1}^{M}\sum_{j=1}^{N}(o_{ap}(i,j))^2 + (o_{fh}(i,j))^2 + (o_{rl}(i,j))^2}} \qquad \text{Equation 5-52}$$

M and N are the image dimensions, o_{ap}, o_{rl}, and o_{fh}, are the original values without noise corruption (reference standard), and $\hat{o}_{ap}$, $\hat{o}_{rl}$, and $\hat{o}_{fh}$, are the filtered images. Noise is only embedded to within 5 pixels of the vessel for two reasons: a) to have noisy and noise-free regions within the same velocity field so that the impact of filtering on both the

regions can be quantified; b) it is logical to embed noise into the system near the vessel border rather than anywhere else since most of the noise is observed along the vessel border. However, it should be noted that the results of the algorithm are unaffected by the choice of pixels selected for noise addition.

The NMSE of VMF is first compared to the filter proposed by Walker et al using the settings described in[100], and a standard Gaussian low pass filter with a kernel size of 15x15 and standard deviation of 1.5. Then, the benefit of using VMF in a fuzzy

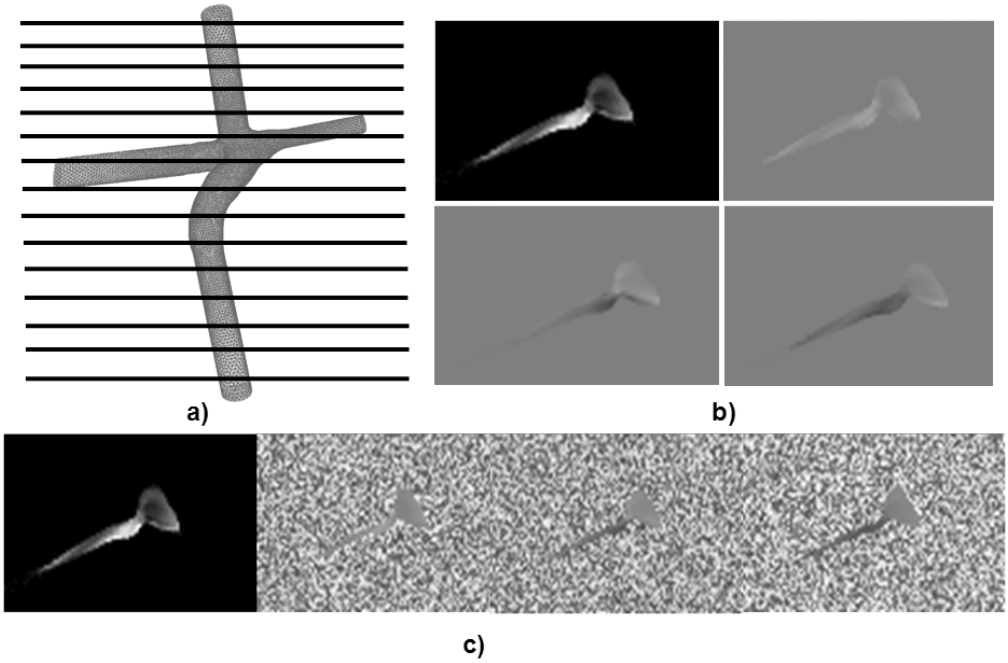

Figure 5.20: The process of noise being embedded into the system. a) The CFD model is first sampled at discrete locations. b) 4 images are acquired per location (Magnitude, and 3 phase images); c) Artificial noise is embedded into the phase images

framework is demonstrated by comparing the NMSE of VMF with FAVMF. In addition, maximum shear rates are computed for the original vector field as well as for the noisy, and the filtered datasets. The results obtained from FAVMF, low pass filter, and the Walker filter are then compared to the shear rates from the original vector field from

CFD. Principal shear rates for the 3D vector field are calculated using the methodology outlined by Tambasco and Steinman[168].

5.6.2 Manual Segmentation Protocol for In Vivo Active Contour Validation

A manual segmentation protocol was designed and implemented to serve as a reference standard for evaluating the performance of the active contour methodology. To ensure the accuracy and reproducibility of this protocol, two independent users manually outlined the vessels of interest on 5 datasets. The protocol was refined until the reproducibility error of the segmentation overlap was less than 5%. Using this protocol, the vessels of interest in all the *in vivo* datasets were manually outlined by the trained user. The total time taken by the manual segmentation process for each dataset was about 30 minutes. The automatic active contour segmentation algorithm was quantitatively compared to the manually outlined contours by evaluating overlap, false positive (percentage of total area included in the automatic segmentation and not present in the manual segmentation), false negative (percentage of total area included in the manual segmentation and not present in the automatic segmentation), sensitivity {true positive/(true positive + false negative)}, and specificity {true negative/(true negative + false positive)} percentages, respectively. True positive is the same as overlap, while true negative is the region excluded from the segmentation common to both the automatic and manual segmentations. The total time taken for the automatic segmentation process was less than 10 minutes for each dataset, which was significantly lesser than the manual process.

5.6.3 Manual Filtering Protocol for In Vivo Optimum Filters Validation

A manual filtering approach was adopted to provide a noise-free control for *in vivo* PC MRI filtering. The manual filtering protocol consisted of displaying the segmented velocities using a vector plot with colors varying from the lowest (blue) to the highest (red) velocities. Figure 5.17 shows an example of a typical vector plot. Color was used instead of grayscale because noise is more easily detected by the human visual system in color. The user was then asked to step through each phase of the cardiac cycle and click on the noise vectors. Due to the large number of noise vectors that are normally present, this process was independently conducted by two users to ensure that all noise was removed from the images. The operators of the manual filtering process were blinded to each other and to the results of the automatic filters used in the study to minimize any bias that may creep into the process. The identified noise pixels were then replaced with the vector median of the surrounding pixels. The presented approach has several benefits: a) Errant vectors that are not part of the flow structure can be easily removed as they clearly stand out in the color vector field; b) Pixel by pixel based error values can be calculated using the manually filtered dataset as the control. A student's unpaired t-test is used for comparing the performance of the proposed segmentation and filtering process.

5.7 Establishment of a velocity database for quantitative flow analysis

After the afore-described validation procedure, the proposed methodology is applied towards the development of a multi-institutional velocity database of over 250 patients. All of these patients were enrolled at either Children' Hospital of Philadelphia (CHOP) or Children's Healthcare of Atlanta (CHOA) over a six year period from March

2001 to June 2007. All protocols were approved by the Institutional Review Boards (IRB) of both institutions and informed consent is obtained from all the patients.

The imaging protocol is described in Chapter 4, Section 4. For each patient, time varying PC MRI data is acquired on the aorta, SVC, IVC, LPA, and the RPA. Once the segmentation and filtering process is complete: a) all the calculated variables are stored in a matlab file for future quantitative analysis; b) a Tecplot file is created for analyzing the vector fields; c) a text file containing the summary of flow rates, area calculations, mean and maximum velocities, pulsatility and resistance indices is created; d) snapshots of the segmentation results, flow, area, and velocity curves are saved.

5.7.1 Patient Selection for Quantitative Flow Analysis

The systematic velocity database created can be used to conduct quantitative analysis on large groups of Fontan patients. A subset of 105 patients are selected for a quantitative hemodynamic analysis. All computed variables are indexed to BSA for comparison. Fractional contribution of IVC and RPA to total blood flow are calculated and correlated with BSA and age. All population statistics are reported as a mean ± the standard deviation. Differences between statistics are reported as mean difference ± the standard error. Total pulmonary blood flow, total caval blood flow, and aortic flow are compared using a paired Student's t-test. The data are disaggregated by Fontan type, superior caval anastomosis type, and the presence or absence of an LSVC. These groups are compared by Student's t-test for independent samples to determine whether flow splits vary by group.

5.8 Chapter 5 Summary

In this chapter the necessary methods for the completion of specific aim 2 and specific aim 4 were presented. Two new methods were developed: a) A novel hybrid-magnitude velocity energy field based active contour model; b) a novel filtering strategy based on Fuzzy set theory. A thorough protocol was then established to validate these methods. These technologies were then applied to *in vivo* Patient PC MRI to establish a large velocity database of over 250 patients with a single ventricle physiology. Out of these 250 patients, 105 were selected for quantitative flow analysis and the results are presented in Chapter 9.

CHAPTER 6

DIVERGENCE-FREE INTERPOLATION

6.1 Overview

Characterizing the *in vivo* 3D hemodynamics of the TCPC requires the development of novel imaging strategies and analysis techniques. Most of the studies thus far have primarily focused on using ultrasound, 2D PC MRI, or computational fluid dynamics for characterizing single ventricle hemodynamics, and very few studies have used 3D PC MRI for looking at the detailed flow structures within the TCPC. This is because of the significant challenges associated with the application of 3D PC MRI in pediatrics such as: a) prolonged scan times of a PC MRI acquisition; b) decreased spatial and temporal resolution due to smaller body sizes (smaller fields of view); c) need for sedation in younger patients; and d) motion artifacts due to patient movement. Although (c) and (d) are issues that cannot be avoided, problems associated with imaging times and resolution can be solved using innovative engineering approaches.

Indeed, there are two possible ways to tackle these problems a) Develop a fast imaging approach such that measurements in 3D can be made quickly and accurately with high spatial and temporal resolution; or b) Develop interpolation strategies where the 3D velocity fields can be reconstructed from low resolution PC MRI datasets. This chapter focuses on (b), where a novel interpolation technique for PC MRI is proposed. The novelty lies in the fact that this approach utilizes the fundamental property of incompressible fluid mechanics: zero divergence; for interpolating missing information in

the PC MRI acquisition. The method is developed and optimized for TCPCs, and is quantitatively and qualitatively validated using theoretical, computational and experimental methods. It is then applied to *in vivo* PC MRI of 24 patients with a TCPC. Quantitative metrics such as energy losses, hepatic flow splits, and vortex sizes are evaluated based on the reconstructed velocity fields, and compared between different Fontan templates. In the following sections, the underlying theory and implementation techniques for this approach are discussed.

6.2 Blood Flow Fundamentals

Blood is a medium for transportation of oxygen and nutrients in the human circulation. It comprises of suspended cells in plasma, and for this reason its chemical properties can be distinguished from other fluids such as water and air. The flow of blood is a complex phenomenon as it travels through intricate, flexible geometries in pulsatile or time-dependent manner, and as it contains different cell types in suspension whose concentrations and cell-to-cell interactions ultimately dictate the global flow behavior. Despite these complexities, blood flow in large vessels resembles that of single-phase incompressible Newtonian fluids of similar viscosity, and traditional fluid mechanics principles are applicable. Therefore, blood in large vessels can be described with a limited number of fluid properties and governing equations, and the assumptions imposed to yield the incompressible Newtonian conservation equations may be considered as valid for blood flows as well.

6.2.1 Conservation Equations

The conservation equations are a set of equations that relate fluid properties to

each other through balance of conserved mass and momentum. The conservation of mass is also known as continuity. The balance equations of mass and momentum for all continuum matter are as follows:

$$\frac{D\rho}{Dt} + \rho\nabla\cdot\vec{u} = 0$$
$$\rho\frac{D\vec{u}}{Dt} = \nabla\cdot\vec{T} + \rho\ \vec{f}$$

Equation 6-1

Here, $(\frac{D}{Dt})$ is the material derivative, $\vec{T}$ is the stress tensor (dyne/cm^2), and $\vec{f}$ is the body force tensor (cm/s^2). The material derivative is the sum of the transient and convective derivatives.

6.2.2 Newtonian Fluid

The balance equations can be simplified for an incompressible, Newtonian fluid. A Newtonian fluid is one that has a linear relationship between shear stress (τ) and the shear strain rate as shown in equation 6-2. The constant of proportionality is the dynamic viscosity. In other words, it can be said that a Newtonian fluid has a constant dynamic viscosity over shear strain rates given by:

$$\tau = \mu\frac{\partial V_x}{\partial y}$$

Equation 6-2

Blood in large vessels at normal, physiologic conditions has a constant dynamic viscosity at 3.5 cP. Plasma has a density of 1.02 g/cm^3, and a dynamic viscosity of 1.2 cP [169] which is similar to that of water (1 cP, 1 g/cm^3). Dynamic viscosity and density rise with increasing hematocrit (volumetric percentage of erythrocytes in blood). Hence, blood cells account for the increased dynamic viscosity of blood.

Due to its complex composition, blood is not always Newtonian. Figure 6.1 indicates that blood has dynamic viscosity at low shear strain rates where the relationship is not necessarily linear. As shear strain rates rise above 100 s^{-1}, dynamic viscosity becomes more constant and blood can be considered to behave like a Newtonian fluid. When shear strain rates are lower than 100 s^{-1}, the dynamic viscosity increases considerably because of the tendency for blood to form rouleaux, or aggregated erythrocytes[169]. Therefore, blood cannot be considered Newtonian at low shear strain rates.

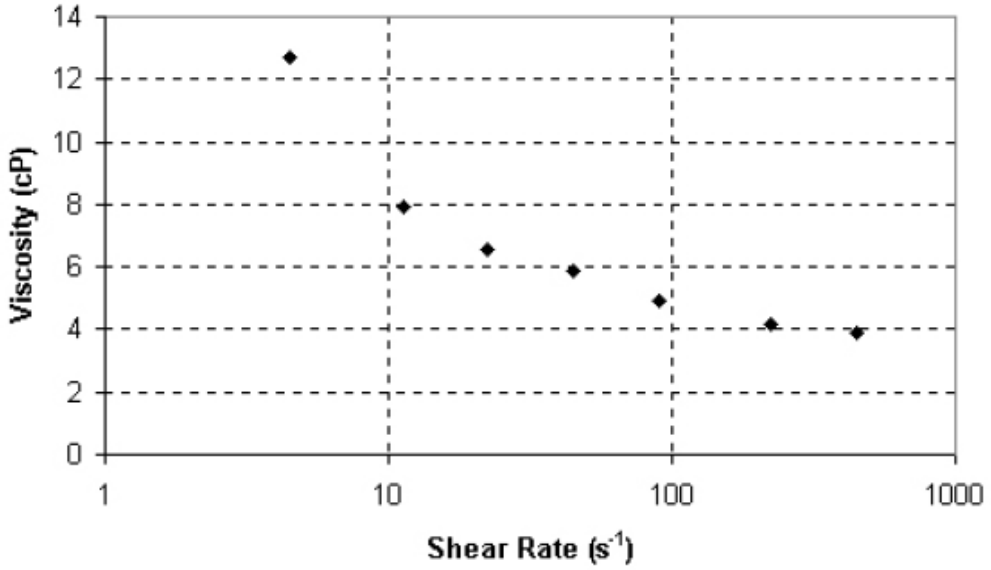

Figure 6.1: The relationship between blood viscosity and shear rate. As the shear rate reduces to below 100 s^{-1}, the viscosity increases dramatically

Blood typically experiences low shear strain rates in the capillaries. Therefore, it would be intuitive from Figure 6.1 to say that as vessel diameter decreases, shear strain

rates decreases, and consequently dynamic viscosity rises. However, in reality blood cells interact less with each other and more with the walls of the capillaries, which dampens the reduction in the shear rate. Despite this phenomenon, the dynamic viscosity of blood in the capillaries is still higher than 3.5 cP and hence cannot be considered Newtonian. In general, if the vessel diameter is greater than 0.5 mm, blood flow within the vessel is considered Newtonian, and if it is less than that, the Newtonian assumption is invalid.

6.2.2.1 Viscosity Considerations

The viscosity of blood is a very important consideration for understanding and modeling cardiovascular pathologies. For example, in patients with congenital heart diseases in elevated altitudes, there is a tendency for the blood viscosity to increase dramatically to account for reduced oxygen levels in the atmosphere. The opposite can happen as well, where conditions such as anemia can lower the hematocrit levels, and subsequently lower blood viscosity and density. In these cases, hemodynamics may vary significantly depending upon the hematocrit levels. Hence, in order to accurately model the hemodynamics, the governing equations of conservation should appropriately account for the changes in blood viscosity.

6.2.3 Navier-Stokes Equations

For most cardiovascular applications, blood can be considered to be a Newtonian fluid as the blood vessels in question are typically larger than 0.5 mm in diameter. Since it is mainly composed of water (plasma), it can also be considered to be an incompressible fluid (the change in density is 0), and hence the first half of equation 6-1 reduces to:

$$\rho \nabla \cdot \vec{u} = 0 \Rightarrow \nabla \cdot \vec{u} = 0$$
$$since \qquad \text{Equation 6-3}$$
$$\frac{D\rho}{Dt} = 0$$

Using the incompressibility criteria and the constitutive relation between shear stress and shear strain rate of a Newtonian fluid, it is possible to simplify the balance equations into the well-known form of the Navier-Stokes equation for incompressible Newtonian fluids as shown:

$$\nabla \cdot \vec{u} = 0$$
$$\rho \frac{D\vec{u}}{Dt} = -\nabla P + \mu \nabla^2 \vec{V} + \rho \vec{f} \qquad \text{Equation 6-4}$$

This set of equations is consistently used for modeling blood flow via computational fluid dynamics.

6.2.4 Incompressibility

The property of incompressibility is fundamental to all blood flow applications. Mathematically, this implies that the divergence of a velocity field is 0. In 3D, this corresponds to:

$$\nabla \cdot \vec{u} = 0$$
$$if\ \vec{u} = (u_x, u_y, u_z),\ then \qquad \text{Equation 6-5}$$
$$\frac{\partial u_x}{\partial x} + \frac{\partial u_y}{\partial y} + \frac{\partial u_z}{\partial z} = 0$$

All velocity fields associated with incompressible fluids have to follow this relationship. Since both computational and experimental methods are discrete in nature, zero divergence can only be enforced within certain error levels. Especially in 3D PC MRI measurements, the divergence error levels can be quite high due to: a) Low spatial

resolution; b) presence of background phase errors; c) high noise levels; d) anisotropic voxel sizes. Therefore, in order to analyze the true velocity fields extracted from PC MRI, some sort divergence-free constraint needs to be enforced, so that the property of continuity is preserved, and more accurate fluid dynamic analysis can be conducted.

6.3 Interpolation and Approximation

The idea of interpolation is to estimate the values of an unknown function **f(x)**, in locations where no data information is available. Often in science and engineering, only a discrete set of measurements are available and there is a need to construct a function which closely fits these measurement points. This process is called curve fitting, or regression analysis, and comprises of minimizing an error term used to estimate the parameters associated with the desired function. Interpolation is a specific case of curve fitting, in which the function must go exactly through those points.

Many times the function is quite complex to estimate, and there is a need to approximate this function using simpler functions. Especially in fluid mechanics applications, the underlying function is essentially unknown except for well understood flow regimes (steady Poiseuille or pulsatile Womersley flows through a straight pipe, for example). In these cases, a few data points are selected from a larger sample, and simpler functions are constructed for interpolation within the selected domain. Of course, when using the simpler function to calculate new data points, results of the actual function itself cannot be reproduced. Such an interpolation approach is also known as approximation. In most applications, the process of approximation is used for the purposes of interpolation. Depending upon the desired application, the interpolation method used to

gain in simplicity might offset the interpolation error.

In the following sections, four common types of interpolating (or approximation) functions are discussed in order of complexity: a) Linear, b) Polynomial, c) Thin-plate splines, and d) Adaptive control grid interpolation. All of these are scalar in nature, i.e., they are used for interpolating scalar functions.

6.3.1 Linear Interpolation

Linear interpolation of functions is conducted by applying linear polynomials to each pair of points in the dataset. In one dimension, if two known points are given by the coordinates (x0, y0) and (x1, y1), the interpolating function y(x) is given by:

$$\frac{y - y0}{y1 - y0} = \frac{x - x0}{x1 - x0}$$

$$y(x) = \frac{(y1 - y0)}{(x1 - x0)}(x - x0) + y0 \qquad \text{Equation 6-6}$$

Therefore an unknown function **f(x)** with 'k' known data points can be estimated by a set of k-1 linear polynomials of the form described in Equation 6-6. The general approach is:

1.) Determine the two points on the measured dataset closest to the desired location

2.) Evaluate the linear interpolating polynomial using those two points

3.) Interpolate the value of the function using the linear polynomial

In multiple (N) dimensions, 2^N points are needed in the interpolation process. For example, in the case of bilinear interpolation in 2 dimensions, the four closest points are determined, and the value is linearly interpolated using 3 operations. In 3D, 8 points are needed, and 7 linear interpolating operations are required. Linear interpolation is quick

and easy to implement, although it is not very accurate. Another disadvantage is that the resulting function may not be differentiable as the linear interpolation process is only C^0 continuous. In situations where C^0 interpolation is inadequate, higher order interpolation techniques such as polynomial and spline approaches are necessary.

6.3.2 Polynomial Approximation

Polynomial approximation is a generalization of the linear interpolation technique. The linear interpolant is now replaced by a polynomial of a different function. For example, in a single dimension consider the sixth degree polynomial given by:

$$f(x) = ax^6 + bx^5 + cx^4 + dx^3 + ex^2 + fx + g \qquad \text{Equation 6-7}$$

Here, 7 parameters need to be evaluated, which implies that a minimum of 7 unique data points are needed for evaluating this function. Similarly, for an interpolating function of order **n**, **n+ 1** data points are needed. These functions are $\mathbf{C^{n-1}}$ continuous, and if a linear combination of these interpolating functions is used, then the interpolated dataset is not differentiable at the boundaries of the interpolating functions. The implementation approach is similar to linear approximation, although it is computationally very expensive and the level of accuracy depends upon the order of the polynomial function.

6.3.3 Thin-Plate Spline Approximation

6.3.3.1 Thin-Plate Spline Definition

Linear and polynomial interpolation strategies work well when the data points are acquired on a regularly spaced grid. Many times the data acquired are scattered and do

not fall on a regular grid. In such situations, the thin-plate spline approximation approach described by Bookstein works very well[170]. The idea is to use an interpolating kernel, defined by the function:

$$z(x,y) = -U(r) = -r^2 \log r^2 \qquad \text{Equation 6-8}$$

Here r is the Euclidian distance in the Cartesian domain defined by $r = \sqrt{x^2 + y^2}$. This function has a value of 0 along the regions where r=1 and attains a maximum value all along a circle of radius 1/sqrt(e)~0.607 concentric with the circle of radius 1. The function satisfies the following relationship:

$$\Delta^2 U \propto \delta_{0,0} \qquad \text{Equation 6-9}$$

Where $\delta_{0,0}$ is the Dirac delta function, that is zero everywhere except in the location where r=0, and has an integral equal to 1. U is also called the fundamental solution of the biharmonic equation $\Delta^2 U = 0$, which is the equation of the thin plate spline lofted as a function **z**(x, y) above the (x, y) plane. This function is the natural generalization to two dimensions of the function $|x|^3$, which is the familiar cubic B-Spline in one dimension.

6.3.3.2 Thin-Plate Splines for Interpolation

Let $P_1=(x_1, y_1)$, $P_2=(x_2, y_2)$, and $P_n= (x_n, y_n)$ be n randomly oriented points in Euclidan space in any coordinate system. The goal is to interpolate some function f taking specified values at points P_i. These points serve as interpolation kernels for the thin-plate spline function. Let r_{ij} be the Euclidian distance between two points (i, j), and let the distance be defined as $|P_i - P_j|$. Define matrices:

$$K = \begin{bmatrix} 0 & U(r_{12}) & U(r_{13}) & U(r_{1n}) \\ U(r_{21}) & 0 & U(r_{23}) & U(r_{2n}) \\ U(r_{31}) & U(r_{32}) & 0 & U(r_{3n}) \\ U(r_{n1}) & U(r_{n2}) & U(r_{n3}) & 0 \end{bmatrix}, n \; x \; n$$

Equation 6-10

$$P = \begin{bmatrix} 1 & x_1 & y_1 \\ 1 & x_2 & y_2 \\ 1 & x_3 & y_3 \\ 1 & x_4 & y_4 \end{bmatrix}, 3 \; x \; n$$

$$L = \begin{bmatrix} K & P \\ P^T & \mathbf{0} \end{bmatrix}, (n+3) \; x \; (n+3)$$

Equation 6-11

In Equation 6-11, **0** is a 3x3 matrix of zeros. Let **V**= (v_1, …, v_n) be any n-vector (or in the presented application, the set of measurements of the function **f**(x, y) at locations (x_i, y_i) respectively), and let **Y**= (V| 0 0 0)^T be a column vector of length n+3. Define the vector **W**=(w_1,…, w_n) and the coefficients a_1, a_x, a_y by the equation:

$$L^{-1}Y = (W \mid a_1 \; a_x \; a_y)$$

Equation 6-12

Using these functions, the thin plate interpolating spline function can now be defined as:

$$f(x,y) = a_1 + a_x + a_y + \sum_{i=1}^{n} w_i U\left(\left|P_i - (x,y,z)\right|\right)$$

Equation 6-13

The role of the last two rows of L is to guarantee that the coefficients $\mathbf{w_i}$ sum up to 0, and that their cross products with x and y of the points Pi are likewise 0. The function U(r) is divided into two parts: a sum of functions U(r), which can be shown to be bounded and asymptotically flat, and an affine part representing the behavior of **f** at

infinity. The thin-plate interpolating spline is guaranteed to equal the value of the measured values v_i at the locations (x_i, y_i). The applications of this function are widespread, ranging from image interpolation to image registration.

6.3.4 Adaptive Control Grid Interpolation

Adaptive control grid interpolation (ACGI) is a method developed by Frakes et al. for the inter-slice interpolation of medical images. This approach utilizes motion estimation techniques for determining the interpolating function. ACGI combines features of optical flow based and block based motion estimation algorithms to enhance insufficiently dense MRI datasets. The ACGI formulation assumes that the pixel displacement functions (d_1 (x,y), d_2(x,y)) within some region ***R*** can be written as:

$$d_1(x,y) = \sum_{i=1}^{p} \alpha_i \theta_i(x,y)$$
$$d_2(x,y) = \sum_{i=1}^{p} \beta_i \phi_i(x,y) \qquad \text{Equation 6-14}$$

Here θ and φ are independent basis functions used to describe the displacement field at (x, y), α_i and β_i are coefficients of the basis functions that need to be estimated, and p is the total number of blocks used in the interpolation. In a vector or matrix form, these equations can be re-written as:

$$\mathbf{d_1(x,y)} = \vec{\boldsymbol{\alpha}}^T \overline{\boldsymbol{\theta}}\mathbf{(x,y)}$$
$$\mathbf{d_2(x,y)} = \vec{\boldsymbol{\beta}}^T \overline{\boldsymbol{\varphi}}\mathbf{(x,y)} \qquad \text{Equation 6-15}$$

Here $\vec{\boldsymbol{\alpha}}^T, \vec{\boldsymbol{\beta}}^T, \overline{\boldsymbol{\theta}},$ and $\overline{\boldsymbol{\varphi}}$ denote vectors with elements α_i, β_i, θ_i, and φ_i, respectively, and (x,y) is the current position. In ACGI, the interpolating basis functions are written explicitly in linear form as follows:

$$\theta_1(x,y)=\phi_1(x,y)=\left(\frac{x^2-x}{x^2-x^1}\right)\left(\frac{y^2-y}{y^2-y^1}\right)$$
$$\theta_2(x,y)=\phi_2(x,y)=\left(\frac{x^2-x}{x^2-x^1}\right)\left(\frac{y-y^1}{y^2-y^1}\right)$$
$$\theta_3(x,y)=\phi_3(x,y)=\left(\frac{x-x^1}{x^2-x^1}\right)\left(\frac{y^2-y}{y^2-y^1}\right)$$
$$\theta_4(x,y)=\phi_4(x,y)=\left(\frac{x-x^1}{x^2-x^1}\right)\left(\frac{y-y^1}{y^2-y^1}\right)$$

Equation 6-16

Here, (x, y) is the position of the pixel, whose intensity has to be interpolated, (x^1, y^1) are the coordinates of the upper left corner, and (x^2, y^2) are the coordinates of the bottom right corner of the interpolating block respectively. This corresponds to the bilinear interpolating model governing the variation of the displacement field within each model. This approach utilizes a connected model, i.e., the parameters associated with a given corner point are also valid for that point in the adjoining regions of which that point is a member. This relationship contributes to the smoothness of the motion field, as the displacements within separate regions are not independent of each other.

The goal herein, is to estimate the parameters of the interpolating model α_i, and β_i, for each control point within the region of support, and is accomplished by minimizing the optical flow constraint equation. Briefly, the optical flow constraint equation describes the motion of pixel between two consecutive frames as follows:

$$I(\mathbf{x},\mathbf{y},\mathbf{k})\approx I(\mathbf{x},\mathbf{y},\mathbf{k}+\mathbf{1})+\frac{\partial I(\mathbf{x},\mathbf{y},\mathbf{k}+\mathbf{1})}{\partial x}\mathbf{d}_1(\mathbf{x},\mathbf{y})+\frac{\partial I(\mathbf{x},\mathbf{y},\mathbf{k}+\mathbf{1})}{\partial y}\mathbf{d}_2(\mathbf{x},\mathbf{y})$$ Equation 6-17

This formulation uses the discrete time approximation of the optical flow equation, where I(x, y, k) and I (x,y, k+1) are the two images between which an image

has to be interpolated. Replacing d_1 and d_2, with the expression of the interpolating model described in Equation 6-15, we obtain:

$$I(\mathbf{x},\mathbf{y},\mathbf{k}) \approx I(\mathbf{x},\mathbf{y},\mathbf{k}+\mathbf{1}) + \frac{\partial I(\mathbf{x},\mathbf{y},\mathbf{k}+\mathbf{1})}{\partial x}\vec{\boldsymbol{\alpha}}^T\overline{\boldsymbol{\theta}}(\mathbf{x},\mathbf{y}) + \frac{\partial I(\mathbf{x},\mathbf{y},\mathbf{k}+\mathbf{1})}{\partial y}\vec{\boldsymbol{\beta}}^T\overline{\boldsymbol{\varphi}}(\mathbf{x},\mathbf{y}) \quad \text{Equation 6-18}$$

Equation 6-18 is expected to hold true for all pixels within the region ***R*** of the two images I(x, y, k) and I (x, y, k+1). In order to estimate the displacement parameters, consider the least squared error between the image intensities of the image, and the model:

$$E(\vec{\boldsymbol{\alpha}},\vec{\boldsymbol{\beta}}) = \sum_{\mathbf{x},\mathbf{y}\in\mathbf{R}}\sum\left[I(\mathbf{x},\mathbf{y},\mathbf{k}) - I(x+\vec{\boldsymbol{\alpha}}^T\overline{\boldsymbol{\theta}}(\mathbf{x},\mathbf{y}), y+\vec{\boldsymbol{\beta}}^T\overline{\boldsymbol{\varphi}}(\mathbf{x},\mathbf{y}),\mathbf{k}+\mathbf{1})\right]^2 \quad \text{Equation 6-19}$$

This equation is minimized iteratively using either the gradient descent or conjugate gradient approach. The algorithm proposed by Frakes et al, minimizes the equation using the adaptive multi-grid approach. The block size is determined based on the feature levels within the image, and the interpolating blocks are adaptively sub divided if certain regions have more features than others. The values of α_i, and β_i are iteratively determined until squared error is minimized. Once the interpolating model is determined, any number of slices can be interpolated between two successive images. This approach has proved to be highly effective for the interpolation of medical images for morphological reconstruction of blood vessels[149], as well as for the reconstruction of blood flow from PC MRI datasets[81].

6.3.5 Shortcomings

In the preceding sections, four interpolating strategies were presented in

increasing order of complexity. Each of these methods have been proven to work in a variety of applications, and are consistently applied in image processing. The biggest shortcoming of these approaches is that they are scalar interpolating methods. This means, for a given set of images, only the intensity of the image, which is a scalar function, is interpolated. When applied to multi-dimensional functions, these techniques are applied independently to each dimension. If each component of such multi-dimensional functions is independent of each other, then these methods work well. In situations where there is a relationship between each component of the function, then there is a significant drop in accuracy. Interpolation of fluid mechanics data is one such application where each data point is a multi-dimensional function $\mathbf{V}$= {$\mathbf{u}$ (x, y, z), $\mathbf{v}$ (x, y, z), $\mathbf{w}$(x, y, z)}, whose relationship is determined by the divergence free constraint and the Navier Stokes equations (Equation 6-3). Hence, in the context of fluid dynamic interpolation, there is a need for a technique that takes this dependence into account in the interpolation process. In the following sections, one such approach is proposed that utilizes the property of incompressibility (or zero divergence) in the process of interpolation.

6.4 Divergence Free Interpolation

In the particular situation of interpolating data that stems from an incompressible fluid, i.e., a fluid having neither sources nor sinks, the velocity field $\mathbf{v}$(x) is considered to have zero divergence (Equation 6-5). Therefore, this physical property should be preserved when the data is being interpolated. Classical interpolating strategies are scalar in nature, and hence do not preserve the zero-divergence property during the process of

interpolation. One obvious approach is to interpolate the data using an arbitrary function and then solve the Navier-Stokes equations using the interpolated field as an initial condition for the partial differential equations. However, such an approach is computationally very expensive and is equivalent to conducting CFD directly without taking any measurements. Fatouree et al., proposed a technique that relied on solving PDEs for regularizing the velocity fields obtained from PC MRI, such that the divergence-free constraint is maintained[101]. Other approaches involve decomposing the velocity field into a divergence-free and curl-free component, and then only retaining the divergence-free component of the velocity field[171]. All of these approaches are based on numerical methods, and can only guarantee zero divergence within some numerical error bounds.

In this section, the divergence-free interpolation is carried out using radial basis functions which are divergence free, C^{∞} continuous, have unbounded support, and more importantly, guarantee zero divergence of the resulting velocity field, and is independent of the numerical implementation. The primary difference between the proposed approach and earlier methods is that the velocity field is represented as a function that has the divergence free property implicit in its formulation, compared to the other techniques that explicitly try to minimize the divergence.

6.4.1 Divergence Free Interpolation- Theory[172]

According to the Helmholtz-Hodge decomposition, any 3D vector field can be decomposed into a divergence-free component and a curl free component as follows:

$$\vec{V}(x,y,z) = \nabla u + \nabla \times \vec{w} + \vec{h} \qquad \text{Equation 6-20}$$

Here, u is a scalar potential field, such that $\nabla \times (\nabla u) = 0$, w is a vector potential field such that $\nabla \cdot (\nabla \times \vec{w}) = 0$, and h is a harmonic vector field whose curl and divergence is 0. This theory implies that any vector field with non-zero divergence has a divergence-free component, and a curl-free component. In the case of experimentally measured data of incompressible flow, the true velocity field can be considered to be the divergence-free component, and measurement noise to be the curl-free component. The process of extracting the divergence-free component of a velocity field can also be considered as the projection of a velocity field to some divergence free space. By constructing appropriate basis functions of this divergence free space, it should be possible to use these basis functions for the continuous divergence-free interpolation of velocity fields.

This problem was first tackled by Narcowich and Ward[173], and later by Lowitzch[172], where such a divergence free subspace was introduced having the general form:

$$\Phi(x) = \left\{ -\Delta I + \nabla \nabla^T \right\} \psi(x) \qquad \text{Equation 6-21}$$

where ψ is a scalar-valued, infinitely supported radial basis function, Δ is the Laplacian operator, ∇ is the gradient, and I is the identity matrix. Let Ω be a compact subset of R^N. In the case where the interpolating data appears in the form $\{x_j, d_j\}_{j=1}^N$, where $d = \{d_j\}_{j=1}^N \in R^N$ are data measurements stemming from an underlying vector valued function **f** at given points $X = \{x_j\}_{j=1}^N \in \Omega$, then the divergence-free interpolant has the

form:

$$V_f(x) = \sum_{j=1}^{N} \Phi(x - x_j) c_j \qquad \text{Equation 6-22}$$

The interpolation problem is now to find $\{c_j\}_{j=1}^{N}$, such that :

$$V_f(x_k) = d_k \quad for\ 1 \le k \le N \qquad \text{Equation 6-23}$$

This problem can be restated as a system of linear equations, with the resulting interpolation matrix being positive definite, symmetric, and sparse depending upon the interpolation radial basis function (ψ) used.

Several choices of ψ can be used for the purposes of interpolation. For example Wendland introduced a new class of compactly supported radial basis functions that can be used in equation 6-21 for the purposes of divergence-free interpolation[174]. We propose to use the continuous radial basis function with infinite support introduced by Narcowich and Ward[173], which is based on the Gaussian function (Figure 6.2):

$$\psi_\alpha(x) = e^{-\alpha\|x\|^2} \in C^\infty, x \in R^N$$
$$\Phi_\alpha(x) = \{-\Delta I + \nabla\nabla^T\}\psi_\alpha(x) \qquad \text{Equation 6-24}$$

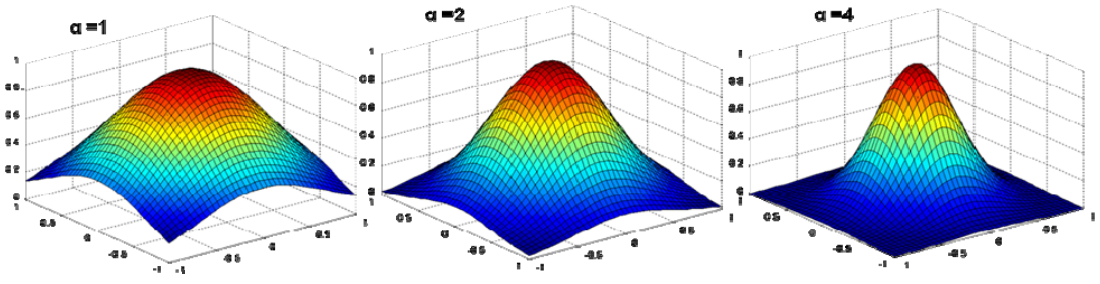

Figure 6.2: The characteristic shape of the radial basis function for different values of α, with a grid spacing of 0.05

The advantage of using such a formulation is that it is smooth, and the interpolation tensor $A_\alpha = (\Phi(x_j - x_k))_{j,k=1}^N$ is strictly positive definite for any set of measured data points. The interpolating function is dense, i.e., any divergence-free vector valued function **f**: $R^N \rightarrow C^N$, contained in a Sobolev space can be approximated arbitrarily well by a linear combination of divergence free matrix valued radial basis functions generated by the Gaussian function of infinite support.

6.4.1.1 *Proof of zero divergence*

Recall that a vector valued function **f** is divergence free if and only if $\nabla \cdot f = 0$ holds for all $x \in R^N$. Let $\Phi_\alpha^i(x)$ be an arbitrary column of $\Phi_\alpha(x)$ for $1 \le i \le N$. Then for N >= 2:

$$\begin{aligned}
\nabla \cdot \phi_\alpha^i &= \nabla \cdot \left\{ -\Delta I + \nabla\nabla^T \right\}_i \psi_\alpha(x) \\
&= \nabla \cdot \left(-\delta_{ij} \sum_{l=1}^{N} \partial^2_{x(l)} + \partial x_{(i)} \partial x_{(j)} \right)_{j=1}^{N} \psi_\alpha(x) \\
&= \left\{ -\sum_{l \neq i} \partial^2_{x(l)} \partial_{x(i)} + \sum_{r \neq i} \partial^2_{x(i)} \partial_{x(r)} \right\} \psi_\alpha(x) \\
&= 0
\end{aligned}$$

Equation 6-25

This proof confirms that the matrix valued radial basis function has zero divergence, and can be used to compactly represent a velocity field of any form. By applying the derivative to Equation 6-24, it can be further simplified to:

$$\begin{aligned}
\Phi_\alpha(x) &= \left\{ -\Delta I + \nabla\nabla^T \right\} e^{-\alpha \|x\|^2} \\
&= \left\{ (2(N-1)\alpha - 4\alpha^2 \|x\|^2) I + 4\alpha^2 x x^T \right\} e^{-\alpha \|x\|^2}
\end{aligned}$$

Equation 6-26

This is the form of the interpolating spline that will be used in the presented

application.

6.4.2 Divergence-Free Interpolation – Implementation

The desired objective is to use a set of measurements from PC MRI, V_M, for reconstructing a velocity field within a blood vessel of interest Ω, at a much higher resoluition V_I, such that the divergence of the resulting velocity field is zero. Since the divergence-free principle holds true only within anatomic structures containing blood flow, there are two problems that have to be tackled:

1.) Identification of the vessel domain Ω to enforce the zero-velocity no-slip condition along the vessel wall $\partial\Omega$

2.) Determination of the divergence-free interpolation function that will hold valid for the entire domain of the blood vessel.

The important thing to note here is that the MRI acquisitions for determining the vessel domain Ω may be different from the PC MRI measurements for velocity. Hence, the interpolation problem has to be set in a framework, where the control points are based off the vascular domain Ω. This section will describe the necessary mathematics and derivations critical for this process.

Recall that the divergence-free interpolation model described using matrix valued radial basis functions has the form:

$$V(\vec{x}) = \sum_{j=1}^{P} \Phi(|\vec{x} - \vec{x}_j|)\vec{c}_j$$

where

$$\vec{x} = (x, y, z)$$

$$\vec{c}j = (c_{j1}, c_{j2}, c_{j3})$$

Equation 6-27

where $V(\vec{x})$, is the interpolating function, $\Phi(\vec{x})$, is the divergence-free matrix valued radial basis function, and $\vec{c}_j$ is the vector valued set of coefficients that have to be determined. For the interpolation process, a set of **P**, stationary, control points are needed. Once the boundary of the vessel is known, these control points can be placed at fixed intervals within the vessel. The radial basis function $\Phi(|\vec{x} - \vec{x}_j|)$ is described as a function of the distance of any point $(\vec{x})$, from the control point $(\vec{x}_j)$.

Before these functions can be used for interpolation, certain modifications have to be made. First and foremost the determination of the coefficients $\vec{c}_j$ is a non-trivial task. It is highly dependent upon where the control points are defined. Furthermore, the velocity measurements may not exactly coincide with these control points. There is a computational challenge as well, where the number of parameters to be estimated increases with increasing number of measured data points. For these reasons, a technique is designed that facilitates the efficient estimation of the coefficients associated with the interpolation model.

The interpolating equation described above can be written in a matrix form as follows:

$$\overline{V} = \overline{\Phi}\,\overline{C} \qquad \text{Equation 6-28}$$

Here $\overline{\Phi}$ is a 3Nx3P matrix associated with the **N** measured and **P** assigned control points, $\overline{C}$ is a 3P x 1 matrix, and $\overline{V}$ is the matrix consisting of the 3 components of the velocity tiled vertically. Let $V_M(\vec{x})$ be the 3Nx1 matrix containing the set of **N** velocity

measurements tiled vertically. Define the error function:

$$\vec{e} = \overline{V} - \overline{V}_M \qquad \text{Equation 6-29}$$

The squared error associated with this function becomes:

$$E = \vec{e} * \vec{e}^T = || \vec{e} ||^2$$
$$E = (\overline{\Phi}\overline{C} - \overline{V}m) * (\overline{\Phi}\overline{C} - \overline{V}m)^T \qquad \text{Equation 6-30}$$

Given this error function, the parameters can be estimated by minimizing the least squared error. Differentiating E with respect to the vector $\overline{C}$, and equating the equation to zero, results in the following expression for $\overline{C}$:

$$\overline{C} = (\overline{\Phi}^T \overline{\Phi})^{-1} \overline{\Phi}^T V_M \qquad \text{Equation 6-31}$$

There are several ways to solve this system of linear equations. Option 1 is to use optimization methods such as gradient descent, conjugate gradient, or multi-resolution methods to iteratively solve for the parameters. Since the matrix to be inverted is positive definite symmetric, but not sparse, no specific computational gains are achieved by taking an iterative approach. Instead, the coefficients can be estimated by directly inverting the symmetric matrix. In doing so, specific properties of positive definite symmetric matrices can be exploited in the inverting process. Hence, the built in ***lscov*** function in Matlab is used for determining the coefficients.

The general algorithm for parameter estimation is as follows:

1. Create a 3P x 1 vector of the control point locations by stacking the x, y, and z co-ordinates of each point on top of each other, i.e:

$$\vec{x}_C = \left[x_1\ y_1\ z_1 \quad x_2\ y_2\ z_2 \quad \ldots \quad x_P\ y_P\ z_P\right]^T$$

2. Create a 3N x 1 vector of the locations where velocity measurements are available by stacking the x, y, and z co-ordinates of each point on top of each other, i.e.,

   $$\vec{x}_M = \left[x_1\ y_1\ z_1 \quad x_2\ y_2\ z_2 \quad \ldots \quad x_N\ y_N\ z_N\right]^T$$

3. Create a 3N x 1 vector of the velocity measurements by stacking the corresponding velocity values for each point, i.e.:

   $$\vec{V}_M = \left[u_1\ v_1\ w_1 \quad u_2\ v_2\ w_2 \quad \ldots \quad u_N\ v_N\ w_N\right]^T$$

4. For each measured point i, let the a 3x1 distance vector from the control point j be: $\vec{d}_{ij} = \left|\vec{x}i - \vec{x}_j\right|$

5. Evaluate the matrix valued radial basis function Φ_{ij} for each $\vec{d}_{ij}$ (3x3 matrix) using Equation 6-26, and tile each of them to form a 3N x 3P matrix.

6. Determine the coefficients by inverting $\Phi^T\Phi$, and multiplying it with $\Phi^T V_M$. The resulting coefficients are stored for use later.

Once the model parameters are estimated, the velocity values can be computed for any point within the flow domain Ω, using Equation 6-28, where Φ is a 3x3P matrix, $\overline{C}$ is a 3P x 1 vector, and V is a 3x1 vector corresponding to the three components of the velocity at that point.

6.4.3 Divergence Free Interpolation - Summary

In the preceding sections, a novel form of the divergence-free interpolation technique was proposed. The approach uses experimentally measured velocities in a divergence free framework for reconstructing a dense, smooth, velocity field within the

domain of interest. The advantages of the proposed technique are three fold: a) The resulting velocity field is divergence-free; b) The interpolating function is smooth and C^{∞} continuous, implying that velocity field can be interpolated up to any desired grid resolution; c) The datasets outlining the domain for interpolation and those containing the velocity measurements, need not be the same. In the following sections, the methodology for using the divergence-free technique in the setting of *in vivo* PC MRI applications is described in detail.

6.5 *In Vivo* Application

In this section, the general algorithm for reconstructing the 4D (3D + time) velocity field from *in vivo* MRI data is described. MRI acquisitions typically consist of 2D images with intensity values corresponding to anatomical structures (anatomic MRI), or components of blood flow velocities (PC MRI). Such formats are not conducive for conducting detailed fluid dynamic analyses, which require the velocities to be part of some discrete geometry (such as a mesh). Therefore, the velocity field needs to have some sort of topology and form necessary for fluid dynamic analyses.

As described in section 6.1, high resolution 3D PC MRI is associated with prohibitively long acquisition times, and hence it is not feasible to acquire them in a pediatric setting. Conversely, high resolution 3D anatomic MRI datasets can be acquired very fast and these datasets can be used for reconstructing accurate 3D anatomic models. This has previously been demonstrated in our laboratory by Frakes and Yoganathan[149, 175]. Therefore, reconstructing a 4D velocity field within the TCPC in a realistic time frame requires the PC MRI data to be acquired at a lower resolution, and the anatomic

data to be acquired in a higher resolution. Two challenges need to be overcome in order to successfully accomplish this task:

1. How is TCPC flow domain automatically determined in both the anatomic MRI and velocity MRI datasets?
2. How can the velocity data from PC MRI be used to reconstruct the velocity fields inside the geometry derived from high resolution anatomic MRI in a divergence free manner?

A new approach has been designed for this purpose and is described in detail in the forthcoming sections.

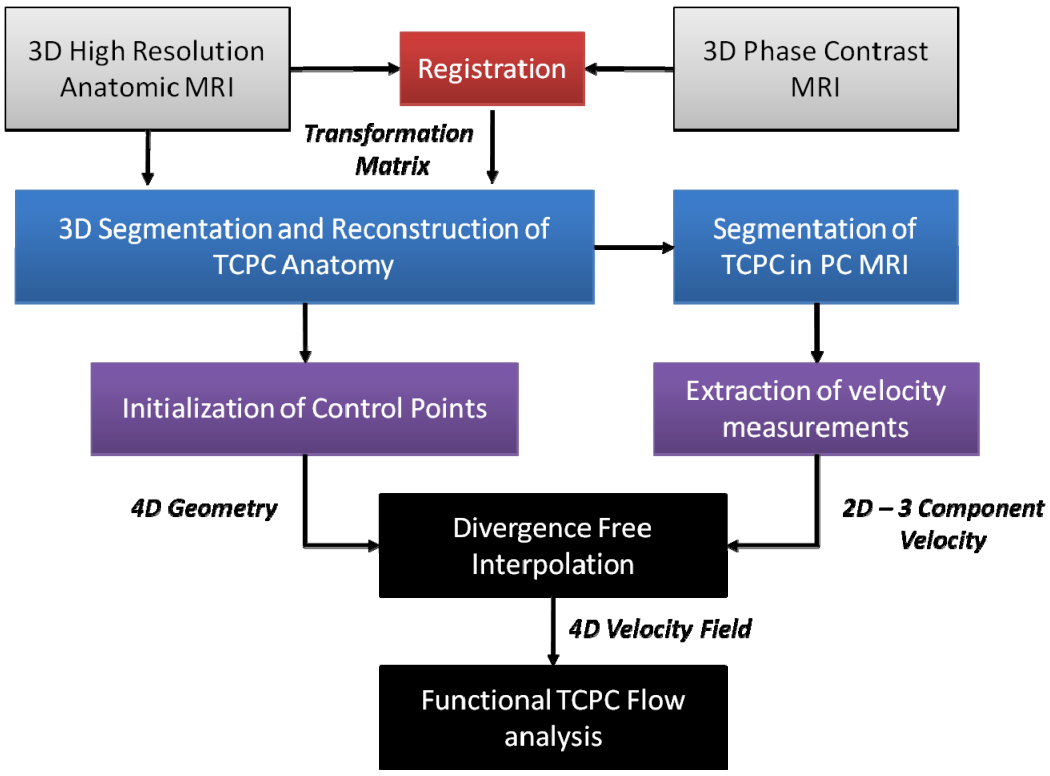

Figure 6.3: Overall Approach for 3D velocity field reconstruction from PC MRI

6.5.1 Overall Approach

The overall approach for the 3D velocity field reconstruction is outlined in Figure 6.3. Such an approach allows for significant computational efficiency as the interpolation is done only within the vessel of interest, and is not extended to the entire MRI domain. Furthermore, the entire process is fully automatic; the only user intervention taking place at the anatomic segmentation process. A finite element mesh is generated at the end of the interpolation process for facilitating the fluid dynamic analysis. This is the first time a 3D *in vivo* velocity field reconstruction methodology has been established that can be implemented using a clinical MRI scan acquired within a realistic time frame. The fully automatic nature of the processing significantly reduces the user time and variability in conducting the analysis for each TCPC case.

6.5.2 Image Acquisition

As described in Figure 6.3, two sets of data are required: a) high resolution 3D anatomic acquisition; b) low resolution 3D PC MRI acquisition. The two datasets are typically acquired in succession, i.e., the anatomic stack is acquired first followed by the velocity stack. Absolute care is taken to make sure that there is no patient motion between, or during the two acquisitions. If that does happen, then both the sequences have to be repeated for the algorithm to work accurately.

6.5.2.1 Anatomic Acquisition

In section 4.2.1, an MRI sequence for 3D reconstruction of the TCPC anatomy is described. The sequence is static, i.e., the anatomic stack is acquired at a single snapshot in time. Such an acquisition works well for extracting rigid geometries for conducting

computational and experimental studies. Indeed, *in vivo* PC MRI acquisitions are pulsatile and the boundaries of the TCPC do move over the cardiac cycle. Hence, time permitting; a cine axial MRI stack will be preferred such that the moving wall and boundary of the TCPC can be captured. The algorithm is designed to be robust enough to handle both the cases.

The patients are primarily recruited and imaged at CHOP (n=20), with a few from Children's Hospital of Boston (CHB, n=4). A Siemens 1.5T Sonata or Avanto scanner (Siemens Medical Solutions, Erlangen, Germany) is used for patients from CHOP and a Philips Intera 1.5T (Philips Medical Systems, Netherlands) for patients from CHB. For the static anatomic stack, the true fast imaging with steady state precession (trueFISP) sequence having a TR of 150-250 ms and a TE of 1.1-1.5ms is used. The scan is taken in a single breath hold, and the resolution and slice thickness is purely dependent upon the patient's age and weight. If the patient is too young for a breath-hold then a free breathing scan is acquired. Axial slices of 3-5 mm thickness with approximately 1 mm^2 in-plane resolution are obtained spanning the entire thorax region. The acquisition is perfectly axial, i.e., the images are parallel to the Right –Left, Anterior-Posterior (X-Y) plane of the MRI coordinate system, and perpendicular to the Superior-Inferior (Z) axis. The order of acquisition is in the increasing Z direction (going from inferior to superior). This is not mandatory, as the algorithm will automatically correct for any orientation.

6.5.2.2 PC MRI Velocity Acquisition

The PC MRI velocity acquisition is comprised of 5-10 contiguous slices of retrospectively gated, 3D phase-encoded velocity maps in an off axis coronal view of the

TCPC. To facilitate the data analysis, the acquisitions are perfectly perpendicular to the axial anatomic slices. The matrix size ranges from 192 x 192 – 320 x 320 and varies depending upon the patient size. The pixel sizes are 1.25 x 1.25 mm^2, the slice thickness is 6 mm, flip angle is 15°, and the TR/TE ratio ranging from 42/3.1 – 69/4.8 is used. A velocity encoding of 80 cm/s is used for the superior-inferior (Z) and the right-left (X) directions, while an encoding of 40 cm/s is used for the anterior-posterior (Y) direction respectively for CHOP, while a venc of 120 cm/s is used for all three directions for patients from CHB. Each component of the velocity in each location is acquired in a single breath hold. Care is taken to capture the entire TCPC baffle, the SVC, IVC, LPA, and the RPA respectively within all the acquired slices. Figure 6.4 shows a typical coronal slice going through the TCPC.

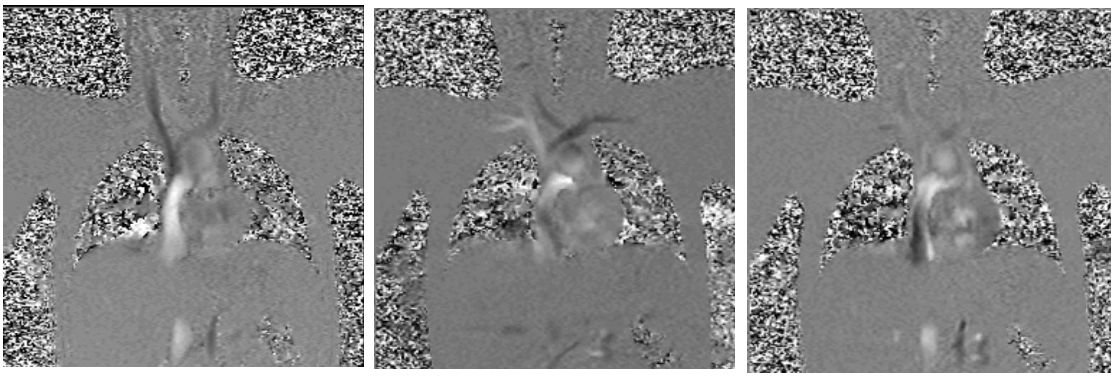

SI RL AP

Figure 6.4: The 3 velocity components images associated with the PC MRI acquisition in a coronal view (SI – Superior Inferior, RL – Right left, AP – Anterior Posterior).

6.5.3 3D Geometric Reconstruction

The next step is the 3D reconstruction of the TCPC anatomy. Frakes et al

proposed and developed a methodology for TCPC reconstruction purposes, where a shape element in the form of a bouncing ball was used to segment the TCPC anatomy (see Section 4.2.2). However, there are two primary deficiencies associated with this method that warrants further improvement:

1.) The segmentation is not smooth
2.) The segmentation is primarily a 2D method
3.) To go from a set of 2D binary images to a 3D model, requires third-party commercial software in the form of MIMICS (Materialize inc) which is expensive and requires significant manual intervention
4.) As a consequence of step (3), the resulting 3D geometry is in a coordinate system defined by MIMICS, and loses all the information inherent in the DICOM headers of the acquisition.
5.) If the axial dataset has multiple phases associated with the acquisition, then the algorithm will have to be run multiple times for each phase, which significantly increases the processing time

To address all these issues, a new fully automatic 3D segmentation and reconstruction algorithm based on the level set algorithm described in Chapter 5 is designed, developed, and implemented. In the following section, the process of extending the 2D method to 3D is presented.

6.5.3.1 3D Level Set Implementation

The extension of the segmentation algorithm from 2D to 3D is quite straightforward. Recall that the partial differential equation governing the level set

evolution as presented in section 5 is written as:

$$\phi_t = \mu\left(\Delta\phi - div\left(\frac{\nabla\phi}{|\nabla\phi|}\right)\right) + \alpha\delta(\phi)div\left(F_I\frac{\nabla\phi}{|\nabla\phi|}\right) + \nu F_I\delta(\phi) \qquad \text{Equation 6-32}$$

Here φ is the zero level set that is evolved until it sits on the boundary of the vessel, μ is a parameter describing the necessary regularization, α governs the emphasis on the external vs. the internal force, and ν specifies the relative location of the initial level set with respect to the geometry to be segmented. For initial first pass segmentation, the geometry is first segmented using the bouncing ball algorithm, and the resulting geometry serves as starting point for the level set algorithm. 3D distances are computed and the zero level set is initialized as the edge of this segmentation. The gradients of the level set function are computed in 3D, and the entire level set is evolved in 3D. This allows the algorithm to maintain smoothness not only in the contour plane but in the through plane direction as well.

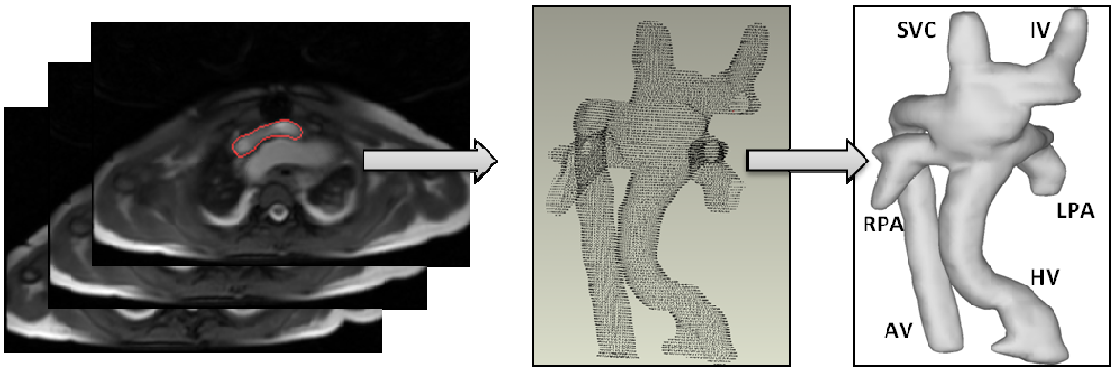

Figure 6.5: Sequence demonstrating the process of level set segmentation for a complex geometry of the TCPC. The segmented 3D contours are exported in point cloud format that is triangulated to form a surface. Shown here is a TCPC model with 4 inlets: SVC, inominate vein (IV), azygous vein (AV), and the IVC, and 2 outlets: LPA and the RPA

The original axial dataset is stacked to form a 3D isotropic dataset (by first interpolating it using ACGI), and the gradient magnitude of this function is used as the external energy for the segmentation algorithm. Once the level set function converged, the zero level set is sampled at a 0.5 mm resolution, and the coordinates are transformed from an image-based to an MRI-based system and the points are exported in a format that can be imported into Raindrop Geomagic software for surface generation. It should be noted that the Geomagic step is only for triangulation, and is used for reconstructing the 3D surface for visual purposes. It plays no role in the velocity field reconstruction process. Figure 6.5 shows an example of this process going from the segmentation to point cloud to surface generation and Figure 6.6 shows a comparison between the

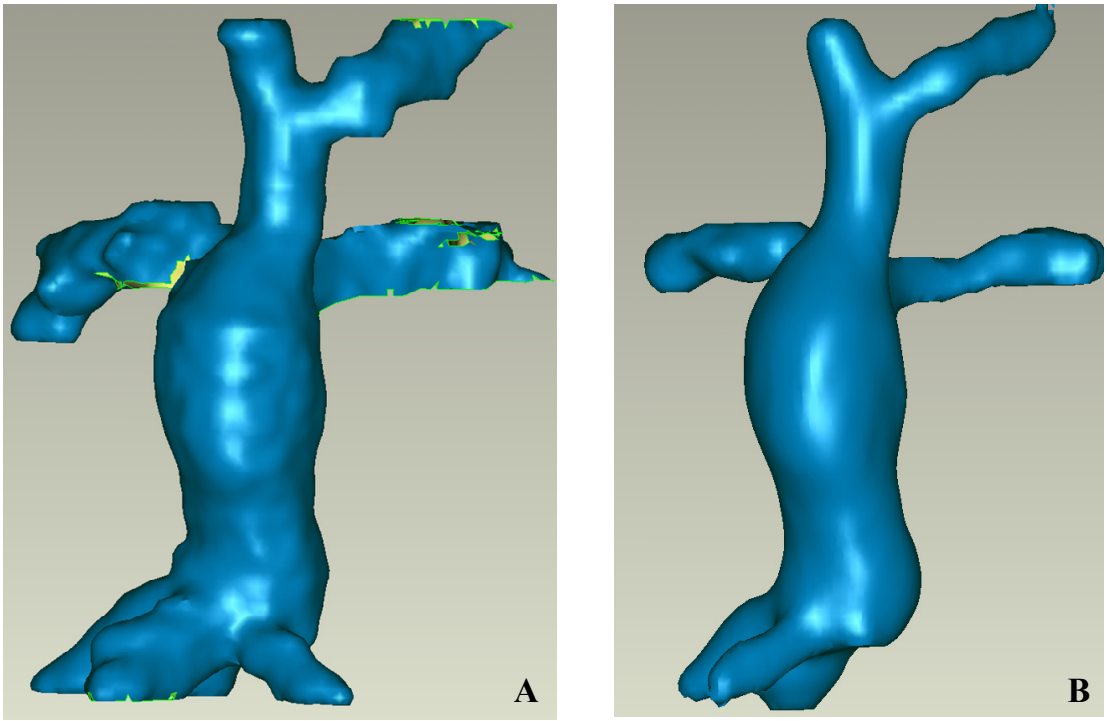

Figure 6.6: Comparison of methods between a reconstruction from the bouncing ball algorithm (A) and the level set approach (B). Notice that the geometry is smooth and there are no open triangles and irregular points within the geometry

bouncing ball approach described in Chapter 4 and the level set method. Notice that the level set method provides significantly smoother geometries compared to the bouncing ball method.

Another advantage of using the level set based segmentation approach is that multiple phases of the anatomy can be segmented automatically. Figure 6.7 shows an example where the difference between using a static segmentation and a time varying level set segmentation is evident.

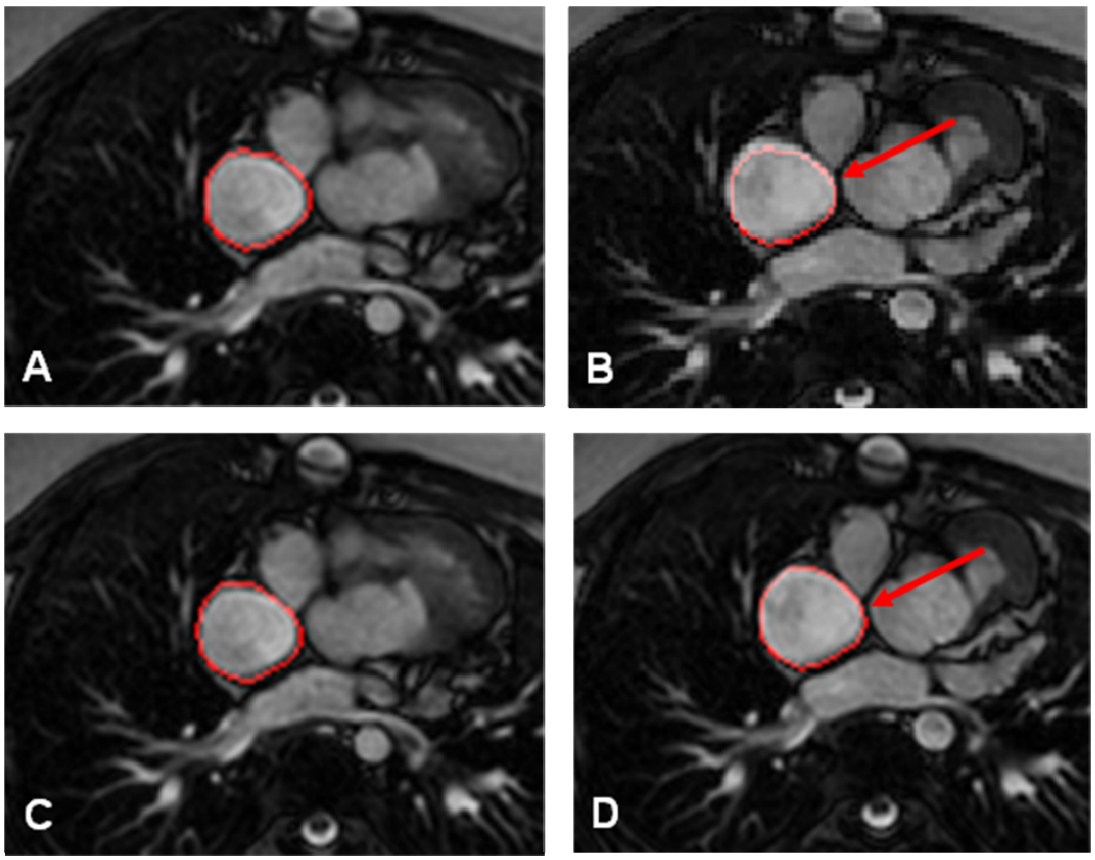

Figure 6.7: A) Segmentation using level sets in the first phase; B) Active contour from phase 1 superimposed onto phase 10 The arrow shows that the vessel moves out of the contour boundary; C) Segmentation using level sets applied to multiple phases – Phase 1; D) Phase 10 – Notice that the contour has been shifted to sit on the vessel boundary.

6.5.4 Data Registration

Once the geometry is segmented for all the cardiac phases, the next step is the segmentation of the PC MRI velocities in the coronal orientation. This is accomplished by registering both the axial anatomic and coronal PC MRI datasets with the MRI coordinate system. The information stored in the DICOM header file is used for this purpose. Recall, that an equation for a point $\vec{x}$ on a plane can be expressed as: $\vec{x}(s,t) = \vec{u} + s\vec{v} + t\vec{w}$, where $\vec{u}$ is the location of a reference point with respect to the origin of the MRI coordinate system, $\vec{v}$ and $\vec{w}$ are linearly independent vectors starting at $\vec{u}$ and pointing in different directions along the plane. The vectors $\vec{u}$, $\vec{v}$ and $\vec{w}$ can be extracted directly from the DICOM header file, in the form of the parameters "ImagePositionPatient" (3x1 vector), and "ImageOrientationPatient" (6x1 vector) respectively. For converting an image from the image coordinate system (i, j), where i and j are the row and column indices of the image matrix respectively, to (x, y, z) in the MRI Coordinate system, the following steps are taken:

1) For each Image I, extract the two parameters $\vec{u}$ ="ImagePositionPatient", and $[\vec{v}\ \vec{w}]$ = "ImageOrientationPatient" from the DICOM header file. The vector $\vec{u}$ is the location of the point associated with the first element in the image matrix (1, 1).
2) For each matrix location I (i, j), calculate the location of the point in the MRI coordinate system according to the formula: $\vec{x}(j,i) = \vec{u} + j\Delta x\vec{v} + i\Delta y\vec{w}$, where Δx, and Δy are the pixel spacing in the X and Y directions, and are also extracted from the DICOM header file.
3) Save the coordinate in three matrices.

This algorithm is applied to both the axial anatomic datasets and the coronal PC MRI datasets. This is equivalent to a rigid body registration done between the two acquisitions.

Once registered, the next step is to segment out the TCPC flow domain using the segmentation from the 3D anatomic dataset. The primary idea is to determine which pixels from the PC MRI coronal acquisition fall inside the segmented TCPC domain, and which ones lie outside. In order to accomplish that task, the following steps are taken:

1.) For each point ($x_{coronal}$, $y_{coronal}$, $z_{coronal}$), its corresponding location on the 3D anatomic dataset is determined as follows:

$$i_{axial} = round((y_{coronal} - \vec{u}_{axial}(2)) / \Delta y_{axial})$$
$$j_{axial} = round((x_{coronal} - \vec{u}_{axial}(1)) / \Delta x_{axial})$$
$$k_{axial} = round((z_{coronal} - \vec{u}_{axial}(3)) / \Delta z_{axial})$$

2.) If the point (i_{axial}, j_{axial}, k_{axial}) lies on the segmented TCPC domain in the 3D anatomic dataset, then ($x_{coronal}$, $y_{coronal}$, $z_{coronal}$) is considered to be inside the flow domain, and

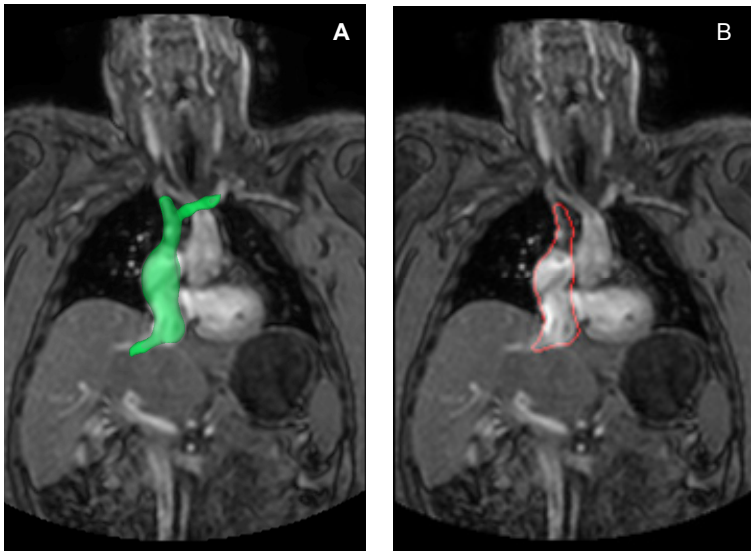

Figure 6.8: A) The 3D TCPC model superimposed on the coronal slice; B) The segmented flow domain

the velocities are retained for interpolation, else it is considered to be outside the flow domain and is discarded. Figure 6.8 shows an example of the TCPC segmented in the domain using this approach.

In a situation where the 3D TCPC segmentation does not exactly correspond to the TCPC in a coronal domain, then a manual rigid body registration is performed to correct this. This happens when there is slight motion between the acquisitions, or if the respiratory phase of the axial and coronal acquisitions is not the same. For example, Figure 6.9 shows a situation when there is a slight offset between the TCPC segmented using the proposed algorithm and the actual TCPC in the coronal domain. The exact offset is determined by manually offsetting the x, y, and z coordinates of the coronal dataset until the contour precisely segments the TCPC domain. This can be done very quickly as the offset is typically very small. It is evident from Figure 6.9 that the manual

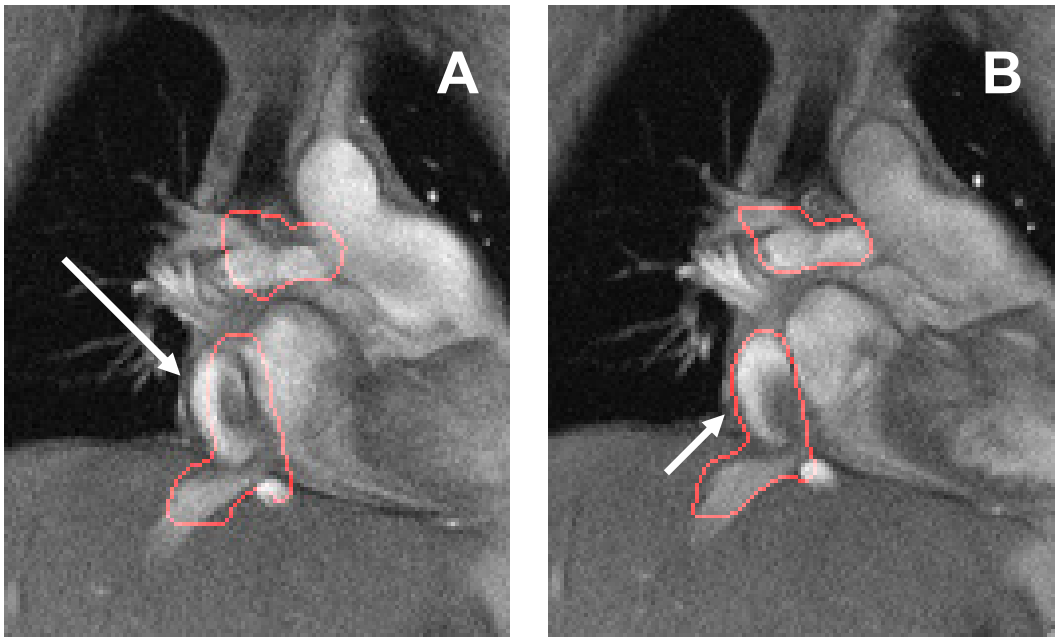

Figure 6.9: A) Segmentation contour offset before correction; B) After correction. The arrow shows the area of the offset.

offsetting method is quite effective in correcting the registration error.

6.5.5 Determination of Interpolation Coefficients

Now that the anatomic reconstruction and the PC MRI datasets are registered and segmented, the coefficients of the divergence free interpolation model can now be determined. The algorithm is as follows:

1) Initialize the control points: Using the anatomic reconstruction, a vector of **P x 1** control point locations is initialized inside the flow domain. Let these vectors be: $\mathbf{X}_{CP}$, $\mathbf{Y}_{CP}$, and $\mathbf{Z}_{CP}$, associated with each component of the position vector.

   Initialize the interpolation coefficients: Let the vectors of the **N x 1** PC MRI velocity measurements and their corresponding locations in the MRI coordinate system be: $\mathbf{U}_{VM}$, $\mathbf{V}_{VM}$, $\mathbf{W}_{VM}$, $\mathbf{X}_{VM}$, $\mathbf{Y}_{VM}$, and $\mathbf{Z}_{VM}$, associated with each component of the velocity and position vectors
2) The **3N x 3P** Φ matrix and the consequent **3P x 1** interpolation coefficient matrix are then evaluated using Equation 6-26 and Equation 6-31 respectively.

6.5.6 Divergence-free Interpolation (DFI)

Once the interpolation coefficients are determined, the next step is to determine the velocity field within enter the TCPC flow domain. This is accomplished as follows:

1) A vector of **M x 1** coordinate locations of every node inside the segmented TCPC anatomy is generated. Let these vectors be: $\mathbf{X}_{AP}$, $\mathbf{Y}_{AP}$, and $\mathbf{Z}_{AP}$.
2) The **3M x 3P** $\mathbf{\Phi}$ matrix is determined.
3) The **3M x 1** interpolated velocity matrix is evaluated using Equation 6-8.

   Once the velocity vectors at each node within the anatomic reconstruction are

determined, a mesh needs to be generated such that fluid dynamic analyses can be performed using these flow fields. This is done using a structured brick mesh by establishing connectivity between each of the anatomic segmented nodes. The connectivity is established as follows:

1) Let the binary segmented axial stack be I(i, j ,k), where i, j, and k are the row, column and height indices of the 3D matrix
2) For k going from 1 to height
    a. For i going from 1 to number of rows
        i. For j going from 1 to number of columns
            1. d(1)=I(i,j,k)
            2. d(2)=I(i+1,j,k)
            3. d(3)=I(i, j+1, k)
            4. d(4)=I(i+1, j+1,k)
            5. d(5)=I(i, j, k+1)
            6. d(6)=I(i+1, j, k+1)
            7. d(7)=I(i, j+1, k+1)
            8. d(8)=I(i+1, j+1, k+1)
            9. if (d(1)*d(2)*d(3)*d(4)*d(5)*d(6)*d(7)*d(8)) not zero
                a. the brick connectivity d is stored
            10. else
                a. it is not stored
            11. end if
        ii. end For

b. end For

3) end For

Once the connectivity is established, and every node is part of some finite element, then the node locations, the velocity values, and the connectivity information are written to a text file in a format that can be read by Tecplot (Amtec Engineering, Bellevue, WA) for further analysis. This approach is followed for the velocity field reconstructed at every phase of the cardiac cycle, and the velocity fields of each phase are stored as a separate Tecplot file.

6.5.7 Analysis Methods

The 3D velocity fields are imported into Tecplot for analysis. Three primary forms of analyses are performed: a) streamtrace plots for quantifying the global flow structures within the TCPC; b) evaluation of the viscous dissipation equation for quantifying the fluid shear losses; c) evaluation of hepatic flow splits to determine how the IVC flow is distributed to the LPA and the RPA; d) average particle transit times.

6.5.7.1 Streamtraces

Once the 3D velocity field dataset is imported into Tecplot, the ***"Extract Slice by Plane"*** feature of Tecplot is used to extract a slice (or multiple slices) from the dataset. The plane is then made as the only zone visible in the workspace. Using the ***"Add a Rake of Streamtraces"*** feature, a set of points are seeded on this plane. Inside the stream trace options tab, the ***"streamtrace format"*** is set to ***"volume"*** to ensure that the streamtraces are 3D. Several streamtrace rakes are initialized using multiple planes in multiple orientations, such that flow structures are clearly visualized in multiple vessels. Figure

6.10 shows an example of the process in an extracardiac geometry.

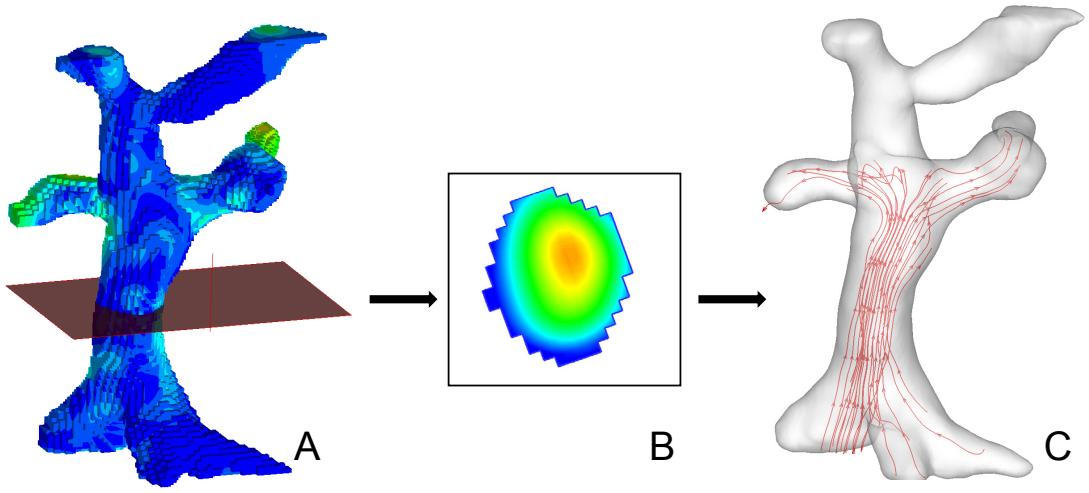

Figure 6.10: A) The process of extracting slice; B) The extracted slice; C) Streamtraces

6.5.7.2 Viscous Dissipation Energy Losses

Calculation of the viscous dissipation energy loss is performed on the reconstructed velocity data using the following equation:

Equation 6-33

$$E_{Loss} = \iiint_{Volumes} \eta \cdot \left[2 \cdot \left(\left(\frac{\partial u}{\partial x} \right)^2 + \left(\frac{\partial v}{\partial y} \right)^2 + \left(\frac{\partial w}{\partial z} \right)^2 \right) + \left(\left(\frac{\partial v}{\partial x} \right) + \left(\frac{\partial u}{\partial y} \right) \right)^2 + \left(\left(\frac{\partial w}{\partial y} \right) + \left(\frac{\partial v}{\partial z} \right) \right)^2 + \left(\left(\frac{\partial u}{\partial z} \right) + \left(\frac{\partial w}{\partial x} \right) \right)^2 \right]$$

In this equation η is the dynamic viscosity; u, v, and w are the velocity components in the x, y, and z directions respectively. The derivatives are computed in Tecplot using the ***"Data ➔ Alter ➔ Specify Equations"*** feature, and the energy loss in mW is evaluated using the ***"Analyze ➔ Perform Integration"*** feature applied to the whole TCPC control volume.

6.5.7.3 IVC Flow Splits

IVC flow splits provide important information about the TCPC physiology and how well it distributes the nutrients from the gastro-intestinal system to the lungs. Clinical studies indicate that effluents from the hepatic veins into the IVC contain proteins that are critical for normal functioning of the lungs. One manifestation of the hepatic flow obstruction to the lungs is the formation of pulmonary arteriovenous malformations (PAVMs). PAVMS are intrapulmonary arterial to venous shunts where the systemic venous blood reaches the pulmonary venous system through abnormal vascular connections proximal to the gas exchange units. The primary consequence of PAVMs is increasing cyanosis and decreased oxygen saturation.

Hence, quantifying IVC flow splits provide a useful diagnostic tool for determining the patency of the TCPC. The only previous study was performed by Fogel et al., who used MR tagging of blood flow to quantify the hepatic flow splits *in vivo*[141]. A more accurate approach is to use the 3D particle streamlines from Section 6.5.7.1 for quantifying the hepatic flow splits. The algorithm is as follows:

1) Extract a plane from the IVC baffle of the TCPC as shown in Figure 6.10.
2) Seed this plane densely with points (or particles).
3) Extract all the streamtraces and export them to a text file.
4) Import the streamtrace locations and velocities into MATLAB.
5) Determine the source and endpoint of every streamtrace, and which one of the streamtraces originating from the IVC exit at the LPA and the RPA.
6) The hepatic flow split percentage is evaluated as: 100*(Total number of streamtraces ending in the LPA) / (Total number of streamtraces).

This process is followed iteratively for each cardiac phase and an average hepatic flow split percentage is evaluated.

6.5.7.4 Vortex Sizes

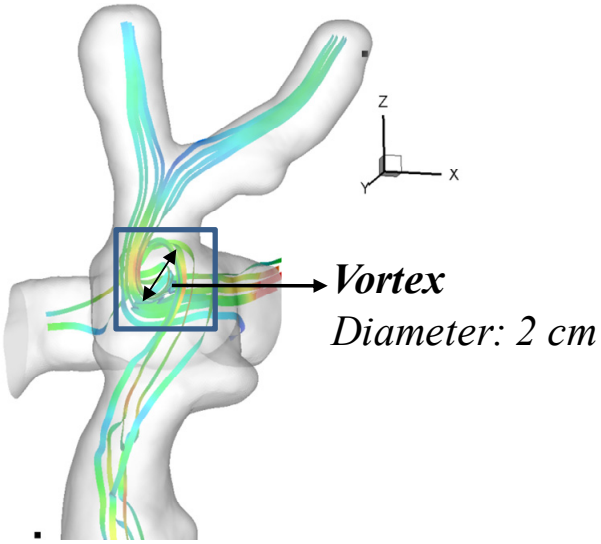

Figure 6.11: The process of measuring the vortex size. The diameter of the largest vortex (shown in the figure) is evaluated in Tecplot

One of the primary differences between intraatrial and extracardiac TCPCs is the presence of a vortex inside the intraatrial baffle. Although this phenomenon has been previously reported, it has never been quantified. This specific flow structure can be quantified using the 3D streamtraces derived from the velocity field as follows.

1) Extract a plane from the IVC baffle of the TCPC as shown in Figure 6.10.
2) Seed this plane with sparsely spaced points
3) Determine the region of the vortex visually by inspecting the streamtraces
4) Measure the diameter of the largest vortex inside the baffle using the ***"Probe***

Data" feature of Tecplot

Only the diameter of the largest vortex is retained for comparison. Figure 6.11 shows an example of how the vortex size is calculated.

6.5.7.5 Average particle transit time

This parameter is evaluated by computing the total time taken by particles along each streamline from the IVC, to exit the connection. The value is then averaged for all the streamtraces.

6.6 Validation Protocol

A multi-step validation is conducted for each of the proposed techniques. The first two cases comprise a theoretical divergence free function, and the 2D steady driven cavity flow problem. These are ideal test cases that have velocity fields which are already divergence-free. In the third test case, a CFD solution of the TCPC will be used followed by *in vitro* PC MRI for the fourth test case respectively. For each of these validation methods, the following quantitative error metrics are defined:

$$RMSError\ (cm/s) = \sqrt{\sum_{FlowDomain}(u_i - u_o)^2 + (v_i - v_o)^2 + (w_i - w_o)^2}$$

$$\%RMS_{Error} = \frac{100 \cdot \sqrt{\sum_{FlowDomain}(u_i - u_o)^2 + (v_i - v_o)^2 + (w_i - w_o)^2}}{\sqrt{\sum_{FlowDomain}u_o^2 + v_o^2 + w_o^2}}$$

$$Average\ Error(u)(cm/s) = \frac{\sqrt{\sum_{FlowDomain}(u_i - u_o)^2}}{N}$$

$$\%Error = \frac{100 \cdot \sqrt{(\bar{u}_i - \bar{u}_o)^2}}{\bar{u}_o}$$

Equation 6-34

Here u_i, v_i, and w_i are the interpolated velocities, u_o,v_o, and w_o are the original (or reference velocities). The average and percentage errors are calculated for each component of the velocity as well as the velocity magnitudes (the u inside the bracket for average error can be any one of the 3 components). Additional validation is performed for testing the efficacy of the method in quantifying viscous dissipation losses.

6.6.1 Divergence-Free Analytical Function

Several divergence free functions exist in the literature. Any of these functions can be used for validation purposes. The function chosen here is as follows:

$$U = 5 \cdot Y^2$$
$$V = (1 - X^2) \cdot (Y - 1) + X \qquad \text{Equation 6-35}$$
$$W = -1 \cdot Z \cdot (1 - X^2)$$

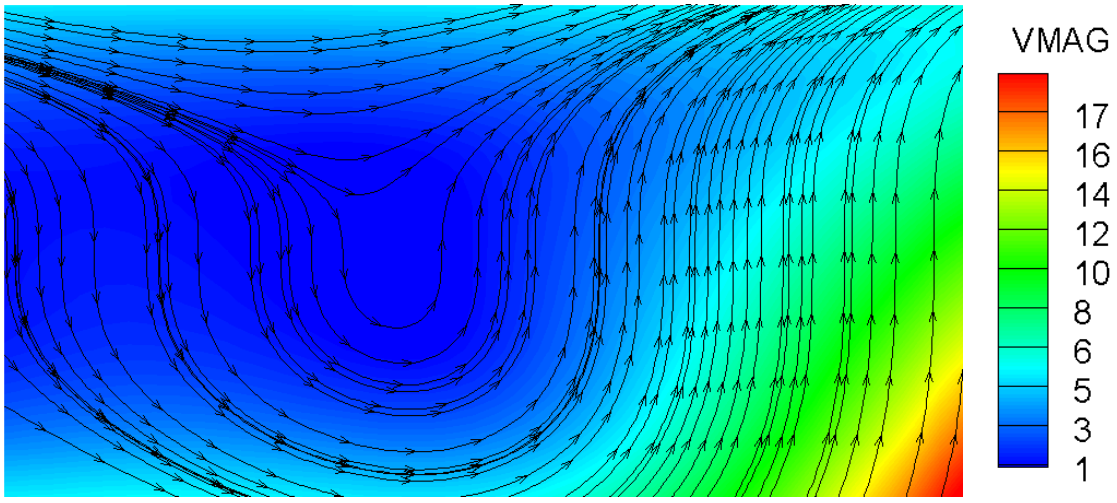

Figure 6.12: The flow field generated by the divergence function described in equation 6-35. The color corresponds to velocity magnitude

This divergence-free function is evaluated on a regular grid bounded by [{-1,3},{-1,1}, {-1,1}], with a uniform spacing of 0.1 in all three directions. The grid is down-

sampled by a factor of 2, 4, 6, and 8, and the corresponding interpolation errors are evaluated. Figure 6.12 shows a contour plot with streamtraces, of the velocity field generated by this function at the location Z=0.

6.6.2 Driven Cavity Flow

One of the cases that are normally used for validation of computational fluid dynamic solvers is the driven cavity problem, which has a well understood and documented flow structure. The flow problem consists of an incompressible fluid enclosed in a two-dimensional square boundary of length 1 m. The fluid within the boundary is motionless at time t=0. However the top boundary starts moving at 1 m/s as

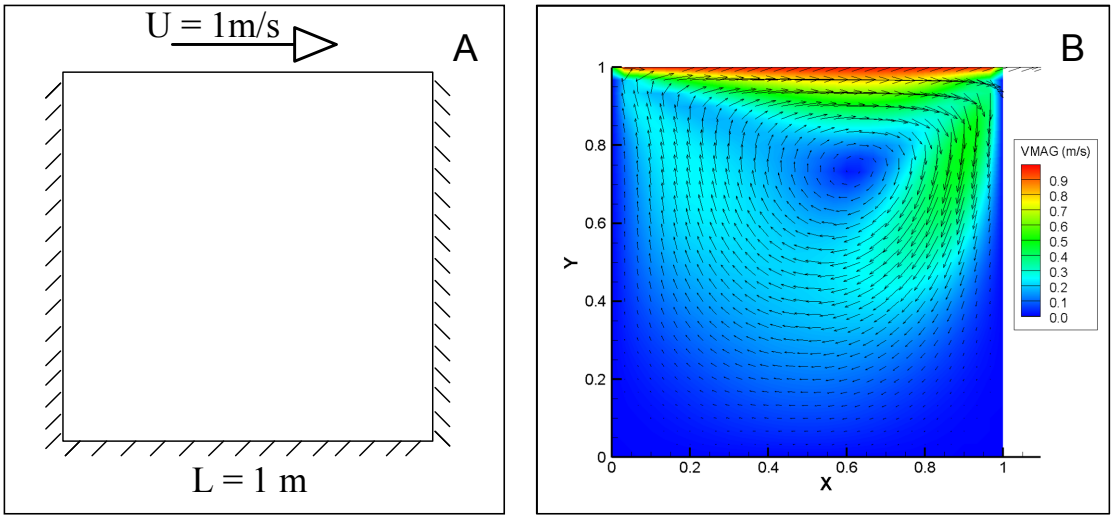

Figure 6.13: A) The schematic of the driven cavity problem; B) The corresponding CFD velocity field. The contour color corresponds to the velocity magnitude and the black arrows depict the velocity field.

shown in the schematic (Figure 6.13A). The induced flow has Reynold's number based on U and L and is equal to 100. The resulting time evolution of the fluid velocity field is governed by the 2D Navier Stokes equations. For a Reynold's number such as 100, the

velocity field assumes a steady behavior as t approaches infinity. Using a Navier-Stokes equation solver (such as the immersed boundary method described in Chapter 4), the velocity field within the cavity can be obtained (Figure 6.13B). To test the divergence-free interpolation algorithm, the grid is progressively down-sampled by a factor 2, 4, and 6, and the errors are compared. In addition, artificial noise is added, and the sensitivity of the algorithm to noise is computed.

6.6.3 3D CFD

The first two validation cases presented earlier are simplified test cases. Moving forward towards more complex scenarios, a 3D CFD solution of a realistic TCPC is used here. Using the methodology described in Chapter 5, a stack of synthetic 3D PC MRI images with isotropic voxel sizes are created. The control point grid is progressively down-sampled by a factor of 2, 4, 5, and 6, the measurement data is down-sampled by a factor of 2, and the missing data is interpolated using the divergence-free interpolation technique. The motivation behind this validation step is to determine how the size of the control grid impacts overall interpolation error.

6.6.4 In Vitro PC MRI

In this section a validation protocol using high resolution *in vitro* PC MRI data is described. The PC MRI acquisition comprises of a stack of 3D PC MRI slices acquired through the TCPC as outlined in section 4.3.3 of Chapter 4. The first three validation strategies comprised using a known velocity field obtained from computational methods, down-sampling it, interpolating the missing data, and comparing the resulting field to the original velocity field. In this section, two forms of validation are presented using high

resolution *in vitro* PC MRI experimental data. Firstly, every alternative slice of the stack is skipped, thus resulting in a dataset with half the number of slices. Then, the dataset is reconstructed to the original resolution using the divergence-free interpolation technique, and the RMS, average, and percent errors e as described in Equation 6-34 are evaluated.

Secondly, all the slices in the acquisition are used for interpolation in the divergence-free framework and a velocity field with isotropic vector spacing is reconstructed. A CFD simulation is conducted in the same geometry for comparison, and is used as the reference velocity field. The performance of the divergence-free interpolation algorithm is then compared to the adaptive control grid interpolation technique (which is the current benchmark for PC MRI interpolation) as well as to the differences between CFD and MRI measurements.

6.7 Clinical Application

After validation, the proposed divergence free velocity field reconstruction approach may be directly applied to clinically acquired PC MRI data, for performing a 3D flow field analysis of the TCPC. 24 Fontan patients (age: 7.88 ± 3.89 years) underwent 3D PC MR imaging at CHOP (n=20) and the CHB (n=4) featuring 11 intraatrials tunnels (LT), 11 extra cardiacs (ECs), and 2 interrupted inferior vena cava with an azygous vein continuation (IIVC). Using the divergence free interpolation technique, the velocity field within the Fontan is reconstructed in 4D (3 spatial + 1 temporal).

Once the velocity field is reconstructed, the clinically relevant parameters described above are derived from the 4D velocity fields. Specifically, the viscous

dissipation energy losses, hepatic flow splits, vortex sizes, and average particle transit times are computed for quantitative comparison between the different TCPC templates. Additionally, stream traces and vector fields are used for a qualitative comparison of velocity fields between the different Fontan templates.

6.8 Chapter 6 Summary

This chapter introduced novel methods for the interpolation and reconstruction of PC MRI that preserves the property of fluid flow in the interpolation process. The proposed technique uses divergence-free radial basis functions that ensure the underlying velocity has zero divergence. The theory, implementation, and the validation approach were described. Finally, the chapter closed with the protocol followed for the application of the 4D PC MRI methodology to 24 patients with a TCPC, as well as the parameters retained for comparing the *in vivo* hemodynamics between the different Fontan types.

CHAPTER 7

MATHEMATICAL MODELING OF THE CARDIOVASCULAR SYSTEM

7.1 Overview

Most of the studies thus far on the Fontan circulation can be broadly categorized into two types: a) those that study the Fontan circulation as a whole using *in vivo* animal and human subjects[37, 38, 176]; and b) those that study the fluid mechanics of the surgically created TCPC in isolation from the single ventricle circulation[18, 19, 43, 67, 69, 78, 138]. There haven't been many studies that have connected the two, i.e.: those that relate the hemodynamics of the TCPC to the upstream hemodynamics and cardiac function. Furthermore, no study to date has quantified TCPC resistances in actual patient TCPCs, which has proved to be a caveat for understanding the true magnitude of TCPC in the context of pulmonary and systemic vascular resistance. For this reason, there are persistent concerns in the clinical community regarding the amount of importance that should be given to optimizing the TCPC geometry.

The previous chapters introduced new methods for evaluating the hemodynamics as well as the energy losses within the TCPC using PC MRI. In this chapter, these energy losses are put in the context of the entire cardiovascular system. Hence, the primary objective of this chapter is to quantify the impact of the hemodynamic energy loss (or resistance) induced by the geometry of the TCPC on two critical aspects of the Fontan circulation: a) exercise performance; b) cardiac function. For the first time, the TCPC

hemodynamics is studied in context of the entire single ventricle circulation using clinically acquired magnetic resonance images and cardiac catheterization data on Fontan patients.

7.2 Patient Data

A multi-center Fontan patient cardiac MRI database of over 200 patients has been established using methods described in Chapter 5 and 6. Briefly, the MRI acquisitions consisted of a stack of axial anatomic images for reconstruction of geometry, and cine phase contrast MRI (PC MRI) acquisitions for flow quantification at the superior vena cava (SVC), inferior vena cava (IVC), left pulmonary artery (LPA), and right pulmonary artery (RPA). For each patient MRI, the 3D anatomies and flows were reconstructed and a database of this information was established.

From this database, 16 patient specific geometries (6 intra-atrial, 9 extra-cardiac, 1 IVC-main pulmonary artery) are selected for computational fluid dynamic (CFD) simulations. The selected geometries are depicted in Figure 7.1. Table 7.1 shows the clinical data associated with each model selected in the study as well as the resting cardiac output obtained from PC MRI. In addition, cardiac catheterization data of 40 patients with a single ventricle physiology are used for estimating the vascular parameters for the systemic and pulmonary circulations. Specifically, systemic vascular resistance (SVR) and pulmonary vascular resistance (PVR) measurements are used in the mathematical model, while the pressure and flow measurements are used for validating the model.

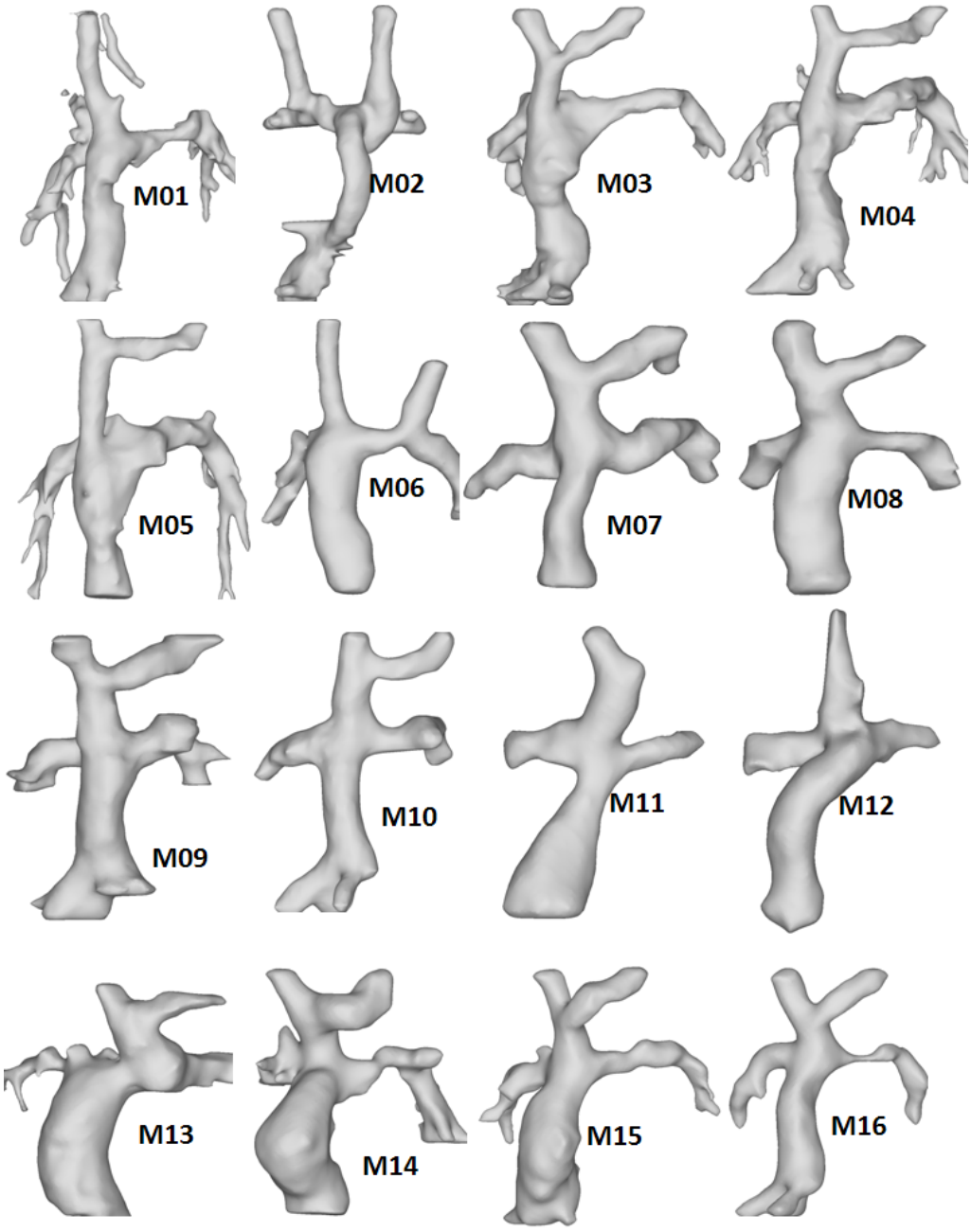

Figure 7.1: Three dimensional anatomic reconstructions of TCPC models used in this study. In total there are 6 intra-atrials (M01, M03, M04, M05, M14, M15), 9 extra-cardiacs (M02, M06, M07, M08, M09, M10, M12, M13, M16) and 1 IVC-MPA TCPC (M11).

Table 7.1: Clinical data of patients used in the study

Model	CHD	Fontan Type	Age	Simulation conditions (L/Min)
M01	HLHS	IA	12	2,4,6
M02	DORV, PA	EC (BL)	9	2.5, 5, 7.5
M03	HLHS	IA	18	2.4, 4.8, 7.2
M04	TA	IA	10	2.9, 5.8, 8.7
M05	PA, HRHS	IA	15	2.75, 5.5, 8.25
M06	Heterotaxy, DC	EC (BL)	4	2.37, 4.72, 4.37
M07	DILV, TGA	EC	9	3.5, 7, 10.5
M08	DC, TA	EC	3	2.7, 3.7, 4.7
M09	TA	EC	7	3.03, 6.06, 9.09
M10	PA, HRHS	EC	8	3, 6, 9
M11	DORV, DC	IVC – MPA	7	3,4,5
M12	HLHS	EC	6	2,3,4
M13	HRHS	EC	5	3,4,5
M14	SV, DIAV	IA	3	2,3,4
M15	HLHS	IA	11	4,6,7
M16	HLHS	EC	6	2,3,4

7.3 Computational Fluid Dynamic (CFD) Simulations

The CFD protocol used for the study is different to the one outlined in Chapter 4. The 3D anatomical reconstructions are used for grid generation in which vessel volumes

are divided into computational elements (meshes). The number of elements varied depending on geometry size and complexity, and ranged from 548,842 to 1,674,440 for the models studied. At each element, the governing Navier-Stokes conservation equations of mass and momentum for laminar fluid flow are solved using FLUENT (Fluent Inc, Lebanon, OH). All solutions are obtained using second order solvers assuming a Newtonian fluid with a density of 1060 kg/m3 and viscosity of 3.71e-3 N-s/m2. The patient-specific TCPC CFD analysis methodology and the *in vitro* validations of these techniques have been described in earlier studies[43, 177]. For each patient-geometry, blood flow is modeled at baseline steady-state flow conditions by setting SVC and IVC flows to values derived from PC MRI averaged over the cardiac cycle. Outflows are defined by pressure boundary conditions, with values tuned to obtain the desired pulmonary flow splits at the equal vascular lung resistance (EVLR) condition described previously[43]. In order to determine the resistance of the TCPC under exercise conditions, simulations are also conducted as 1 L/Min increases for younger patients (3-7 years), and 2x and 3x the resting flow rates for older patients (>7 years), with the only exception being M15.

7.4 TCPC Resistance Evaluation

The CFD simulations are used to provide the pressure (P) and flow (Q) measurements throughout the TCPC pathway. Using the measurements at the inlets (SVC and IVC) and the outlets (LPA and RPA), the control volume energy loss is computed according to the following equation:

$$\dot{E}_{Loss} = P_{SVC} * Q_{SVC} + P_{IVC} * Q_{IVC} - P_{LPA} * Q_{LPA} - P_{RPA} * Q_{RPA} \quad \text{Equation 7-1}$$

An energy loss based pressure drop term is then evaluated to estimate the resistance of the TCPC as follows:

$$\Delta P_{TCPC} = \frac{\dot{E}_{Loss}}{Q_{SVC} + Q_{IVC}} \qquad \text{Equation 7-2}$$

$$R_{TCPC} = \frac{\Delta P_{TCPC}}{\frac{(Q_{SVC} + Q_{IVC})}{BSA}} \qquad \text{Equation 7-3}$$

7.5 Description of the Lumped Parameter Model

An electric-circuit analog of the cardiovascular system similar to the lumped parameter model (closed-loop) developed previously by Pekkan et al is used[178]. This model is based on an earlier technique proposed by Peskin et al. for the whole cardiovascular system, and is adapted here to study the Fontan physiology[179]. This is a fairly simple model of the circulatory system (compared to the more complex models proposed by Magosso and Migliavacca)[39, 139, 140], and has been used extensively to study normal and diseased configurations[178-181]. Figure 7.2 shows the mathematical model for both the normal and SV circulations used in this study. The vascular parameters are the same for both biventricular and univentricular physiologies except for the: a) presence of a TCPC, b) absence of right ventricle, c) venous compliance.

The arteries, veins, and heart chambers are treated as pure time-dependent compliance chambers with lumped capillary and valve resistances. For the normal circulation, there is a chamber each for the left heart, systemic arteries, systemic veins, right heart, pulmonary arteries, and pulmonary veins. For the Fontan circulation, the right

heart is replaced by a chamber representing the TCPC. Each of these chambers (except the heart and the TCPC) has a resistance and compliance component mimicking the arterial and venous vessels in the cardiovascular system. As explained previously, SVR and PVR values are obtained from clinical cardiac catheterization data. Systemic and pulmonary compliance reflect typical Fontan values and are outlined in Table 7.2[45, 140, 182, 183]. The TCPC is treated as a dynamic resistance that changes with cardiac output and is evaluated using CFD simulations described above.

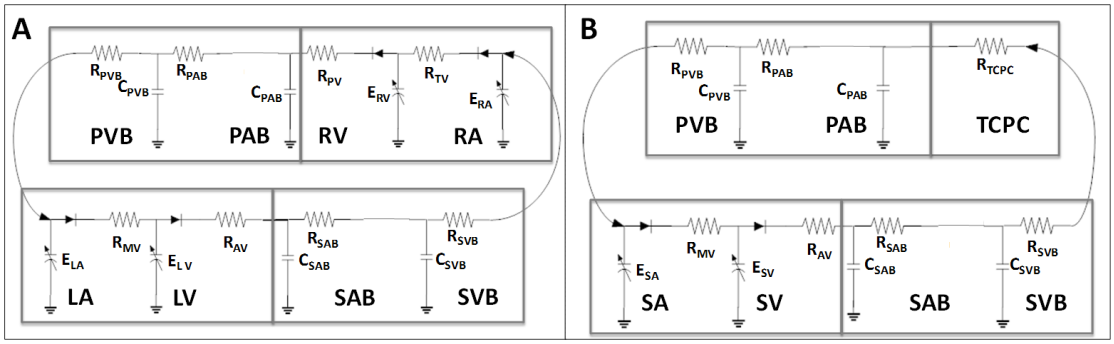

Figure 7.2: The schematics describing the lumped parameter models used in the study. Shown on the left is the biventricular circulation (A), and to the right is the univentricular circulation (B). The abbreviations stand for: LA (Left Atrium), LV (Left Ventricle), SAB (Systemic Arterial Bed), SVB (Systemic Venous Bed), RA (Right Atrium), RV (Right Ventricle), PAB (Pulmonary Arterial Bed), PVB (Pulmonary Venous Bed), SA (Single Atrium), SV (Single Ventricle), TCPC (Total Cavopulmonary Connection), MV: Mitral Valve, AV: Aortic Valve.

The advantage of such a mathematical model is that additional chambers or shunts can be introduced into the system, which is an option particularly valuable in congenital heart defect research. The instantaneous flow and pressure from compartment "i" to compartment "j" can be evaluated by solving the following set of differential equations:

$$E(t) = \frac{1 - e^{-t/Tc}}{1 - e^{-Ts/Tc}} \qquad 0 \le t \le Ts$$

$$CV(t) = CVD * (CVS / CVD)^{E(t)}$$

$$E(t) = \frac{1 - e^{-(t-Ts)/Tr}}{1 - e^{-(T-Ts)/Tr}} \qquad Ts \le t \le T \quad \text{Equation 7-4}$$

$$CV(t) = CVS * (CVD / CVS)^{E(t)}$$

Table 7.2: Parameters used in the lumped parameter model. * Parameters extracted from patient data in the current study. WU is equivalent to mmHg/(L/Min).

Parameter	**Normal Ventricle**	**Single Ventricle**
C_{SVB} (mL/mmHg) [32]	1517	332.5
C_{SAB} (mL/mmHg)[32]	1.75	1.75
R_{SAB} (WU)*	17.2	17.2
R_{SVB} (WU) *	1.2	1.2
C_{PAB} (mL/mmHg)	4.12	4.12
C_{PVB} (mL/mmHg)	80	80
R_{PAB} (WU) *	1.7	1.7
R_{PVB} (WU) *	0.11	0.11

Tc (0.0025 minutes) and Tr (0.0075 minutes) are time constants governing the contraction and relaxation of the myocardial muscle during systole and diastole. T is the duration of one cardiac cycle (1/Heart Rate), Ts is the length of systole (T/3 at rest, T/2 at exercise), and t is the current point in the cardiac cycle. Systole and diastole are switched for modeling atrial contraction. CVD and CVS are the minimum and maximum

compliance values of the chamber. The valves are modeled as linear unidirectional resistors with a resistance of 0.01 WU. Please note that 1 WU is equivalent to 1 mmHg/(L/Min) and is a commonly used clinical parameter to describe resistance to blood flow. The parameter values used in Equation 7-4 for each heart chamber are shown in Table 7.3.

Table 7.3: Parameters used for describing the heart chambers in the mathematical model.

Parameter	**Normal Heart**	**Single Ventricle Heart**
CVD_{RA} (L/mmHg)	0.03	N/A
CVS_{RA} (L/mmHg)	0.0003	N/A
CVD_{RV} (L/mmHg)	0.0365	N/A
CVS_{RV} (L/mmHg)	0.0002	N/A
CVD_{LA} (L/mmHg)	0.01	0.01
CVS_{LA} (L/mmHg)	0.0003	0.0003
CVD_{LV} (L/mmHg)	0.0146	0.0146
CVS_{LV} (L/mmHg)	0.00003	0.00003
R_{Mi} (WU)	0.01	0.01
R_{Tr} (WU)	0.01	N/A
R_{Ao} (WU)	0.01	0.01
R_{Pu} (WU)	0.01	N/A

7.6 Modeling Rest / Exercise Conditions and Data Analysis

Rest: To simulate the impact of TCPC resistance on cardiac output, R_{TCPC} in the model is uniformly varied from 0 WU to 1.8 WU (0 to 90% PVR) and its corresponding

effect on cardiac output for the biventricular and univentricular circulations are evaluated. The range of TCPC resistances are selected based on computational models described above and are used to evaluate the sensitivity of the model to the TCPC resistance. For a biventricular circulation, since there is no TCPC, the pulmonary vascular resistance is increased by an equivalent amount. In addition, pressure volume analysis is conducted for a normal subject and TCPC cases with the highest, mean, and lowest resistances to demonstrate how the operating point of the univentricular circulation changes with resistance.

Exercise Conditions: In order to isolate the impact of just the TCPC resistance, the following parameters are changed for simulating exercise conditions:

1. The heart rate is uniformly increased from 70 to 150 beats per minute simulating the primary response to exercise as outlined by several human and animal studies[29, 37-40, 145, 147, 176, 184-189]. For the normal circulation, the ventricular contraction properties (CVD and CVS) are changed in addition to heart rate to model the typical response to exercise for a normal heart. This is not done for the SV circulation, as it has been previously demonstrated that Fontan patients increase CO primarily by increasing their heart rate, and do not change their ventricular contraction properties to increase stroke volume[37, 38, 176]. Therefore, only the heart rate is increased in the SV circulation as the primary response to exercise.
2. SVR typically goes down with exercise demonstrating the impact of the peripheral muscular dynamics and the vasodilation that occurs to aid the increase in cardiac output[190]. Studies have shown a drop of almost 50% in SVR. This is

accomplished in the model by decreasing the SVR progressively from 18.5 WU as measured from catheterization data to 11 WU for both the normal and the SV circulation.

3. There is also a significant impact of the pulmonary system and the lungs during exercise, especially in Fontan patients, where the negative intra-thoracic pressure greatly augments flow. Studies have reported a 40% drop in the PVR as a result of this phenomenon in addition to the local vasodilation that occurs to improve exercise tolerance[190]. Therefore the PVR in the model is gradually dropped from 1.96 WU as measured from catheterization to 1.1 WU based on the severity of exercise.
4. As the cardiac output increases with increasing heart rate, so does the resistance of the TCPC. Figure 7.3 shows the dynamic range of TCPC resistances and how they change between the different geometries. As can be observed there is a non-linear increase in resistance with cardiac output. This phenomenon becomes important during elevated cardiac output conditions. To take this characteristic into account, the resistance of the TCPC (R_{TCPC}) is treated as a dynamic element that increased with an increase in cardiac output. TCPC resistance curves shown in Figure 7.3 is used for evaluating the correct resistance for each exercise condition.

Based on these exercise conditions, the following parameters are evaluated as a function of heart rate for the normal and SV circulations respectively: cardiac output (CO), end systolic pressure (ESP), central venous pressure (CVP), afterload (Ea), preload (Ees), ventricular-vascular coupling ratio (Ea/Ees), R_{TCPC}, and ratio of R_{TCPC} to

pulmonary vascular resistance (R_{TCPC}/PVR). Pressure volume loops are used to evaluate the slope of the end-systolic volume elastance or preload (Ees) and the vascular afterloading (Ea) property. These parameters are evaluated based on the methodology outlined by Nogaki[40].

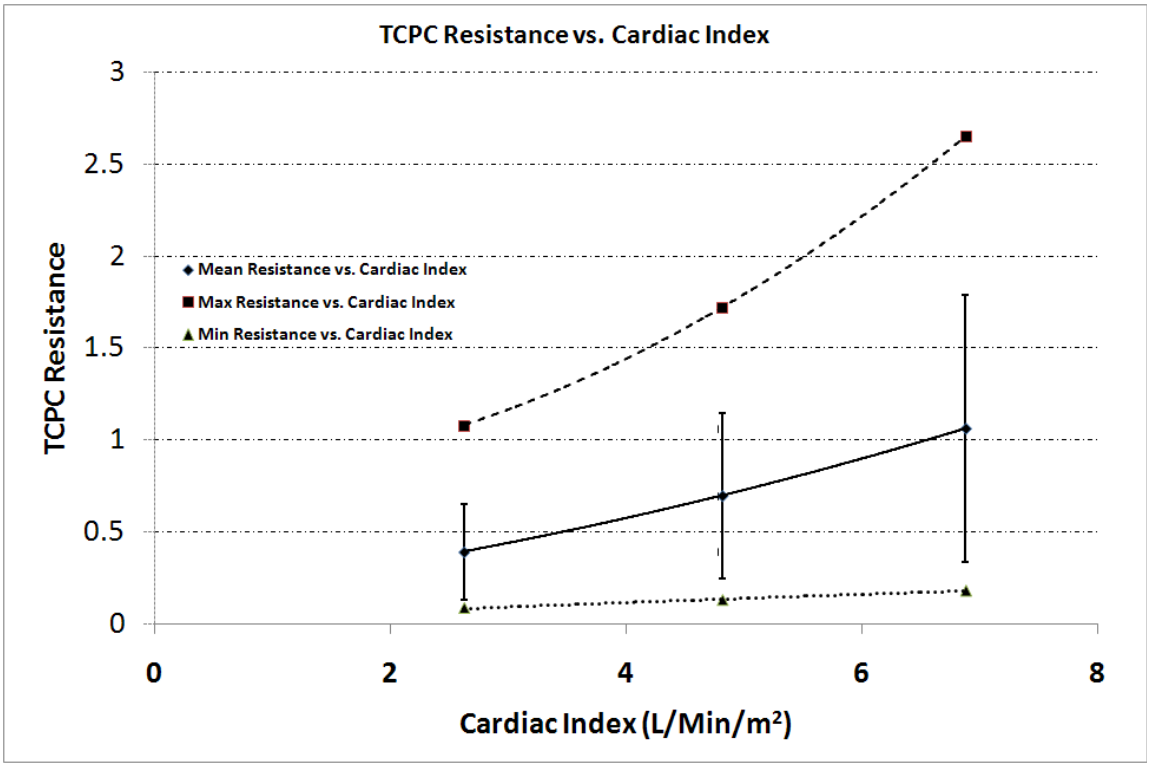

Figure 7.3: TCPC resistance plotted as a function of cardiac index representing 16 geometries used in the study. These curves were used as inputs to the lumped parameter model. The maximum resistance curve corresponds to M16, while the minimum resistance model corresponds to M6. The mean resistance curve is the mean resistance at resting, moderate exercise, and severe exercise respectively.

7.7 Chapter 7 Summary

In this chapter, a mathematical model for investigating the impact of the TCPC

resistance on the entire cardiovascular system was presented. The model was based on the electrical circuit analogue of the cardiovascular system, and represented the different cardiovascular components in terms of resistances and capacitances. Parameters for this model were obtained from clinical MRI, cardiac catheterization data and from the literature. The model was used for evaluating the impact of the TCPC resistance on cardiac function and exercise capacity of Fontan patients. The results are presented and discussed in Chapter 11.

CHAPTER 8

RESULTS AND DISCUSSION – *IN VITRO* PC MRI EXPERIMENTS

8.1 Overview

The results presented in this chapter are associated with the *in vitro* PC MRI experiments conducted on 3 patient specific models: CHOA006, CHOA007, and CHOA011 based on the methodology outlined in Chapter 4. The bulk of the chapter will focus on the comparison of *in vitro* PC MRI experiments with CFD simulations, with the first few sections comprising of the validation of the experimental methodology. Results would primarily be presented for CHOA007 and CHOA006, since experiments on these models were conducted in MRI scanners of different field strengths.

8.2 Experimental Validation

Experiments were successfully conducted for:

1.) CHOA006 at 3 liters per minute (LPM) (flow splits: 30% RPA, 70% RPA) and 5LPM (flow splits: 30% RPA, 50% RPA, 70% RPA)

2.) CHOA007 at 2LPM (50% RPA, 60% RPA, 70% RPA) and 4 LPM (50% RPA, 60% RPA, 70%RPA)

3.) CHOA011 at 4LPM (30%RPA, 50% RPA, 70% RPA) and 6 LPM (30% RPA, 50% RPA)

Figure 8.1 shows the locations where the measurements were made. As described in Chapter 4, a dense stack of axial images were acquired (50 slices total) through the TCPC. The average flow rates through the slices at the SVC and the IVC as shown in

Table 8.1 are compared to the true flow rates.

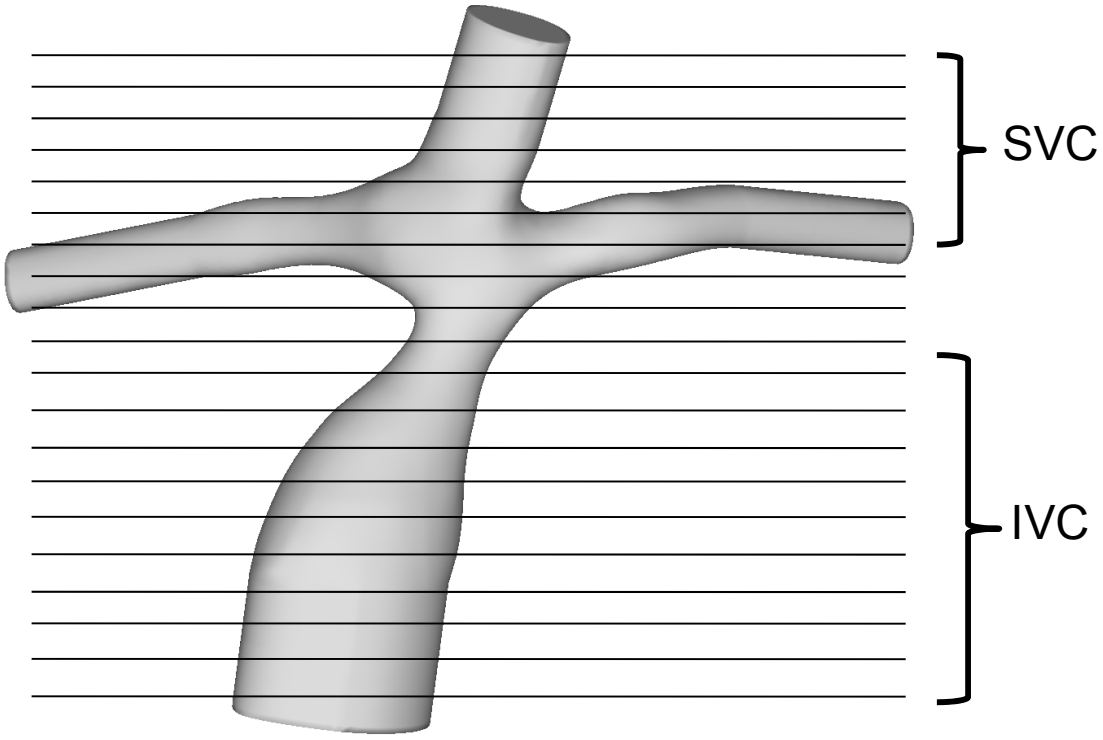

Figure 8.1: Locations where the PC MRI slices were acquired. A dense contiguous stack was obtained throughout the geometry of the TCPC. Average flow rates through each of the slices were used for comparison with the values that were prescribed during the experiment.

Three sets of data (CHOA006 3LPM, flow split 50% RPA and CHOA011 4LPM, flow split 30% RPA, and 6LPM, flow split 70% RPA) had to be discarded due to excessive acquisition noise rendering the datasets unusable. For the rest of the datasets, the average error in flow rate measurements for the IVC and SVC were 6 ± 3% and 8 ± 6 % respectively using the rotameter reading as the reference standard. The total flow rate (SVC + IVC) error was 4.2 ± 4%.Table 8.1 shows the error breakdown for all the

experiments conducted successfully.

Table 8.1: Experimental error in the measurement of flow rates. The experimental condition is labeled as: CHOA0XX- Flow Rate- Flow Condition

Expt. Condition	IVC True (LPM)	IVC MRI (LPM)	IVC Error (%)	SVC True (LPM)	SVC MRI (LPM)	SVC Error (%)	Total True (LPM)	Total MRI (LPM)	Total Error (%)
06-3-30	1.8	1.62	10	1.2	1.1	8.3	3	2.63	12.3
06-3-70	1.8	1.8	0	1.2	1.15	3.9	3	2.96	1.3
06-5-30	3	2.8	6.7	2	2.17	8.5	5	4.97	0.6
06-5-50	3	3.14	4.7	2	1.96	2	5	5.1	2
06-5-70	3	2.79	7	2	1.83	8.5	5	4.6	8
07-2-50	1.2	1.3	8.3	0.8	0.75	6.25	2	2.06	3
07-2-60	1.2	1.27	5.8	0.8	0.69	13.8	2	1.95	2.5
07-2-70	1.2	1.23	2.5	0.8	0.72	10	2	1.95	2.5
07-4-50	2.4	2.6	8.3	1.6	1.58	1.3	4	4.18	4.5
07-4-60	2.4	2.65	10.4	1.6	1.65	3.1	4	4.3	7.5
07-4-70	2.4	2.48	3.3	1.6	1.47	8.1	4	3.95	1.3
11-4-50	2.4	2.66	10.8	1.6	1.34	16.3	4	4	0
11-4-70	2.4	2.32	3.3	1.6	1.2	25	4	3.5	12.5
11-6-30	3.6	3.72	3.3	2.4	2.44	1.67	6	6.15	2.5
11-6-50	3.6	3.9	8.3	2.4	2.25	6.25	6	6.15	2.5
Average	2.36	2.42	6.18	1.57	1.48	8.2	3.93	3.9	4.2
Stdev	0.8	0.84	3.24	0.53	0.56	6.34	1.33	1.39	4

As can be observed from the table most of the errors are below 10%, which shows that the prescribed experimental conditions were successfully maintained. There were a few cases where errors higher than 10% were observed, and this could be attributed to several reasons: a) MRI measurement error; b) the failure of the flow resistances to maintain the desired flow splits; c) soft tubing compliance that could result in dissipation

of the pump energy over time; d) overheating of the pump. Previous studies have shown error in MRI flow measurements are in the range of 10-21% [107, 191], and hence it can be said that the error in flow measurements observed in this study are acceptable. One problem that was experienced consistently was the progressive drop in flow rates over time due to the long lengths of soft tubing used for conducting the experiments. In order to account for this drop in flow rate, the rotameters were consistently checked, and the resistances were adjusted accordingly to ensure that the correct flow rate was maintained over the entire duration of the experiment.

8.3 Reproducibility of *In Vitro* PC MRI Experiments

High resolution *in vitro* PC MRI experiments have never been conducted on anatomically realistic TCPC geometries. Consequently, the error bounds of PC MRI experimental and post processing methodology for comparing velocity fields from two identical TCPC geometries are unknown. Hence, a reproducibility study was conducted on one of the TCPC anatomic models (CHOA007) to determine the errors in 3D PC MRI for the measurement of velocities in all three components.

In vitro PC MRI experiments were conducted twice on two separate days in the Philips 1.5T Intera scanner located at the Emory University Hospital using identical experimental protocols as described in Chapter 4. Three sets of data were collected at 4 LPM and flow splits of 50%, 60%, and 70% respectively. The datasets were processed and then registered using the protocols described in Chapter 4 for a quantitative comparison. For brevity, results are shown for the 4LPM, 50% RPA case but the general trends hold true for all the 3 test cases.

8.3.1 Quantitative Comparison

Table 8.2 shows the experimental errors associated with the 3 components of the velocity and the velocity magnitude for CHOA007 4LPM, 50% RPA case *for all the planes that were acquired (N=50).* For the correlation plots, a mean absolute velocity for each component was evaluated for each slice in the acquisition, and then correlated with those from the repeated MRI scan. The experimental measurement in the Z direction (which is the through plane direction for a majority of acquired PC MRI slices) had a much lower error compared to the transverse components in the X, and Y directions respectively. This was consistent with previous *in vitro* PC MRI studies, which showed that the transverse components of the velocities have much higher errors compared to the through plane components[112]. The mean velocities of both sets of experiments were nearly identical, but when the RMS errors were quantified as a percentage of mean velocity in each region, the highest error was observed the X component of the velocity at 20.55% followed by the Y component at 14.86% and the Z component at 7.29% respectively.

Table 8.2: PC MRI reproducibility error

	Original (cm/s)	**Repeated (cm/s)**	**RMS Error (cm/s)**	**% Error**
X Velocity	13.48 ± 8.87	12.23 ± 8.16	1.84 ± 1.16	20.55 ± 15.5
Y Velocity	8.61 ± 4	8.62 ± 4.59	1.34 ± 1.20	14.86 ± 8.83
Z Velocity	23.25 ± 6.61	23.93 ± 6.4	1.38 ± 1.06	7.29 ± 8.25
Velocity Magnitude	32.5 ± 2.32	31.91 ± 2.77	2.05 ± 1.64	6.21 ± 4.79

Figure 8.2 shows the correlation and Bland- Altman plots of the original and the repeated acquisition respectively.

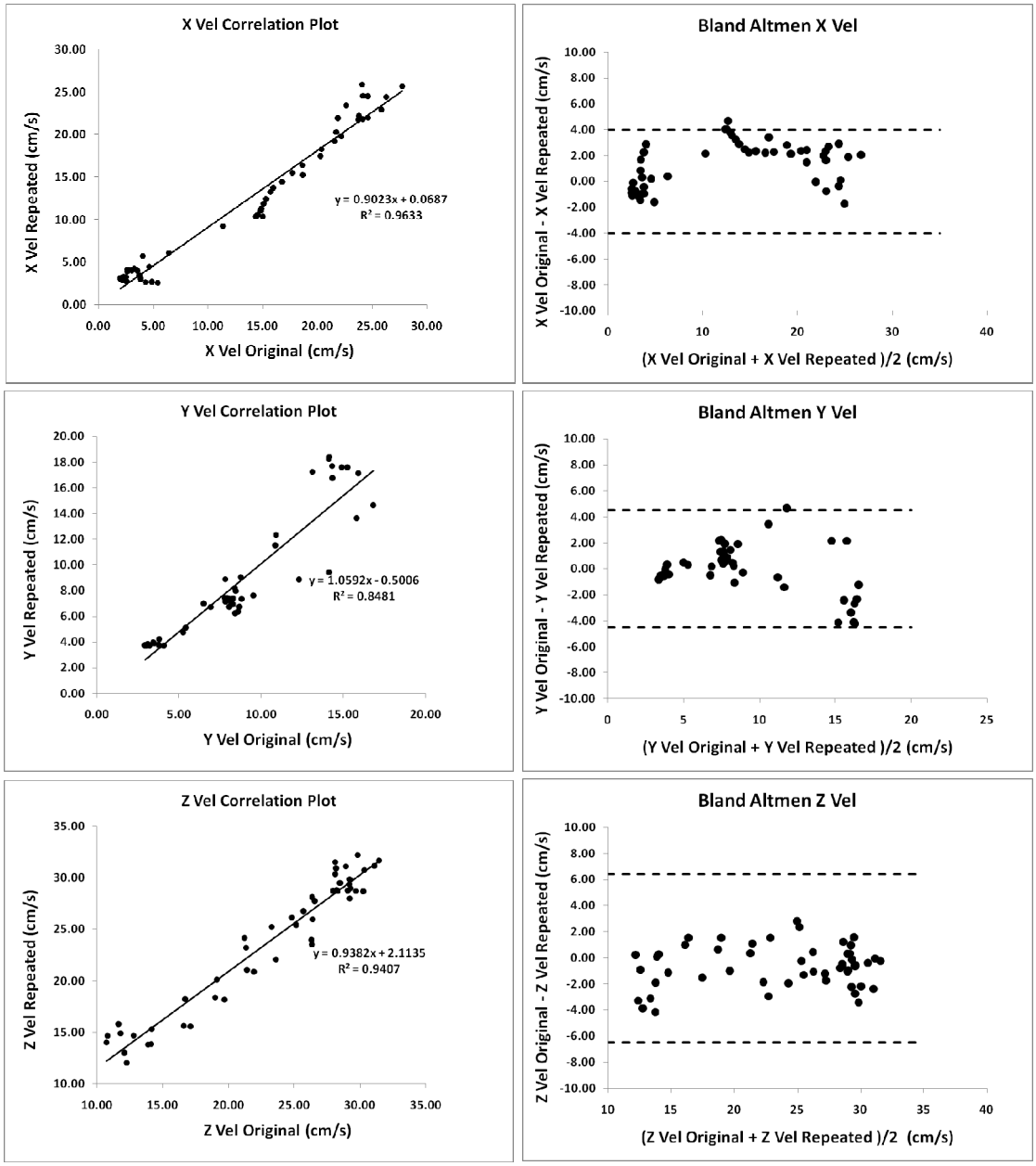

Figure 8.2: Correlation and Bland-Altman Analysis demonstrating the reproducibility of PC MRI experiments. The dotted lines on the Bland-Altman plots represent 1 standard deviation from the mean velocity. As can be observed, the errors clustered around 0, and are within 1 standard deviation of the mean velocity

Correlation analysis conducted on all three components of velocity demonstrated an excellent match between the two sets of measurements ($p < 0.05$). The Pearson correlation coefficients (R) were 0.92, 0.98, and 0.97 for the X, Y, and Z velocities respectively. The slope of the regression line ranged from 0.9 to 1.06 indicating that the there was minimal bias in the velocity magnitudes. Bland Altman plots revealed that more than 96% of the error values were within one standard deviation of the mean velocities for all three components. The error values were primarily clustered around zero and did not seem to be dependent upon the magnitude of the velocity. One of the reasons why a higher percentage error was noticed for the in plane components, was that they had lower velocity magnitudes in the first place. While the errors were more spread out for the X and Y components, those for the Z component were clustered close to each other. Overall, the quantitative analysis demonstrated that the *in vitro* PC MRI experimental methodology and the associated post processing steps were highly reproducible.

8.3.2 Qualitative Comparison

Figure 8.3 shows a qualitative comparison of the PC MRI velocity magnitude contour plots for the two sets of experiments at the SVC and IVC of the TCPC, and their corresponding cross sectional velocity profiles taken along the diameter of the vessel superimposed on top of each other. Although significant attempts were made to ensure a fully developed flow profile, it is evident from the plots, that such a profile was not maintained. There is some evidence of a parabolic flow profile, although some sort of a flattening effect can be observed in both the SVC and the IVC. This phenomenon was observed for both the experimental conditions.

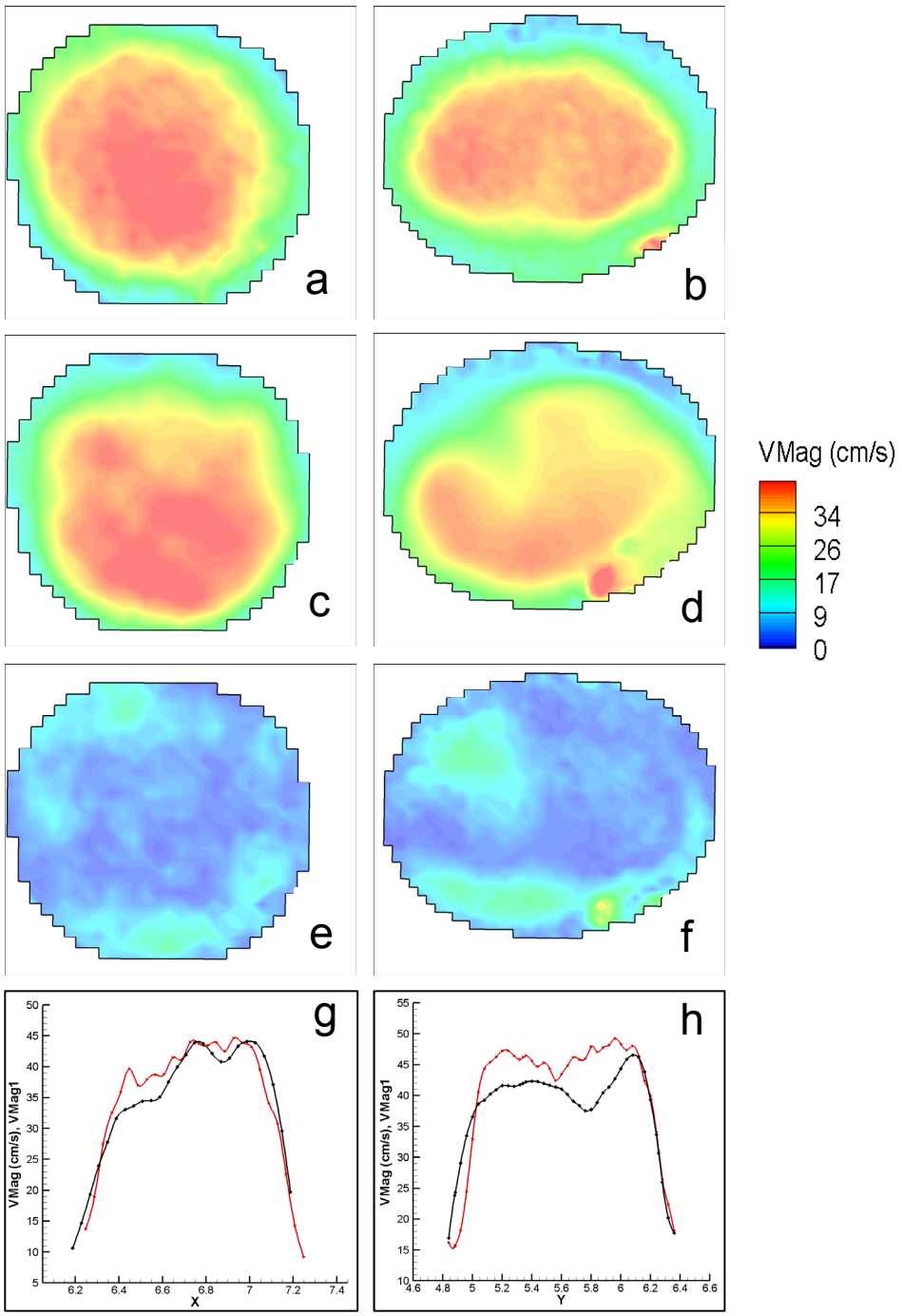

Figure 8.3: Cross sectional velocity magnitude plots of the SVC (a, c) and IVC (b, d) of the original acquisition (a, b), and the repeated acquisition (c, d), followed by velocity magnitude differences for the SVC (e), and the IVC (f). Figure g and h are the cross sectional velocity profiles along the diameter of the vessel for the SVC (g) and IVC (h). The red line corresponds to the original acquisition and the black line corresponds to the repeated acquisition

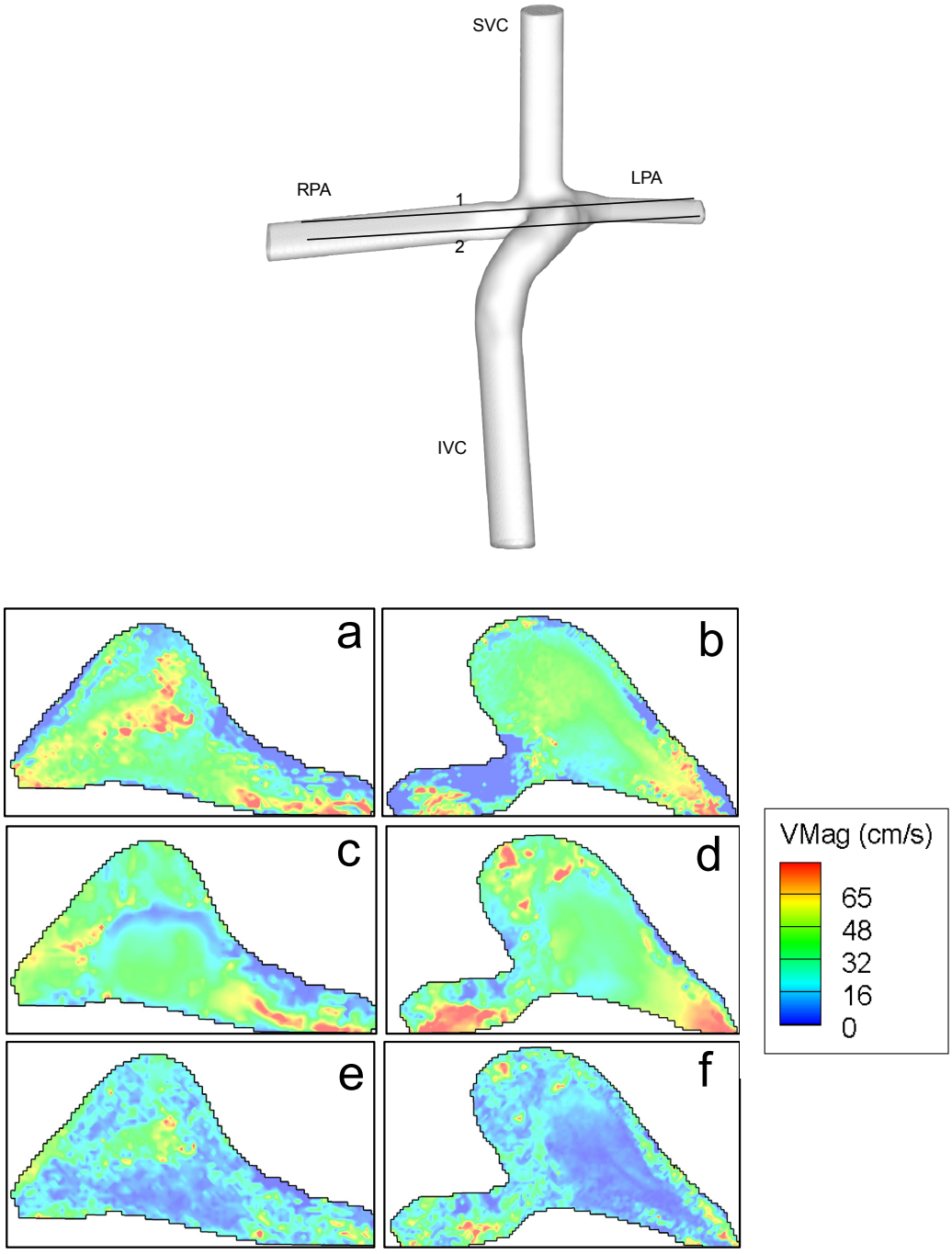

Figure 8.4: Cross section velocity magnitude profiles in two locations of the IVC to pulmonary artery junction for the original (a, b), and the repeated (c, d) acquisition. The differences between the two scans are shown as part of the contour plots (e,f). Notice that maximum disagreement between the two scans is along the vessel walls

The flattening of the flow profile can be attributed to the abrupt change in shape going from circular feeding tubes to the native shape of the SVC and the IVC. Although care is taken to keep the tubing long enough such that the flow through the individual inlets become fully developed prior to entering the two vessels, the parabolic nature of the flow is disrupted when it enters the primary inlets. The only way that this problem can be avoided is by having extremely long inlets built into the model itself. This is not experimentally feasible as the models will then be abnormally huge, and conducting PC MRI experiments will not be possible.

Figure 8.4 shows the velocity magnitude contour plots at two locations in the IVC to pulmonary artery junction. Although global flow features matched, significant errors as high as 60% were observed as a result of salt and pepper noise as well as low signal to noise ratio (SNR). One of the primary reasons for this phenomenon, is that flow from the larger vessels in the form of the SVC and IVC enters the smaller vessels of the LPA, and the RPA, which causes unsteady behavior in the connection region. Prior computational and experimental studies on the TCPC have shown that this region experiences unsteady flow phenomena despite the inlet boundary conditions being steady[177]. Such unsteady flow behavior causes de-phasing of the underlying proton spins and intravoxel dispersion, consequently affecting the SNR. These were the locations where the highest measurement errors were observed.

8.3.3 Summary

In this section, the reproducibility of the *in vitro* PC MRI experimental and post processing methodology was evaluated. Besides validating the experimental approach,

this section also provided error bounds that can be expected for comparing the PC MRI simulations to numerical simulations. The protocol involved conducting two experiments on two separate days on the same *in vitro* phantom model of the TCPC (CHOA007), using the same MRI acquisition and post processing protocol. The resulting flow fields were quantitatively and qualitatively compared to each other. There was an excellent qualitative and quantitative agreement between the two acquisitions, which validated the *in vitro* PC MRI experimental methodology. The overall accuracy evaluated (the total RMS error) was quite good between the two scans, and was quantified (according to the formula in Chapter 4) to be 3 cm/s, which amounted to a normalized RMS error percentage of 9%.

8.4 PC MRI – CFD Comparison

In this section, quantitative and qualitative comparisons of PC MRI with CFD are presented. The validation and comparison methodology adopted is identical to the one utilized for conducting the MRI reproducibility study. The only difference was that instead of comparing the velocities at 50 locations, the velocities were instead compared at 180 different locations. The CFD solution was registered to the PC MRI volumetric dataset, and the velocities from CFD were interpolated onto the PC MRI volumetric mesh. Although, volumetric mesh was not isotropic, it could still be sliced at arbitrary locations using Tecplot that allowed for a quantitative as well as a qualitative comparison. For each slice that was extracted, the mean absolute velocities were used for conducting the correlation study. It was not possible to correlate measurements at every single measurement point, as there were over 200,000 measurement points. Due to the

significant volume associated with the acquired data, the results are primarily presented for CHOA007 and CHOA006 at resting and exercise conditions.

8.4.1 CHOA007 (1.5T)

8.4.1.1 Quantitative Comparison

Table 8.3 shows the average root-mean-squared error associated with each component of velocity at both resting and exercise conditions, while Figure 8.5 and Figure 8.6 show the corresponding correlation and Bland Altman plots. The overall RMS error at resting flow conditions was 3.16 cm/s, and the normalized RMS error percentage was 15%. At exercise flow conditions, the overall RMS error doubled to 6.57 cm/s, and the normalized error percentage went up to 23%.

Table 8.3: Quantitative comparison between PC MRI and CFD velocities over the entire CHOA007 flow domain. Data presented as Mean ± SD

Flow Condition	**Velocity Component**	**PC MRI (cm/s)**	**CFD (cm/s)**	**RMS Error (cm/s)**	**% Error**
2 LM	X Velocity	7.05 ± 7.8	8.43 ± 7.2	2.86 ± 1.9	40.1 ± 19.48
2 LM	Y Velocity	5.15 ± 3.5	5.17 ± 3.8	0.62 ± 0.7	10.48 ± 7.4
2 LM	Z Velocity	12.37 ± 3.3	12.85 ± 3.6	0.72 ± 0.5	5.49 ± 3.32
2 LM	Velocity Magnitude	17.86 ± 4.8	22.25 ± 6.2	4.74 ± 2.6	20.83 ± 7.22
4 LM	X Velocity	7.67 ± 4.5	5.4 ± 6.1	3.76 ± 2.78	46 ± 29.3
4 LM	Y Velocity	6 ± 5.8	4.28 ± 5.2	2.07 ± 1.7	40.1 ± 17.5
4 LM	Z Velocity	29.43 ± 5.9	25.51±6.6	4 ± 1.6	14.68 ± 8
4 LM	Velocity Magnitude	33.73 ± 2.7	28.94 ± 3.5	5 ± 2.1	14.89 ± 6.1

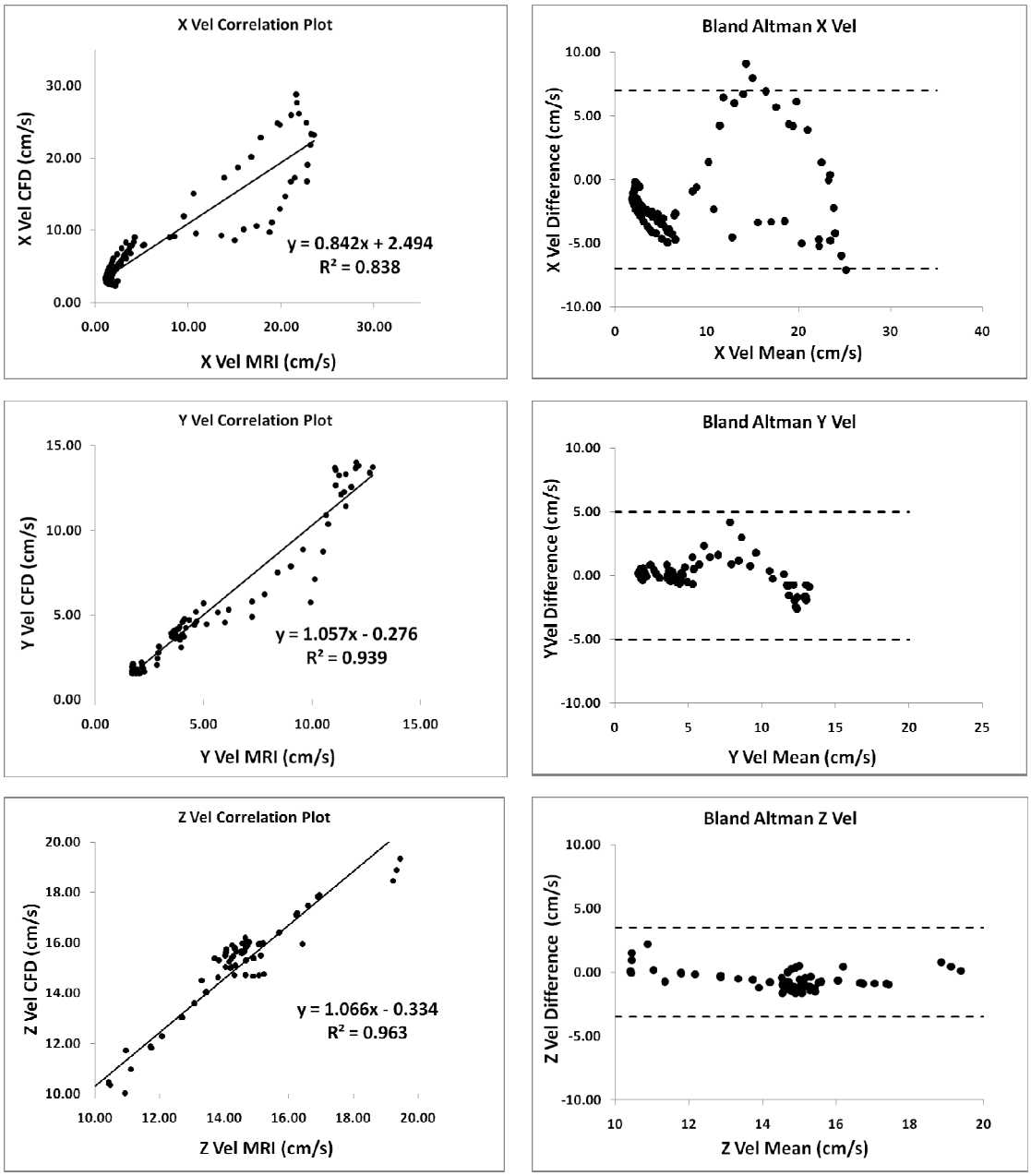

Figure 8.5: Correlation and Bland-Altman Analysis comparing the PC MRI velocities with CFD at the resting flow rate of 2 LPM. The dotted lines on the Bland-Altman plots represent ± 1 standard deviation from the mean velocity. PC MRI and CFD velocities were highly correlated, and except for a few outliers, an excellent match was observed between the two modalities. Maximum error was observed in the X component of the velocity, while minimum error was observed in the Z component of the velocity

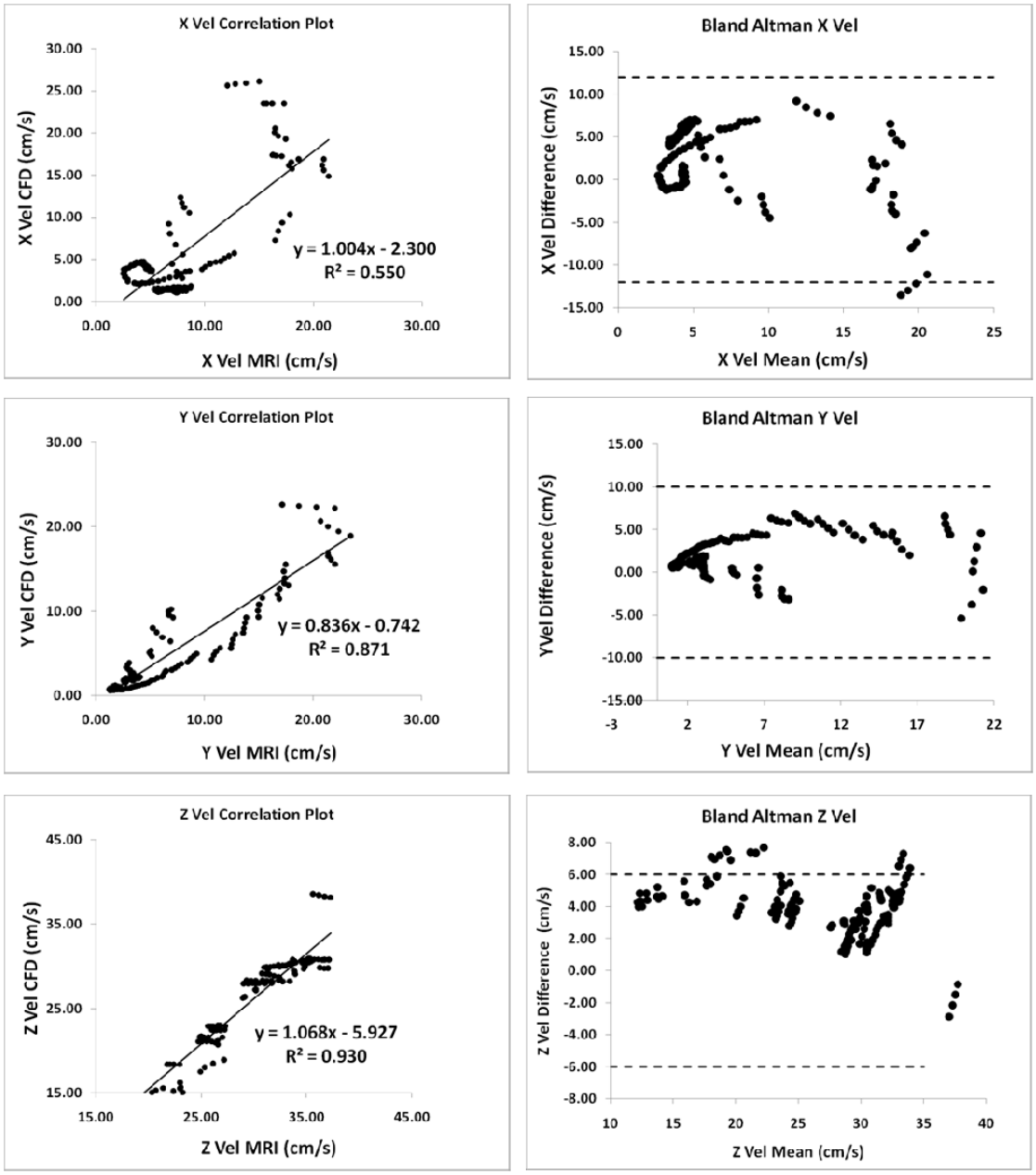

Figure 8.6: Correlation and Bland-Altman Analysis comparing the PC MRI velocities with CFD at the resting flow rate of 4 LPM. The dotted lines on the Bland-Altman plots represent ± 1 standard deviation from the mean velocity. PC MRI and CFD velocities were highly correlated for velocities in the Z direction, but the correlation was not very strong for velocities in the X direction.

At resting flow conditions, there was an excellent match in the Z component of the velocity between CFD and PC MRI. The average error was about 5.5% which was lower than the PC MRI reproducibility error of 7.29%. However, error in the X (40%) and Y (10%) directions were significantly higher than those in the Z direction. The velocities from both CFD and PC MRI were highly correlated for each of the 3 components with R^2 values of 0.84, 0.94, and 0.96 for X, Y, and Z components respectively. Bland-Altman analysis revealed that more than 96% of the error values were within 1 standard deviation of the mean values for all three components of velocity.

At higher flow rates going from resting to exercise, the error magnitude increased for all three components. Average X velocity error went up from 40 to 46%, Y velocity from 10 to 40%, and the Z velocity from 5.6 to 14.68 %. There was also a drop in the overall strength of the correlation between PC MRI and CFD, with the R^2 values dropping from 0.84 to 0.55, 0.94 to 0.87, and 0.96 to 0.93 for the X, Y, and Z components of the velocity respectively. It is important to note that the drop in the X component of the velocity was significantly more than either the Y or Z components of the velocity. Most of the errors were observed in the plane where then IVC connects to the pulmonary arteries where significant instabilities in the flow take place causing significant data loss in the PC MRI acquisition. Increasing the number of signal averages did not particularly improve the quality of the acquisition, and there were still significant number of missing data points in the pulmonary artery plane. The inherent drop in accuracy due to the low SNR associated with small pixel sizes could also be one of the reasons for data loss. This phenomenon will become more evident in the following sections.

8.4.1.2 Qualitative Comparison

In order to compare the flow fields between CFD and PC MRI, several planes were extracted at different orientations from the respective 3D flow fields. Since the two modalities were already registered, it was quite straightforward to acquire the slices at the exact same locations. Figure 8.7 shows the specific locations where all the different planes were acquired. Slices 1 and 4 corresponding to the SVC and the IVC were taken directly from the axial acquisitions, while locations 2 and 3 were taken from the connection region where the IVC is anastomosed to the pulmonary arteries. Location 5 is an oblique sagittal view of the connection showing the interaction between the SVC and the IVC, which differed slightly for the 2LPM and 4LPM acquisition. Figure 8.8 - Figure 8.18 show the corresponding contour plots, and vector plots comparing the flow fields between the two methodologies, as well as magnitude images at locations 2 and 3.

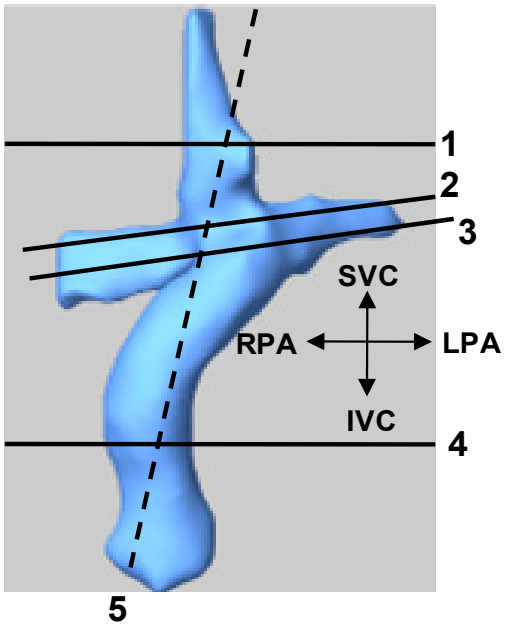

Figure 8.7: Slices extracted for comparison between CFD and PC MRI

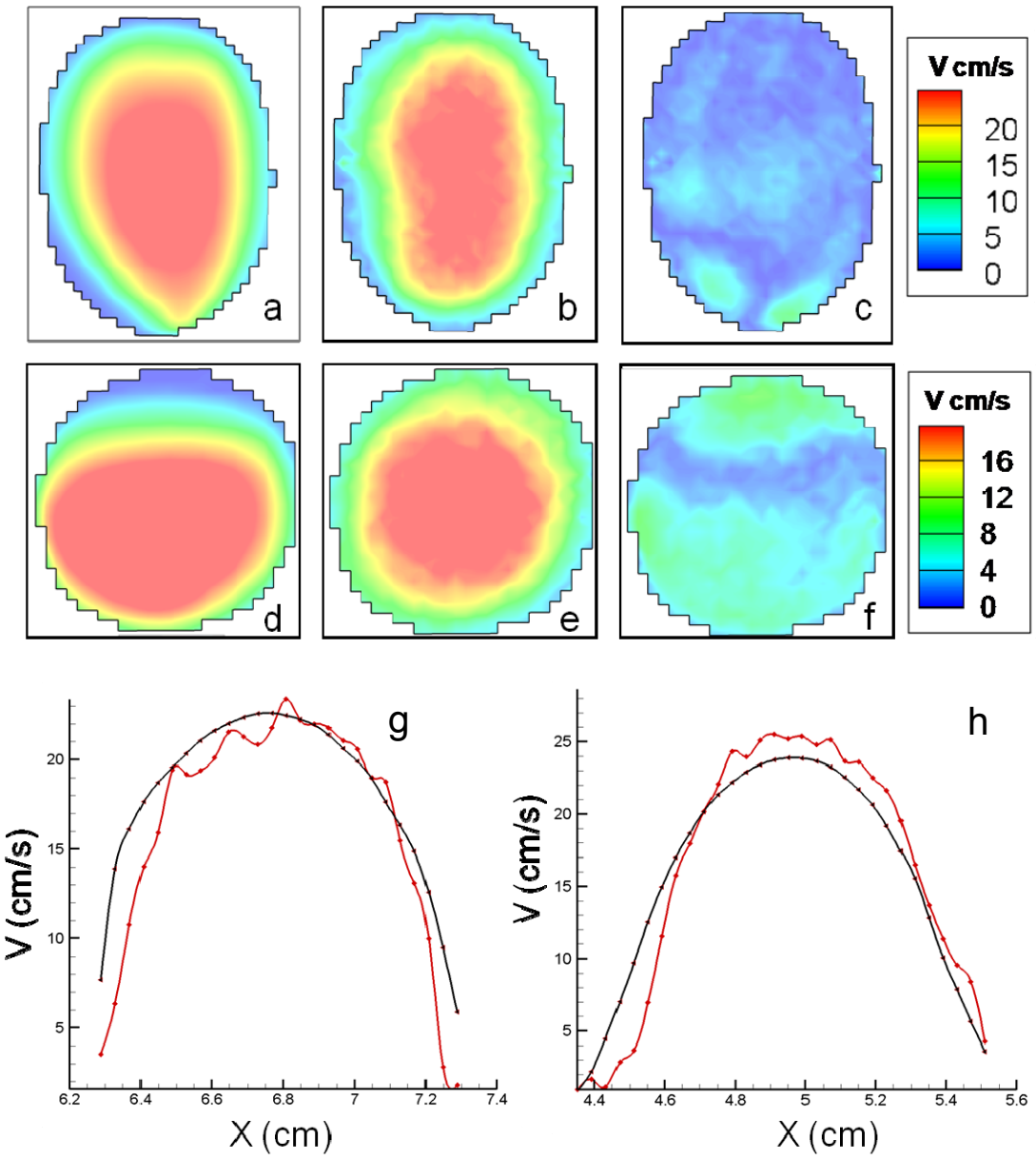

Figure 8.8: CHOA007 cross sectional velocities at 2LPM in: a) IVC using CFD; b) IVC using PC MRI; c) CFD-MRI error at the IVC; d) SVC using CFD; e) SVC using PC MRI; f) CFD-PC MRI error at the SVC. The cross sectional flow profiles (through plane velocity) taken along the diameter of the vessel for the SVC (g) and IVC (h) are shown below the contour plots. The black line corresponds to the CFD profile, while the red lines correspond to the PC MRI acquisition. Overall, an excellent match is evident between the two modalities.

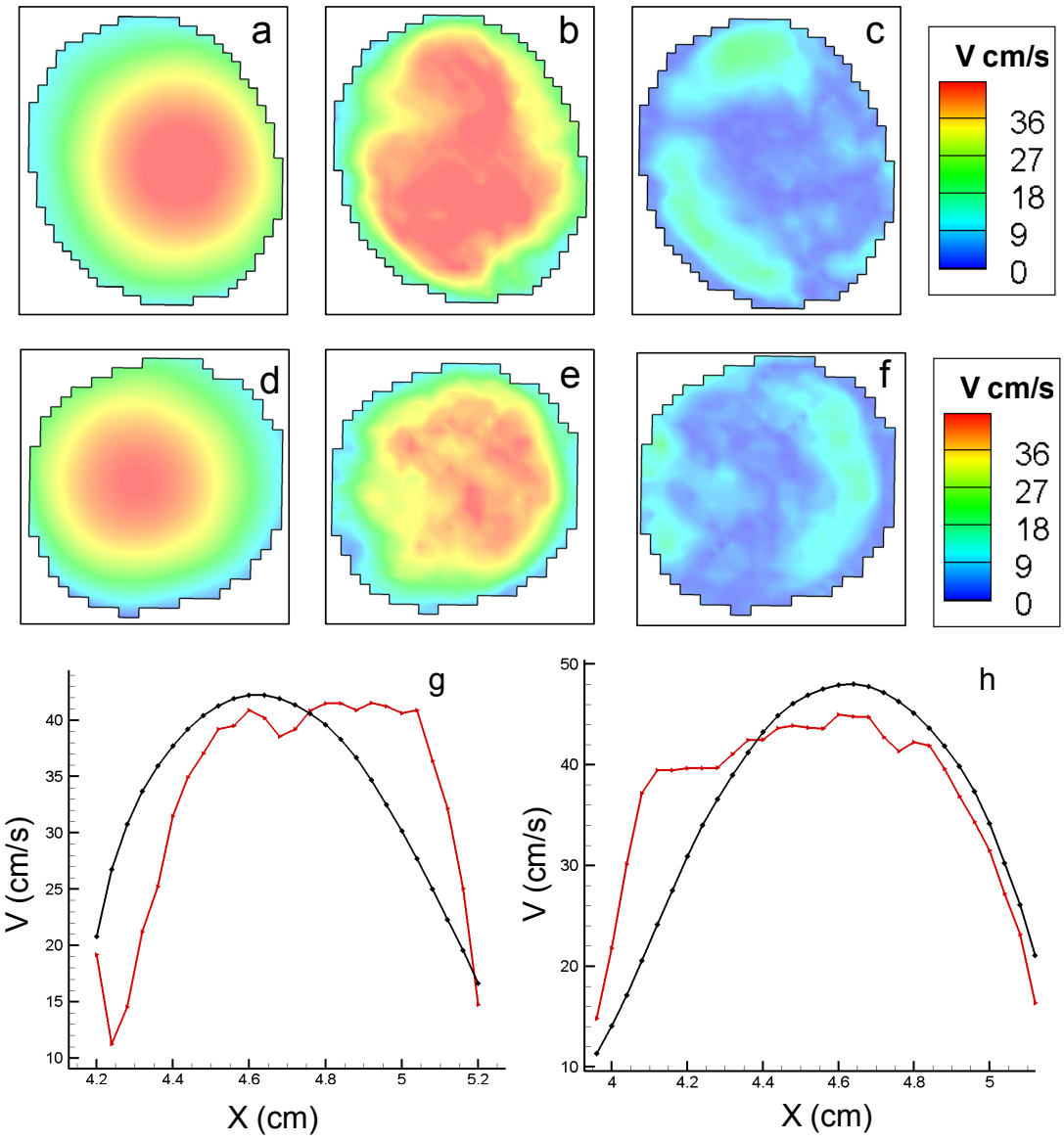

Figure 8.9: CHOA007 cross sectional velocities at 4LPM in: a) IVC using CFD; b) IVC using PC MRI; c) CFD-MRI error at the IVC; d) SVC using CFD; e) SVC using PC MRI; f) CFD-PC MRI error at the SVC. The red and blue colors correspond to the highest and lowest velocities observed in the CFD simulation The cross sectional flow profiles (through plane velocity) taken along the diameter of the vessel for the SVC (g) and IVC (h) are shown below the contour plots. The black line corresponds to the CFD profile, while the red lines correspond to the PC MRI acquisition. There is a slight offset in the flow profiles, which can be attributed to the registration error of the CFD with PC MRI.

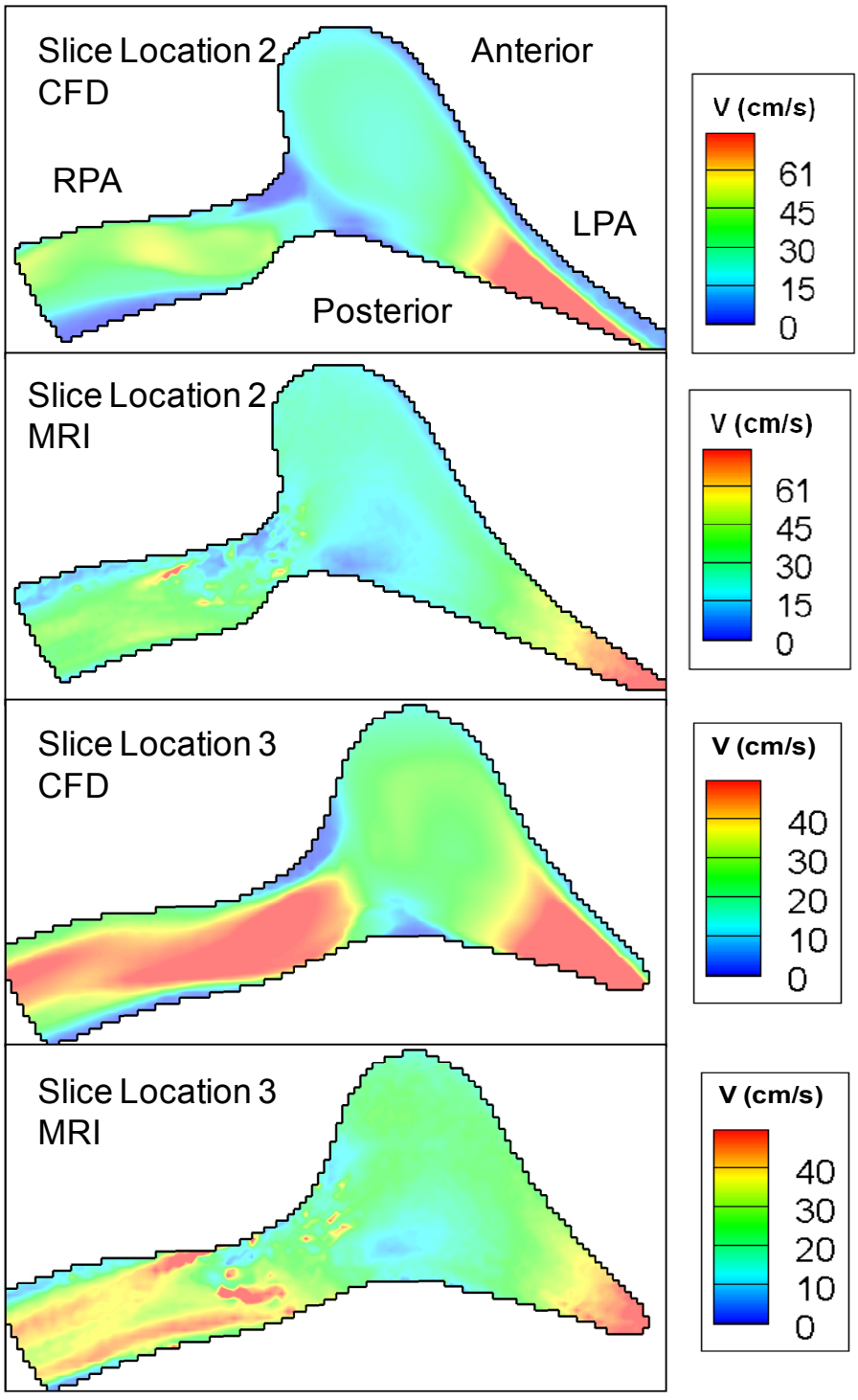

Figure 8.10: Contour plots of the velocity magnitude taken at slice locations 2 and 3 at 2 LPM. A slight registration mismatch is evident, but outside of that, the match between the two modalities is quite good.

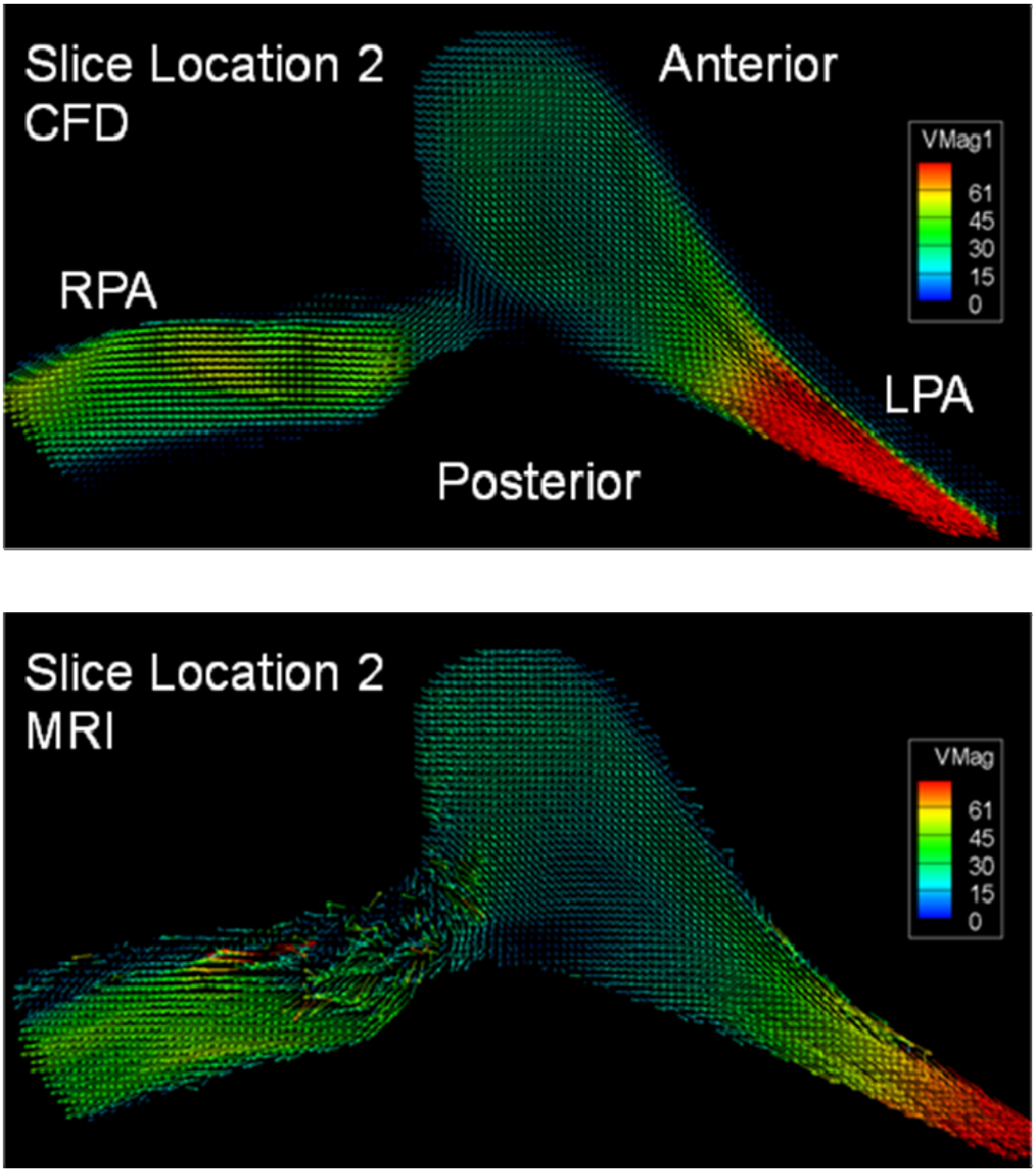

Figure 8.11: Comparison of CFD and MRI vector fields extracted at slice location 2 for the flow condition 2LPM. Notice that some vectors have a random orientation in the MRI acquisition as the flow enters the RPA.

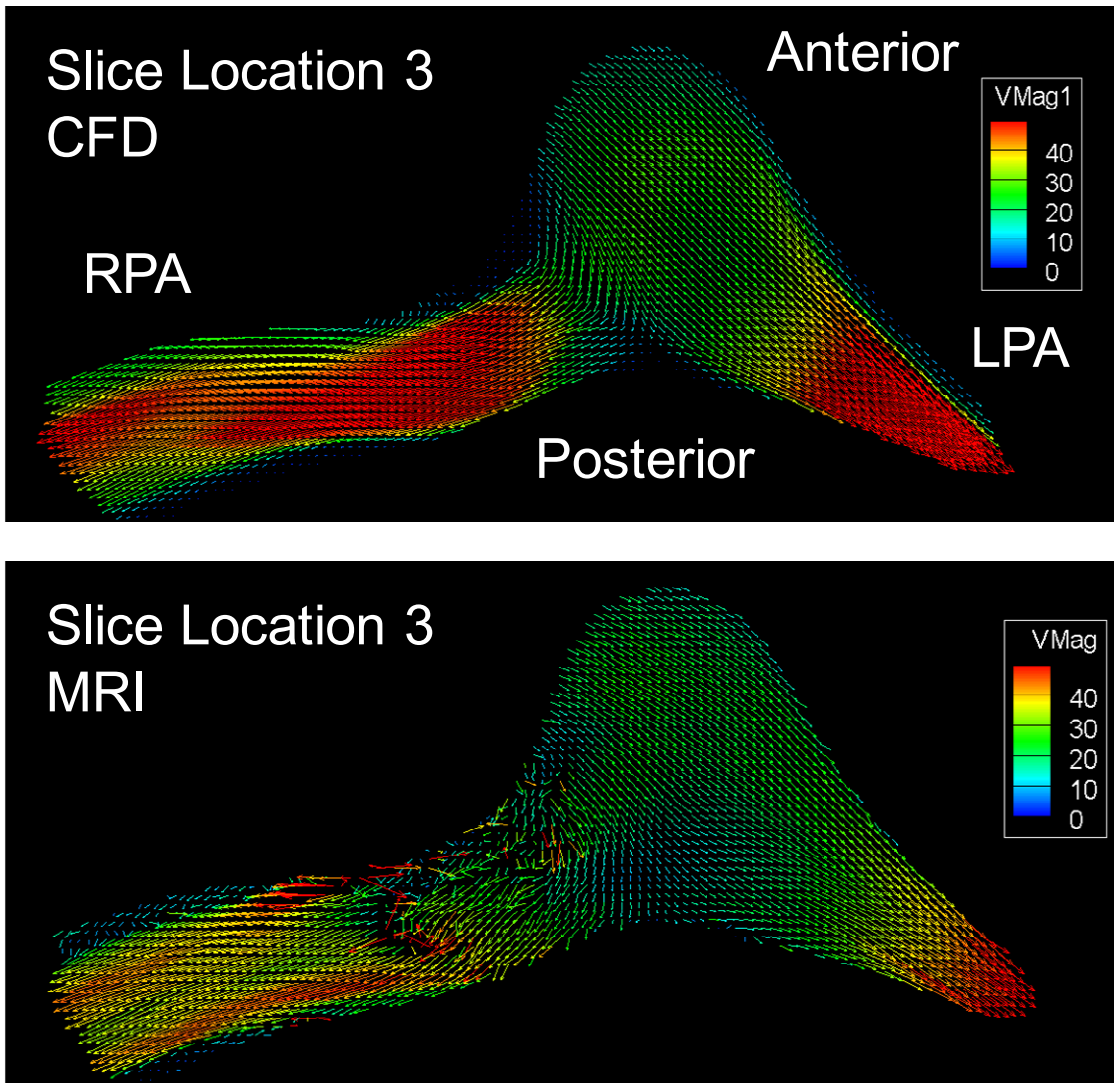

Figure 8.12: Comparison of CFD and MRI vector fields extracted at slice location 3 for the flow condition 2LPM. Notice that are still some vectors that have a random orientation in the MRI acquisition as the flow enters the RPA. The red and blue colors correspond to the highest and lowest velocities observed in the CFD simulation

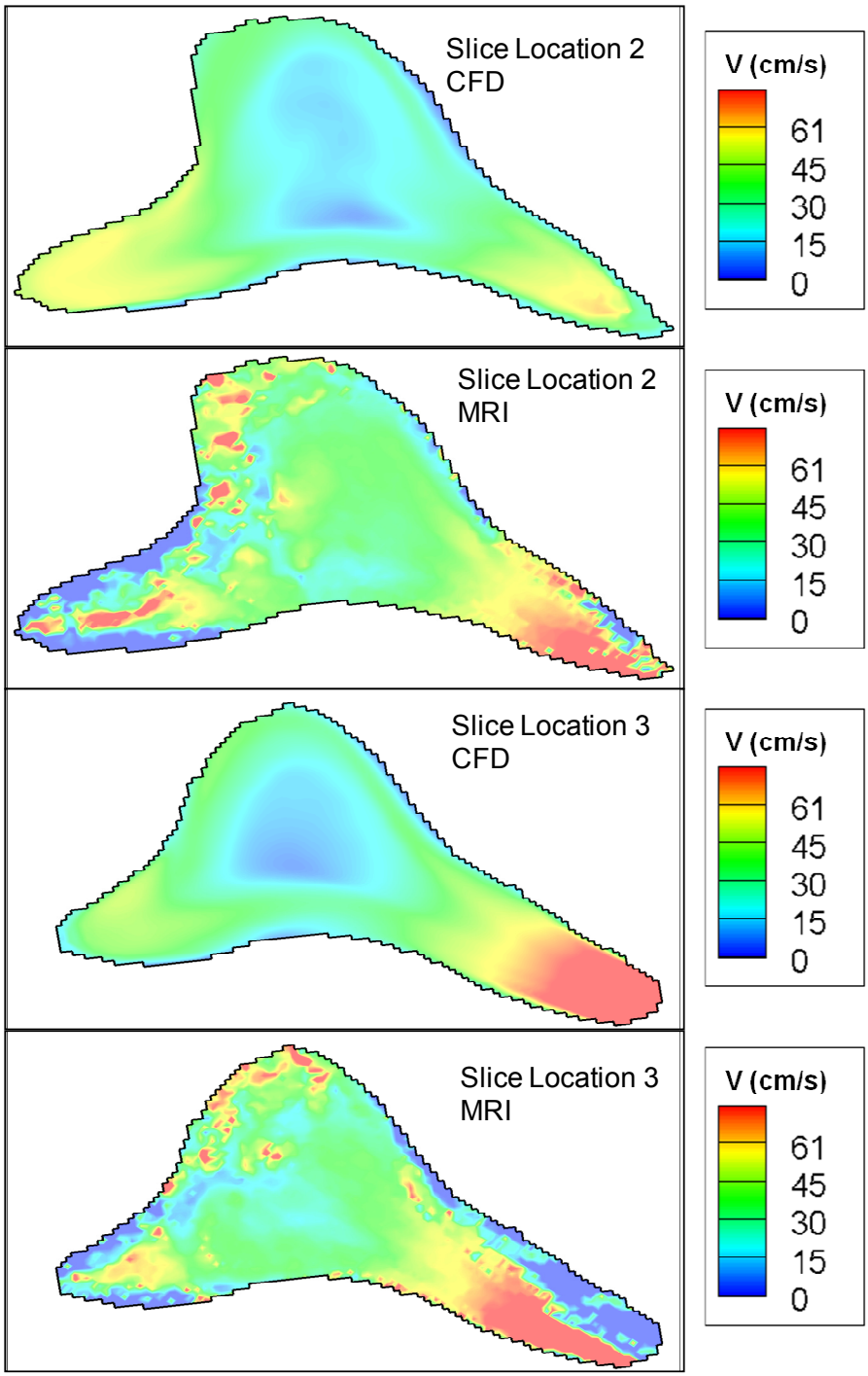

Figure 8.13: Contour plots of the velocity magnitude taken at slice locations 2 and 3 at 4 LPM. Notice that there is a lot of data-loss in the MRI associated with the low magnitude contour plots. The red and blue colors correspond to the highest and lowest velocities observed in the CFD simulation

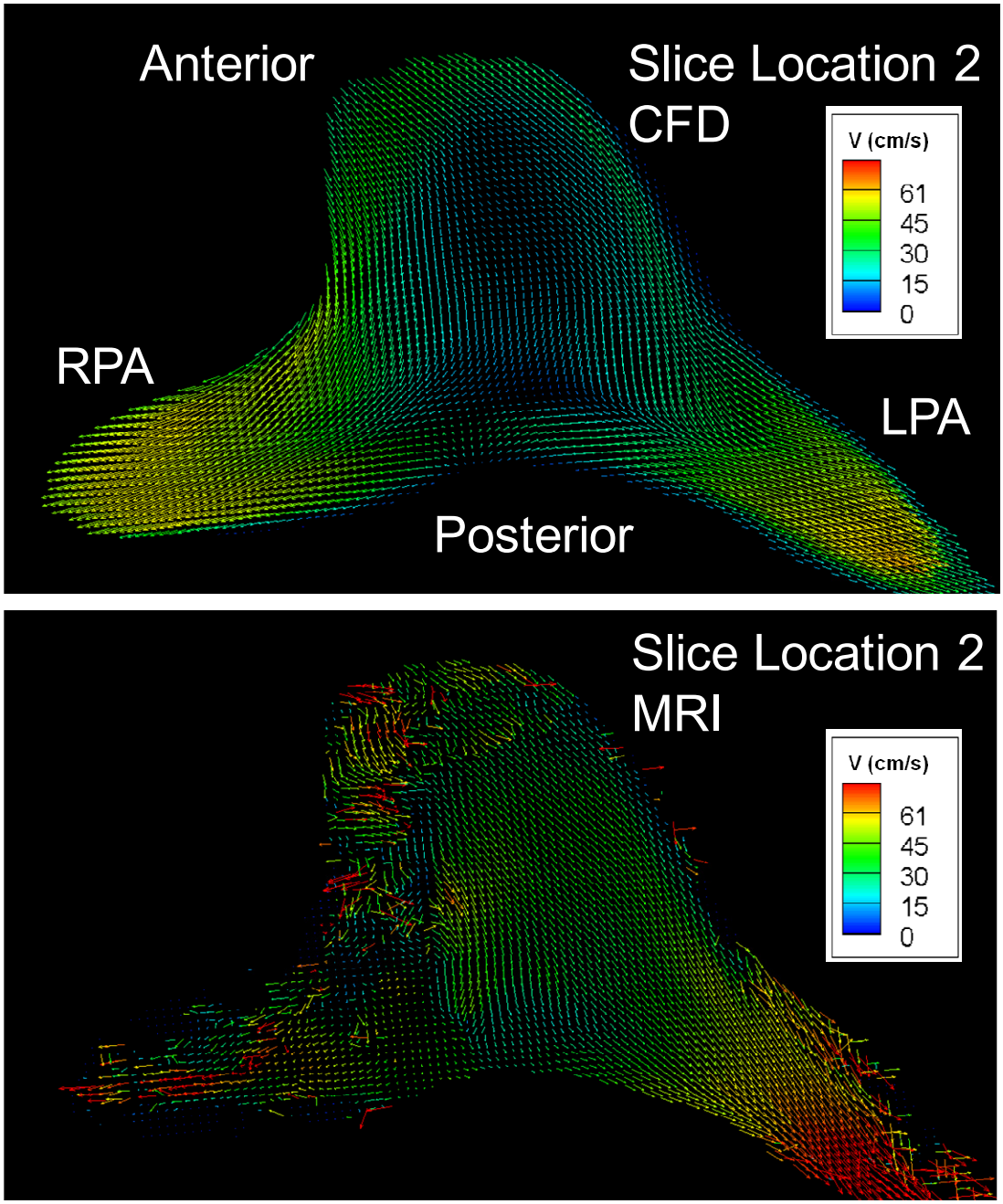

Figure 8.14: Comparison of vector fields extracted at slice location 2 (approximately) for the exercise flow condition 4 LPM. There are more vectors that seem to have random orientation in the MRI acquisition compared to CFD.

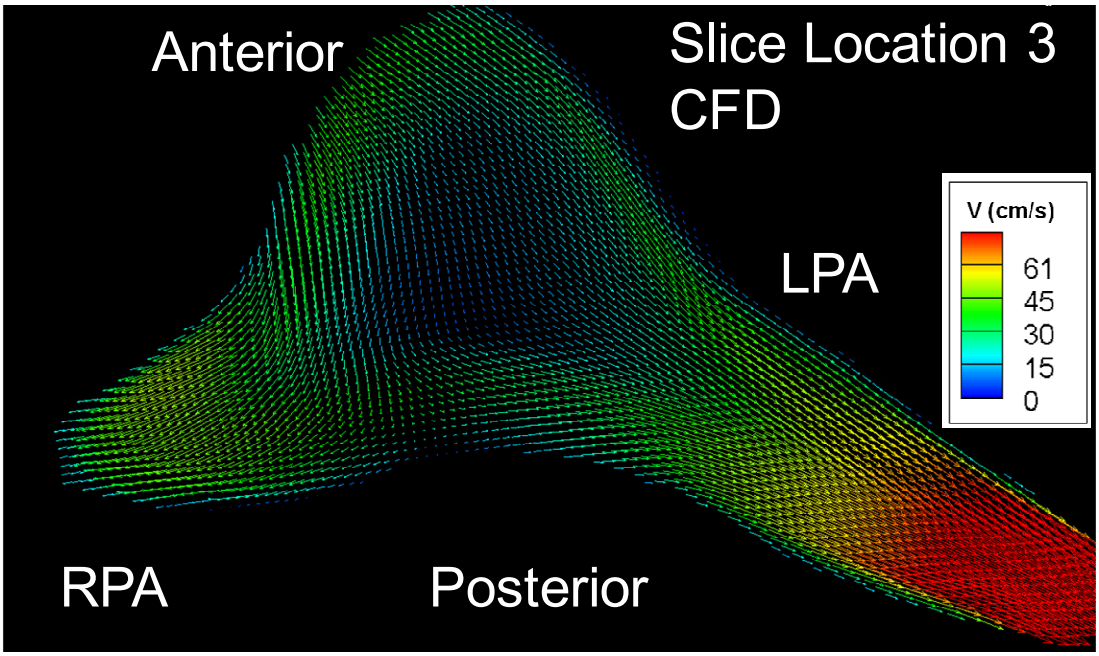

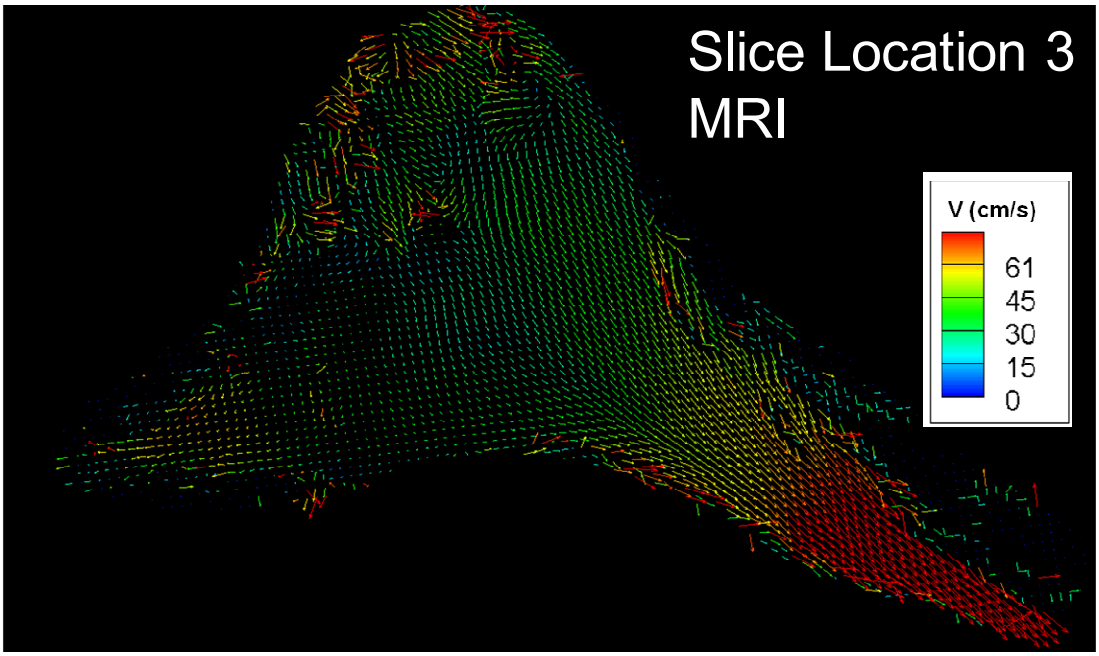

Figure 8.15: Comparison of vector fields extracted at slice location 3 (approximately) for the exercise flow condition 4 LPM. The loss of data in the MRI acquisition is clearly evident along the RPA and the LPA

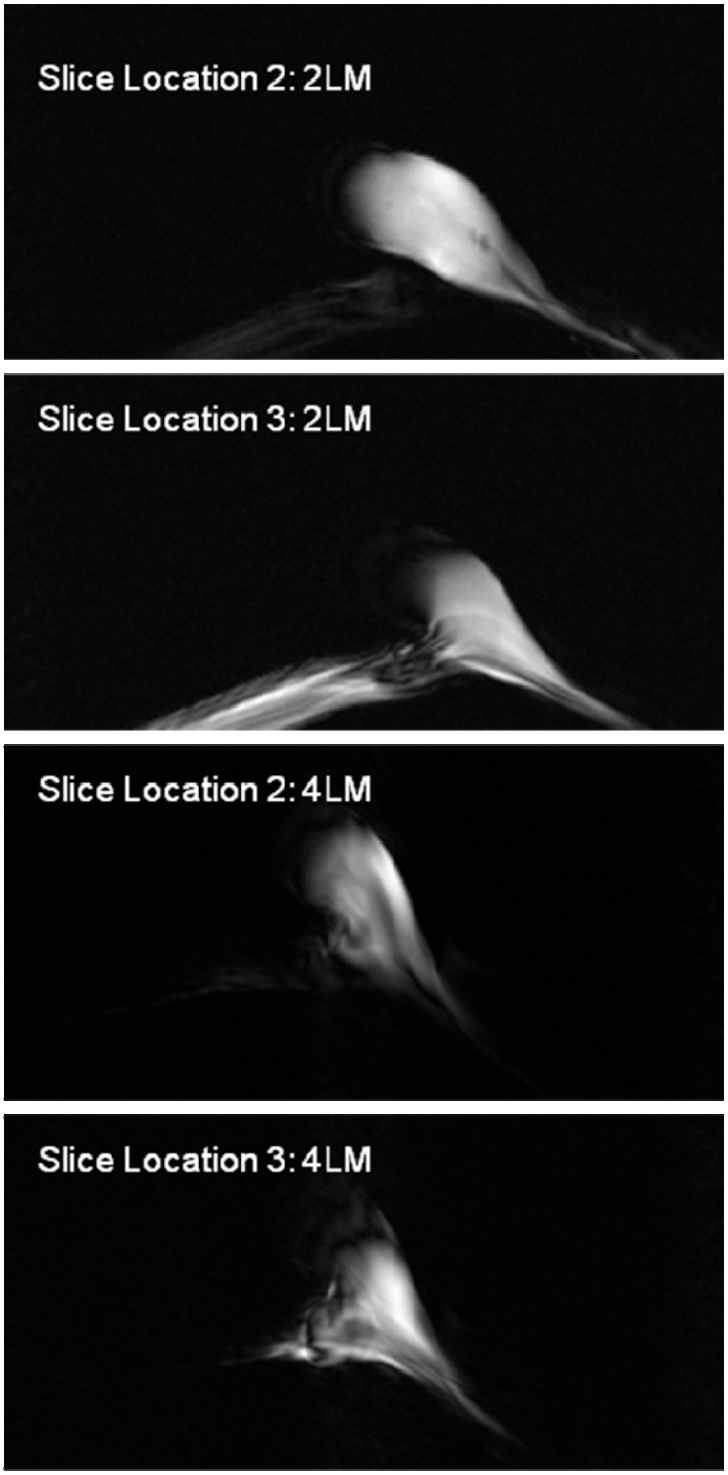

Figure 8.16: The corresponding magnitude images acquired in the connection region close to locations 2 and 3. Notice how there are dark spots within the flow field at 4 LPM compared to the 2LPM especially along the pulmonary arteries

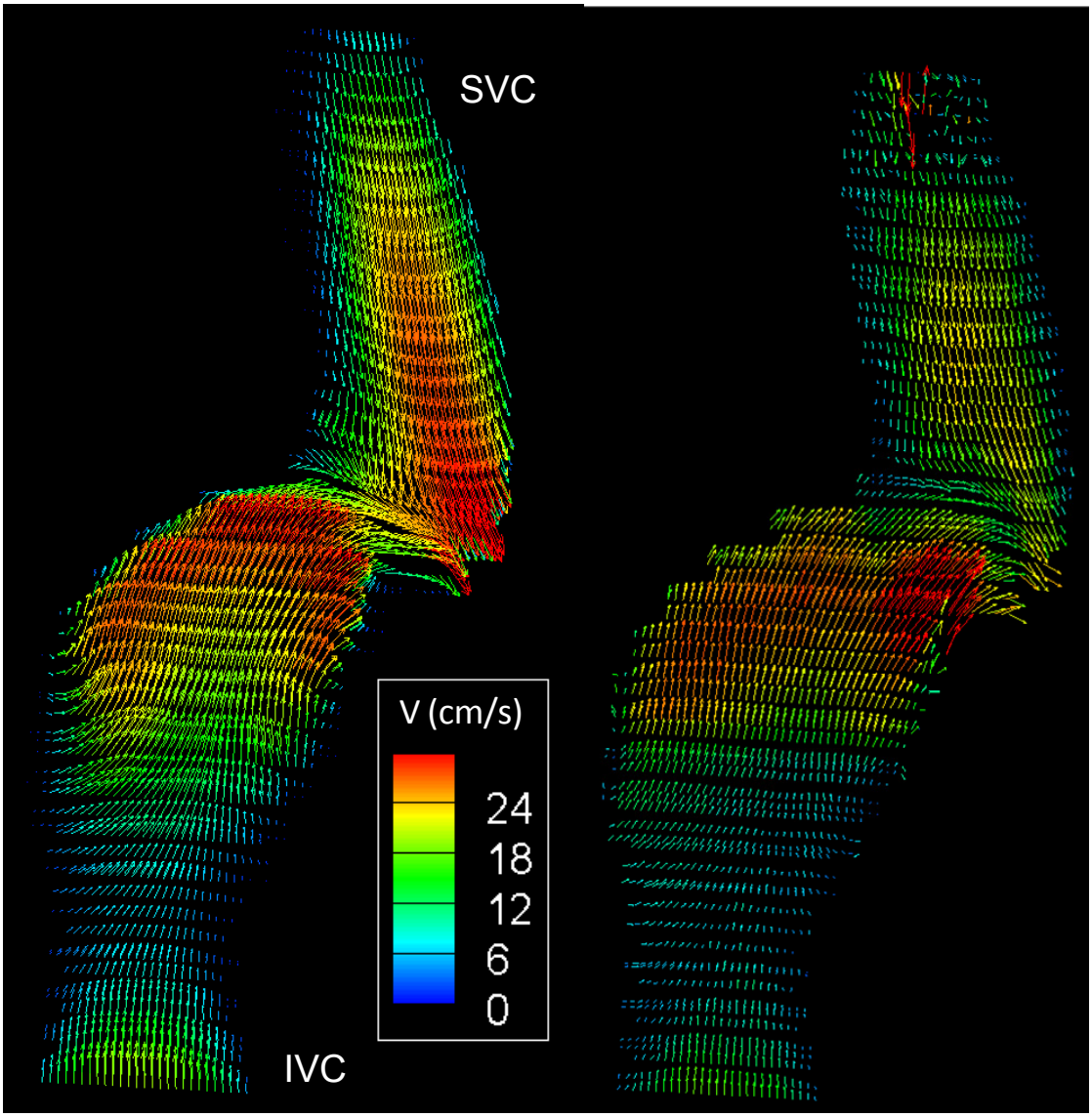

Figure 8.17: The vector field associated with an oblique coronal view (location 5) comparing CFD (left) and PC MRI (right) at 2LPM. There is a good match overall in the global flow features between PC MRI and CFD

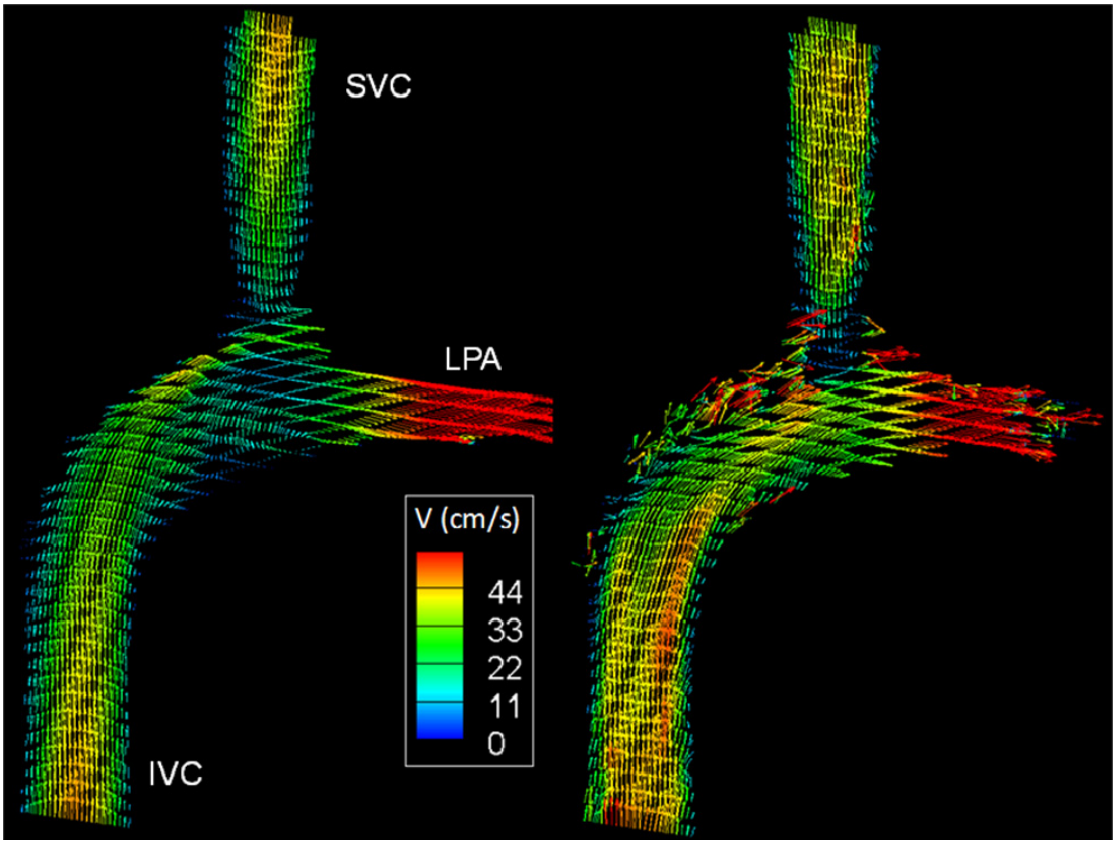

Figure 8.18: The vector field associated with an oblique coronal view (location 5 slightly rotated) comparing CFD (left) and PC MRI (right) at 4LPM. As can be observed, the global features match well between PC MRI and CFD, although slight differences in flow profiles can be observed at the IVC.

8.4.1.3 CHOA007 - Summary

The comparison between CFD and *in vitro* PC MRI experiments conducted at 1.5T yielded a good match between the two modalities. Particularly at 2LPM, the quantitative match was excellent in the primary flow direction, which in this case was the Z direction. Maximum errors were observed in the in-plane components primarily because the observed velocity magnitudes were much smaller compared to the dominant through plane component. The errors were highest in the location of the model where the

IVC connected to the pulmonary arteries, due to signal loss in the PC MRI acquisitions. Errors as high as 100% were observed in regions within the flow field where there was a loss of MRI signal. These effects were further pronounced at higher flow rates. Figure 8.19 shows the error as a function of flow rate, where the increase in error with flow rate is statistically significant. There were no significant differences in the errors in the X component of the velocity, while significant differences in error were observed for the Y and Z components respectively. However, there was a drop in the average error in velocity magnitudes going from 2 LPM to 4LPM. The reason is that velocity magnitudes are a function of three independent quantities, and even though the net error in the individual components may go down, it may still be possible that the velocity magnitude error is high.

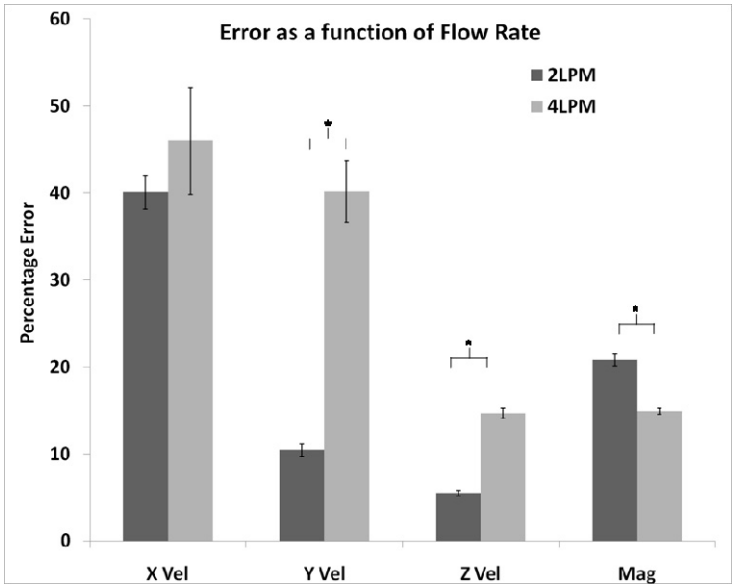

Figure 8.19: Error as a function of flow rate for CHOA007

In summary, it can be concluded that the comparison between high resolution PC

MRI and CFD was excellent at 1.5T for resting flow rates and moderately good for exercise flow rates.

8.4.2 CHOA006 (3.0T)

8.4.2.1 Quantitative Comparison

Table 8.4 shows the average root-mean-squared error associated with each component of velocity at both resting and exercise conditions, while Figure 8.20 and Figure 8.21 show the corresponding correlation and Bland Altman plots. At the resting flow condition, the overall RMS error was 5.96 cm/s which translated to an average normalized RMS percentage error of 25%. At the exercise flow condition, the overall RMS error increased to 7.67 cm/s, which translated to an average normalized RMS percentage error of 30%.

Table 8.4: Quantitative comparison of velocity values between CFD and PC MRI. Data presented as Mean ± SD

Flow Condition	**Velocity Component**	**PC MRI (cm/s)**	**CFD (cm/s)**	**RMS Error (cm/s)**	**% Error**
3 LM	X Velocity	10.45 ± 9.8	10.74 ± 8.6	2.2 ± 1.9	22.15 ± 12.8
3 LM	Y Velocity	6.23 ± 4	9.47 ± 6.3	4.25 ± 3.6	39.18 ± 23.1
3 LM	Z Velocity	11.9 ± 4.6	14.66 ± 5.9	2.77 ± 1.92	17.4 ± 9
3 LM	Velocity Magnitude	19.47 ± 11.2	22.39 ± 12.2	3.47 ± 3.2	14.53 ± 10.9
5 LM	X Velocity	11.67 ± 7.8	15.77 ± 12.6	4.9 ± 5.8	25.9 ± 20
5 LM	Y Velocity	11.54 ± 5.4	11 ± 8.11	4.02 ± 2.6	36 ± 20
5 LM	Z Velocity	18.88 ± 8	18.57 ± 8	2.33 ± 2.7	10.68 ± 12.4
5 LM	Velocity Magnitude	27.78 ± 12.2	29.22 ± 16.1	5.69 ± 5.7	17.98 ± 13.5

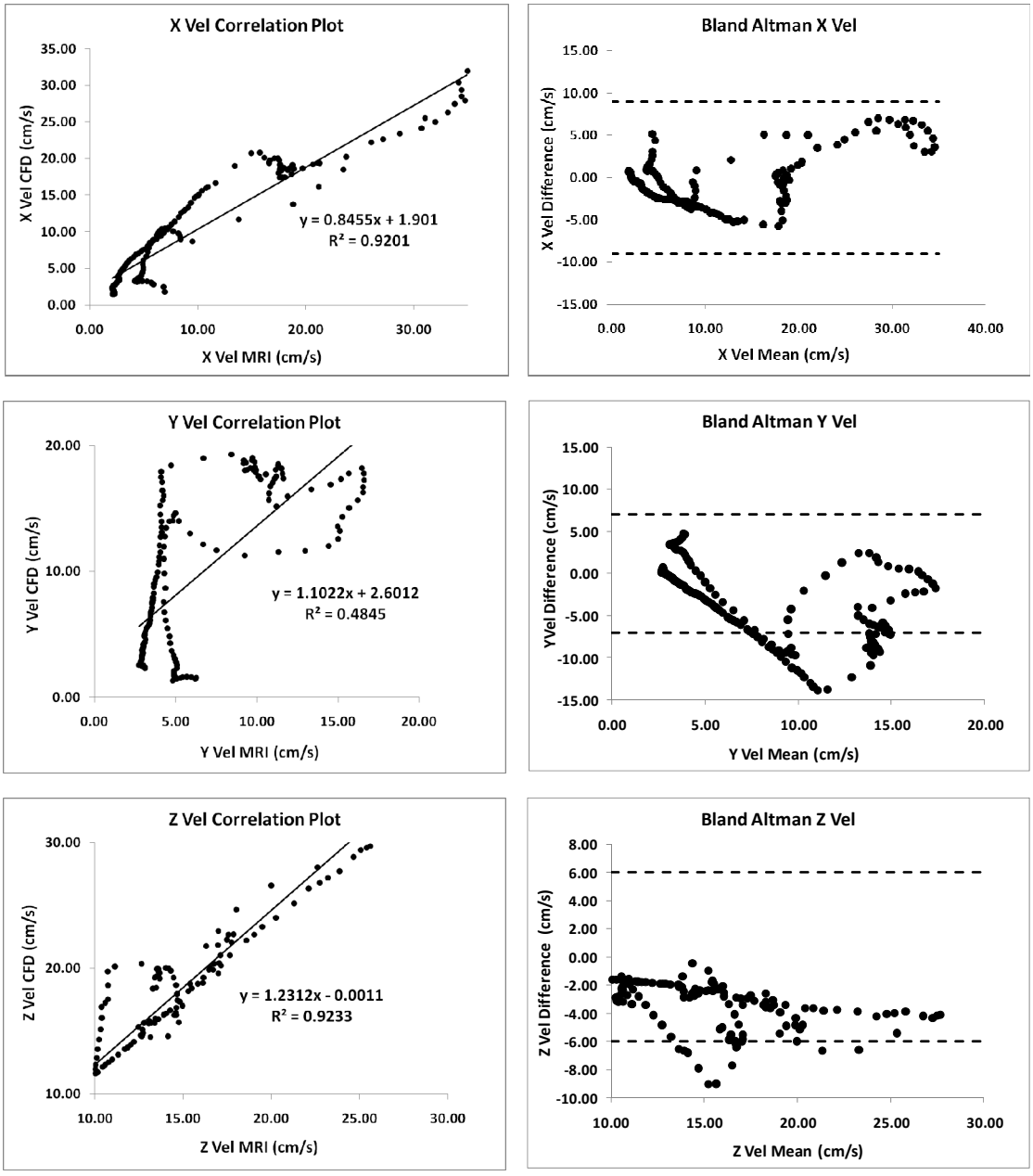

Figure 8.20: Correlation and Bland-Altman Analysis comparing the PC MRI velocities with CFD at the resting flow rate of 3 LPM for CHOA006. The dotted lines on the Bland-Altman plots represent ± 1 standard deviation from the mean velocity. PC MRI and CFD velocities were highly correlated, and except for a few outliers, an excellent match was observed between the two modalities. Maximum error was observed in the Y component of the velocity, while minimum error was observed in the Z component of the velocity

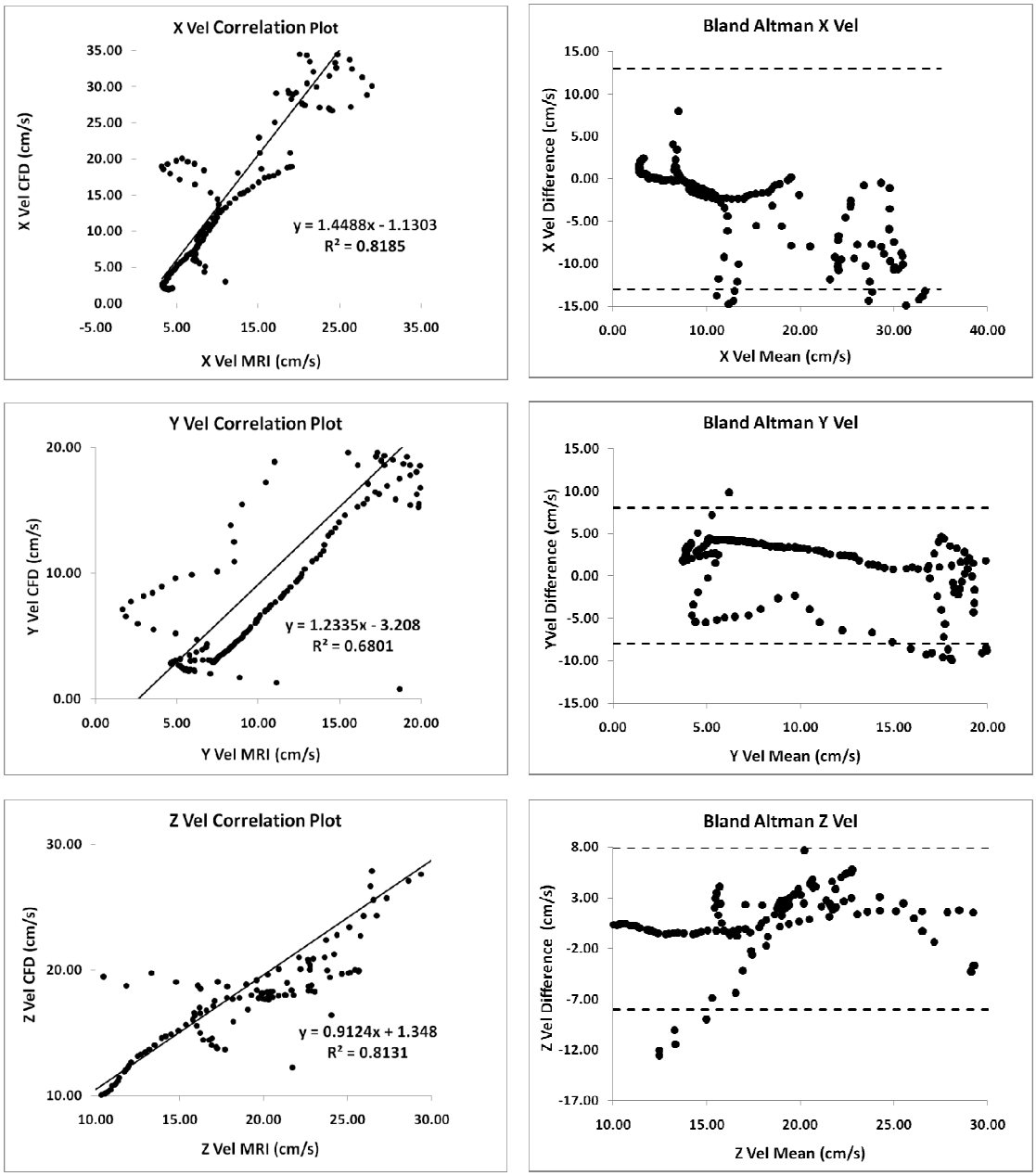

Figure 8.21: Correlation and Bland-Altman Analysis comparing the PC MRI velocities with CFD at a flow rate of 5 LPM for CHOA006. The dotted lines on the Bland-Altman plots represent ± 1 standard deviation from the mean velocity. PC MRI and CFD velocities were highly correlated, and except for a few outliers, a good match was observed between the two modalities. Maximum error was observed in the X component of the velocity, while minimum error was observed in the Z component of the velocity

At resting flow conditions of 3 LPM, there was an excellent quantitative match between PC MRI and CFD for the X and Z component of the velocities respectively. The average X and Z velocity error were 22.15 ± 12.8% and 17.4 ± 9 % respectively. However, there was a poor match between the two modalities in the Y component of the velocity, where an average error of 39.2 ± 23% was observed. The velocities seemed to be uncorrelated between the two modalities (Figure 8.20) for the Y component. Bland-Altman Analysis revealed that at low velocity magnitude of less than 10 cm/s there was a linear bias in the velocities, which hints towards the influence of background phase in distorting the Y velocity values. This is because lower Y velocities (in this particular model) are typically observed in the SVC and the IVC, which are not in the isocenter of the magnet. The same phenomenon is observed in the Bland Altman plots for the Z velocities as well, although the bias is quite small compared to the velocity value itself.

At exercise flow conditions of 5 LPM, the match between PC MRI and CFD was good for all three components. The average error for X velocities increased slightly to 25 ± 20%, while the average error for the Y and Z velocities dropped to 36 ± 20% and 10.7 ± 12 % respectively. Contrary to the 3LPM case, the Y velocities in this condition were highly correlated with the CFD velocities, with the R^2 value increasing from 0.48 to 0.68. Some distortion was still observed at lower velocity values, but for values greater than 10 cm/s, the correlation was almost perfectly linear. Bland Altman analysis confirmed this observation. For the X and Z components, the match was excellent with most of the velocity differences being around 0. There were still a few values that were scattered, which could be due to: a) MRI signal loss due to the dephasing of proton spins, b) low SNR.

8.4.2.2 Qualitative Comparison

Similar to CHOA007, several planes were extracted at different locations in order to compare the flow fields between the two modalities. The slices were extracted at 5 different locations, with 3 extracted at perfectly axial locations, and 2 at oblique angles depicting the flow transition from the IVC/SVC to the two pulmonary arteries. Flow profile plots are shown for the SVC and the IVC in addition to the velocity magnitude contour plots. Velocity magnitude contour plots are shown for the slices acquired in the axial orientation, while velocity vector plots are primarily used for the slices taken at oblique orientations. Figure 8.22 shows the locations of the slices while Figure 8.23 to Figure 8.28 show the contour plots and vector plots for each slice and experimental condition. Figure 8.29 shows the magnitude image at slice location 2.

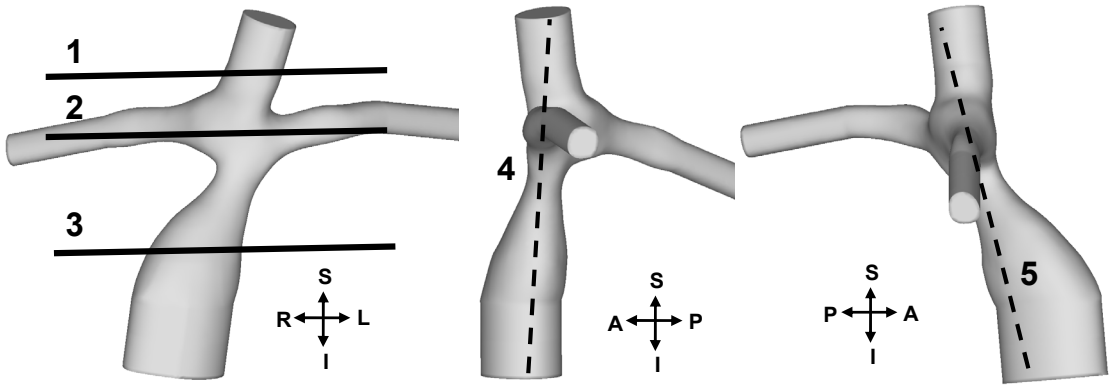

Figure 8.22: Orientation of the different slices used for comparing the flow fields between PC MRI and CFD. 'S' stands for Superior, 'I' for Inferior, 'A' for anterior, 'P' for Posterior, 'L' for Left, and 'R' for Right. Slices 1-3 are perfectly axial acquisitions while 4 and 5 are taken at an oblique angle with respect the model

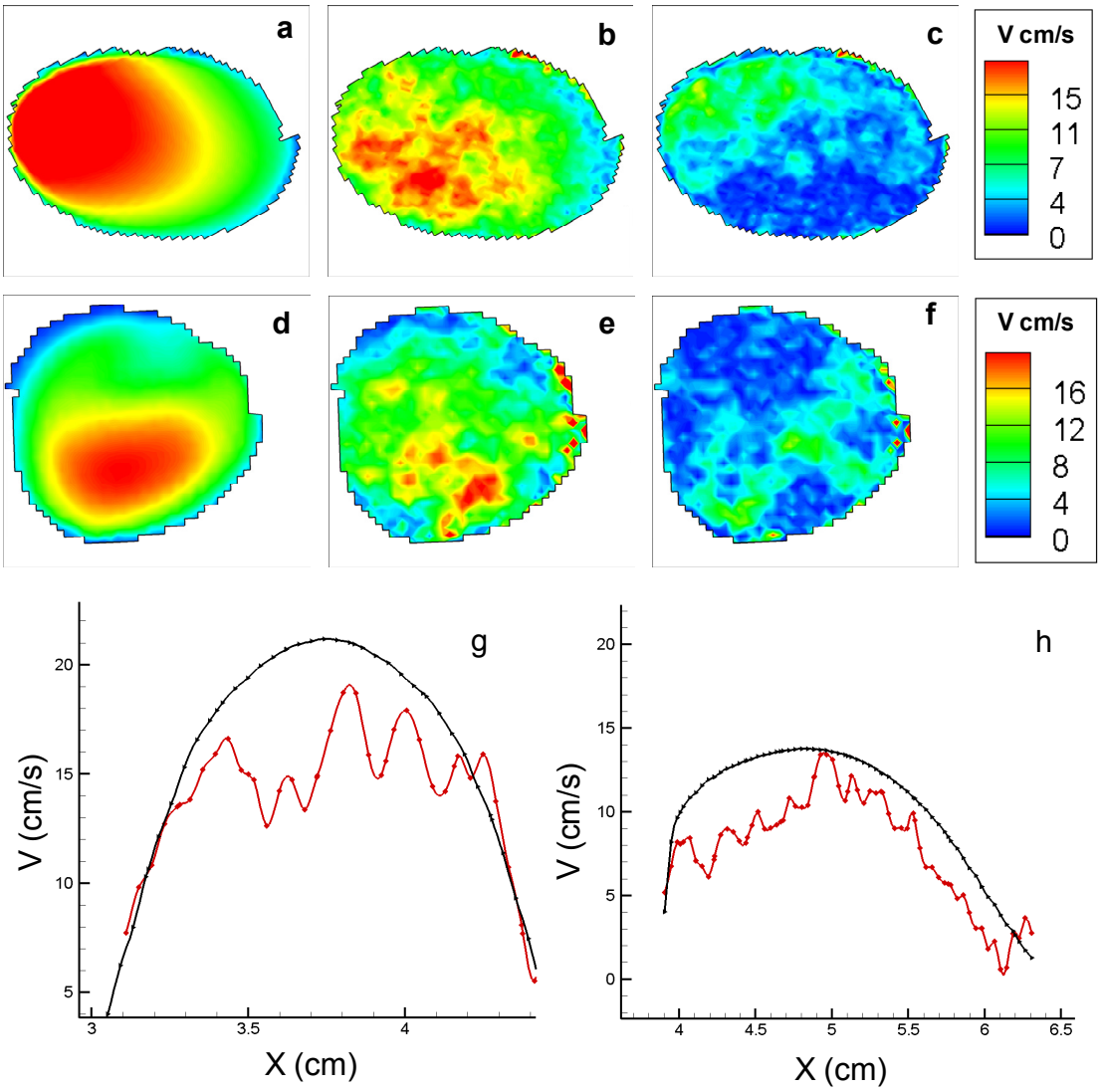

Figure 8.23: CHOA006 cross sectional velocities at 3LPM in: a) IVC using CFD; b) IVC using PC MRI; c) CFD-MRI error at the IVC; d) SVC using CFD; e) SVC using PC MRI; f) CFD-PC MRI error at the SVC. The cross sectional flow profiles (through plane velocity) taken along the diameter of the vessel for the SVC (g) and IVC (h) are shown below the contour plots. The black line corresponds to the CFD profile, while the red lines correspond to the PC MRI acquisition. Fluctuations in the velocity profile are clearly evident from both the PC MRI locations at SVC and the IVC. Furthermore, the peak values for the MRI were below those for the CFD.

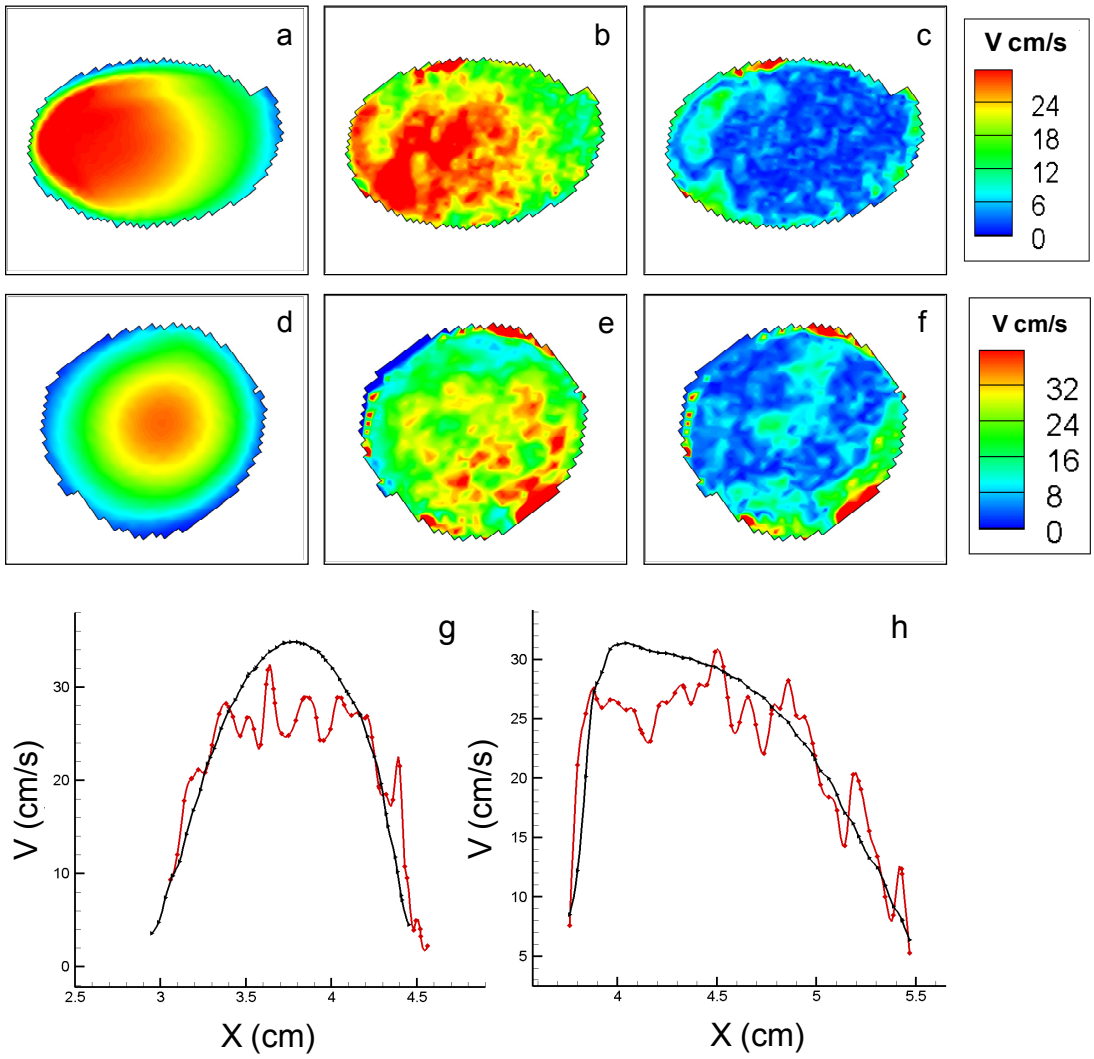

Figure 8.24: CHOA006 Cross sectional velocities at 5LPM in: a) IVC using CFD; b) IVC using PC MRI; c) CFD-MRI error at the IVC; d) SVC using CFD; e) SVC using PC MRI; f) CFD-PC MRI error at the SVC. The cross sectional flow profiles (through plane velocity) taken along the diameter of the vessel for the SVC (g) and IVC (h) are shown below the contour plots. The black line corresponds to the CFD profile, while the red lines correspond to the PC MRI acquisition. Fluctuations in the velocity profile are clearly evident from both the PC MRI locations at SVC and the IVC. Furthermore, the peak values for the MRI were below those for the CFD.

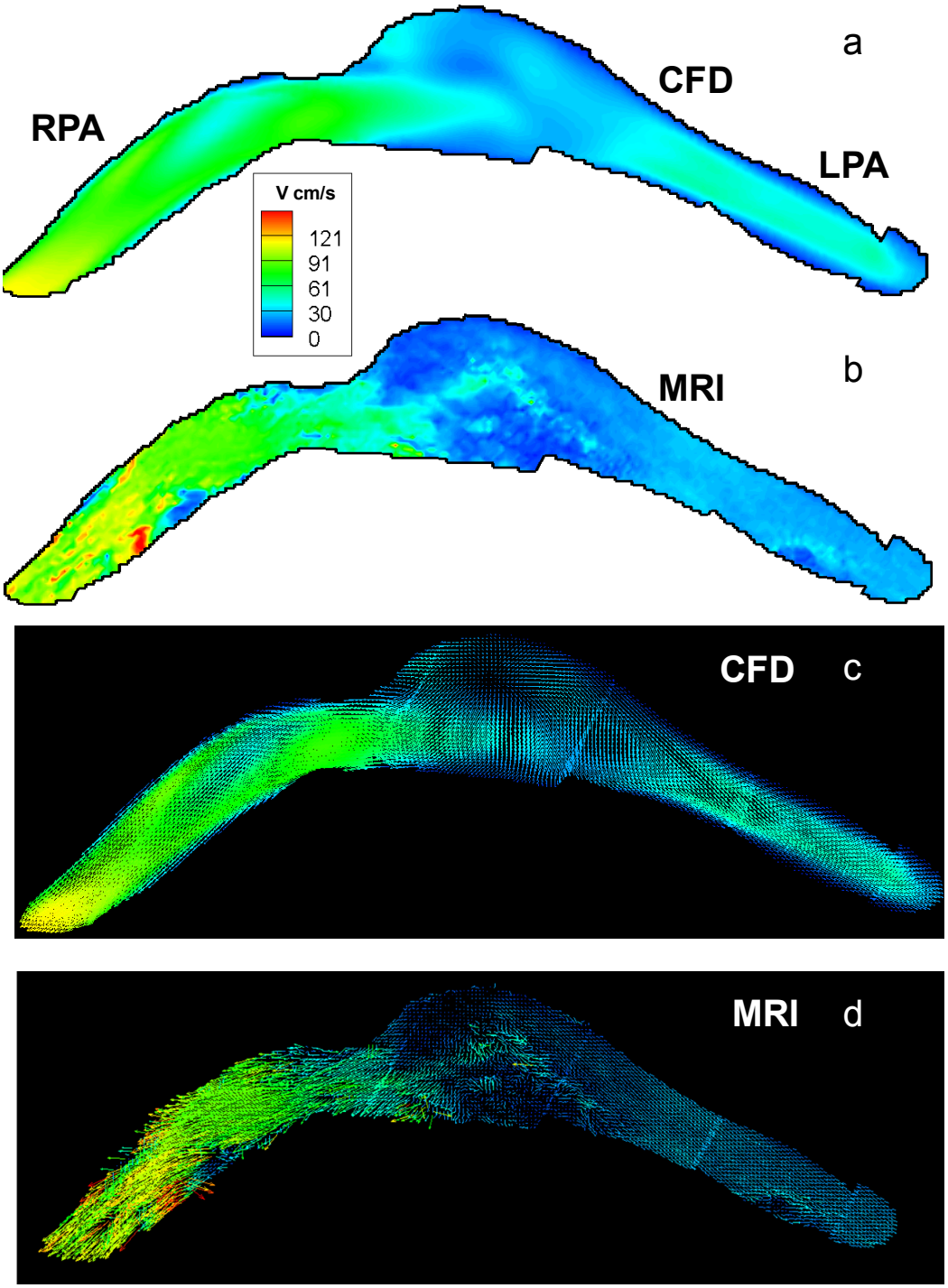

Figure 8.25: The contour plots (a, b) and the associated vector plots (c, d) for CHOA006 at slice location 3 for the 3LPM flow condition. A good qualitative agreement between the two modalities is evident from the both the contour plots and the vector plots. Slightly lower velocity magnitudes were observed for the PC MRI measurement (b, d) compared to CFD (a,c).

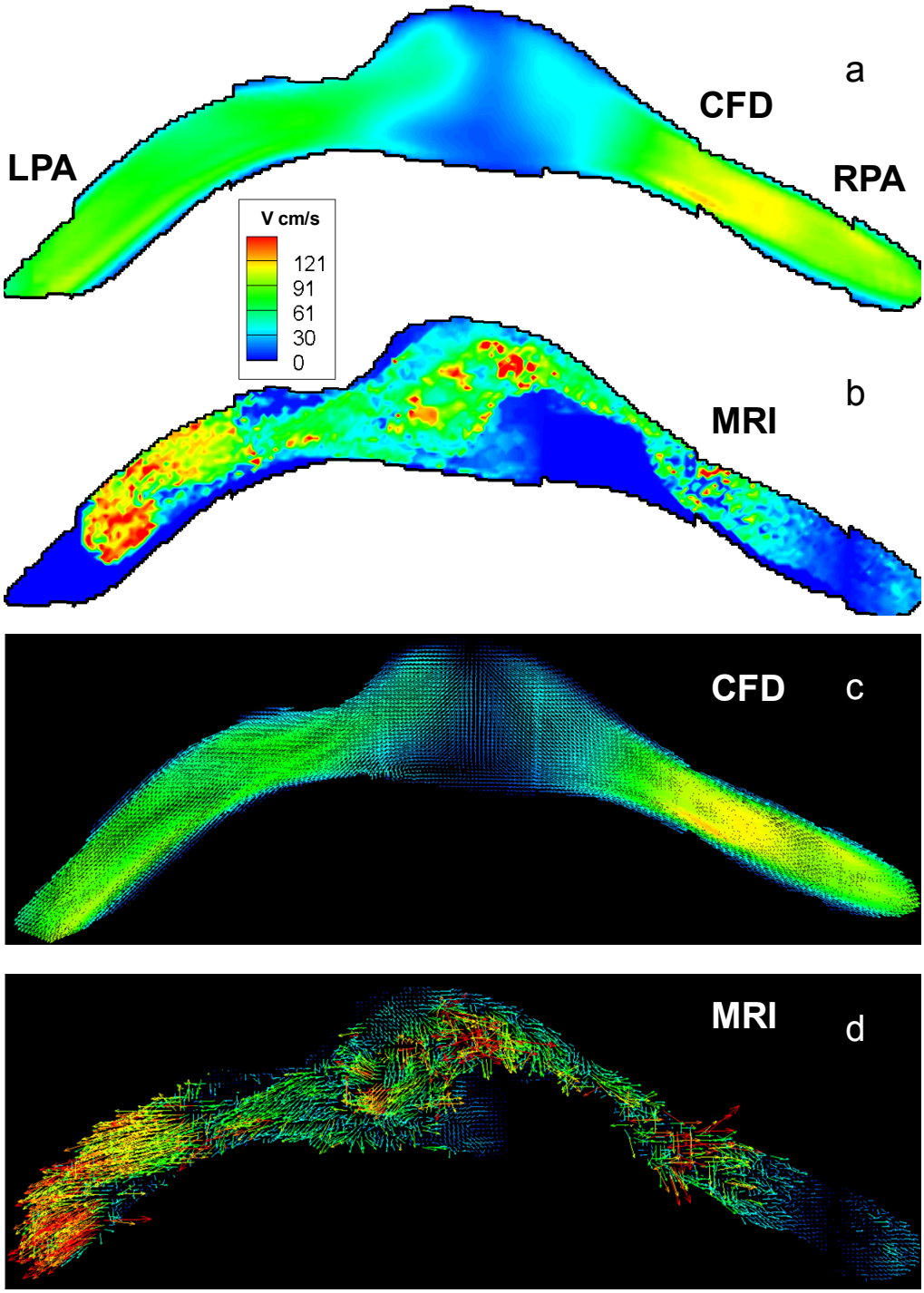

Figure 8.26: The contour plots (a, b) and the associated vector plots (c, d) for CHOA006 at slice location 3 for the 5LPM flow condition. The match between CFD and MRI was not good in this slice location. There was a big area in the center of the model where PC MRI data was missing, possibly due to low signal to noise ratio

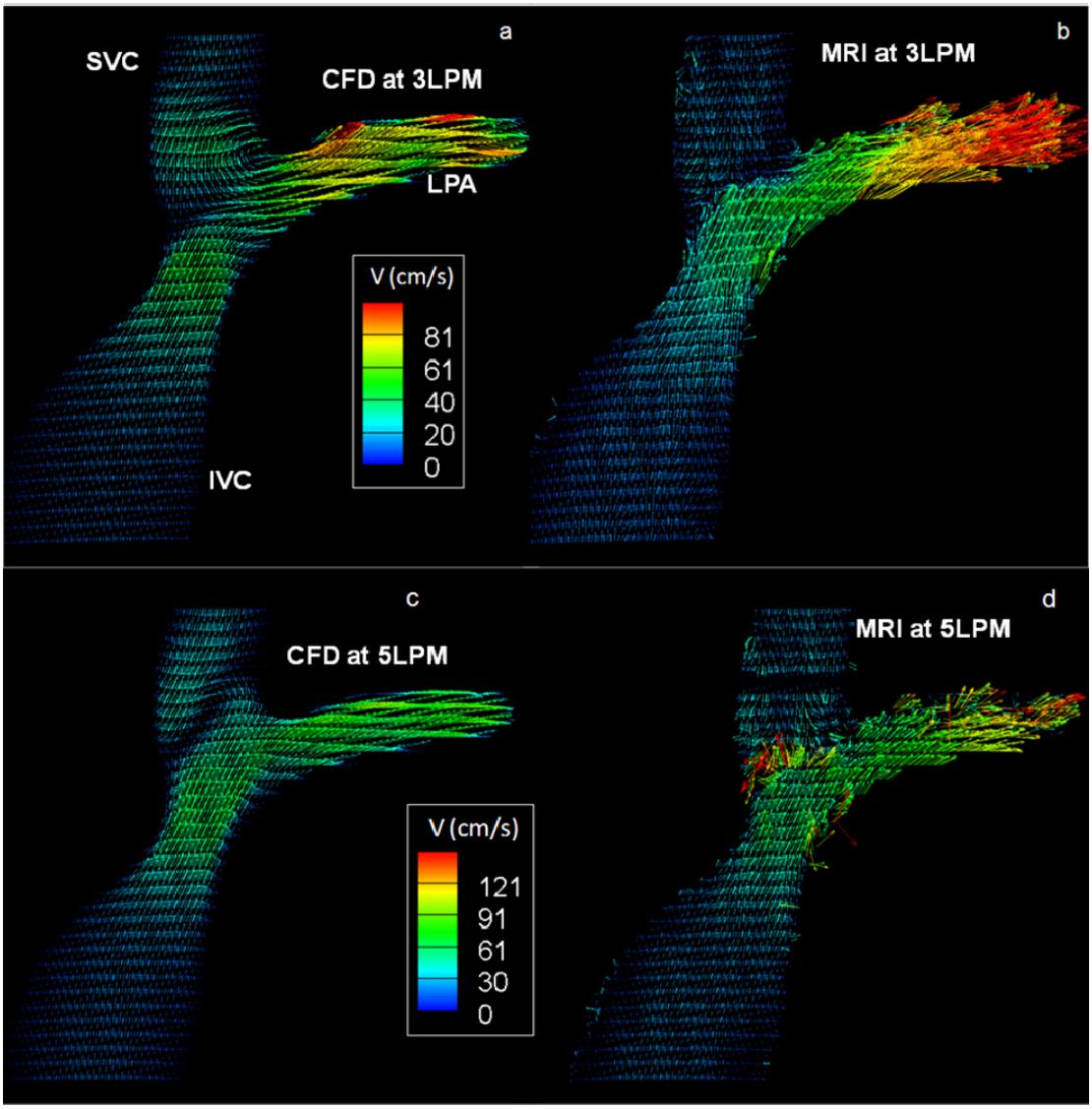

Figure 8.27: The CFD (a,c) and PC MRI (b,d) vector plots associated with slice location 4 for the experimental conditions 3LPM (a,b) and 5 LPM (c,d). At 3 LPM there is a good match between CFD and PC MRI, although a vortex just superior of the LPA is missing in the PC MRI vector field. Similarly, there is a shear layer that is clearly observed in the CFD velocity field at 5 LPM which is absent for the PC MRI velocity field.

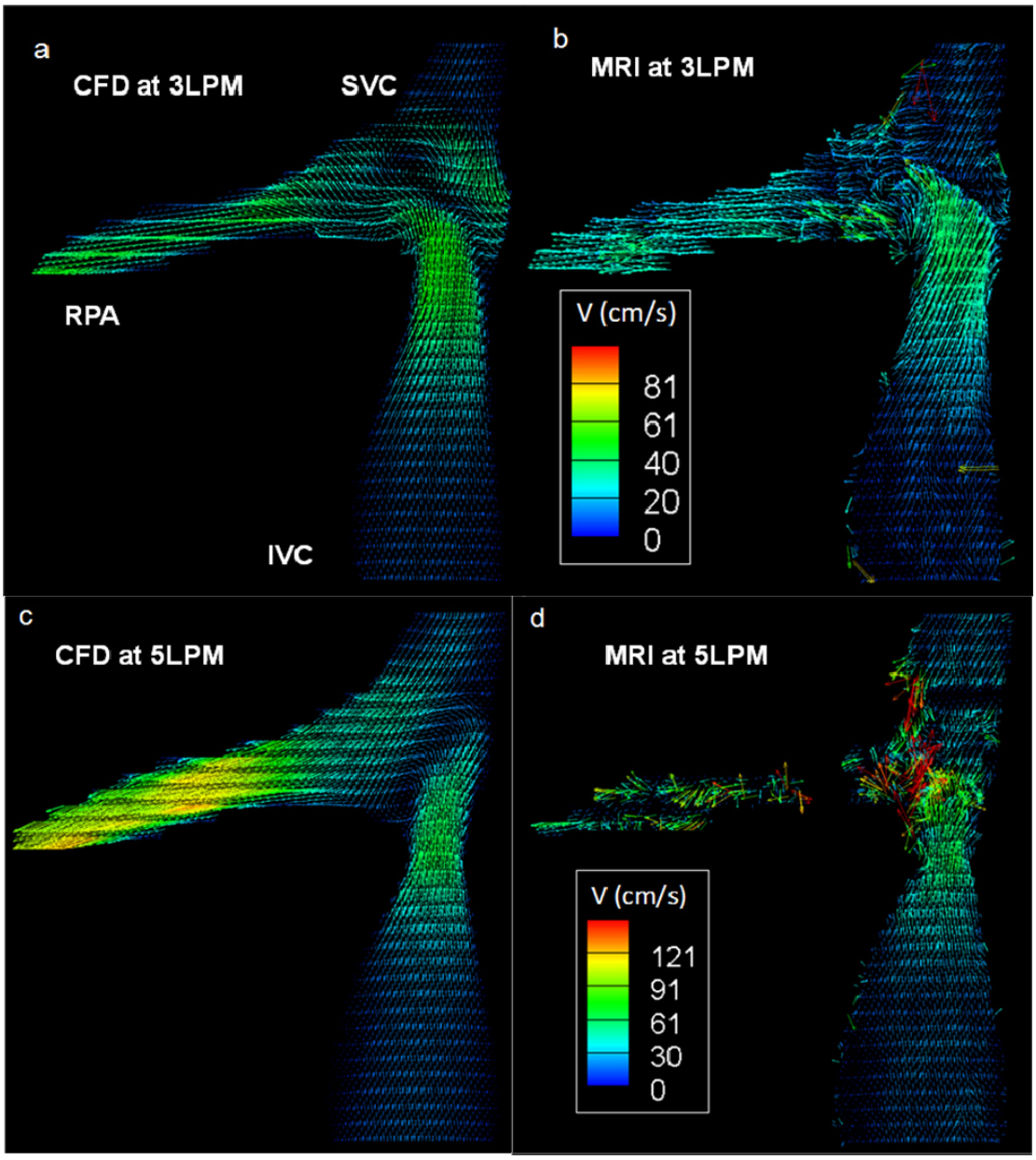

Figure 8.28: The CFD (a,c) and PC MRI (b,d) vector plots associated with slice location 5 for the experimental conditions 3LPM (a,b) and 5 LPM (c,d). At 3 LPM there is an average match between CFD and PC MRI, although a vortex just superior of the RPA is missing in the PC MRI vector field. At 5 LPM the match is very poor, because the data is altogether missing for the RPA.

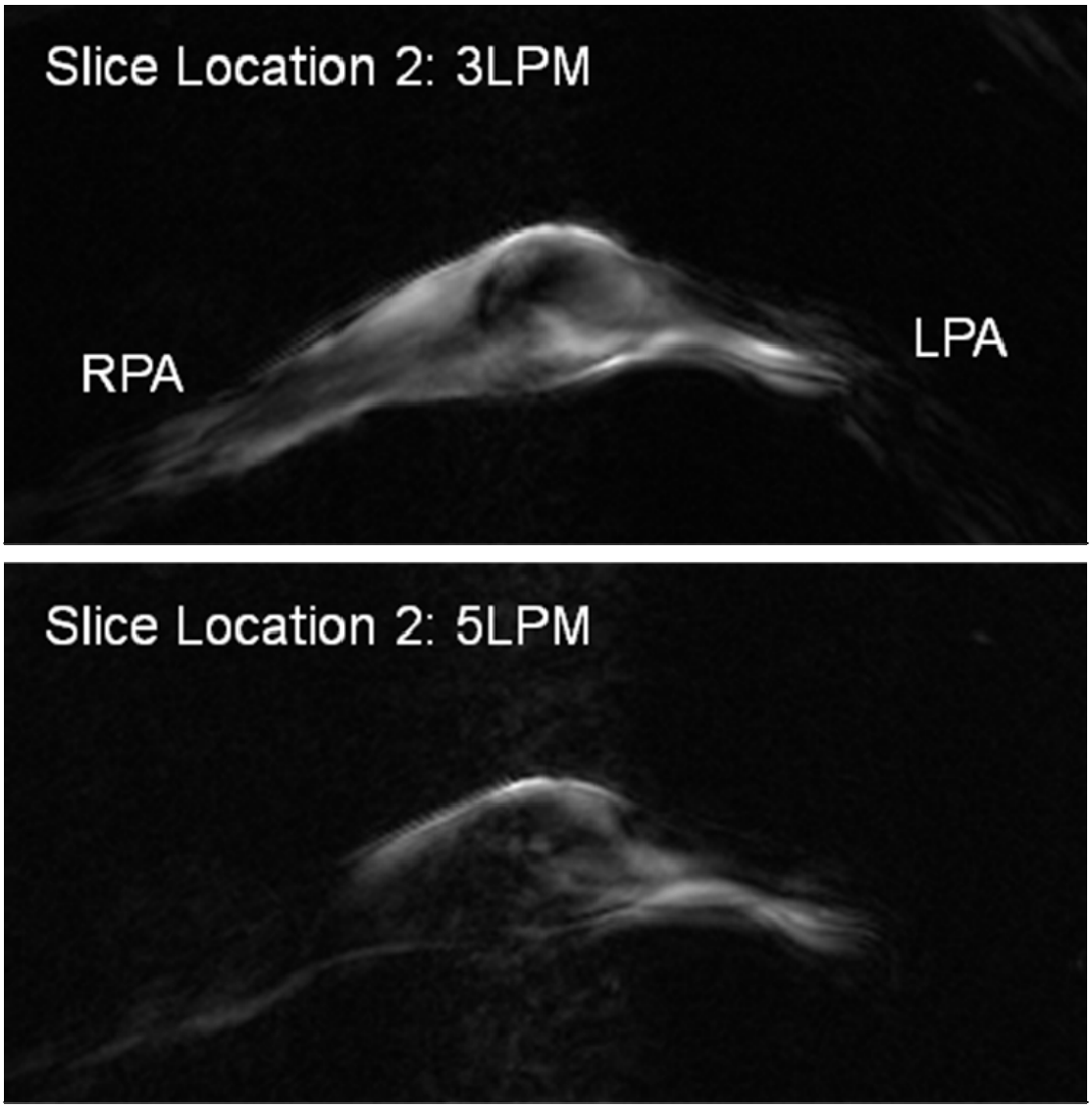

Figure 8.29: The magnitude images for CHOA007 at slice location 2 for flow conditions 3 LPM and 5LPM respectively

The qualitative comparison of flow fields between CFD and MRI for CHOA006 at 3T revealed some very interesting shortcomings of PC MRI applied to a complex anatomic configuration such as the TCPC. The flow profiles of the SVC and the IVC at both resting and exercise conditions had significant fluctuations compared to the smooth profile that is expected for a parabolic inflow condition. Particularly at 5LPM, there was an entire region near the RPA where data was missing. At both 3LPM and 5LPM, PC MRI failed to catch the formation of certain vortices and shear layers near the connection region. Instead, low magnitude velocity vectors were observed, which hints that the small scale vortices are either being averaged out over the PC MRI acquisition, or PC MRI is not sensitive enough to capture these secondary flow structures. The higher SNR expected at 3T did translate into improved error percentages at higher flow rates, but no major improvement was observed at resting flow rates.

8.4.2.3 CHOA006 Summary

A detailed quantitative and qualitative comparison between PC MRI and CFD was conducted with the goal of evaluating the potential of high resolution PC MRI for quantifying the 3D flow fields within the TCPC at 3.0T. There was good agreement at resting flow condition for the X and Z components of flow, but a high error was observed for Y component. It is important to note that lower velocities were observed in general, for the Y component which could be one of the reasons why a higher percentage error was observed. The average error in the Y direction was double that of those in X and Z directions, which hinted that perhaps magnetic field in-homogeneities could be playing a role in distorting the MRI acquisition. This phenomenon was somewhat alleviated at

higher flow rates with the percentage error going down at 5LPM. The error at the higher flow rate was still approximately 4 cm/s, but the velocity magnitude increased resulting in a drop in the overall percentage error. Figure 8.30 shows a graph of the percentage error as a function of flow rate for each component of velocity. The difference in percentage errors for the X and Y components of velocity was not statistically significant, while the change in error percentages for the Z component of the velocity and the velocity magnitude was statistically significant ($p < 0.05$). There was a drop in the error magnitude of the Z component of the velocity, as is evident from Figure 8.24, where a much improved match in the flow profile can be observed. However, the average error in the velocity magnitudes went up, which can be attributed to the poor MRI signal in the pulmonary arteries at 5LPM; a phenomenon which is clearly evident from the contour and vector plots Figure 8.26 and Figure 8.28 respectively.

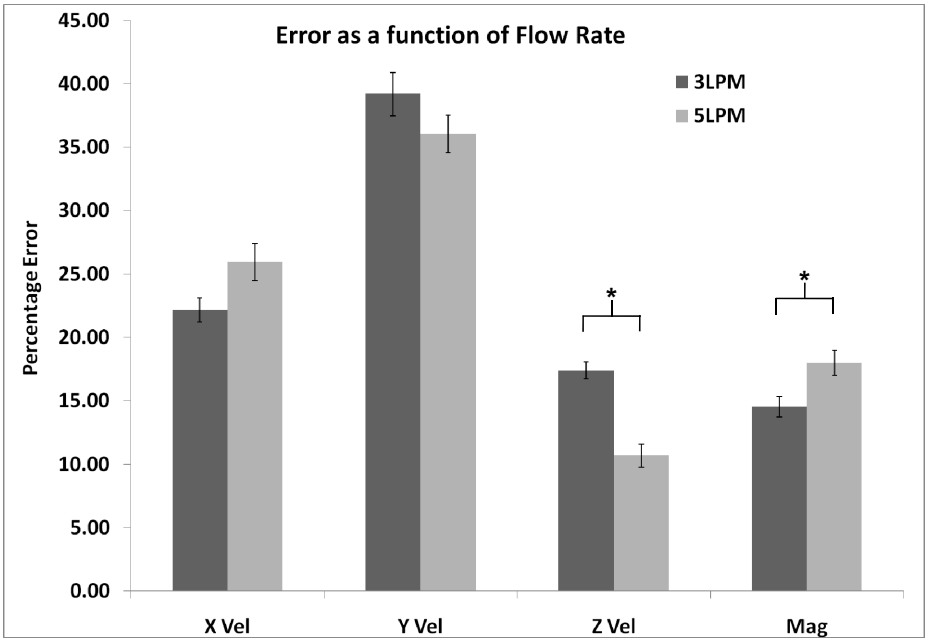

Figure 8.30: Percentage error as a function of flow rate for CHOA006

8.5 Discussion

Controlled validation of 3D flow fields of experimental and computational methodologies for biological applications has not been extensively performed. The importance of such validation processes cannot be understated, considering the growing impact of Phase Contrast MRI and CFD for elucidating the mechanisms of blood flow in a clinical setting. Corroborations of computational findings with MR measurements have been very few, and those that exist have been qualitative or cursory[192-194]. Studies have demonstrated that shortcomings of PC MRI combined with the shortcomings of CFD have resulted in significant errors between the two methodologies[112]. One of the reasons why a quantitative comparison between the two approaches has been missing thus far is the lack of methodologies for 3D flow field validation. Hence, a robust method for flow field validation is necessary, particularly in the realm of complex experimental fluid dynamics. Towards this end, a novel approach to validation was presented in Chapter 4 that has enabled a comprehensive quantitative comparison between PC MRI and CFD.

High resolution PC MRI experiments were conducted at resting and exercise flow conditions on TCPC phantom models at magnetic field strengths of 1.5T and 3.0T. The feasibility and reproducibility of experimental methodology was thoroughly validated. Each experimental dataset was processed and a 3D velocity field was reconstructed. CFD simulations were conducted on identical geometries and the flow fields were registered to the PC MRI experiments in a fully automatic fashion for comparison. The registration of the flow fields enabled a quantitative and qualitative comparison that had previously been missing in earlier *in vitro* PC MRI experimental studies[62, 81, 112, 192].

The velocity magnitudes in all three directions were comparable to those obtained

from CFD measurements. Qualitatively, the dominant flow features matched very well between CFD and MRI. However, there were regions within the PC MRI datasets close to the pulmonary arteries where velocity data was missing. This was evident in the contour and vector plots at exercise flow conditions for both the models. One possible explanation could be the flow instabilities that arise from the SVC/IVC flow collision even at Reynold's numbers well within the laminar range. Furthermore, there is rapid change in direction from superior-inferior to left right, which could be causing fluctuations in velocity magnitudes. Rapid changes in velocities causes intra-voxel phase dispersion, resulting in signal loss over time. Since each PC MRI acquisition takes about 10 minutes, the fluctuations may induce de-phasing of proton spins resulting in the loss of MRI signal. Further studies need to be done to confirm this observation.

Quantitatively, the agreement between PC MRI and CFD was excellent and within the MRI reproducibility error for two out of the three components of velocity (Table 8.2). There was one component of velocity for experiments conducted at both 1.5T and 3.0T, where the match wasn't good. For experiments conducted at 1.5T, the biggest discrepancy was in the X component of the velocity with an average error of 40%. Similarly at 3.0T, the biggest discrepancy was in the Y component of the velocity with the average error being around 40%. Three major sources could potentially be contributing towards this error: a) background phase distortion; b) low SNR at small pixel sizes; c) registration mismatch between CFD and PC MRI.

Background phase errors are non-linear signal distortions induced within the MR signal receiver coil as a result of magnetic field in-homogeneities within the bore of the MRI scanner. These errors are minimal and close to zero near the isocenter of the

magnet, but tend to increase in regions farther away from the isocenter. The characteristics of background phase error are not really well understood. The most common way to correct for this problem is to adopt a linear error model, by fitting a plane to the error measurements[100]. Although the method is quite simple and straightforward, the underlying linear assumption may not be exactly valid and could potentially be introducing other artifacts into the velocity measurements. In this study, no specific background phase error correction was performed, which could explain the high percentage errors at low velocity magnitudes.

The second source of error was low SNR at smaller pixel sizes. It is well known that SNR in a PC MRI acquisition drops as a function of resolution, which could be one of the reasons why there were areas of missing data at higher flow rates. This brings up an interesting observation. At lower flow rates, background phase is the primary source of error. Since background phase doesn't change as a function of flow rate, the net contribution of background phase goes down at higher flow rates. However, from Figure 8.19, it is evident that velocity errors actually went up at exercise flow conditions. This indicates that at higher flow rates, intra voxel phase dispersion is another source of error that impacts the quality of PC MRI measurements at small pixel sizes.

The third source of error was the registration mismatch between CFD and PC MRI. This problem is evident in Figure 8.10, where the CFD solution is rotated compared to the PC MRI acquisition. In these situations, a point-wise error comparison may yield a high error even if the models are oriented correctly, as the profiles do not overlap. Therefore registration is an important consideration for quantitative flow field validation.

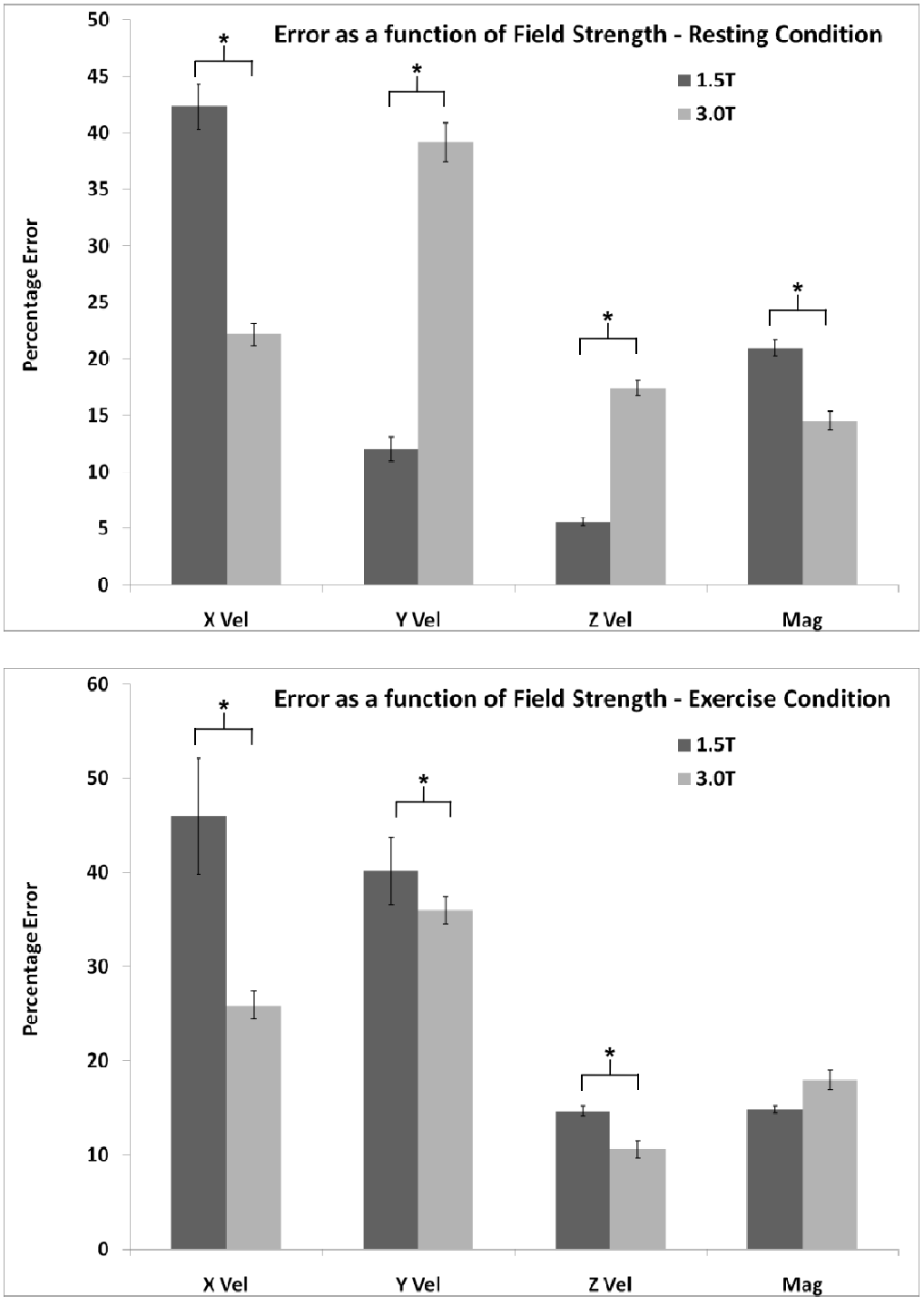

Figure 8.31: Comparison of error as a function of magnetic field strength at resting and exercise flow conditions

There was no significant benefit of imaging at higher field strengths of 3.0T on the overall error of PC MRI measurements at resting flow conditions. Figure 8.31 shows a comparison of error percentages for each velocity component between experiments conducted at 1.5T and 3.0T. Results from the experiments conducted at 1.5T, performed better than the 3.0T for the Y and Z velocity components respectively, while the opposite was true for the X component and the overall velocity magnitude ($p < 0.05$). This could be attributed to the higher background phase error in the X direction for the 1.5T, and in the Y direction for 3.0T. So for imaging at resting conditions, there is no clear winner between 1.5T and 3.0T.

Interestingly, the trends reversed going from resting to exercise flow conditions. Experimental error was significantly lower at 3.0T for all velocity components. This improvement could be partially attributed to increased SNR achieved at higher field strengths, as well as the decreased contribution of background phase error for all three components of velocity. There was a marginal increase in the velocity magnitude error at 3.0T, which was not statistically significant ($p=0.4$). Therefore, PC MRI acquisitions at exercise flow conditions are much more favorable at 3.0T than 1.5T.

Despite the improvement in SNR, several important considerations have to be kept in mind before 3.0T is routinely used in pediatric applications. The background phase error is a significant problem and has a higher impact at 3.0T than 1.5T. There is also a problem of tissue heating as a result of high specific absorption rates (SAR) of electromagnetic energy at 3.0T. This could potentially result in patient discomfort and significantly reduce the quality of images consequently acquired. Despite these shortcomings, 3.0 T does offer an attractive option for quantitative flow imaging in the

TCPC. The major limitation of the present study was that no background phase error correction was performed. For future PC MRI studies to be conducted *in vitro*, it will be important to place a static phantom close to the model so that phase error correction can be performed.

8.6 *In Vitro* PC MRI studies – Summary

In this chapter, *in vitro* fluid dynamic experiments were conducted in order to comprehensively evaluate the potential of high resolution 3D PC MRI for quantifying the hemodynamics within the TCPC. Both quantitative and qualitative comparisons with CFD confirmed the hypothesis that high resolution PC MRI can be used for accurately characterizing the 3D hemodynamics within the TCPC. As with all experimental modalities, there are certain shortcomings of PC MRI that still need to be addressed. Background phase errors as a result of magnetic field in-homogeneities and low SNR at high resolutions are the two major limitations which have to be taken into consideration before any clinical inferences are made. Imaging at higher field strengths did provide improved SNR at higher flow rates, although no clear benefit was evident at resting flow rates. Furthermore, there are several technical issues still associated with 3.0T imaging, which need to be addressed before it is actively used in pediatric applications. In conclusion, it can be said that high resolution PC MRI at 1.5T is sufficient for routine pediatric scans, while 3.0T may offer improved results if the effect of exercise need to be evaluated.

CHAPTER 9

RESULTS AND DISCUSSION: *IN VIVO* PC MRI STUDIES - I

9.1 Overview

The goal of this chapter is to characterize the global hemodynamics prevalent in single ventricle patients, addressing specific aims 2 and 4 of this thesis respectively. The chapter is split into three sections:

1) In section 9.2, the validation of the segmentation and filtering approach outlined in chapter 5 is presented.
2) In section 9.3, 105 patients are randomly selected from the velocity database, and various hemodynamic parameters are analyzed for different cohorts of Fontan patients using PC MRI of the SVC, IVC, LPA, and the RPA.
3) In section 9.4, the differences in energetics and hemodynamics between hypoplastic left heart syndrome (HLHS) and other single ventricles are investigated, using PC MRI of the ascending aorta.

9.2 Segmentation Validation

9.2.1 Automatic Segmentation

Table 9.1 shows the numerical comparison of the manually and the automatically segmented datasets for the aorta, SVC, IVC, LPA, and RPA. Table 9.2 shows the net flow rates in L/Min evaluated using the manual and automatic segmentation techniques respectively. Figure 9.1 shows a comparison of manual and automatic segmentation techniques superimposed on top of each other.

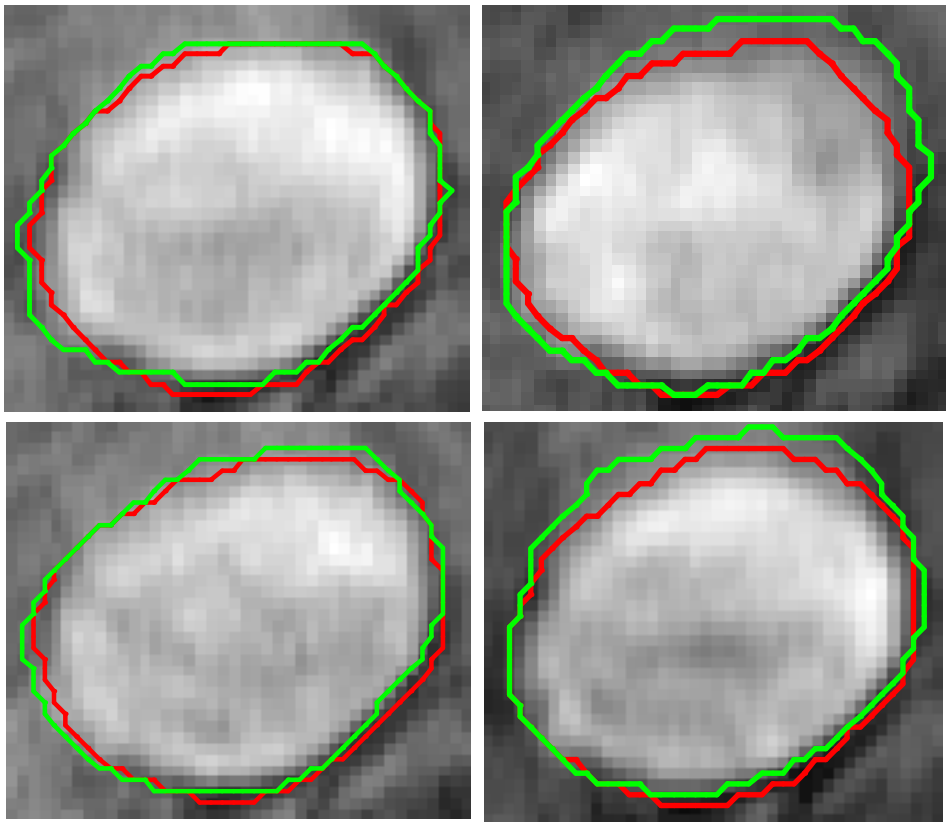

Figure 9.1: Comparison of manual (green) and automatic (red) segmentation techniques for the IVC at four different cardiac phases. Overall, there is a good match between the automatic and manual segmentation techniques

Table 9.1: Comparison of manual and automated segmentation techniques

Vessel	Overlap (%)	False Positive (%)	False Negative (%)	Sensitivity (%)	Specificity (%)
AO	93 ± 4.6	6.9 ± 4.6	4.7 ± 3.6	95.4 ± 3.2	93.7 ± 3.9
IVC	93.3 ± 4.4	6.6 ± 4.4	7.7 ± 4.4	92.8 ± 3.4	94 ± 3.6
SVC	93.4 ± 4.3	6.5 ± 4.3	6.2 ± 4.4	94 ± 3.9	94 ± 3.7
LPA	87 ± 4.5	12.9 ± 4.5	7.49 ± 8.2	93 ± 7	89 ± 3.6
RPA	88 ± 8.6	11.8 ± 4.6	9.4 ± 4.6	91.1 ± 4.7	90.0 ± 6.5

For the ascending aorta, 93 ± 4.6% of the automatically segmented region overlapped with the manually segmented region. The false positive rate was 6.9 ± 4.6 % and the false negative was 4.7 ± 3.6%. The percentage of the total flow through the overlapping, false positive and false negative regions were 98%, 2%, and 1%, respectively. For both the IVC and SVC, the percentage of total flow through the overlapping, false positive and false negative regions were 98%, 2%, and 2%, respectively. In the LPA and the RPA, the overlapping regions between the automatic and manual segmentation techniques were lower since the diameter of these vessels is much smaller than the IVC and the SVC. However, the net flow through the overlapping regions still remained at 98% for the LPA and the RPA. This showed that regions excluded from the automatic segmentation were generally characterized by slow velocity flow. For each vessel the automatic and manual segmentation results (flow rates) were statistically identical with a type II (β) error < 0.05.

Table 9.2: Comparison of flows through the manually (MS) and automatically segmented (AS) regions (L/Min)

Vessel	**AS Flow**	**MS Flow**	**Overlap Flow**	**False Positive Flow**	**False Negative Flow**
AO	3.27 ± 1.57	3.27 ± 1.53	3.26 ± 1.55	0.00 ± 0.12	0.01 ± 0.07
IVC	1.88 ± 0.99	1.89 ± 1	1.85 ± 0.99	0.02 ± 0.02	0.04 ± 0.04
SVC	0.83 ± 0.45	0.88 ± 0.32	0.8 ± 0.44	0.02 ± 0.015	0.02 ± 0.02
LPA	1.22 ± 0.81	1.22 ± 0.78	1.19 ± 0.79	0.03 ± 0.05	0.02 ± 0.02
RPA	2.08 ± 0.76	2.12 ± 0.79	2 ± 0.76	0.07 ± 0.08	0.11 ± 0.10

9.2.2 Automatic Filtering

9.2.2.1 Synthetic Datasets

Figure 9.2 shows the error associated with using the vector median filters (VMF) (without the fuzzy framework), Walker filter, and a low pass filter as a function of increasing noise levels. As can be observed, the normalized mean squared error (NMSE) obtained with the VMF technique was significantly lower than the low pass filter and the Walker filter at all noise levels ($p < 0.05$). There were no significant differences between the Walker filter and low pass filter at low noise levels, but the difference at high noise levels was statistically significant ($p<0.05$). The increase in NMSE with increasing noise

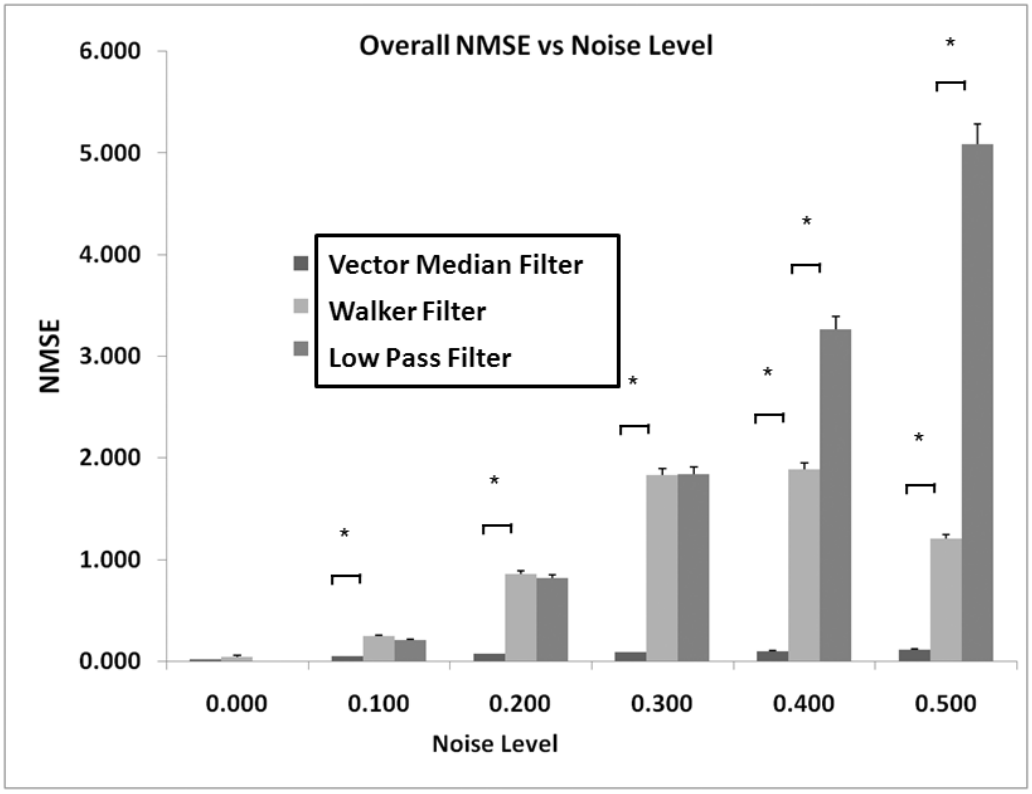

Figure 9.2: Comparison of VMF with the Walker filter, and a standard low pass filter. VMF had the lowest error compared to the two other filters.

levels was quite small for the VMF, when compared to the other two techniques. This justified the use of VMF in the hybrid multi-channel fuzzy adaptive vector median filtering (FAVMF) framework.

Figure 9.3 shows the overall benefit of using VMF in a fuzzy framework compared to VMF alone. There is a statistically significant drop in the overall NMSE at all levels of noise using the FAVMF technique ($p < 0.05$). The Fuzzy filter was also able to accurately differentiate between noise and flow as can be observed in Figure 9.3b, where the NMSE is compared between VMF and FAVMF in regions where there was no noise. FAVMF had extremely low error when compared to the VMF technique demonstrating that it had minimal impact on the true velocity field. In regions where noise was present, FAVMF performed as well as the VMF. This adaptive feature is highly desirable in applications which require quantification and visualization of complex flow patterns, especially where filtering artifacts can alter the measured velocity field.

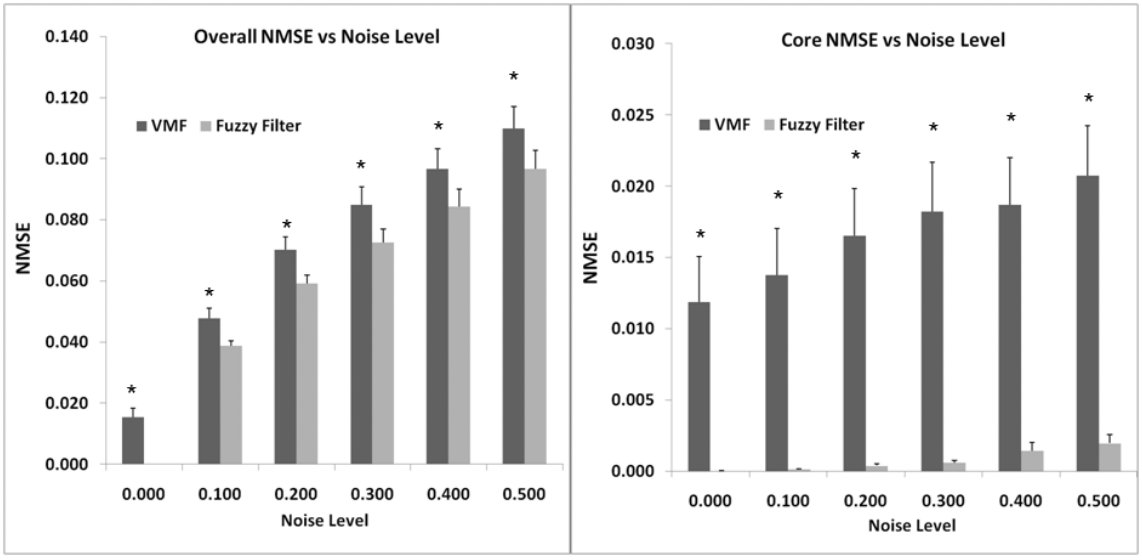

Figure 9.3: a) Comparison of VMF with FAVMF; b) Comparison of VMF with FAVMF in regions where no noise is present. Using VMF in the fuzzy framework further reduced the error.

The maximum shear rates evaluated using the vector fields derived after FAVMF, Walker filtering, low pass filtering, and no filtering were 240 ± 40.3, 346 ± 11.6, 370 ± 15.9, and 453 ± 16 s-1 respectively. Maximum shear rates derived from FAVMF were much closer to the true shear rate derived from computational fluid dynamics (176.1 ± 30.4) compared to the other filtering methodologies.

9.2.2.2 In Vivo Datasets

Figure 9.4a shows the drop in error that can be accomplished using the automated FAVMF technique when compared to the unfiltered dataset using the manually segmented dataset as reference. When no filtering was performed, the average error in the velocity measured was about 2 cm/s/pixel. This error was reduced to < 1cm/s/pixel after the dataset was filtered using the FAVMF technique. Figure 9.4b shows the peak velocities in close proximity of the vessel wall for 3 different cases: a) Segmentation + No Filtering; b) Segmentation + Manual Filtering; c) Segmentation + FAVMF. Unrealistically high peak velocities were observed in the unfiltered dataset, which are not characteristic of the flows in the TCPC and the aorta. After filtering, the peak velocities significantly dropped to less than 50% of the original values ($p<0.05$). The peak velocities evaluated using the automatic filtering technique was statistically identical to the reference with a type II error <0.05. Figure 9.4c shows the ratio of the peak velocities along the vessel wall to those measured in the core of the vessel. This ratio should be between 0 (parabolic profile) and 1 (flat profile) for a physiological velocity field. For the unfiltered dataset, this ratio was about 2, which cannot be true, indicating that pixels giving such high values were noise pixels. This ratio dropped significantly to less than 1

once the filtering was performed ($p<0.05$). The performance of the automatic FAVMF technique was statistically identical to the reference with a type II error < 0.05.

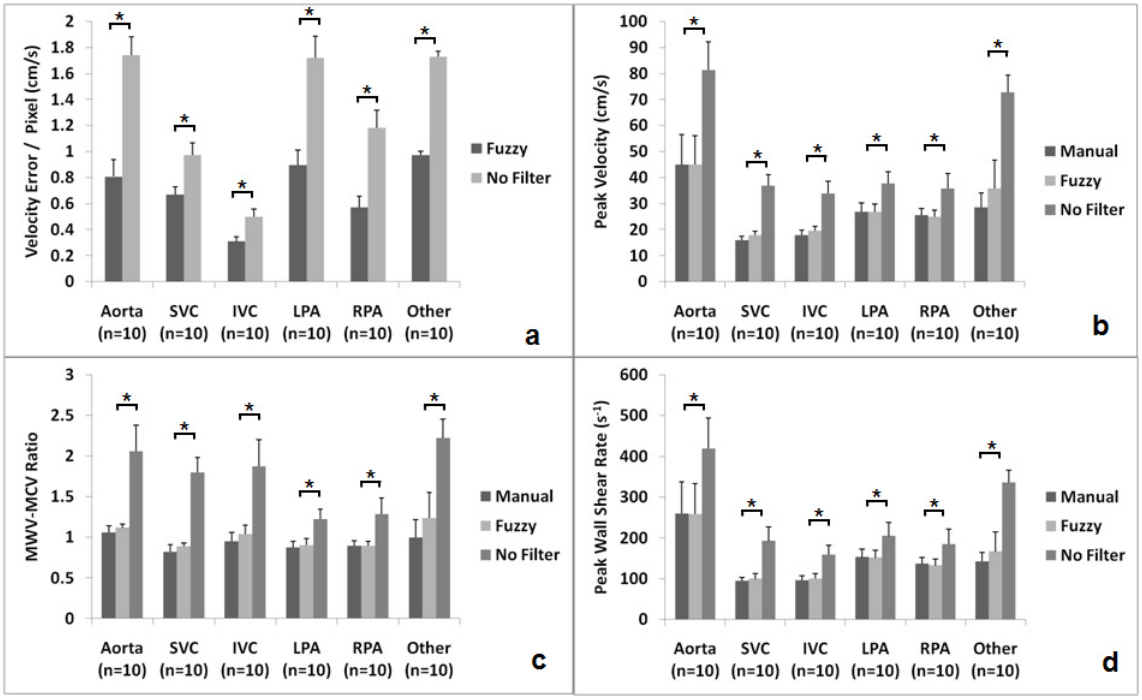

Figure 9.4: The benefit of filtering using the FAVMF approach. a) The reduction in error/pixel achieved after filtering with FAVMF compared to no filtering; b) Comparison of peak velocities close to the wall between manual filtering, FAVMF, and No Filtering; c) Comparison of mean peak wall velocity to mean peak core velocity (MWV-MCV) ratio between manual filtering, FAVMF, and No Filtering; d) Comparison of wall shear rates evaluated using manual filtering, FAVMF, and No Filtering.

One important clinically relevant parameter that can be evaluated using PC MRI is wall shear stress. Wall shear stresses are evaluated by first computing the velocity shear rates along the wall. Figure 9.4d shows the peak wall shear rates computed for the 3 cases mentioned above. The peak wall shear rates in the unfiltered dataset were significantly higher compared to the filtered datasets ($p=0.05$). The peak wall shear rate for all the vessels dropped by about 50% after the filtering was performed. This

mechanism is depicted in Figure 9.5 where the velocity fields (Figure 9.5 a-c) and the corresponding velocity shear rate contour plots (Figure 9.5 d-f) for the 3 cases are shown on a coronally acquired dataset. The noise present along the SVC resulted in an abnormally high shear region, which really doesn't exist. Once the noise is filtered out using either the manual or the automatic technique, this region disappears. Overall, the two-step segmentation process produced much cleaner velocity fields, preserving key features of the flow field at the same time. For example, the recirculation region circled in Figure 9.5c is preserved, while the noise vectors circled in Figure 9.5a are removed. This demonstrates the benefit of using the FAVMF technique in conjunction with the segmentation process for velocity field quantification.

9.2.3 Segmentation Validation – Discussion and Summary

With the growing application of 3D PC MRI for quantifying *in vivo* velocity fields, it is important that accurate post processing methodologies are developed and validated. Most of the current automated methodologies for PC MRI post processing, use a single step process for segmentation. In chapter 5, a new two step segmentation and filtering process was proposed. In step 1, the vessel of interest is first segmented using an active contour methodology that uses both magnitude and phase images. In step 2, the resulting velocity field is automatically filtered using a novel FAVMF technique. This two-step approach produced velocity fields that are cleaner and more accurate for performing quantitative analysis, than the single step approach adopted by current methodologies.

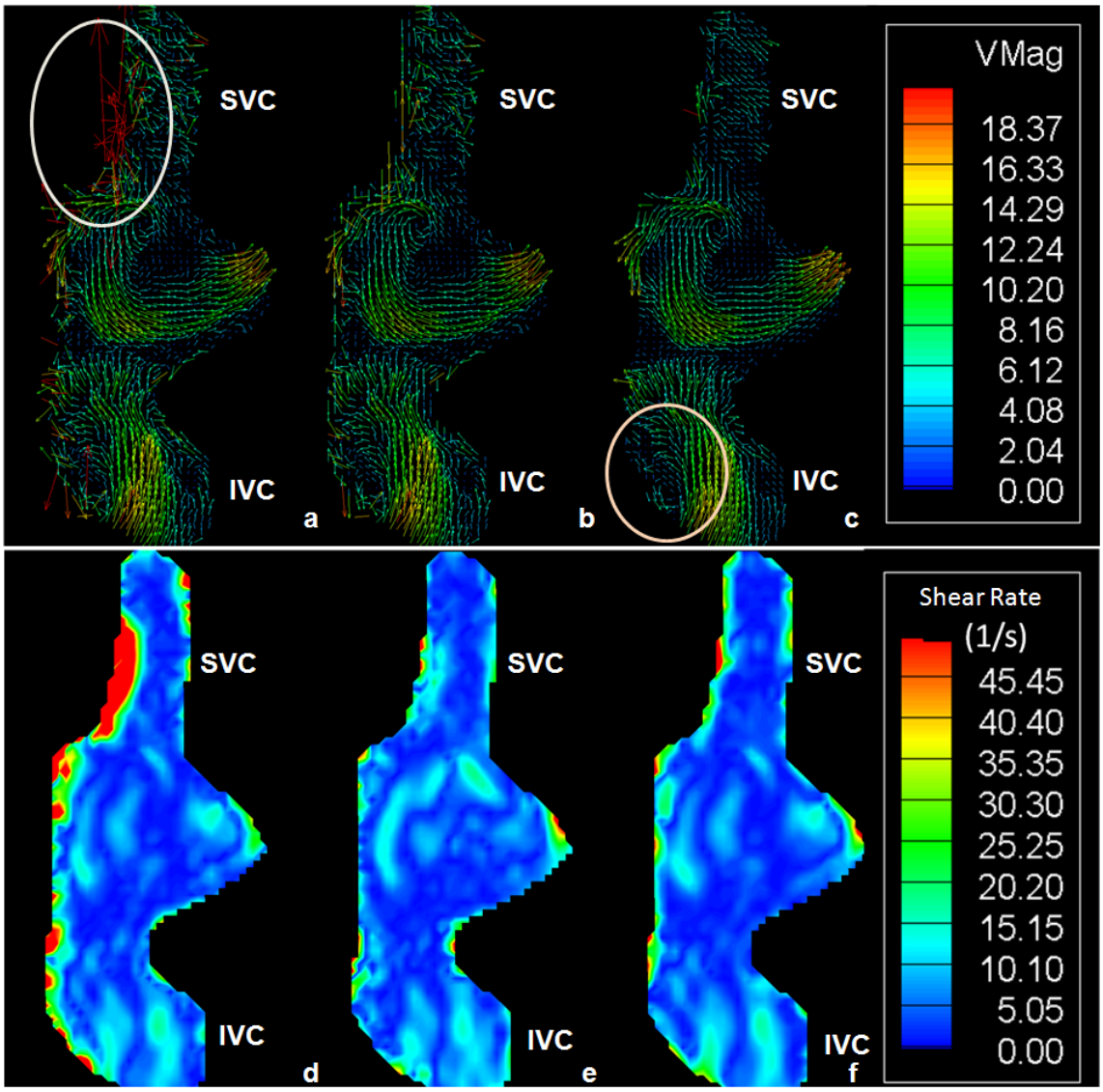

Figure 9.5: (a-c) The vector field of CHOP073 reconstructed from a coronally acquired velocity field. a) Unfiltered dataset; b) Dataset manually filtered; c) Dataset filtered with FAVMF. Notice the vortex region is preserved while the noise is removed. d-e) The velocity shear rate map: d) Unfiltered dataset; b) Dataset manually filtered; e) Dataset filtered with FAVMF. Notice the reduction in wall shear rates along the SVC after the filtering is performed

The automatic segmentation based on active contours for step 1 of the segmentation process, is not novel by itself. Kozerke et al, were the first to use active contours for automatic PC MRI segmentation[96]. This paper improves the robustness of the active contour methodology by using an implicit approach for contour evolution, and the hybrid magnitude-velocity potential field for the external energy function. The strength of this methodology is that vessels of arbitrary shapes can be segmented, and the resulting velocity field is clean and free of noise. The Fuzzy framework presented here is a significant improvement over both generic noise removal strategies from multi-dimensional image processing and current filtering methods popular for PC MRI. This framework requires no *a priori* knowledge for determination of the membership function and exploits differences between random noise and flow in the filtering process. It uses both velocity magnitude and direction information to achieve this objective. Techniques such as those proposed by Song et al, which use divergence as a parameter, cannot be applied to single velocity slices since one of the velocity derivatives is unavailable and hence the true divergence is unknown. The proposed Fuzzy filter is not subject to this limitation.

While the proposed methodology was tested here on 3D PC MRI slices, it can easily be adapted to 3D PC MRI volumes for newer sequences such as those proposed by Markl et al[92, 195]. The Fuzzy framework is robust enough, that the parameters in the filtering process can be easily evaluated for window sizes of 3X3X3. This may increase the total processing time, but will be negligible compared to the overall segmentation process. Besides flow applications, the framework can also be used in other situations where filtering can play a role on 3D data. For example, in displacement encoding using

stimulated echo (DENSE)[196] and PC MRI of the myocardial wall[111, 121], the presence of noise complicates the estimation of regional biomechanical parameters such as strains in the ventricle. The proposed filtering technique has significant potential in improving the quality of the vector fields acquired from any of these modalities if certain constraints on the quality of acquired images are met. Since this approach uses vector median filters with a minimum window size of 3 x 3, the resolution of the images should be high enough so that filtering can actually be performed within the region of interest; i.e. the number of pixels enclosed within the segmentation should be much higher than 9. This is typically not a problem for a majority of PC MRI and DENSE acquisitions where large cardiac structures are being analyzed. Another requirement is that the signal to noise ratio and contrast to noise ratio should be sufficiently high, such that the bulk features of the flow field can be visualized. If these constraints are met, then the proposed FAVMF technique offers significant advantages for noise filtering over traditional scalar filters as it preserves the inherent characteristics of vector fields.

The primary application targeted here is the segmentation and analysis of hemodynamics within the TCPC, which is characterized by complex flow patterns. Recirculation regions and vortex patterns are common in these geometries, and may be an indication of high energy losses within the system. The ability to accurately quantify such structures can tremendously improve clinical evaluation of the surgically altered connection. Hence the proposed Fuzzy filter plays a significant role as it offers an attractive solution for removing such noise vectors while preserving flow features at the same time. While not all noise is filtered, performance is seldom worse than the manual technique, and usually better.

Although, there are several benefits of using the proposed two-step segmentation process for accurately quantifying flow from PC MRI data, certain limitations of the methodology are well acknowledged. Firstly, the performance of the filtering done during second stage is highly dependent upon the quality of the segmentation done in stage one. Therefore care should be taken that the vessel is not under segmented, i.e., all flow vectors are included in the segmentation. If there is a doubt that flow-vectors are being excluded during stage one of the segmentation process, then a dilation operation can be performed to include more vectors in the segmentation. If noise vectors get included in the process, then they can be removed during stage two. Secondly, there was a lack of true reference data for comparing the results of the filtering algorithm on *in vivo* datasets. A manual filtering algorithm was designed and developed to serve as a reference to get around this issue. However, data acquired from alternative computational and experimental fluid dynamic modalities may have served as better controls. Unfortunately, such data were not available for the patients used in this study. Finally, the proposed algorithm is ultimately dependent upon the quality of the MRI data acquired and is limited by SNR and CNR constraints. Although the algorithm works well with data having low SNR, the quality of the reconstructed velocity field goes down considerably as the noise components of the velocity field increase.

In conclusion, a two-step segmentation and filtering framework for multi-dimensional PC MRI is presented, which is more accurate compared to a single step process of segmentation alone. This is the first time a filtering technique based on fuzzy theory has been proposed and optimized for quantifying velocity fields from PC MRI. The framework is robust and easily extensible to other multi-dimensional MRI

applications where noise is a significant problem.

9.3 Fontan Flow Analysis

The segmentation and filtering methodology described previously was applied to a large cohort of Fontan patients to establish a Fontan flow database of over 200 patients. The patients were enrolled at either Children's Hospital of Philadelphia (CHOP) or Children's Healthcare of Atlanta (CHOA) over a six year period from March 2001 to June 2007. All protocols were approved by the Institutional Review Boards of both institutions and informed consent obtained from all participants. 105/200 (Table C.3) patients were selected from this database, and flow dynamics through the aorta, SVC, IVC, LPA, and the RPA were quantitatively analyzed. Figure 9.6 shows a schematic of the different forms of analyses conducted in this study.

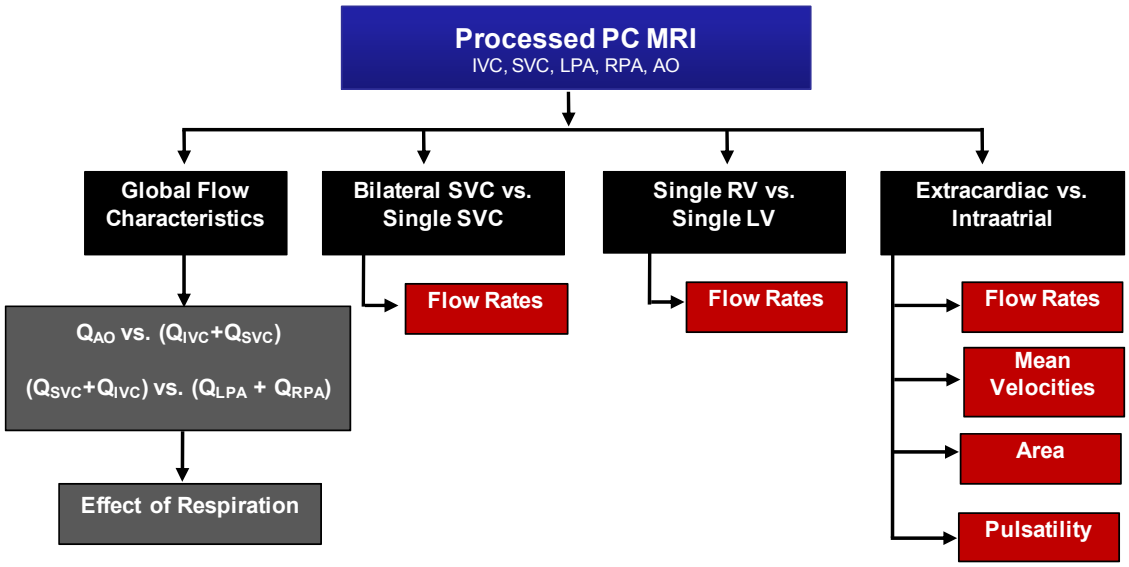

Figure 9.6: Overall schematic of the different forms of data analysis that are conducted on the processed PC MRI data. A more detailed analysis is performed for comparing intraatrial and extracardiac TCPC types

First the global flow characteristics of all the patients are analyzed. All flow rates are indexed to BSA for comparison. Fractional contributions of IVC (IVC/(SVC+IVC)) and RPA (RPA/(RPA+LPA)) to the total blood flow are calculated and correlated with BSA and age. This is followed by a study evaluating the impact of breath-holding on flow rates through all 5 vessels. Following the global flow analysis, the data are separated into different templates and several comparisons are made to establish the differences between the templates. First, patients with bilateral SVCs are compared to patients with single SVCs. This is followed by a comparison of flow characteristics between morphological single RVs and single LVs respectively. Finally, a detailed comparison of several flow parameters evaluated for intraatrial and extracardiac TCPCs is performed. More attention is given to this comparison, since considerable interest exists in the surgical community regarding the differences in hemodynamics between these two Fontan types. For each comparison, a Student's t-test for independent samples is performed to determine if group differences are statistically significant. All population statistics are reported as a mean ± the standard deviation. Differences between statistics are reported as mean difference ± the standard error.

9.3.1 Patient Characteristics

The mean subject age was 11.5 years, ranging from 2 to 28 years. The mean time from the Fontan operation for the 82 patients, where the data were available was 8.2 years. The SVC anastomosis and Fontan type were recorded from the medical records for each patient, when available. There were 40 patients with bidirectional Glenns, 53 with hemi-Fontans, and 12 who either had older atriopulmonary-type connections or

there was insufficient information to determine the type of superior caval connection. The Fontan type included 69 intraatrial baffles, 28 extracardiac conduits, and 4 classic atriopulmonary connections. Four patients had their surgeries at outside institutions and their Fontan types were not completely defined. There were 15 patients with bilateral SVC's. The presence of an open fenestration was recorded from the surgical notes documenting whether a surgical fenestration was made, and from the most recent echocardiogram documenting whether the fenestration was still patent.

9.3.2 Global Flow Characteristics

The contribution of IVC flow to total systemic venous return was 59%±15%. The contribution of RPA flow to total pulmonary blood flow was 55%±13%, which was significantly greater than half ($p = 0.003$). Total pulmonary flow was measured at 2.4±0.7 l/min/m^2, compared to 2.8 L/min/m^2 for the measured total caval flow; this was a difference of 14% ($p < 0.001$). Age and BSA were correlated with the IVC fraction of total systemic venous return ($r = 0.60$ and 0.74 respectively, $p<0.05$). The IVC fraction appeared to increase in a logarithmic pattern with BSA (Figure 9.7). Conversely, there was no correlation between RPA fraction of pulmonary blood flow with age or BSA.

9.3.2.1 Comparing Fontan flows to Aortic Flow

When compared to aortic flow data, the total caval (SVC + IVC) flow was generally about 12% lower across the range of measured flows and the total pulmonary (LPA + RPA) blood flow was on an averge 22% lower than the aortic flow. This appeared to be primarily a systematic rather than a random difference since there was an excellent correlation between the total pulmonary blood flow, total caval blood flow, and

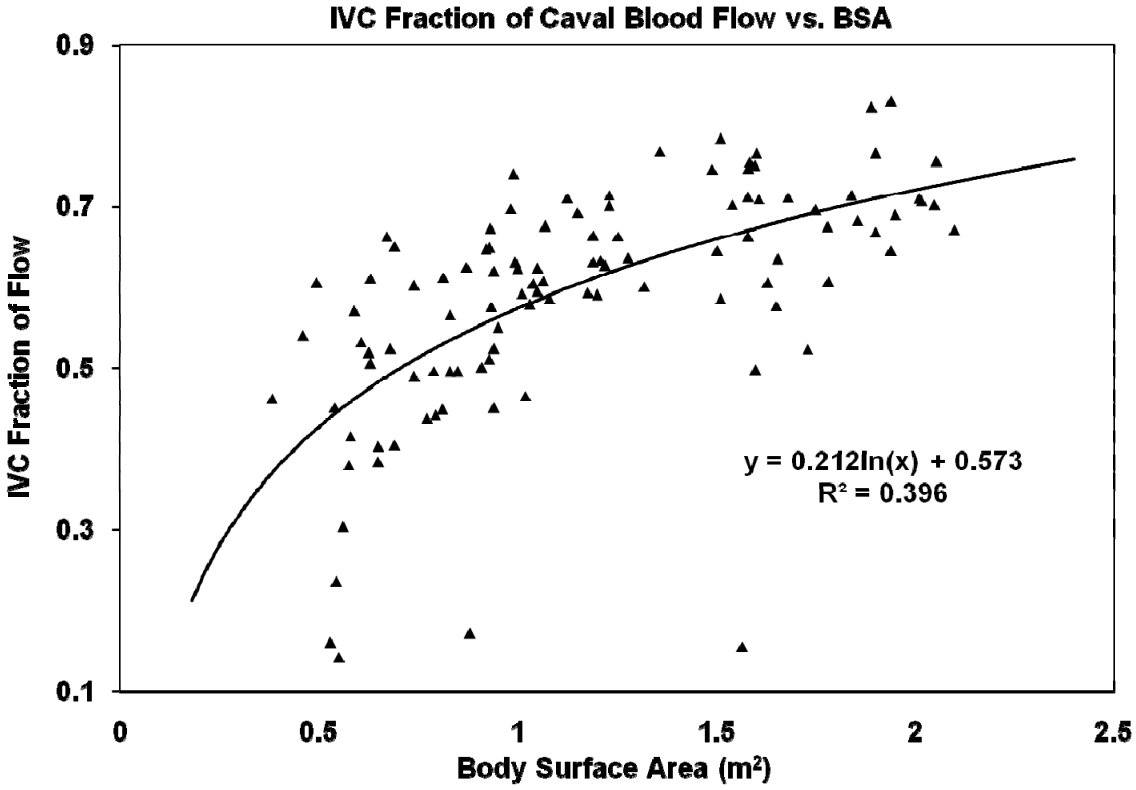

Figure 9.7: Relationship between the IVC fraction of caval flow and body surface area. There was a strong correlation between IVC fraction and BSA

aortic flow (Figure 9.8). Note in the Bland-Altman plot for the caval data that there were almost no data points in which the caval flow exceeded aortic flow, with most patients having measured caval flow significantly less than the aortic flow.

A potential source of difference between the systemic venous and pulmonary flows could be the presence of a fenestration in the Fontan, which would allow a right to left shunt prior to blood reaching the branch pulmonary arteries. To investigate this, the data were separated by the presence or absence of a fenestration at the time of the MRI. While the ratio of pulmonary to caval blood flow was slightly higher in patients without an open fenestration (0.86±0.24 vs. 0.84±0.20), the difference was small and not

statistically significant. Another source of error could be the presence of aorto-to-pulmonary collaterals which could drain some of the flows from the aorta. However, in order to confirm this hypothesis, pulmonary vein flow is needed, which was not acquired as part of this study.

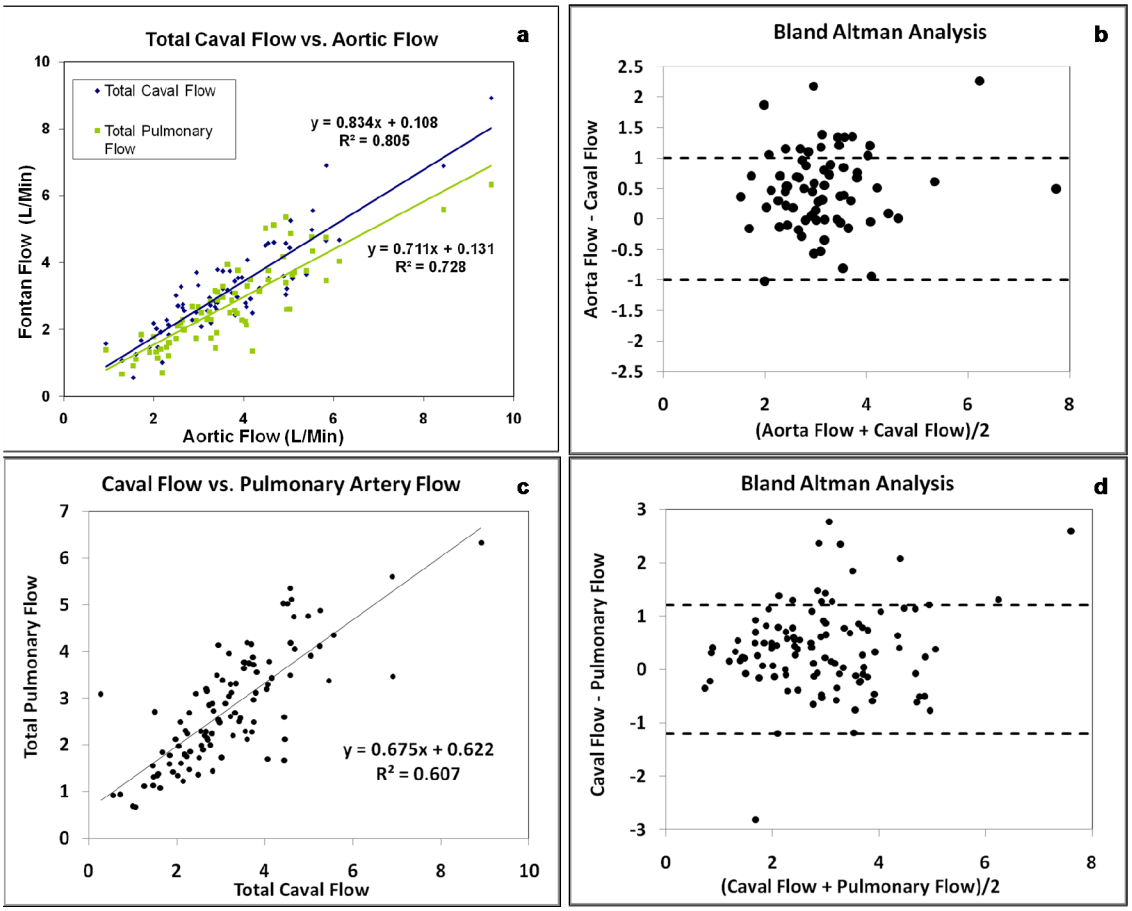

Figure 9.8: a: Correlation plots comparing the total cardiac output to the total caval flow (blue) and total pulmonary artery flow (green); b: Bland-Altman analysis of the aortic flow and the total caval flow; c: Correlation plot comparing total cavalo flow to total pulmonary artery flow respectively; d) Bland-Altman Analysis of the total caval and total pulmonary artery flow. The dotted lines on the Bland Altman plots correspond to +/- 1 standard deviation of the mean velocity

9.3.2.2 Effect of Respiration on Flow

In order to investigate the impact of breath-hold phase on TCPC flow, PC MRI measurements were performed on 10 patients at both end-inspiration and end-expiration. Figure 9.9 shows the plot comparing the two cases for the aorta, SVC, IVC, LPA, and RPA.

Average flow rates were higher at end expiration for all vessels, which was statistically significant for the IVC and the LPA. Due to the presence of the diaphragm immediately below the IVC, the state of respiration plays more of a role in the IVC rather than any of the other vessels, which explains why the results were most significant for the IVC. The preferential flow of the IVC to the LPA, as reported by Fogel and colleagues, resulted in significant differences for the LPA as well[142]. However, no significant differences were observed for the SVC and the RPA.

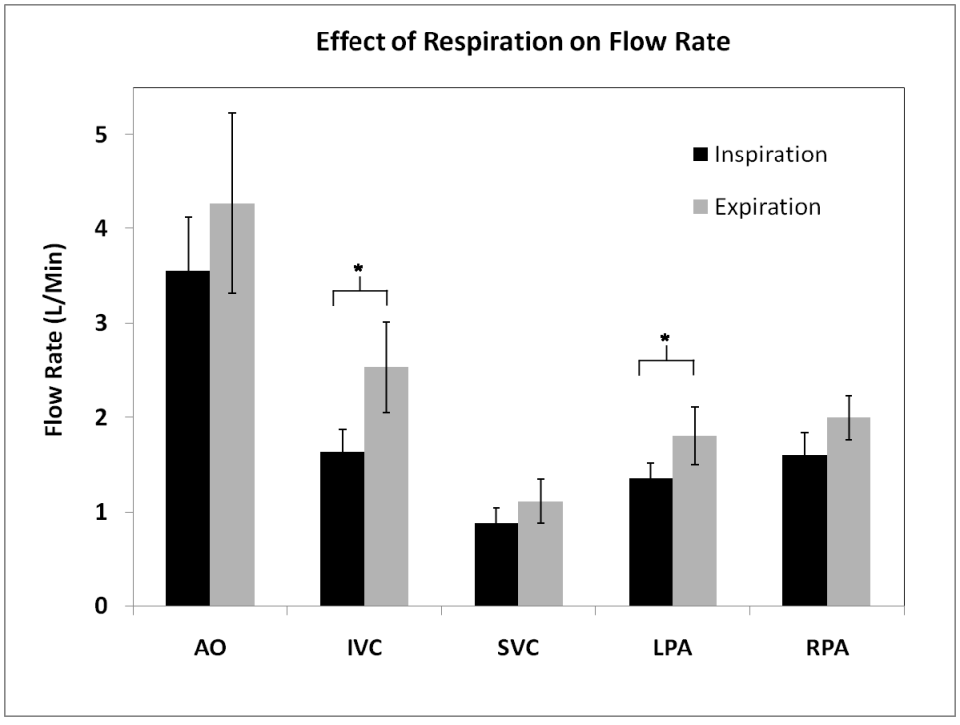

Figure 9.9: Effect of respiration on Fontan flow rate. The error bars correspond to standard deviation

It is important to differentiate these results from those earlier reported by Hjordtal and colleagues[146], where increased flow during inspiration was observed. The fundamental difference between the two studies was the methodology adopted for the flow measurement. In their study, the measurements were taken using a real-time free breathing sequence, with respiratory gating performed at end inspiration and end expiration. This is fundamentally different from our study, where the patients were asked to hold their breath at end inspiration and end expiration, followed by PC MRI acquisition at each breath hold. This highlights that the process of breath-holding may have an impact on Fontan flow physiology. Since the exact bias that may occur as a result of these differences in measurement states is not known, care should be taken to make sure that images are always collected at the same respiratory state. Controlled studies with respiratory gating should be performed in the future to determine the true variation in flow rates due to respiration.

9.3.3 Bilateral SVC vs. Single SVC TCPC

The goal of this study was to determine if the presence or absence of a bilateral SVC had any impact on the total flow rates observed through the Fontan connection. A majority of the patients in this study comprised of a single SVC (90), which hinted that bilateral SVCs are not commonly observed in Fontan patients. Table 9.3 summarizes the flow comparison of patients with bilateral SVC's to those without. No signicant differences in cardiac index, total caval flow, or total pulmonary artery flow were observed between the two groups. The only statistically significant result was that the patients with a bilateral SVC were older and had a larger body surface area compared to

the other group. In patients with bilateral SVC's, the right SVC accounted for 52%±14% of the total superior caval flow. No significant difference was noted in the pulmonary flow splits for patients with bilateral SVC's, with the right pulmonary artery carrying about 48%±19% of the total flow.

Table 9.3: Summary of flow data for caval and pulmonary artery flows and comparisons between the presence and absence of an LSVC. Values reported as Mean±S.D.

Flows in l/min/m^2 **Ratios as fraction**	**No LSVC**	**With LSVC**	**LSVC vs. no LSVC**
N	90	15	p
Age	11.0±5.8	14.8±6.9	0.03
BSA	1.13±0.44	1.41±0.55	0.03
(IVC+SVC)	2.9±1.0	2.7±0.8	0.61
(RPA+LPA)	2.5±0.8	2.2±0.6	0.17
IVC/(IVC+SVC)	0.59±0.15	0.61±0.11	0.59
RPA/(LPA+RPA)	0.55±0.13	0.50±0.16	0.22
(RPA+LPA)/(IVC+SVC)	0.92±0.2	1.1±1.7	0.38
N	67	11	p
Aortic Flow/BSA	3.7±1.6	3.2±0.7	0.40
(IVC+SVC) / Ao	0.88±0.5	0.88±0.2	0.99
(RPA+LPA) / Ao	0.78±0.6	0.73±0.3	0.79

9.3.4 Single RV vs. Single LV

The first part of Table 9.4 summarizes the flow results for patients with dominant right (62 pts) or dominant left ventricles (37 pts). The remaining 6 patients either had a morphologically ambiguous systemic ventricle or had two good sized ventricles.

Table 9.4: Summary of flow data and comparisons between the systemic LV and RV. All values reported as Mean±S.D

Flows in l/min/m^2 **Ratios as fraction**	**RV**	**LV**	**RV vs. LV**
N	62	37	p
Age	11.6±5.8	12.5±6.1	0.4
BSA	1.15±0.47	1.26±0.44	0.27
(IVC+SVC)/BSA	2.9±0.8	2.8±1.2	0.66
(RPA+LPA)/BSA	2.4±0.8	2.5±0.8	0.74
IVC/(IVC+SVC)	0.61±0.11	0.58±0.16	0.23
RPA/(LPA+RPA)	0.55±0.13	0.52±0.14	0.34
(RPA+LPA) / (IVC+SVC)	0.87±0.24	1.2±1.7	0.13
N	50	25	p
Aortic Flow/BSA	3.5±1.6	3.7±1.3	0.67
(IVC+SVC) / Ao	0.93±0.5	0.82±0.3	0.32
(RPA+LPA)/ Ao	0.82±0.6	0.72±0.2	0.43

There were no significant differences between the two groups. The most common types of congenital heart disease included hypoplastic left heart syndrome (HLHS) (42 pts), tricuspid atresia (18 pts), various forms of double outlet right ventricle

(DORV) (15 pts), D Transposition of the Great Arteries (D-TGA) (8 pts), and pulmonary atresia with intact ventricular septum (PA-IVS) (7 pts). The remaining patients were a mix of more unusual heart defects. The two statistically significant findings were: the indexed caval flow for the PA-IVS group (2.2 L/min/m2) was significantly less than the HLHS group (2.8 L/min/m2); and HLHS patients had significantly lower cardiac index compared to those with tricuspid atresia.

Table 9.5: Summary of flow data by heart disease. All values reported as Mean±S.D

Flows in l/min/m^2 **Ratios as fraction**	**HLHS**	**Tricuspid Atresia**	**DORV**	**PA-IVS**	**D-TGA**
N	42	18	15	7	8
Age	10.0±5.0	11.4±6.5	13.6±7.1	15.0±3.9	14.9±7.4
BSA	1.09±0.42	1.16±0.47	1.24±0.49	1.4±0.23	1.3±0.6
(IVC+SVC)/BSA	2.8±0.7	3.2±1.4	3.1±1.0	2.2±0.8	3.0±1.1
(RPA+LPA)/BSA	2.3±0.7	2.7±1.0	2.9±0.9	2.2±0.7	2.4±1.1
IVC/(IVC+SVC)	0.60±0.12	0.54±0.17	0.60±0.10	0.62±0.21	0.65±0.11
RPA/(LPA+RPA)	0.56±0.12	0.49±0.13	0.51±0.08	0.60±0.22	0.50±0.11
(RPA+LPA) / (IVC+SVC)	0.85±0.26	0.9±0.27	0.95±0.21	1.0±0.18	0.82±0.21
N	32	10	12	4	4
Aortic Flow/BSA	3.3±0.8	3.9±1.6	3.7±1.5	3.2±0.3	2.8±0.6
(IVC+SVC) / Ao	0.88±0.22	0.88±0.16	0.90±0.17	0.78±0.10	1.0±0.3
(RPA+LPA) / Ao	0.74±0.21	0.73±0.16	0.83±0.20	0.76±0.12	0.7±0.1

9.3.5 Extracardiac vs. Intraatrial

Table 9.6 shows a summary of results comparing the flow rates between intraatrial and extracardiac Fontan types. There were no statistically significant differences in total caval flows between the two groups, although some parameters were leaning towards statistical significance.

Table 9.6: Summary of flow data for caval and pulmonary artery flows and comparisons between intraatrial (IA) and extracardiac (EC) fontan. Values reported as Mean±S.D.

Flows in l/min/m^2 **Ratios as fraction**	**IA**	**EC**	**IA vs. EC**
N	69	28	p
Age	11.9±5.5	8.5±4.9	0.005
BSA	1.2±0.5	0.9±0.3	0.003
(IVC+SVC)/BSA	2.8±1.0	3.0±1.0	0.43
(RPA+LPA)/BSA	2.3±0.8	2.7±0.8	0.03
IVC/(IVC+SVC)	0.60±0.15	0.55±0.11	0.17
RPA/(LPA+RPA)	0.55±0.13	0.51±0.13	0.14
(RPA+LPA)/(IVC+SVC)	0.88±0.3	1.26±1.9	0.1
N	52	22	
Aortic Flow/BSA	3.4±1.5	4.1±1.5	0.11
(IVC+SVC) / Ao	0.92±0.5	0.82±0.3	0.41
(RPA+LPA) / Ao	0.80±0.6	0.70±0.2	0.48

The ratio of pulmonary to caval flow was not statistically different from unity for the extracardiac Fontans. However, the mean ratio of pulmonary to caval flow for the

intraatrial Fontans was statistically different from unity. Even though the patients with extracardiac conduits were younger, their cardiac index seemed to be higher than intraatrials.

9.3.5.1 Comparison of Mean velocities

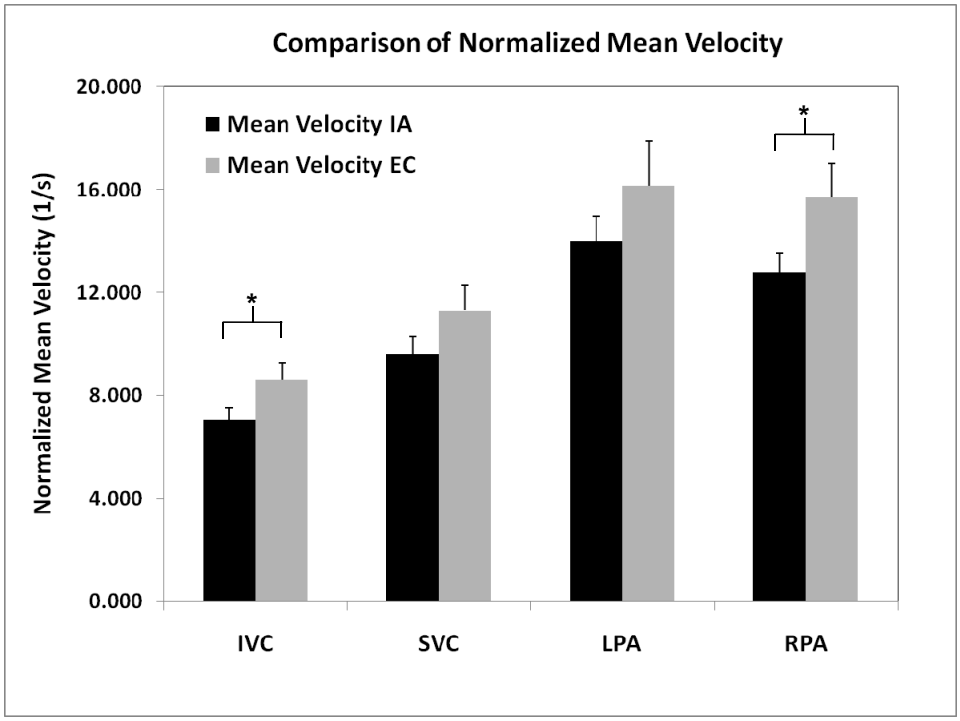

Figure 9.10: Effect of Fontan type on normalized mean velocities. IA: intraatrial; EC: extracardiac. Error bars depict standard error. P values for the IVC and the RPA were 0.05 and 0.006 respectively.

Figure 9.10 shows a comparison of normalized mean velocities (mean velocity/sqrt(body surface area)) between intraatrial and extracardiac Fontan types. The normalization factor of sqrt(BSA) was chosen to correctly account for the dimension of velocity (m/s), since BSA has units of m^2. Hence, normalizing by sqrt (BSA), correctly results in the normalization factor of 'm'[197]. The normalized velocities were generally higher for the extracardiacs when compared to the intraatrials, with the differences being

statistically significant for the IVC (p=0.05) and the RPA (p=0.006). The extracardiac TCPCs typically have a smooth conduit which is generally smaller in diameter (see next section) compared to the intraatrial TCPC, which explains the higher velocities in extracardiac Fontan geometries. Higher velocities in the baffle could translate to lower pressures and faster clearing of blood cells thereby preventing platelet aggregation and thrombi formation. A more detailed analysis of the particle transit times and 3D hemodynamics within intraatrial and extracardiac TCPCs are presented in Chapter 10.

9.3.5.2 Comparison of Vessel Area

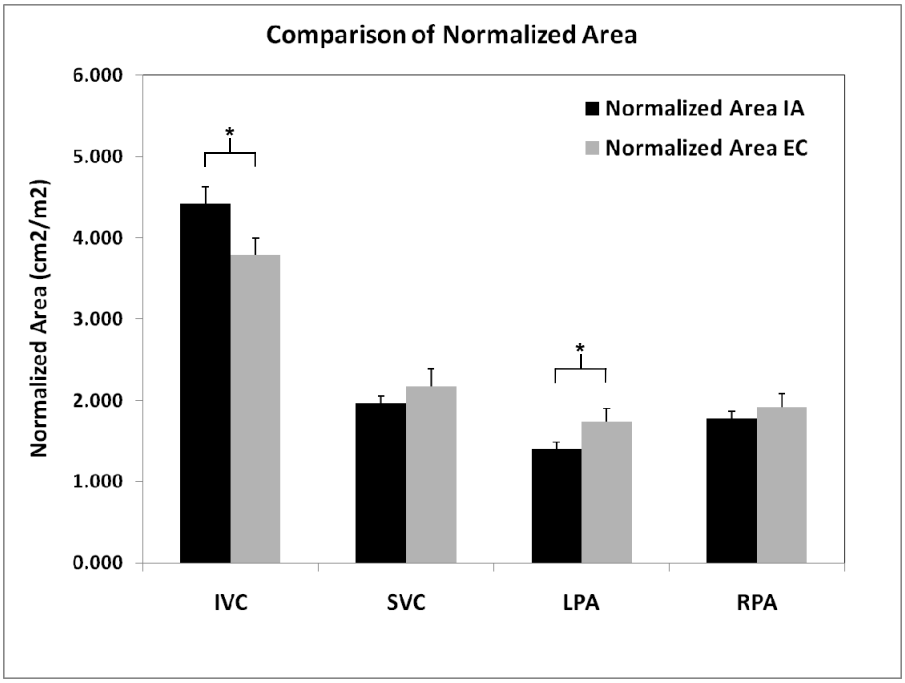

Figure 9.11: Effect of Fontan type on vessel cross sectional area. IA: intraatrial; EC: extracardiac. Error bars depict standard error

Normalized vessel cross sectional areas were compared between intraatrial and extracardiac TCPCs at the location where PC MRI measurements were acquired (Figure 9.11). Intraatrial Fontans had significantly larger cross sectional area for the IVC (p =

0.04), while extracardiacs had signifantly larger area for the LPA (p = 0.02). Extracardiac TCPCs also seemed to have larger area for the RPA and the SVC, but the differences were not statistically different. The normalized pulmonary artery area (Nakata Index) is clinically considered to be a good indicator of clinical outcome as higher pulmonary artery diameters have been correlated with improved long term clinical outcome. Both the groups had pulmonary arteries (1.5 cm^2/m^2) which were significantly smaller than published normal values (3.3 cm^2/m^2)[198].

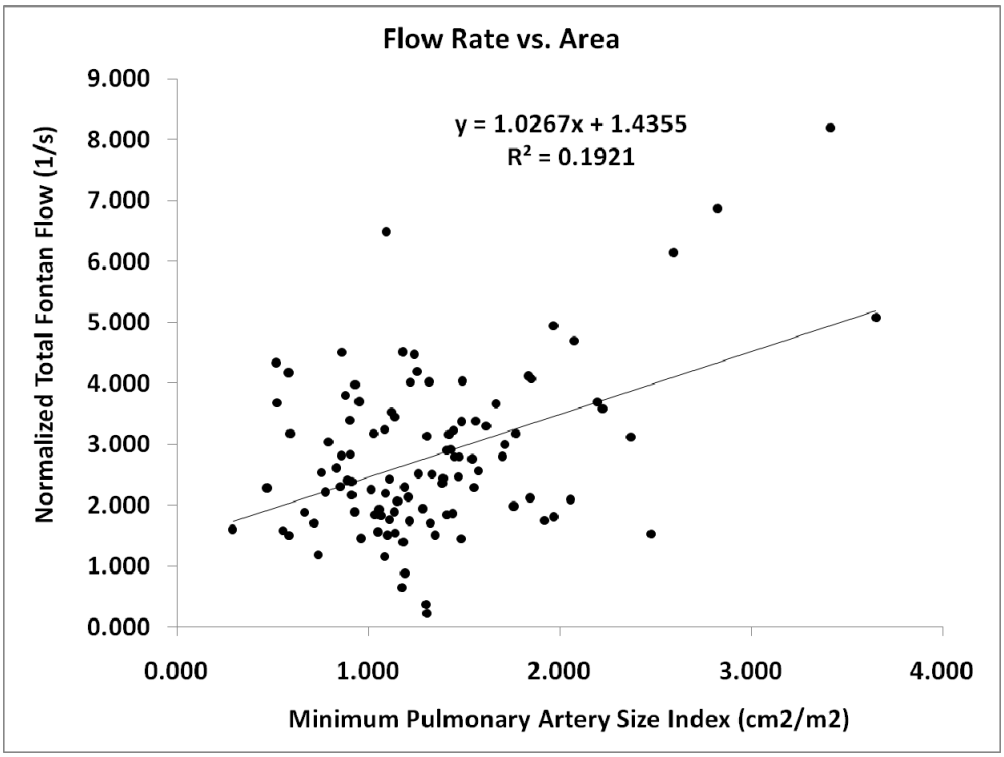

Figure 9.12: Correlation of normalized Fontan flow with minimum pulmonary artery size index.

This brings to the forefront, the importance of pulmonary artery diameter in regulating cardiac index. Figure 9.12 shows the correlation of normalized Fontan flow (IVC + SVC) with the minimum pulmonary artery size index (minimum of LPA and the

RPA) for all the patients in the current study. There was a significant positive correlation ($p < 0.0005$) between the Fontan flow and pulmonary size index. Most of the pulmonary artery size indices were clustered between 1 and 2 cm^2/m^2 with only a few being between 2 and 5 cm^2/m^2. Clearly, the pulmonary artery growth is stunted in these patients due to the lack of a right ventricle. Pulmonary artery sizes can directly impact ventricular function upstream and downstream by controlling the overall resistance of the TCPC. Smaller pulmonary arteries imply higher resistance, which decreases the preload and increases the afterload experienced by the single ventricle (see chapter 11 for a detailed analysis), consequently decreasing the cardiac output. This is particularly important for patients with intraatrial TCPCs, in whom flow has to go from a larger sized IVC (compared to extracardiacs) to a smaller sized LPA and RPA, resulting in a higher resistance configuration. This could explain why intraatrials appear to have lower cardiac index compared to extracardiac Fontans.

9.3.5.3 Comparison of Flow Pulsatility

It is generally believed that the presence of the atrial wall in an intraatrial fontan would result in increased pulsatility, when compared to an extracardiac connection. To test this hypothesis, pulsatility indices (as defined in Chapter 5) were evaluated and compared between the two Fontan types. Figure 9.13 shows the differences between the two Fontan types. The pulsatility of flow in the LPA and the RPA for intraatrial Fontans was significantly higher in intraatrials compared to extracardiacs ($p < 0.006$). The pulsatility of flow in the IVC was not significantly different between the two groups. This highlights that the presence of the atrial wall in intraatrials *does* add pulsatility to flow in

the forward direction going into the pulmonary arteries, but has minimal impact on the pulsatility upstream in the IVC.

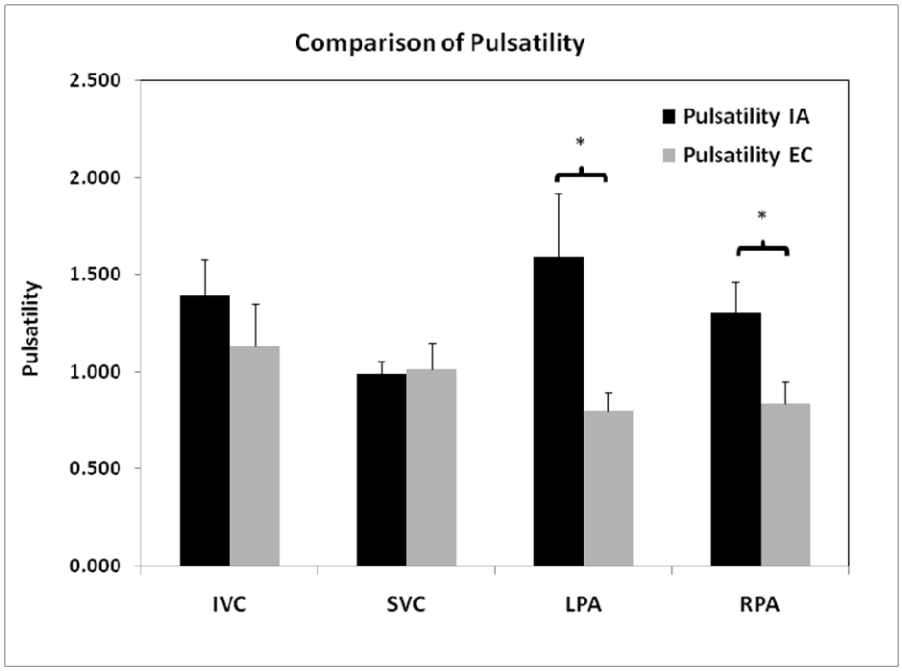

Figure 9.13: Comparison of pulsatility between intraatrial (IA) and extracardiac (EC) Fontan types for different vessel sizes.

9.3.6 Fontan Flow Analysis – Discussion

The velocity and flow database on Fontan patients established as part of this study is the largest one that exists in the world today. Its agreement with prior data using both mass spectrometry[199] and the Fick method[200, 201] suggests that cardiac magnetic resonance (CMR) can accurately measure blood flow in the Fontan baffle. The importance of a large series of patients in establishing normative data for this unique population should not be understated. Prior series are at best anecdotal and certainly cannot be viewed as establishing normal values.

Many investigators are performing computer and *in vitro* modeling of the Fontan pathway in order to better understand the hemodynamics of the connection. They rely on normal values reported in the literature upon which to base their models. As the previous reported series have been quite limited, the current data will provide a more comprehensive range of normal flows and flow splits which these investigators can use. Age and body surface area were correlated with IVC flow contribution. This study demonstrated that total caval flow was 2.9 l/min/m^2, with measured total pulmonary flow slightly lower at 2.4±0.7 l/min/m2, and an IVC contribution of nearly 60%. Flows to both lungs and from both SVCs, when present, were nearly equal. Type of SVC anastomosis or Fontan type did not seem to significantly affect the global pulmonary flow splits.

There was a relatively small but significant difference between measured pulmonary and systemic venous flows. Part of this may be explained by the Fontan fenestration, although attempts to control for this did not account for the differences. One potential source may be in the measurement of the RPA flow, as the origin of the right upper lobe branch of the pulmonary artery is often extremely close to the SVC-RPA junction. It is therefore often very challenging to choose an imaging plane that will exclude the SVC but include the right upper lobe branch.

There was excellent correlation between aortic and both pulmonary and venous flow measurements. However, the measured systemic venous and pulmonary artery flows were significantly lower than the measured aortic flows. This may in part be explained by coronary blood flow, which is included in aortic velocity maps when measured near the valve. A more likely explanation for this difference is the presence of significant aortopulmonary collaterals as these collaterals are known to be present in

Fontan patients, especially after prolonged pleural effusions[202]. This difference deserves further investigation. The quantification of collateral flow has classically been quite difficult and this data points to a potential mechanism for quantifying this flow. The precise difference can be quantified by measuring flow through the pulmonary veins, and checking if it matches aortic flow. If it does, then the presence of collaterals can be acknowledged. A different study has to be performed in order to fully establish this mechanism.

Another potential source of error in the Fontan pathway flow measurements is in the breath-holding technique employed during routine PC-MRI acquisitions. It has been previously demonstrated that Fontan blood flow, especially the IVC, increases during inspiration and decreases during expiration[146]. In this study, the opposite phenomenon was observed. There were significant differences between flow rates measured at end-inspiration and end-expiration, with end expiration flow rates being higher than end inspiration by 45%. Although the data collection approach was different for the two studies, it does bring to fore, the important effects of respiration in controlling the hemodynamics within the Fontan connection. This mismatch could also contribute towards the bias that exists between the aorta and the Fontan pathway, as many of the sequences were acquired during expiratory breath-holds.

The increase in IVC fraction with age shown in Figure 9.7 is consistent with previous studies in normal children. A Doppler study by Salim et al. in 1995 looked at SVC flow compared to total pulmonary blood flow in a group of 145 healthy children[203]. They determined that the IVC flow reached a peak of 45% of total caval flow at 2.5 years of age and then increased to 65% of the total pulmonary blood flow by 6.6 years of age.

While the IVC contributions were slightly lower than those suggested in our study, the overall trend is quite similar. Note that the initial decline in IVC fraction was not captured in our study as most of our patients were greater than 2.5 years of age, where the Salim study suggests the peak occurs. This indicates that the presence of a Fontan does not have a significant effect on the relationship between SVC and IVC contributions of caval flow.

To date, there have been very few studies which have systematically examined the flow rates and flow distribution in the Fontan baffle. In 1999, Fogel et al. used CMR presaturation pulse sequences to measure the IVC and SVC flow contribution to each pulmonary artery. In this study, 10 patients underwent CMR with presaturation pulses applied individually to the SVC and IVC, with the relative flow contribution to each pulmonary artery measured using the relative signal decrease. It was shown that in their cohort of 2 year olds, on average 40% of the total systemic venous return was from the IVC, with relatively more flow from the IVC directed toward the LPA. This is consistent with our study in which approximately 37% of the caval flow was from the IVC in this age group (see Figure 9.7). Absolute flows were not measured in their study[142]. The largest series on Fontan patients to date came from Rosenthal et al. in 1995. This study used respiratory mass spectrometry with acetylene to measure effective pulmonary blood flow during rest and exercise in 43 Fontan patients. The resting pulmonary blood flow was measured at 2.2 L/min/m2 for atriopulmonary Fontans and 2.3 L/min/m2 for TCPC Fontans[199]. These data agree very well the pulmonary blood flow measured in this study.

Finally, this study also demonstrated that the Fontan type has a direct impact on single ventricle hemodynamics. Patients with extracardiac Fontans appeared to have

higher cardiac index which approached statistical significance ($p = 0.1$). This difference in cardiac index could be partly explained by the mismatch in vessel areas that was observed between the two groups. Intraatrial TCPCs had larger IVCs and smaller pulmonary arteries, which meant that the flow from a large IVC had to go to the smaller pulmonary arteries. This vessel diameter mismatch results in increased power losses which translates to increased TCPC resistance experienced by the upstream single ventricle. Increased TCPC resistance has a direct impact on the preload and afterload of the single ventricle (see Chapter 11), which impairs the ability of the ventricle to generate adequate cardiac output. This is an important finding, which could help in demonstrating the benefit of one surgical procedure over the other.

Higher velocities were also observed in extracardic Fontans. This was because extracardiacs generally have smaller size IVCs, which automatically results in increased velocities within the baffle. The smaller size IVC in extracardiacs may not be bad, especially if it reduces the mismatch in areas between the IVC and the pulmonary arteries. This could reduce the effective "stenosis" created as a result of flow going from a larger vessel to a smaller one, and could potentially help reduce the overall resistance of the TCPC.

Another important finding of this study was that patients with extracardiac Fontan types have larger pulmonary artery indices compared to intraatrials. Pulmonary artery sizes have been shown to be good indicators of clinical performance in patients with congenital heart disease[198]. In this study, pulmonary artery size index (Nakata index) was quantified for normal subjects, and for patients with CHD. This study quantified the normal value of the pulmonary artery size index to be 3.3 cm^2/m^2. The pulmonary artery

size indices of all Fontan patients in our study (except 1) was less than this value. Furthermore, the study by Nakata showed that mortality rates were higher for patients with pulmonary artery indices less than 1.5 cm^2/m^2. The average value for patients with intraatrial Fontans was lower than this value, which suggests that they maybe at risk for Fontan failure earlier than those with extracardiac Fontans. This is an important result, as it may directly impact the surgeon's decision to choose between an intraatrial and extracardiac Fontan.

9.3.7 Fontan Flow Analysis - Summary

In this section, global flow characterists through the TCPC pathway were analyzed for a large cohort of Fontan patients. The trends suggest that CMR can be used to accurately measure blood flow through the Fontan baffle. There was a bias between the flow rates measured in the aorta and the vena cavae, with the aortic flow being significantly higher than the caval and pulmonary artery flows. Significant differences were observed between between intraatrial and extracardiac Fontan types. Differences in cardiac index leaned towards statistical significance ($p=0.1$), while significant differences were observed in the magnitude of flow velocities and vessel cross sectional area between the extracardiac and intraatrial Fontan types. The larger pulmonary artery sizes highlighted extracardiac Fontan types may facilitate pulmonary artery growth, which could have implication in the long term clinical outcome of these patients.

9.4 Energetics of the single ventricle circulation

In a biventricular circulation, the right ventricle is morphologically designed to handle the low energy pulmonary circulation. However, in patients with hypoplastic left

heart syndrome (HLHS), the dominant pumping chamber for the entire systemic and pulmonary circulation is the single right ventricle, which may result in abnormal cardiac mechanics in these patients. This was partially evident from the results presented in the previous section (Table 9.5), where the cardiac index was lower for patients with HLHS compared to those with tricuspid atresia. To better understand this mechanism, a more detailed analysis of flow through the aorta is conducted in this study. *The primary hypothesis of this is that patients with HLHS have lower power capacity compared to other single ventricle defects.* This hypothesis is tested two parts: a) Output power differences between HLHS and other ventricle defects are first investigated using PC MRI of the ascending aorta; b) the dependence of output power on ventricular function is determined using cine short-axis MRI of the single ventricle.

9.4.1 Power Output of the Single Ventricle

18 patients with HLHS (Table 9.7) and 18 patients with other single ventricle defects (non-HLHS) (Table 9.8) were selected from the velocity database. The basis for the selection was the availability of PC MRI through the aorta and the availability of the measurement of cuff blood pressures. Out of the 18 HLHS patients, there were 15 Fontans (8 intra-atrials and 7 extra-cardiacs), 2 BDGs, 1 Hemi-Fontan, and all of them underwent the stage 1 aortic reconstruction (Norwood) procedure. Non-HLHS patients consisted of 14 patients with a Fontan (8 intra-atrials, 5 extra-cardiacs, and 1 atriopulmonary), 4 with a bidirectional Glenn, and 2 who had an aortic reconstruction (Damus-Stansel-Kaye) procedure done.

Table 9.7: HLHS patients used in the current study, ASD: Atrial Septal Defect; VSD: Ventricular Septal Defect; IA: intraatrial; EC: extracardiac; BDG: Bidirectional Glenn; HF: Hemi-Fontan

Patient	**Diagnosis**	**Fontan**	**Age (Years)**	**BSA m^2)**
CHOA017	HLHS	BDG	1.2	0.36
CHOA020	HLHS	IA	10.5	1.16
CHOA026	HLHS	IA	5	0.63
CHOA034	HLHS	BDG	1.2	0.4
CHOP006	HLHS	EC	13	1.05
CHOP013	HLHS, ASD	EC	8.5	0.83
CHOP016	HLHS	IA	16	1.68
CHOP018	HLHS	IA	13	1.73
CHOP019	HLHS, bilateral SVC	EC	9	0.91
CHOP023	HLHS	IA	8.5	0.79
CHOP025	HLHS	IA	19.6	1.59
CHOP026	HLHS	IA	11	1.08
CHOP035	HLHS	IA	11.5	1
CHOP039	HLHS	IA	17.9	1.22
CHOP042	HLHS	HF	6.2	0.80
CHOP044	HLHS	IA	20.5	1.97
CHOP045	HLHS	IA	19	1.4
CHOP046	HLHS, VSD, LV	HF	2.9	0.57

Table 9.8: Non-HLHS patients used as part of this study: SV: Single Ventricle; DILV: Double Inlet Left Ventricle; HRHS: Hypoplastic Right Heart Syndrome; TA: Tricuspid Atresia. See list of abbreviations for the rest.

Patient	**Diagnosis**	**Fontan**	**Age (Years)**	**BSA (m^2)**
CHOA024	SV with DI-LV	IA	5	0.65
CHOA029	SV with DI-LV	BDG	5	0.49
CHOA031	SV with DI-LV	IA	3.8	0.54
CHOA032	SV with DI-LV	BDG	1.8	0.51
CHOP007	HRHS	EC	10.5	1.02
CHOP021	TA	IA	9	0.74
CHOP022	Dextrocardia	EC	12.6	1.01
CHOP024	TA	IA	10.4	0.88
CHOP028	SLV	IA	8.8	0.94
CHOP029	TA	IA	20.5	1.61
CHOP030	TA, VSD	IA	12.5	1.32
CHOP032	DORV	EC	19.8	1.97
CHOP033	DORV	EC	10.4	0.69
CHOP041	Dextrocardia	IA	20.5	1.46
CHOP043	TA	APC	20.7	1.84
CHOP049	DORV	EC	4.2	0.62
CHOP050	TGA, LAVV atresia, severe sub-PS	IA	20	1.47
CHOP053	Heterotaxy	BDG	5	1.73

The PC MRI plane acquired in the ascending aorta was used for comparing the hemodynamics between the two groups. The vessel was segmented and flow was quantified using the methodology previously described in Chapter 5. The output power was computed using the modified Bernoulli equation: Power = $(0.5* \rho v^2_{systole} + P_{mean})*Q_{mean(systole)}$; where ρ = blood density (a constant value of 1060 kg/m^3), v = mean systolic velocity, P_{mean}= mean static pressure, and Q=mean systolic flow rate. In order to evaluate this equation, the mean arterial pressure (MAP) was used as the static pressure. The computed power was indexed to BSA for ease of comparison across all patient sizes. Additional parameters that were compared included quadrant flow, mean velocity, maximum velocity, time of forward flow, stroke index, and time to peak flow.

The statistical methods employed for comparisons include two-sampled two-tailed students' t-test with Bonferroni correction to test for group differences. The effect of quadrant flow for differences between the groups was analyzed using a dummy variable regression model. BSA had a strong correlation with both power and systemic vascular resistance index (SVRI), and was used as a covariate in the model. The descriptive statistics are presented as mean, median, minimum, and maximum values. For quadrant flow analysis, the log transformation was not effective for establishing normality and hence an F-approximation to a non-parametric repeated measures analysis of variance was used to look for group differences in quadrant flow. The reported p values are two sided unless otherwise stated, and a p value of 0.05 or less indicated statistical significance. A summary of results are shown in Table 9.9.

Table 9.9: A summary of the results comparing HLHS and Non-HLHS patients. The measured variables are those that are directly obtained from patient measurements, while the computed variables are those that were computed from PC MRI data

Variable	**HLHS**	**Non-HLHS**	
N	18	18	p
Measured Variables			
Age (yrs)	10.8±6.14	11.14±6.6	.88
BSA (m^2)	1.04±0.44	1.03±0.47	.95
Heart Rate (B/Min)	83.3±0.3	90.5±22.5	.33
Systolic BP (mmHg)	112.9±22.4	115.2±23	.73
Diastolic BP (mmHg)	60.11±11.1	64.7±9.52	.19
LPA Pressure mmHg)	10.33±2.8	11.8±2.82	.09
Mean Velocity (cm/s)	18.15±7.53	28.2±10.7	.003
Mean Diameter (cm)	3.09±0.56	2.69±0.60	0.05
Max Flow (L/ Min)	12.1±2.61	14.7±7.2	0.31
Forward flow time (s)	0.30±0.06	0.26±0.04	0.03
Time to Max Flow (s)	0.17±0.04	0.16±0.04	0.24
Computed Variables			
Output Power (W)	1.46±0.75	1.85±1	.20
CO (L/Min)	3.18±1.34	4.08±2.0	.13
CI ($L/Min/m^2$)	3.15±0.98	4.09±1.24	0.009
Power Index (W/m^2)	1.39±0.39	1.77±0.38	0.004

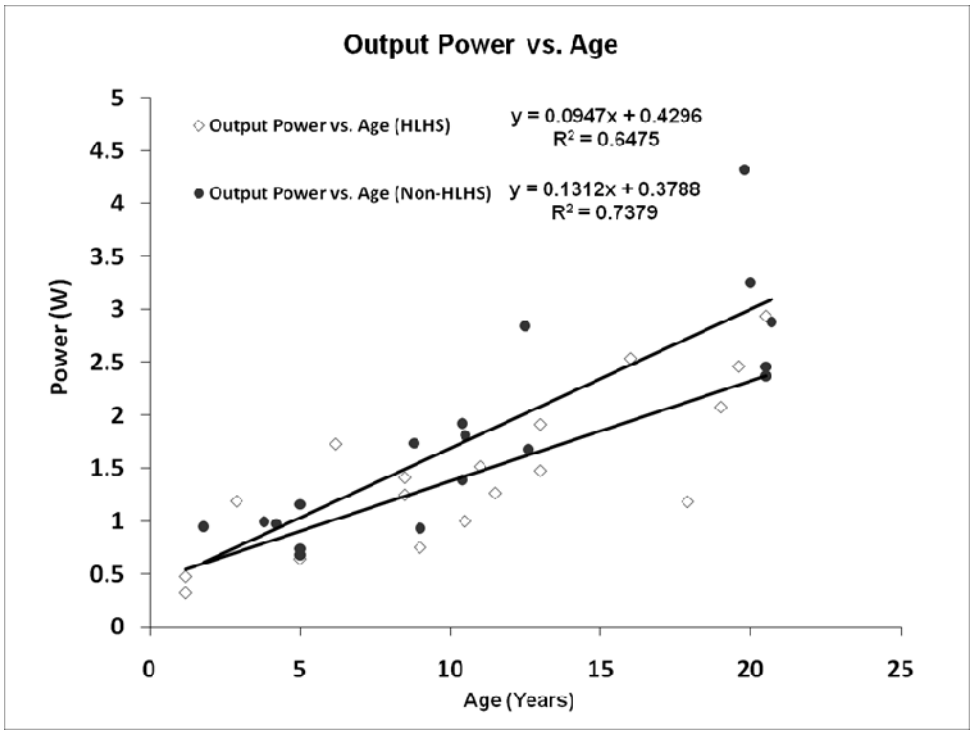

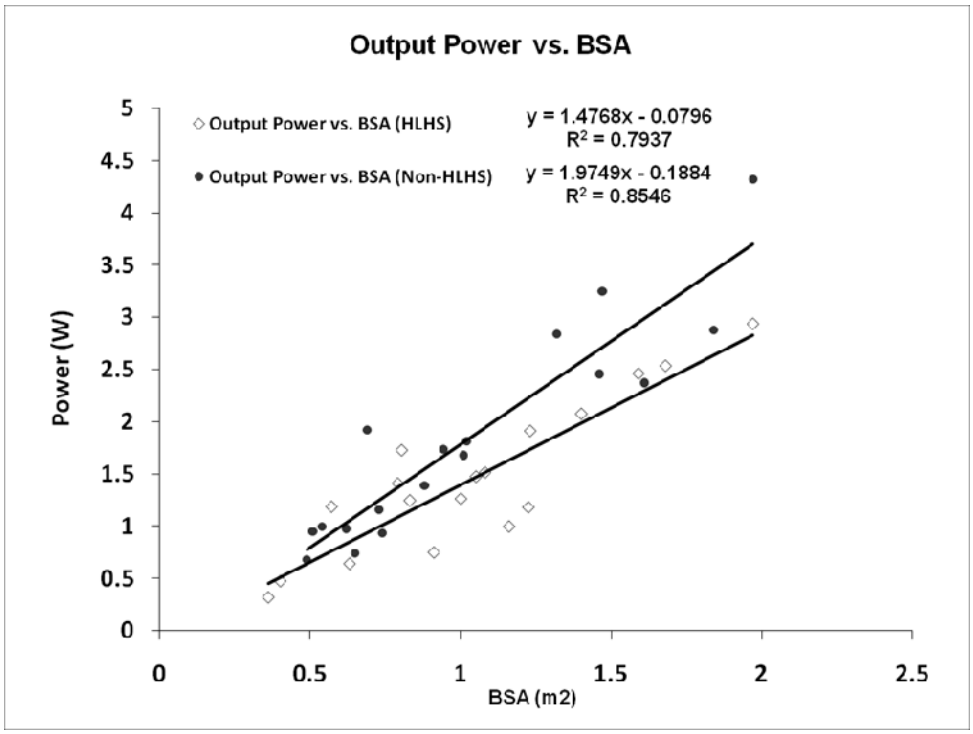

Figure 9.14: Variation of output power with age and body surface area (BSA).

The patient age and BSA were comparable in both the groups. The mean age of HLHS patients was 10.8±6.14 years, while for the non-HLHS category it was 11.14±6.6 years. There were no significant differences in age (p=0.88) and BSA (p=0.99) indicating that the two groups of patients used in the study were similar in physical characteristics. Due to the large variation in age and BSA of patients, the primary variables of interest are indexed to BSA for comparison.

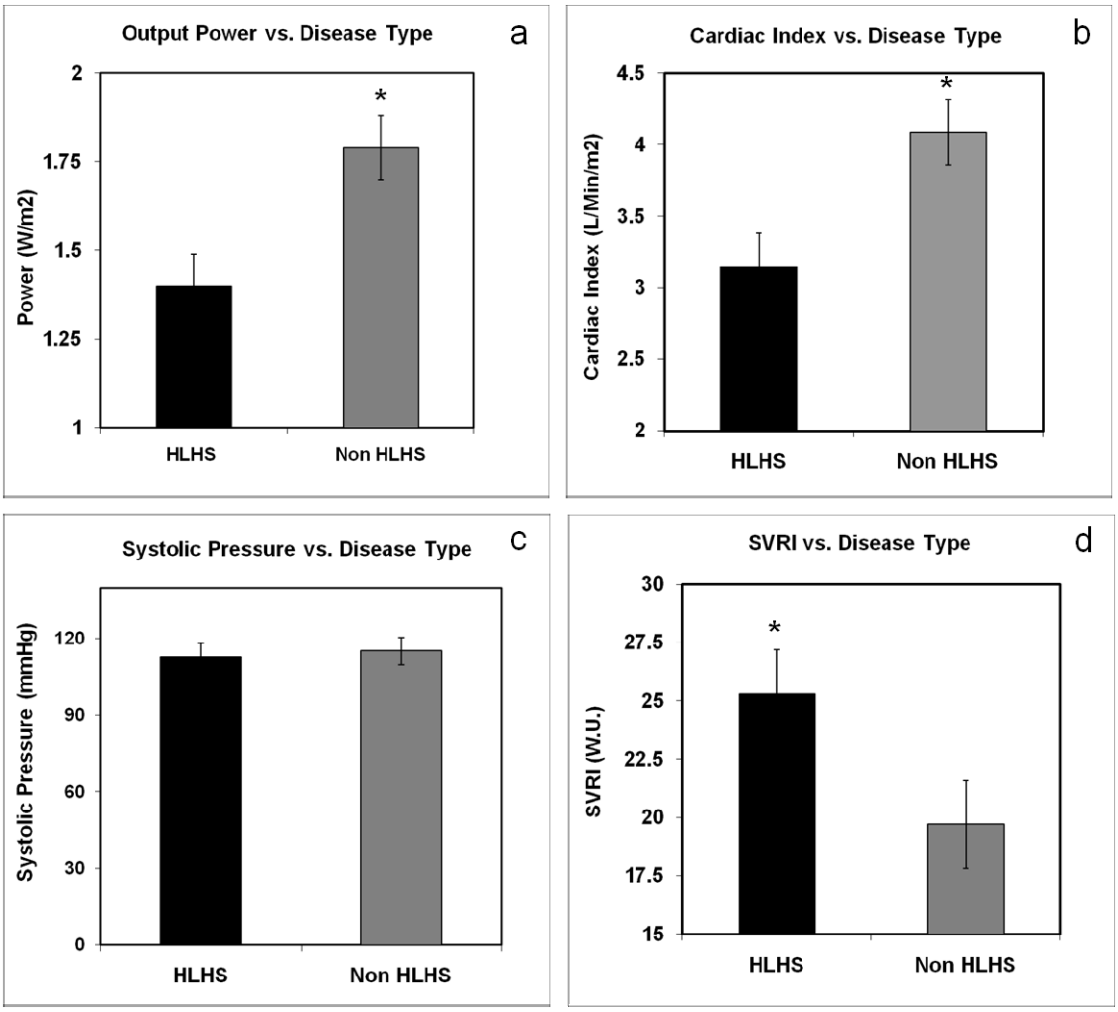

Figure 9.15: Bar graphs showing differences between HLHS and non-HLHS in: a) Output Power normalized by BSA, b)Cardiac Index, c) Systolic Pressure. and d) Systemic Vascular Resistance Index (SVRI)

There was a strong correlation of power with BSA and age (Figure 9.14). For both the groups, power increased with increase in BSA and age, though for HLHS patients the slope was smaller than for non-HLHS patients. The mean power output for HLHS group was 1.46 ± 0.75 W, and for the non-HLHS group it was 1.85 ± 0.98 W. When indexed to BSA, the results yielded significantly lower values for HLHS compared to non-HLHS ($p < 0.004$) as depicted in Figure 9.15a. There were no significant differences in the blood pressures in the two groups (Figure 9.15c), though there were significant differences in the cardiac index of these patients (Figure 9.15b). This indicated that patients with HLHS may be experiencing higher resistances and for this reason SVRI was computed for each of the patients and group differences were evaluated.

Figure 9.16a depicts bar graphs of the quadrant flow ratios computed for each of the patient groups. An outlier was in the HLHS group (CHOA026) which was removed for better comparison (Figure 9.16b). Table 9.10 also shows flow differences between each of the quadrants. The four quadrants were defined to be anterior-left (AL), anterior right (AR), posterior left (PL) and posterior right (PR). The methodology of how these quadrants were divided is described in Chapter 5. There were clear differences between the HLHS and the non-HLHS group in the AL and PR quadrants, respectively. Pairwise comparisons revealed group differences in AL flow ratio approached statistical significance ($p < 0.07$) as is evident in Table 9.10. Within the HLHS group, statistically significant differences existed between AL and AR quadants showing greater skewness towards AL in HLHS. A repeated measures analysis of variance on the ranked data confirmed that there were statistically significant differences in flow between the quadrants, indicating that flow is not uniform for HLHS ($p<0.05$).

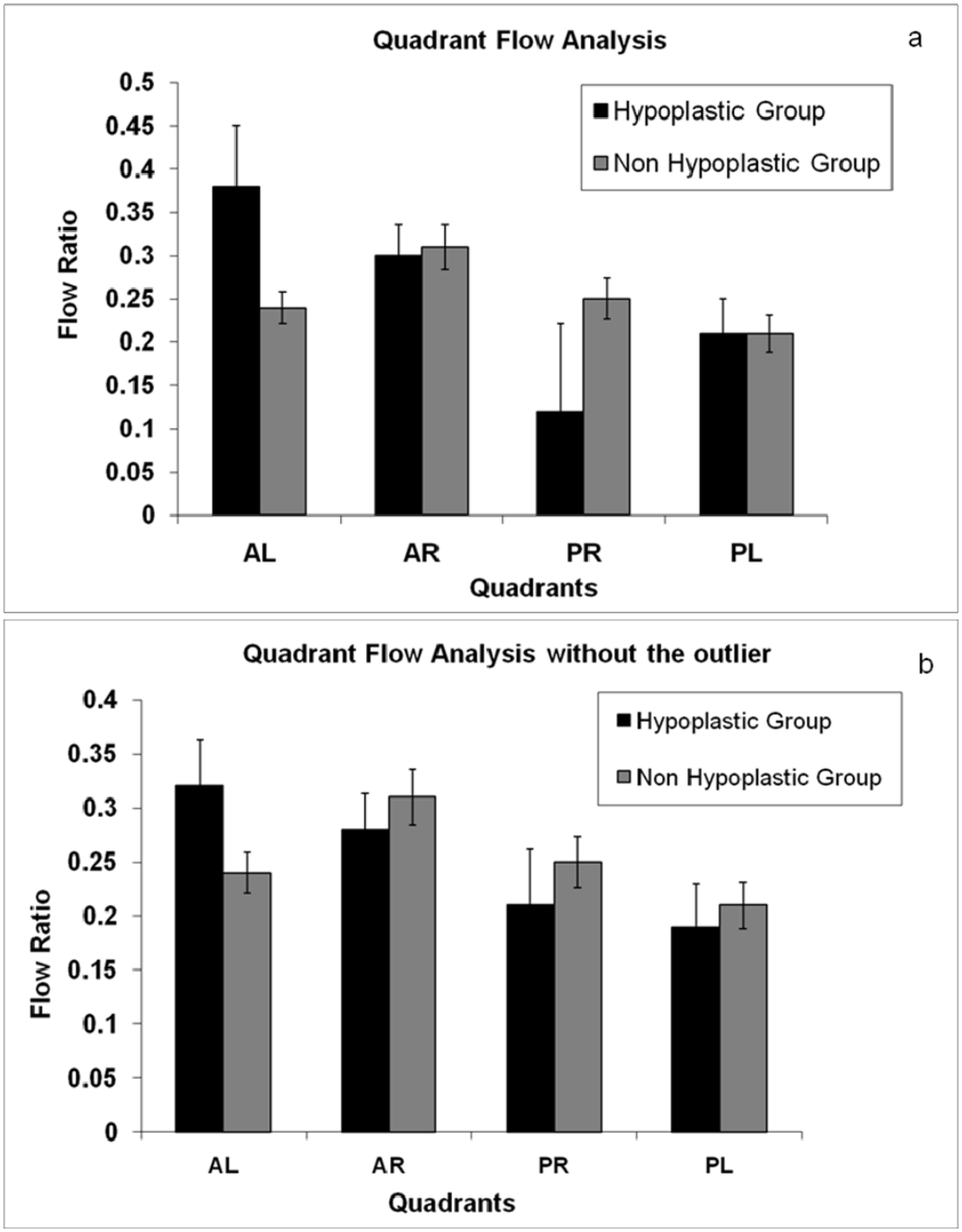

Figure 9.16: Quadrant flow ratio across the aorta: AL: Anterior Left; AR: Anterior Right; PR: Posterior Right; PL: Posterior Left. a) Analysis conducted on all the points; b) Analysis without the outlier skewing the data

Table 9.10: Summary of quadrant flow ratios seen in the ascending aorta. Significant differences were observed in the difference between anterior-left and anterior right quadrants between HLHS and non-HLHS groups. AL – Anterior Left, AR – Anterior Right, PR – Posterior Right, PL – Posterior Left. All values reported as Mean ± S.D.

Quadrant Flow	***HLHS***	***Non-HLHS***	
N	18	18	p
AL	0.37 ± 0.29	0.23 ± 0.09	.07
AR	0.30 ± 0.60	0.31 ± 0.12	.30
PR	0.13 ± 0.44	0.25 ± 0.10	.24
PL	0.20 ± 0.17	0.21 ± 0.09	.41
Differences			
AL – AR*	0.08 ± 0.23	-0.06 ± 0.14	0.05
AL – PR	0.26 ± 0.72	0.00 ± 0.17	0.15
AL – PL	0.10 ± 0.28	0.03 ± 0.11	0.24
AR – PR	0.18 ± 0.54	0.06 ± 0.16	0.50
AR– PL	-0.10 ± 0.49	0.10 ± 0.2	0.39
PR – PR	-0.09 ± 0.5	0.03 ± 0.14	0.19

In order to establish a relationship between quadrant flow and output power, a regression model was setup: Output Power = $\beta o+\beta 1*(AL-AR) + \beta 2*BSA$. AL-AR had a significant negative impact ($\beta 1(estimate)= -0.15$) on the output power ($p<0.04$) for the HLHS group. The negative trend was expected since a higher skew towards the anterior wall of the aorta could result in higher frictional losses at the wall, which in turn could account for some of the reduced power, lower velocities, and lower cardiac output. Other combinations of parameters were also tried, although they were not significant. Figure

9.17 shows examples of velocity profiles at peak systole for two of the cases.

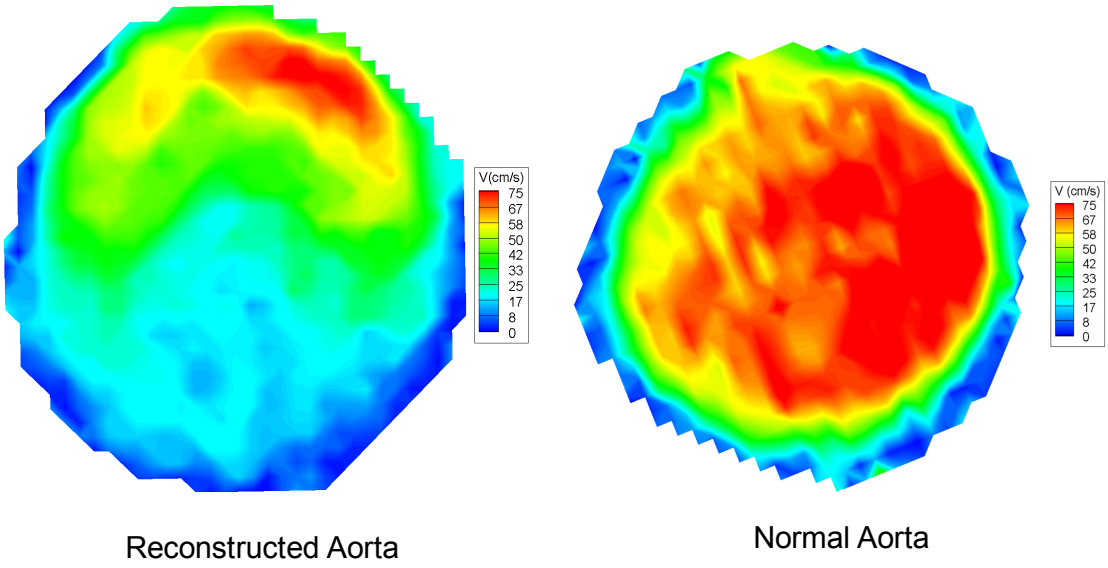

Figure 9.17: Comparisons of velocity profiles between a reconstructed aorta (CHOP006) and normal aorta (CHOP022) at peak systole. Notice the anterior skewness of the velocity profile for the HLHS case. Animations of these two cases are provided as an addendum to this thesis

9.4.2 Impact of Ventricular Function on Output Power

In order to investigate the impact of ventricular function on output power, end diastolic volume (EDV), end systolic volume (ESV), stroke volume (SV), and ejection fractions (EF) were correlated with total power output. 22 patients from the database were selected (Table C.2) on whom a short axis cine MRI scan of the single ventricle was performed as part of the study. Ventricular function was evaluated by manually outlining the endocardial borders. Note that this group was different from the group used in the previous study since short axis cine MRI was not available on all the patients in the previous group. 13/22 patients had HLHS (Age: 11.9 ± 6.71 years, BSA: 1.11 ± 0.47 m^2),

while the remaining 9 had tricuspid atresia/hypoplastic right syndrome with a morphological left systemic ventricle (Age: 9.81 ± 6.49 years, BSA: 1.07 ± 0.42 m^2). In order to account for the large variation in patient age and size, the volume data (EDV, ESV, and SV) was normalized by $(BSA)^{1.5}$ to obtain a dimensionless parameter.

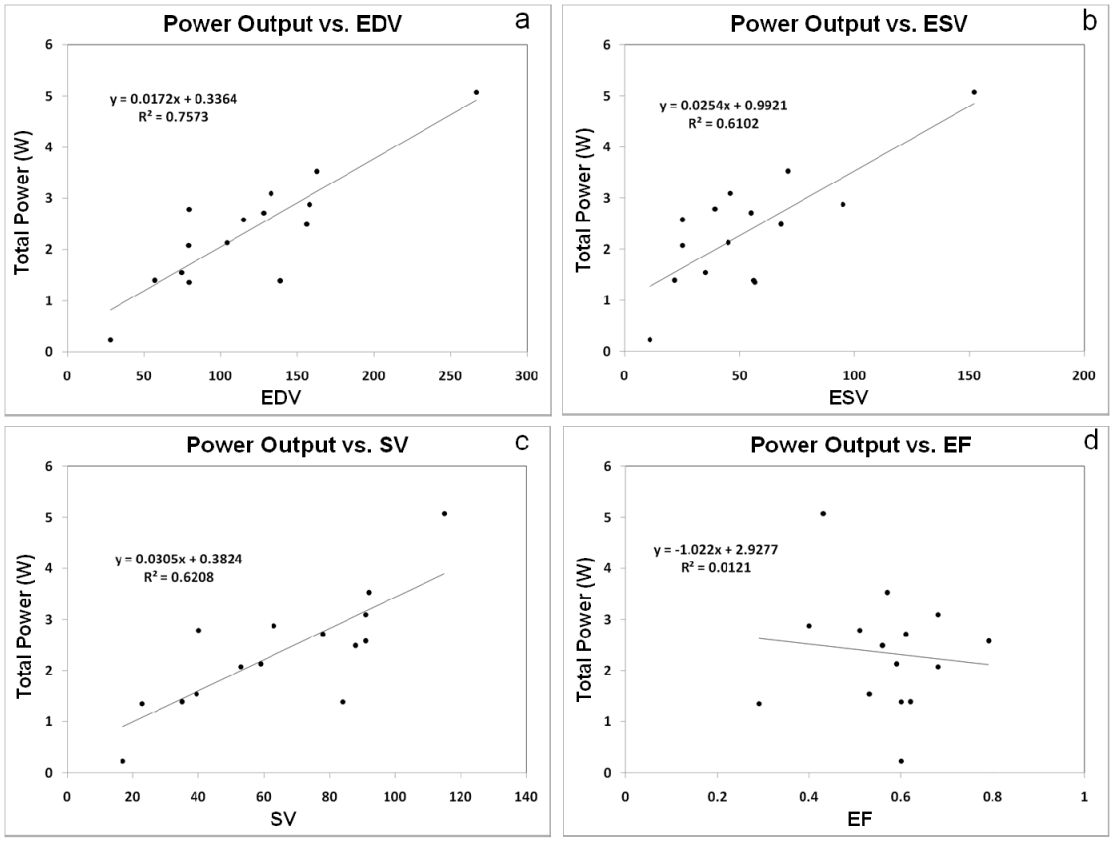

Figure 9.18: a) Power output vs. End Diastolic Volume (EDV); b) Power output vs. End Systolic Volume (ESV); c) Power Output vs. Stroke Volume (SV); d) Power output vs. Ejection Fraction (EF). A positive correlation was observed between output power and ventricular volumes while no correlation was observed between output power and ejection fraction

Figure 9.18 shows regression plots correlating the total power output with ventricular volumes and ejection fraction. There was an excellent positive correlation

between the output power, EDV, ESV, and SV ($p<0.0005$). This is not surprising as power output is a function of cardiac output, which in turn is a function of ventricular volume. In order to eliminate the impact of cardiac output, output power was non-dimensionalized by normalizing it with ($\rho Q^3/BSA^2$), where ρ is the density (1025 kg/m^3 for blood), Q is the cardiac output, and BSA is the body surface area. This normalization factor is obtained from dimensional analysis as described by Dasi et al[197]. Once normalized, there was no statistically significant correlation between the two, which highlights that the single ventricle primarily increases its power capacity by increasing its volume.

Table 9.11: Comparison of Ventricular Function between HLHS and non HLHS

	HLHS	**Non HLHS**	
N	13	9	p
Age (yrs)	11.9 ± 6.7	9.81 ± 6.5	0.47
BSA (m^2)	1.11 ± 0.5	1.07 ± 0.4	0.80
EDV (cc)	114 ± 64.5	77.73 ± 41.2	0.12
ESV (cc)	56.05 ± 36.9	35.9 ± 20.5	0.12
SV (cc)	59.2 ± 33.9	41.8 ± 21.2	0.15
EF	0.52 ± 0.13	0.54 ± 0.06	0.5

To further differentiate the ventricular performance depending upon the original clinical diagnosis, the analysis here again was separated into HLHS and non-HLHS patients. Table 9.11 shows the comparison of ventricular function between the two groups, while Table 9.12 shows a comparison of these dimensionless parameters (EDVI: end diastolic volume index; ESVI: end systolic volume index; SVI: stroke volume index) between the two groups. All statistical tests were done using the students' unpaired t-test

having a two-tailed distribution with unequal variance. There were no statistical significant differences between the two groups, although patients with HLHS seemed to have larger end diastolic volumes, end systolic volumes, and stroke volumes compared to the non HLHS group.

Table 9.12: Comparison of normalized volumes between HLHS and Non HLHS

	HLHS	Non HLHS	
N	13	9	p
Age (yrs)	11.9 ± 6.7	9.81 ± 6.5	0.47
BSA (m^2)	1.11 ± 0.5	1.07 ± 0.4	0.80
EDVI	103.4 ± 43.6	79.9 ± 38.9	0.2
ESVI	52.47 ± 29.4	37.74 ± 20.6	0.18
SVI	51.26 ± 17.4	42.16 ± 18.5	0.26

9.4.3 Discussion: Energetics of the Single Ventricle Circulation

HLHS is one of the most complex and lethal forms of single ventricle diseases whose management is critical at the neonatal stage[8, 204-215]. If left untreated, the disease is fatal resulting in mortality within the first year of birth. With the introduction of the staged reconstruction process and improved diagnosis of HLHS by fetal echocardiography, the early survival rate has markedly improved[214]. Even though right ventricular (RV) function has not directly been linked with operative survival in most of the studies, they do have an impact on the long term survival of HLHS patients[204, 205, 213, 216]. Altmann et al observed that qualitative assessment of RV function was the best predictor for operative survival[216]. They reported that the survival rate of patients with diminished qualitative RV function was only 35% compared to 70% with normal or

hyperdynamic function. In our study, the power output of the single ventricle was evaluated using flow through the ascending aorta, and significant differences between HLHS and non-HLHS patients were elucidated. Furthermore, ventricular function was

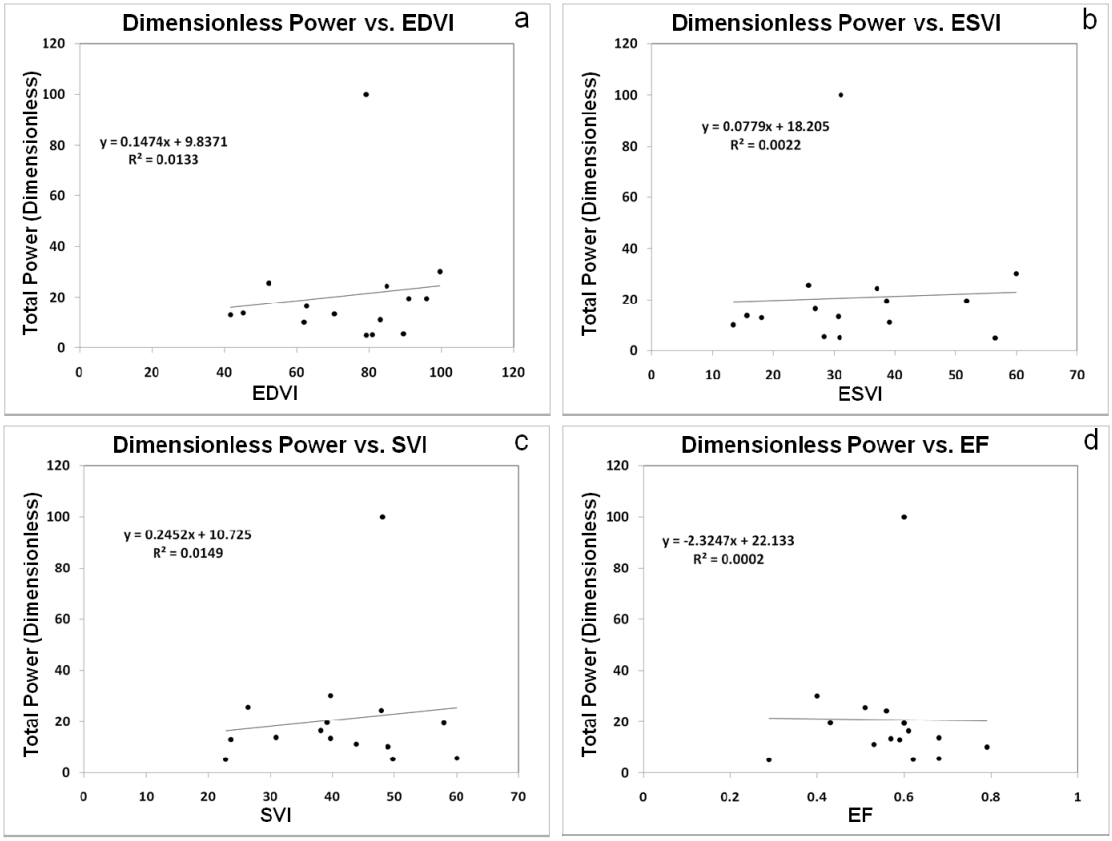

Figure 9.19: a) Dimensionless Power output vs. End Diastolic Volume Index (EDVI); b) Dimensionless Power output vs. End Systolic Volume Index (ESVI); c) Dimensionless Power Output vs. Stroke Volume Index (SVI); d) Dimensionless Power output vs. Ejection Fraction (EF). No significant correlation was observed between any of the parameters

quantified as well, which demonstrated that the power output does strongly correlate with ventricular volumes.

Various studies are currently being done on flow dynamics in the TCPC and one

of the performance measures constantly used for evaluating its efficacy is power loss[19, 43, 61, 62, 67]. However, power loss through the TCPC is meaningless without knowledge of the power supplied to the system. In this study, a simple method for evaluating energetic parameters was proposed based upon classical fluid mechanics principles using non-invasive PC MRI. Power losses through the TCPC and the ascending aorta can now be expressed as a percentage of the total power input into the system. This has the potential to be a useful diagnostic tool for clinical evaluation of Fontan patients.

Power differences observed between HLHS and other variations of single ventricles may seem obvious, but does bring into fore the importance of flow efficiencies for long term performance of single right ventricles. Senzaki et al demonstrated that the hydraulic power cost per unit of forward flow was 40% less in a dual chamber circulation than in the single ventricle circulation[176]. Consequently, a pressure overloaded right ventricle may not be able to handle the high power losses that are seen in the TCPC during normal and elevated activity compared to single LV. This may provide an explanation for the high rate of morbidity associated with HLHS patients in the first 10 years of life and highlights the importance of designing efficient Fontan circuits, especially in the case of HLHS patients.

No significant differences in blood pressures were observed between the two groups. This indicates that differences in output power are arising from the differences in kinetic energy imparted by the single ventricle. This is confirmed by the mean velocities measured in the ascending aorta which were significantly higher for the non-HLHS group compared to the HLHS group. The ability to generate high velocities in the ascending aorta is a measure of the myocardial contraction effectiveness. It is well known from

muscle physiology that the relationship between power and force is given by: Power=Force*Velocity. In cardiac physiology, this power is generated by the myocardial muscle and converted to fluid dynamic energy. Assuming the power consumed by the ventricle itself is negligible, and the energy transfer process is efficient, the power measured at the ascending aorta will be a representative measure of myocardial contraction power. Therefore, the lower velocities seen in the ascending aorta of patients with HLHS maybe an indicator of the decreased contraction velocities associated with the myocardial muscle wall. Unfortunately, myocardial wall velocities were not measured as part of this study, a component that is very important in order to confirm this hypothesis. A possible future study could be to correlate the blood velocities observed in the ascending aorta with the myocardial wall velocities.

A statistically significant correlation between power output and ventricular volume was observed. This is not surprising, especially since cardiac index is one of the primary variables used for evaluating the output power, which is in turn dependent upon the stroke volume. However, it was interesting to note that the output power correlated with end diastolic volume as well, which suggests that increasing ventricular volume is one possible mechanism by which HLHS patients respond to increased power demands. This is further evident as the correlation disappears when the power output is non-dimensionalized by normalization with cardiac index and body surface area (Figure 9.19). No significant correlation was observed between ejection fraction and output power.

Non-uniform flow profile was observed in some of HLHS patients that could have an impact on cardiac efficiency. The skewness of the flow profile could either be due to

the abnormally angled aorta, or it could be due to the pumping mechanism of the right ventricle itself. This is consistent with previous studies that have shown marked differences in aortic flow profiles in patients who have reconstructed aortas compared to other single ventricle patients with normal aortas[34]. Flows through the reconstructed aortas in our study were skewed anteriorly (Figure 9.17) as well, and was in good agreement with the previous study. However, we did observe larger variations in flow profiles within the HLHS group. The conclusions of this study are that patients with HLHS are subject to further power losses and other possible long term aortic wall complications as a result of the skewed velocity profile.

9.4.4 Conclusion: Energetics of the single ventricle circulation

This study showed marked cardiac performance differences between HLHS patients and patients with other forms of single ventricle physiology, in an attempt to provide a physiological explanation for the poor long term performance of HLHS patients. Clearly, there are significant differences in cardiac mechanics between the two groups, since the ability of the single systemic right ventricle to pump blood effectively is impaired. Hence, any minimization of power losses through efficient surgical procedures, could significantly impact the clinical outcome of HLHS patients.

9.5 Summary: *In vivo* PC MRI studies - I

In this chapter, the results of clinical studies conducted on a large cohort of Fontan patients were presented. In the first section, the PC MRI post processing methodology was validated. In the second section, hemodynamics of the Fontan surgical pathway was quantitatively analyzed and similarities and differences between intraatrial

and extracardiac Fontan types were established. In the final section, cardiac energetics and mechanics of the single ventricle circulation were quantified. The results highlighted the impaired ability of single right ventricles (in the HLHS category) for providing the adequate power necessary to maintain normal cardiac function. In the following chapter, the hemodynamics of the TCPC are investigated in more detail using 4D flow fields reconstructed from *in vivo* PC MRI.

CHAPTER 10

IN VIVO PC MRI STUDIES – II

10.1 Overview

In this chapter, the results from specific aim 3 of this thesis are presented. The validation of the divergence free interpolation (DFI) methodology is presented first, followed by the clinical application of the interpolation technique on coronal PC MRI acquired on 24 Fontan patients.

10.2 Divergence Free Interpolation – Validation

As described in chapter 6, the validation of the divergence free interpolation technique was performed on 4 test cases: 1) analytical divergence free function; 2) 2D computational fluid dynamic (CFD) simulation of the driven cavity problem; 3) 3D CFD simulation of an anatomically realistic TCPC geometry; 4) 3D velocity field reconstruction from *in vitro* PC MRI. For test cases a-c, the reference velocity field or the gold standard is directly available in the form of the original velocity field. For test cases a-c, the value of the interpolation parameter α from equation 6-26 is determined based on an optimization study conducted for different spacing of control points. Recall from equation 6-26:

$$\Phi_{\alpha}(x) = \left\{ -\Delta I + \nabla\nabla^{T} \right\} e^{-\alpha \|x\|^2}$$
$$= \left\{ (2(N-1)\alpha - 4\alpha^2 \|x\|^2) I + 4\alpha^2 x x^{T} \right\} e^{-\alpha \|x\|^2}$$

Here, the parameter α can be thought of as 1/standard deviation of the Gaussian component of the radial basis interpolating function. Since the argument is the distance

function, one possible option for α is the average distance between the control points. Hence, the value of α is optimized as a function of distance between the control points. For test case d, a CFD simulation conducted independently on an identical TCPC geometry (CHOA007) is used as a reference.

10.2.1 Validation Test Case #1: Analytical Divergence Free Function

Figure 10.2 shows the percentage error as a function of the parameter α for control point spacing ranging from 2-8. A control point spacing of 2, implies that every 2nd node is retained for interpolation purposes; a spacing of 3 implies that every 3rd node is retained and so on. As expected, the error increased as a function of control point spacing. Choosing an α value between 1 and 2 times the average control point spacing, resulted in lower interpolation errors. Please note that the control grid size and the measurement grid size are the same.

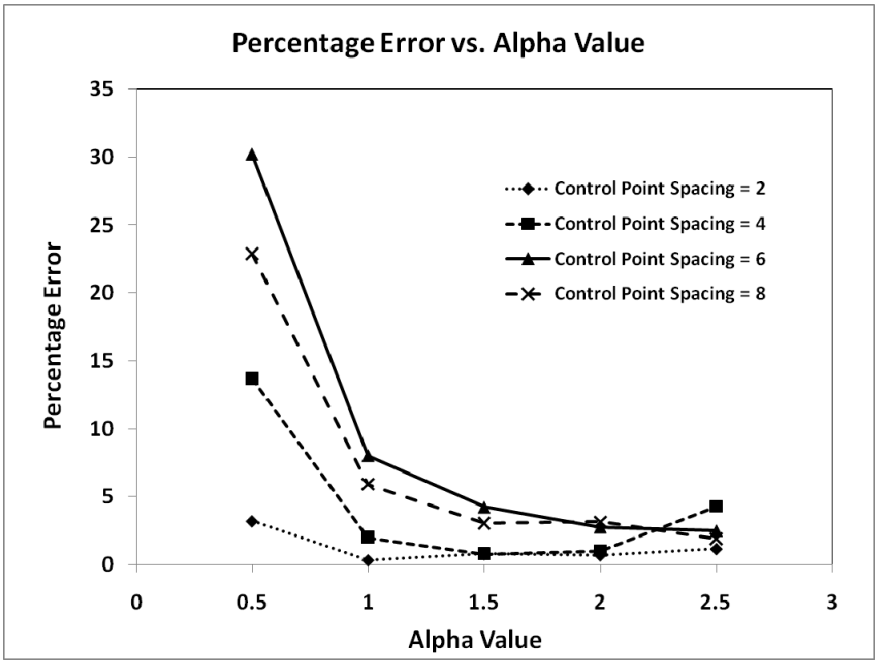

Figure 10.1: Interpolation error as a function of the parameter alpha

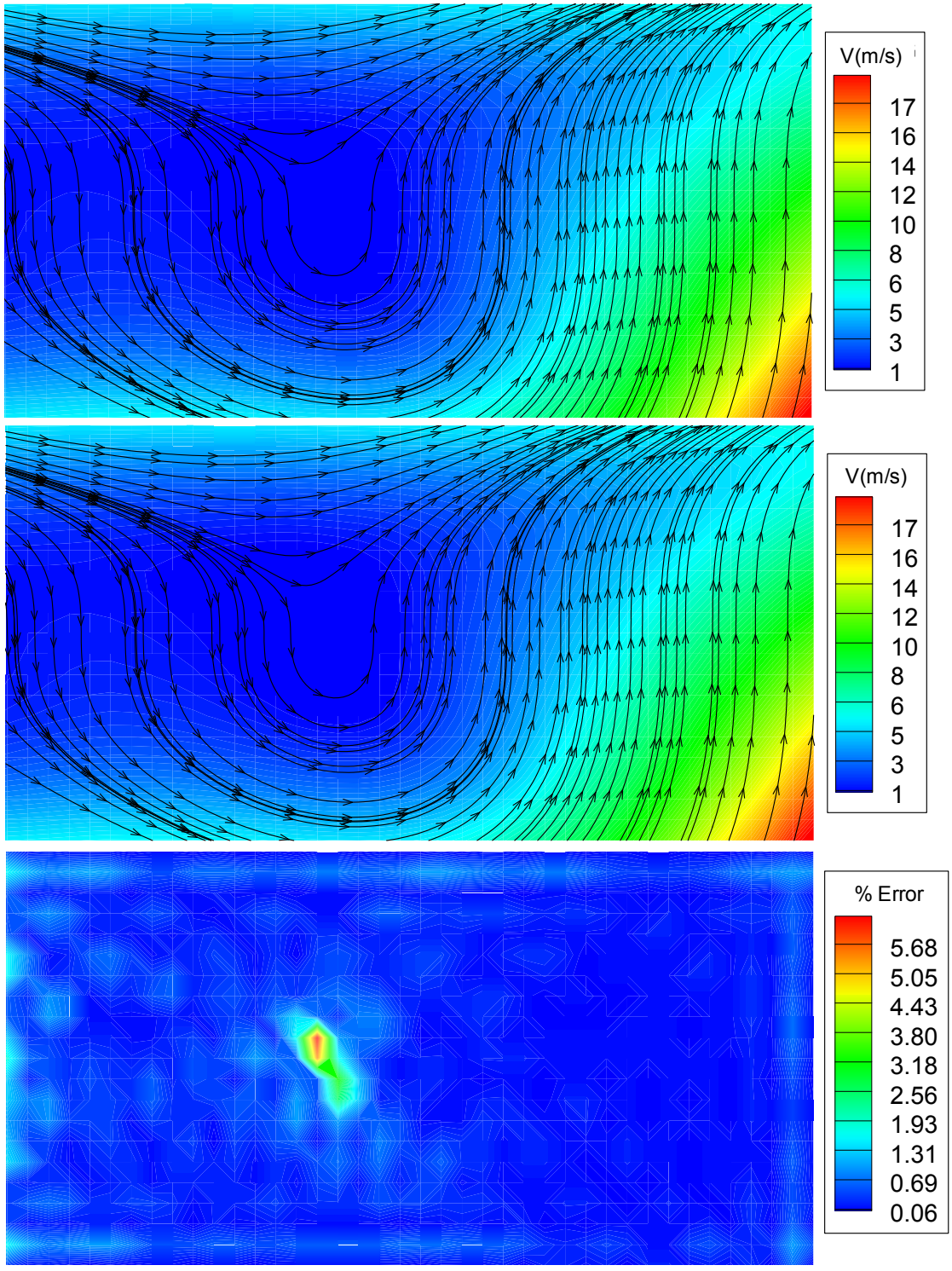

Figure 10.2: Comparison of the original velocity field (top), and the interpolated field with a control point spacing of 2. The average error is below 1%, with the maximum error of 5% occurring at the stagnation point.

Figure 10.2 shows a comparison of the original velocity field (with streamtraces), and the DFI model with a control point spacing of 2 and an α value of 1.5. The error between the interpolated and original velocity field was negligible except in the center of the velocity field where the peak error was about 6 %. Table 10.1 shows a comparison of the DFI and thin plate splines (TPS) techniques, respectively. At a control point spacing of 2, the root mean squared (RMS) error of TPS was comparable to the DFI model. However, this error increased rapidly for TPS as the data available for interpolation became sparse with increasing spacing between the control points.

Table 10.1: Percent RMS error comparison between Thin Plate Splines and Divergence Free Splines (α = 1.1)

Control Point Spacing	**TPS RMS % Error**	**DFI RMS % Error**
2	0.13	0.32
4	1.42	0.77
6	7.72	4.2
8	15.82	3.04

10.2.2 Validation Test Case #2: Driven Cavity Problem

Figure 10.3 shows the percentage RMS interpolation error as a function of α for control point spacing ranging from 2-6 (grid size: 15x15 – 5x5 respectively). Since the original CFD simulation was performed on a grid of 31x31, a control point spacing of 8 could not be used. The resulting grid size was too small (3 x 3) and insufficient for reconstructing the velocity field. Table 10.2 shows a comparison between TPS and DFI model for the driven cavity problem. Figure 10.4, Figure 10.5, and Figure 10.6 show the comparison of the interpolated velocity field, divergence, and through plane vorticity

contour maps at control point spacing of 2 and 6, with the original CFD velocity field. Please note that the size of the control point grid and the measurement grid was the same.

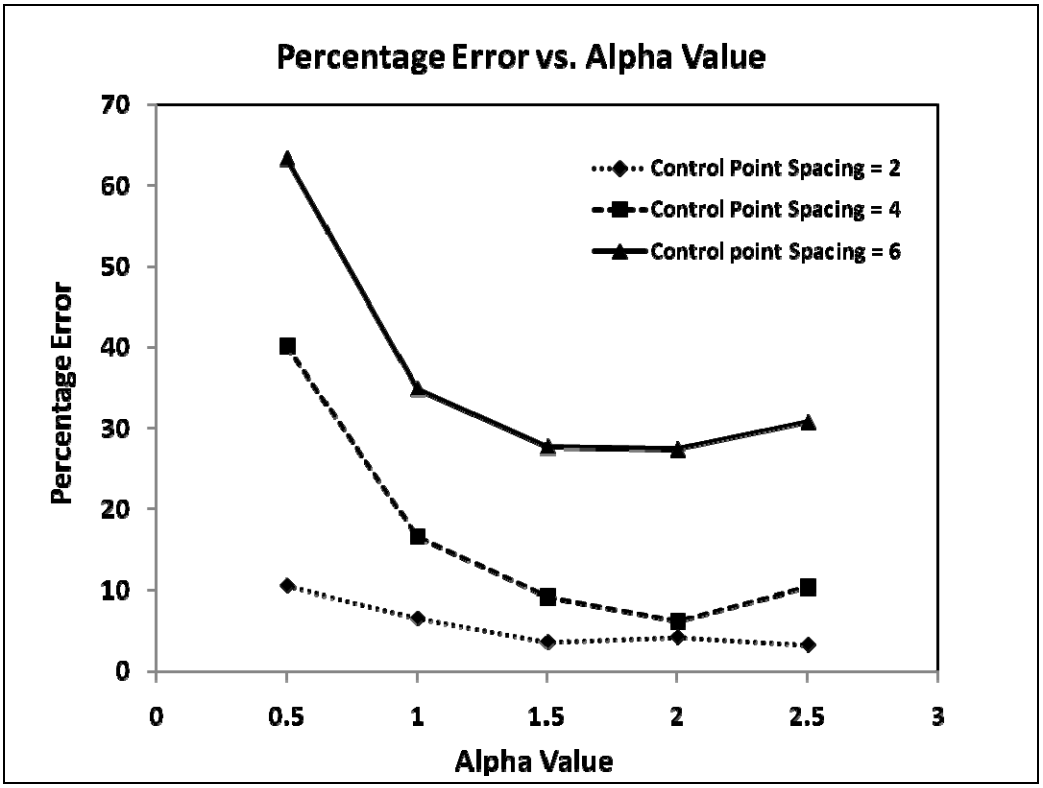

Figure 10.3: Interpolation error as a function of alpha for control point spacing for the driven cavity test case

Table 10.2: Percent RMS interpolation error comparison between TPS and DFI for the driven cavity problem

Control Point spacing	TPS RMS % Error	DFI RMS % Error
2	2.3	3.6
4	18.7	6.2
6	28.23	20.4

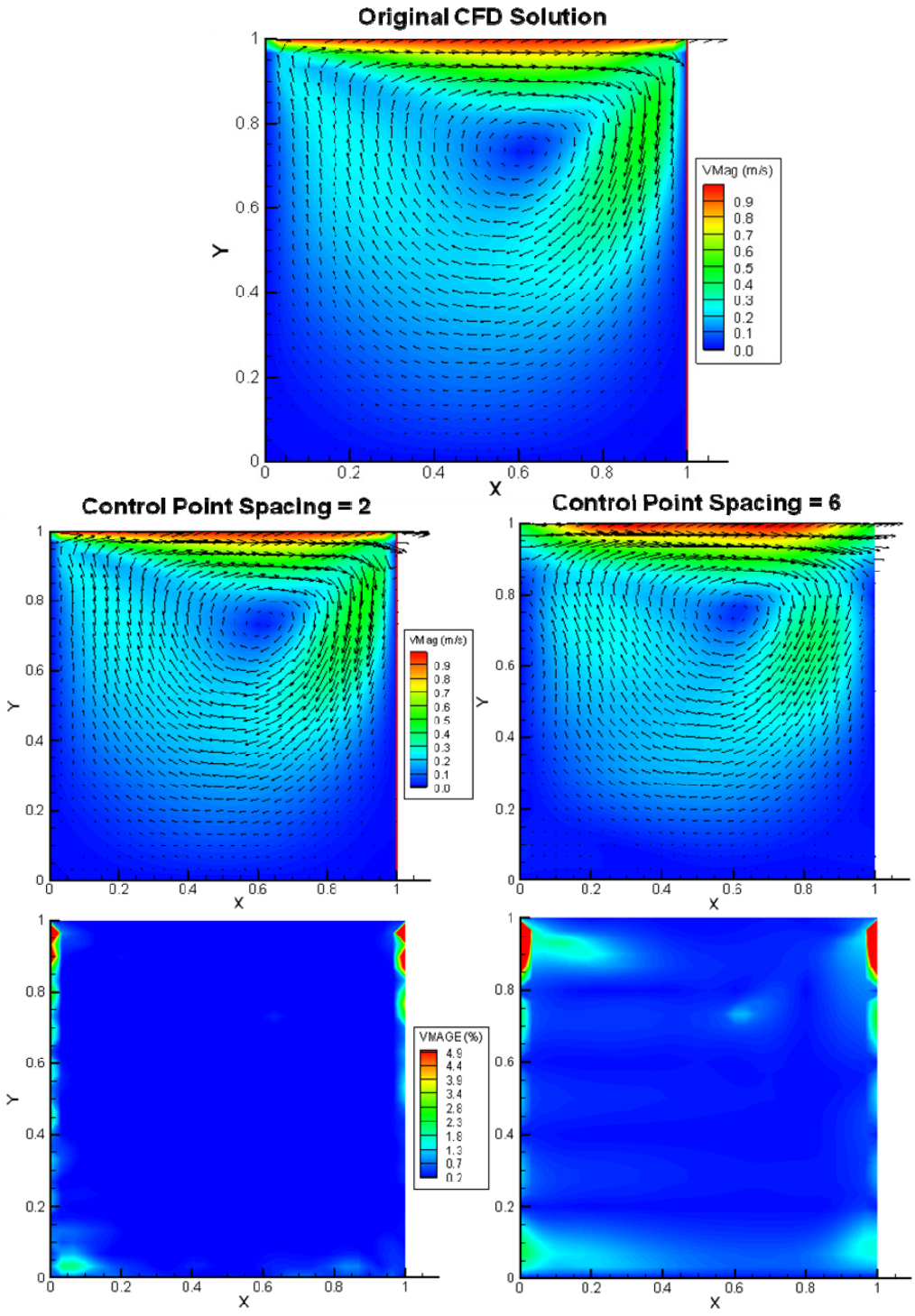

Figure 10.4: Comparison of velocity fields reconstructed from a control point spacing of 2 (left column) and 6 (right column) with the original velocity field (top). The bottom row depicts the RMS percentage error contour plot

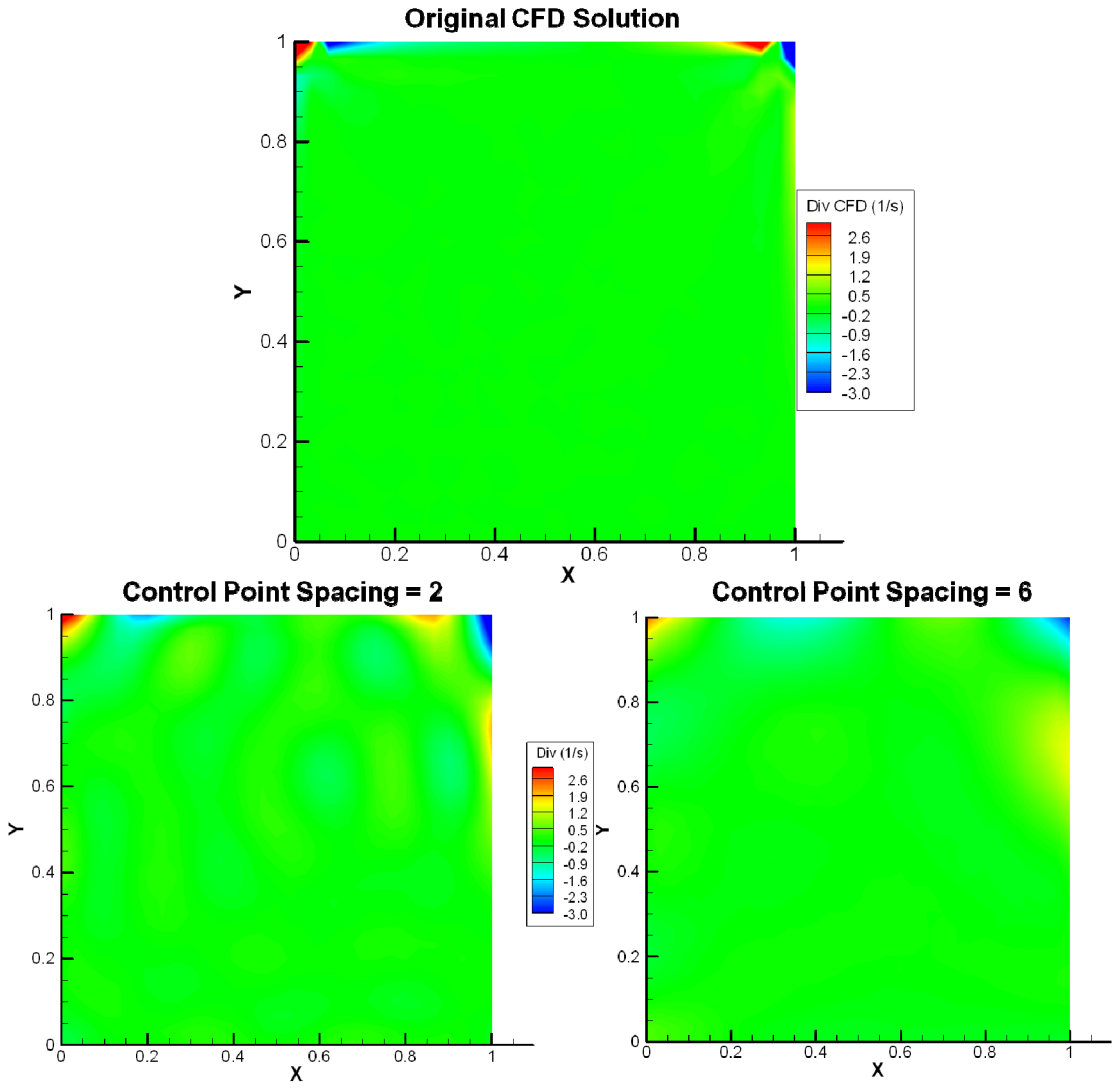

Figure 10.5: Divergence contour plots of the original CFD simulation, and the ones reconstructed with a uniform control point spacing of 2 and 6. The same color scheme is used in all plots ranging from -3.0 (blue) to 2.6 (red). The dominant green color demonstrates that, as expected, the divergence is zero (or close to zero) for both control point spacings. .

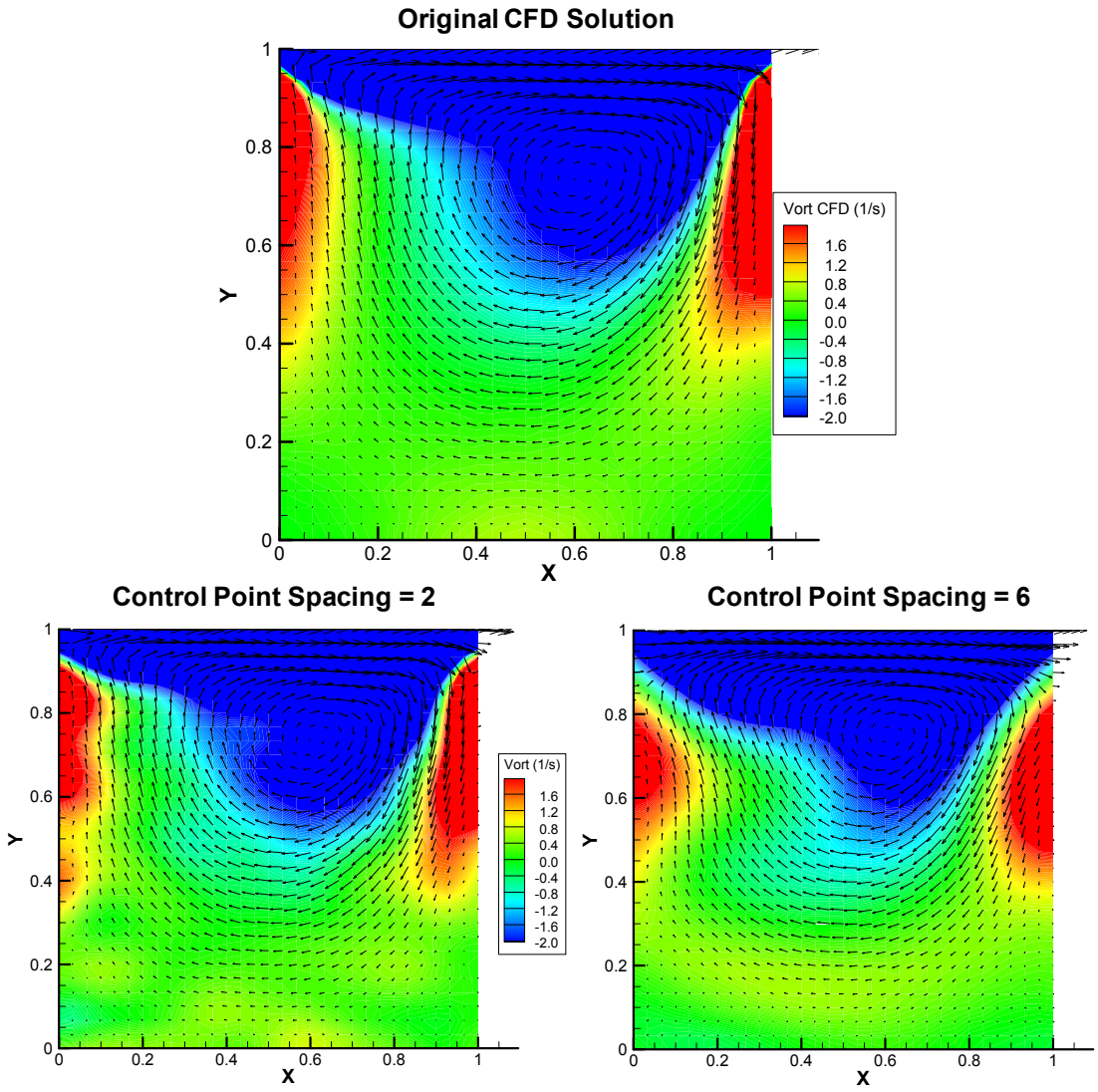

Figure 10.6: Through plane vorticity contour plots comparing the secondary flow structures of the original CFD solution, and those reconstructed using divergence free splines at a control point spacing of 2 and 6. The dominant flow structures are preserved, even with a lower number of control points

There was an excellent qualitative and quantitative match between the original velocity field and the one reconstructed using the DFI model ($\alpha = 1.1$). Dominant primary and secondary flow structures were preserved, irrespective of the control point spacing. In the presented divergence free test case, the velocities were interpolated to a full grid size of 31 x 31 (original CFD simulation) using a control point spacing of 2 (grid size of 15 x 15) and 6 (grid size of 5 x 5). The errors increased as the number of data points available for the interpolation reduced, but compared to the TPS approach, they were still lower. Figure 10.7 shows the sensitivity of the DFI technique to noise. Noisy images were created by systematically adding Gaussian white noise to each velocity component. High SNR corresponded to low noise and low SNR corresponded to high noise in the figure.

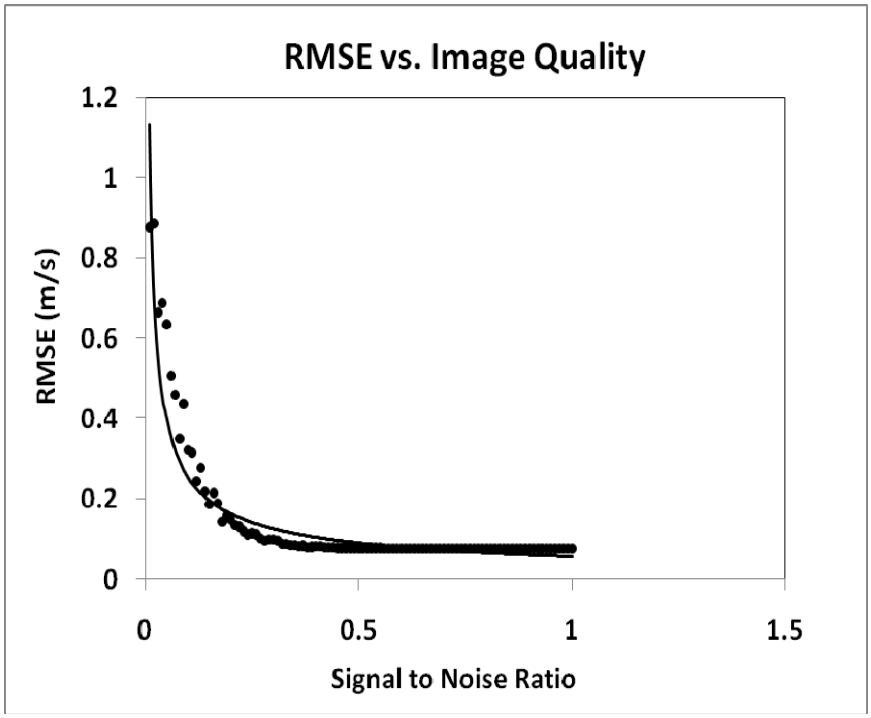

Figure 10.7: Relationship between root mean squared error and image quality for the

10.2.3 Validation Test Case #3: 3D CFD

The primary objective of this test case was to ensure that the values of α used in the 3D DFI model were comparable to the values used in the 2D case. Contrary to previous test cases, the control point grid here was of lower resolution compared to the measurement grid. Every 2nd fluid node in each direction (down-sample factor of 2) from the original CFD simulation was retained as a measurement grid to initialize the DFI model, while the control grid spacing was varied from 2 - 5. Figure 10.8 shows the plot of the RMSE percent error as a function of α for different control point grid sizes. Similar to the 2D case, the errors increased with control point spacing, although there were no significant differences for α-values between 1 and 2.

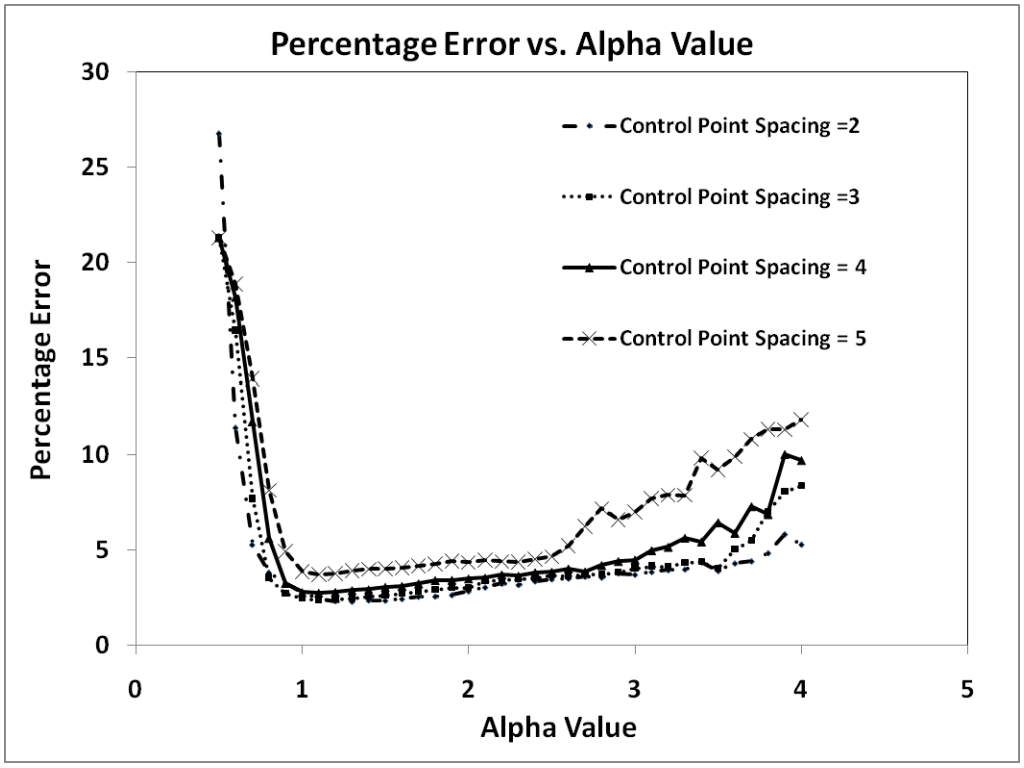

Figure 10.8: RMSE percentage error as a function of alpha for different control point sizes

Control grids with large spacing significantly reduce the computational time, as lesser number of interpolation coefficients have to be estimated. The improvement in computational speed achievable can be appreciated by the fact that for '**N**' control points in each direction; $3\mathbf{N}^3$ linear equations have to be solved, requiring a matrix inversion of size $3\mathbf{N}^3$ x $3\mathbf{N}^3$. This phenomenon becomes critical when large datasets need to be interpolated in 3D. In such situations placing control points at every measurement location puts a tremendous strain on computational resources available for a relatively small decrease in error. Based on this study, a uniform constant control grid comprising of the original grid down-sampled by a factor of 5 and an α value of 1.1 x the average control point spacing was determined to be optimum value for 3D interpolation.

10.2.4 Validation Test Case #4: In vitro PC MRI

High resolution PC MRI acquired as part of specific aim 1 on CHOA007 was used for the final validation test case. Recall that this dataset comprised of 50 PC MRI slices acquired with velocity encoding in all three directions. In the first step of the validation, only 25 out of the 50 slices were retained for initializing the DFI model. More slices were not discarded, since the LPA was visible only in 3 slices. The 25 discarded slices served as experimental control. The DFI model was then used to interpolate the velocities at the locations of the discarded slices, and the errors between interpolated velocities and the original velocities were evaluated.

In the second test case, all the slices were retained (voxel size: 0.4 x 0.4 x 2 mm^3) and the entire dataset was interpolated to achieve an isotropic voxel size of 0.4 x 0.4 x 0.4 mm^3. The entire velocity field was then quantitatively and qualitatively compared to a

CFD simulation.

10.2.4.1 In Vitro PC MRI Test Scenario #1

Table 10.3 depicts the RMS error values for each component of the velocity, the velocity magnitude, as well as the overall error of the DFI model. Since a suitable comparison was absent, the MRI reproducibility error for the exact same model was used for comparison. Figure 10.9 depicts the same error metrics expressed as percentages of the mean velocities. The DFI model interpolation errors were comparable to the 3D PC MRI reproducibility error. Statistically there were no differences between the two groups. Although lower errors in cm/s were observed for the DFI model (as evident in the table), the percentage errors were similar in both groups. This is because the normalized error values were calculated for only 25 slices within the DFI group, while the MRI reproducibility error was calculated for all 50 slices. This study demonstrated that the DFI model can be used for interpolating 3D velocity fields from PC MRI with great accuracy maintaining the physical properties of blood flow at the same time.

Table 10.3: DFI reconstruction error evaluated for each velocity component. The mean velocity interpolation error using the DFI technique was comparable to the MRI reproducibility error. The data is expressed as mean ± standard error

Variable	**MRI Reproducibility Error (cm/s)**	**DFI Reconstruction Error (cm/s)**
X Velocity	1.84 ± 0.23	1.4 ± 0.22
Y Velocity	1.34 ± 0.24	0.75 ± 0.15
Z Velocity	1.38 ± 0.21	1.63 ± 0.3
Velocity Magnitude	2.05 ± 0.33	2.47 ± 0.47
Overall RMS Error	3.06 ± 0.25	2.51 ± 0.34

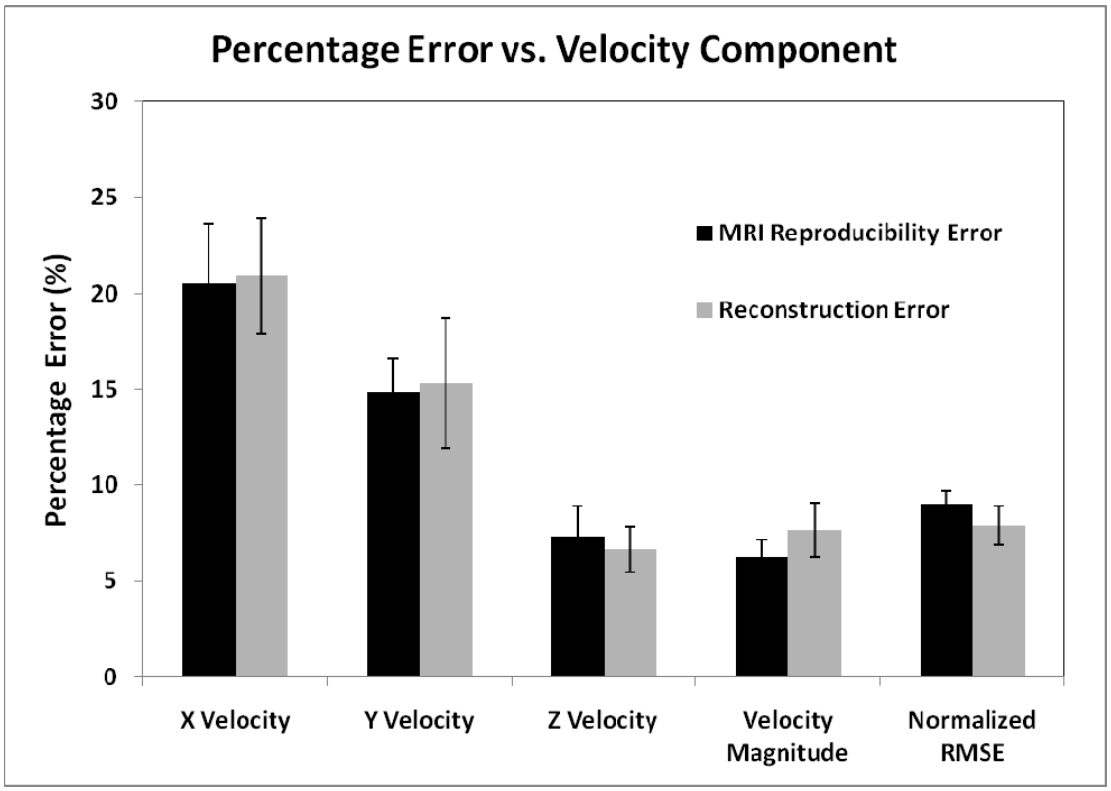

Figure 10.9: Percentage error associated with the DFI reconstruction for the 3 velocity components, the velocity magnitude and the overall root mean squared error compared to the MRI Reproducibility error. There were no significant differences between the two groups

10.2.4.2 In Vitro PC MRI Test Scenario #2

Table 10.4 shows a comparison of velocities, energy dissipation, and absolute divergence errors for the CFD simulation, un-interpolated MRI measurements, ACGI velocity field reconstruction, and the DFI velocity field reconstruction respectively. Table 10.4 also shows the error values for all three cases using the CFD simulation as a control. Energy dissipation and absolute divergence errors were not evaluated for the MRI measurements as the voxel sizes were not isotropic. A uniform grid size was required in

order to evaluate the derivatives accurately in the energy dissipation equation.

Figure 10.10 shows the percentage errors for the MRI measurements, and the reconstruction errors associated with the ACGI and DFI reconstruction techniques respectively using CFD as the reference standard. For a qualitative comparison, a representative sagittal slice through the model was extracted, and velocity magnitudes, energy dissipation, and divergence were displayed as color contour plots. Figure 10.11 shows the location where the slice was acquired with respect to the TCPC geometry. The qualitative contour plots are shown as part of Figure 10.12-Figure 10.14.

Table 10.4: Comparison of mean velocities, velocity errors, energy dissipation, and the divergence error between CFD simulations, MRI measurements, ACGI reconstruction, and the DFI reconstruction. For the error values, the CFD solution was used as control. The data is expressed as mean ± standard error

Variable	**CFD**	**MRI**	**ACGI**	**DFI**
X Velocity (cm/s)	5.67± 0.49	7.67 ± 0.34	7.5 ± 0.33	6.6 ± 0.32
Y Velocity (cm/s)	4.37 ± 0.4	6 ± 0.43	5.98 ± 0.42	5.3 ± 0.39
Z Velocity (cm/s)	23.9 ± 0.46	29.43 ± 0.44	27.54 ± 0.43	26.37 ± 0.48
Magnitude (cm/s)	27.73 ± 0.26	33.73 ± 0.2	31.72 ±0.2	30.11 ± 0.19
X Error (cm/s)	0 ± 0	3.76 ± 0.21	3.67 ± 0.21	3.12 ± 0.19
Y Error (cm/s)	0 ± 0	2.07 ± 0.13	2.09 ± 0.14	1.68 ± 0.13
Z Error (cm/s)	0 ± 0	4 ± 0.12	3.6 ± 0.13	2.47 ± 0.1
Magnitude error (cm/s)	0 ± 0	5.03 ± 0.16	4.54 ± 0.16	3.35 ± 0.15
Dissipation ($1/s^2$)	48.97 ± 4	N/A	243.18 ± 18.73	37.50 ± 16.5
Divergence (1/s)	2.89 ± 0.14	N/A	50.70 ± 2.56	0.024 ± 0.011

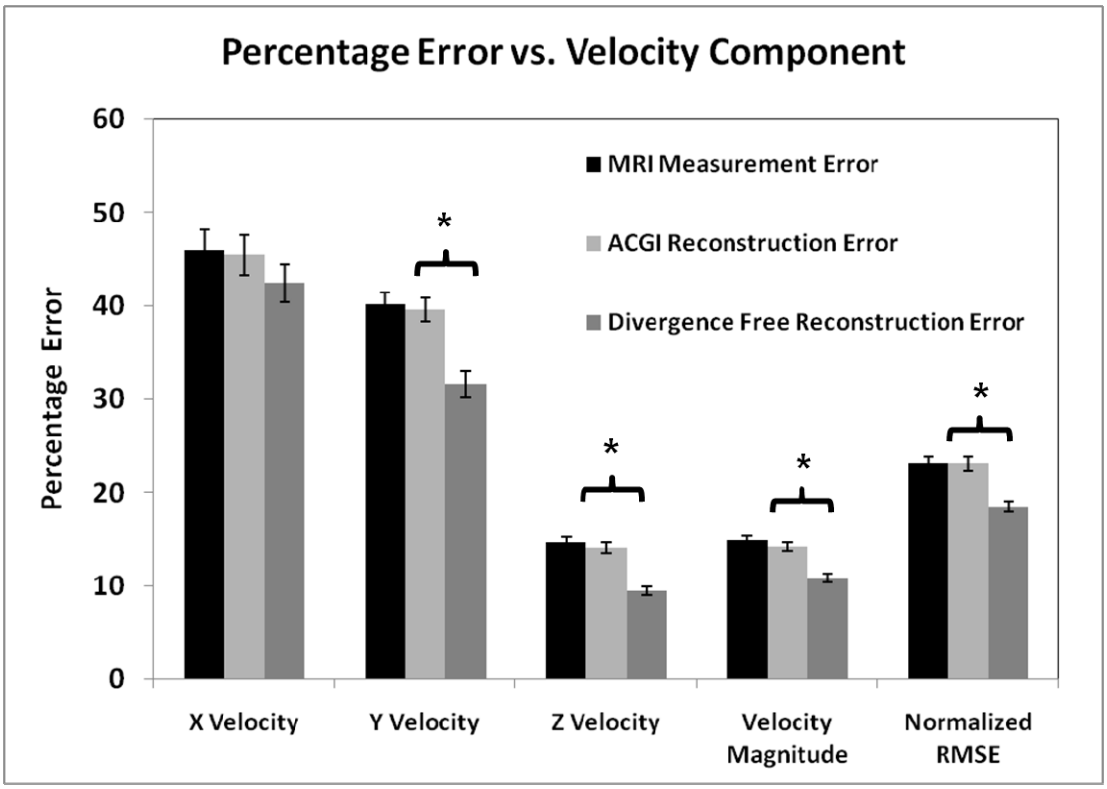

Figure 10.10: Percentage error comparing, X velocity, Y velocity, Z velocity, magnitude and the normalized RMSE respectively. Statistically significant results were obtained for all cases except the X velocity

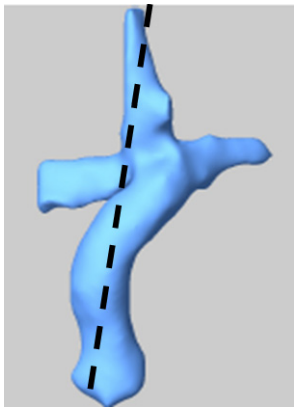

Figure 10.11: Location where the slice for the qualitative comparison was obtained

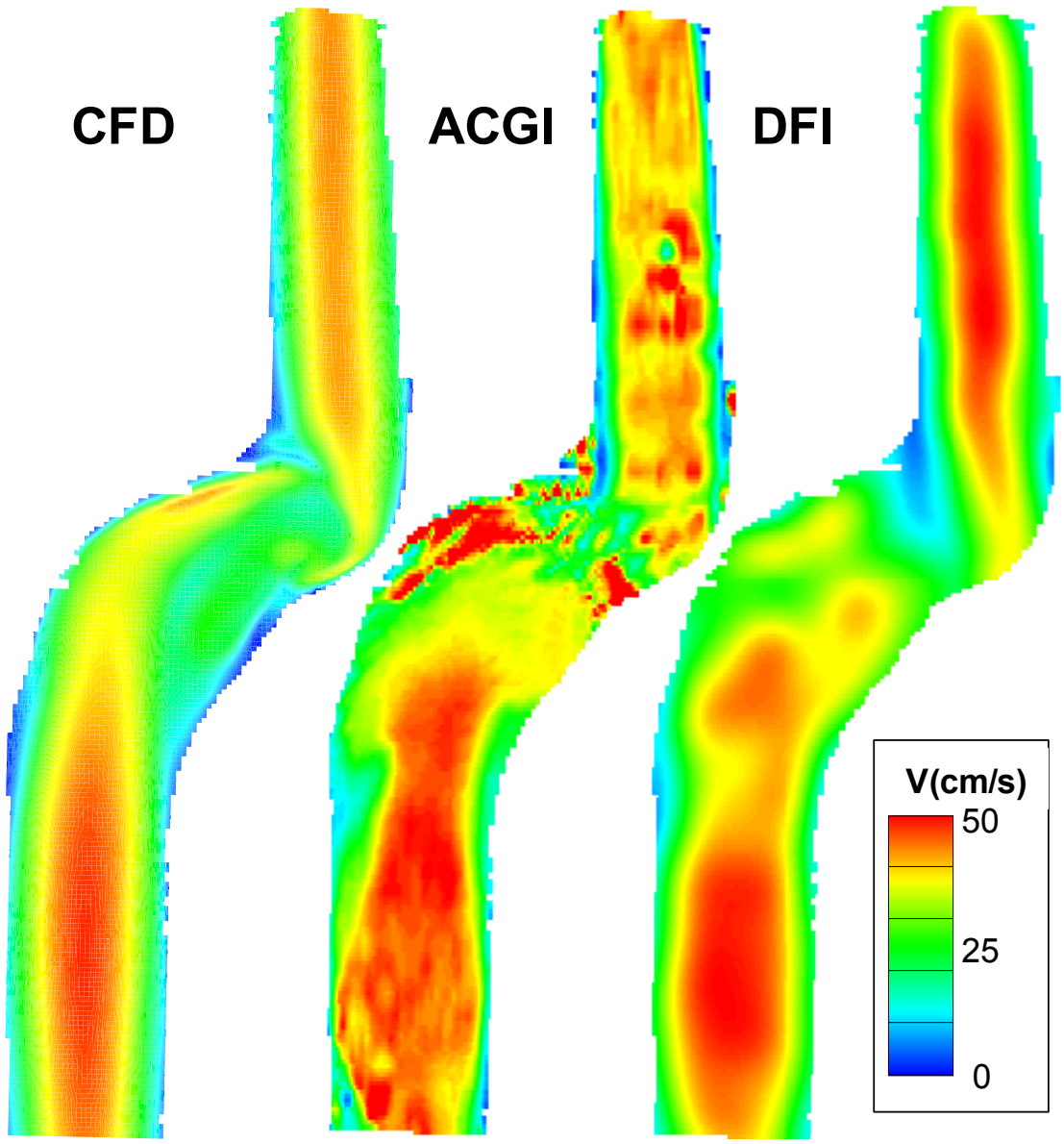

Figure 10.12: Comparison of velocity magnitude maps between the CFD simulation, ACGI reconstruction, and the DFI reconstruction. Notice that the DFI reconstruction is significantly smoother than the ACGI reconstruction, and resembles the CFD reconstruction a lot more. The red color in the contour map is the maximum velocity observed in the CFD simulation.

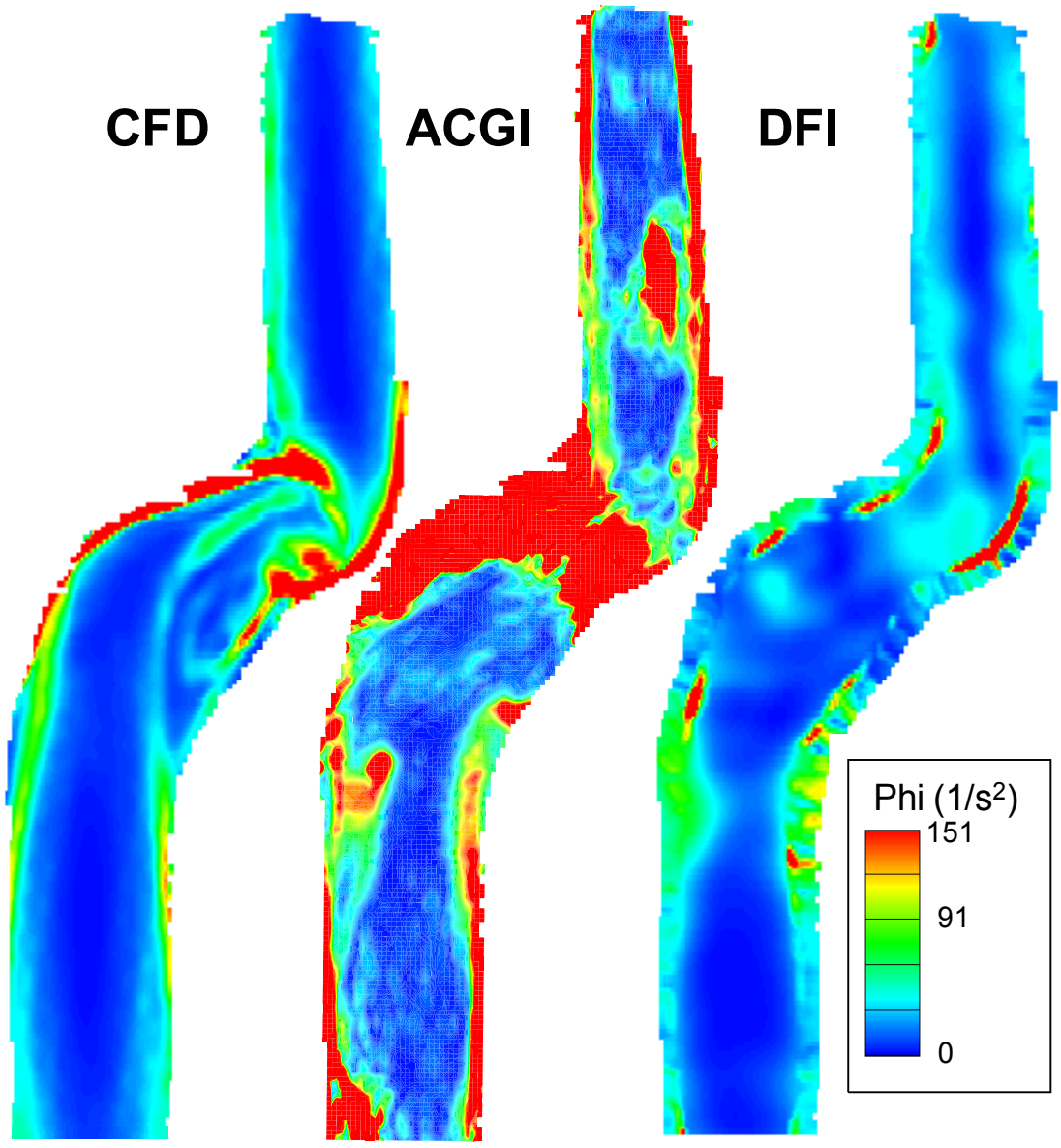

Figure 10.13: Comparison of viscous dissipation energy loss evaluated for the CFD, ACGI, and the DFI reconstructions respectively. The red color in the contour map corresponds to the maximum dissipation observed in the CFD simulation. Notice that ACGI gives dissipation values that are significantly higher than the CFD, while those for DFI are similar to CFD. Furthermore, certain shear layers observed in CFD along the walls towards the center of the connection are observed in the DFI reconstruction as well

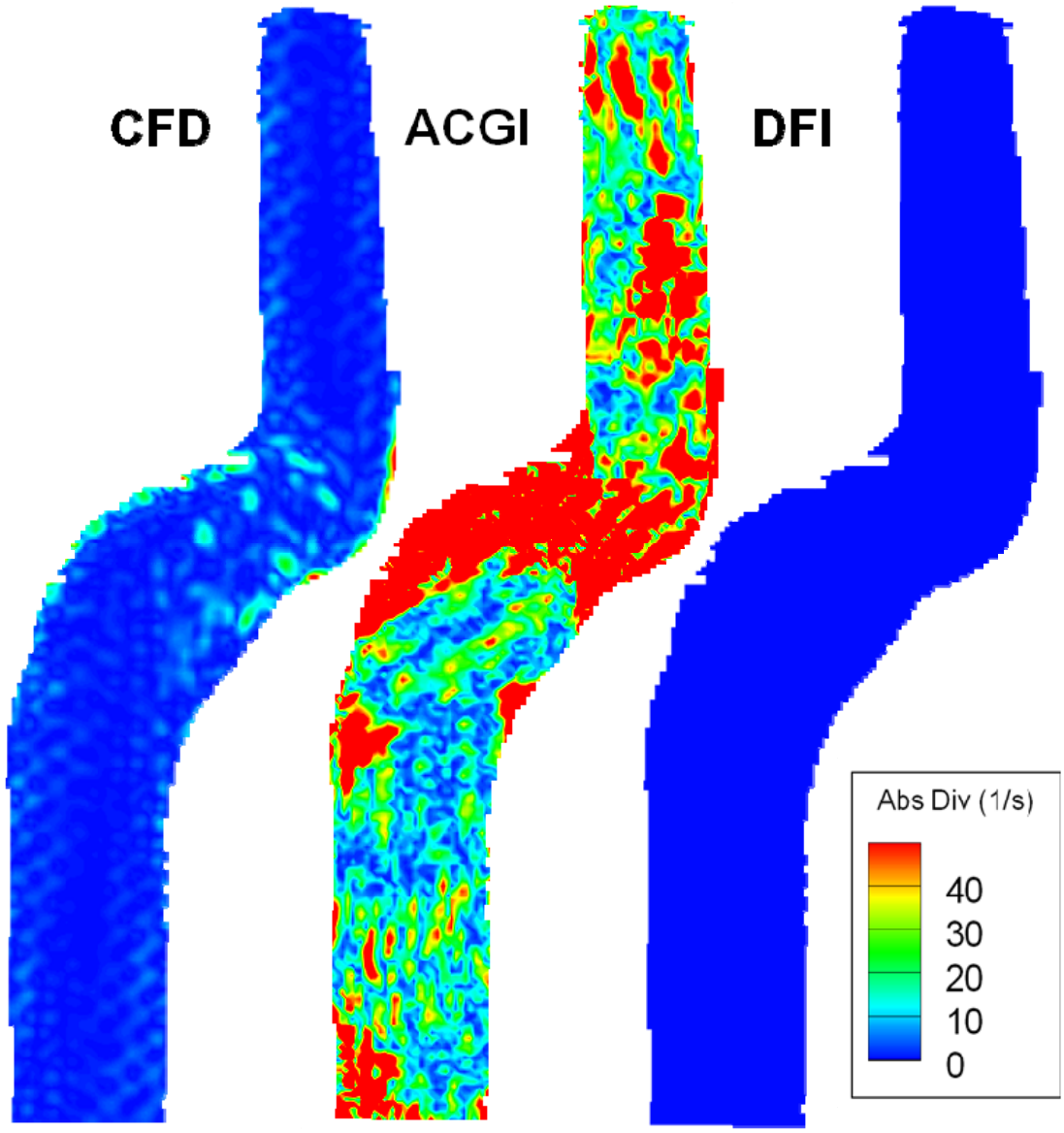

Figure 10.14: Absolute divergence plots comparing CFD, ACGI, and DFI respectively. The red color in the contour map corresponds to the maximum divergence error observed in the CFD simulation. The divergence error associated with ACGI is significantly higher than CFD and DFI techniques respectively, highlighting that the physical property of incompressibility is not preserved in the ACGI interpolation process.

10.2.5 Discussion: Divergence Free Interpolation

Several clinical applications require the visualization of blood flow velocity fields *in vivo*. PC MRI is one attractive clinical imaging modality, as it allows for the measurement of these *in vivo* velocity fields non-invasively and with reasonable accuracy and repeatability. However, the spatial accuracy that is typically used in clinical scans is not high enough in order to accurately and reliably perform fluid dynamic analyses to extract clinically relevant information from the data, and high resolution PC MRI scans typically require prohibitively long scan times and/or high magnetic fields. Interpolation strategies have thus been used to increase spatial resolution a posteriori. Methods that are dominant in the literature are primarily scalar in nature, and are not effective for interpolating vector fields that are governed by the laws of physics. To address this limitation, a novel vector field interpolation strategy was developed in this thesis that preserves the incompressible property of blood by ensuring that the velocity field has zero divergence. This approach was based on the idea of divergence free splines introduced first by Narcowich and Ward[173], and developed further by Lowitzch[172]. These splines were further optimized and improved for the realistic application to PC MRI data.

In the first half of this chapter we presented a thorough, qualitative and quantitative validation of the proposed DFI technique. A comprehensive approach was undertaken utilizing a variety of test cases in order to demonstrate the efficacy of DFI for interpolating 3D velocity fields. The results highlighted the strength of utilizing an interpolation strategy based on fluid mechanics' principles, for accurately reconstructing velocity fields from sparsely sampled data. The validation exercise was performed using idealized datasets obtained from analytical test functions and CFD simulations, as well as

PC MRI datasets acquired using *in vitro* experiments. DFI was first compared to TPS for the 2D case studies, and then to ACGI for the 3D PC MRI studies.

Quantitative validation using the analytical test case revealed that the DFI technique was able to accurately interpolate the data despite significant down sampling of the test dataset. By choosing an appropriate value for the interpolation parameter α, the differences in error between the dataset that was down-sampled to $1/8^{th}$ of the original size (in each direction) and the one down-sampled to ½ of the original size (in each direction) was minimal. Qualitatively, the DFI technique was able to perfectly reconstruct the velocity field with a negligible normalized RMSE of 3% for the lowest sampled dataset. Conversely, errors associated with the TPS technique increased significantly as the number of data points available for the interpolation reduced.

Contrary to the previous case, the driven cavity problem does not have a closed form analytical solution. Hence this test case provided a more challenging scenario for testing the DFI technique. When compared qualitatively to the original dataset, there were no visual differences in the velocity fields reconstructed using ½ and $1/6^{th}$ the number of data points in each direction. The vorticity contour plots revealed that the dominant flow structures were preserved for the two extreme cases as the central recirculation region was accurately resolved. Quantitatively, the errors increased with control point spacing, although the increase was much smaller compared to the TPS approach. The maximum RMS interpolation error was 20%, which was observed for the case down-sampled to $1/6^{th}$ of the original matrix size, which was still lower compared to the TPS technique (28%).

3D interpolation of datasets with large measurement samples requires significant

computational resources. In order to reduce the computational time, an alternative implementation of DFI was described in Chapter 6. In this approach, the interpolation control points were not placed exactly on the measurement nodes. Instead, the control point grid and the measurement nodes were considered as two separate entities. A low resolution control grid was used for determining the parameters of the interpolation model, subject to the constraint that the least squared error was minimized for the velocities evaluated at the measurement locations. Such an approach has been successful in several previous applications including the ACGI[175], where the interpolating function was evaluated on control grids of lower resolution. Figure 10.8 showed that the difference in interpolation error between the velocity fields reconstructed using a control point spacing of 2, 3, 4, and 5 were minimal for α-values between 1 and 1.5. Using such a model significantly reduced the computational time, for 3D interpolation of PC MRI data.

The primary motivation behind developing the DFI technique was to analyze the 3D hemodynamics within the TCPC using PC MRI. Hence, the final aspect of the validation process was to evaluate the performance of the DFI technique on PC MRI datasets. In the first step, the interpolation error was quantified using PC MRI itself as the experimental control. The results demonstrated encouraging results with RMS error values less than 10%, which were comparable to the MRI reproducibility error. However, for the X and Y components of the velocities, the errors were higher than 10%. This was also true for the MRI reproducibility error. There are several explanations for this: a) the noisy nature of the PC MRI acquisitions; b) low magnitude nature of the transverse velocities; c) background phase error; and d) interpolation error. Some of these are limitations of the PC MRI acquisitions themselves. Consequently, the error was

systematically compounded as the property of incompressibility does not apply to noise and background phase error. For this reason, another validation was performed, where a CFD simulation conducted on an identical TCPC geometry was used as control.

Quantitatively and qualitatively the comparison of the DFI technique with CFD was excellent. The velocity fields reconstructed using the DFI technique had significantly lower errors compared to ACGI. Interestingly, the average DFI reconstruction error was also lower than the un-interpolated PC MRI -CFD error. This underscores an important feature of the DFI technique: denoising. Since noise is a critical issue in 3D PC MRI acquisitions, the DFI technique also has the potential application for use as a filter. Comparatively, the ACGI reconstruction error did not lower the PC MRI-CFD error, since it is an image-based interpolation technique, and inherently cannot remove the error in the PC MR images themselves.

One of the important clinically relevant parameters that can be evaluated from 3D PC MRI is viscous dissipation energy loss. This parameter is very much dependent upon the quality of the velocity field reconstructed. The DFI technique was significantly better than the ACGI technique for the evaluation of the viscous dissipation energy loss. This was evident from Figure 10.13 and Table 10.4, where the average dissipation evaluated on 182 slices extracted from the DFI, was much closer in magnitude to CFD than ACGI. Furthermore, the shear layers found in the center of the connection were resolved by the DFI reconstruction technique. Conversely, an abnormally high shear region was observed in the ACGI reconstruction. This was because data points were missing in the PC MRI acquisition, which artificially inflated the dissipation error. This contributed towards the abnormally large dissipation evaluated by the ACGI technique. The DFI technique on the

other hand recognized that the velocities in those regions were incorrect, and interpolated in those regions using velocities that were physically more accurate.

Although, the proposed DFI technique was implemented on a stack of 3 component PC MRI slices, it can easily be extended to newer sequences such as those proposed by Markl etl al[92, 195]. These are sequences where PC MRI can be acquired over a 3D volume with isotropic voxel sizes. However, one of the major drawbacks associated with the clinical application of these sequences, are the prolonged acquisition times with acquiring such datasets. This can be circumvented using a sparsely sampled dataset, and then interpolating them using the DFI technique. The robustness of the DFI technique ensures that it could be used seamlessly in conjunction with emerging technologies in MR Imaging.

10.2.6 Conclusion: Divergence Free Interpolation

In this section, the validation of the DFI technique for reconstructing 3D fluid flow fields was presented. The results confirmed that the DFI technique can be used to reconstruct 3D velocity fields accurately for a wide variety of incompressible flows. The computational time for determining the interpolation parameters can be reduced using a lesser number of control point grid nodes, in order to facilitate the interpolation of large sets of 3D PC MRI data. Energy losses evaluated from the DFI velocity fields were comparable in magnitude to those from CFD simulations, which established the validity of the DFI approach for quantifying energy losses directly from PC MRI. Finally, the interpolation guaranteed zero divergence of the velocity field, highlighting the physical accuracy of the reconstruction method. In the following sections, the DFI technique is

directly applied on *in vivo* datasets for characterizing the detailed 4D hemodynamics within the TCPC.

10.3 *In Vivo* TCPC Flow Analysis

Recall from Chapter 2 that the primary hypothesis of specific aim 3 was: *Significant differences in flow structures exist between intraatrial and extracardiac Fontan geometries and these differences can be quantified using 3D PC MRI.* To test this hypothesis, a comparison of flow fields between intraatrial and extracardiac TCPCs was performed and the results are presented in this section. Viscous dissipation power losses, hepatic flow splits, vortex sizes, and particle transit times were the quantitative parameters used for comparing the two Fontan types. 3D pulsatile streamtraces were extracted from the velocity fields, and then used for elucidating the qualitative differences in flow structures between intraatrial and extracardiac TCPCs.

10.3.1 DFI for reconstructing 3D PC MRI velocity fields

Figure 10.15 and Figure 10.16 show a comparison of velocity fields obtained from PC MRI measurements and the DFI reconstructions respectively. The flow fields illustrate the effectiveness of the DFI technique for velocity field reconstruction. The secondary flow structures such as the swirl observed in Figure 10.16, were accurately resolved using the DFI technique. Furthermore, the velocity magnitudes match perfectly, except along the vessel borders where noise is evident in the actual PC MRI measurement. The primary direction of the flow jet in the IVC (Figure 10.15) is preserved, and noise vectors along the vessel walls were correctly removed and smoothened out.

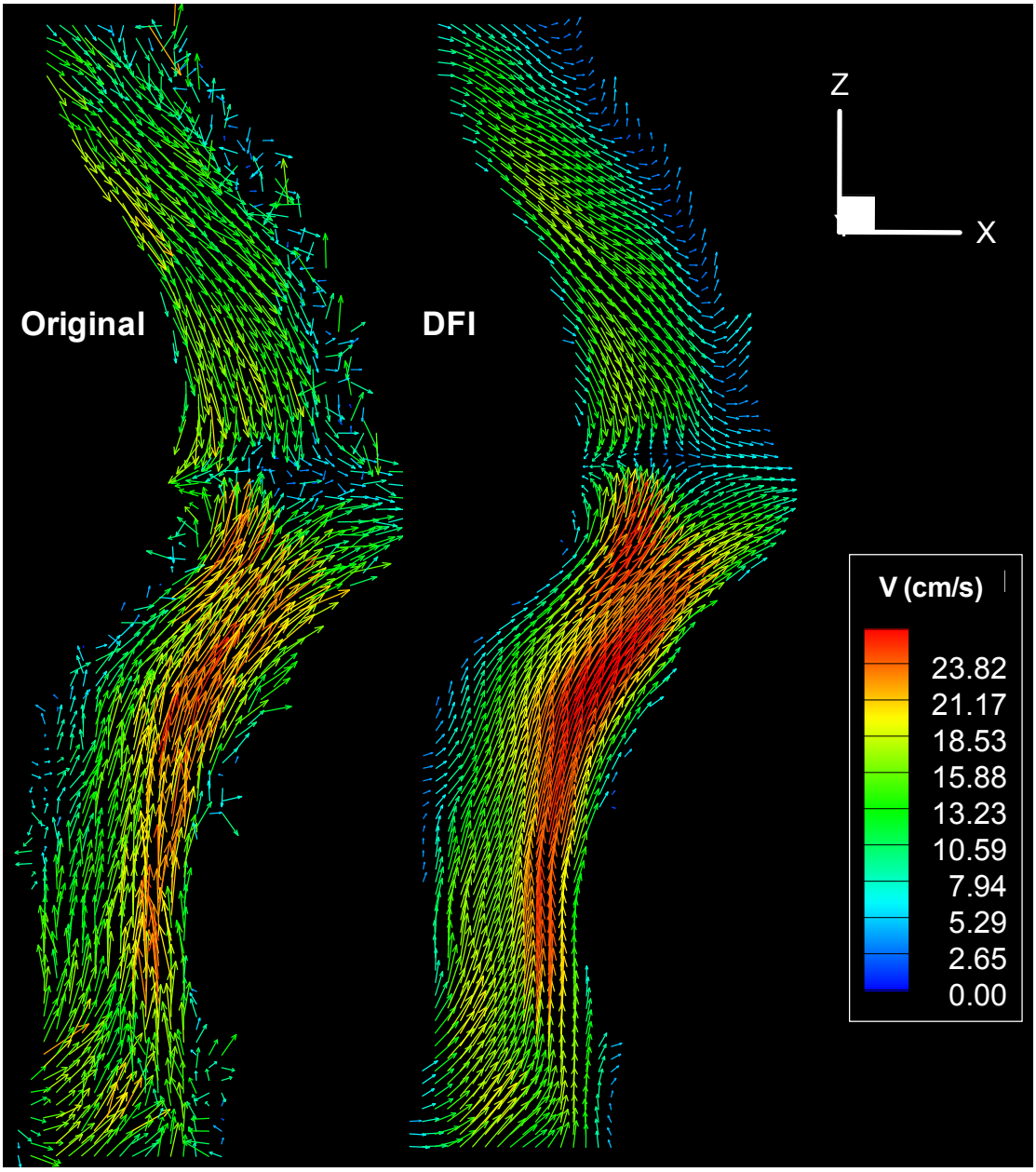

Figure 10.15: Comparison of velocity fields extracted from the original PC MRI measurements, and the DFI reconstruction at the central plane of the coronal stack acquired on CHOP091. The location of the IVC jet-like pattern is accurately resolved, while errant noise vectors are correctly filtered out

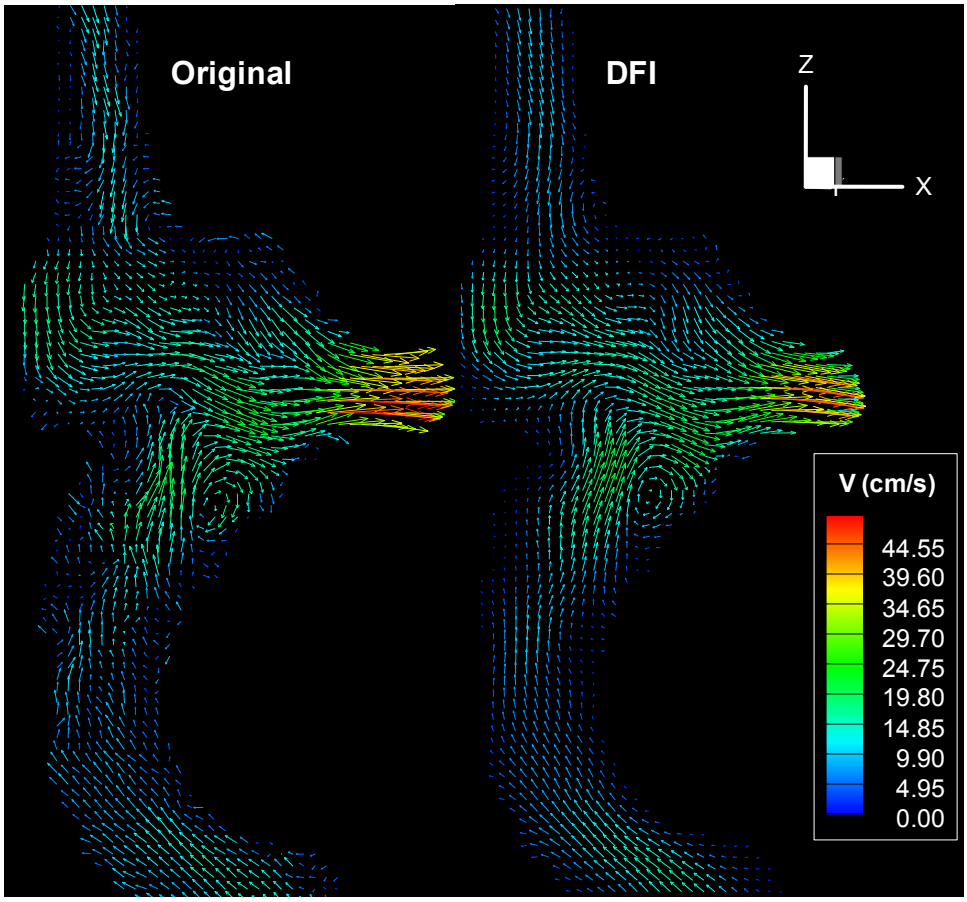

Figure 10.16: Comparison of velocity fields extracted from the PC MRI measurements and those reconstructed using the DFI technique for a central coronal slice acquired from CHOP_M1. There were no artifacts that were evident in the interpolation model. Notice that the vortex in the region where the IVC connected to the SVC was accurately resolved using the DFI technique

10.3.2 In vivo Intraatrial vs. Extracardiac Comparison

In this section, results of the 4D hemodynamics reconstructed from 20 patients with intraatrial and extracardiac TCPCs are presented. First, the hemodynamics are analyzed for each patient selected in the study. 3D flow streamtraces for each patient as well as quantitative metrics (power loss, IVC flow splits, vortex sizes, and particle transit times) are provided for each model. These metrics were evaluated based on the protocol

described in Chapter 6. Table 10.5 shows a clinical summary of all the patients used in the study.

Table 10.5: Clinical data of patients used for comparing the 3D hemodynamics of patients with intraatrial and extracardiac Fontan types

Model	Fontan Type	Disease	Age	BSA (m^2)
CHOP068	Intraatrial	HLHS	6	0.94
CHOP073	Intraatrial	HLHS	9	0.96
CHOP078	Intraatrial	HLHS	12	N/A
CHOP089	Extracardiac	Tricuspid Atresia	7	0.87
CHOP090	Extracardiac	Pulmonary Atresia	8	1.15
CHOP091	Extracardiac	HLHS	8	0.99
CHOP094	Intraatrial	L-Transposition, I-TGA	5	0.81
CHOP095	Extracardiac	DILV, Pulmonary Atresia	8	1.25
CHOP105	Intraatrial	HLHS,	5	0.67
CHOP115	Extracardiac	HLHS	8	N/A
CHOP125	Intracardiac conduit	HLHS	15	1.75
CHOP129	Extracardiac	DORV	5	0.771
CHOP130	Extracardiac	Tricuspid Atresia	4	0.756
CHOP132	Extracardiac	DORV	5	0.75
CHOP148	Extracardiac	DORV, HLHS	4	0.65
CHOP150	Extracardiac	VSD, RV Hypoplasia	4	0.63
CHOP_M1	Interrupted IVC, Azygous vein (extracardiac)	Dextrocardia, Heterotaxy Syndrome	4	0.6
CHB004	Intraatrial	N/A	N/A	N/A
CHB006	Intraatrial	N/A	N/A	N/A
CHB008	Intraatrial	N/A	N/A	N/A

10.3.2.1 Flow characteristics of patient specific geometries

Figure 10.17 - Figure 10.54 show 3D flow streamtraces extracted from the 3D velocity fields as well as the IVC flow split and power losses curves for all the models used in the study. The cardiac cycle chosen to display the results is the beginning of systole. For each patient, three streamtrace figures are provided. The first figure corresponds to the streamtraces color-coded by their source of origin. If the streamtrace originated from the SVC, the color is red. If the streamtrace originated from the IVC, the color is blue. The second figure corresponds to the flow streamtraces color-coded by velocity magnitude, and the third figure shows the streamtraces in black without any color-coding (for illustrating the flow structures). Streamtrace animations are provided for 4 TCPC cases and are included as an addendum to this thesis for the following patients: CHOP068, CHOP078, CHOP091, and CHOP_M1, respectively. In addition to the streamtraces, time-varying power loss and IVC flow split curves are provided for each patient as well. In order to evaluate the viscous dissipation power losses, the entire TCPC geometry was defined as the control volume, with the final coronal plane in the pulmonary arteries as the end of the control volume. For the SVC and the IVC, the control volume was determined by the first and last slice associated with the axial anatomic acquisition used in the 3D reconstruction. The flow characteristics of each TCPC model are discussed within the figure legends. The first 9 figures are associated with intraatrial geometries, while the remaining 11 are for extracardiac TCPCs.

The flow structures of intraatrials with a Hemi-Fontan (Figure 10.17-Figure 10.27) were all characterized by a vortex in the center of the connection. The direction of this vortex was in the anti-clockwise direction. The angle of the IVC anastomosis and the

presence of the Hemi-Fontan pouch were responsible for the vortex formation. The presence of large vortices in intraatrial geometries with a Hemi-Fontan connection has been shown before using *in vitro*[19] and CFD studies[17], and the overall characteristics as described by these studies were observed in our study as well. One positive consequence of this Hemi-Fontan pouch was better mixing of caval flows, which ensured that nutrients from the liver were adequately distributed to the two lungs. However, there were two drawbacks of having these vortices: a) increased particle residence time which may increase the possibility of thrombus formation; b) unstable flow environment when the cardiac output increases to exercise flow rates (2x and 3x resting flow rate). A study using *in vitro* experiments by de Zelicourt et al[19], demonstrated that these vortices were highly complex in intraatrial Fontan connections, with a progressive increase in complexity at exercise flow conditions. Although the vortices observed in our study had a well-defined morphology, they could quickly become unsteady and more complex with increasing flow rates.

In CHOP105, the size of the vortex was not as significant as the other intraatrial TCPCs with a Hemi-Fontan. This was because the IVC (70%) fractional contribution to the total flow was much higher than the contribution of the SVC (30%). Consequently, the momentum of the flow from the SVC was not sufficiently high enough in order to create a large enough vortex inside the connection region. The average size of the vortex seen in this geometry was only 1 cm, which was significantly lower than the mean vortex size of 1.6 cm.

For the intraatrial geometries with a bidirectional Glenn procedure performed in the second stage, only one of the geometries had a vortex present in the center of the

connection. This geometry had a pouch that was present below the superior caval anastomosis (as opposed to being at the site of the connection like the Hemi-Fontan intraatrials). The nature of the vortex induced as a result of this pouch had a different morphology compared to the intraatrials with a Hemi-Fontan. The difference in vortex morphology arose from the difference in the TCPC geometry. As the IVC flow entered the intraatrial connection, it experienced a sudden increase in cross-sectional area. This expansion in vessel cross-sectional area was followed by a constriction at the location of the bidirectional Glenn anastomosis. This geometrical feature created a large vortex in the intraatrial pouch, with the axis of rotation in an oblique superior-posterior direction. The rotation itself was in the anti-clockwise direction. For the other two intraatrial geometries with a bidirectional Glenn (CHB006 and CHB008), there was no offset between the SVC and the IVC, resulting in a direct collision of the caval flows. Consequently, the power losses in these models were also the highest observed amongst the intraatrials. In general, the magnitude of power losses seen in intraatrials with a bidirectional Glenn were higher than the power losses observed in intraatrials with a Hemi-Fontan, although the study was limited by a small sample size (7 intraatrials with a Hemi-Fontan vs. 3 intraatrials with a bidirectional Glenn).

For all the intraatrial patients (except CHOP078, CHOP105and CHOP115), the particle transit time was higher than 1 second. Since Fontan patients have heart rates greater than 80 BPM under resting conditions[37], this would mean that it takes a particle more than 1 cardiac cycle to enter and exit the Fontan connection. If a particle spends longer time in the IVC baffle, and if this particle is an activated platelet, it would have a greater tendency to aggregate, and hence could increase the risk of thrombo-embolism.

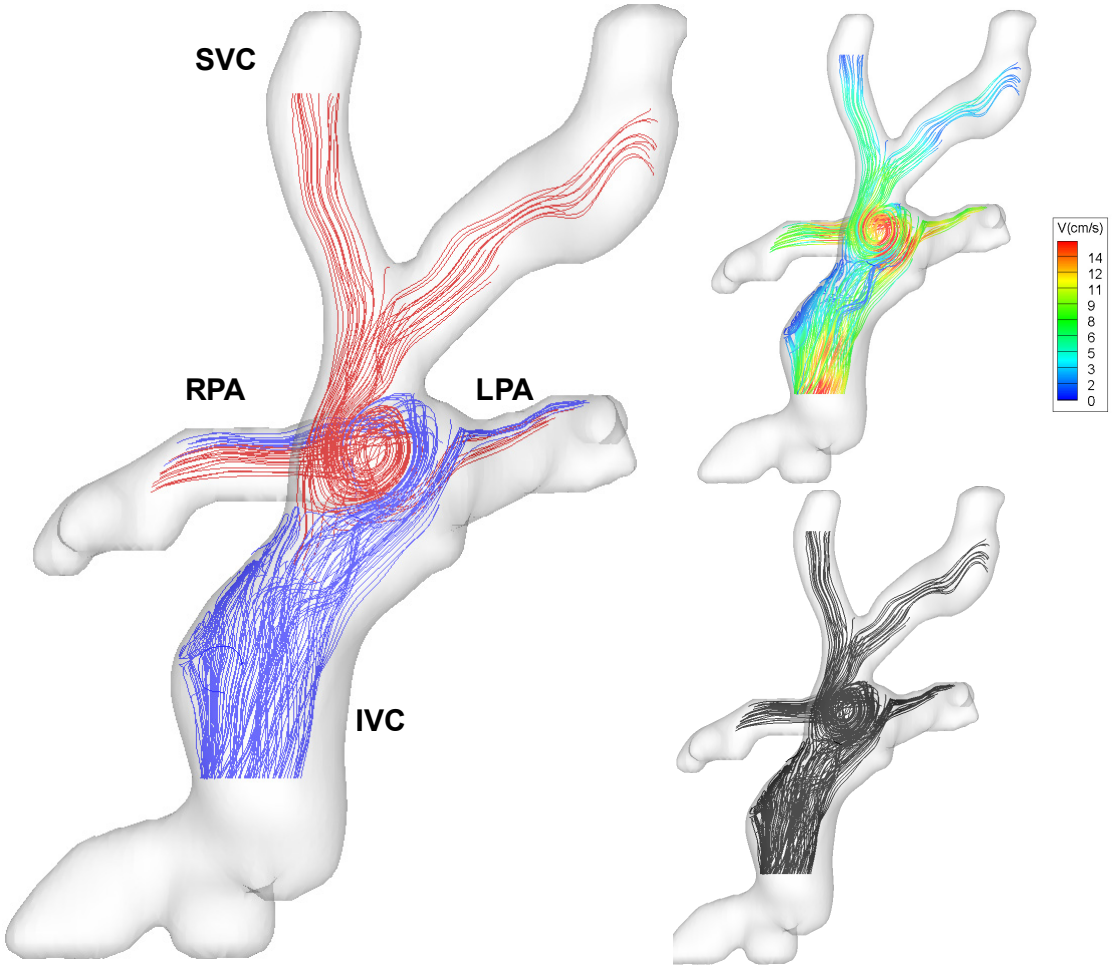

Figure 10.17: Flow fields within an intraatrial TCPC having a Hemi-Fontan connection (CHOP068) at beginning systole. The streamtraces are color-coded by their source of origin (red – SVC, blue – IVC), their velocity magnitudes, and without any color-coding to illustrate the flow structures. Notice the large vortex in the center of the connection. The diameter of the largest vortex measured was about 1.9 cm, which was almost as big as the Hemi-Fontan pouch itself. As a result the average particle transit time was quite high at 1.76s. The color-coded velocity streamtraces indicated that flow from the IVC was getting distributed adequately to the pulmonary arteries.

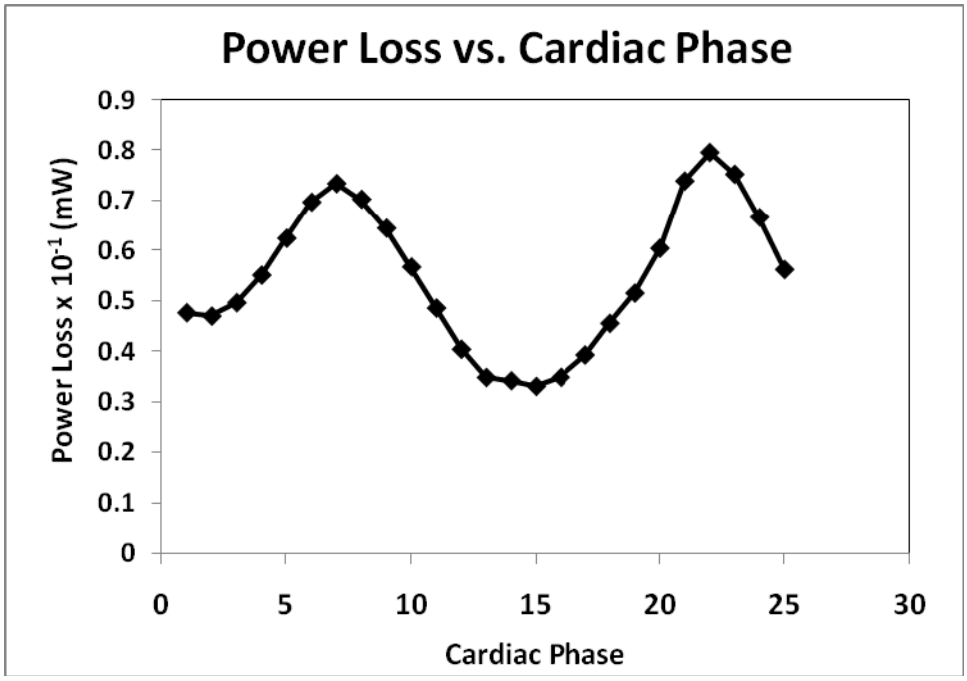

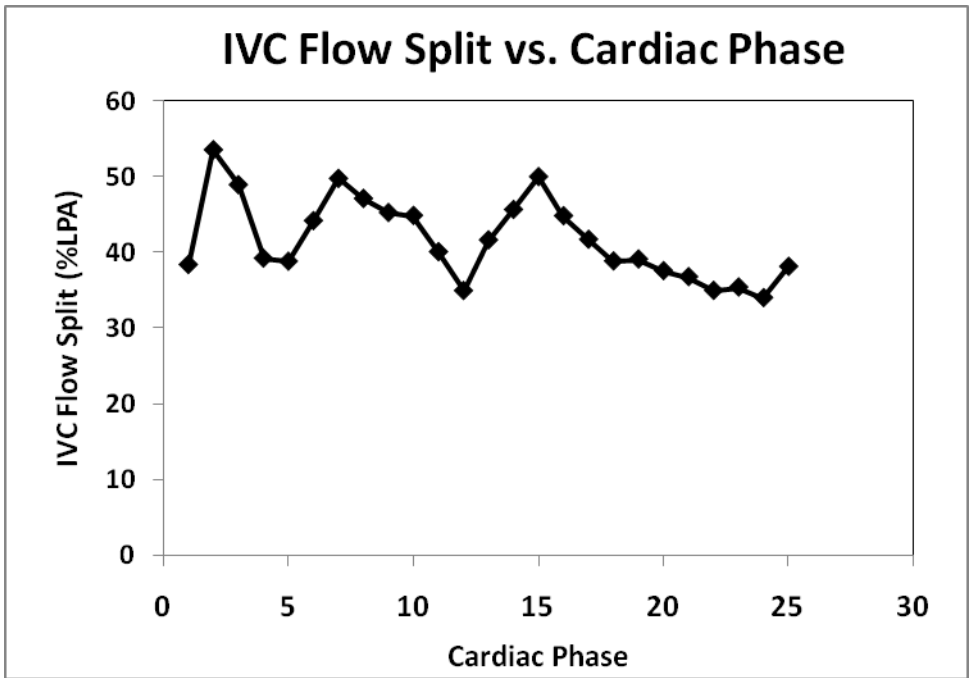

Figure 10.18: Power loss and IVC flow splits evaluated over the cardiac cycle for CHOP068. Notice that the power losses have an oscillatory pattern, while the IVC flow split seems to vary between 40%-50%, with an average IVC flow split to the LPA at 42%.

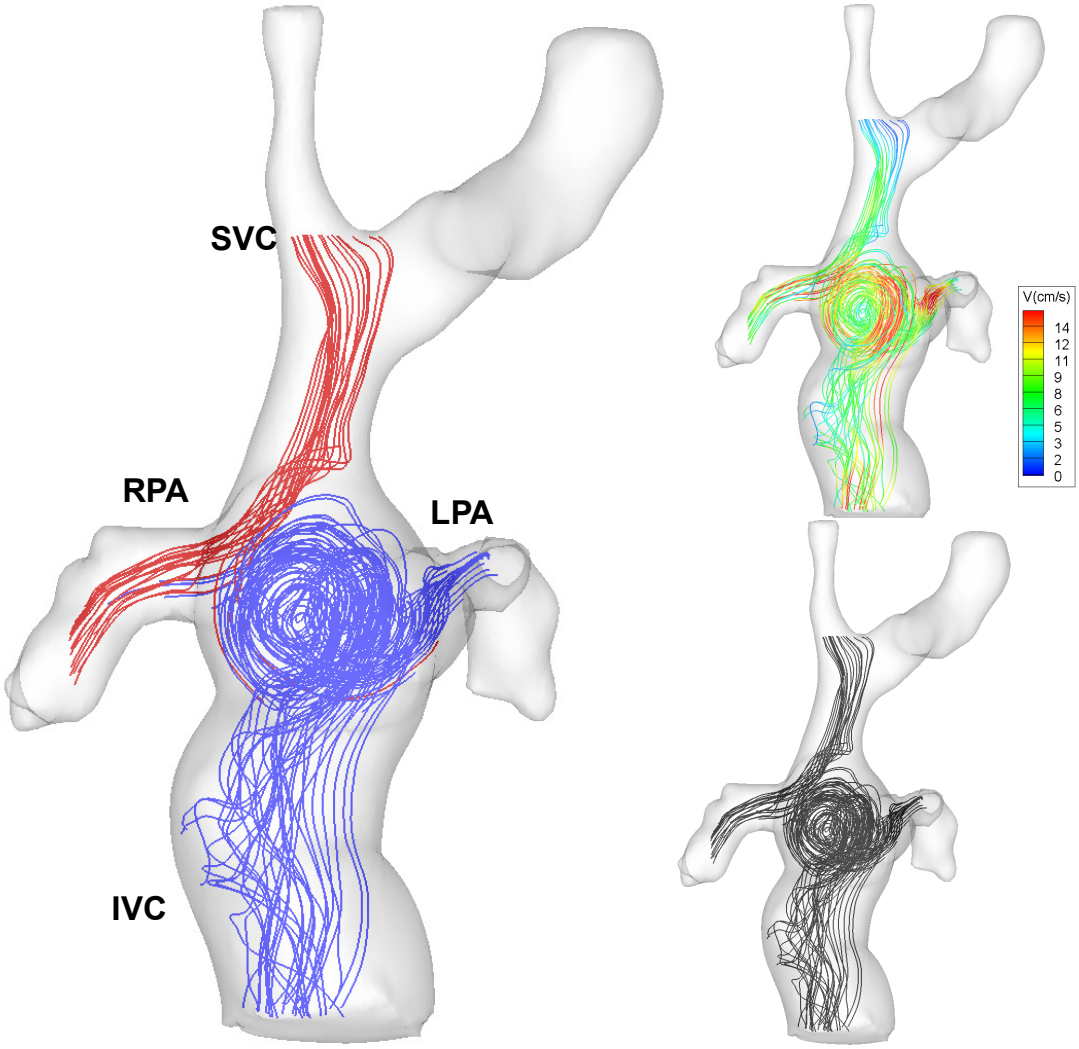

Figure 10.19: Shown here are the velocity streamtraces for another intraatrial connection with a Hemi-Fontan (CHOP073) at beginning of systole. Notice that an even larger vortex is present (compared to CHOP068) in the Hemi-Fontan pouch that had a maximum diameter of 3cm. The average particle transit time for this model was quite high at 2.24s. Furthermore, the flow was much more disturbed in the IVC baffle before it entered the Hemi-Fontan pouch in the center of the TCPC.

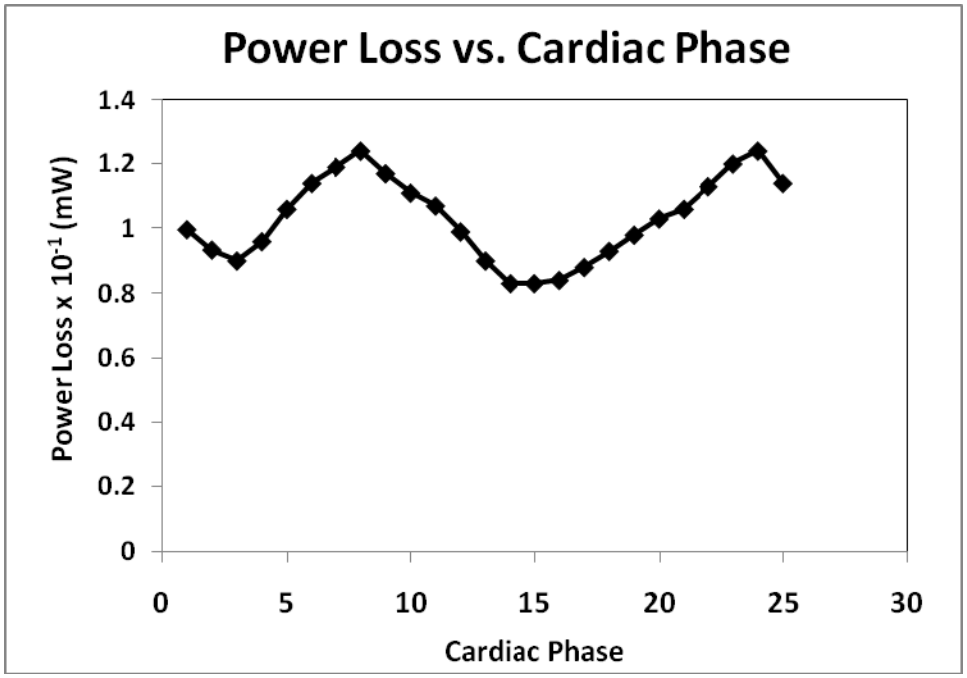

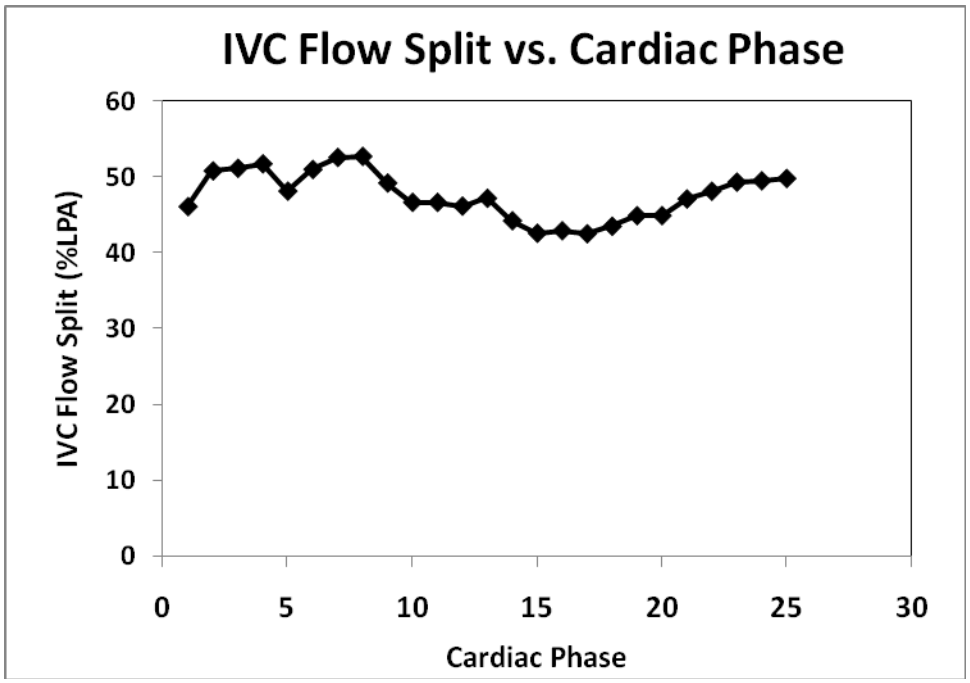

Figure 10.20: Power loss and IVCflow splits evaluated over the cardiac cycle for CHOP073. Notice that the power losses have an oscillatory pattern, while the IVC flow splits seem to be steady at 50%. The average IVC flow split was evaluated to be 47.6%

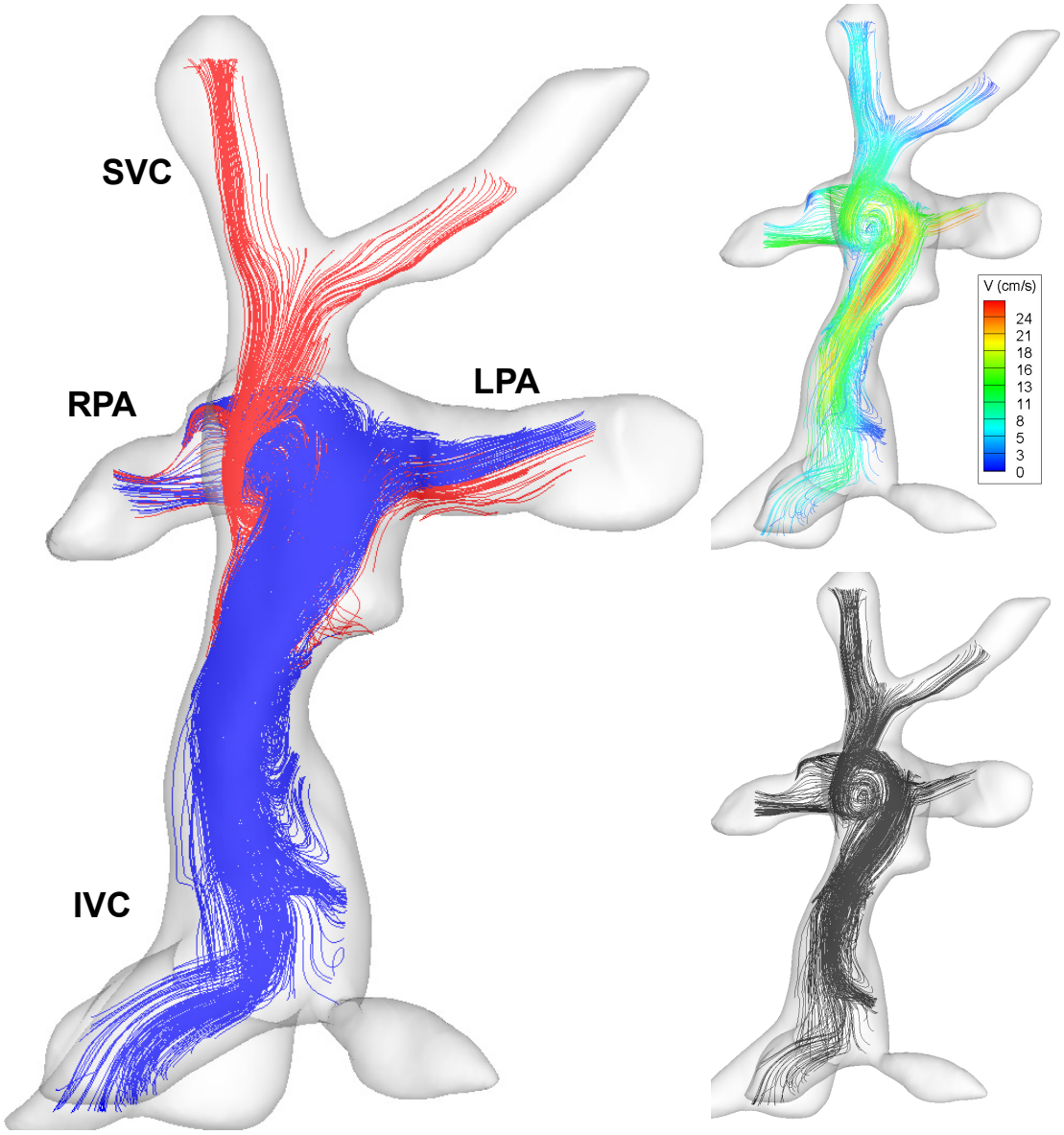

Figure 10.21: Shown here are the velocity streamtraces for another intraatrial connection with a Hemi-Fontan (CHOP078) at beginning of systole. The size of the maximum vortex was measured to be 1.8 cm in this case. The average particle transit time was measured to be 0.9s. This was lower than the previous models, primarily because the velocity magnitude was higher for this case. There was some evidence of a helical flow pattern in the IVC before it entered the Hemi-Fontan pouch. Overall, the flow characteristics were quite similar to the previous intraatrials with a Hemi-Fontan configuration.

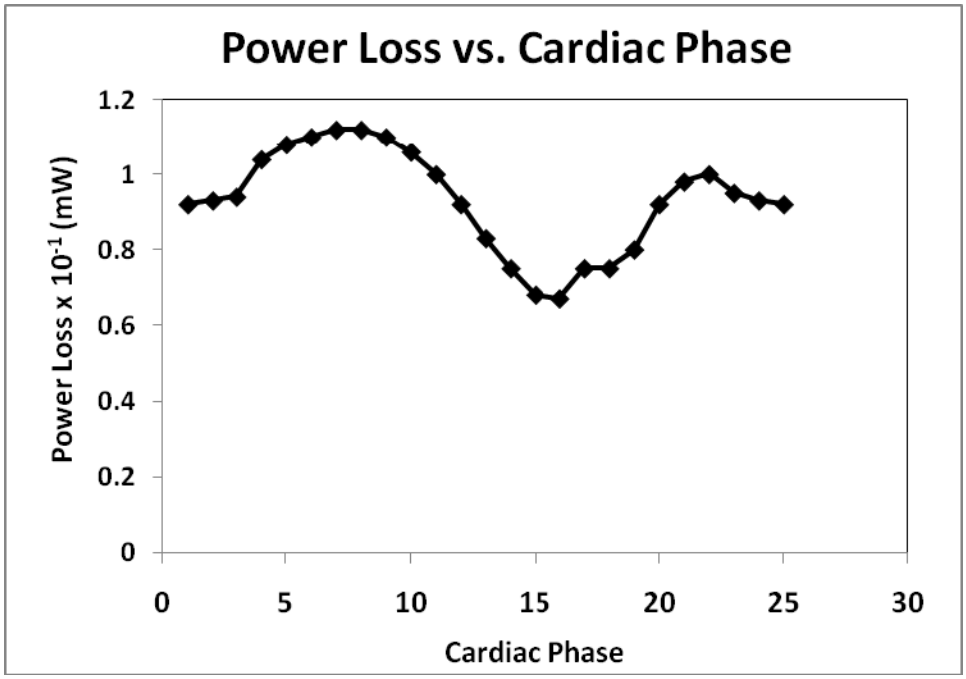

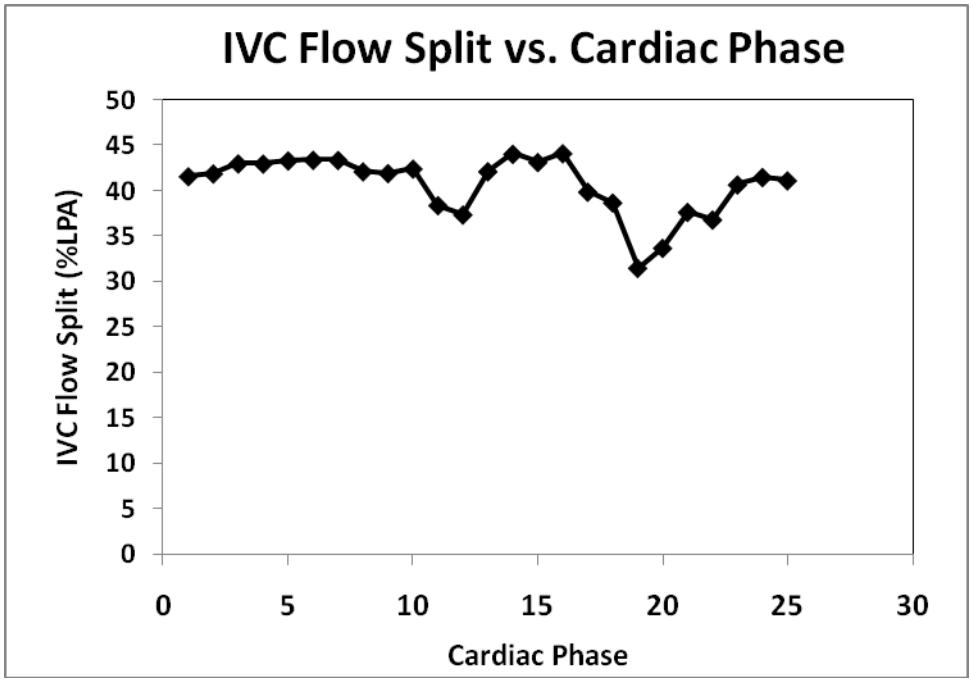

Figure 10.22: Power losses and IVC flow split curves for CHOP078. The magnitude of the fluctuation was along the same range as those observed in previous intraatrial models. The IVC flow splits were steady at around 40% throughout the cardiac cycle, with an average IVC flow split of 40.7% to the LPA

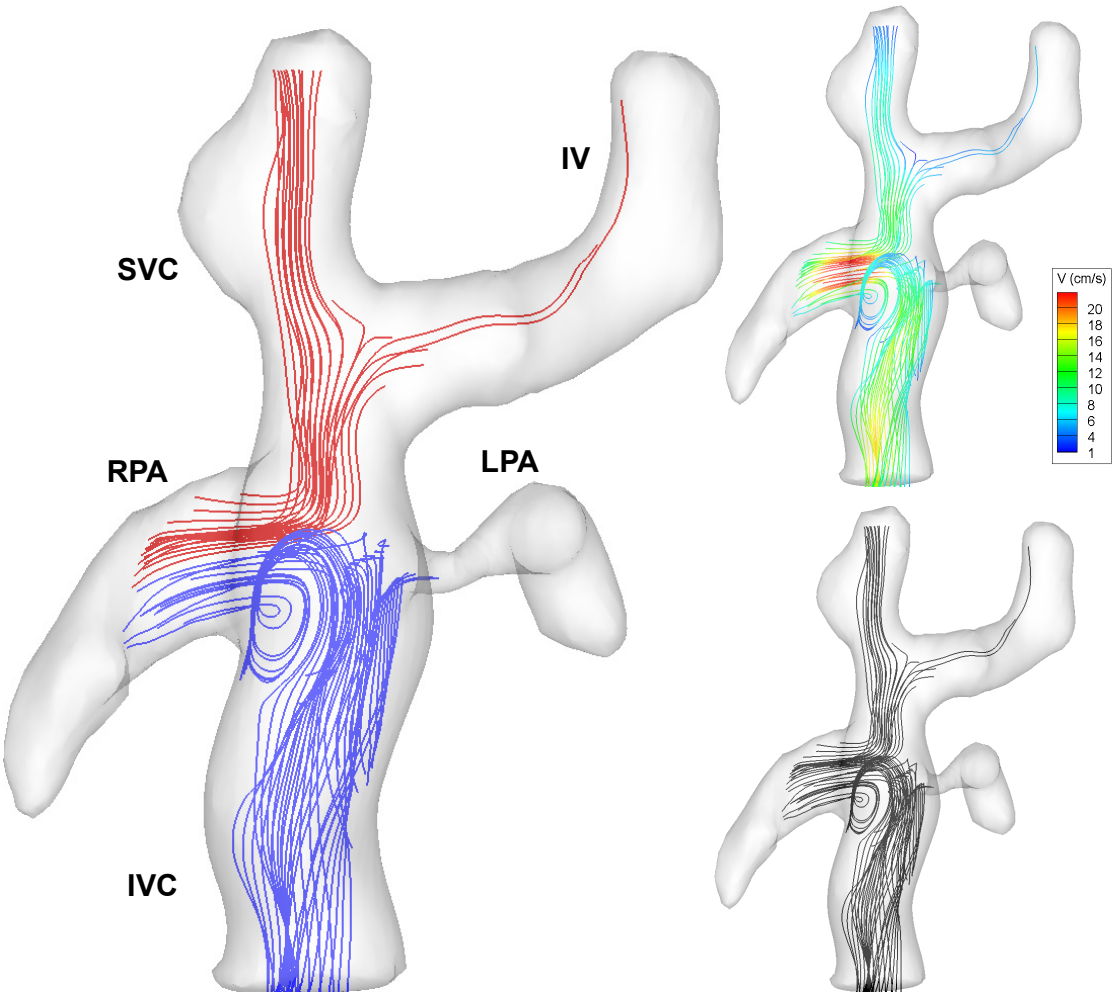

Figure 10.23: Shown here are the velocity streamtraces for CHOP094 (Stage 2: Hemi-Fontan) at beginning systole. The largest vortex present in the center of the connection had a diameter of 1.8 cm which was similar to the size of the vortices observed in the previous cases. The average particle transit time for this model was quite high at 3.45s. This patient also had an LPA stenosis, which resulted in a majority of the superior caval flow getting directed to the RPA. Consequently, the LPA received flow only from the IVC.

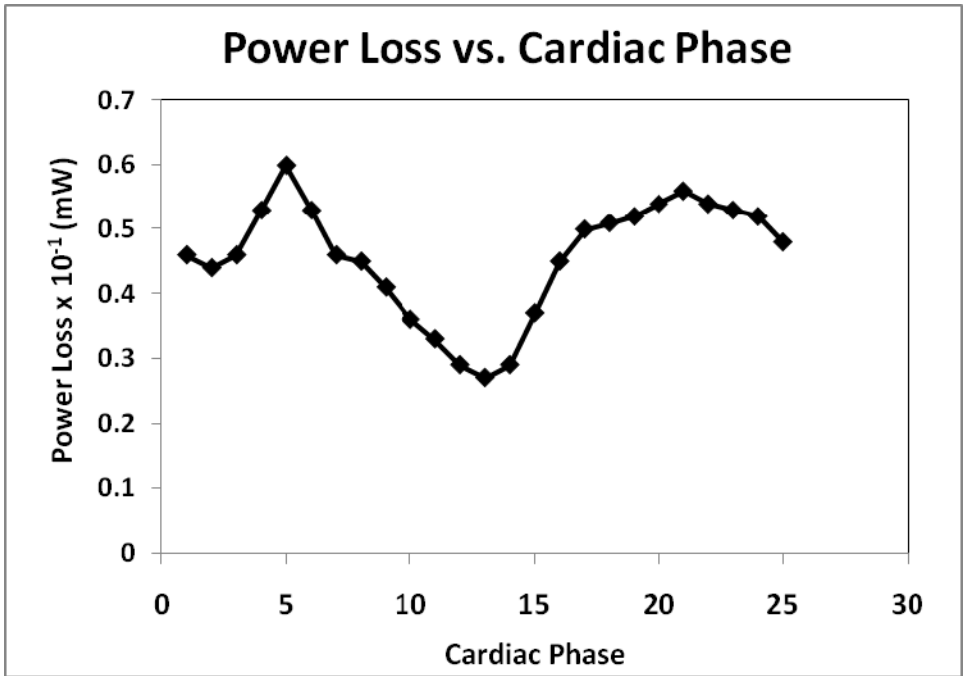

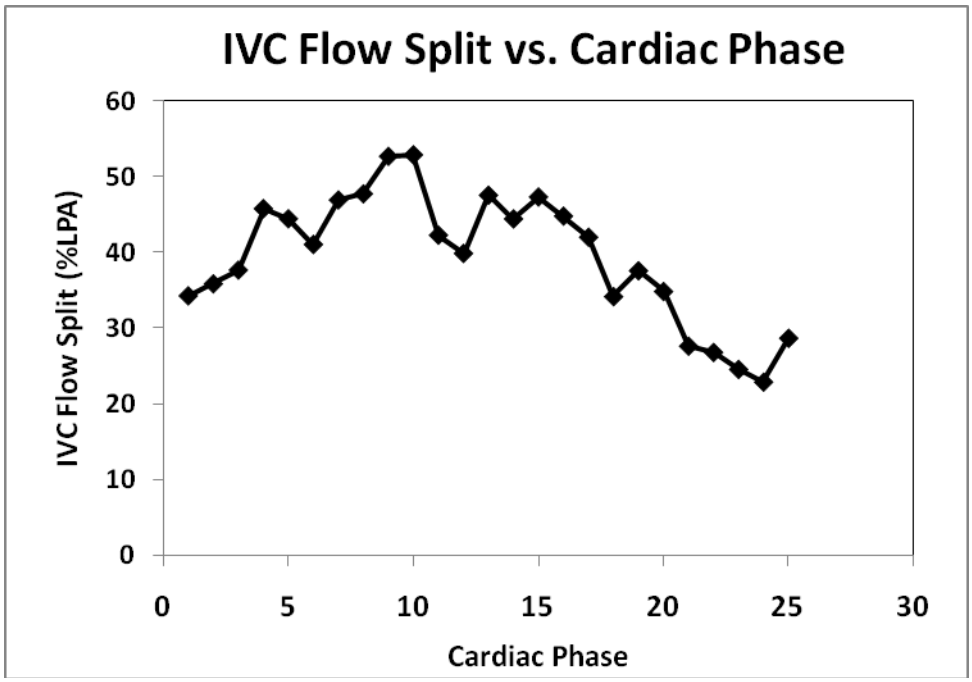

Figure 10.24: Power losses and IVC flow split curves for CHOP094. The magnitude of the fluctuation was along the same range as those observed in previous intraatrial models, although the mean power loss was lower (due to lower velocity magnitudes). The IVC flow splits varied from 30% to 50% over the cardiac cycle, with a mean value of 39% going to the LPA.

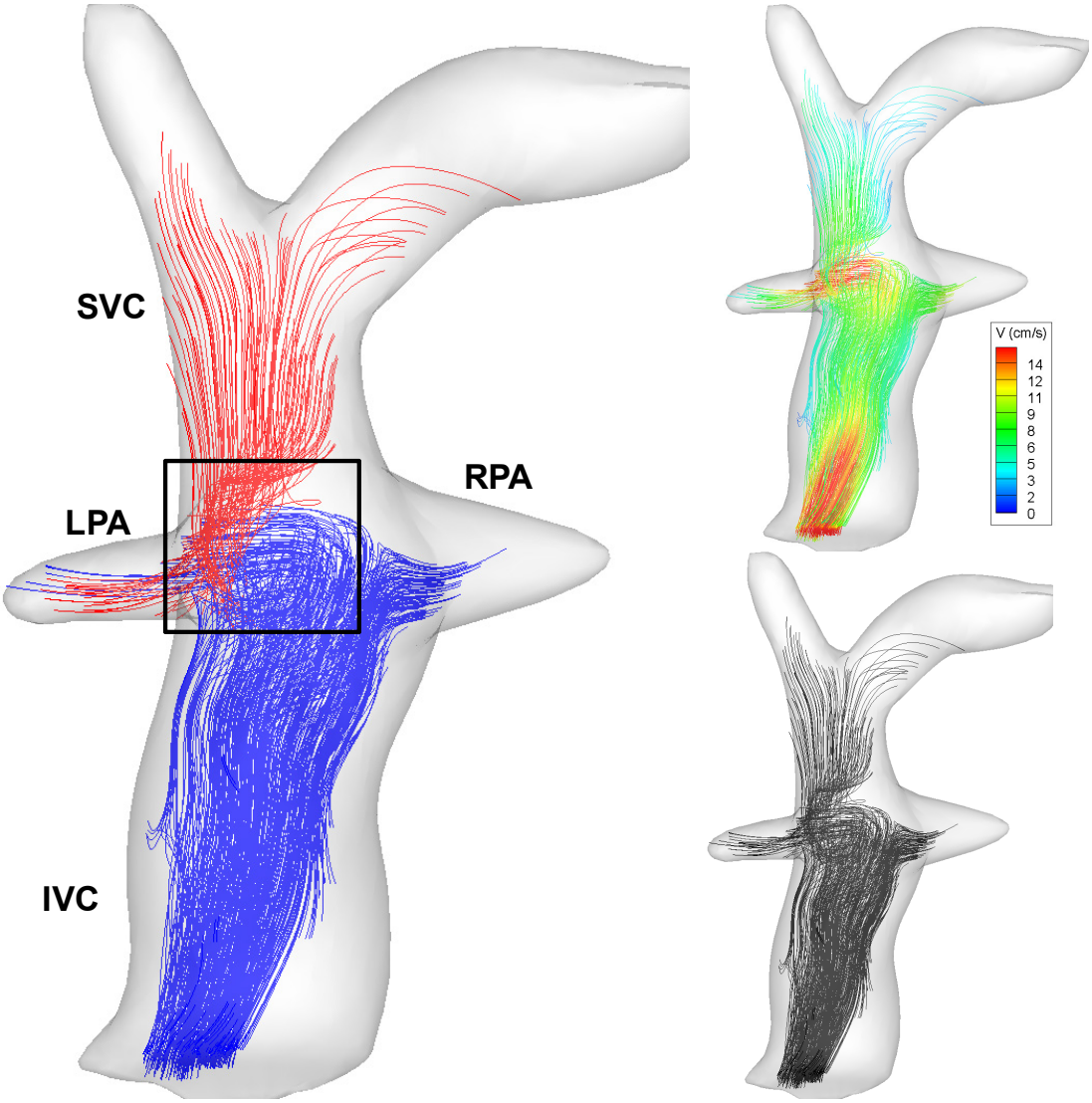

Figure 10.25: Shown here are the velocity streamtraces for CHOP105 (stage 2: Hemi-Fontan) at beginning systole. The largest vortex present in the center of the connection had a diameter of 1 cm which was much smaller compared to the previous models. In fact, the vortex was difficult to spot because of its small size. One of the reasons was that the SVC flow (0.77 LPM) was much lower in magnitude compared to the IVC flow (1.5LPM). As a result the SVC jet was not strong enough to create a vortex as big as those in the previous cases. The box indicates the area where the vortex was observed. The average particle residence time for this model was only 0.6s.

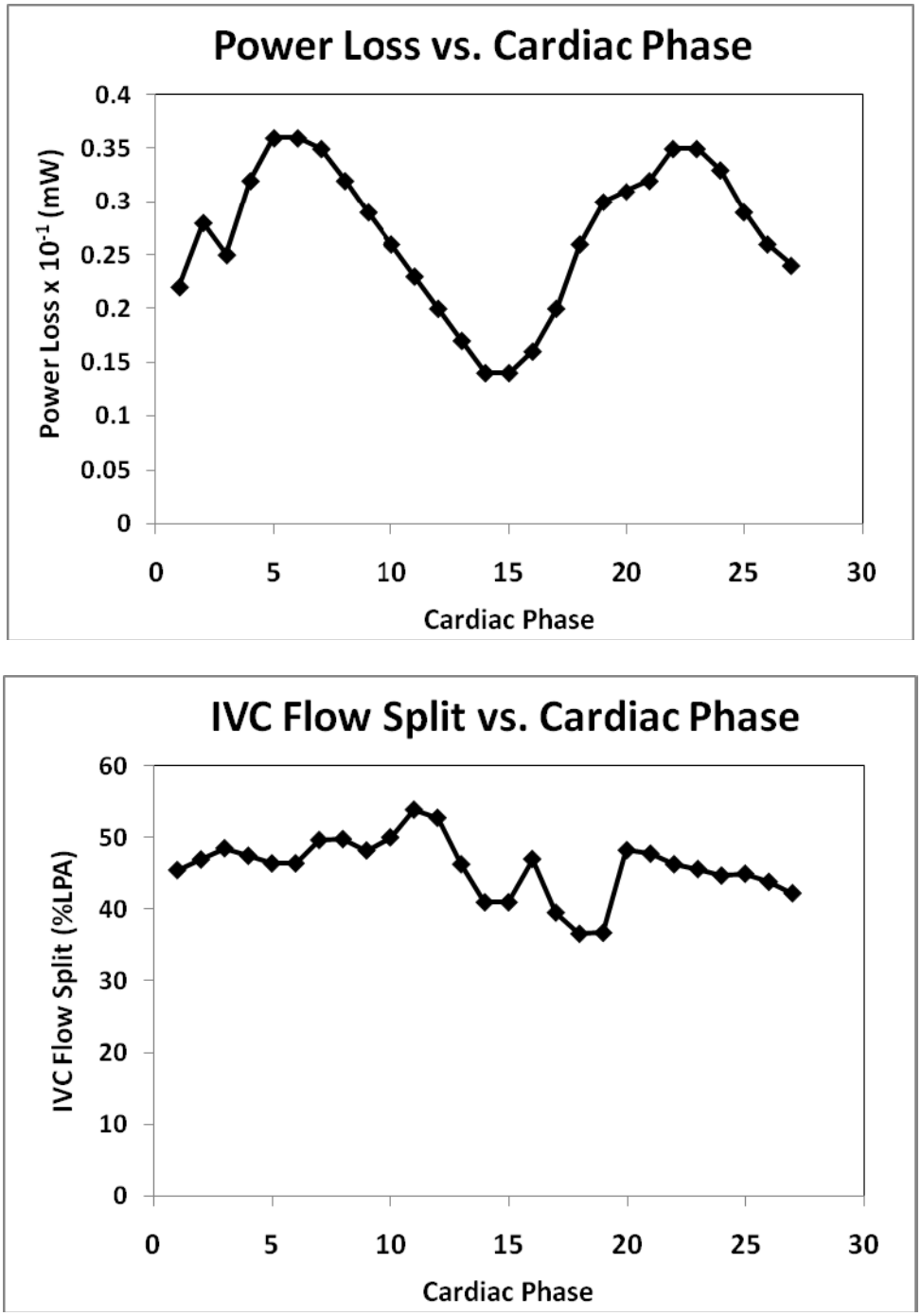

Figure 10.26: The power loss and IVC flow splits associated with CHOP105. The magnitude of power losses was even lower in this case, partly due to the larger sized Fontan connection and the lower magnitude of velocities. The IVC flow split ranged between 35% and 55%, with a mean value of 45%.

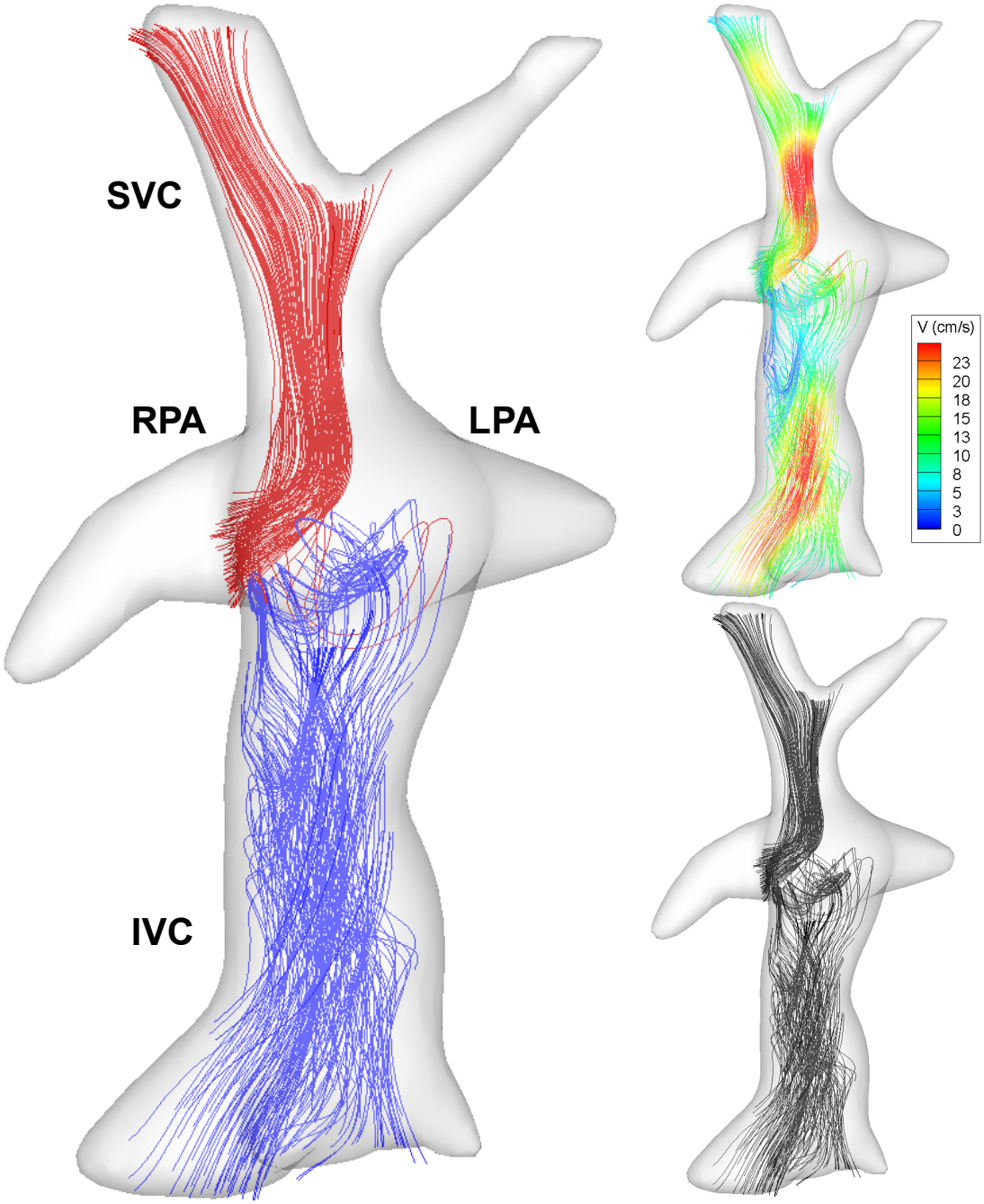

Figure 10.27: Shown here are the streamtrace velocity fields of CHOP115 at the beginning of systole. The size of the largest vortex measured in this case was 1.2 cm. This vortex can be observed in the center of the connection where a few streamtraces from the SVC form a vortex with the streamtraces from the IVC, and exit towards the LPA. The particle transit times were quite low at for this model as well at 0.65s. Also, there seems to be a strong helical flow pattern within the IVC of this patient. Most of the IVC flow had a tendency to go towards the RPA.

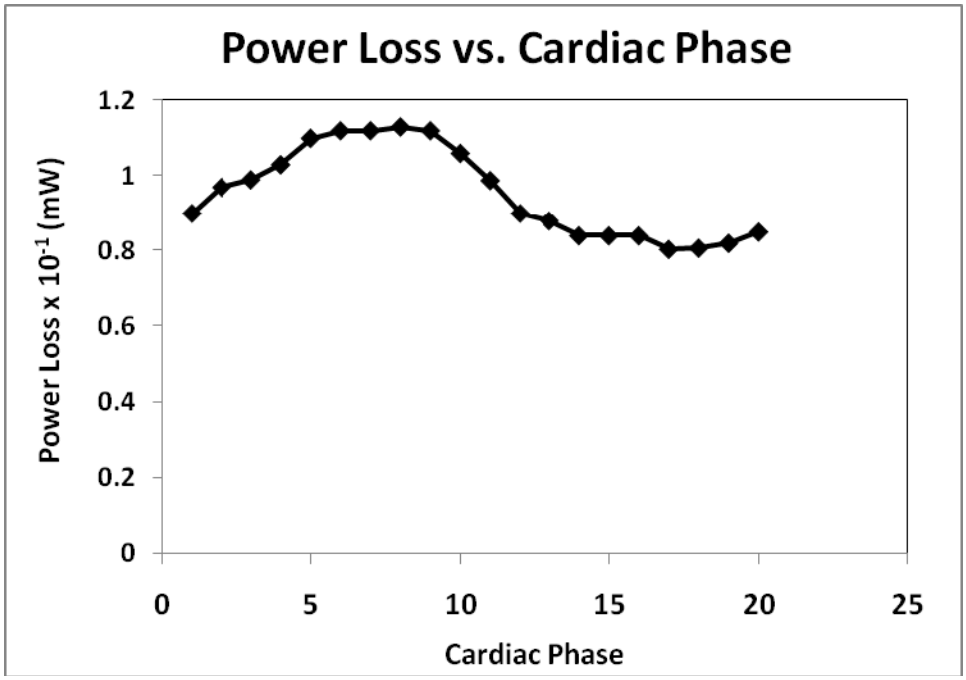

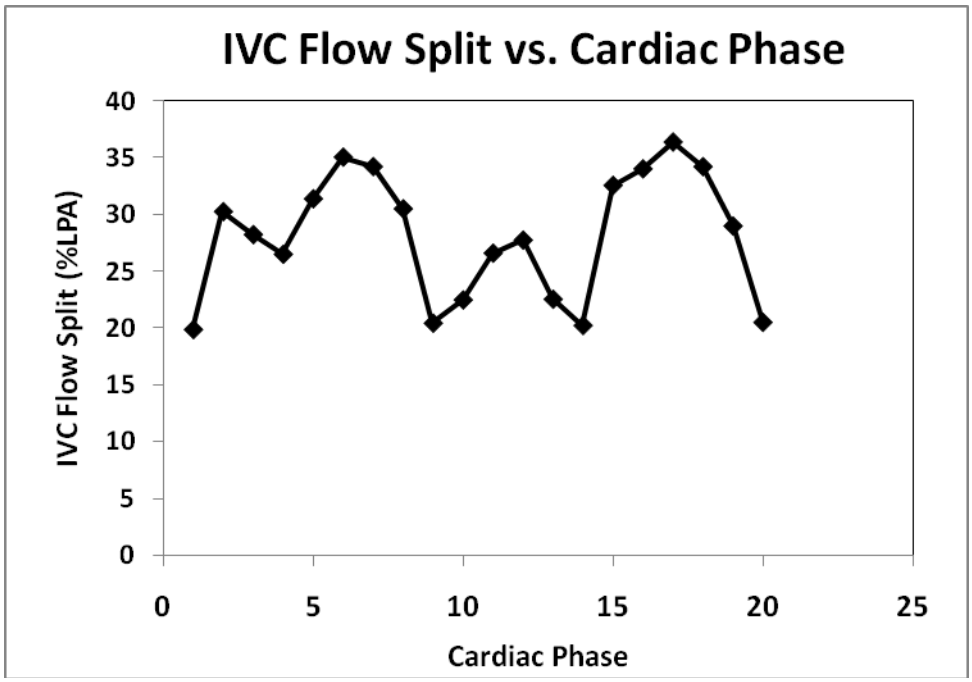

Figure 10.28: Power loss and IVC flow split curves for CHOP115. The magnitude of power losses in this case was much higher than what was observed previously. Higher velocities (as evident in the color-coded streamtraces) within the Fontan connection compared to the previous case contributed to this increased power loss. The average IVC flow split was about 28%. Since the coronal slices were not acquired all the way till the pulmonary arteries in this case, the IVC flow split had to be calculated by the directionality of the flow before it entered the pulmonary arteries

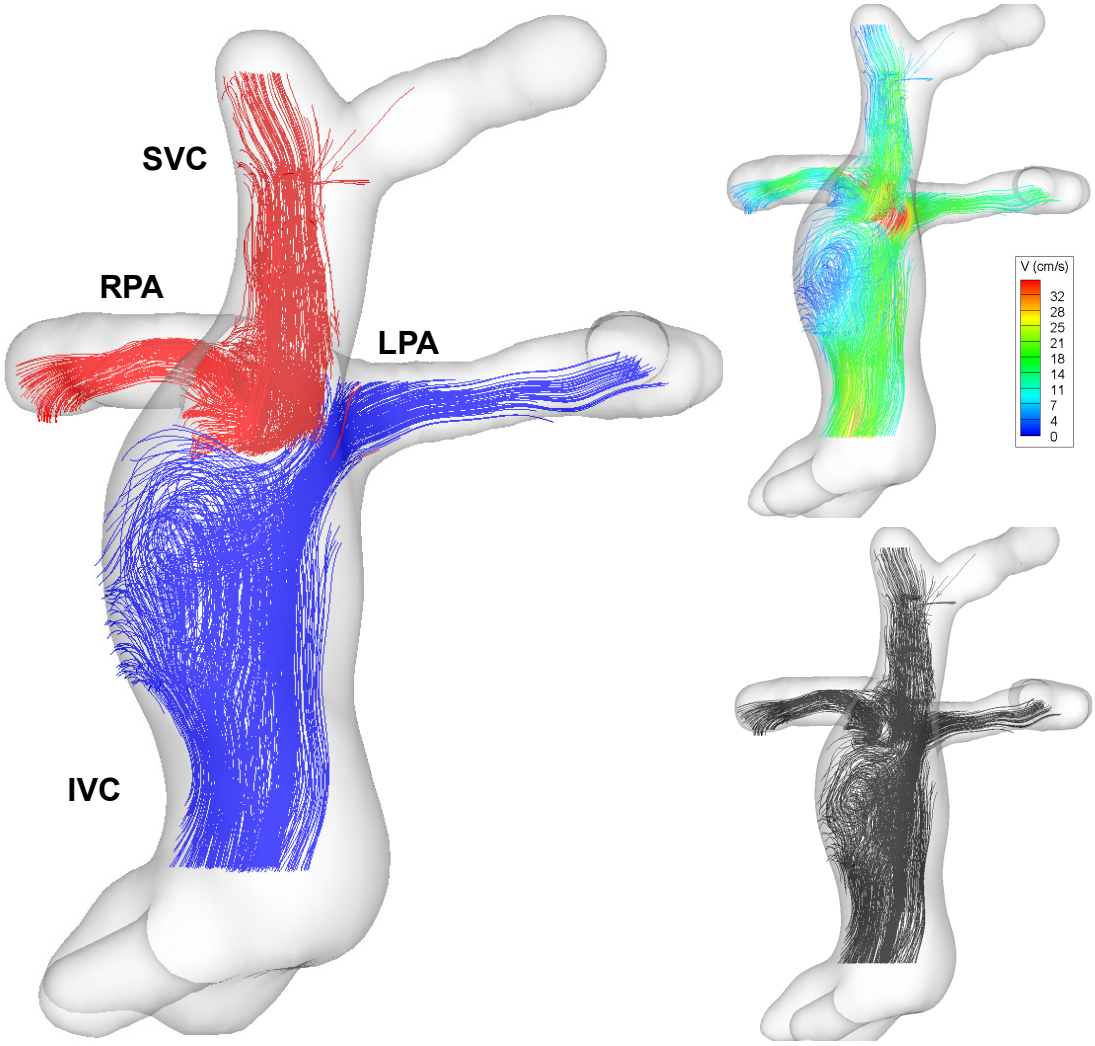

Figure 10.29: Shown here are flow fields within CHB004 (Stage2: bidirectional Glenn). There was a slow moving recirculation region in the center of intraatrial pouch below the bidirectional Glenn anastomosis. Notice how the SVC flow impinges upon the IVC flow, before turning and going back up towards the LPA. Interestingly the magnitude of velocities that were observed in this case were much higher than those observed in intraatrial Fontans with a Hemi-Fontan. The size of the largest vortex was 2.2cm, and due to significant recirculation within the intraatrial baffle, the average particle residence time was quite high at 6.26s. Although it seems like most of the flow from the IVC is actually going towards the LPA, there is a stagnation region at the location where the IVC flow splits evenly to go to both the LPA and the RPA. However, due to the resolution of the anatomic mesh, the streamtraces do not go all the way into the RPA. Since the IVC flow split was evaluated by the direction of the flow vectors at the stagnation region, it was possible to evaluate the IVC flow split despite the streamtraces not ending at the RPA.

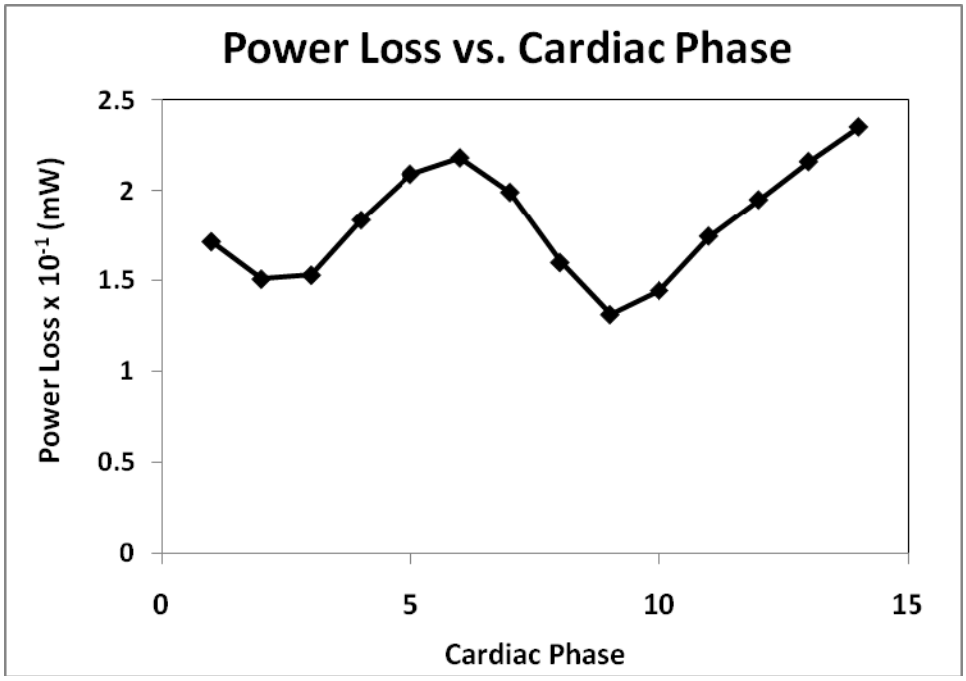

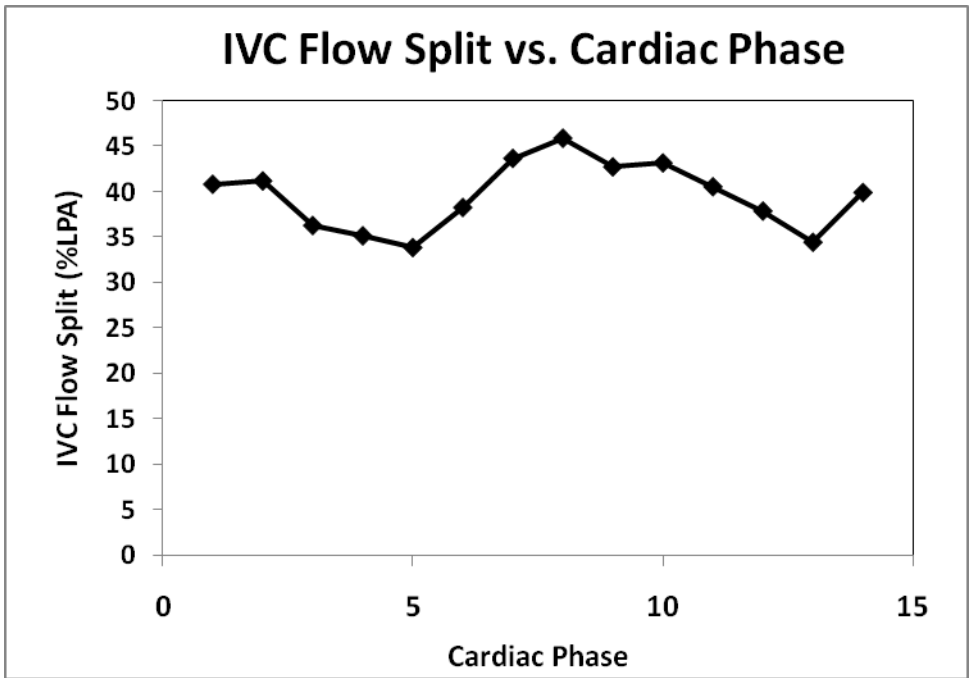

Figure 10.30: Power loss and IVC flow split curves for CHB004. Although the oscillatory pattern of power loss was evident in this case as well, the magnitude was much higher than the previous cases, primarily because of the higher velocities observed in the TCPC (max velocity of 36 cm/s). A steady IVC flow split was observed throughout the cardiac cycle, with an average of 40% of the IVC flow going towards the LPA.

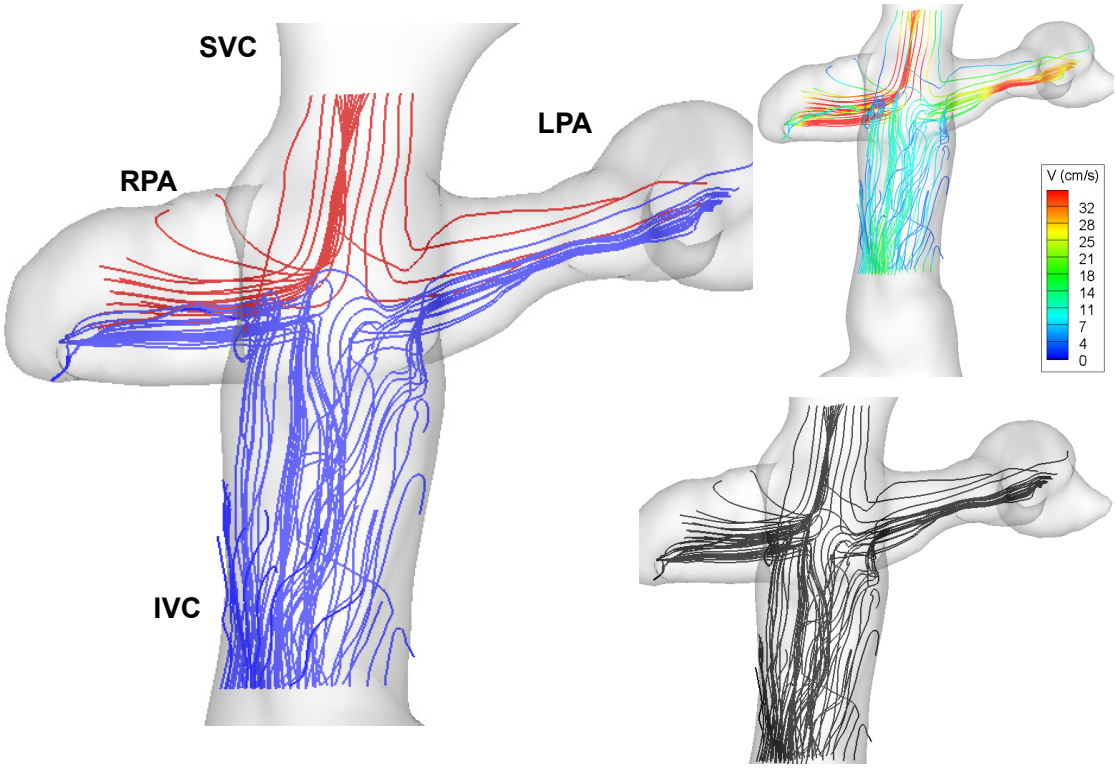

Figure 10.31: Shown here are flow streamtraces within CHB006 (Stage2: bidirectional Glenn). Only a very small vortex of size 0.5 cm, was present close to the IVC-RPA anastomosis region. There seemed to be an almost even split of flows coming from the SVC and the IVC going into the LPA and the RPA. The flow structures within the IVC seemed to be a bit disturbed with a few streamtaces from the IVC not making all the way to the pulmonary arteries. This could be partly attributed to a low SNR PC MRI acquisition, or the fact that the chaotic flow pattern within the IVC baffle is only partially captured by PC MRI. Due to the lack of a significantly sized vortex, the particle residence times were lower for this patient at 1.73s.

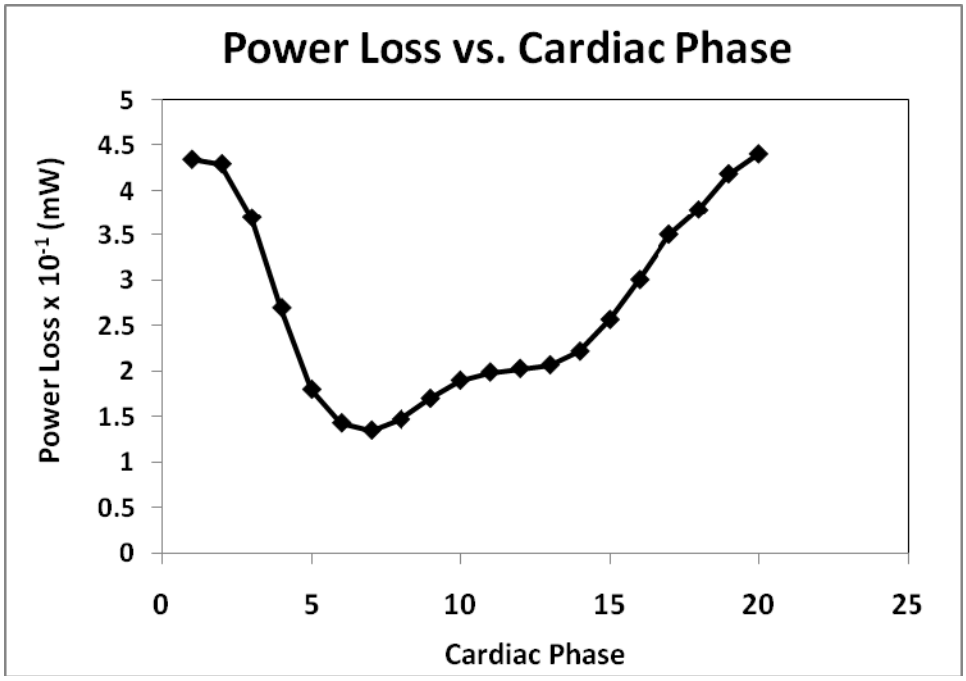

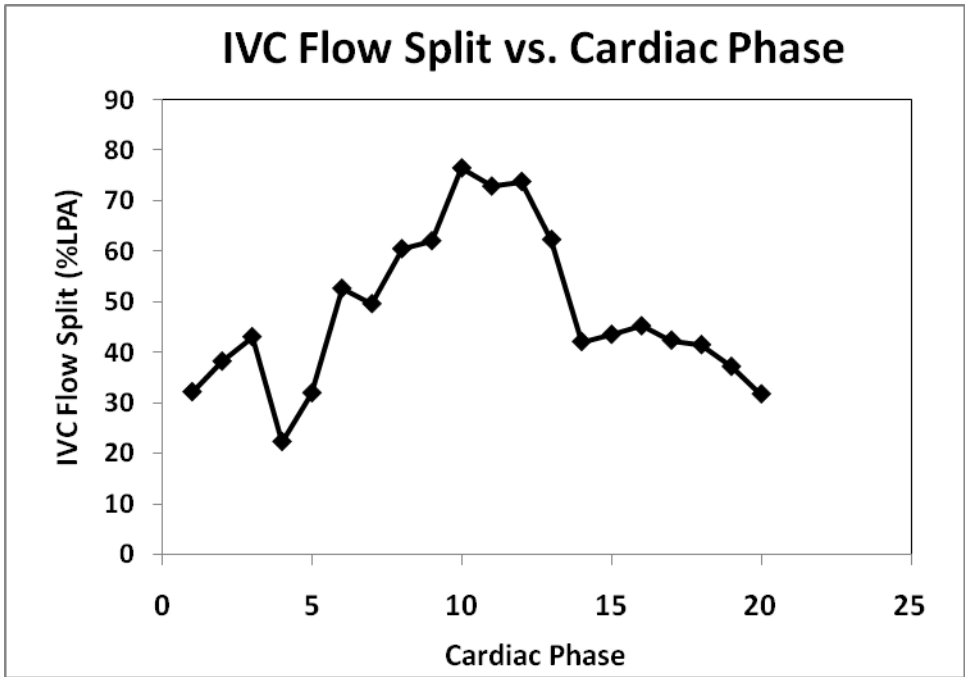

Figure 10.32: Power loss and IVC flow splits for CHB006. The peak power loss observed was quite high (4.5 x 10^{-1} mW) in the beginning of systole, and dropped significantly midway through the cardiac cycle, before going back up towards the end of the cardiac cycle. There was significant variation in the IVC flow split, with an average of 48% of the IVC flow going towards the LPA.

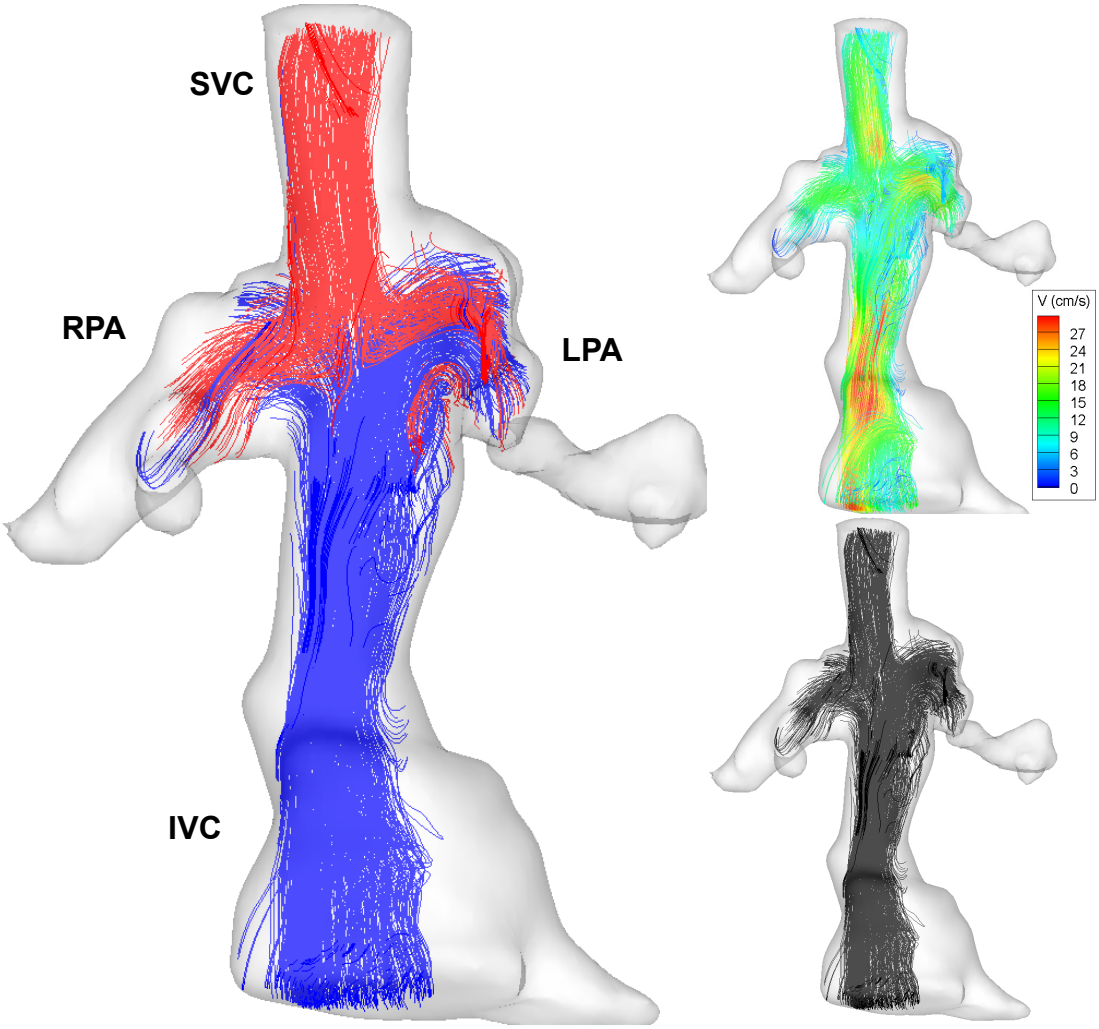

Figure 10.33: Shown here are flow streamtraces within CHB008 (Stage2: Bidirectional Glenn). Only a very small vortex of size 0.5 cm, was present close the IVC-LPA anastomosis region. Although flow from the SVC got smoothly split into the RPA and the LPA, the IVC flow had a preference to go towards the LPA.

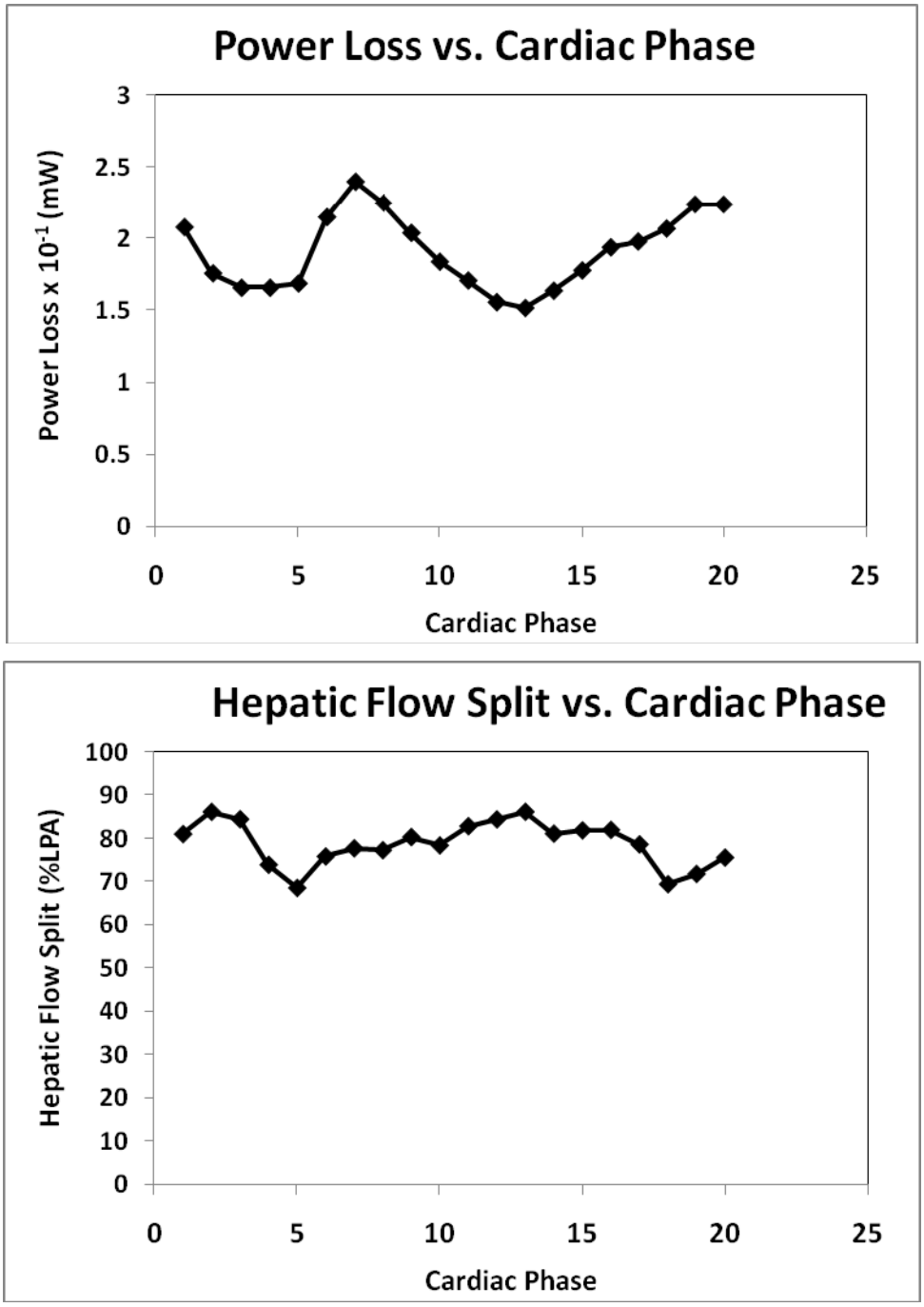

Figure 10.34: Power loss and IVC flow splits for CHB008. Notice that the peak power loss was less pulsatile and seemed to remain between 1.6 and 2.5. Throughout the cardiac cycle there was a preference for the IVC flow to go towards the LPA, with the average IVC flow split hovering around the 78% mark.

For the extracardiac TCPCs, flow seemed to be streamlined in the IVC for all cases except a few situations where the flow was chaotic (CHOP130 and CHOP148). Figure 10.39 depicts a typical extracardiac, with smooth flow structures and slightly preferential venous return distribution to the LPA. In this geometry, almost 100% of the SVC went to the RPA but the IVC flow (and in turn the hepatic venous return) was biased towards the LPA with an LPA/RPA flow ratio of 65/35 averaged over the cardiac cycle. Another interesting observation was that the IVC flow distribution to the LPA increased to almost 90 % during mid-systole, which seemed to correlate with the increased velocities in the IVC baffle. Contrastingly, Figure 10.41 shows another extracardiac TCPC (CHOP095), but with an offset between the SVC and the IVC. Although, such an offset has been shown before to reduce energy losses within the Fontan connection, it did bias the flow from the IVC in the direction of the offset. This particular patient had an LPA/RPA IVC flow split of 12/88 % highlighting a significant bias to the right side. Figure 10.43 shows, perhaps, the most intriguing extracardiac geometry of all the models selected. The patient had a Hemi-Fontan operation performed at stage 2, which explained the presence of a large pouch like structure. This patient did not have an SVC, and as a result the innominate vein carried all the superior caval flow. Flow from the innominate vein entered the Hemi-Fontan pouch, formed a vortex, and got redirected towards the RPA. Almost all of the flow from the IVC got directed towards the left lung resulting in an LPA/RPA flow split of 93/7%.

Figure 10.53 shows the flow fields associated with the most complex geometric configuration of all the models used in the study: an interrupted IVC with an azygous vein continuation. In order to truly visualize the complex flow structures, stream ribbons

instead of stream traces were used to display the flow structures. The highly uneven distribution of hepatic flow was evident, where majority of hepatic flow tends to go towards the right lung. The average LPA/RPA hepatic flow spit was quantified to be 5/95 % using the reconstructed PC MRI velocity fields. A close examination of e flow fields provided insights into why such poor hepatic flow distribution was observed. First, the orientation of the azygous vein in the Kawashima configuration constrained flow from the SVC and IVC into the LPA. Since the interrupted IVC only carried the hepatic blood (ie. 21% of the cardiac output), the relative fluid dynamic energy was lower compared to the superior caval flows. As a result, the IVC stream was observed to detach from the left side of the IVC baffle, where the superior inflows engulfed and recirculated, further constraining the IVC flow towards the right and into the RPA. Hence, although the connection was designed with a preferential orientation of the IVC towards the LPA, the hemodynamic consequence was similar to having a unidirectional Fontan with the IVC flow getting directed to the RPA and SVC flow getting directed to the LPA.

Compared to intraatrials, higher magnitude of power losses were observed in patients with extracardiac Fontans. On closer inspection, it was found that the higher power losses were a characteristic of higher velocity magnitudes. Extracardiac Fontans had higher velocities in the IVC baffle (as a result of the smaller sized conduit), resulting in higher velocity shear, and consequently higher viscous dissipation power losses. There were no differences in IVC flow splits between the two groups, although there was more variation amongst extracardiac Fontan types. This variation could be attributed to the differing angle of the IVC anastomosis as well as the SVC-IVC offset at the connection region.

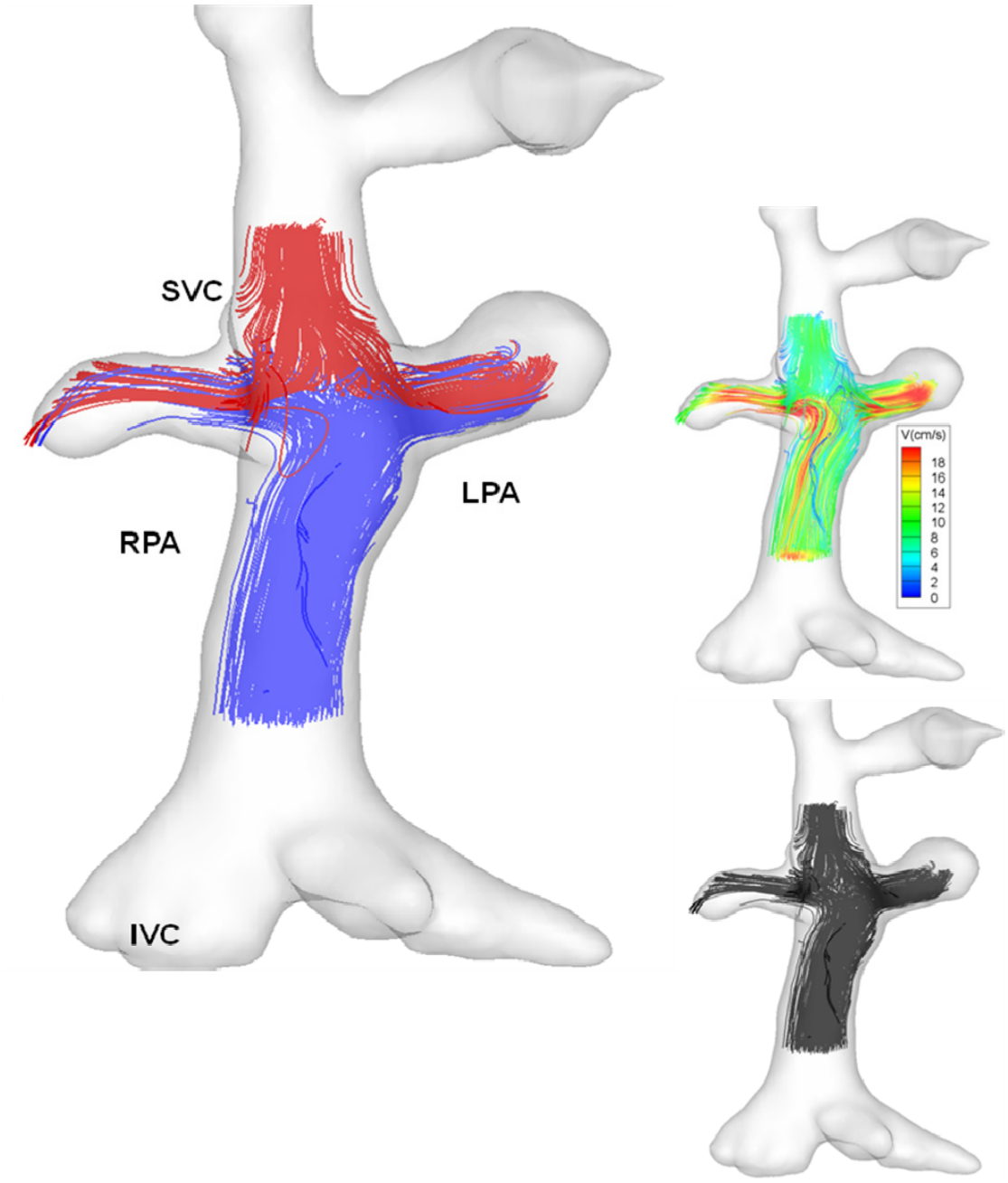

Figure 10.35: Shown here are the 3D flow streamtraces for CHOP089. The IVC flow is quite streamlined, and the flows from the SVC and the IVC get equally distributed to both the LPA and the RPA. There was a small vortex anterior of the connection, where some streamtraces from the SVC re-circulated and entered the RPA. The magnitude of velocities were quite low with a maximum of 20 cm/s observed in the pulmonary arteries. The average particle transit time was evaluated to be 1.05s for this patient.

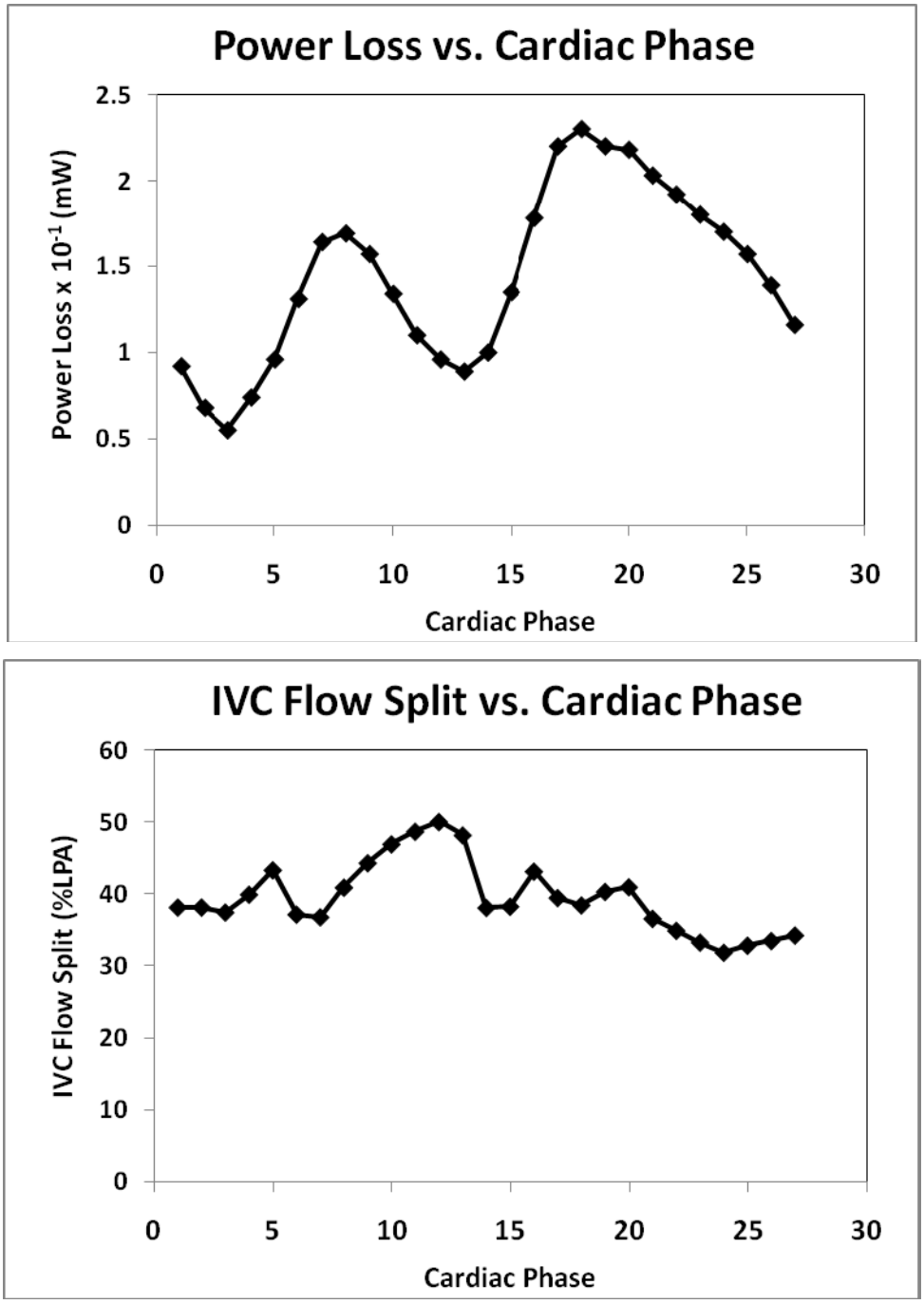

Figure 10.36: Power loss and IVC flow splits for CHOP089. There is significant pulsatility in the power loss with a variation of almost 50 %. The IVC flow split was steady at around 45% and did not seem to vary over the cardiac cycle.

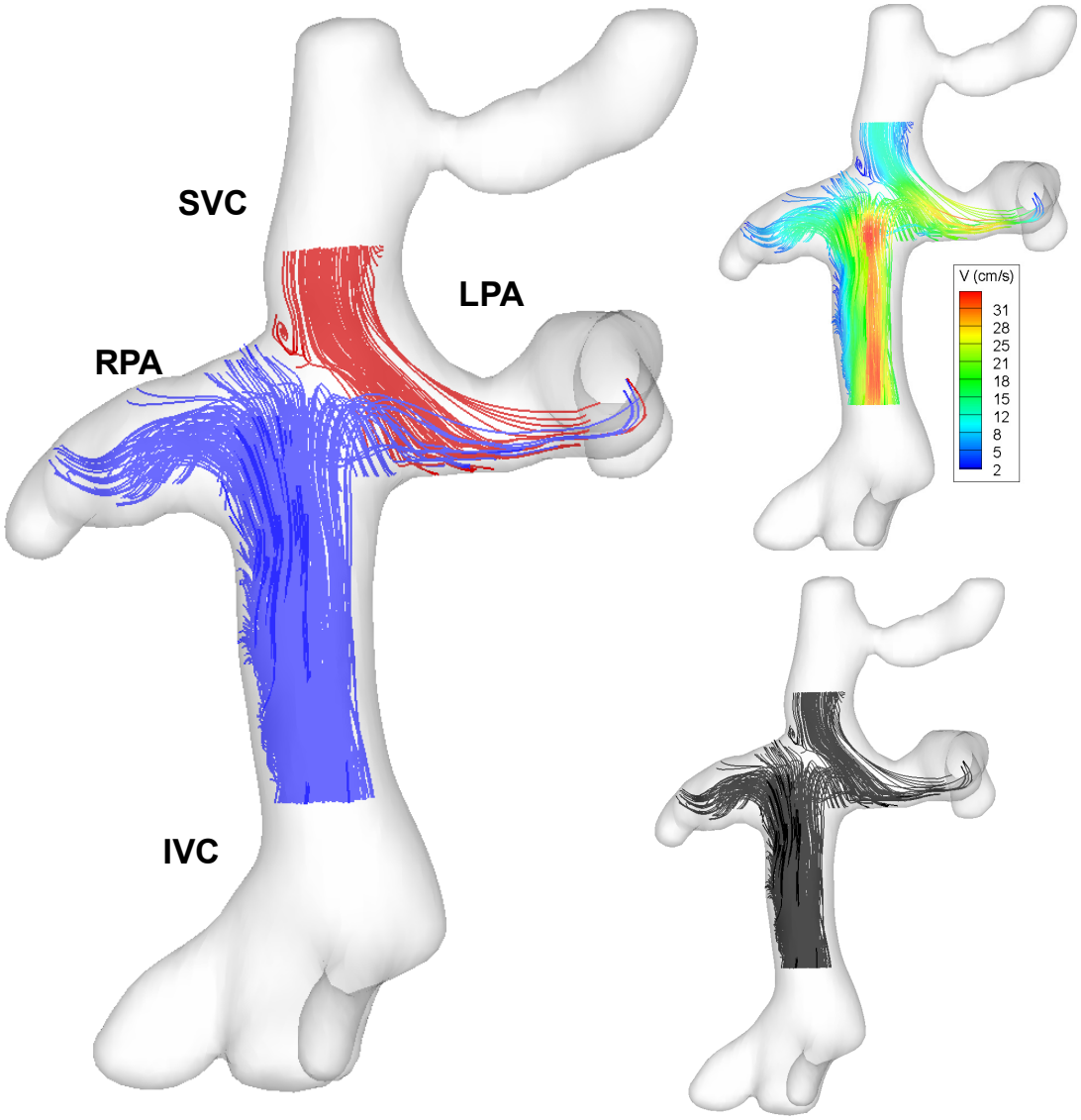

Figure 10.37: Shown here are the 3D flow streamtraces for CHOP090. The IVC flow was quite streamlined, although it had a tendency to go towards the RPA. If observed closely, there was an offset placed between the SVC and the IVC during the surgery, which is why IVC flow tends to go towards the RPA, while all the SVC flow goes towards the LPA. A clear helical flow pattern is evident going into the LPA and the RPA. This patient also seemed to have a smaller conduit, which resulted in higher velocities inside the IVC baffle. This geometry had the shortest particle residence time of 0.53s.

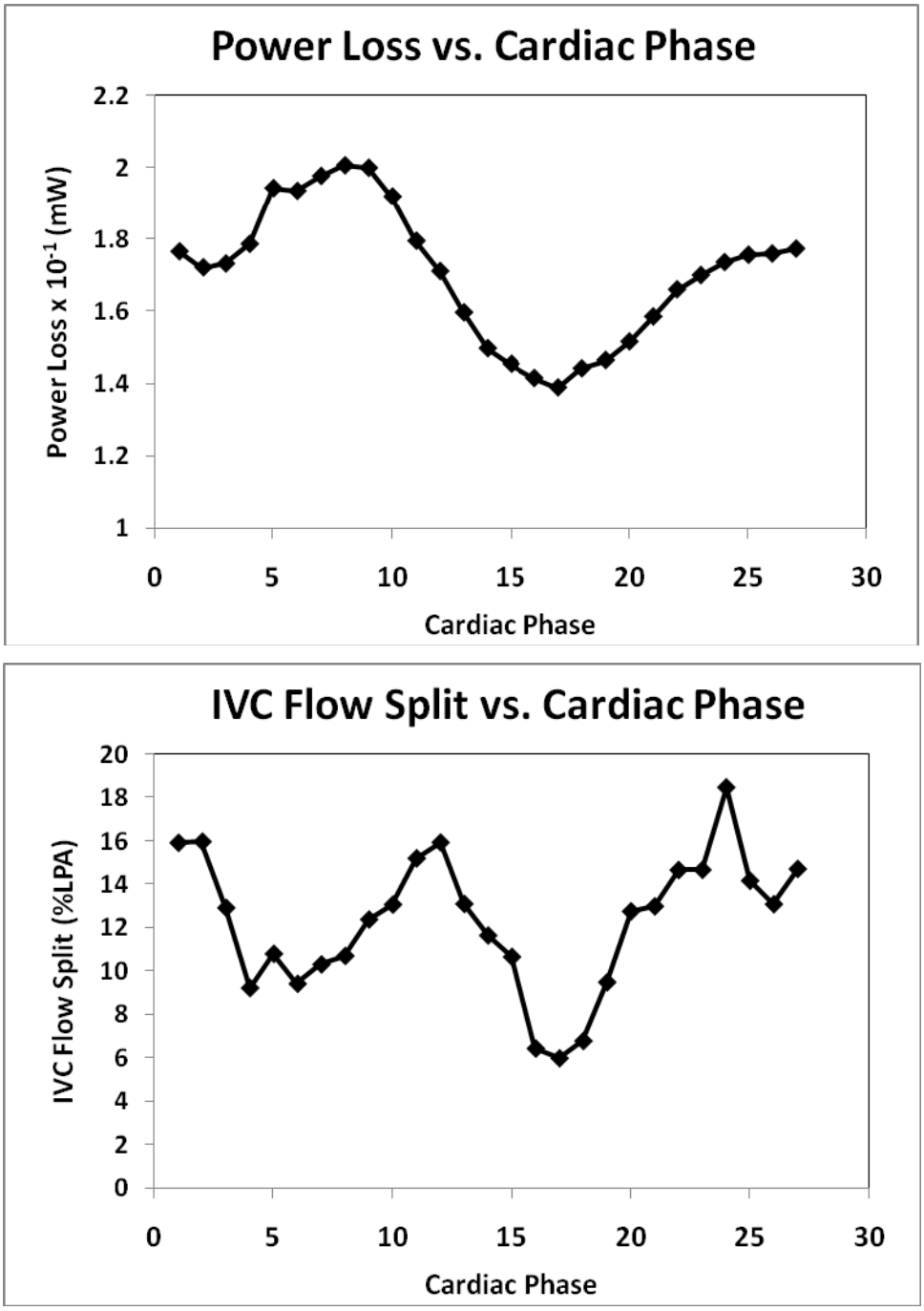

Figure 10.38: Power loss and IVC flow split curves for CHOP090. The magnitude of power losses were high which correlated with the increased velocities observed within the baffle. The IVC flow split was biased towards the RPA, with an average of only 12% going towards the left pulmonary artery.

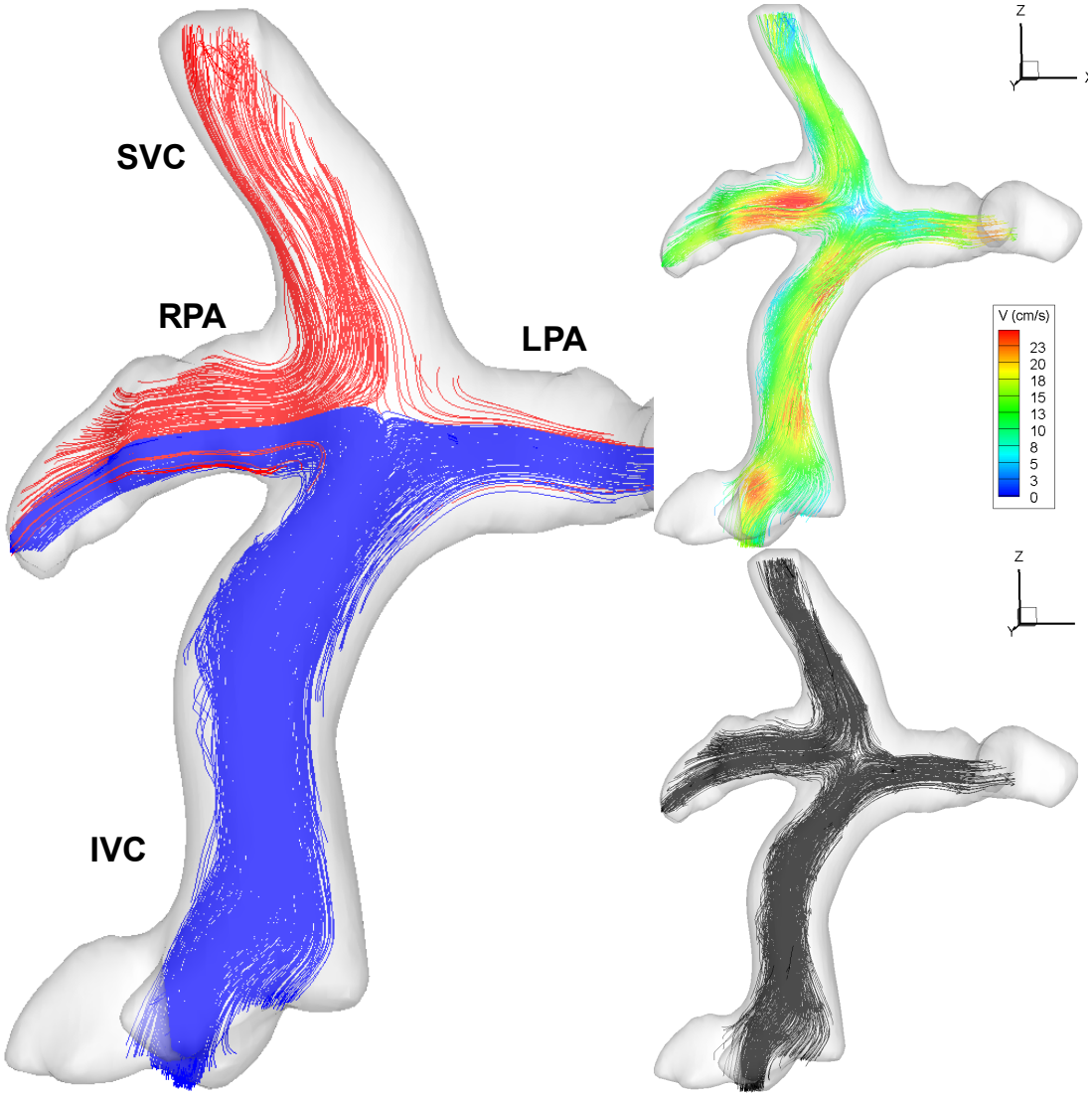

Figure 10.39: Flow structures through CHOP091 with no SVC-IVC offset, but with a flaring of the IVC towards the LPA in the beginning of systole. Notice that there was an almost even splitting of the IVC flow to both the LPA and the RPA in this phase, although there was a bias of the IVC flow to the LPA in some of the other phases of the cardiac cycle (see next figure). The IVC to LPA flow split averaged over the cardiac cycle was 65%. Almost all of the SVC flow appeared to go towards the RPA. This patient had no vortex present, and had an average particle transit time of 0.61s.

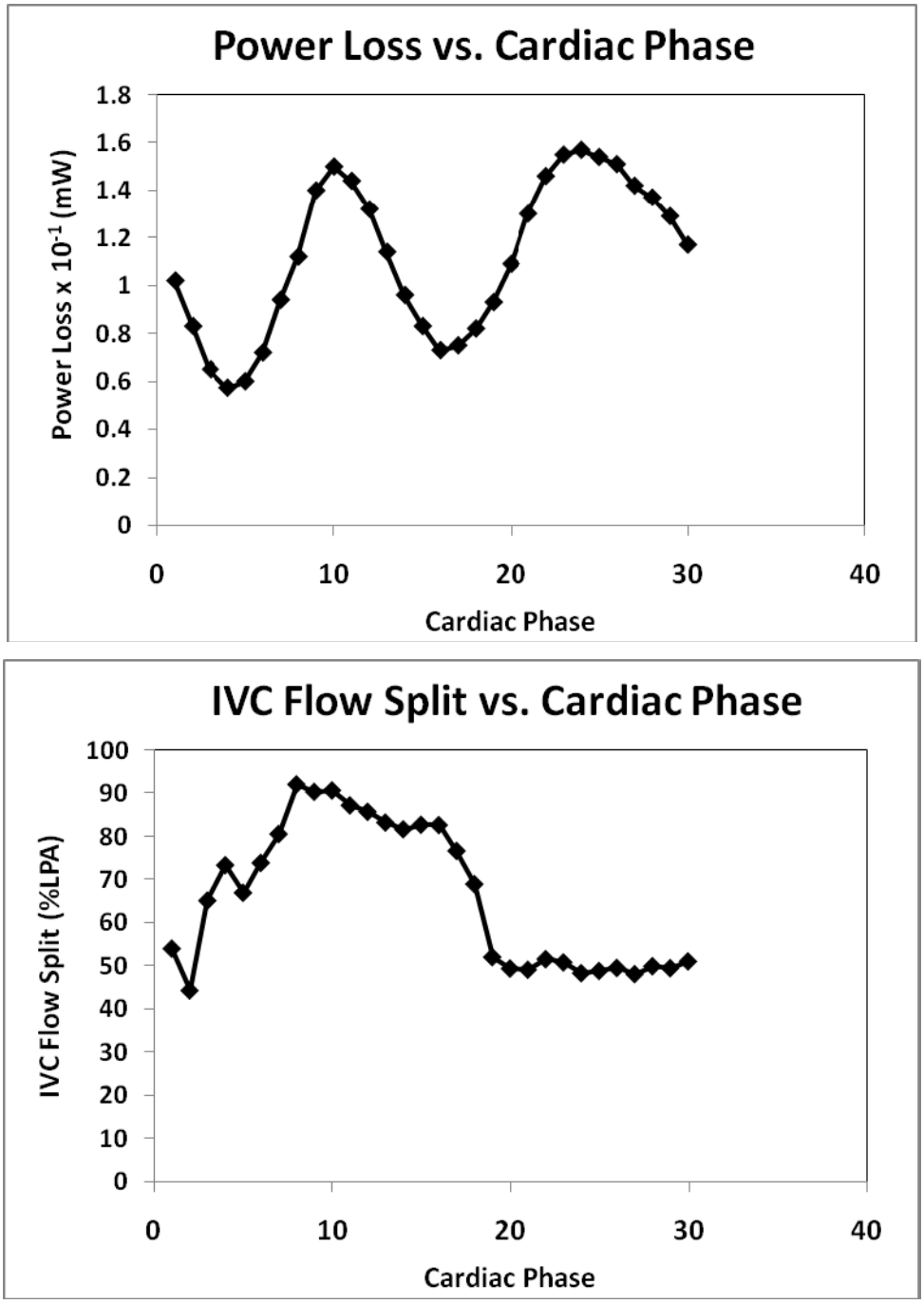

Figure 10.40: Power loss and IVC flow split curves for CHOP091. The power loss curve was quite pulsatile with a variation of 50% over the mean value of 1.2. Notice how there was a sharp increase in the bias of the IVC flow split towards the LPA over the cardiac cycle during mid systole. As the flow through the IVC increased, the angle with which the IVC was connected to the pulmonary arteries forced more flow from the IVC to go into the LPA, which resulted in a the higher IVC flow split at mid systole.

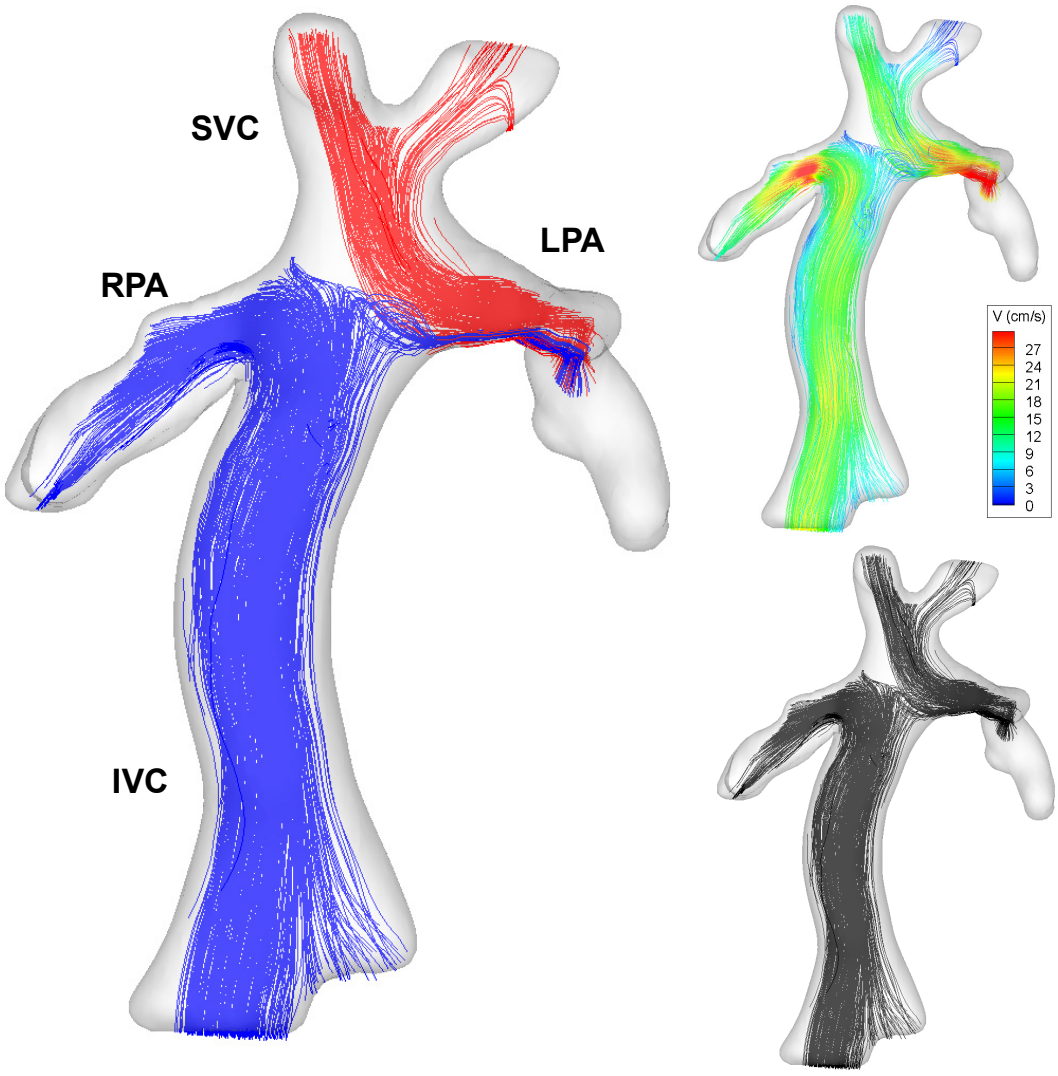

Figure 10.41: Flow structures through CHOP095, which had an IVC offset to the right side of the SVC. As a result there was a bias for flow from the IVC to go towards the RPA. Furthermore, the angle with which the SVC was connected to the pulmonary arteries, guaranteed that most of the superior caval flow went into the LPA. This was another example where the offset had more of an impact in governing the flow splits, even though the global LPA/RPA flow split was 53/47%. Overall, the flow structures through the baffle were quite smooth and streamlined. No vortex was present, and this model has a particle transit time of 0.58s.

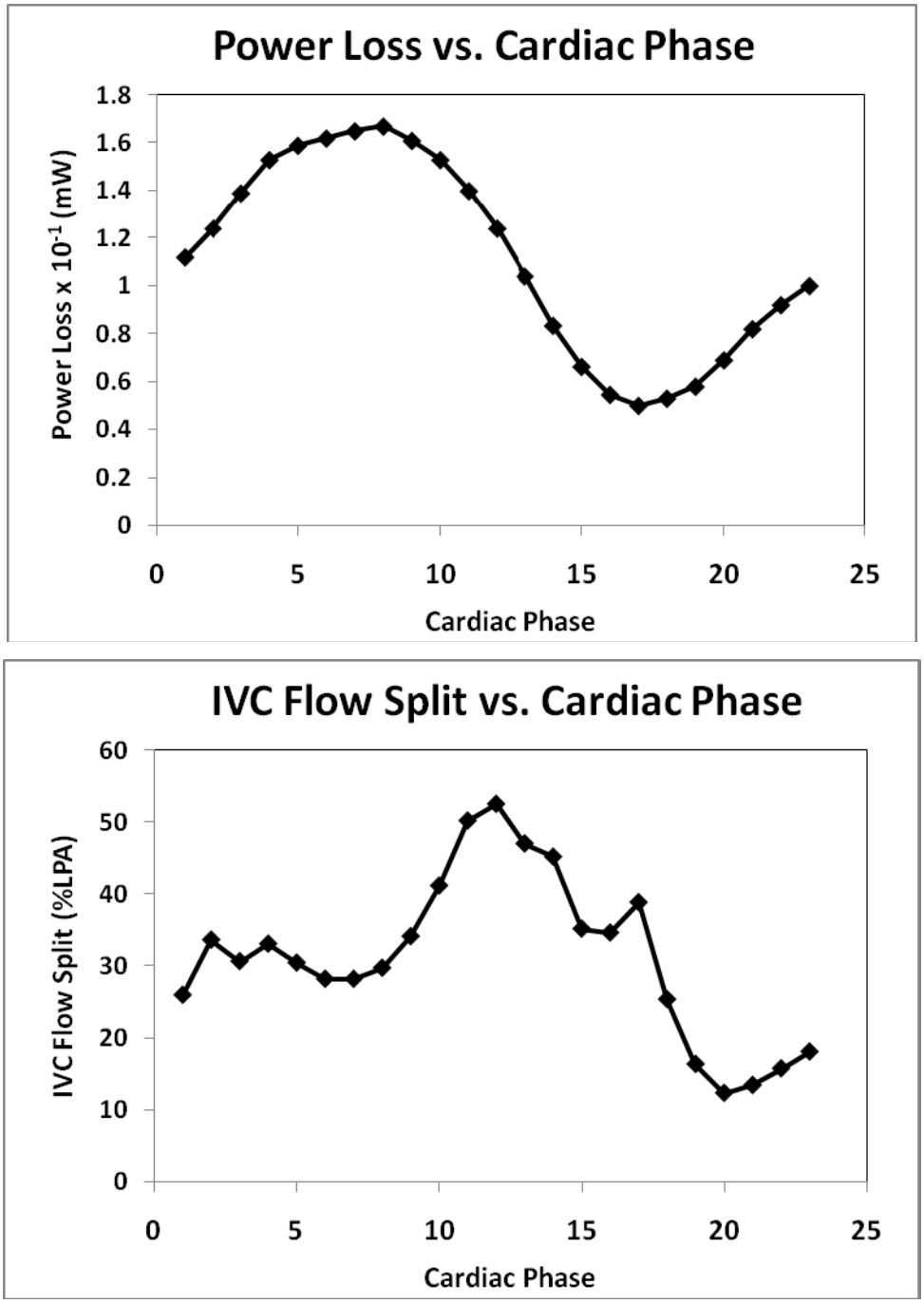

Figure 10.42: Power loss and IVC flow split curves for CHOP095. The power loss curve was quite pulsatile and behaved like a perfect sinusoid with a variation of 50% over the mean value of 1.2. The IVC flow split hovered around the 30% mark (average 31%)) and decreased to almost 10% late in the cardiac cycle, an effect that was evident from the flow streamtrace plots in the previous figure.

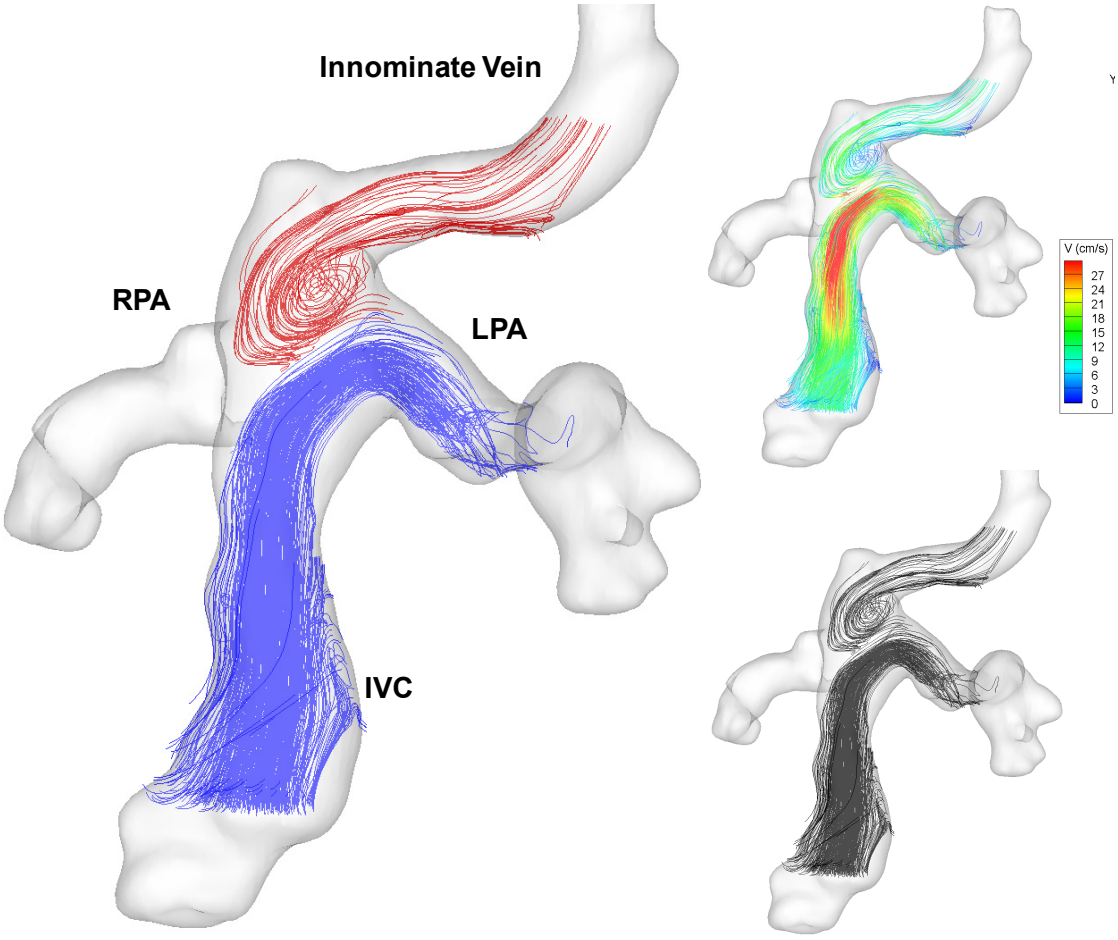

Figure 10.43: Streamtraces through CHOP125, which had a conduit connected to the Hemi-Fontan from inside the atrium. There was a large vortex that formed as a result of the Hemi-Fontan. There was no mixing between the SVC and the IVC except along the edge of the vortex. Most of the IVC flow had a tendency to go towards the LPA, while all the flow from the innominate vein seemed to go towards the RPA. However, no PC MRI slices were available for the RPA which is why no streamtraces were observed in the RPA. The size of the vortex was 1.5 cm, with an average particle transit times of 1.1s.

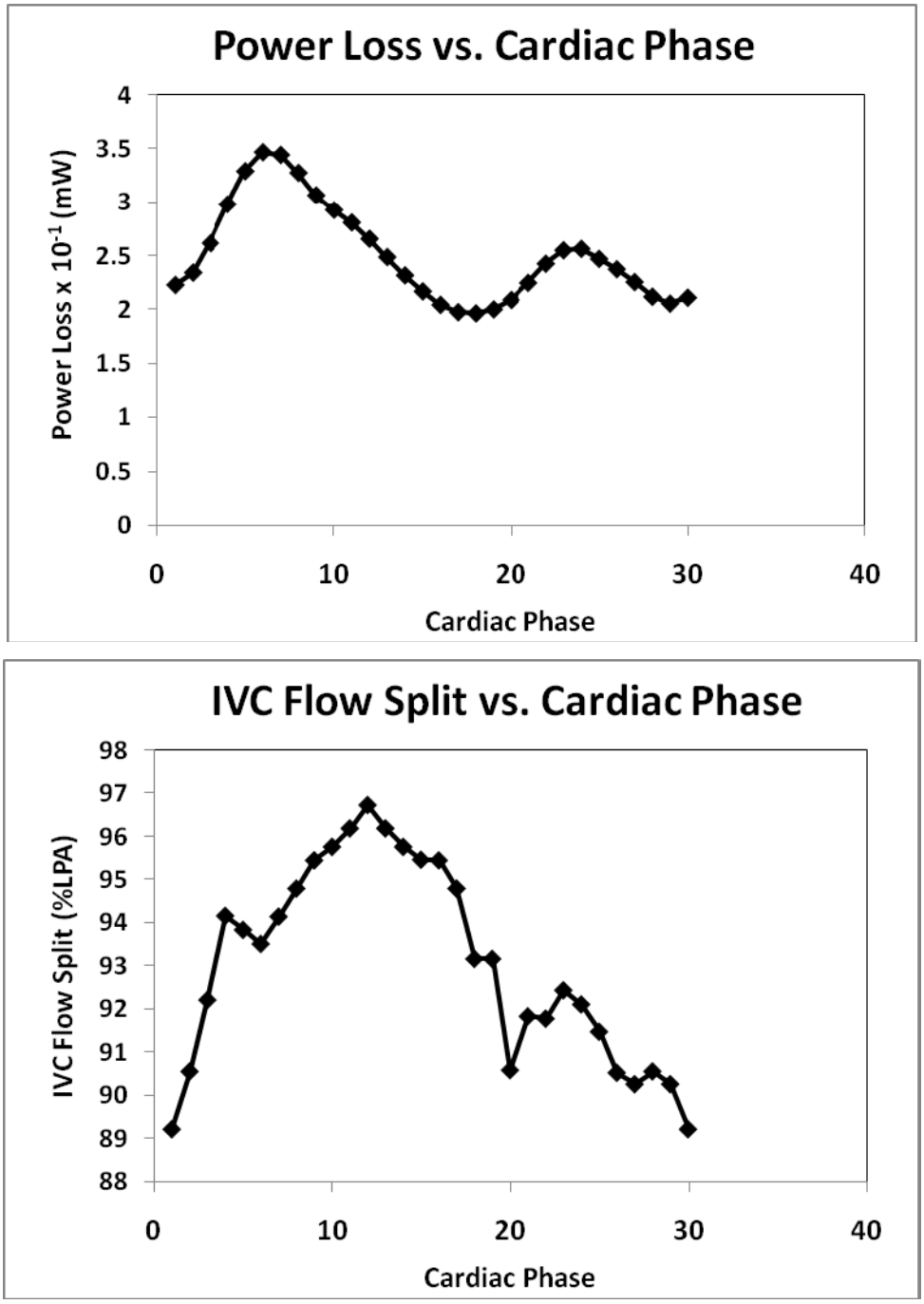

Figure 10.44: Power loss and IVC flow split curves for CHOP125. The power loss curve was quite pulsatile and there was a variation of almost 50 % around the mean value of 2.8. Most of the flow from the IVC had a tendency to go towards the LPA, as is clearly evident in the figure, with an average IVC-LPA flow split of 93%.

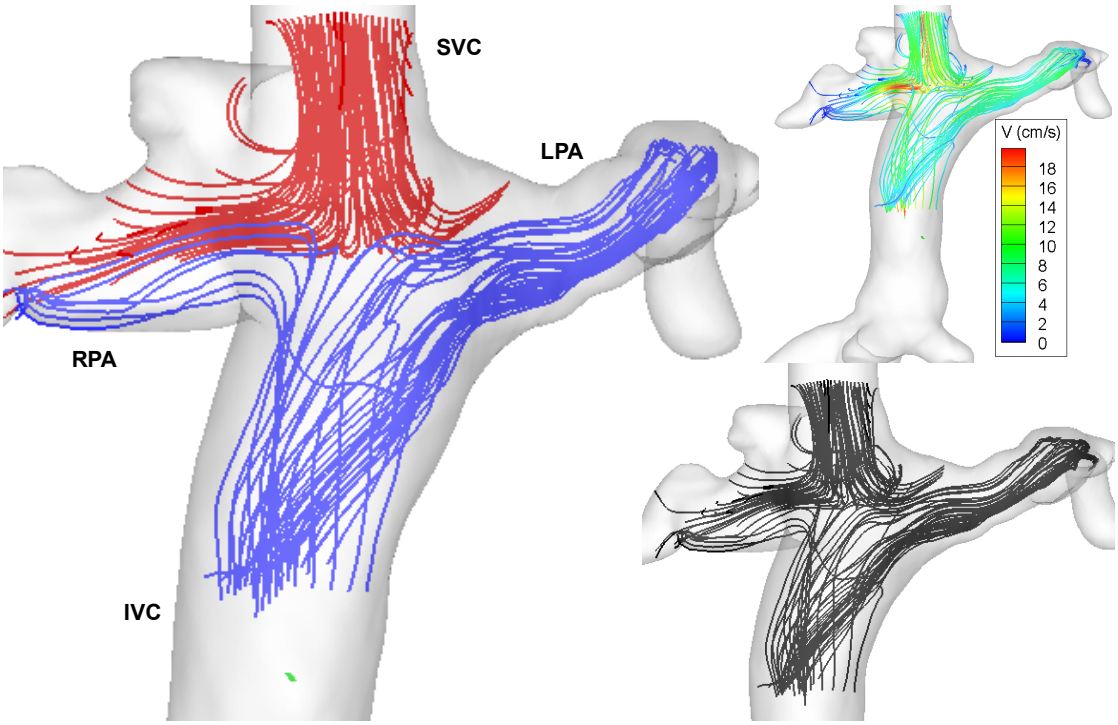

Figure 10.45: Streamtrace plots through CHOP129, which had an IVC conduit without an SVC/IVC offset. Notice that the flow fields through the IVC were quite smooth and streamlined. An even split of both the SVC and the IVC flow was achieved. An RPA upper lobe was present which resulted in some of the flow from the SVC getting redirected towards the RPA upper lobe. The velocity magnitudes were much lower in this model (peak velocity of 20 cm/s), which resulted in a slightly longer particle transit time of 0.97s.

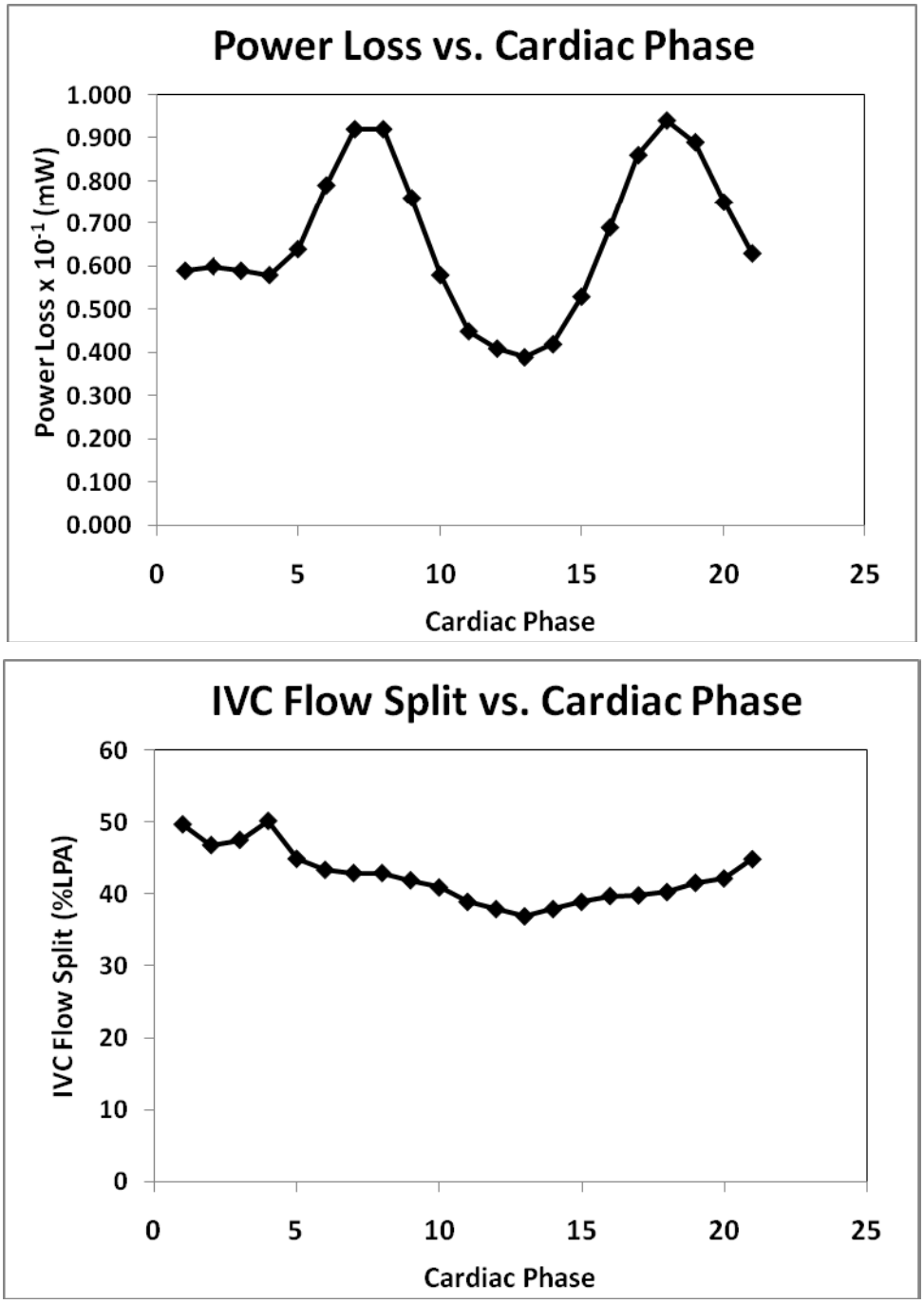

Figure 10.46: Power loss and IVC flow split curves for CHOP129. The magnitudes of the power losses were quite low fluctuating around a mean value of 0.67 x 10^{-1} mW, which was much lower than the previous cases. The lower power losses were because of the smaller magnitude of velocities (peak velocity of 20 cm/s vs. 30 cm/s). The IVC flow split was fairly uniform with a mean value of 42% throughout the cardiac cycle, which was consistent with the global LPA/RPA flow split of 34%/66%.

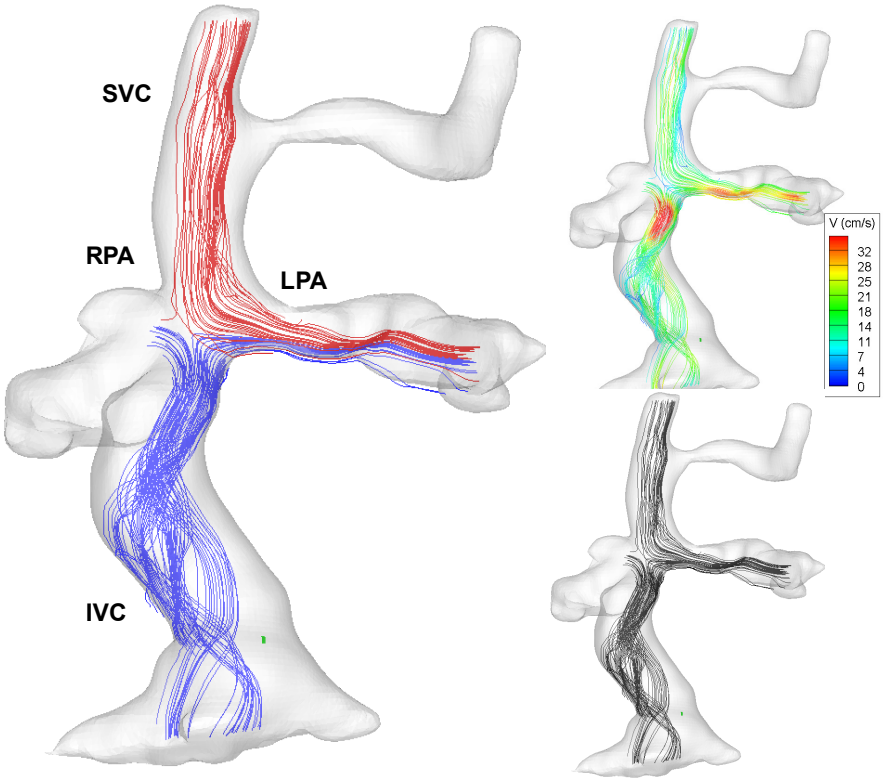

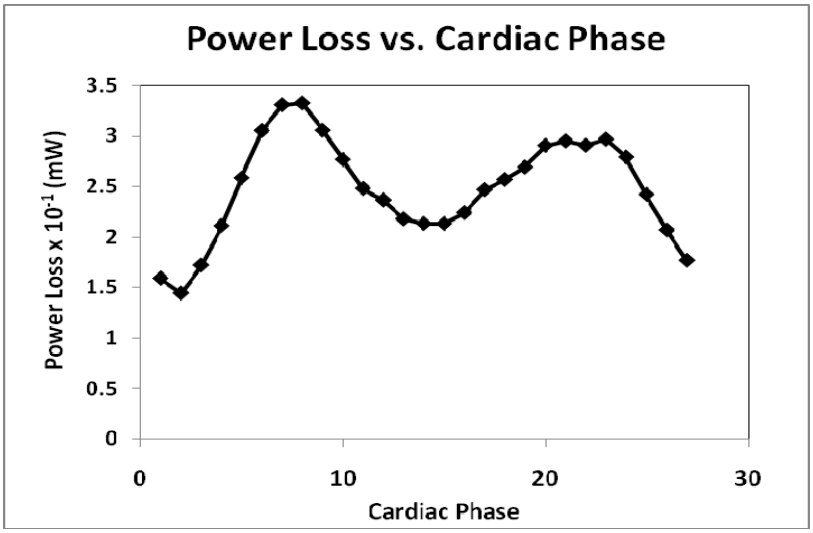

Figure 10.47: Flow stream trace and power loss curves for CHOP130. The IVC flow split curves over the entire cardiac cycle were not available for this patient. Only for one phase (phase 24) was it possible to reliably evaluate the IVC flow split (for the phase shown in the figure), while it was not possible to do so accurately for the rest of the phases. Low SNR from the PC MRI acquisition was one of the reasons why particles seeded at the IVC did not successfully end up at either the LPA or the RPA. The average particle transit time for the phase 24 was 0.38s.

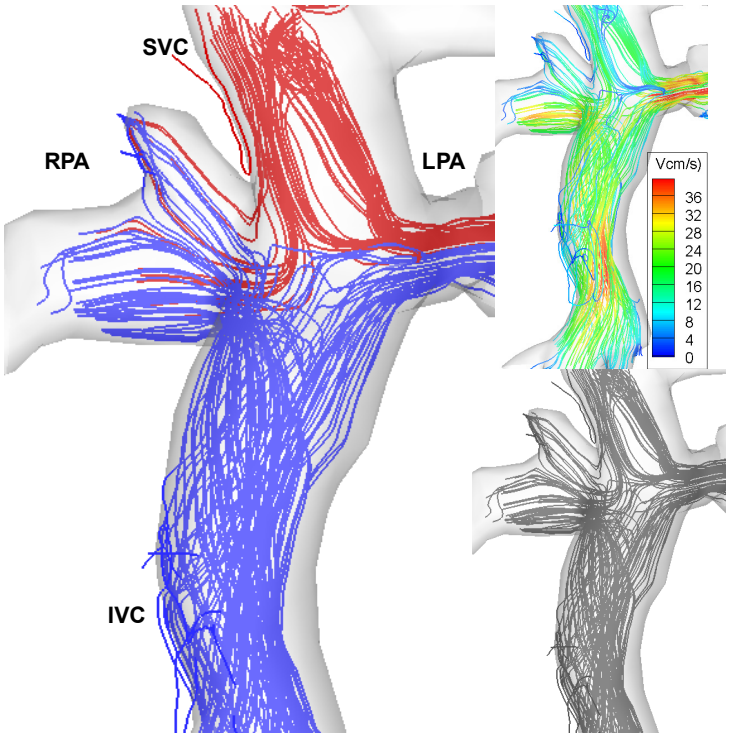

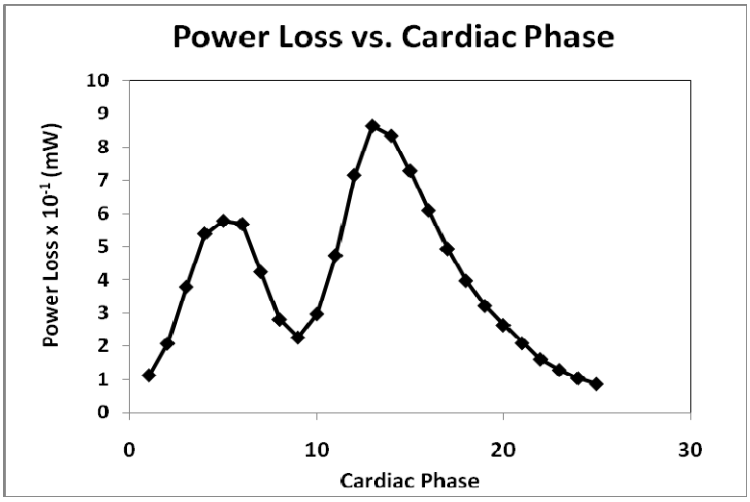

Figure 10.48: Flow streamtraces and power loss curves for CHOP132. IVC flow split curve over the entire cardiac cycle was not available for this model. It was not possible to extract accurate streamtraces for the remaining cardiac phases as most of the streamlines did not terminate at the pulmonary arteries (mostly due to the limited spatial resolution of the anatomic MRI stack). The IVC flow split evaluated was 32% for phase 17 which is the phase displayed in the figure. There were significant fluctuations in the velocity magnitude, ranging from 20 cm/s to 40cm/s (peak velocity), which resulted in high fluctuations in power losses (highest among all the patients used in the study).

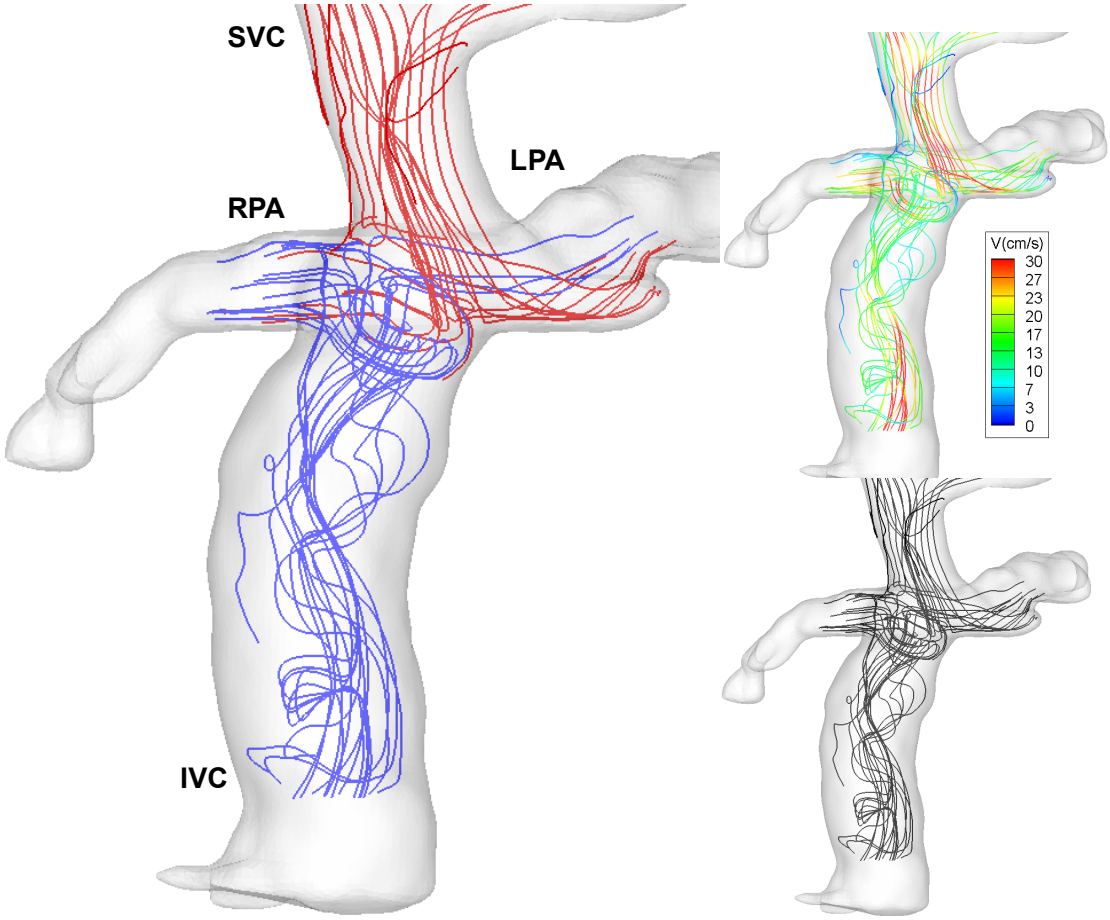

Figure 10.49: Flow structures through CHOP148. Only a few streamtraces are used here, in order to distinctly demonstrate the chaotic flow pattern in the IVC baffle. In this patient, chaotic flow patterns were observed in the IVC, which was different compared to other extracardiac patients. There was a strong jet that entered the IVC (as evident in the plot color-coded by velocity magnitude). Once the flow entered the extracardiac baffle, there seemed to be a lot of random motion before the flow entered the pulmonary arteries. This model also had a vortex that was present in the center of the connection, which was about 1 cm in diameter. The average residence time for a particle inside the IVC of this model was also quite high at 3.8 seconds.

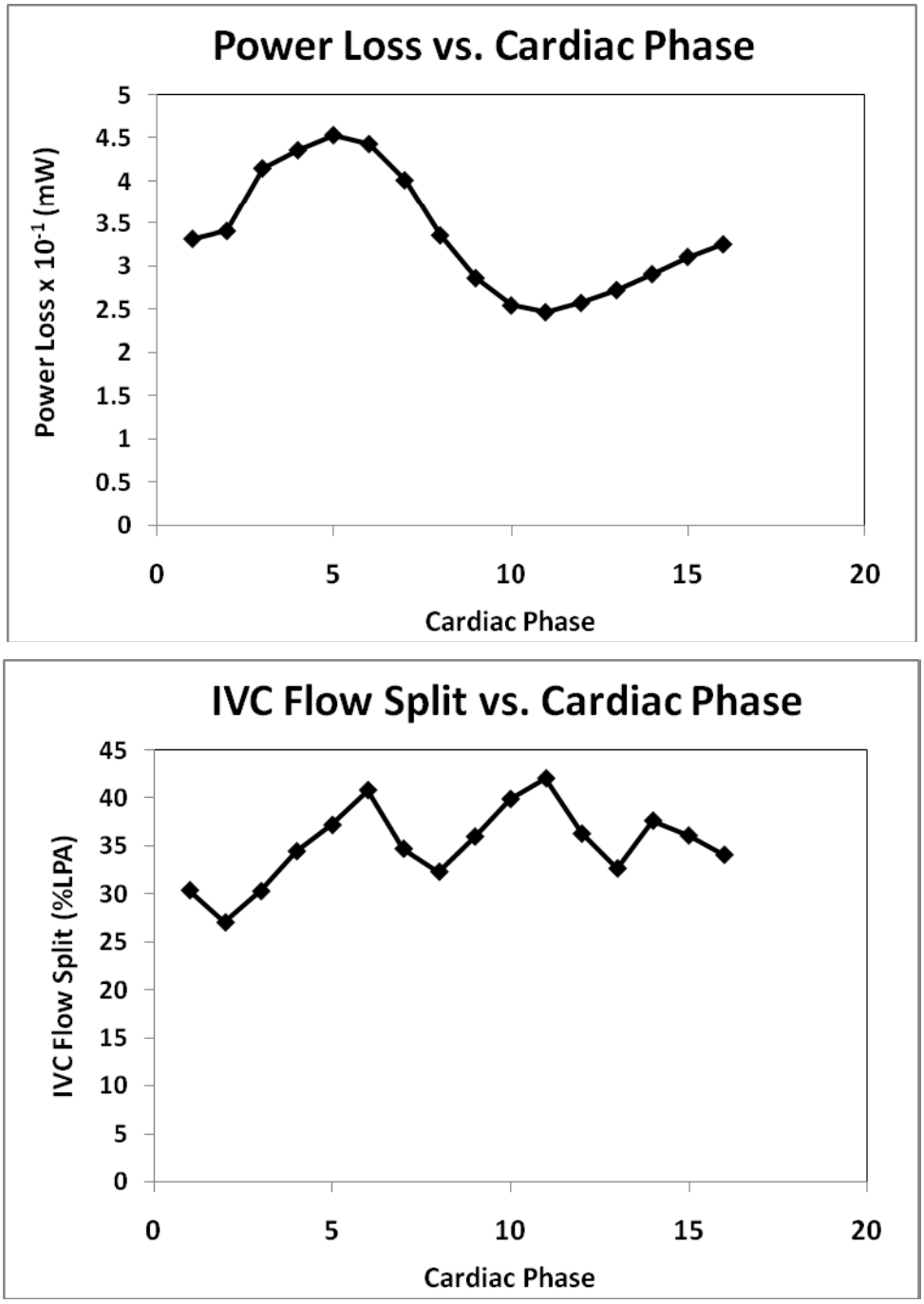

Figure 10.50: Power loss and IVC flow split curves for CHOP148. The power loss curve followed a perfect sinusoidal pattern for this geometry oscillating around a mean value of 3.5 x 10^{-1} mW. The power loss was higher than other extracardiac Fontan geometries, primarily because of the chaotic flow pattern that is evident in the previous figure. The IVC flow split followed a saw-toothed pattern having a mean value of 35%.

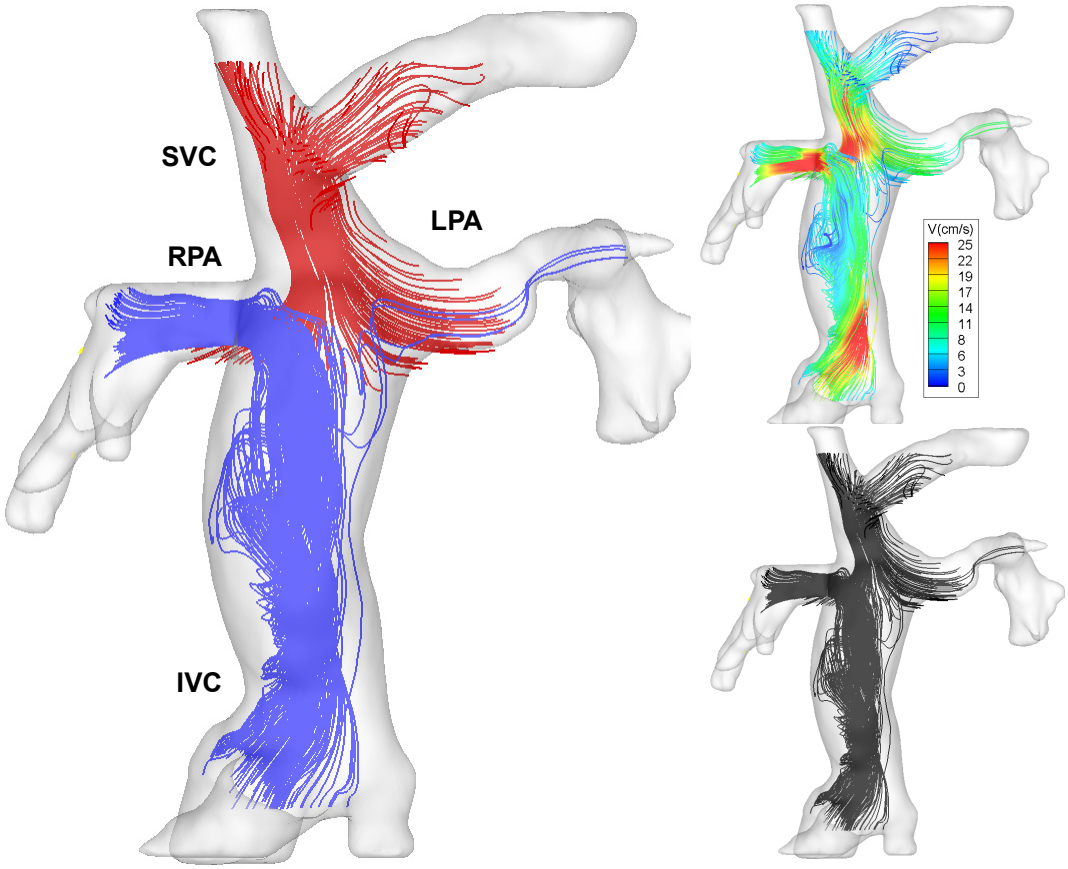

Figure 10.51: Flow structures through CHOP150. In this case, a clear helical flow pattern was observed in the IVC. Even though no offset was present between the SVC and the IVC, most of the flow from the IVC preferred to go to the RPA, while the SVC flow seemed to be well distributed between the LPA and the RPA. One of the reasons for the biased hepatic flow split was that the global LPA/RPA flow split was 37/63%, which meant that the right lung had lower resistance compared to the left lung. The average transit time for a particle was also quite high for this case at 2.54s

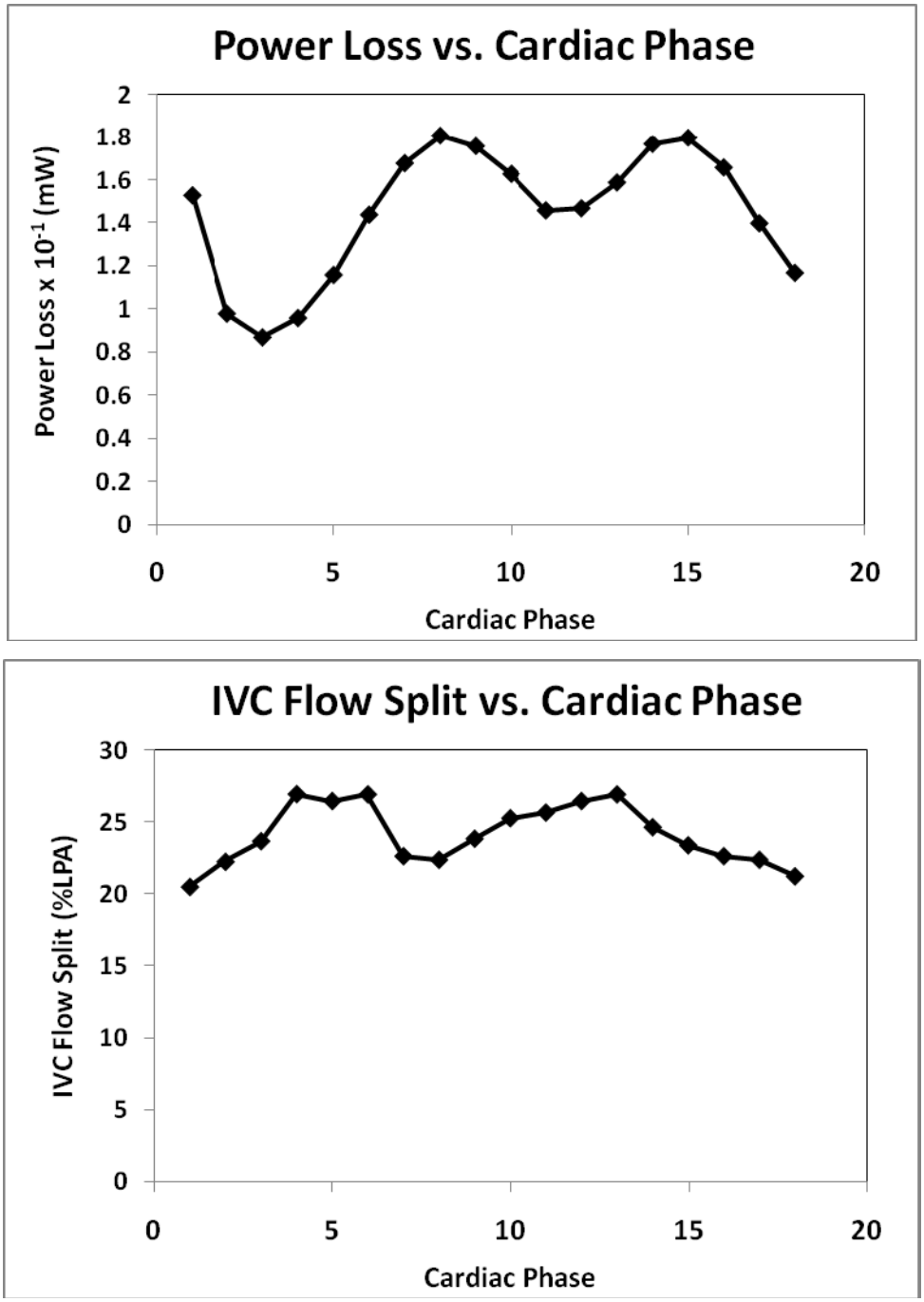

Figure 10.52: Power loss and IVC flow split curves for CHOP150. The power loss curve was biphasic, with two peaks towards the end of diastole. The IVC flow split to the LPA was quite steady at 24% over the cardiac cycle.

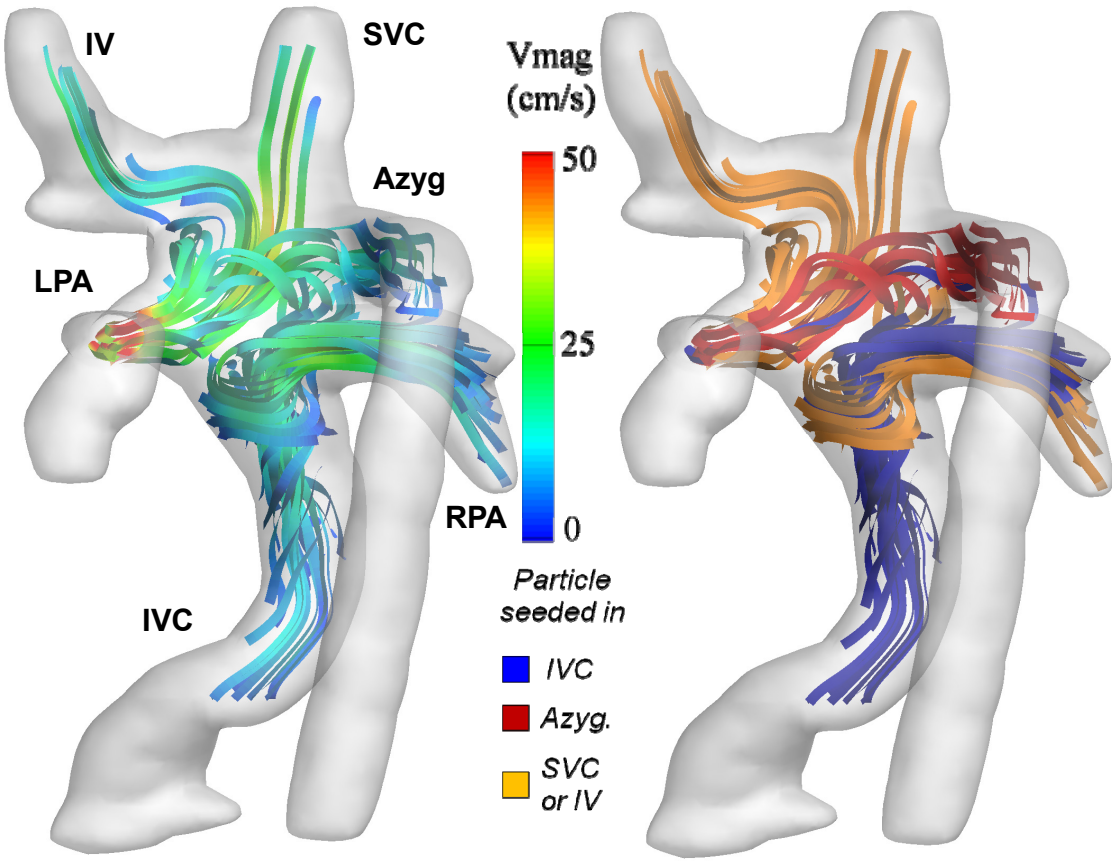

Figure 10.53: Flow through the TCPC with an interrupted IVC having an azygous vein continuation (CHOP_M1). The extracardiac conduit primarily carried the flow from the hepatic veins. On the left are stream-ribbons color-coded by their velocity magnitude and on the right are stream-ribbons color-coded by their origin. The vessels involved in this complex configuration were Azyg: Azygous vein; IV: innominate vein; SVC; IVC; LPA; and the RPA. Observe that most of the flow from the IVC entered the RPA. The azygous vein forced all the superior caval flow into the left pulmonary artery, leaving little room for the flow from the IVC to enter the LPA. This patient had a severe case of pulmonary arteriovenous malformations that resulted due to this abnormal hepatic flow distribution.

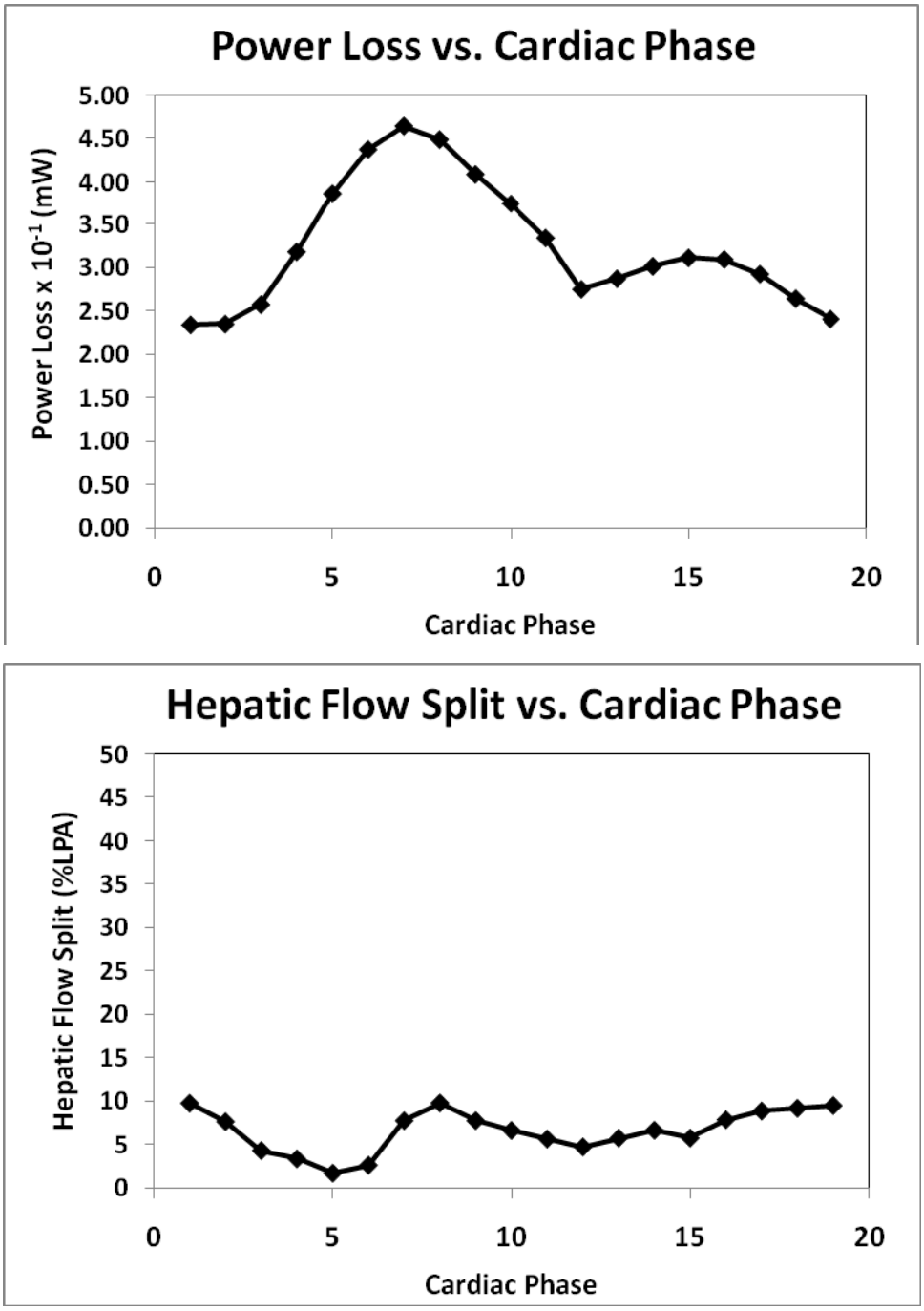

Figure 10.54: The power loss and hepatic flow split curves associated with CHOP_M1. Significant variation in power losses were observed over the entire cardiac cycle, while there was minimum variation in hepatic flow splits, with an average value of 9.7%.

10.3.2.2 Effect of flow pulsatility

Shown in Figure 10.55 are time-varying flow fields (animations included) over the entire cardiac cycle for CHOP091 (extracardiac) and CHOP068 (intraatrial). The global flow features for both the models did not change significantly over the cardiac cycle. This was confirmed by the vector plots of the original velocity fields extracted from the central plane of the coronal stack. All the dominant flow features (vortex in the intraatrial, and helical flow pattern in the extracardiac) were evident through out the cardiac cycle. The diameter of the vortex in CHOP068 appeared to reduce in size towards end diastole. An acceleration of velocities over the cardiac cycle was evident along the edge of the vortex. Throughout the cardiac cycle, the flow from the IVC seemed to get well distributed to both the pulmonary arteries.

For CHOP091, the flow was streamlined throughout the cardiac cycle, with the superior caval flow preferentially going towards the RPA and flow from the IVC getting distributed to both the pulmonary arteries with a slight bias towards the LPA. As the flow velocities increased in the IVC, there was a corresponding increase in LPA velocities, highlighting the preferential flow of the IVC to the LPA. This phenomenon was evident in the IVC flow split curves (Figure 10.40) as well where the IVC contribution of flow to the LPA increased significantly with increasing flow rates. Similarly when velocities increased in the SVC, a corresponding increase was observed in the RPA demonstrating the preferential flow going of the SVC to the RPA. Even though there was no offset between the SVC and the IVC, and their connection angle to the pulmonary arteries were the same, IVC flow favored to go towards the LPA (higher momentum), while the SVC flow turned and went into the RPA.

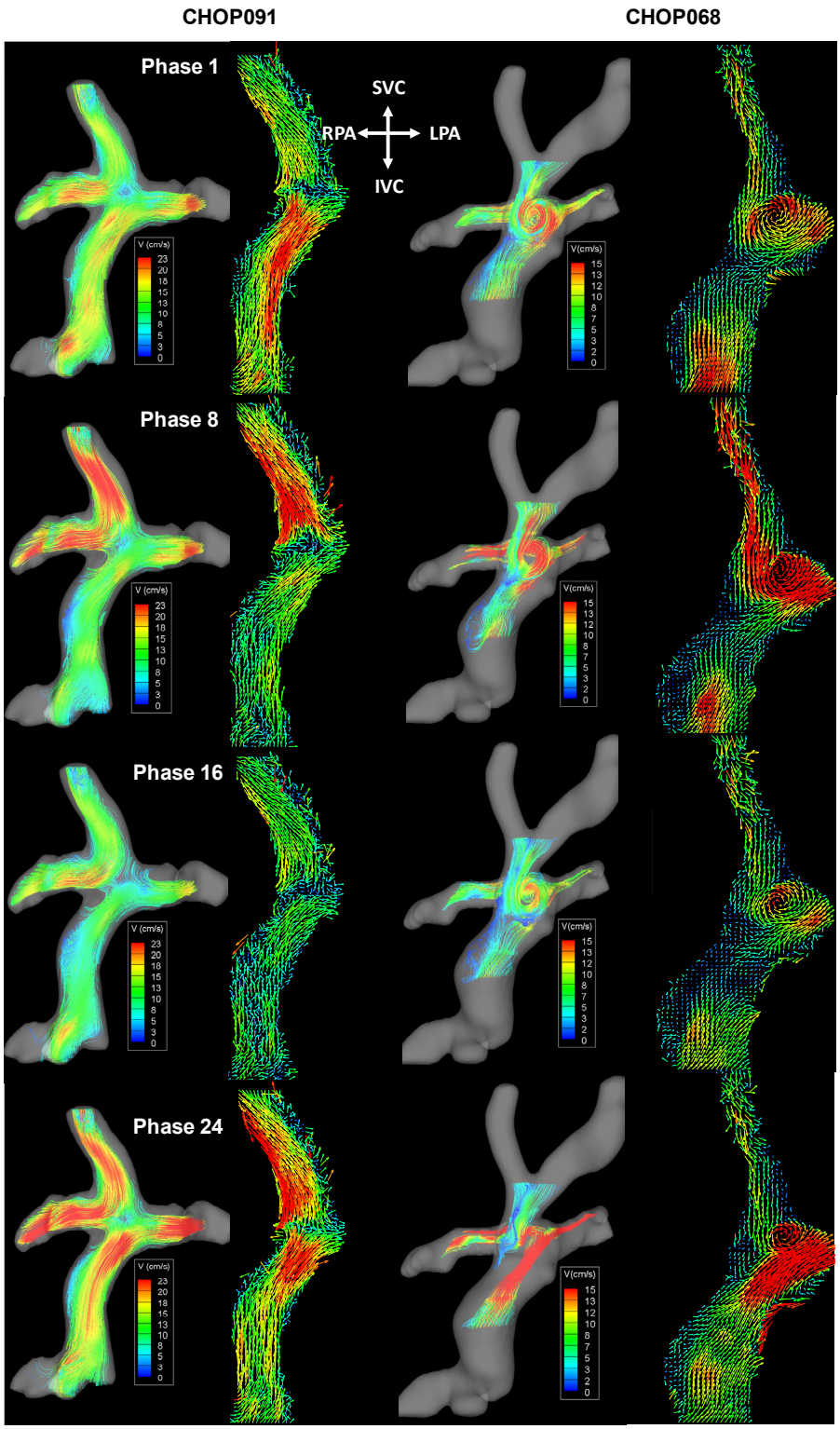

Figure 10.55: Time-varying velocity fields (3D interpolated and the original vector field) through an extracardiac (CHOP091) and an intraatrial connection (CHOP068)

10.3.2.3 Quantitative summary of intraatrials vs. extracardiac Fontans

Table 10.6 shows a summary of results comparing the quantitative hemodynamic parameters of intraatrial and extracardiac TCPCs. The results were spatially and temporally averaged to obtain a single number for the entire TCPC. The results were then averaged for all the patients in the specific group. Differences in power losses, power loss pulsatility, and particle transit time were close to being statistically significant, while the IVC flow splits were not statitistically different between the two groups. All intraatrial (except CHB006 and CHB008) flow fields were characterized by a large vortex in the center of the connection. This vortex was absent from all the extracardiac TCPCs analyzed in this study, except for CHOP125. This model had a Hemi-Fontan operation performed during the second stage procedure that resulted in the vortex.

Table 10.6: Comparison of hemodynamic parameters between extracardiac and intraatrial TCPCs

Parameter	**Extracardiac**		**Intraatrial**		**p**
	Mean ± S.D.	**(Min, Max)**	**Mean ± S.D.**	**(Min, Max)**	
Age	6.7 ± 3.4	(4, 15)	7.1 ± 2.7	(5, 12)	0.77
BSA	0.96 ± 0.35	(0.63, 1.75)	0.86 ± 0.1	(0.67, 1)	0.45
Power Loss (10^{-1} mW)	1.99 ± 1	(0.66, 4)	1.18 ± 0.81	(0.27, 2.72)	0.08
Hepatic Flow Splits	42.36 ± 23	(12, 92.9)	45.8 ± 13.67	(29.3, 78.96)	0.72
Vortex Sizes	0.54 ± 0.54	(0, 1.5)	1.6 ± 0.76	(0.5, 3)	0.004
Particle Transit Time	1.19 ± 1.12	(0.37, 3.88)	2.17± 1.8	(0.64, 6.27)	0.19
Energy Loss Pulsatility	0.89 ± 0.44	(0.36, 1.94)	0.64 ± 0.26	(0.34, 1.13)	0.15

10.3.3 3D TCPC Flow Analysis: Discussion

In this section, a comparison of 3D hemodynamics in 20 patients with a Fontan connection was presented. This is the first time that *in vivo* flow structures inside the TCPC have been reconstructed and quantified. Prior studies have primarily focused on quantifying the global hemodynamics within the TCPC using ultrasound[217] and 2D MRI[146, 147]. The only two studies that sought to evaluate the flow structures within the Fontan baffle were from Be'eri[143] and Sharma[71], who mapped the velocities in a single plane of the TCPC geometry. Such 2D analyses do provide significant insights into Fontan hemodynamics, but in order to truly understand the three dimensionality and complexity of TCPC flow fields, 3D flow analyses is required. In this study, the entire 3D flow field inside the TCPC was resolved using a novel divergence free interpolation technique applied on a stack of PC MRI data acquired on Fontan patients. Quantitative parameters such as power losses, hepatic flow splits, particle transit times, vortex sizes, and power loss pulsatility were computed, and 3D flow streamlines for each cardiac phase were reconstructed for all Fontan patients used in this study.

Significant strides have been made in the last two decades towards improving the surgical management and care of Fontan operations. Thanks to these efforts, many children with a single ventricle physiology are now entering adulthood and a new phase in their lives. However, the single ventricle circulation is not perfect, and these children are bound to experience a lot of complications in their adult lives. Abnormal long term effects are currently unknown, except for few documented Fontan failure modes such as ventricular dysfunction and protein losing enteropathy. This poses new challenges for cardiologists in adult congenital heart disease programs, and demands new diagnostic

tools in order to better understand the Fontan physiology. The technologies developed as part of this thesis, are a significant step at this direction.

The time varying 3D velocity fields evaluated using the DFI technique allowed for the direct *in vivo* quantification of parameters such as power losses, hepatic flow splits, vortex sizes, and particle transit times which could be of significant diagnostic importance for Fontan patients. Currently, CFD is the only possible way these parameters can be quantified. Although CFD is a powerful technology and has the potential to play a significant role in clinical cardiovascular research, it is quite cumbersome to implement routinely in the clinic. Furthermore, CFD is quite complex and requires engineering expertise to be conducted correctly. On the contrary, the DFI technique presented in this chapter is fully automatic, and with minimal user interaction, can be used to fully reconstruct the time varying 3D flow fields within the TCPC directly from *in vivo* PC MRI measurements.

Differences in power losses between intraatrial and extracardiac Fontan types were close to being statistically significant at a p value of 0.08. The higher power losses that were evident in extracardiac geometries were primarily due to the smaller IVC baffle size. This was consistent with the observation in Chapter 9, where extracardiac TCPCs had significantly higher velocities compared to the intraatrial geometries. When the power losses were normalized to BSA, the statistical significance of the p-values dropped from 0.08 to 0.41. This was consistent with prior studies, where pulmonary artery diameter, rather than the Fontan type, seemed to influence the total energy loss in Fontan connections the most. Within intraatrial Fontans themselves, those with a bidirectional Glenn had significantly higher power losses (2.15 ± 0.5 mW) compared to those with a

Hemi-Fontan (0.7 ± 0.3). However, only 3/9 had an intraatrial with a BDG, and therefore the sample size was quite small in order to derive any significant conclusions.

Although no differences in power losses were observed, there were significant differences in flow structures between intraatrial and extracardiac TCPCs. Large vortices were clearly evident within the baffle of intraatrial Fontan types. Furthermore, the nature of the vortex differed between intraatrials with a Hemi-Fontan and those with a BDG. All Hemi-Fontan intraatrials had a large vortex present in the region where the SVC and IVC were connected to the pulmonary arteries. For the intraatrial model with a BDG, the vortex was present inferior to the pulmonary arteries for one model, where the intraatrial pouch was present (CHB004). The sudden expansion in area going from the IVC to the intraatrial baffle, resulted in this slow recirculation region. For the other models, there was no pouch that was evident, and hence the size of vortex was quite small. The presence of a vortex has been previously documented using CFD models by several groups[4, 17, 58, 68, 218], but this phenomenon has only now been reported using *in vivo* imaging methods. Such a vortex was completely absent in extracardiac Fontan patients. Instead, the superior venous returns typically collided and split at the center of the connection, resulting in a characteristic flow stagnation point. Interestingly, the hemodynamics observed in the other two intraatrial TCPCs with a BDG (CHB006 and CHB008), were similar to those observed in extracardiac TCPCs. This suggests that the type of second stage palliation (BDG vs. Hemi-Fontan) could play a significant role determining the hemodynamics after the final stage Fontan operation.

There were no differences in IVC flow splits between the two groups, although extracardiac TCPCs had more variability in the percentage of IVC flow going to the left

lung. While the intraatrial Fontans fostered good caval flow mixing, the offset between the SVC and the IVC seemed to play a significant role in determining the IVC flow splits. If the offset was to the right of the SVC, then the IVC flow had a tendency to go towards the right lung, and if the offset was towards the left lung, then the opposite phenomenon was observed. Similarly, the presence of an azygous vein and its orientation with respect to the Fontan connection also seemed to play a significant role in governing the hepatic flow splits as is evident in Figure 10.53.

Achieving equal hepatic flow to both the lungs plays an important role in maintaining good cardiovascular function in Fontan patients. Abnormal hepatic flow distribution, which has been implicated in the development of pulmonary arteriovenous malformations (PAVMs), is often controlled by the geometry of the TCPC. Therefore, care should be taken during the Fontan surgery, to ensure that the offset is just enough to ensure an optimal hepatic flow distribution.

The primary flow structures did not change significantly over the cardiac cycle for both intraatrial and extracardiac TCPCs, as is evident in Figure 10.55. For some extracardiac geometries (CHOP091 and CHOP095), variations in IVC flow splits were observed, which stemmed from the geometric configuration of the IVC relative to the pulmonary arteries. All the results in this study demonstrate that geometry plays a significant role in governing the hemodynamics of the TCPC. This brings up an important consideration when choosing the right surgical procedure for the final stage of the Fontan procedure: offsetting the IVC relative to the SVC. Although offsetting the SVC and IVC has been shown beneficial from a power loss perspective, it does result in a biased IVC flow to the pulmonary artery in the direction of the offset.

Finally, the average transit times for a particle to enter and exit the Fontan connection were quantified as well. Although particles tended to reside for longer periods of times within intraatrial TCPCs, this observation was not statistically significant. One of the reasons was that there were two extracardiac geometries (CHOP148 and CHOP150) where particle transit times wer quite high. This was because significant instabilities in flow structures were present in the IVC (Figure 10.49 and Figure 10.51). Higher particle transit times could have important implication in the development of thrombi in Fontan baffles. Prolonged particle transition times, and presence of recirculation regions, could promote the aggregation of activated platelets, which may eventually result in a thrombus. However, further clinical studies correlating this parameter with the incidence of thrombus formation is necessary in order to prove this hypothesis.

10.3.4 3D TCPC Flow Analysis – Limitations

Despite the promise of the DFI technique for reconstructing 3D TCPC flows, there are certain limitations associated with the current approach that need to be addressed. The DFI technique is dependent upon the quality of the measured velocity field, and hence if a coronal dataset is used, then maximum care should be taken to ensure that there is no motion between successive PC MRI acquisitions. If there is motion between the acquisitions, then the resulting measured velocity vector field for determining the interpolating coefficients will be inaccurate, and any analysis performed as a consequence would be incorrect. In this study, 4/24 patients selected had this problem, which is why they were not included in the analysis. Another weakness is that

the DFI technique cannot be used to interpolate a vector field when there is minimal or no flow. In such a situation, the original PC MRI produces a vector field that has low magnitude and random direction, and consequently the interpolated vector field will not be accurate. From an image acquisition stand-point, the strategy of using the coronal dataset for 3D flow reconstruction requires that the images be acquired at the exact same respiratory cycle, with minimum respiratory artifacts. This can be accomplished by using a faster sequence with respiratory gating minimizing any motion artifacts.

Another limitation is that power losses evaluated using images acquired in the coronal orientation maybe underestimating the true power losses within the Fontan baffle. Since only 3-4 slices are acquired spanning the IVC conduit, the resolution of the measured velocities along the walls is low, and hence power losses due to wall friction may not be well resolved. Acquiring more slices will alleviate this problem. Another potential weakness is that any flow instabilities in the Fontan baffle would result in the dephasing of the MRI signal, which may also result in the underestimation of power losses. Although the accuracy of the DFI technique for quantifying power losses were evaluated using *in vitro* experiments, unfortunately no CFD simulations or *in vitro* experiments were available for the *in vivo* datasets used in this study.

The particle transit times evaluated in this study were not the true particle transit times in the strictest sense, as they were evaluated using instantaneous particle streamlines. In order to evaluate the true particle transit times, pulsatile streaklines have to be used by taking the entire time-varying flow field into account. Previous studies on the systemic arterial side[168] have shown that a high temporal resolution of 12,000 time points over the cardiac cycle is needed in order to evaluate particle pathways using

streaklines. However, the temporal resolution of the PC MRI acquisition is not high enough (15-30 phases/cardiac cycle) to evaluate particle streaklines accurately. Hence, instantaneous streamlines were used as the alternative. The non-pulsatile nature of the systemic venous flow compared to the systemic arterial side, hints that particle transit times evaluated using streamlines should provide an order of magnitude approximation of true particle transit times. However, a more thorough validation will have to be performed in order to precisely identify the errors associated with using instantaneous streamlines for evaluating particle pathways.

10.3.5 3D TCPC Flow Analysis: Conclusion

In this study, the 4D (3D space+time) flow fields were evaluated for the first time within the TCPC using *in vivo* PC MRI. The new techniques developed allowed for detailed qualitative and quantitative analyses of intraatrial and extracardiac TCPCs. Significant differences in flow structures between the two groups were illustrated, which highlighted the advantages and disadvantages of both intraatrial and extracardiac TCPCs. The goal of this study was not to recommend one surgical procedure over the other, but to provide the surgeon with valuable quantitative hemodynamic endpoints that should be combined with other clinically relevant data in order to make informed surgical decisions.

10.4 Chapter Summary: *In vivo* PC MRI studies – 2

The studies presented in this chapter demonstrated that PC MRI can be used to quantify the detailed 3D hemodynamics within the TCPC if appropriate post-processing methods are used. In the first section, a comprehensive validation of the novel divergence

free interpolation algorithm was presented, which was an important step before the technique could be applied to *in vivo* datasets. The strength of the technique was evident in subsequent sections, where significant insights into the TCPC hemodynamics were gained. At the conclusion of sections 10.2 and 10.3, the sub-hypothesis associated with specific aim 3 was successfully tested.

CHAPTER 11

RESULTS AND DISCUSSION: MATHEMATICAL MODELING OF THE SINGLE VENTRICLE CIRCULATION

11.1 Overview

This chapter ties in the hemodynamics of the TCPC with the entire single ventricle circulation using a lumped parameter mathematical model described in Chapter 7. In the previous chapters the hemodynamics of the TCPC were quantified in significant detail. Specifically new techniques for the direct assessment of ventricular power output, and power losses of the TCPC were described. However, it is still not known how the power loss of the TCPC impacts the overall resting and exercise hemodynamics of the single ventricle circulation. To investigate this impact in greater detail, a lumped parameter mathematical model was developed in Chapter 7. The results are presented and described in this chapter.

11.2 Results: Impact of TCPC Resistance on Single Ventricle Hemodynamics

As explained in Chapter 7, computational fluid dynamic simulations conducted on 16 models were used for characterizing the TCPC resistances in this study. The pulmonary vascular resistance and the systemic vascular resistance were obtained from cardiac catheterization data on 40 patients (see Appendix C.5 for a summary of the patients) who were different from the 16 patients used for the CFD simulations. Since this was a mathematical modeling study, and not a patient specific study, these values only served as parameters for the model. Please note that the CFD simulations were

carried out be Dr. Kevin Whitehead from Children's Hospital of Philadelphia. The characteristics of 16 patients used in the study are described in

Table 11.1. Please note that this information is also available in Chapter 7. The only difference is that the patient number is provided in addition to the model number.

Table 11.1: Patient characteristics for the CFD study

Model	Patient Number	CHD	Fontan Type	Simulation conditions (L/Min)
M01	CHOP018	HLHS	IA	2,4,6
M02	CHOP022	DORV, PA	EC (BL)	2.5, 5, 7.5
M03	CHOP025	HLHS	IA	2.4, 4.8, 7.2
M04	CHOP030	TA	IA	2.9, 5.8, 8.7
M05	CHOP037	PA, HRHS	IA	2.75, 5.5, 8.25
M06	CHOP055	Heterotaxy, DC	EC (BL)	2.37, 4.72, 4.37
M07	CHOP067	DILV, TGA	EC	3.5, 7, 10.5
M08	CHOP088	DC, TA	EC	2.7, 3.7, 4.7
M09	CHOP089	TA	EC	3.03, 6.06, 9.09
M10	CHOP090	PA, HRHS	EC	3, 6, 9
M11	CHOA006	DORV, DC	IVC – MPA	3,4,5
M12	CHOA007	HLHS	EC	2,3,4
M13	CHOA008	HRHS	EC	3,4,5
M14	CHOA009	SV, DIAV	IA	2,3,4
M15	CHOA011	HLHS	IA	4,6,7
M16	CHOP013	HLHS	EC	2,3,4

11.2.1 Single Ventricle Resistance

The average age and body surface area of the 16 patients used in this study (with CFD data) were 8.25 ± 4.28 (min= 2, max= 18) years, and 0.97 ± 0.28 (min=0.54, max=1.49) m^2 respectively. The average PVR and SVR measured on the 40 patients with cardiac cath data were 1.96 ± 0.80 (min = 1, max = 4.3) WU, and 18.4 ± 7.2 (min= 10.6, max= 47.8) WU respectively. Figure 7.3 depicted the change in TCPC resistance with exercise for the 16 CFD models used in the study. TCPC resistances were 0.39 ± 0.26 WU (min=0.1, max=1.08) during rest, 0.70 ± 0.45 (min=0.13, max=1.72) during moderate exercise, and 1.06 ± 0.73 (min=0.18, max= 2.65) WU under severe exercise. The most efficient TCPCs at rest and exercise were M7 and M9, respectively. The least efficient TCPCs at rest and exercise were M13 and M17. The average TCPC resistance evaluated using CFD was found to be a significant percentage of the PVR measured using cardiac catheterization (22% at rest).

11.2.2 Lumped Parameter Model Validation

For a simulated resting heart rate of 70 BPM, and an average TCPC resistance of 0.39 WU, systolic/diastolic aortic pressures were 117/85 mmHg and 115/73 mmHg for the normal and SV cases respectively. The lower diastolic pressures resulted in a lower mean aortic pressure of 95 mmHg (compared to 103 mmHg) for the single ventricle circulation. Cardiac output was significantly lower for the SV circulation at 3.8 L/Min compared to 5.1 L/Min for the normal circulation. This can be attributed to the increased afterload experienced by the single ventricle due the lack of a pumping chamber on the right side. Pulmonary artery pressures were non-pulsatile in the single ventricle

circulation that resulted in non-pulsatile flow in the pulmonary arteries. This finding was in agreement with previous clinical studies. Table 11.2 shows a comparison of the modeled hemodynamic data vs. observed data from cardiac catheterization. Please note that the central venous pressure was only available for 13 patients, while cardiac output, systolic and diastolic pressures were available for all 40 patients. There was a good match between the values predicted by the model and what was observed in the cardiac catheterization reports demonstrating that this model could be used for analyzing the hemodynamics of single ventricle patients.

Table 11.2: Comparison of predicted and observed values of hemodynamic parameters from cardiac catheterization data acquired on patients with a single ventricle physiology.

Variable	**Predicted**	**Observed**	**Average Percent Difference**
CO (L/Min)	3.8	3.6 ± 1.7	5.2 %
$P_{systole}$ (mmHg)	115	114 ± 22	0.8 %
$P_{diastole}$ (mmHg)	73	63 ± 10	15.8 %
P_{SVB} (mmHg)	13	13.5 ± 3	0.6%

11.2.3 Effect of TCPC Resistance at Rest

Figure 11.1 shows the impact of TCPC resistance on hemodynamics in a single ventricle circulation and a normal circulation at a resting heart rate of 70 beats per minute (BPM). There is a drop in cardiac output going from a biventricular to a univentricular circulation at zero resistance, which is due to the lack of a systemic ventricle and the serial configuration of the two circulations. The sensitivity of cardiac output to the resistance of the TCPC in single ventricles was -0.88, which was significantly higher

compared to -0.064 for the normal biventricular circulation. This implies that for every 10% increase in resistance, there is an 8.8% drop in cardiac output. Figure 11.1c shows the impact of TCPC resistance on CVP. The sensitivity of CVP to increase in the resistance of the TCPC was 0.64 implying that a 10% increase in resistance results in a 6.4% increase in CVP. The increase in CVP in single ventricles has been shown before in acute *in vivo* animal experiments[38], human studies[37], and theoretical studies[39, 40]. Elevated CVP in patients with a single ventricle is a phenomenon that happens due to the lack of a true right ventricle. A systolic pressure of about 40 mmHg is typically generated by the right ventricle to pump blood through the pulmonary circulation. Since this ventricle is now absent, the pressures have to be elevated in order for the blood to go through the pulmonary system. Concurrently there is a remodeling of the systemic venous compliance in order to account for such increased pressures.

Until now, the impact of the TCPC resistance on elevated central venous pressure has not been known. These results show that with increasing TCPC resistances (or increasing power losses), the pressures in the systemic venous bed have to be higher in order to compensate for the increased pressure drops across the TCPC. Any further increases in CVP as a result of a poorly designed TCPC could result in flow backup into the hepatic system, which could potentially lead to problems with the gastro-intestinal system. Therefore, it is important that power losses within the TCPCs are viewed from the perspective of CVP as well.

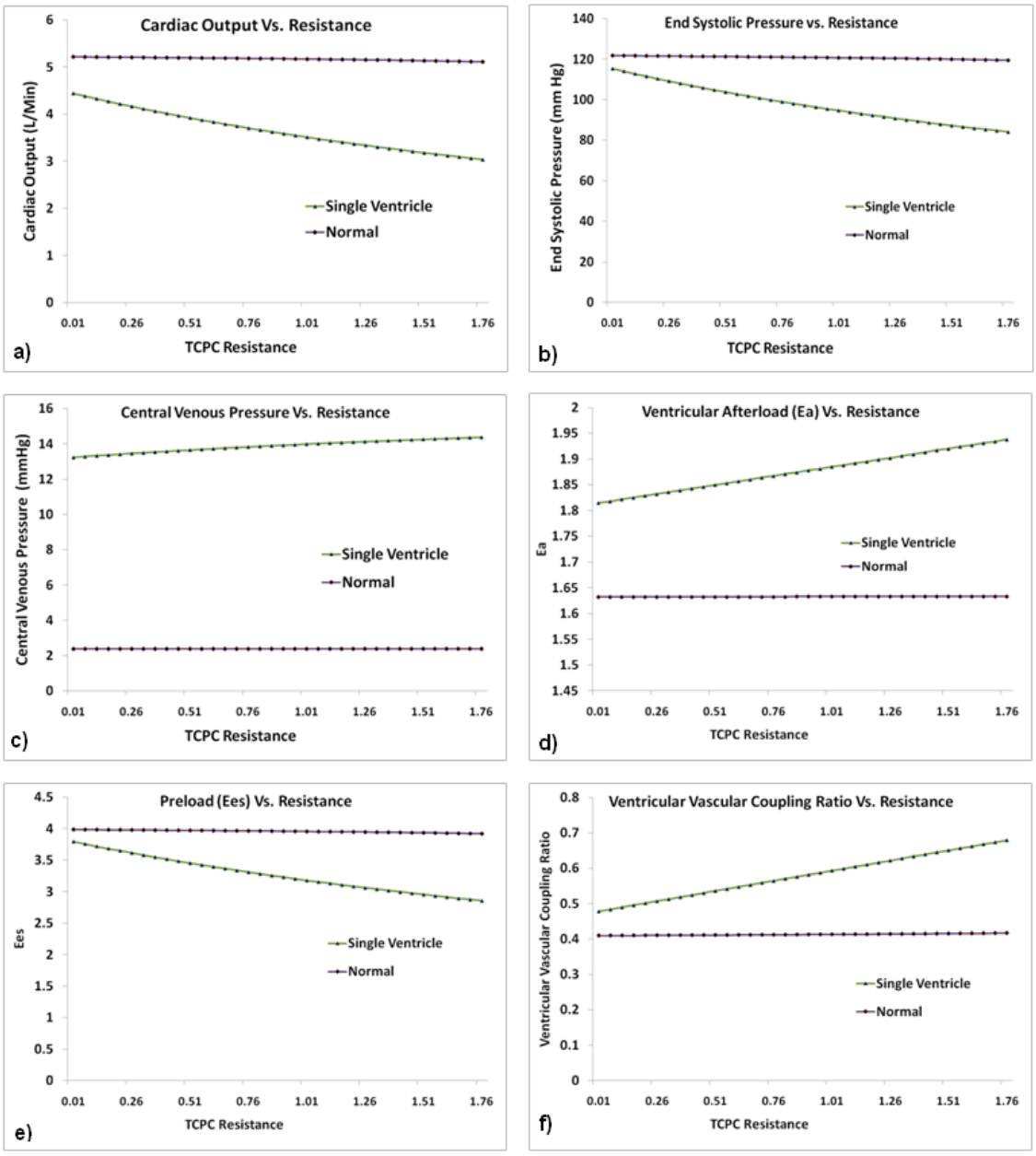

Figure 11.1: The impact of TCPC resistance at resting conditions on: a) Cardiac Output; b) End Systolic Pressure (ESP); c) Central Venous Pressure (CVP); d) ventricular afterload (Ea); e) Ventricular Preload (Ees), f) Ventricular Vascular Coupling ratio.

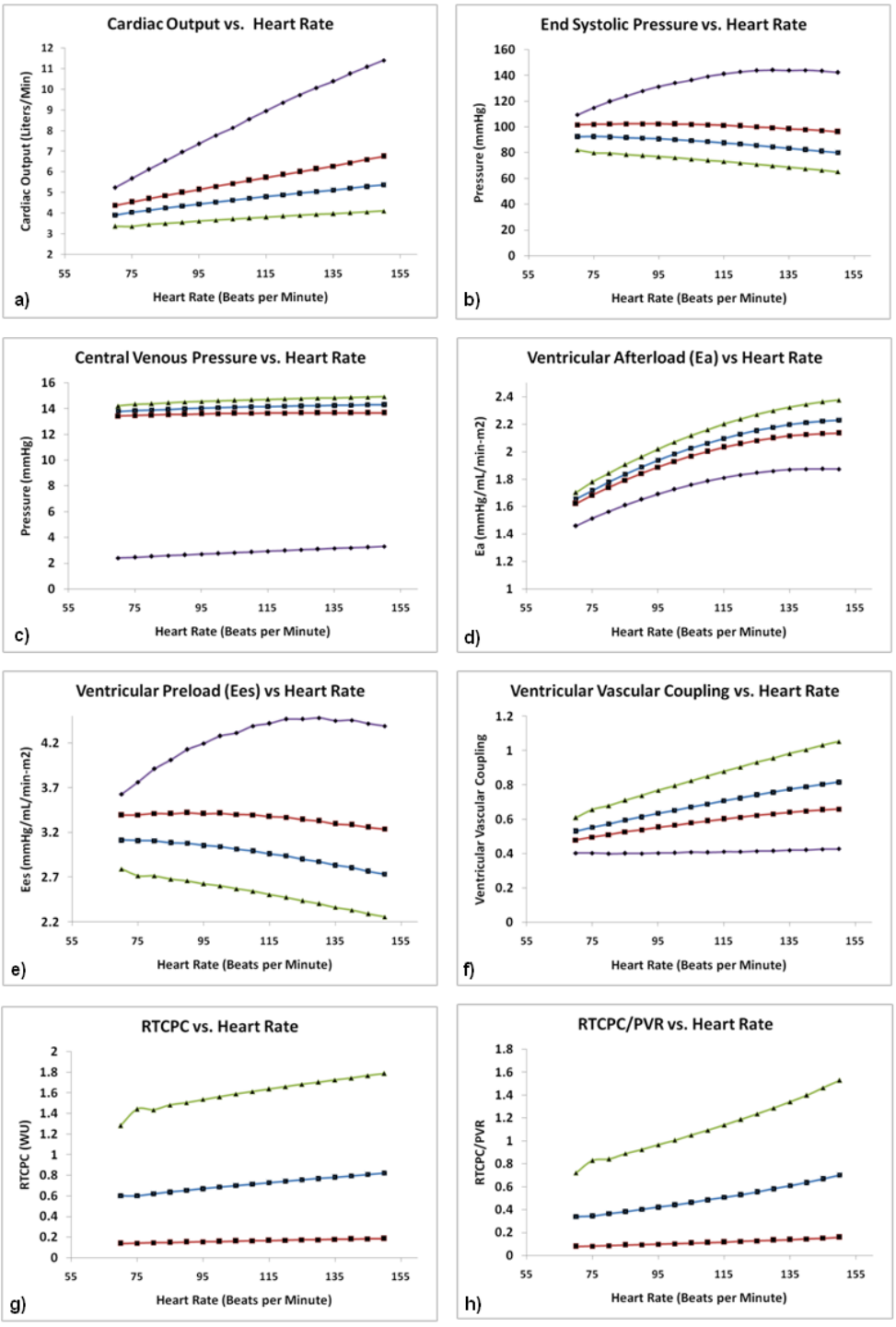

Figure 11.2: The impact of exercise on: a) Cardiac Output; b) ESP; c) CVP; d) Ea; e) Ees; f) ventricular vascular coupling ratio; g) R_{TCPC}; h) R_{TCPC}/ PVR. (Rhombus): Normal biventricular circulation; (squares) SV with the lowest R_{TCPC}; (circles) SV with average R_{TCPC}; (triangles); SV with highest R_{TCPC}.

11.2.4 Effect of TCPC resistance during Exercise

Figure 11.2 depicts the hemodynamic responses to exercise as predicted by the model. The biventricular circulation was able to increase the cardiac output of 5.2 L/Min at 70 BPM to 11.4 L/Min at an exercise heart rate of 150 BPM (Figure 11.2a). This ability to increase CO was blunted in the SV circulation. In the SV, the increase in CO was only from 3.8 L/Min to 5.4 L/Min for a mean TCPC resistance of 0.39 WU; 4.4 L/Min to 6.8 L/Min for the TCPC with a minimum resistance of 0.1 WU; and 3.3 L/Min to 4.1 L/Min for a highly dissipative TCPC with a resistance of 1.08 WU. There was an increase in end systolic pressure with exercise for the biventricular circulation, but not so for the single ventricle circulation (Figure 11.2b). The CVP was consistently higher for the TCPC with high resistance (Figure 11.2c).

The afterload (E_a) experienced by the SV significantly increased with exercise compared to the biventricular circulation (Figure 11.2d). The presence of a highly dissipative TCPC further increased the afterload. The increases were from 1.65, 1.62, and 1.7 to 2.23, 2.14, and 2.54 mmHg/mL for mean, minimum, and maximum R_{TCPC} values, respectively. Although similar at rest, the differences increased with exercise. In comparison, the afterload only increased from 1.46 to 1.87 mmHg/mL for the biventricular circulation. Ventricular preload (E_{es}) increased (3.63 to 4.39 mmHg/mL) in the normal circulation, while it decreased in the case of the SV circulation (Figure 5e). For the three SV scenarios, Ees dropped from 3.12, 3.40 and 2.79, to 2.73, 3.24, and 2.26 mmHg/mL for mean, minimum, and maximum R_{TCPC} values, respectively. This resulted in a mismatch in the preload and afterload experienced by the ventricle, resulting in an abnormal increase in the ventricular vascular coupling ratio (E_a/E_{es}) for the univentricular

circulation, which was further worsened by the presence of a high resistance TCPC. While E_a/E_{es} remained almost flat for a biventricular circulation, it increased for the univentricular circulation (Figure 11.2f). The increases were from 0.53, 0.48, and 0.61, to 0.82, 0.66, and 1.05 for mean, minimum, and maximum R_{TCPC} values, respectively.

Finally, human studies have established that the PVR and the SVR go down with exercise[190]. However, the TCPC resistance increases with exercise as shown in Figure 7-3 implying that the TCPC bottleneck becomes more significant during exercise. Figure 11.2g and Figure 11.2h, demonstrate that although at rest the TCPC resistance is a fraction of the pulmonary resistance (22%), this fraction significantly increases with exercise (50%). In fact, for the TCPC with a high resistance, this fraction increased from 55% at rest to 155 % during exercise, while for a low resistance TCPC this change was comparatively smaller from 7% to 16%. This demonstrates the significant improvement that could be accomplished by optimizing the TCPC geometry.

11.3 Discussion

This study demonstrated that the total cavopulmonary connection, which is in series with the pulmonary vascular resistance and the systemic vascular resistance, plays a significant role in regulating the cardiac output and exercise performance in single ventricle patients. It brings to fore, that the TCPC resistance is not insignificant compared to the downstream pulmonary vascular resistance, and any obstruction in the TCPC pathway can have a more significant impact on the cardiac function of a single ventricle circulation than a biventricular circulation. Most studies until now have only demonstrated this phenomenon in a global sense by looking at the single ventricle

circulation as a whole[37, 38, 40, 176, 187, 188] and the hydrodynamic role of the TCPC has not been investigated in these studies. This study shows for the first time, utilizing mathematical modeling with patient-specific imaging, CFD flow simulations and cardiac catheterization measurements, the important role played by the surgically altered TCPC geometry and the mechanisms by which it impacts the resting and exercise hemodynamic capacity of patients with a Fontan circulation.

The reduced capacity to increase cardiac output with exercise in single ventricle circulations has been well documented in the literature[2, 184, 187, 188, 219]. However, the exact quantitative relationship between TCPC resistance and this phenomenon has been unclear, primarily because of two reasons: 1) lack of appropriate methods for quantifying TCPC efficiency; and 2) complex interrelationships that exist between the respiratory, skeletal, and cardiovascular system that make it difficult to establish correlations between the TCPC and exercise capacity. Therefore, there is a tendency to disregard the impact of the TCPC on exercise capacity. Although PVR drops as a result of exercise, the increased resistance of the TCPC with increasing cardiac output makes it the primary bottleneck during increased cardiovascular demand.

The significant variability of Fontan geometries translates to significant variability in TCPC resistances. The resistance of the "worst" TCPC was 10 times higher than the resistance of the "best" TCPC. This suggests that the TCPC procedures performed today are far from optimal, and more emphasis needs to be given to optimizing the geometries pre-operatively. Especially, since the sensitivity of the univentricular circulation to changes in resistance is quite significant with a 10% increase in resistance resulting in an 8.8% decrease in cardiac output. To verify if this

phenomenon is observed *in vivo*, cardiac index measured using PC MRI was plotted against the resistance evaluated using CFD for all the patients used in this study Figure 11.3. Clearly a weak, but significant ($p < 0.05$) negative correlation can be observed between the TCPC resistance and the resting cardiac index measured on these patients. It should be noted that the TCPC resistance (as defined in the current study) is independent of the downstream PVR. The only dependence is indirect, as PVR can regulate cardiac output, and the TCPC resistance changes with cardiac output (Figure 11.1). But outside of this phenomenon, the TCPC resistance is largely governed by its geometry.

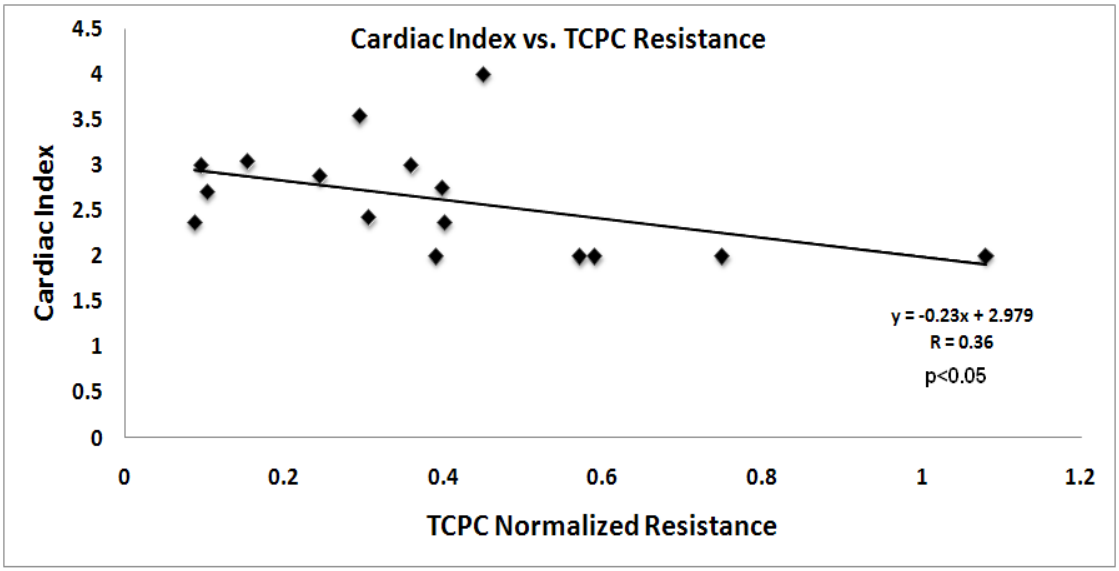

Figure 11.3: Cardiac Index vs. Resistance for the 16 patients used in the study. The Cardiac Index was evaluated using MRI, and the resistance was evaluated using computational fluid dynamics.

This study sought to bring to the clinician's attention the following messages: a) the final stage TCPC surgery has not yet been optimized, which is evident from the significant variability in the observed resistances; and b) the resistance of the TCPC itself is not secondary to the PVR as commonly believed, and physiologically it plays a greater

role when going from rest to exercise. Here in lies the clinical significance of the study. The TCPC resistance is directly proportional to the afterload (as higher systolic pressures are needed to maintain cardiac output for TCPCs with higher resistance), and inversely proportional to preload (as higher pressure drops across the TCPC results in lower filling pressures). This phenomenon is similar to mitral stenosis where, the preload of the left ventricle is directly affected due to the high pressure drops (and consequently a higher resistance) across the mitral valve. This observation points towards a unique property of the single ventricle circulation: both preload and afterload are impacted in identical manner by the TCPC as the right ventricle is replaced by a dynamic resistance in the form of the TCPC.

Not only does optimizing TCPC resistance improve cardiac function, it drops central venous pressures which is critical to maintain normal gastro-intestinal function. As explained previously, the single ventricle circulation is prone to an increase in CVP as a result of the series configuration of the systemic and pulmonary circulations. Any further increase in CVP as a result of the increased TCPC resistance could potentially result in damage to the tissue lining of the hepatic venous system, resulting in significant problems in liver function.

In addition, optimal TCPC geometries have improved flow dynamics in the baffle that may reduce the risk of thromboembolic complications. Hence, new TCPC designs that reduce energy losses need to be investigated in more detail, and more emphasis needs to be given for improving the hemodynamic efficiency within the TCPC. Surgical planning approaches combining pre-operative MRI, computational fluid dynamics, and the presented lumped parameter modeling can prove to be beneficial in

determining the optimum TCPC geometry. Previous optimization studies using idealized *in vitro* models and computational fluid dynamic studies have shown that significant improvements with reductions of over 50% in energy losses can be accomplished[18, 61, 62, 70, 72, 220]. If appropriate surgical planning strategies are used then it is possible to accomplish similar improvements in energy losses *in vivo* as well.

11.4 Study Limitations

Although the proposed model has a sound basis on clinically measured data and compares well with other clinical studies, the inherent limitations of this work are well acknowledged. As with all modeling studies, the results are idealized as many components of the cardiovascular system are missing. The biochemical response to exercise, cardiopulmonary interactions, baroreflex response have not been modeled, in order to achieve a simpler model with less variables. Since this is more of a comparative study between different single ventricle circulations and the normal circulation, the only parameter that was changed between different cases was the TCPC resistance. Incorporating a more complex model will no doubt improve the accuracy of the model's predictions, but the relative importance andimpact of the TCPC resistance is not expected to change.

11.5 Conclusions

This is the first time the impact of TCPC resistance on the overall hemodynamics of the univentricular circulation has been demonstrated. TCPC resistance has a direct impact on the afterload and the preload of the univentricular circulation and significantly impacts the resting and exercise hemodynamics. The inability to increase cardiac output

with exercise limits their ability to exercise and hence worsens their overall functional outcome. This can be countered by optimizing the geometry of the TCPC prior to the Fontan surgery that may result in decreased afterload and consequently an improvement in cardiac function and quality of life.

CHAPTER 12

CONCLUSIONS

At the beginning of this research endeavor, it was hypothesized that phase contrast magnetic resonance imaging (PC MRI) can be used for characterizing the hemodynamics of the single ventricle circulation. Based on the studies conducted, it can be concluded that PC MRI combined with advanced image processing techniques, can be used for reconstructing, quantifying, and visualizing the complex flow characteristics evident in Fontan patients. Towards this end, the primary contributions of this thesis are in two fronts: a) new method development for PC MRI data analysis; b) application of these techniques for understanding single ventricle hemodynamics.

From the perspective of new technique development, the major contributions of this thesis are as follows: a) development of a novel segmentation tool based on implicit active contour models, that is optimized for PC MRI applications; b) development of a multi-dimensional filtering methodology based on fuzzy set theory, that can be used to clean up noise in segmented PC MRI datasets; c) development of a novel divergence free interpolation algorithm, that can be used for reconstructing 3D vector fields from PC MRI datasets.

The segmentation methodology comprised of a novel two-step segmentation and filtering approach, which was shown to be more accurate compared to a single step process of segmentation alone. The novel hybrid magnitude-velocity based energy function used in the active contour segmentation step, was shown to be much more effective in segmenting the vessel of interest than an energy function based on just

magnitude images. The automatic segmentation methodology was thoroughly validated against manually segmented data, and was shown to be as effective as manual segmentation. The second step of the segmentation step comprised of a novel noise-filtering strategy based on fuzzy principles that was optimized for quantifying velocity fields from PC MRI. This was the first time a noise filtering strategy for PC MRI-based fluid dynamic data was developed and validated. This two-step segmentation/filtering approach for post-processing of PC MRI data was shown to be very accurate for quantifying clinically relevant parameters, and robust enough to be easily extended to other multi-dimensional MRI applications.

The third technique that was developed was a novel divergence free interpolation algorithm. The results of a thorough quantitative and qualitative validation affirm that this technique can be used to reconstruct three-dimensional velocity data accurately. Specifically, this methodology provided superior quality velocity fields reconstructed from sparsely sampled PC MRI data, compared to other 3D reconstruction techniques. Furthermore, the technique can be readily applied to any PC MRI dataset, if morphological information is available for suitable boundary conditions. This technique was instrumental for conducting the detailed hemodynamic analysis of extracardiac and intraatial Fontan connections.

These techniques were then applied to clinical PC MRI data acquired on a large cohort of Fontan patients. Several clinically relevant parameters were evaluated, and differences between intraatrial and extracardiac Fontan types were quantified in significant detail. For the first time, 3D *in vivo* hemodynamics within the different templates of Fontan geometries were visualized and parameters such as power losses,

IVC flow splits, vortex sizes, flow rates, and flow velocities were directly evaluated. It was observed that extracardiac connections had significantly smoother flow fields, higher velocity magnitudes, and lesser flow recirculation regions compared to intratrial connections. Interestingly, the extracardiac Fontan connections also had higher normalized pulmonary artery diameters, which hint that over long term, their clinical function maybe better. However, for both extracardiac and intraatrial Fontans, the normalized pulmonary artery diameter was much smaller than normal values. On the other hand, intraatrial Fontan connections did foster improved mixing between the SVC, and the IVC compared to extracardiacs, which could have clinical implications in the long term normal development of the pulmonary circulation.

When the energetics between patients with hypoplastic left heart syndrome and those with other forms of single ventricle defects were compared, a marked difference between the two groups was observed. Significant differences in power output, cardiac index, and aortic flow dynamics demonstrated that the ability of the single systemic right ventricle to pump blood effectively is impaired. Lower energetic performance of the right ventricle under pressure overloaded conditions highlights the importance of hydrodynamic efficiency of the surgical procedures resulting in the Fontan connection. Clinically, this implies that having an efficient TCPC with minimum power loss, could play a significant role in improving the long term functional outcome and quality of life in these patients, especially for those with impaired cardiac power capacity.

All the PC MRI studies that were conducted involved either studying the TCPC hemodynamics or the ventricular function, and in order to connect the two, a lumped parameter model was developed to investigate the impact of the TCPC resistance on

ventricular function. The study shows that TCPC resistance has a direct impact on the afterload and the preload of the univentricular circulation and significantly impacts the resting and exercise hemodynamics. The inability to increase cardiac output with exercise limits their ability to exercise and hence worsens their overall functional outcome. This was the first time that the TCPC hemodynamics and cardiac function were related by means of a mathematical model.

In conclusion of all these studies, there is no doubt that hemodynamics play a significant role in the Fontan physiology. There is still a lot to be learnt about these patients, and these clinical studies have only taken a small step towards understanding the Fontan problem. The tools that were developed as part of this thesis, now allow the clinician to quantify and visualize several hemodynamic patterns that were previously thought not possible, and has opened doors for future research in this area. The next step would be to conduct a much larger clinical study, correlating the hemodynamic patterns with parameters of clinical outcome, to better optimize the care and management of single ventricle patients.

CHAPTER 13

FUTURE DIRECTION

In this thesis, novel techniques were developed for the processing and analysis of PC MRI data. The segmentation, filtering, and interpolation techniques were designed with the specific goal of quantifying clinically relevant parameters directly from PC MRI. There are several opportunities for taking these technologies one step further for performing the analyses faster and with higher accuracy. I will be outlining some of these avenues in the forthcoming sections.

13.1 Controlled *in vitro* PC MRI experiments

In specific aim 1 of this thesis, controlled PC MRI experiments were conducted for the first time on patient specific TCPC models. The studies demonstrated that PC MRI can be used to accurately reconstruct the 3D hemodynamics in patients with a single ventricle physiology. These studies can be taken one step further, by designing new experiments to obtain a better understanding of 3D TCPC flow dynamics.

13.1.1 Pulsatile input waveforms

The studies conducted as part of this thesis, used a steady flow pump. The next step would be to use pulsatile waveforms obtained from *in vivo* measurements. These waveforms can be used to prescribe flow velocities in the SVC and IVC using an MRI compatible flow pump. The PC MRI acquisition can then be gated to these waveforms, and high resolution 3-component PC MRI data can be acquired over the entire cardiac cycle. Depending upon the available sequences, either a fully 3D acquisition sequence

can be utilized, or a stack of 3 component PC MRI slices can be acquired similar to the present study. 3D pulsatile flow fields can then be reconstructed, and more interesting temporally varying flow features can be studied in greater detail. The divergence free interpolation technology developed in this thesis could serve as a medium for converting the 3 component 2D data, into 4D data with isotropic voxel sizes. The ensuing 4D velocity field could also serve as a validation method for 3D CFD studies, where new technologies are currently being developed for modeling unsteady pulsatile flow in the TCPC.

13.1.2 Validation of the coronal PC MRI acquisition

In Chapter 6 and Chapter 10, new techniques for the interpolation of data from coronal PC MRI acquisitions were presented. However, it was never investigated if coronal PC MRI was accurate enough for quantifying power losses, IVC flow splits and particle transit times. To address this issue, an *in vitro* PC MRI study can be designed where datasets are acquired in both the coronal and axial orientations. 3D flow fields reconstructed using the techniques described in Chapter 6 can be used to evaluate quantitative parameters such as power losses, IVC flow splits, and particle transit times for both the acquisitions. The differences between the two acquisitions can be quantified, and used for determining the optimum number of slices that can be obtained in the coronal orientation with minimum loss of accuracy.

13.2 Automatic PC MRI Segmentation

In Chapter 5, a new approach for the segmentation of PC MRI data based on level set active contours was presented. This approach utilized energy functions derived from

both magnitude and phase images for segmenting the vessel of interest in a single cardiac cycle. Each phase of the cardiac cycle was handled independently from the other. This approach can be further refined by treating the time component of the cine PC MRI as the 3rd dimension for the segmentation. The level set implementation in 3D (as described in Chapter 5) can then be directly applied to this 3D (2D space + 1D time) dataset. In this manner, a fully coupled space-time segmentation technique can be developed by utilizing the connectivity that exists between each image in the cardiac cycle. Furthermore, smoothness constraints in the 3rd dimension can be enforced to ensure that the segmentation does not fail in any cardiac cycle. This approach will not only speed up the computation time for the algorithm, but will also improve the reliability and reproducibility of the segmention approach.

13.2.1 Extension of active contours for other imaging modalities

Level set based active contours are quite powerful for segmenting anatomic structures of any shape and size. In the current study, the application targeted was primarily MRI datasets. However, MRI is not the most popular and cost efficient modality for *in vivo* imaging in clinical use today. Most clinical institutions prefer to use echocardiography (echo) for diagnostic imaging. With developments in 3D echo, it is now possible to acquire 3D images of cardiovascular anatomies cheaply and quickly. Hence, new segmentation and image analysis techniques are needed in order to fully utilize the 3D information obtained from such 3D echocardiograms. 3D level set based segmentation technique developed as part of this thesis can be readily applied to reconstructing 3D anatomies from 3D echo data. This ability to reconstruct 3D anatomies

directly from echo would open doors for several clinical applications, such as improved quantification of ventricular function, surgical planning, as well as real-time robotic surgery. 3D echo is an exciting new imaging modality, and has the potential to significantly impact the field of diagnostic imaging.

13.3 Optimum Fuzzy Filters

A new technique based on Fuzzy filters for noise cleaning of fluid dynamic data was presented in Chapter 5. This technique proved to be quite powerful for selectively cleaning out noise vectors without affecting the true velocity field. In the current implementation of the algorithm, a fuzzy membership function is determined by iteratively minimizing a cost function. However, once determined, it is applied only once in combination with vector median filters. Sometimes, the noise vector maybe surrounded by several noise vectors, in which case the vector median is also a noise vector. Consequently, the output of the Fuzzy filter is a noise vector as well. This problem can be alleviated by iteratively applying the filter until every noise vector is filtered, and can be a feature for the next generation Fuzzy filter.

Although the Fuzzy filter was only applied to fluid dynamic data obtained from PC MRI datasets in this study, it can easily be extended to other multi-dimensional data where noise is a problem. For example, particle image velocimetry (PIV) is a measurement technique where flow velocities are evaluated using optical techniques. In this modality, noise could be a significant problem along the boundaries of the flow domain. The Fuzzy filter can provide significant data enhancement by cleaning out these noise vectors, so that quantitities such as wall shear stress can be evaluated accurately.

The only requirement is that data needs to a rectangular array.

13.4 Divergence free interpolation

The first generation of the DFI technique for interpolating 3D flow data was presented in Chapter 6. There are several new features that can be incorporated for improving the speed and accuracy of the algorithm. Some of these features are outlined below.

13.4.1 Adaptive optimization of the radial basis function support

The parameter α, which is an important parameter in the current DFI implementation, is set to be a constant depending upon the average spacing between the interpolating control grid nodes. However, depending upon the flow behavior, setting the value of α as a constant may not be the the most accurate approach. One improvement that can be made is to adaptively determine the value of α by implementing an optimization algorithm that minimizes an error function between the DFI model and the measured velocity field. Currently, only coefficients of the radial basis functions are determined by minimizing the least squared error. This minimization can be further extended by factoring in α into the optimization process.

13.4.2 Adaptive control grid spacing

In the current DFI implementation, the control point nodes which serve as interpolating kernels are distributed uniformly within the flow domain. If the DFI model is used for interpolating more complex flow environments, then there is a possibility that secondary flow features may get smoothened out. In order to handle this problem, the

control grid nodes can be seeded in an adaptive fashion inside the flow domain. In such an implementation, we would first start with a coarse grid seeding, which will be adaptively subdivided based on some sort of an error measure. This way areas of smooth flow can be represented using a coarse set of interpolating nodes, while ares of complex flow can be represented using a finer control point grid.

13.4.3 Automatic anatomic and velocity registration

One problem, that is experienced when the anatomic data and velocity measurements are acquired in different orientations, is registration. The implementation described in Chapter 6 assumes that there is no significant motion between the two acquisitions. In several situations, registration mismatches may occur due to respiration artifacts, or patient movement in which case the anatomic and velocity data cannot be used concurrently. Hence, an automatic registration technique that aligns images from both these acquisitions quickly and accurately may improve the robustness of the algorithm.

13.4.4 PC MRI combined with CFD

The output of the DFI algorithm is a 3D velocity field that is divergence free. However, zero divergence is not the only criteria that need to be successfully satisfied for fluid dynamic data. Blood flow velocity fields need to satisfy the conservation of mass and momentum as described by Navier-Stokes equations. By combining the immersed boundary CFD approach with the DFI 3D velocity reconstructions, it is possible to obtain a full 3D velocity field that correctly satisfies all the governing equations of flow. The CFD process itself should not take a long time, as the initial velocity field is not zero.

This should ensure faster convergence of the CFD solution.

13.5 Concluding Remarks

The work presented as part of this thesis has opened up the doors for analyzing PC MRI data, which is a significant step in improving the understanding of the single ventricle physiology. It is noteworthy, however, that the techniques developed are not limited in application to just the single ventricle circulation. The 3D segmentation, filtering, and interpolation techniques can be applied to any cardiovascular morphology. The fully 3D nature of the proposed methodologies can be used directly on 3D data, whether it is acquired in serial planar format, or in a 3D volume, and hence is modality independent. Results presented in Chapter 9 and 10 fully support this claim. Future directions described in this chapter have shown how these technologies can be taken many steps further towards an integrated post-processing package for medical image analysis.

APPENDIX A: DETERMINATION OF VELOCITY ENCODING VALUES FOR IN VITRO PC MRI EXPERIMENTS

Table A.1: Mean velocities calculated for each of the four vessels of the TCPC. 30R, 50R, 60R, and 70R correspond to the percentage of the total flow going to the RPA.

Model	Flow Rate/Flow Condition	IVC (cm/s)	SVC (cm/s)	LPA (cm/s)	RPA (cm/s)
CHOA006	3 LPM / 30R	9.55	12.28	16.57	9.21
CHOA006	3 LPM / 50R	9.55	12.28	11.84	15.36
CHOA006	3 LPM / 70R	9.55	12.28	7.10	21.49
CHOA006	5 LPM / 30R	15.92	20.47	27.62	15.35
CHOA006	5 LPM / 50R	15.92	20.47	19.73	25.59
CHOA006	5 LPM / 70R	15.92	20.47	11.84	35.83
CHOA007	2 LPM / 50R	5.89	6.16	14.26	14.74
CHOA007	2 LPM / 60R	5.89	6.16	11.41	17.69
CHOA007	2 LPM / 70R	5.89	6.16	8.56	20.64
CHOA007	4 LPM / 50R	11.77	12.33	28.52	29.48
CHOA007	4 LPM / 60R	11.77	12.33	22.82	35.38
CHOA007	4 LPM / 70R	11.77	12.33	17.11	41.27
CHOA011	4 LPM / 30R	8.7	12.03	49.12	10.74
CHOA011	4 LPM / 50R	8.7	12.03	35.08	17.90
CHOA011	4 LPM / 70R	8.7	12.03	21.05	25.06
CHOA011	6 LPM / 30R	13.05	18.05	73.67	16.10
CHOA011	6 LPM / 50R	13.05	18.05	52.63	26.85
CHOA011	6 LPM / 70R	13.05	18.05	31.57	37.59

Table A.2: Maximum velocities calculated for each of the four vessels of the TCPC. 30R, 50R, 60R, and 70R correspond to the percentage of the total flow going to the RPA.

Model	Flow Rate/Flow Condition	IVC (cm/s)	SVC (cm/s)	LPA (cm/s)	RPA (cm/s)
CHOA006	3 LPM / 30R	19.1	24.57	33.14	18.52
CHOA006	3 LPM / 50R	19.1	24.57	23.67	30.71
CHOA006	3 LPM / 70R	19.1	24.57	14.2	43
CHOA006	5 LPM / 30R	31.84	40.94	55.24	30.71
CHOA006	5 LPM / 50R	31.84	40.94	39.46	51.18
CHOA006	5 LPM / 70R	31.84	40.94	23.67	71.65
CHOA007	2 LPM / 50R	11.77	12.32	28.52	29.48
CHOA007	2 LPM / 60R	11.77	12.32	22.82	35.37
CHOA007	2 LPM / 70R	11.77	12.32	17.11	41.27
CHOA007	4 LPM / 50R	23.55	24.65	57.04	58.96
CHOA007	4 LPM / 60R	23.55	24.65	45.63	70.75
CHOA007	4 LPM / 70R	23.55	24.65	34.22	82.54
CHOA011	4 LPM / 30R	17.4	24.07	98.23	21.48
CHOA011	4 LPM / 50R	17.4	24.07	70.17	35.8
CHOA011	4 LPM / 70R	17.4	24.07	42.1	50.12
CHOA011	6 LPM / 30R	26.1	36.1	147.35	32.22
CHOA011	6 LPM / 50R	26.1	36.1	105.25	53.7
CHOA011	6 LPM / 70R	26.1	36.1	63.15	75.18

Table A.3: Reynold's Numbers calculated for the different models used in the study. 30R, 50R, 60R, and 70R correspond to the percentage of the total flow going to the RPA.

Model	Flow Rate/Flow Condition	IVC Re	SVC Re	LPA Re	RPA Re
CHOA006	3 LPM / 30R	545.78	505.36	776.52	379.01
CHOA006	3 LPM / 50R	545.78	505.36	554.66	631.69
CHOA006	3 LPM / 70R	545.78	505.36	332.79	884.31
CHOA006	5 LPM / 30R	909.6	842.3	1294.2	631.7
CHOA006	5 LPM / 50R	909.6	842.3	924.4	1052.8
CHOA006	5 LPM / 70R	909.6	842.3	554.7	1476.9
CHOA007	2 LPM / 50R	349.86	292.25	497.07	505.36
CHOA007	2 LPM / 60R	349.86	292.25	347.66	606.43
CHOA007	2 LPM / 70R	349.86	292.25	298.24	707.5
CHOA007	4 LPM / 50R	699.7	584.5	994.1	1010.7
CHOA007	4 LPM / 60R	699.7	584.5	795.3	1212.9
CHOA007	4 LPM / 70R	699.7	584.5	596.5	1415.0
CHOA011	4 LPM / 30R	601.4	577.5	1543.6	422.5
CHOA011	4 LPM / 50R	601.4	577.5	1102.6	787.6
CHOA011	4 LPM / 70R	601.4	577.5	661.6	1102.6
CHOA011	6 LPM / 30R	902.1	866.3	2315.4	708.8
CHOA011	6 LPM / 50R	902.1	866.3	1653.9	1181.3
CHOA011	6 LPM / 70R	902.1	866.3	992.3	1653.9

APPENDIX B: TABLE LOCATION OF VARIOUS STUDIES

Study	Table Number
Chapter 8 – Patient specific models used for the *in vitro* PC MRI study	Table 4.1
Chapter 9 – Patients used for *in vivo* validation of the automatic segmentation technique	Table C.1
Chapter 9 – Patients used for *in vivo* validation of Optimum Fuzzy Filters	Table C.2
Chapter 9 – Patients used for *in vivo* Fontan flow analysis	Table C.3
Chapter 9 – Patients used for single ventricle power output analysis	Table 9.7 and Table 9.8
Chapter 9 – Patients used for single ventricle function study	Table C.4a and Table C.4b
Chapter 10 – Patients used for 3D flow comparison of intraatrial and extracardiac Fontan types	Table 10.5
Chapter 11- Patients used for the CFD study	Table 11.1
Chapter 11 – Data available from cardiac catheterization for lumped parameters study	Table C.5

APPENDIX C: PATIENTS USED FOR THE VARIOUS STUDIES NOT INCLUDED IN THE THESIS

Table C.1: Patients used for the validation of the automatic segmentation technique

Patient	Age (years)	CHD	Fontan Type
CHOP097	10	Tricuspid atresia, VSD	Intraatrial
CHOP098	27	D transposition,VSD, Subaortic stenosis	Unknown Type
CHOP099	18	Single ventricle-pulmonary stenosis	Unknown Type
CHOP103	3	Hypoplastic aortic arch and mild hypoplastic left ventricle	Bidirectional Glenn
CHOP105	6	HLHS	Intraatrial
CHOP106	2	TGA, DILV	Bidirectional Glenn
CHOP107	3	HLHS	Bidirectional Glenn
CHOP108	21	HRHS	Intraatrial
CHOP109	1	Heterotaxy, TGA	Bidirectional Glenn
CHOP110	25	Heterotaxy, DORV	Modified Fontan
CHOP111	4.16	HLHS	Intraatrial
CHOP112	22	HLHS, DORV	Intraatrial

Table C.2: Patients used for the validation of Optimum Fuzzy Filters

Patient	**Age (years)**	**CHD**	**Fontan Type**
CHOP028	7	Single left ventricle	Intraatrial
CHOP029	19	Double supero-inferior ventricles	Intraatrial
CHOP030	11	Tricuspid Atresia	Intraatrial
CHOP031	14	DILV, TGA	Intraatrial
CHOP033	9	TGA, DORV	Extracardiac
CHOP035	10	DC, HLHS	Intraatrial
CHOP039	17	HLHS	Intraatrial
CHOP041	20	DC, Malaligned AV canal	Intraatrial
CHOP042	5	HLHS	Hemi-Fontan
CHOP051	15.2	Pulmonary Atresia with intact ventricular septum	Intraatrial
CHOP068	6	HLHS	Intraatrial
CHOP073	9	HLHS	Intraatrial
CHOP078	12	HLHS	Intraatrial
CHOP089	7	Tricuspid Atresia	Extracardiac
CHOP090	9	Pulmonary Atresia	Extracardiac
CHOP091	8	HLHS, DORV	Extracardiac

Table C.3: Patients used in the velocity database study

Patient	Age (years)	CHD	Fontan Type (second stage)
CHOA001	9	HLHS	Extracardiac
CHOA002	3	HLHS	Interrupted IVC
CHOA004	3	Tricuspid Atresia	Intraatrial (Glenn)
CHOA005	6	Tricuspid Atresia	Intraatrial (Glenn)
CHOA006	7	Ventricular septal defect	IVC-MPA, 4 mm gortex graft from SVC to RA appendage, 5mm with bidirectional shunting
CHOA007	6	HLHS	Extracardiac
CHOA008	5	Tricuspid Atresia	Extracardiac
CHOA009	2	Single ventricle with double inlet AV connection	Intraatrial (Glenn)
CHOA010	11	HLHS	Intraatrial (Glenn)
CHOA011	11	HRHS	Intraatrial (Glenn)
CHOA015	21	Tricuspid Atresia	Intraatrial (Glenn)
CHOA024	4	Single ventricle with double inlet AV connection	Intraatrial (Glenn)
CHOA025	2	Single ventricle with double inlet AV connection	Intraatrial (Glenn)
CHOA026	2	HLHS	Intraatrial (Glenn)

CHOA031	3	Single ventricle with double inlet AV connection	Intraatrial (Glenn)
CHOA037	2	Single ventricle with double inlet AV connection	Other
CHOA038	8	TGA with VSD, PS, hypoplastic MV	Other
CHOA039	3	HLHS	Extracardiac (Bilateral SVC)
CHOA040	15	Tricuspid Atresia	Intraatrial (Glenn)
CHOP003	15	HLHS	Intraatrial (Hemi-Fontan)
CHOP006	10	HLHS	Extracardiac (Hemi-Fontan)
CHOP007	8	HRHS	Extracardiac
CHOP008	16	HLHS	Intraatrial (Hemi-Fontan)
CHOP009	16	Hypoplastic Left Ventricle	Extracardiac (Bilateral)
CHOP010	9	Double inlet LV, single ventricle, L-transposition	Extracardiac (Hemi-Fontan)
CHOP011	24	Tricuspid Atresia	Atriopulmonary (PA Band)
CHOP013	6	HLHS	Extracardiac (Hemi-Fontan)
CHOP014	13	Pulmonary atresia, intact	Extracardiac (Glenn)

		ventricular septum and right ventricular hypertrophy	
CHOP015	7	Pulmonary Stenosis	Intraatrial (Hemi-Fontan)
CHOP016	14	HLHS	Intraatrial (Hemi-Fontan)
CHOP017	15	Tricuspid Atresia	Intraatrial (Hemi-Fontan)
CHOP018	12	HLHS	Intraatrial (Hemi-Fontan)
CHOP019	7	HLHS	Extracardiac (Bilateral SVC)
CHOP020	12	Double Outlet Right Ventricle	Intraatrial (Hemi-Fontan)
CHOP021	7	Tricuspid Atresia	Intraatrial (Hemi-Fontan)
CHOP022	9	Heterotaxy	Intraatrial (Bilateral SVC, Hemi-Fontan)
CHOP023	6	HLHS	Intraatrial (Hemi-Fontan)
CHOP024	8	Tricuspid Atresia	Extracardiac (Hemi-Fontan)
CHOP025	18	HLHS	Intraatrial (Hemi-Fontan)
CHOP026	9	HLHS	Intraatrial (Hemi-Fontan)
CHOP028	7	Single left ventricle, L-transposition, superoinferior ventricles, straddling left AV valve	Intraatrial (Hemi-Fontan)

CHOP029	18	Tricuspid Atresia	Intraatrial (Hemi-Fontan)
CHOP030	10	Tricuspid Atresia	Intraatrial (Hemi-Fontan)
CHOP031	14	DILV, TGA	Intraatrial (Hemi-Fontan)
CHOP032	18	DORV with Pulmonary Stenosis	Intraatrial (Bilateral SVC, Hemi-Fontan)
CHOP033	9	LTGA, DORV	Extracardiac Glenn)
CHOP034	11	HRHS	Intraatrial (Hemi-Fontan)
CHOP035	10	HLHS	Intraatrial (Hemi-Fontan)
CHOP037	15	Hypoplastic Right Ventricle	Intraatrial (Hemi-Fontan)
CHOP038	18	Malaligned AV Canal	Bilateral SVC (other)
CHOP039	12	HLHS	Intraatrial (Hemi-Fontan)
CHOP040	10	HLHS	Intraatrial (Hemi-Fontan)
CHOP041	19	Dextrocardia	Intraatrial (Hemi-Fontan)
CHOP042	5	HLHS	Intraatrial (Bilateral SVC, Hemi-Fontan)
CHOP043	20	Tricuspid Atresia	Atriopulmonary (PA Band)
CHOP044	19	DORV, HLHS	Intraatrial (Hemi-Fontan)
CHOP045	18	HLHS	Intraatrial (no stage 2)

CHOP051	15	Pulmonary Atresia	Intraatrial (Glenn)
CHOP055	4	Heterotaxy Syndrome	Extracardiac (Glenn)
CHOP058	4	HLHS	Intraatrial (Hemi-Fontan)
CHOP061	21	Ventricular septal defect	Extracardiac (Hemi-Fontan)
CHOP065	10	HLHS	Intraatrial (Hemi-Fontan)
CHOP066	12	Single ventricle-PA, IVS, Hypoplastc RV	Intraatrial (Hemi-Fontan)
CHOP067	9	Single ventricle-DILV	Extracardiac (Glenn)
CHOP068	6	HLHS	Intraatrial (Hemi-Fontan)
CHOP069	16	HLHS	Unknown (Hemi-Fontan)
CHOP070	14	HLHS	Intraatrial (Hemi-Fontan)
CHOP076	14	Single Ventricle DORV	Intraatrial (Hemi-Fontan)
CHOP077	20	DORV	Intraatrial (Hemi-Fontan)
CHOP079	18	HLHS	Intraatrial (Hemi-Fontan)
CHOP085	3	HLHS	Extracardiac (Glenn)
CHOP088	3	Tricuspid Atresia, Dextrocardia	Extracardiac (Glenn)
CHOP089	7	Tricuspid atresia, VSD	Extracardiac (Glenn)
CHOP090	8	Pulmonary Atresia	Extracardiac (Glenn)
CHOP091	8	DORV	Extracardiac (Glenn)
CHOP092	1	HLHS	Intraatrial (Hemi-Fontan)

CHOP093	6	Hypoplastic Right Ventricle	Extracardiac (Glenn)
CHOP095	8	DILV, Pulmonary Atresia	Extracardiac (Glenn)
CHOP097	10	Tricuspid atresia, VSD	Intraatrial (Hemi-Fontan)
CHOP098	27	D transposition,VSD, Subaortic stenosis	Unknown Type
CHOP099	18	Single ventricle-pulmonary stenosis	Unknown Type
CHOP105	5	HLHS	Intraatrial (Hemi-Fontan)
CHOP108	19	Tricuspid Atresia	Intraatrial (Hemi-Fontan)
CHOP110	25	Heterotaxy, DORV, LAVV, atresia	Unknown
CHOP111	4	HLHS	Intraatrial (Hemi-Fontan)
CHOP112	22	DORV	Intraatrial (Hemi-Fontan)
CHOP114	10	Dtransposition of great vessels, VSD and valvular and subvalvular PS	Intraatrial (Hemi-Fontan)
CHOP115	8	HLHS	Intraatrial (Hemi-Fontan)
CHOP116	8	Ebsteins Anomaly	Extracardiac (Glenn)
CHOP117	21	Dextrocardia, Hypoplastic Left Ventricle	Intraatrial (Hemi-Fontan)
CHOP119	8	HLHS	Intraatrial (Hemi-Fontan)

CHOP125	15	HLHS	Intraatrial (Hemi-Fontan)
CHOP129	5	DORV	Extracardiac (Glenn)
CHOP132	5	DORV	Extracardiac (Glenn)
CHOP133	15	HLHS	Intraatrial (Hemi-Fontan)
CHOP138	13	Tricuspid Atresia	Intraatrial (Hemi-Fontan)
CHOP140	20	TGA, HLHS	Unknown (Bilateral SVC)
CHOP141	10	VSD, TGA	Intraatrial (Hemi-Fontan)
CHOP143	11	Pulmonary Atresia	Extracardiac (Glenn)
CHOP146	15	Pulmonary Atresia	Intraatrial (Hemi-Fontan)
CHOP148	4	DORV	Extracardiac (Glenn)
CHOP149	10	HLHS	Intraatrial (Hemi-Fontan)
CHOP150	4	Tricuspid Atresia	Extracardiac (Glenn)
CHOP151	20	Pulmonary Atresia	Intraatrial (Hemi-Fontan)
CHOP155	15	HLHS	Intra-atrial (Hemi)

Table C.4a: Patient Number and Age of the patients used for Ventricular Function Studies for HLHS patients

HLHS Patient	**Age (years)**
CHOP035	10
CHOP069	16
CHOP070	14
CHOP079	18
CHOP092	1
CHOP117	21
CHOP118	2
CHOP119	8
CHOP124	18
CHOP125	15
CHOP133	15
CHOP147	2
CHOP155	15

Table C.4b: Patient Number and Age of the patients used for Ventricular Function Studies for Non-HLHS patients

Non-HLHS Patient	**Age (years)**
CHOP014	13
CHOP017	15
CHOP030	10
CHOP034	14
CHOP043	20
CHOP059	2
CHOP060	2
CHOP096	10
CHOP126	2.3

Table C.5: Cardiac catheterization data used in the lumped parameter modeling study

Patient	**PVRI (mmHg-m^2-Minute/Liter)**	**SVRI (mmHg-m^2-Minute/Liter)**	**IVC Pressures-mmHg**
CHOP006	N/A	N/A	20
CHOP007	4.3	47.8	N/A
CHOP018	N/A	N/A	10
CHOP022	1.5	20.7	9
CHOP023	1.3	23.8	N/A
CHOP024	N/A	N/A	16
CHOP028	1.7	22.9	8
CHOP032	N/A	N/A	11
CHOP041	1.6	24.4	11
CHOP042	1.91	30.15	N/A
CHOP046	1.7	19.2	N/A
CHOP049	1.7	11.8	N/A
CHOP050	4.23	24.06	N/A
CHOP053	3.4	22.3	N/A
CHOA00D	1.7	15.7	N/A
CHOA001	1	18.6	N/A
CHOA002	3.2	21.2	N/A
CHOA003	2.2	21.4	N/A
CHOA005	2.1	15.5	N/A

CHOA007	2.7	19.2	N/A
CHOA009	2	20.3	N/A
CHOA011	3.52	18.77	N/A
CHOA013	2.3	14.9	N/A
CHOA016	1.5	10.7	N/A
CHOA017	1	18.7	N/A
CHOA018	2.5	27	N/A
CHOA019	2	11.2	N/A
CHOA020	1.9	11.4	8
CHOA022	1.6	13.5	N/A
CHOA024	2.6	12.00	6
CHOA025	1	14.2	N/A
CHOA026	N/A	N/A	7
CHOA27	1.6	12.5	N/A
CHOA028	1.6	20.3	N/A
CHOA029	1.7	14.5	7
CHOA031	1.3	14.6	14
CHOA032	1.4	15.1	11
CHOA039	2	10.6	N/A
CHOA040	1.7	30.4	N/A
CHOA042	1.1	13	N/A
CHOA046	1.5	14.5	N/A

CHOA047	2.7	14.8	N/A
CHOA048	1.8	33	N/A
CHOA049	1.8	10.9	N/A
CHOA051	1	12.9	N/A

REFERENCES

1. Fontan F, Baudet E. Surgical repair of tricuspid atresia. Thorax 1971;26(3):240-8.
2. Marino BS. Outcomes after the Fontan procedure. Curr Opin Pediatr 2002;14(5):620-6.
3. Kreutzer GO, Vargas FJ, Schlichter AJ, Laura JP, Suarez JC, Coronel AR, et al. Atriopulmonary anastomosis. J Thorac Cardiovasc Surg 1982;83(3):427-36.
4. de Leval MR, Kilner P, Gewillig M, Bull C. Total cavopulmonary connection: a logical alternative to atriopulmonary connection for complex Fontan operations. Experimental studies and early clinical experience. J Thorac Cardiovasc Surg 1988;96(5):682-95.
5. Marcelletti C, Corno A, Giannico S, Marino B. Inferior vena cava-pulmonary artery extracardiac conduit. A new form of right heart bypass. J Thorac Cardiovasc Surg 1990;100(2):228-32.
6. Laschinger JC, Ringel RE, Brenner JI, McLaughlin JS. Extracardiac total cavopulmonary connection. Ann Thorac Surg 1992;54(2):371-3.
7. Laks H, Ardehali A, Grant PW, Permut L, Aharon A, Kuhn M, et al. Modification of the Fontan procedure. Superior vena cava to left pulmonary artery connection and inferior vena cava to right pulmonary artery connection with adjustable atrial septal defect. Circulation 1995;91(12):2943-7.
8. Norwood WI, Kirklin JK, Sanders SP. Hypoplastic left heart syndrome: experience with palliative surgery. Am J Cardiol 1980;45(1):87-91.
9. Stansel HC, Jr. A new operation for d-loop transposition of the great vessels. Ann

Thorac Surg 1975;19(5):565-7.

10. Reemtsen BL, Pike NA, Starnes VA. Stage I palliation for hypoplastic left heart syndrome: Norwood versus Sano modification. Curr Opin Cardiol 2007;22(2):60-5.

11. Sano S, Ishino K, Kawada M, Arai S, Kasahara S, Asai T, et al. Right ventricle-pulmonary artery shunt in first-stage palliation of hypoplastic left heart syndrome. J Thorac Cardiovasc Surg 2003;126(2):504-9; discussion 509-10.

12. Pizarro C, Mroczek T, Malec E, Norwood WI. Right ventricle to pulmonary artery conduit reduces interim mortality after stage 1 Norwood for hypoplastic left heart syndrome. Ann Thorac Surg 2004;78(6):1959-63; discussion 1963-4.

13. Sano S, Ishino K, Kado H, Shiokawa Y, Sakamoto K, Yokota M, et al. Outcome of right ventricle-to-pulmonary artery shunt in first-stage palliation of hypoplastic left heart syndrome: a multi-institutional study. Ann Thorac Surg 2004;78(6):1951-7; discussion 1957-8.

14. Cua CL, Thiagarajan RR, Gauvreau K, Lai L, Costello JM, Wessel DL, et al. Early postoperative outcomes in a series of infants with hypoplastic left heart syndrome undergoing stage I palliation operation with either modified Blalock-Taussig shunt or right ventricle to pulmonary artery conduit. Pediatr Crit Care Med 2006;7(3):238-44.

15. Tabbutt S, Dominguez TE, Ravishankar C, Marino BS, Gruber PJ, Wernovsky G, et al. Outcomes after the stage I reconstruction comparing the right ventricular to pulmonary artery conduit with the modified Blalock Taussig shunt. Ann Thorac Surg 2005;80(5):1582-90; discussion 1590-1.

16. Lardo AC, Webber SA, Iyengar A, del Nido PJ, Friehs I, Cape EG. Bidirectional superior cavopulmonary anastomosis improves mechanical efficiency in dilated atriopulmonary connections. J Thorac Cardiovasc Surg 1999;118(4):681-91.

17. de Leval MR, Dubini G, Migliavacca F, Jalali H, Camporini G, Redington A, et al. Use of computational fluid dynamics in the design of surgical procedures: application to the study of competitive flows in cavo-pulmonary connections. J Thorac Cardiovasc Surg 1996;111(3):502-13.

18. de Zelicourt DA, Pekkan, K.,Parks, J.,Kanter, K.,Fogel, M.,Yoganathan, A. P. Flow study of an extracardiac connection with persistent left superior vena cava. J Thorac Cardiovasc Surg 2006;131(4):785-91.

19. de Zelicourt DA, Pekkan K, Wills L, Kanter K, Forbess J, Sharma S, et al. In vitro flow analysis of a patient-specific intraatrial total cavopulmonary connection. Ann Thorac Surg 2005;79(6):2094-102.

20. Amodeo A, Galletti L, Marianeschi S, Picardo S, Giannico S, Di Renzi P, et al. Extracardiac Fontan operation for complex cardiac anomalies: seven years' experience. J Thorac Cardiovasc Surg 1997;114(6):1020-30; discussion 1030-1.

21. Choussat A, Fontan F, Besse F. Selection Criteria for Fontan's procedure. Pediatr Cardiol 1978:559-66.

22. Driscoll DJ. Long-term results of the Fontan operation. Pediatr Cardiol 2007;28(6):438-42.

23. Mair DD, Puga FJ, Danielson GK. The Fontan procedure for tricuspid atresia: early and late results of a 25-year experience with 216 patients. J Am Coll Cardiol 2001;37(3):933-9.

24. Gaynor JW, Bridges ND, Cohen MI, Mahle WT, Decampli WM, Steven JM, et al. Predictors of outcome after the Fontan operation: is hypoplastic left heart syndrome still a risk factor? J Thorac Cardiovasc Surg 2002;123(2):237-45.

25. Lemler MS, Scott WA, Leonard SR, Stromberg D, Ramaciotti C. Fenestration improves clinical outcome of the fontan procedure: a prospective, randomized study. Circulation 2002;105(2):207-12.

26. Seliem M, Muster AJ, Paul MH, Benson DW, Jr. Relation between preoperative left ventricular muscle mass and outcome of the Fontan procedure in patients with tricuspid atresia. J Am Coll Cardiol 1989;14(3):750-5.

27. Fogel MA, Rychik J. Right ventricular function in congenital heart disease: pressure and volume overload lesions. Prog Cardiovasc Dis 1998;40(4):343-56.

28. Fogel MA, Weinberg PM, Gupta KB, Rychik J, Hubbard A, Hoffman EA, et al. Mechanics of the single left ventricle: a study in ventricular-ventricular interaction II. Circulation 1998;98(4):330-8.

29. Joshi VM, Carey A, Simpson P, Paridon SM. Exercise performance following repair of hypoplastic left heart syndrome: A comparison with other types of Fontan patients. Pediatr Cardiol 1997;18(5):357-60.

30. Fogel MA. Assessment of cardiac function by magnetic resonance imaging. Pediatr Cardiol 2000;21(1):59-69.

31. Fogel MA, Weinberg PM, Chin AJ, Fellows KE, Hoffman EA. Late ventricular geometry and performance changes of functional single ventricle throughout staged Fontan reconstruction assessed by magnetic resonance imaging. J Am Coll Cardiol 1996;28(1):212-21.

32. Fogel MA, Weinberg PM, Fellows KE, Hoffman EA. A study in ventricular-ventricular interaction. Single right ventricles compared with systemic right ventricles in a dual-chamber circulation. Circulation 1995;92(2):219-30.

33. Fogel MA, Weinberg PM, Haselgrove J. Nonuniform flow dynamics in the aorta of normal children: a simplified approach to measurement using magnetic resonance velocity mapping. J Magn Reson Imaging 2002;15(6):672-8.

34. Fogel MA, Weinberg PM, Hoydu AK, Hubbard AM, Rychik J, Jacobs ML, et al. Effect of surgical reconstruction on flow profiles in the aorta using magnetic resonance blood tagging. Ann Thorac Surg 1997;63(6):1691-700.

35. Huddleston CB. The failing Fontan: options for surgical therapy. Pediatr Cardiol 2007;28(6):472-6.

36. Fogel MA, Weinberg PM, Fellows KE, Hoffman EA. Magnetic resonance imaging of constant total heart volume and center of mass in patients with functional single ventricle before and after staged Fontan procedure. Am J Cardiol 1993;72(18):1435-43.

37. Senzaki H, Masutani S, Ishido H, Taketazu M, Kobayashi T, Sasaki N, et al. Cardiac rest and reserve function in patients with Fontan circulation. J Am Coll Cardiol 2006;47(12):2528-35.

38. Szabo G, Buhmann V, Graf A, Melnitschuk S, Bahrle S, Vahl CF, et al. Ventricular energetics after the Fontan operation: contractility-afterload mismatch. J Thorac Cardiovasc Surg 2003;125(5):1061-9.

39. Magosso E, Cavalcanti S, Ursino M. Theoretical analysis of rest and exercise hemodynamics in patients with total cavopulmonary connection. Am J Physiol

Heart Circ Physiol 2002;282(3):H1018-34.

40. Nogaki M, Senzaki H, Masutani S, Kobayashi J, Kobayashi T, Sasaki N, et al. Ventricular energetics in Fontan circulation: evaluation with a theoretical model. Pediatr Int 2000;42(6):651-7.

41. Guyton AC. Cardiac Output, Venous Return, and Their Regulation: Saundersm Philadelphia, PA; 1961.

42. Guyton AC, Abernathy B, Langston JB, Kaufmann BN, Fairchild HM. Relative importance of venous and arterial resistances in controlling venous return and cardiac output. Am J Physiol 1959;196(5):1008-14.

43. Pekkan K, de Zelicourt D, Ge L, Sotiropoulos F, Frakes D, Fogel MA, et al. Physics-driven CFD modeling of complex anatomical cardiovascular flows-a TCPC case study. Ann Biomed Eng 2005;33(3):284-300.

44. Wang C, Pekkan K, de Zelicourt D, Horner M, Parihar A, Kulkarni A, et al. Progress in the CFD modeling of flow instabilities in anatomical total cavopulmonary connections. Ann Biomed Eng 2007;35(11):1840-56.

45. Kelley JR, Mack GW, Fahey JT. Diminished venous vascular capacitance in patients with univentricular hearts after the Fontan operation. Am J Cardiol 1995;76(3):158-63.

46. Kiesewetter CH, Sheron N, Vettukattill JJ, Hacking N, Stedman B, Millward-Sadler H, et al. Hepatic changes in the failing Fontan circulation. Heart 2007;93(5):579-84.

47. Brown JW, Ruzmetov M, Vijay P, Rodefeld MD, Turrentine MW. Pulmonary arteriovenous malformations in children after the Kawashima operation. Ann

Thorac Surg 2005;80(5):1592-6.

48. Duncan BW, Desai S. Pulmonary arteriovenous malformations after cavopulmonary anastomosis. Ann Thorac Surg 2003;76(5):1759-66.

49. Moore JW, Kirby WC, Madden WA, Gaither NS. Development of pulmonary arteriovenous malformations after modified Fontan operations. J Thorac Cardiovasc Surg 1989;98(6):1045-50.

50. Pandurangi UM, Shah MJ, Murali R, Cherian KM. Rapid onset of pulmonary arteriovenous malformations after cavopulmonary anastomosis. Ann Thorac Surg 1999;68(1):237-9.

51. Shinohara T, Yokoyama T. Pulmonary arteriovenous malformation in patients with total cavopulmonary shunt: what role does lack of hepatic venous blood flow to the lungs play? Pediatr Cardiol 2001;22(4):343-6.

52. Pike NA, Vricella LA, Feinstein JA, Black MD, Reitz BA. Regression of severe pulmonary arteriovenous malformations after Fontan revision and "hepatic factor" rerouting. Ann Thorac Surg 2004;78(2):697-9.

53. AboulHosn J, Danon S, Levi D, Castellon Y, Child J, Moore J. Regression of pulmonary arteriovenous malformations after transcatheter reconnection of the pulmonary arteries in patients with unidirectional Fontan. Congenit Heart Dis 2007;2(3):179-84.

54. Steinberg J, Alfieris GM, Brandt B, 3rd, Smith F, Byrum CJ, Fink GW, et al. New approach to the surgical management of pulmonary arteriovenous malformations after cavopulmonary anastomosis. Ann Thorac Surg 2003;75(5):1640-2.

55. Uemura H, Yagihara T, Hattori R, Kawahira Y, Tsukano S, Watanabe K.

Redirection of hepatic venous drainage after total cavopulmonary shunt in left isomerism. Ann Thorac Surg 1999;68(5):1731-5.

56. Wu IH, Nguyen KH. Redirection of hepatic drainage for treatment of pulmonary arteriovenous malformations following the Fontan procedure. Pediatr Cardiol 2006;27(4):519-22.

57. Atz AM, Cohen MS, Sleeper LA, McCrindle BW, Lu M, Prakash A, et al. Functional state of patients with heterotaxy syndrome following the Fontan operation. Cardiol Young 2007;17 Suppl 2:44-53.

58. Amodeo A, Grigioni M, Oppido G, Daniele C, D'Avenio G, Pedrizzetti G, et al. The beneficial vortex and best spatial arrangement in total extracardiac cavopulmonary connection. J Thorac Cardiovasc Surg 2002;124(3):471-8.

59. Dubini G, de Leval MR, Pietrabissa R, Montevecchi FM, Fumero R. A numerical fluid mechanical study of repaired congenital heart defects. Application to the total cavopulmonary connection. J Biomech 1996;29(1):111-21.

60. Dubini G, Redaelli A. Mesh updating in fluid-structure interactions in biomechanics: an iterative method based on an uncoupled approach. Ann Biomed Eng 1997;25(1):218-31.

61. Ensley AE, Lynch P, Chatzimavroudis GP, Lucas C, Sharma S, Yoganathan AP. Toward designing the optimal total cavopulmonary connection: an in vitro study. Ann Thorac Surg 1999;68(4):1384-90.

62. Ensley AE, Ramuzat A, Healy TM, Chatzimavroudis GP, Lucas C, Sharma S, et al. Fluid mechanic assessment of the total cavopulmonary connection using magnetic resonance phase velocity mapping and digital particle image

velocimetry. Ann Biomed Eng 2000;28(10):1172-83.

63. Healy TM, Ensley A.E., Ramuzat A., Lucas C., and Yoganathan A.P. Numerical Simulation of Flow in Model Total Cavopulmonary Connections. In: BMES-EMBS First Joint Conference; 1999; Atlanta, GA, USA; 1999.

64. Healy TM, Ensley A.E., Ramuzat A., Sharma S., and Yoganathan A.P. . Reconstruction and Visualization of Three-Dimensional, Time-Dependent Velocity Fields Obtained from Magnetic Resonance Imaging. In: ASME Bioengineering Conference; 1999; Big Sky, MT, USA; 1999.

65. Lardo AC, Webber SA, Friehs I, del Nido PJ, Cape EG. Fluid dynamic comparison of intra-atrial and extracardiac total cavopulmonary connections. J Thorac Cardiovasc Surg 1999;117(4):697-704.

66. Masters JC, Ketner M, Mill M, Yoganathan AP, and Lucas CL. . Assessing the effect of compliance on the efficacy of the total cavopulmonary connection. . Journal of Biomechanical Engineering. Under revision.

67. Migliavacca F, de Leval, M.R., Dubini G. Pietrabissa, R., and Fumero, R. Computational Fluid Dynamic Simulations of Cavopulmonary Connections with an Extra-Cardiac Lateral Conduit. Medical Engineering Physics 1999;21:187-193.

68. Migliavacca F, Kilner PJ, Pennati G, Dubini G, Pietrabissa R, Fumero R, et al. Computational fluid dynamic and magnetic resonance analyses of flow distribution between the lungs after total cavopulmonary connection. IEEE Trans Biomed Eng 1999;46(4):393-9.

69. Pekkan K, Kitajima HD, de Zelicourt D, Forbess JM, Parks WJ, Fogel MA, et al. Total cavopulmonary connection flow with functional left pulmonary artery

stenosis: angioplasty and fenestration in vitro. Circulation 2005;112(21):3264-71.

70. Ryu K, Healy TM, Ensley AE, Sharma S, Lucas C, Yoganathan AP. Importance of accurate geometry in the study of the total cavopulmonary connection: computational simulations and in vitro experiments. Ann Biomed Eng 2001;29(10):844-53.

71. Sharma S, Ensley AE, Hopkins K, Chatzimavroudis GP, Healy TM, Tam VK, et al. In vivo flow dynamics of the total cavopulmonary connection from three-dimensional multislice magnetic resonance imaging. Ann Thorac Surg 2001;71(3):889-98.

72. Sharma S, Goudy S, Walker P, Panchal S, Ensley A, Kanter K, et al. In vitro flow experiments for determination of optimal geometry of total cavopulmonary connection for surgical repair of children with functional single ventricle. J Am Coll Cardiol 1996;27(5):1264-9.

73. Hsia TY, Migliavacca F, Pittaccio S, Radaelli A, Dubini G, Pennati G, et al. Computational fluid dynamic study of flow optimization in realistic models of the total cavopulmonary connections. J Surg Res 2004;116(2):305-13.

74. Migliavacca F, de Leval MR, Dubini G, Pietrabissa R. A computational pulsatile model of the bidirectional cavopulmonary anastomosis: the influence of pulmonary forward flow. J Biomech Eng 1996;118(4):520-8.

75. Migliavacca F, Dubini G, Pennati G, Pietrabissa R, Fumero R, Hsia TY, et al. Computational model of the fluid dynamics in systemic-to-pulmonary shunts. J Biomech 2000;33(5):549-57.

76. Migliavacca F, Dubini G, Pietrabissa R, de Leval MR. Computational transient

simulations with varying degree and shape of pulmonic stenosis in models of the bidirectional cavopulmonary anastomosis. Med Eng Phys 1997;19(4):394-403.

77. Migliavacca F, Pennati G, Di Martino E, Dubini G, Pietrabissa R. Pressure drops in a distensible model of end-to-side anastomosis in systemic-to-pulmonary shunts. Comput Methods Biomech Biomed Engin 2002;5(3):243-8.

78. de Zelicourt D, Pekkan K, Kitajima H, Frakes D, Yoganathan AP. Single-step stereolithography of complex anatomical models for optical flow measurements. J Biomech Eng 2005;127(1):204-7.

79. Masters JC, Ketner M, Bleiweis MS, Mill M, Yoganathan A, Lucas CL. The effect of incorporating vessel compliance in a computational model of blood flow in a total cavopulmonary connection (TCPC) with caval centerline offset. J Biomech Eng 2004;126(6):709-13.

80. Kim YH, Walker PG, Fontaine AA, Panchal S, Ensley AE, Oshinski J, et al. Hemodynamics of the Fontan connection: an in-vitro study. J Biomech Eng 1995;117(4):423-8.

81. Frakes D, Smith M, de Zelicourt D, Pekkan K, Yoganathan A. Three-dimensional velocity field reconstruction. J Biomech Eng 2004;126(6):727-35.

82. Webb A. Magnetic Resonance Imaging. In: Webb A, editor. Introduction to Biomedical Imaging. Piscataway: John Wiley & Sons; 2003. p. 157-220.

83. Box FM, van der Geest RJ, van der Grond J, van Osch MJ, Zwinderman AH, Palm-Meinders IH, et al. Reproducibility of wall shear stress assessment with the paraboloid method in the internal carotid artery with velocity encoded MRI in healthy young individuals. J Magn Reson Imaging 2007;26(3):598-605.

84. Ebbers T, Wigstrom L, Bolger AF, Engvall J, Karlsson M. Estimation of relative cardiovascular pressures using time-resolved three-dimensional phase contrast MRI. Magn Reson Med 2001;45(5):872-9.

85. Oshinski JN, Curtin JL, Loth F. Mean-average wall shear stress measurements in the common carotid artery. J Cardiovasc Magn Reson 2006;8(5):717-22.

86. Pantos I, Patatoukas G, Efstathopoulos EP, Katritsis D. In vivo wall shear stress measurements using phase-contrast MRI. Expert Rev Cardiovasc Ther 2007;5(5):927-38.

87. Wu SP, Ringgaard S, Pedersen EM. Three-dimensional phase contrast velocity mapping acquisition improves wall shear stress estimation in vivo. Magn Reson Imaging 2004;22(3):345-51.

88. Venkatachari AK, Halliburton SS, Setser RM, White RD, Chatzimavroudis GP. Noninvasive quantification of fluid mechanical energy losses in the total cavopulmonary connection with magnetic resonance phase velocity mapping. Magn Reson Imaging 2007;25(1):101-9.

89. Groen HC, Gijsen FJ, van der Lugt A, Ferguson MS, Hatsukami TS, van der Steen AF, et al. Plaque rupture in the carotid artery is localized at the high shear stress region: a case report. Stroke 2007;38(8):2379-81.

90. Wentzel JJ, Corti R, Fayad ZA, Wisdom P, Macaluso F, Winkelman MO, et al. Does shear stress modulate both plaque progression and regression in the thoracic aorta? Human study using serial magnetic resonance imaging. J Am Coll Cardiol 2005;45(6):846-54.

91. Acevedo-Bolton G, Jou LD, Dispensa BP, Lawton MT, Higashida RT, Martin AJ,

et al. Estimating the hemodynamic impact of interventional treatments of aneurysms: numerical simulation with experimental validation: technical case report. Neurosurgery 2006;59(2):E429-30; author reply E429-30.

92. Markl M, Harloff A, Foll D, Langer M, Hennig J, Frydrychowicz A. Sclerotic aortic valve: flow-sensitive 4-dimensional magnetic resonance imaging reveals 3 distinct flow-pattern changes. Circulation 2007;116(10):e336-7.

93. Tanaka K, Makaryus AN, Wolff SD. Correlation of aortic valve area obtained by the velocity-encoded phase contrast continuity method to direct planimetry using cardiovascular magnetic resonance. J Cardiovasc Magn Reson 2007;9(5):799-805.

94. Chung AC, Noble JA, Summers P. Fusing speed and phase information for vascular segmentation of phase contrast MR angiograms. Med Image Anal 2002;6(2):109-28.

95. Chung AC, Noble JA, Summers P. Vascular segmentation of phase contrast magnetic resonance angiograms based on statistical mixture modeling and local phase coherence. IEEE Trans Med Imaging 2004;23(12):1490-507.

96. Kozerke S, Botnar R, Oyre S, Scheidegger MB, Pedersen EM, Boesiger P. Automatic vessel segmentation using active contours in cine phase contrast flow measurements. J Magn Reson Imaging 1999;10(1):41-51.

97. Cho J, Benkeser P. Elastically deformable model-based motion-tracking of left ventricle. Conf Proc IEEE Eng Med Biol Soc 2004;3:1925-8.

98. Cho J, Benkeser PJ. Cardiac segmentation by a velocity-aided active contour model. Comput Med Imaging Graph 2006;30(1):31-41.

99. Pluempitiwiriyawej C, Moura JM, Fellow, Wu YJ, Ho C. STACS: new active contour scheme for cardiac MR image segmentation. IEEE Trans Med Imaging 2005;24(5):593-603.

100. Walker PG, Cranney GB, Scheidegger MB, Waseleski G, Pohost GM, Yoganathan AP. Semiautomated method for noise reduction and background phase error correction in MR phase velocity data. J Magn Reson Imaging 1993;3(3):521-30.

101. Fatouraee N, Amini AA. Regularization of flow streamlines in multislice phase-contrast MR imaging. IEEE Trans Med Imaging 2003;22(6):699-709.

102. Caputo GR, Kondo C, Masui T, Geraci SJ, Foster E, O'Sullivan MM, et al. Right and left lung perfusion: in vitro and in vivo validation with oblique-angle, velocity-encoded cine MR imaging. Radiology 1991;180(3):693-8.

103. Evans AJ, Iwai F, Grist TA, Sostman HD, Hedlund LW, Spritzer CE, et al. Magnetic resonance imaging of blood flow with a phase subtraction technique. In vitro and in vivo validation. Invest Radiol 1993;28(2):109-15.

104. Lee VS, Spritzer CE, Carroll BA, Pool LG, Bernstein MA, Heinle SK, et al. Flow quantification using fast cine phase-contrast MR imaging, conventional cine phase-contrast MR imaging, and Doppler sonography: in vitro and in vivo validation. AJR Am J Roentgenol 1997;169(4):1125-31.

105. Chatzimavroudis GP, Oshinski JN, Pettigrew RI, Walker PG, Franch RH, Yoganathan AP. Quantification of mitral regurgitation with MR phase-velocity mapping using a control volume method. J Magn Reson Imaging 1998;8(3):577-82.

106. Powell AJ, Maier SE, Chung T, Geva T. Phase-velocity cine magnetic resonance imaging measurement of pulsatile blood flow in children and young adults: in vitro and in vivo validation. Pediatr Cardiol 2000;21(2):104-10.

107. Beerbaum P, Korperich H, Gieseke J, Barth P, Peuster M, Meyer H. Blood flow quantification in adults by phase-contrast MRI combined with SENSE--a validation study. J Cardiovasc Magn Reson 2005;7(2):361-9.

108. Isoda H, Hirano M, Takeda H, Kosugi T, Alley MT, Markl M, et al. Visualization of hemodynamics in a silicon aneurysm model using time-resolved, 3D, phase-contrast MRI. AJNR Am J Neuroradiol 2006;27(5):1119-22.

109. Wentland AL, Korosec FR, Vigen KK, Wieben O, Fine JP, Grist TM. Cine flow measurements using phase contrast with undersampled projections: in vitro validation and preliminary results in vivo. J Magn Reson Imaging 2006;24(4):945-51.

110. Markl M, Benk C, Klausmann D, Stalder AF, Frydrychowicz A, Hennig J, et al. Three-dimensional magnetic resonance flow analysis in a ventricular assist device. J Thorac Cardiovasc Surg 2007;134(6):1471-6.

111. Delfino JG, Bhasin M, Cole R, Eisner RL, Merlino J, Leon AR, et al. Comparison of myocardial velocities obtained with magnetic resonance phase velocity mapping and tissue Doppler imaging in normal subjects and patients with left ventricular dyssynchrony. J Magn Reson Imaging 2006;24(2):304-11.

112. Canstein C, Cachot P, Faust A, Stalder AF, Bock J, Frydrychowicz A, et al. 3D MR flow analysis in realistic rapid-prototyping model systems of the thoracic aorta: comparison with in vivo data and computational fluid dynamics in identical

vessel geometries. Magn Reson Med 2008;59(3):535-46.

113. Kohler U, Marshall I, Robertson MB, Long Q, Xu XY, Hoskins PR. MRI measurement of wall shear stress vectors in bifurcation models and comparison with CFD predictions. J Magn Reson Imaging 2001;14(5):563-73.

114. Long Q, Xu XY, Kohler U, Robertson MB, Marshall I, Hoskins P. Quantitative comparison of CFD predicted and MRI measured velocity fields in a carotid bifurcation phantom. Biorheology 2002;39(3-4):467-74.

115. Papathanasopoulou P, Zhao S, Kohler U, Robertson MB, Long Q, Hoskins P, et al. MRI measurement of time-resolved wall shear stress vectors in a carotid bifurcation model, and comparison with CFD predictions. J Magn Reson Imaging 2003;17(2):153-62.

116. Marshall I, Zhao S, Papathanasopoulou P, Hoskins P, Xu Y. MRI and CFD studies of pulsatile flow in healthy and stenosed carotid bifurcation models. J Biomech 2004;37(5):679-87.

117. Kilner PJ, Manzara CC, Mohiaddin RH, Pennell DJ, Sutton MG, Firmin DN, et al. Magnetic resonance jet velocity mapping in mitral and aortic valve stenosis. Circulation 1993;87(4):1239-48.

118. Kilner PJ, Yang GZ, Mohiaddin RH, Firmin DN, Longmore DB. Helical and retrograde secondary flow patterns in the aortic arch studied by three-directional magnetic resonance velocity mapping. Circulation 1993;88(5 Pt 1):2235-47.

119. Kilner PJ, Yang GZ, Wilkes AJ, Mohiaddin RH, Firmin DN, Yacoub MH. Asymmetric redirection of flow through the heart. Nature 2000;404(6779):759-61.

120. Delfino JG, Fornwalt BK, Eisner RL, Leon AR, Oshinski JN. Determination of transmural, endocardial, and epicardial radial strain and strain rate from phase contrast MR velocity data. J Magn Reson Imaging 2008;27(3):522-8.

121. Delfino JG, Johnson KR, Eisner RL, Eder S, Leon AR, Oshinski JN. Three-directional myocardial phase-contrast tissue velocity MR imaging with navigator-echo gating: in vivo and in vitro study. Radiology 2008;246(3):917-25.

122. Johnson KR, Patel SJ, Whigham A, Hakim A, Pettigrew RI, Oshinski JN. Three-dimensional, time-resolved motion of the coronary arteries. J Cardiovasc Magn Reson 2004;6(3):663-73.

123. Oshinski JN, Ku DN, Mukundan S, Jr., Loth F, Pettigrew RI. Determination of wall shear stress in the aorta with the use of MR phase velocity mapping. J Magn Reson Imaging 1995;5(6):640-7.

124. Chatzimavroudis GP, Oshinski JN, Franch RH, Pettigrew RI, Walker PG, Yoganathan AP. Quantification of the aortic regurgitant volume with magnetic resonance phase velocity mapping: a clinical investigation of the importance of imaging slice location. J Heart Valve Dis 1998;7(1):94-101.

125. Chatzimavroudis GP, Oshinski JN, Franch RH, Walker PG, Yoganathan AP, Pettigrew RI. Evaluation of the precision of magnetic resonance phase velocity mapping for blood flow measurements. J Cardiovasc Magn Reson 2001;3(1):11-9.

126. Chatzimavroudis GP, Walker PG, Oshinski JN, Franch RH, Pettigrew RI, Yoganathan AP. The importance of slice location on the accuracy of aortic regurgitation measurements with magnetic resonance phase velocity mapping.

Ann Biomed Eng 1997;25(4):644-52.

127. Chatzimavroudis GP, Walker PG, Oshinski JN, Franch RH, Pettigrew RI, Yoganathan AP. Slice location dependence of aortic regurgitation measurements with MR phase velocity mapping. Magn Reson Med 1997;37(4):545-51.

128. Frydrychowicz A, Arnold R, Harloff A, Schlensak C, Hennig J, Langer M, et al. Images in cardiovascular medicine. In vivo 3-dimensional flow connectivity mapping after extracardiac total cavopulmonary connection. Circulation 2008;118(2):e16-7.

129. Frydrychowicz A, Arnold R, Hirtler D, Schlensak C, Stalder AF, Hennig J, et al. Multidirectional flow analysis by cardiovascular magnetic resonance in aneurysm development following repair of aortic coarctation. J Cardiovasc Magn Reson 2008;10(1):30.

130. Frydrychowicz A, Berger A, Russe MF, Stalder AF, Harloff A, Dittrich S, et al. Time-resolved magnetic resonance angiography and flow-sensitive 4-dimensional magnetic resonance imaging at 3 Tesla for blood flow and wall shear stress analysis. J Thorac Cardiovasc Surg 2008;136(2):400-7.

131. Frydrychowicz A, Bley TA, Dittrich S, Hennig J, Langer M, Markl M. Visualization of vascular hemodynamics in a case of a large patent ductus arteriosus using flow sensitive 3D CMR at 3T. J Cardiovasc Magn Reson 2007;9(3):585-7.

132. Frydrychowicz A, Bley TA, Winterer JT, Harloff A, Langer M, Hennig J, et al. Accelerated time-resolved 3D contrast-enhanced MR angiography at 3T: clinical experience in 31 patients. MAGMA 2006;19(4):187-95.

133. Frydrychowicz A, Harloff A, Jung B, Zaitsev M, Weigang E, Bley TA, et al. Time-resolved, 3-dimensional magnetic resonance flow analysis at 3 T: visualization of normal and pathological aortic vascular hemodynamics. J Comput Assist Tomogr 2007;31(1):9-15.

134. Frydrychowicz A, Markl M, Harloff A, Stalder AF, Bock J, Bley TA, et al. [Flow-sensitive in-vivo 4D MR imaging at 3T for the analysis of aortic hemodynamics and derived vessel wall parameters]. Rofo 2007;179(5):463-72.

135. Frydrychowicz A, Schlensak C, Stalder A, Russe M, Siepe M, Beyersdorf F, et al. Ascending-descending aortic bypass surgery in aortic arch coarctation: four-dimensional magnetic resonance flow analysis. J Thorac Cardiovasc Surg 2007;133(1):260-2.

136. Frydrychowicz A, Weigang E, Langer M, Markl M. Flow-sensitive 3D magnetic resonance imaging reveals complex blood flow alterations in aortic Dacron graft repair. Interact Cardiovasc Thorac Surg 2006;5(4):340-2.

137. Frydrychowicz A, Winterer JT, Zaitsev M, Jung B, Hennig J, Langer M, et al. Visualization of iliac and proximal femoral artery hemodynamics using time-resolved 3D phase contrast MRI at 3T. J Magn Reson Imaging 2007;25(5):1085-92.

138. Migliavacca F, de Leval MR, Dubini G, Pietrabissa R, Fumero R. Computational fluid dynamic simulations of cavopulmonary connections with an extracardiac lateral conduit. Med Eng Phys 1999;21(3):187-93.

139. Migliavacca F, Lagana K, Pennati G, de Leval MR, Bove EL, Dubini G. Global mathematical modelling of the Norwood circulation: a multiscale approach for the

study of the pulmonary and coronary arterial perfusions. Cardiol Young 2004;14 Suppl 3:71-6.

140. Migliavacca F, Pennati G, Dubini G, Fumero R, Pietrabissa R, Urcelay G, et al. Modeling of the Norwood circulation: effects of shunt size, vascular resistances, and heart rate. Am J Physiol Heart Circ Physiol 2001;280(5):H2076-86.

141. Fogel MA, Weinberg PM, Hoydu A, Hubbard A, Rychik J, Jacobs M, et al. The nature of flow in the systemic venous pathway measured by magnetic resonance blood tagging in patients having the Fontan operation. J Thorac Cardiovasc Surg 1997;114(6):1032-41.

142. Fogel MA, Weinberg PM, Rychik J, Hubbard A, Jacobs M, Spray TL, et al. Caval contribution to flow in the branch pulmonary arteries of Fontan patients with a novel application of magnetic resonance presaturation pulse. Circulation 1999;99(9):1215-21.

143. Be'eri E, Maier SE, Landzberg MJ, Chung T, Geva T. In vivo evaluation of Fontan pathway flow dynamics by multidimensional phase-velocity magnetic resonance imaging. Circulation 1998;98(25):2873-82.

144. Morgan VL, Graham TP, Jr., Roselli RJ, Lorenz CH. Alterations in pulmonary artery flow patterns and shear stress determined with three-dimensional phase-contrast magnetic resonance imaging in Fontan patients. J Thorac Cardiovasc Surg 1998;116(2):294-304.

145. Pedersen EM, Stenbog EV, Frund T, Houlind K, Kromann O, Sorensen KE, et al. Flow during exercise in the total cavopulmonary connection measured by magnetic resonance velocity mapping. Heart 2002;87(6):554-8.

146. Hjortdal VE, Emmertsen K, Stenbog E, Frund T, Schmidt MR, Kromann O, et al. Effects of exercise and respiration on blood flow in total cavopulmonary connection: a real-time magnetic resonance flow study. Circulation 2003;108(10):1227-31.

147. Hjortdal VE, Christensen TD, Larsen SH, Emmertsen K, Pedersen EM. Caval blood flow during supine exercise in normal and Fontan patients. Ann Thorac Surg 2008;85(2):599-603.

148. Frakes DH, Conrad CP, Healy TM, Monaco JW, Fogel M, Sharma S, et al. Application of an adaptive control grid interpolation technique to morphological vascular reconstruction. IEEE Trans Biomed Eng 2003;50(2):197-206.

149. Frakes DH, Smith MJ, Parks J, Sharma S, Fogel SM, Yoganathan AP. New techniques for the reconstruction of complex vascular anatomies from MRI images. J Cardiovasc Magn Reson 2005;7(2):425-32.

150. Lotz J, Doker R, Noeske R, Schuttert M, Felix R, Galanski M, et al. In vitro validation of phase-contrast flow measurements at 3 T in comparison to 1.5 T: precision, accuracy, and signal-to-noise ratios. J Magn Reson Imaging 2005;21(5):604-10.

151. Perona P, Malik J. Scale Space and Edge Detection Using Anisotropic Diffusion. IEEE Transactions on Pattern Analysis and Machine Intelligence 1990;12(7):629-639.

152. Gilmanov A, Sotiropoulos, F, Balarus, E. A General Reconstruction Algorithm For Simulating Flows with Complex 3D Immersed Boundaries on Cartesian Grids. Journal of Computational Physics 2003;191(2):660-669.

153. Gilmanov A, Ge, L., Wang, C., de Zelicourt, D. Pekkan, K., Sotiropolous, F., and Yoganathan, A.P. . Numerical Simulations of Flow in Anatomically Realistic Total Cavopulmonary Connections. In: 57th Annual Meeting of the Division of Fluid Dynamics,APS; 2004 November; Seattle, WA; 2004.

154. Kass MW, A., Terzopoulos, D. Snakes: Active Contour Models. International Journal of Computer Vision 1988:321-331.

155. Xu C, Prince, JL. Snakes, Shapes, and Gradient Vector Flow. IEEE Trans Image Processing 1998;7(3).

156. Osher S, Sethian J. Fronts propagating with curvature dependent speed: Algorithms based on Hamilton-Jacobi Formulation. Journal of Computational Physics 1988;79:12-49.

157. Mulder W, Osher S, Sethian JA. Computing Interface Motion in Compressible Gas Dynamics. Journal of Computational Physics 1992;100(2):209-228.

158. Caselles V, Kimmel R, Sapiro G. Geodesic Active Contours. International Journal of Computer Vision 1997;22(1):61-79.

159. Adalsteinsson D, Sethian J. A Fast Level Set Method for Propagating Interfaces. Journal of Computational Physics 1995;118:269-277.

160. Adalsteinsson D, Sethian J. The Fast Construction of Extension Velocites in Level Set Methods. Journal of Comptutational Physics 1999;148:2-22.

161. Malladi R, Sethian J, Vemuri BC. Shape Modeling with Front Propagation: A Level Set Approach. IEEE Transactions on Pattern Analysis and Machine Intelligence 1995;17(2):158-175.

162. Li C, Xu C, Gui C, Fox M. Level Set Evolution Without Re-Initialization: A New

Variational Formulation. In: IEEE Computer Society Conference on Computer Vision and Pattern Recognition IEEE; 2005.

163. Alperin N, Lee SH. PUBS: Pulsatility-based segmentation of lumens conducting non-steady flow. Magnetic Resonance in Medicine 2003;49(5):934-944.

164. Soerensen DD. Optimization and Analysis of the Total Cavopulmonary Connection [MS Thesis]. Atlanta: Georgia Institute of Technology; 2005.

165. Astola J. Vector Median Filters. Proceedings of IEEE 1990;78:678-689.

166. Lukac R. Adaptive Vector Median Filtering. Pattern Recognition Letters 2003;24:1889-1899.

167. Sonka M, Fitzpatrick, M.J. Handbook of Medical Imaging Volume 2: Medical Image Processing and Analysis. Boston: SPIE Press; 2000.

168. Tambasco M. Lagrangian Hemodynamics of the Stenosed Carotid Bifurcation [PhD Thesis]. London: University of Western Ontario; 2002.

169. Nichols W, O'Rourke MF, McDonald DA. Blood Flow in Arteries: Theoretical, Experimental, and Clinical Principles. London; 1990.

170. Bookstein FL. Principal Warps: Thin-plate splines and the decomposition of deformations. IEEE Transactions on Pattern Analysis and Machine Intelligence 1989;11(6):567-586.

171. Tong Y, Lombeyda, S, Hirani, AN, Desbrun, M. Discrete Multiscale Vector Field Decomposition. Association of Computed Machinery 2003:445-452.

172. Lowitzch S. A Density Theorem For Matrix-Valued Radial Basis Functions. Numerical Algorithms 2005;39:253-256.

173. Narcowich FJ, Ward JD. Generalized Hermite Interpolation via Matrix Valued

Conditionally Positive Definite Functions. Mathematics of Computation 1994;63:661-687.

174. Wendland H. Piecewise, polynomial, positive definite, and compactly supported radial basis functions of minimal degree. Advanced Computational Math 1995;4:389-396.

175. Frakes D, Healy, T., Sharma, S., Fogel, M., Monaco, J., Smith, M., andYoganathan, A.P. . Adaptive Control Grid Interpolation-Based MR Data Reconstruction for Surgical Planning and Evaluation. In: IBB Educational Partners Symposium; 2002 February; Atlanta, GA; 2002.

176. Senzaki H, Masutani S, Kobayashi J, Kobayashi T, Sasaki N, Asano H, et al. Ventricular afterload and ventricular work in fontan circulation: comparison with normal two-ventricle circulation and single-ventricle circulation with blalock-taussig shunts. Circulation 2002;105(24):2885-92.

177. Wang C, Gilmanov A., Ge L., Sotiropoulos F., and Yoganathan, A.P. The Hemodynamics of Total Cavo-Pulmonary Connection Anatomies. In: Meeting of The American Physical Society; 2005 November; Chicago, IL; 2005.

178. Pekkan K, Frakes D, De Zelicourt D, Lucas CW, Parks WJ, Yoganathan AP. Coupling pediatric ventricle assist devices to the Fontan circulation: simulations with a lumped-parameter model. Asaio J 2005;51(5):618-28.

179. Peskin CS, Tu C. Hemodynamics in congenital heart disease. Comput Biol Med 1986;16(5):331-59.

180. Palladino JL, L.C. R, Noordergraaf A. Human System Circulation Model Based on the Frank Mechansim. In: Ottesen JT, Danielson M, editors. Mathematical

Modeling in Medicine: IOP Press; 2000. p. 29-40.

181. Sun Y, Beshara M, Lucariello RJ, Chiaramida SA. A comprehensive model for right-left heart interaction under the influence of pericardium and baroreflex. Am J Physiol 1997;272(3 Pt 2):H1499-515.

182. Milanesi O, Stellin G, Colan SD, Facchin P, Crepaz R, Biffanti R, et al. Systolic and diastolic performance late after the Fontan procedure for a single ventricle and comparison of those undergoing operation at <12 months of age and at >12 months of age. Am J Cardiol 2002;89(3):276-80.

183. Penny DJ, Redington AN. Diastolic ventricular function after the Fontan operation. Am J Cardiol 1992;69(9):974-5.

184. Durongpisitkul K, Driscoll DJ, Mahoney DW, Wollan PC, Mottram CD, Puga FJ, et al. Cardiorespiratory response to exercise after modified Fontan operation: determinants of performance. J Am Coll Cardiol 1997;29(4):785-90.

185. Reybrouck T, Mertens L. Physical performance and physical activity in grown-up congenital heart disease. Eur J Cardiovasc Prev Rehabil 2005;12(5):498-502.

186. Minamisawa S, Nakazawa M, Momma K, Imai Y, Satomi G. Effect of aerobic training on exercise performance in patients after the Fontan operation. Am J Cardiol 2001;88(6):695-8.

187. Ohuchi H. Cardiopulmonary response to exercise in patients with the Fontan circulation. Cardiol Young 2005;15 Suppl 3:39-44.

188. Ohuchi H, Arakaki Y, Yagihara T, Kamiya T. Cardiorespiratory responses to exercise after repair of the univentricular heart. Int J Cardiol 1997;58(1):17-30.

189. Sanghavi DM, Flanagan M, Powell AJ, Curran T, Picard S, Rhodes J.

Determinants of exercise function following univentricular versus biventricular repair for pulmonary atresia/intact ventricular septum. Am J Cardiol 2006;97(11):1638-43.

190. Bendien C, Bossina KK, Buurma AE, Gerding AM, Kuipers JR, Landsman ML, et al. Hemodynamic effects of dynamic exercise in children and adolescents with moderate-to-small ventricular septal defects. Circulation 1984;70(6):929-34.

191. Lew CD, Alley MT, Bammer R, Spielman DM, Chan FP. Peak velocity and flow quantification validation for sensitivity-encoded phase-contrast MR imaging. Acad Radiol 2007;14(3):258-69.

192. Khunatorn Y, Shandas R, DeGroff C, Mahalingam S. Comparison of in vitro velocity measurements in a scaled total cavopulmonary connection with computational predictions. Ann Biomed Eng 2003;31(7):810-22.

193. Ku JP, Elkins CJ, Taylor CA. Comparison of CFD and MRI flow and velocities in an in vitro large artery bypass graft model. Ann Biomed Eng 2005;33(3):257-69.

194. Migliavacca F, Dubini G, Bove EL, de Leval MR. Computational fluid dynamics simulations in realistic 3-D geometries of the total cavopulmonary anastomosis: the influence of the inferior caval anastomosis. J Biomech Eng 2003;125(6):805-13.

195. Markl M, Harloff A, Bley TA, Zaitsev M, Jung B, Weigang E, et al. Time-resolved 3D MR velocity mapping at 3T: improved navigator-gated assessment of vascular anatomy and blood flow. J Magn Reson Imaging 2007;25(4):824-31.

196. Spottiswoode BS, Zhong X, Hess AT, Kramer CM, Meintjes EM, Mayosi BM, et al. Tracking myocardial motion from cine DENSE images using spatiotemporal

phase unwrapping and temporal fitting. IEEE Trans Med Imaging 2007;26(1):15-30.

197. Dasi LP, Pekkan K, Katajima HD, Yoganathan AP. Functional analysis of Fontan energy dissipation. J Biomech 2008;41(10):2246-52.

198. Nakata S, Imai Y, Takanashi Y, Kurosawa H, Tezuka K, Nakazawa M, et al. A new method for the quantitative standardization of cross-sectional areas of the pulmonary arteries in congenital heart diseases with decreased pulmonary blood flow. J Thorac Cardiovasc Surg 1984;88(4):610-9.

199. Rosenthal M, Bush A, Deanfield J, Redington A. Comparison of cardiopulmonary adaptation during exercise in children after the atriopulmonary and total cavopulmonary connection Fontan procedures. Circulation 1995;91(2):372-8.

200. Shachar GB, Fuhrman BP, Wang Y, Lucas RV, Jr., Lock JE. Rest and exercise hemodynamics after the Fontan procedure. Circulation 1982;65(6):1043-8.

201. Shekerdemian LS, Bush A, Shore DF, Lincoln C, Redington AN. Cardiopulmonary interactions after Fontan operations: augmentation of cardiac output using negative pressure ventilation. Circulation 1997;96(11):3934-42.

202. Triedman JK, Bridges ND, Mayer JE, Jr., Lock JE. Prevalence and risk factors for aortopulmonary collateral vessels after Fontan and bidirectional Glenn procedures. J Am Coll Cardiol 1993;22(1):207-15.

203. Salim MA, DiSessa TG, Arheart KL, Alpert BS. Contribution of superior vena caval flow to total cardiac output in children. A Doppler echocardiographic study. Circulation 1995;92(7):1860-5.

204. Bando K, Turrentine MW, Sun K, Sharp TG, Caldwell RL, Darragh RK, et al.

Surgical management of hypoplastic left heart syndrome. Ann Thorac Surg 1996;62(1):70-6; discussion 76-7.

205. Checchia PA, Larsen R, Sehra R, Daher N, Gundry SR, Razzouk AJ, et al. Effect of a selection and postoperative care protocol on survival of infants with hypoplastic left heart syndrome. Ann Thorac Surg 2004;77(2):477-83; discussion 483.

206. Forbess JM, Cook N, Roth SJ, Serraf A, Mayer JE, Jr., Jonas RA. Ten-year institutional experience with palliative surgery for hypoplastic left heart syndrome. Risk factors related to stage I mortality. Circulation 1995;92(9 Suppl):II262-6.

207. Forbess JM, Cook N, Serraf A, Burke RP, Mayer JE, Jr., Jonas RA. An institutional experience with second- and third-stage palliative procedures for hypoplastic left heart syndrome: the impact of the bidirectional cavopulmonary shunt. J Am Coll Cardiol 1997;29(3):665-70.

208. Gillum RF. Epidemiology of congenital heart disease in the United States. Am Heart J 1994;127(4 Pt 1):919-27.

209. Hoshino K, Ogawa K, Hishitani T, Kitazawa R, Uehara R. Hypoplastic left heart syndrome: duration of survival without surgical intervention. Am Heart J 1999;137(3):535-42.

210. Jenkins PC, Flanagan MF, Jenkins KJ, Sargent JD, Canter CE, Chinnock RE, et al. Survival analysis and risk factors for mortality in transplantation and staged surgery for hypoplastic left heart syndrome. J Am Coll Cardiol 2000;36(4):1178-85.

211. Kern JH, Hayes CJ, Michler RE, Gersony WM, Quaegebeur JM. Survival and risk factor analysis for the Norwood procedure for hypoplastic left heart syndrome. Am J Cardiol 1997;80(2):170-4.

212. Mahle WT, Spray TL, Wernovsky G, Gaynor JW, Clark BJ, 3rd. Survival after reconstructive surgery for hypoplastic left heart syndrome: A 15-year experience from a single institution. Circulation 2000;102(19 Suppl 3):III136-41.

213. Razzouk AJ, Chinnock RE, Gundry SR, Johnston JK, Larsen RL, Baum MF, et al. Transplantation as a primary treatment for hypoplastic left heart syndrome: intermediate-term results. Ann Thorac Surg 1996;62(1):1-7; discussion 8.

214. Reis PM, Punch MR, Bove EL, van de Ven CJ. Outcome of infants with hypoplastic left heart and Turner syndromes. Obstet Gynecol 1999;93(4):532-5.

215. Tweddell JS, Hoffman GM, Mussatto KA, Fedderly RT, Berger S, Jaquiss RD, et al. Improved survival of patients undergoing palliation of hypoplastic left heart syndrome: lessons learned from 115 consecutive patients. Circulation 2002;106(12 Suppl 1):I82-9.

216. Altmann K, Printz BF, Solowiejczky DE, Gersony WM, Quaegebeur J, Apfel HD. Two-dimensional echocardiographic assessment of right ventricular function as a predictor of outcome in hypoplastic left heart syndrome. Am J Cardiol 2000;86(9):964-8.

217. Korperich H, Gieseke J, Barth P, Hoogeveen R, Esdorn H, Peterschroder A, et al. Flow volume and shunt quantification in pediatric congenital heart disease by real-time magnetic resonance velocity mapping - A validation study. Circulation 2004;109(16):1987-1993.

218. de Leval MR, Kilner P, Gewillig M, Bull C. Total cavopulmonary connection. J Thorac Cardiovasc Surg 1989;97(4):636.

219. McCrindle BW, Williams RV, Mital S, Clark BJ, Russell JL, Klein G, et al. Physical activity levels in children and adolescents are reduced after the Fontan procedure, independent of exercise capacity, and are associated with lower perceived general health. Arch Dis Child 2007;92(6):509-14.

220. Soerensen DD, Pekkan K, de Zelicourt D, Sharma S, Kanter K, Fogel M, et al. Introduction of a new optimized total cavopulmonary connection. Ann Thorac Surg 2007;83(6):2182-90.

VITA

Kartik Sundareswaran was born on 25th July 1981 in the beautiful city of New Delhi, India. He spent the first 12 years of his life growing up in New Delhi, before his family decided to move to Dubai, United Arab Emirates. The Sundareswarans comprising of T.S. Sundareswaran, Seethalakshmy, Sowmya, and Kartik settled down in Dubai, where Kartik completed his high school education.

In 1999, Kartik began his higher education in Georgia Tech pursuing a Bachelor of Science degree in Computer Engineering and finished with Highest Honors in May 2003. During his undergraduate studies, Kartik had the opportunity to be enrolled in the Georgia Tech Coop program and worked for Dell Computers for 4 semesters before deciding to pursue his PhD in Biomedical Engineering. In August 2003, Kartik started his PhD under the guidance of Dr. Ajit Yoganathan. Through the course of his doctoral studies, Kartik received the American Heart Association's predoctoral fellowship award, and the Gandy/Diaz teaching fellowship awards. In the Fall of 2008, Kartik successfully defended his PhD thesis. He will be pursuing a career in medical devices by working for Thoratec Corporation.